ANL/FPP/TM-100

INL Technical Library
312868

PLEASE RETURN TO
MFC BRANCH LIBRARY

ANL PARAMETRIC SYSTEMS STUDIES

November 1977

RETURN TO REFERENCE FILE
TECHNICAL PUBLICATIONS
DEPARTMENT

FUSION POWER PROGRAM

Argonne National Laboratory
9700 South Cass Avenue
Argonne, Illinois 60439

The facilities of Argonne National Laboratory are owned by the United States Government. Under the terms of a contract (W-31-109-Eng-38) between the U. S. Department of Energy, Argonne Universities Association and The University of Chicago, the University employs the staff and operates the Laboratory in accordance with policies and programs formulated, approved and reviewed by the Association.

MEMBERS OF ARGONNE UNIVERSITIES ASSOCIATION

The University of Arizona
Carnegie-Mellon University
Case Western Reserve University
The University of Chicago
University of Cincinnati
Illinois Institute of Technology
University of Illinois
Indiana University
Iowa State University
The University of Iowa
Kansas State University
The University of Kansas
Loyola University
Marquette University
Michigan State University
The University of Michigan
University of Minnesota
University of Missouri
Northwestern University
University of Notre Dame
The Ohio State University
Ohio University
The Pennsylvania State University
Purdue University
Saint Louis University
Southern Illinois University
The University of Texas at Austin
Washington University
Wayne State University
The University of Wisconsin

NOTICE

This report was prepared as an account of work sponsored by the United States Government. Neither the United States nor the United States Department of Energy, nor any of their employees, nor any of their contractors, subcontractors, or their employees, makes any warranty, express or implied, or assumes any legal liability or responsibility for the accuracy, completeness or usefulness of any information, apparatus, product or process disclosed, or represents that its use would not infringe privately-owned rights. Mention of commercial products, their manufacturers, or their suppliers in this publication does not imply or connote approval or disapproval of the product by Argonne National Laboratory or the U. S. Department of Energy.

ANL Parametric Systems Studies*

Compiled by Mohamed Abdou

M. A. Abdou, Project Manager
Fusion Power Program
Argonne National Laboratory
Argonne, Illinois 60439

ANL/FPP Technical Memorandum Number 100

Results reported in the FPP series of memoranda frequently are preliminary and subject to revision. They should not be quoted nor referenced without the author's permission.

* Work supported by the U.S. Department of Energy.

FOREWORD

Parametric systems studies for fusion reactors are currently being carried out at Argonne National Laboratory (ANL). At present, the effort is focused mainly on tokamak power plants. This document is a collection of reports summarizing the work performed over the past year. These ANL/FPP reports cover the following areas:

ANL/FPP/TM-97, "Parametric Systems Analyses for Tokamak Power Plants," is a summary report for the global parametric systems studies and the detailed subsystems analysis. The conclusions of the work carried out to date are stated in this report.

ANL/FPP/TM-94, "Thermal Hydraulic Analyses of Two Fusion Reactor First Wall/Blanket Concepts," is a detailed subsystem analysis of the primary energy conversion system. This report also documents the thermal hydraulic analysis model in the ANL systems code.

ANL/FPP/TM-95, "A Systematic Survey of Tokamak Reactor Physics Design Parameters," presents the results of the plasma physics analysis. The plasma physics model and data base are also described.

ANL/FPP/TM-87, "Plasma Driving Systems Requirements for Commercial Tokamak Fusion Reactors," is a detailed analysis of the plasma driving system (ohmic heating and equilibrium field coils and their power supplies) for commercial tokamak reactors.

ANL/FPP/TM-92, "Radiation Considerations for Superconducting Fusion Magnets," is a comprehensive treatment of the shield subsystem. The shield/magnet interface is examined in detail and the shielding requirements are delineated.

ANL/FPP/TM-84, "Modeling of Life-Limiting Properties of Fusion Reactor Structural Materials," describes the modeling of life-limiting properties of stainless steel and vanadium alloys.

ANL/FPP/TM-88, "Computational Model for Superconducting Toroidal-Field Magnets for a Tokamak Reactor," describes a model for predicting the performance characteristics and cost of superconducting toroidal-field coils.

ANL/FPP/TM-83, "Tokamak Fusion Power Reactors," describes a plausible path along which tokamak power reactors could evolve towards a commercial reactor.

Work is being performed in several other technical areas. A report that describes all the subsystem models and the cost algorithms in the ANL tokamak system code will be issued in the future.

October 31, 1977 ANL/FPP/TM-97

PARAMETRIC SYSTEMS ANALYSES FOR TOKAMAK POWER PLANTS

M. A. Abdou,* J. N. Brooks, C. Dennis, D. A. Ehst,
K. Evans, Jr., R. Kustom, V. A. Maroni, R. Mattas,
J. Norem, B. Misra, D. L. Smith, W. M. Stacey, Jr.,†
H. C. Stevens, and L. R. Turner

ANL/FPP Technical Memorandum No. 97

---

*Study Manager.

†Present address: School of Nuclear Engineering, Georgia Institute of Technology, Atlanta, Georgia 30332.

TABLE OF CONTENTS

	Page
ABSTRACT	1
1. INTRODUCTION	2
2. GENERAL ECONOMICS CONSIDERATIONS	4
3. REACTOR THERMAL POWER RATING	6
4. DESIRABLE TOROIDAL-FIELD STRENGTH AND PLASMA β_t	7
5. ASPECT RATIO AND PLASMA ELONGATION	11
6. INNER BLANKET/SHIELD THICKNESS	14
7. NEUTRON WALL LOAD AND STRUCTURE LIFETIME	18
8. THERMAL HYDRAULIC ANALYSIS OF FIRST-WALL BLANKET	23
8.1 Development of the Computational Algorithms	24
8.2 RESULTS AND DISCUSSION	26
8.3 CONCLUSIONS OF THERMAL HYDRAULIC ANALYSIS	29
9. PLASMA SUBSYSTEM ANALYSIS AND DATA BASE	31
10. PLASMA DRIVING SYSTEM REQUIREMENTS	35
11. SUMMARY AND CONCLUSIONS	39
REFERENCES	44
TABLES	48
FIGURES	52
DISTRIBUTION LIST	81

PARAMETRIC SYSTEMS ANALYSES FOR TOKAMAK POWER PLANTS

M. A. Abdou, J. N. Brooks, C. Dennis, D. A. Ehst,
K. Evans, Jr., R. Kustom, V. A. Maroni, R. Mattas,
J. Norem, B. Misra, D. L. Smith, W. M. Stacey, Jr.,
H. C. Stevens, and L. R. Turner

Fusion Power Program
Argonne National Laboratory
Argonne, Illinois 60439

ABSTRACT

A parametric systems studies program is now in an active stage at Argonne National Laboratory (ANL). This paper presents a summary of the results from this systems analysis effort over the past year. The impact of major design parameters on the economics of tokamak power plants is examined. The major parameters considered are: (1) the plant power rating; (2) toroidal-field strength; (3) plasma β_t; (4) aspect ratio; (5) plasma elongation; (6) inner blanket/shield thickness; and (7) neutron wall load. The performance characteristics and economics of tokamak power plants are compared for two structural materials (stainless steel and a vanadium alloy) and two coolants (lithium and helium). The plasma driving systems requirements are analyzed.

1. INTRODUCTION

Numerous conceptual designs for tokamak power reactors [1-15] have been developed and investigated in the past several years. These design studies have elucidated many of the important features of tokamaks and have identified many technological problems that require a vigorous research and development program. These designs taken collectively demonstrate the presence of a huge space of design parameters and a diversity of design concepts. The required technological developments depend greatly on the features of the perceived commercial tokamak. Therefore, a resource-limited research and development program inevitably has to select and focus on a very limited number of paths to the commercialization of fusion power. An exceedingly important concern with this inevitable approach is the decision-making process to identify a low-risk high payoff path. One great difficulty is that much of the technical information required for scientifically evaluating the various paths is often not available. This situation is not unique to fusion research but is common to the development of most new energy sources, and is actually faced in many facets of life. There is no unique scientific formula for dealing with this situation; there are only guidelines.

Global parametric systems studies represent a useful framework for providing critical information to help guide the research and development and selection of the most fruitful path to commercialization of fusion power. In these studies, all the performance characteristics and the complex interrelations among and within the power plant components are modeled into a computer program. Trade-off studies are performed and design variables, options, and concepts are compared in a systems context. The economics, safety, and cost of required technological developments provide the primary basis for comparison. The systems approach is general and can be utilized for comparative

evaluation of different plasma confinement schemes as well as comparing the different design concepts within a given confinement approach.

A parametric systems studies program is now in an active stage at Argonne National Laboratory (ANL). Up to the present, the studies have focused only on commercial power-producing tokamaks. The studies are divided into three areas: (1) detailed subsystems analyses; (2) system code development; and (3) global reactor systems parametric analysis. The detailed subsystems analysis is concerned with the development of information necessary to describe the performance of each reactor component under a variety of design and operating conditions. Trade-off studies are performed for each subsystem to eliminate those design options that are technically not feasible, to identify the more promising ones, and to point out the critical issues that should be addressed in the area of global parametric analysis. An important product of the detailed subsystems analysis is a mathematical model to describe the performance of each component in the reactor power plant. In the area of the system code development, these models are synthesized into a computer systems code that is capable of predicting the performance characteristics and economics of the entire power plant. An important feature of the code is that "scaling" from existing conceptual designs is avoided. Rather, design algorithms are built into the code to ensure the relative validity of the results in the huge parameter space of tokamaks. A modular approach is utilized in developing the code to permit upgrading of existing models and the incorporation of new ones. The global systems parametric analysis phase employs the integrated systems code together with the results from the detailed subsystems analysis to investigate, in a truly systems context, the critical issues concerning tokamak reactor development. Trade-off studies are performed to determine the most promising design options and the best range of design parameters for economical and safe

operation of the entire reactor system. Another useful product of the study is the identification of attractive new design points and technological options to guide the design studies. In addition, the payoff, in terms of fusion power economics, of different technology development can be quantified.

The purpose of this paper is to present a summary of some of the results from the parametric systems analysis effort at ANL. Section 2 is intended as a background for the economics analysis. Sections 3 through 7 deal with the impact of major design parameters on the economics of tokamak power plants. The major parameters considered are: (1) the plant power rating; (2) toroidal-field strength; (3) plasma β_t; (4) aspect ratio; (5) plasma elongation; (6) inner blanket/shield thickness; and (7) neutron wall load. Sections 8 through 10 are devoted to results from detailed systems analyses of the first-wall/blanket, plasma, and plasma-driving systems and they serve to provide some of the information bases utilized in Sections 3 through 7. Section 11 is a summary of the conclusions.

Space limitations constrain the amount of detail in this paper. The interested reader should consult Refs. 16-26 for additional details.

2. GENERAL ECONOMICS CONSIDERATIONS

Two important figures of merit characterize the economics of a power producing plant. One of these is the cost per unit power, $/KWe, which is the ratio of the total plant capital cost to the design value of the plant electrical power output. A more important figure of merit is the cost of producing usable energy. In this work, electrical energy is considered as the only form of usable energy from a tokamak reactor plant. The unit energy production cost is calculated from annual costs by

$$\text{Unit Energy Cost} = 114.2\ C_a/P_eF \quad \text{mills/kWh},$$

where

C_a = the annual cost, millions of dollars

P_e = the net electric power of the plant in MW

F = the plant capacity factor.

The capital cost, C_T, is the cost of building the tokamak power plant and placing it in commercial operation. It consists of direct plus indirect costs [27]. The direct cost covers the costs associated on an item-by-item basis with all the components that comprise a power plant. The indirect cost covers primarily expenses for services which apply to all or many portions of the physical plant, such as construction facilities, engineering and design, contingency, and interest during construction. Our cost estimates indicate that the indirect cost is roughly 50% of the direct cost.

The annual cost, C_a, consists of four general types of cost: (a) the return on capital; (b) the fuel cost; (c) the operation and maintenance cost; and (d) the component rebuilding cost. The annual return on capital is computed as 15% of the total capital cost, C_T. The fuel cost for tritium is assumed to be zero but the small cost of deuterium is included. The operation and maintenance cost (O&M) covers regular expenditures for salaries, consumable supplies, etc. The component rebuilding cost covers the cost of planned component replacement, primarily the first wall and the blanket structure. This replacement cost is the initial cost of materials plus fabrication plus labor. The annual cost of component rebuilding is computed as a prorated share of the total replacement cost. For a typical tokamak power plant, the return on capital represents approximately 90 to 95% of the cost of energy. The fuel cost is very small, <0.1% of the cost of energy. The operation and maintenance cost

varies typically from approximately 0.5% to 1.5%. The cost of first-wall and blanket structure replacement varies widely from approximately 1 to 10% of the cost of energy depending on the type of structural material and its lifetime as well as the reactor operating conditions.

The plant capacity factor calculations allow for 28 days miscellaneous outage time per year and a prorated share of the total downtime, t_d, for first-wall and blanket rebuilding. The net electrical power is obtained from the gross electrical power by subtracting all the recirculating power losses.

3. REACTOR THERMAL POWER RATING

The optimum values of many of the tokamak design variables depend to a great extent on the selected reactor thermal power. The desirable power rating of a power plant depends on several factors that include the relationship between the cost of electricity and the plant power rating as well as the generating capacity and the operating conditions of the utilities.

Figure 1 shows the dependence of the cost of electricity on the reactor thermal power for the design conditions specified in the figure caption. Results are shown for both cases of stainless steel and advanced vanadium alloys as the construction material for the first-wall and blanket structure. The results in Fig. 1 demonstrate the "economy of scale" for tokamak power plants with thermal power in the range of 3000 to 9000 MWt, i.e., the cost of electricity is lower for larger power plants. Therefore, there is an economics incentive to build tokamak power plants with larger capacity. Since tokamak plants represent a large capital investment and a small operating cost, they are particularly suited for a "base load" operation. The demand on the reliability is more stringent, however, for larger power base-load power plants. An important factor to the reliability of tokamaks is the

structural integrity of the first-wall and energy-conversion system. The radiation environment is more severe for larger power plants as they produce higher neutron wall loads (see Fig. 1). These aspects and the comparison of stainless steel with advanced alloys will be discussed in a later section.

Despite the strong incentives of the economy of scale, the largest desirable power will be limited by many of the financial and operating considerations of the electric utilities. These considerations vary from one country to another and they differ among utilities. In the United States, nuclear power plants with capacities in the range of 1000 to 1500 MWe, i.e. 3000 to 4500 MWt, are presently under construction. Assuming only 3% growth per year in the electric generating capacity of the United States, one would expect that power plants with capacities in the range 7000 to 10,000 MWt will be in demand by some of the larger utilities by the year 2020. Most of the utilities, however, are still likely to prefer smaller power plants of approximately 3000 MWt.

4. DESIRABLE TOROIDAL-FIELD STRENGTH AND PLASMA β_t

Knowledge of the highest desirable toroidal-field (TF) strength is important because of the technology developments required for high fields. Niobium-titanium superconductors are ductile and can be designed for a high strain but the maximum practical magnetic field with niobium-titanium is limited to only ~9 T. Higher fields can be produced by Nb_3Sn but its brittleness casts some doubt on its viability in large superconducting magnets. Many of the technological developments required for high-field Nb_3Sn magnets are more difficult than those for niobium-titanium. Therefore, it is essential to quantify the economic benefits, if any, associated with Nb_3Sn. We have examined this question in some detail and a summary of the results is presented below.

Consider the class of reactors with thermal power, P_{th} = 3000 MWt; aspect ratio, A = 3; plasma D-shape height-to-width ratio, κ = 1.65; a scrape-off region thickness, Δ_v = 0.2 m; and a blanket/shield thickness, Δ^i_{BS} = 1 m. Three major parameters remain to be determined to fully describe the basic features of a reactor. These are the major radius, R, the maximum toroidal-field strength, B_m, and the average plasma toroidal beta, β_t. Since the MHD stability limits on β_t have not been established yet, a plausible range of β_t is considered. The relationships among the three parameters are discussed in Section 9. The size (major radius) of the reactor decreases as B_m and/or β_t are increased since the power density in the plasma increases as $B_m^4\beta_t^2$ (for a fixed R, A, and Δ^i_{BS}). This underlines the often-mentioned motive for a high field capability; smaller-size reactors are generally less expensive. Figure 2 shows the cost of energy production in mills/kWh as a function of B_m and β_t for the class of reactors specified above. In these calculations, NbTi with a maximum strain of 0.2% is used for $B_m \leq 9$ T and Nb_3Sn, with a maximum strain of 0.1%, is employed at higher fields.

The results in Fig. 2 show that, in the range $0.06 \leq \beta_t \leq 0.14$ and $6\ T < B_m < 9\ T$, larger β_t and higher toroidal-field reactors produce electricity at a cheaper cost. For $B_m \geq 10$ T, the cost of electricity increases substantially at higher fields and the benefits of high β_t are poorly utilized and turned into disadvantages. The reasons for this large increase in cost at high fields and high β_t are explained below.

The type of reactor examined in this study is based on the conventional design concept of locating the solenoid ohmic-heating (OH) coil outside the bores of the TF coils and inside the central core formed by the inner legs of these TF coils. Increasing the toroidal-field strength decreases the OH flux core area in two ways: (1) the major radius decreases; and (2) the thickness

of the TF coils increases. Although the volt-second requirements to achieve a particular burn cycle decrease with a smaller major radius, the reduction in the OH flux core area is so large that the OH field increases very rapidly at higher toroidal field. In the calculations presented here, the OH field is permitted to exceed the technological limits on pulsed magnets and the cost algorithms are assumed to be extrapolatable to these very high OH fields. Figure 3 shows the total capital cost for all cases corresponding to those in Fig. 2. The direct capital cost is roughly two-thirds of the total capital cost. The capital cost of the poloidal (ohmic-heating and equilibrium) coils and associated power supply is shown in Fig. 4. For the low toroidal-field ($B_m < 9$ T) cases the power supply cost is approximately 15% of the direct capital cost of the plant. For higher toroidal fields, i.e. $B_m > 9$ T, the power-supply cost increases very rapidly until it represents approximately 60 to 70% of the direct capital cost at $B_m \sim 14$ T.

From the above discussion it is clear that the difficulty with high toroidal fields is the smallness of the available OH central flux core area. Situations that might alleviate this problem can be considered. Figure 5 is similar to Fig. 2 except a larger aspect ratio, A = 4, and a lower degree of noncircularity, $\kappa = 1.3$, are considered. An additional case of low β_t ($\beta_t = 0.04$) is also included. The same trends observed earlier are once again evident in Fig. 5. For $\beta_t \geq 0.06$, the minimum cost is achievable with NbTi at 9 T. However, the rate of cost increase at higher fields is less for the larger aspect ratio lower κ cases. An important result in Fig. 5 is that for $\beta_t = 0.04$, the cost of energy continues to decrease beyond $B_m = 9$ T and has a minimum at $B_m \sim 12$ T. However, this minimum is only <1 mill/kWh lower than the cost of energy at $B_m = 9$ T. This is a marginal difference, well within design and cost uncertainties, and cannot alone justify costly and high-risk new technology development.

In the above discussions, reactors with 3000-MW thermal power were considered. Figure 6 shows the cost of energy as a function of β_t and the toroidal-field strength for larger power reactors, P_{th} = 7000 MW, with A = 4, κ = 1.3, and the other parameters are the same as those used above. Other parameters being fixed, a larger power reactor has larger major radius and central flux core area. For these larger power reactors, the minimum cost is obtainable with a toroidal-field of 9 T for $\beta_t \geq 0.08$. For reactors with $\beta_t = 0.06$, the cost of energy is slightly smaller at B_m = 12 T than that at 9 T. The cost of energy for reactors with $\beta_t \leq 0.04$ has a markedly different behavior. In general, it decreases gradually as the toroidal-field is increased up to ∿13 T. The largest reduction in cost is accomplished by increasing B_m from 6 to 9T. The lowest cost of energy, which occurs at 13 T, is ∿7% lower than that at 9 T. We also examined the 7000 MWt class of reactors at higher plasma elongation and lower aspect ratios. For reactors with κ = 1.65 and A = 3, the minimum cost occurs at 9 T for $\beta_t \geq 0.06$. For the lower β_t cases ($\beta_t = 0.04$) the cost at 12 T is insignificantly smaller than that at 9 T.

An outstanding conclusion from these results is the great dependence of cost on β_t. Reactors designed properly can always benefit from higher β_t equilibria — if achievable — by reducing the reactor size and/or by operating at a lower toroidal field. Higher β_t equilibria are likewise more tolerable to the levels of impurity buildup. However, the economic benefits of increasing β_t are smaller at high β_t. A β_t of ∿0.08 seems to achieve most of the economic potential of tokamaks.

Our analyses, a part of which has been presented above, show no economics incentive for developing magnets that can operate at fields higher than 9 T if plasma stability can be assured for $\beta_t \geq 0.06$. If the stability limit on β_t

is 0.04 or lower, then tokamaks will be considerably more expensive. In this case, it might be worthwhile to develop high-field (~12 T) magnets if the economic competitiveness with other energy sources dictate that. However, two points have to be carefully considered then:

(1) There will be very strong motives to develop other design concepts for the OH system. One such concept has been suggested [11] although its technical feasibility has not been established yet. Concurrently with this, new design concepts that permit smaller toroidal-field magnet thickness become more important.

(2) Tokamak power plants with the conventional central OH solenoid will have to be designed at large power levels ($P_{th} \gtrsim 5000$ MWt), large aspect ratios ($A \gtrsim 4$), and small elongation ($\kappa \lesssim 1.3$) to realize significant economic advantages from high toroidal fields. As discussed in the next section, there are indications that β_t will decrease significantly as the aspect ratio increases. It is unfortunate that the high-field approach dictated by low β_t has to employ a large aspect ratio and does not make a good utilization of β_t.

5. ASPECT RATIO AND PLASMA ELONGATION

It has often been stated that tokamaks are better designed at lower aspect ratios because the β_t stability limit may be higher. A similar reason has been argued for greater plasma elongation, i.e. higher κ. In addition, elongating the plasma permits a larger volume of the plasma to be positioned in the high magnetic field region. On the other hand, tokamaks with lower aspect ratio have more difficult engineering-related problems concerning accessibility, assembly, and disassembly. Highly shaped plasmas may require locating the equilibrium-field (EF) coils inside the blanket which creates the problems of maintenability and replacement in a geometrically difficult

configuration and radioactive environment. All these questions are difficult to resolve at present because the quantitative dependence of β_t on κ and A is not known, and quantifying the economics of the engineering problems require considerable design details that vary from one design concept to another. In this section, we examine the possibility of the presence of economic effects for A and κ other than the β_t dependence and the engineering-related problems. In addition, we examine the sensitivity of the cost of energy to several possible scenarios for the variation of β_t with A and κ.

Figure 7 shows the cost of energy as a function of the aspect ratio for three assumed cases of the β_t dependence on A: (1) β_t is fixed and independent of A; (2) $\beta_t \sim C_1/A^2$ with C_1 in the range of 0.5 to 1.0; and (3) $\beta_t \sim C_2/A$ with C_2 varying from 0.2 to 0.3. In all cases in Fig. 7 we fix P_{th} = 3000 MWt, B_m = 9 T, κ = 1.3, and Δ^i_{BS} = 1 m. Several interesting results are noted from Fig. 7.

For a fixed value of β_t, in the range β_t = 0.04 to 0.1, the cost of energy decreases by approximately 10% as the aspect ratio is increased from 2.5 to 4. This trend of lower cost of energy at larger A was observed for other values of κ (1-2) and reactor power (3000-10,000 MWt). There are two reasons for this:

(a) Increasing the aspect ratio increases the magnetic field in the plasma region. The increase in the power density at larger A makes it possible to reduce the plasma volume and the first-wall area. This results in a reduction in the costs of the first-wall, blanket, shield, and toroidal-field coils.

(b) The cost of the poloidal coils and their power supply decreases significantly as A increases due to several factors. The central OH flux core area increases as A increases. The reduction in the plasma cross section area at larger A results in a significant decrease in the plasma current as discussed in Section 9. Furthermore, the equilibrium field also decreases as A increases.

Figure 7 shows that if the β_t stability limit depends strongly on A such that $\beta_t \sim C/A^2$ then the cost of energy increases at larger A. The rate of increase is less significant at larger β_t-values (i.e. larger C) and low-aspect ratio. For moderately high β_t ($\gtrsim$8% at A = 2.5), the increase in the cost of energy resulting from increasing A from 2.5 to 3 is so small that it will almost certainly be compensated for by the ease of assembly/disassembly and maintenance.

If the dependence of the β_t-stability limit on A is moderate, i.e. $\beta_t \sim C/A$, the results of Fig. 7 show that the cost of energy actually decreases as A increases for $A \gtrsim 3.5$. Taking the engineering-related problems into consideration, it appears that $A \sim 3.5$ is a favorable design point if $\beta_t \sim C/A$.

Figure 8 shows the cost of energy as a function of the plasma height-to-width ratio, κ. Results are shown for three scenarios of the β_t-stability limit on κ: (1) β_t is fixed and independent of κ; (2) $\beta_t \sim CS^2$ where S is the shape factor (the ratio of the plasma perimeter to the circumference of an inscribed circle); and (3) $\beta_t \sim CS$. We have chosen the D-triangularity parameter, d, to vary with κ as follows: d = 0.0 at κ = 1.0, d = 0.25 at k = 1.3, d = 0.5 at k = 1.65, and d = 0.75 at κ = 2. Thus, the shape factor, S, is equal to 1, 1.16, 1.36, and 1.56 at κ = 1, 1.3, 1.65, and 2, respectively. All results in Fig. 8 are for P_{th} = 3000 MW, A = 3, B_m = 9 T, and Δ^i_{BS} = 1 m.

A clear observation from Fig. 8 is that for a fixed β_t, the variation of the cost of energy with κ is very small with a broad minimum in the range of κ = 1.3-1.6. This weak dependence of the cost of energy on κ when β_t is fixed was also found for reactors with larger power and aspect ratio. There are several counteracting effects with increasing κ. The plasma major radius and width decrease resulting in reduction in the costs of the TF coils, the reactor containment building, and the piping for the heat transport system. On the other hand, the height of the plasma increases and the costs of the first-

wall, blanket, and shield increase. Very strong effects come from large increases in the plasma current and the equilibrium-field at higher κ as will be discussed in Section 9. Although the reduction in the area of central OH flux core is moderate, the rapid increase in the volt-second requirements result in a significant increase in the OH field. The cost of the power supply for the OH and EF coils increases significantly with κ.

If the β_t-stability limit is strongly dependent on the shape factor, i.e. $\beta_t \sim CS^2$, the results in Fig. 8 show a significant economics benefit from increasing κ. The savings from the reduction in the size of the reactor at larger κ significantly exceed the increase in the power supply cost. If the β_t stability limit depends only moderately on κ, i.e. $\beta_t \sim CS$, the cost of energy also decreases as κ is increased from 1 to 1.3 but at a much slower rate than in the previous case of $\beta_t \sim CS^2$. The cost of energy exhibits little variation as κ is increased from 1.3 to 1.65 for the case of linear dependence of β_t on κ.

6. INNER BLANKET/SHIELD THICKNESS

One of the strongest interactions between the blanket/shield subsystem and the entire tokamak reactor system concerns the attenuation requirements and the thickness, Δ^i_{BS}, of the blanket and primary shield on the inner side of the torus. There are conflicting requirements on the value of Δ^i_{BS}. Satisfying the energy conversion and tritium breeding requirements in the blanket and providing the radiation attenuation in the blanket/shield necessary for magnet protection favors a relatively large Δ^i_{BS}. On the other hand, there are strong incentives to conserve on the space on the inner side of the torus. These incentives can be viewed in three different ways:

(1) If the maximum toroidal field, B_m, is assumed to be fixed by technological constraints the reactor thermal power, P_{th}, varies with Δ^i_{BS} as

$$P_{th} \sim B_0^4 \sim \left[1 - \frac{r_w + \Delta^i_{BS}}{R}\right]^4 B_m^4 , \tag{1}$$

where B_0 is the toroidal field at the plasma center and r_w is the first-wall radius (or width). Therefore, a very significant increase in P_{th} is obtainable by reducing Δ^i_{BS}. Plasma confinement may also improve with B_0.

(2) For the same R, r_w, B_0, and P_{th} reducing Δ^i_{BS} reduces B_m and Δ_m, and increases r_v, where Δ_m is the thickness of the TF coil and its support structure and r_v is the OH central flux core radius. The result is a significant reduction in the TF coil cost, which increases as $\sim B_m^2$, and a reduction in the ohmic heating field, B_{OH}. Besides the technological constraints on B_{OH}, the cost of the OH coils, and more importantly the cost of the power supply decreases substantially as B_{OH} is reduced.

(3) For the same P_{th} and B_m reducing Δ^i_{BS} makes it possible to reduce the reactor size.

It is clear, therefore, that tokamak reactor designs must be based on prudent utilization of the space on the inner side of the torus. This can be accomplished by proper design concepts and economic optimization of the entire reactor system that accounts for all the important interrelations such as those of the shield and magnet interface.

The requirement of tritium breeding in the blanket necessitates the use of a lithium-containing material in the blanket. Employing natural lithium causes approximately 20% increase in Δ^i_{BS} compared with an all stainless-steel blanket. Two solutions are possible:

(1) The volume of the inner portion of the blanket is only approximately 10% of the total volume. Calculations with present data indicate that it is feasible to achieve a breeding ratio greater than 1.0 without employing any lithium in the inner portion of the blanket.

(2) If the previous solution does not prove feasible, then only a thin (∿2-5 cm) layer of lithium highly enriched in ^{6}Li can be employed in the inner blanket. High-breeding ratios are then attainable with a minor or no increase in Δ^i_{BS}.

The primary shielding functions of the blanket/shield subsystem are:

(1) To reduce the nuclear heating in the TF coils to the levels allowed by (a) total power required to run the refirgerators; and (b) maximum local heating rates imposed by practical limits for coil design.

(2) To attenuate the nuclear radiation to the levels allowed by tolerable radiation damage to the components of the superconducting magnet. These components are (a) the superconductor; (b) the normal (stabilizing) conductor; (c) electrical and thermal insulators; and (d) structure.

The refrigeration power requirements and radiation damage to the components of the magnet can be translated into economics terms. For example, the reduction in the critical current density of the superconductor when the radiation level increases must be compensated by adding more superconductor and the effect is reflected in a higher magnet cost. All these factors are built into the ANL tokamak systems program.

An extensive study of the tradeoffs in the magnet/shield design has been carried out using the System Program. An example of the results is shown in Fig. 9. This figure shows the cost of energy as a function of the inner blanket/shield thickness for tokamaks with aspect ratio of 3, and neutron wall loading of 3 MW/m^2. The blanket/shield material composition is an effective

mixture of stainless steel and boron carbide with 15% of the thickness provided for vacuum, engineering, and maintenance space. Results are shown for tokamaks with major radius R = 6, 7, 8, and 9 m. Annealing of the superconducting toroidal-field magnets was assumed to coincide with the first-wall replacement which occurs every 11.4 yr and requires downtime of 80 days. Niobium-titanium was employed for fields ≤ 9 T and Nb_3Sn was used for higher fields. The plant capacity factor, F, is 0.9. The results in Fig. 9 show that the minimum energy cost is obtainable with $\Delta^i_{BS} \sim 1$ m. Increasing Δ^i_{BS} beyond the optimum value increases the cost of energy due to the larger capital cost when B_m and B_{OH} increase. The relative increase in the cost of energy is more significant at smaller major radius, R. This can be readily explained by recalling that the ratio B_m/B_0 increases as the ratio Δ^i_{BS}/R increases. In other words, the gradient of the TF field is steeper and the space on the inner side of the torus is more valuable for smaller-size machines. On the other hand, decreasing Δ^i_{BS} below the optimum value results in a dramatic increase in the cost of energy that is not overly sensitive to R. This increase in the cost of energy results from an increase in the refrigeration power requirements and an increase in the capital cost of the magnet to accommodate the increased radiation level at the magnet. The radiation level at the magnet is not sensitive to R when the neutron wall load is fixed.

In carrying out the parametric study discussed above, we purposely assumed that all insulators will perform satisfactorily for the lifetime of the plant in all cases. However, Table I shows the actual dose in the TF magnet insulators as a function of Δ^i_{BS} at the end of plant life of 30 yr. For the optimum shield, $\Delta^i_{BS} \sim 1$ m, the maximum dose in the insulator is 1.8×10^{10} rad. Therefore, TF insulators that can function properly up to that dose level are required in order to operate tokamaks in economically optimum conditions.

Radiation damage data on organic insulators at ∿4°K are lacking. Extrapolation of irradiation data at higher temperatures show that mylar can be operated up to a dose of $\sim 10^8$ rad and that epoxy-base insulators can withstand higher doses of $\sim 10^9$-5×10^9 rad. Table I shows that such limits would dictate the use of a thicker shield and result in higher costs of energy than what is achievable otherwise. Therefore, accurate low-temperature irradiation data for organic insulators is necessary. These results may prove the need for development of more radiation-resistant insulators or new concepts for magnet design that can permit the utilization of inorganic insulators.

7. NEUTRON WALL LOAD AND STRUCTURE LIFETIME

A major problem relating to the successful operation of tokamak power plants is the satisfactory performance of the first-wall and blanket structure. The neutron wall load is an important measure of the severity of the operational environment for the first-wall and blanket. The useful lifetime of the structural material, on the other hand, is an important indication of the performance of the first-wall and blanket. In this section, the tradeoffs concerned with the neutron wall loading and the structure lifetime are examined. The results provide a useful input to determining the desirable goals for structural alloy development.

The neutron wall loading, P_w, is strongly related to the reactor thermal power, P_{th}, the surface area of the first wall, A_w, the plasma power density, P_p, and the plasma volume. The motive for a higher P_w capability is that it makes it possible to design higher power density, smaller size, and potentially more economical reactors. However, there are upper limits, on the highest wall load that can be realized, arising from: (a) physics constraints on the power

density achievable in the plasma; and (b) limitations unique to tokamaks on the smallness of the reactor size. There are also limits on the usability of high P_w dictated by the structure cooling capability and its lifetime in a harsh radiation environment.

An extensive parameter survey was made to determine the range of wall loads producible in tokamaks. A sample of the results is given in Fig. 10 which shows P_w as a function of the maximum toroidal field, B_m, for a reactor with P_{th} = 3000 MWt. The results are shown at four values of plasma average β_t: 0.04, 0.06, 0.08, and 0.1 for an aspect ratio of 4 and D-shaped plasma elongation, κ, of 1.3. P_w varies from 1 to 9 MW/m^2 in the range $6 < B_m < 13$ T and $0.04 < \beta_t < 0.1$. Systems studies results discussed in an earlier section indicate that the optimum magnetic field is $\sim$9 T. At B_m = 9 T, P_w varies from $\sim$3 MW/m^2 at β_t = 0.06 to $P_w \sim 5$ MW/m^2 at β_t = 0.1. For a larger power reactor with P_{th} = 7000 MWt, P_w at B_m = 9 T varies from $\sim$5 MW/m^2 at β_t = 0.06 to $\sim$8 MW/m^2 at β_t = 0.1. The producible P_w is sensitive to the aspect ratio, A. For B_m = 9 T, β_t = 0.08, and κ = 1.3 increasing A from 3 to 4 increases P_w from $\sim$3 MW/m^2 to $\sim$4 MW/m^2 for P_{th} = 3000 MWt. The wall load decreases slightly as the plasma elongation, κ, is increased from 1 to 1.65. P_w is particularly sensitive to β_t and P_{th}. The uncertainties in the plasma stability limit on β_t and in the projected optimum plant power rating at the time fusion is commercialized complicates the task of determining a target wall load for structural alloy development.

One technological constraint on the usability of a high wall load is the ability to cool the first-wall. This technological constraint varies with the properties of the structural material and the type of coolant. This question is examined in the next section which shows that a lithium-cooled vanadium alloy can be operated in the presence of a divertor up to $P_w \sim 8$ MW/m^2 with

B_m = 9 T. Lower wall-load limits are derived for higher fields, no divertor, helium cooling, and/or stainless-steel structure. Provided that this cooling constraint is met, the neutron wall load affects the economics of the power plant in two ways. A higher wall load results in a lower exit temperature, a lower thermodynamic efficiency and a smaller electric power output. Furthermore, for a given fluence lifetime (MW-yr/m^2) of the structural material, a higher wall load results in a shorter calendar lifetime (years) of the structural material, a lower plant capacity factor, and a higher cost of structure replacement. All these effects are accounted for in the ANL Tokamak Systems Program which was utilized to derive the results given below.

One substantial difficulty with determining an optimum neutron wall load is the strong economic dependence on many major design parameters and options for tokamaks. For the purpose of this work, we choose a common set of parameters that generally result in favorable economic conditions. These are: B_m = 9 T, κ = 1.65, A = 3, and Δ^i_{BS} = 1 m. The reactor thermal power and the plasma β_t are left as variables because of the large uncertainties in determining desirable and feasible values for them as well as their large effect on the wall load. Lithium cooling and two structural materials are considered.

Figure 11 shows the cost of energy, mills/kWh, as a function of the neutron wall load obtainable at various values of β_t and P_{th}. The lines of constant β_t and those of constant P_{th} are shown in Fig. 11. The results are for a structural material with properties and cost similar to those of an advanced vanadium alloy with a relatively long lifetime of $\sim$34 MW-yr/m^2 and a maximum operating temperature of 650°C. The total downtime, t_d, for replacement of the first wall and blanket structure is assumed to be 80 days. The results show a significant economic benefit for operating at a higher neutron wall load. Figure 11 also shows that the lines of constant β_t are much steeper than those of constant P_{th}.

In other words, a more substantial cost saving is achieved at higher wall loads obtainable by increasing the reactor thermal power from 3000 to 9000 MW than by increasing β_t from 0.06 to 0.14. This difference in the cost saving is attributable to the economy of scale discussed earlier in this paper.

Figure 12 is similar to Fig. 11, except that the vanadium structure is replaced with stainless steel operating at a maximum temperature of 500°C with a predicted lifetime of 3.1 MW-yr/m^2. Figure 12 shows that under these conditions the cost of energy for any given reactor thermal power increases as the neutron wall is increased to values greater than $\sim$2 MW/m^2.

Therefore, structural materials with stainless steel-like properties impose a limitation on the neutron wall load and do not permit a full utilization of the economics potential of tokamaks. In contrast, structural materials with vanadium-like properties permit operation at higher wall loads at a significantly lower cost of energy. The economics benefits of advanced structural alloys compared with stainless steel are obvious in Fig. 1. With the assumption that the material plus fabrication cost is 30 \$/kg for stainless steel and 440 \$/kg for vanadium alloys, the capital cost of the power plant is higher with the advanced alloys. However, our trade-off studies indicate that the optimum operating temperature is 650°C for vanadium structure compared with only 500°C for stainless steel. Therefore, for the same reactor thermal power, the net electrical power output is significantly larger with the advanced alloys. The net effect is that the cost per unit power is roughly the same for power plants employing advanced alloys or stainless steel. The large saving, $\sim$20%, in the cost of energy obtainable with vanadium alloys is due mostly to the much longer lifetime compared with that of stainless steel.

Figure 13 shows the cost of energy as a function of the structure lifetime (MW-yr/m^2) at several values of the reactor power and a fixed β_t of 0.08. A reference set of parameters (B_m = 9 T, κ = 1.65, A = 3, and Δ^i_{BS} = 1 m, t_d =

160 d) is fixed as above and a structural material with properties and cost similar to vanadium alloys is employed. The neutron wall load at each reactor power is shown in the figure. These results show that the cost of energy will always decrease as the lifetime of the structure is increased. At any given reactor power and wall load, a large reduction (∿20-30%) in the cost of energy is achieved by increasing the lifetime from 5 to 12 MW-yr/m^2. The reduction in the cost of energy obtainable by further increase in the structure lifetime is smaller but is still significant.

Based on the results of this study, goals for structural alloy development can be recommended regarding the wall load capability, calendar lifetime (years), and fluence lifetime (MW-yr/m^2). The goals are classified into two categories: (a) very important (Priority 1); and (b) important (Priority 2). Achieving the goals in Priority 1 category ensures that the structural materials do not pose serious limitations on the economic competitiveness of tokamak power plants. The Priority 1 goals are 3 MW/m^2, 4 yr, and 12 MW-yr/m^2. Accomplishing the goals in the Priority 2 category will provide an important step in a comprehensive research and development program to improve the utilization of the tokamak potential as a relatively inexpensive energy source. The Priority 2 goals are 5 MW/m^2, 6 yr, and 30 MW-yr/m^2. These results are based on our present understanding of tokamaks. Future results, experience, and the burden of economic competitiveness may require appreciable modification of these goals. For example, material resources limitations, long-term radioactive inventory problems, and benefits of simpler designs obtainable with relaxation of requirements on frequency of shutdown and length of downtime may demonstrate a more pressing need for longer structure lifetime. In this regard we reached two conclusions that supplement the above goals:

(1) Remote maintenance for the first wall and blanket is necessary for all

structural materials of practical interest. Therefore, the only requirement on structure activation is a low long-term radioactivity so that the structural material can be recycled after a reasonable cooldown period (∿30-100 yr). This requirement satisfies two objectives: (a) a substantial reduction in the material resources required for an all fusion power economy. This is a most desirable objective to be consistent with the major advantage of fusion as an energy source with "inexhaustible" fuel ; (b) reduced storage and sociopolitical costs associated with very long-term radioactivity. It is of interest to note that vanadium-titanium alloys have the greatest potential of satisfying this requirement as they can be recycled in ∿40-70 yr.

(2) The above goals for lifetime assume that the total downtime, t_d, for replacement of the first wall and blanket structure is in the range of 80 to 160 days. Longer t_d will require longer lifetime. In order to limit the increase in the cost of energy due to downtime for replacement of the first wall and blanket rebuilding to less than 10%, the following condition must be met

$$t_d(\text{days}) < 30 \cdot t_w(\text{years})$$

where t_w is the structure lifetime.

8. THERMAL HYDRAULIC ANALYSIS OF FIRST-WALL/BLANKET

As a first step in providing a basis for parametric investigations of energy conversion systems for commercial reactors, analyses of first-wall/blanket thermal-hydraulic response were performed with the life-limiting properties of the structural materials as the primary constraints. The thermal hydraulic calculations are based on a set of reference design parameters: major radius of 8 m, first-wall minor radius of 3.4 m, and thicknesses of the blanket, shield, and TF coils are 0.6 m, 0.9 m, and 0.52 m, respectively.

Two generally similar first-wall/blanket concepts have been evaluated. One involves the use of flowing lithium as a heat transfer and breeding medium in a modular blanket cell of the type shown in Fig. 14. The other uses pressurized helium as the heat transfer fluid flowing (in channels) through a "sea" of stagnant liquid lithium as illustrated in Fig. 15. Solution-annealed, Type 316 stainless steel and vanadium-base alloys were selected for initial study of the structural material effects.

8.1 Development of the Computational Algorithms

Mathematical models to describe the thermal hydraulic response of the two blanket concepts illustrated in Figs. 14 and 15 were formulated and programmed into a computer code capable of performing steady-state energy balance calculations [22]. The computational model is summarized briefly herein.

8.1.1 Flowing Lithium-Cooled First-Wall Blanket Concept

The use of an electrically conducting fluid, like lithium, in the presence of large magnetic fields, gives rise to a number of adverse fluid dynamic effects of which the most serious is the pressure loss due to magnetohydrodynamic (MHD) interactions. In calculating the total pressure drop for the blanket cell concept in Fig. 14, the coolant flow path was divided into four regions: (1) inlet to blanket; (2) return through the blanket cell annulus; (3) inlet and exit through shield; and (4) inlet and exit through magnets. As the magnetic field is not constant across the blanket, the shield, and the magnet, the magnetic field strength, B, was integrated over each of the regions inside the toroidal field coil to obtain a properly averaged value of the gross MHD effect. The pressure loss in each region was then determined [22] using the corresponding average value of B^2 for that region. Because the actual lengths of the coolant flow paths, the sizes of the inlet and outlet headers, and the locations of

bends, fittings, etc., for a commercial reactor are subject to considerable uncertainty, a safety factor of two was employed in calculating each pressure drop. The thicknesses of the inlet piping to the blanket cell, the cell wall itself, and the manifolds were calculated based on the stress requirements corresponding to the prevailing operating conditions (temperature and pressure) with the assumptions that (1) the pressure stress cannot exceed one-third the yield strength [21]; and (2) the wall thicknesses cannot be less than 2.5 mm in the blanket region and 5 mm in the shield and magnet regions due to fabrication constraints.

The heat transfer calculations for the flowing lithium concept (Fig.14) were performed using standard empirical equations [22,23]. A one-dimensional steady-state analysis was carried out by dividing the blanket cell into (1) inlet piping; (2) first-wall; (3) cell annulus; and (4) cell side walls (see Fig. 14). These calculations were used to set the required coolant velocity for a given wall loading and to establish the general thermal characteristics of the system. The overall heat balance was determined based on a given wall loading due to (1) particles and radiation that create a first-wall surface flux; and (2) neutrons that create internally generated heat. As the particle and surface radiation power fraction depends on whether the reactor has a divertor or not, two representative cases were considered — the particle and surface radiation loading factor was set equal to 25% of the neutron wall loading without divertor and 10% of the wall loading with divertor.

8.1.2 Helium-Cooled Stagnant Lithium First-Wall/Blanket Concept

The thermal hydraulic analyses of a helium-cooled tubular first-wall coupled to a stagnant lithium blanket were based on the configuration shown in Fig. 15. The first-wall is assumed to be made of a single row of tightly packed tubes and the blanket is in essence a "sea" of lithium extending radially outward from the

back of the first-wall and having an appropriately dispersed array of helium-carrying tubes. The radiation power deposited on the first-wall and the nuclear heat generated within Zone 1 (see Fig. 15) are removed by the helium flowing through the first-wall tube bundle. Zone 2 (blanket) is divided into several regions and the number and size of the coolant tubes throughout these regions are calculated based on the internal heat generation rate so that the coolant exit temperatures for all regions are the same. The criteria for materials property limitations were the same as those described above for the lithium-cooled blanket concept.

8.2 Results and Discussion

8.2.1 Thermal Hydraulic Analyses of the Flowing Lithium-Cooled, First-Wall/Blanket Concept

Typical results of thermal hydraulic analyses for four reference cases (stainless steel with and without a divertor and vanadium alloy with and without a divertor) are summarized in Table II and are presented in greater detail in Refs. 22 and 23. For stainless steel (with or without a divertor), the maximum neutron wall loading generally occurs at relatively low wall thicknesses (i.e. $\leq$2.5 mm) and is limited by the thermal stress criterion (maximum thermal stress = material yield strength). For vanadium alloys this maximum occurs at somewhat larger wall thickness values (3 to 6 mm) and is limited by the minimum coolant inlet temperature criterion. The values of the maximum allowable neutron wall loading for 8, 10, and 12 T maximum toroidal fields are listed in the lower half of Table II. The total pressure drops were nominally in the range from 3 to 6 MPa (including the safety factor of 2.0 on all calculated pressure losses).

The effect of maximum toroidal field and cell wall thickness on the maximum allowable neutron wall loading is illustrated more clearly in Figs. 16 and 17

for the four cases described above. As can be seen in Figs. 16 and 17 and in Table II, there is some advantage (in terms of overall thermal hydraulic performance) to having the lower toroidal fields. For most cases, the actual advantage is, in fact, even greater than is indicated in Table II, because the increased cell wall thicknesses required to support the maximum neutron wall loading at the higher toroidal fields have the concommitant effect of reducing the coolant exit temperature.

Early trade-off studies on the coolant temperature rise showed that the values in Table II (i.e. 225°C for stainless steel and 325°C for vanadium alloy) are near to optimum for each material based on the thermal-hydraulic model and maximum structural temprature limits used herein. Also, the pumping power to thermal power ratio (based on geometrically averaged values of the actual magnetic field strength inside the reactor) was found to be <1.0, <1.5, and <2.0% for maximum toroidal fields of 8, 10, and 12 T, respectively.

Data of the type presented in Refs. 22 and 23 have permitted the derivation of a series of empirical equations which relate the coolant exit temperature T(CE) to maximum material temperature, T(max), neutron wall loading, P_w, and cell wall thickness, t, for each of the material and divertor options investigated. For stainless steel

$$T(CE) = T(max) - t\left[1.2\ P_w + 0.5\right] \text{ with divertor,}$$

and

$$T(CE) = T(max) - t\left[\frac{T(max) - 400}{100}\right]\left[1.3\ P_w + 0.25\right] \text{ without divertor.}$$

For vanadium

$$T(CE) = T(max) - t\left[\frac{T(max) - 400}{100}\right]\left[0.8\ P_w - 2.7\right] \text{ with divertor,}$$

and

$$T(CE) = T(max) - t\left[\frac{T(max) - 400}{100}\right]\left[2.0\ P_w - 3.8\right] \text{ without divertor,}$$

where T is in °C, t is in mm, and P_w is in MW/m^2. Only in the case of stainless steel with a divertor present did the value of T(max) - T(CE) show negligible dependence on the value of T(max).

8.2.2 *Thermal Hydraulic Analyses of the Helium-Cooled Stagnant Lithium First-Wall/Blanket Concept*

One of the primary objectives of the thermal hydraulic analysis for the helium-cooled stagnant lithium concept was to make the coolant operating parameters and characteristics reasonably consistent with existing HTGR experience [28]. Table III contains a summary of results with stainless steel as construction material and with the following sets of conditions: (1) the presence of or absence of a divertor; (2) maximum allowable structural temperatures of 500°C or 650°C; (3) thermal stress limits of 17 or 34 ksi; and (4) heat transfer coefficient and friction factor multipliers of 2.2 and 4.0, respectively [24]. The asterisked parameters were fixed in the calculation and the primary iteration was done by increasing the neutron wall loading until the thermal stress limit at the first wall was exceeded.

In the thermal hydraulic analysis of the first wall, the coolant velocity is fixed at 200 ft/s, the tube diameter is fixed at 25.4 mm (1 in.), and the tube wall thickness is not allowed to be less than 1.25 mm (50 mil). In the thermal hydraulic analysis of the blanket, the coolant void fraction, VF, is fixed at 5% and the temperature drop through the lithium $\Delta T(Li)$, is set at 25°C. Trade studies on the latter two parameters have been completed for VF = 5, 7, and 10% and $\Delta T(Li)$ = 25, 50, and 100°C. These studies show that,

in terms of maximum coolant exit temperature, VF = 5% and $\Delta T(Li) = 25°C$ are closer to optimum than the other values tested. Other parameters that were fixed in these analyses are given in Table III. The coolant exit temperature, from the first wall region, T(CE), may be represented empirically in terms of the neutron wall loading, P_w, and the maximum allowable structural temperature, T(max), by:

$$T(CE) = T(max) - 17.9\ P_w - 21.9 \text{ (with divertor)}$$

$$T(CE) = T(max) - 41.3\ P_w - 21.4 \text{ (without divertor).}$$

where T is in °C and P_w is in MW/m^2. The coolant exit temperature from the blanket region is nominally 30 to 50°C below the maximum structural temperature and seems to be relatively independent of wall loading or divertor status.

8.3 Conclusions of Thermal Hydraulic Analysis

The key conclusions from the study of the liquid lithium-cooled, first-wall/blanket concept may be summarily stated as follows:

(a) The maximum allowable neutron wall loading for a given reactor design can be increased from 40 to ∿90% by the addition of a divertor. The magnitude of the increase depends primarily on which criteria set the maximum wall loading, e.g., increases tend to be greatest in thermal stress-limited systems.

(b) With respect to overall thermal hydraulic performance, austenitic alloys will tend to be thermal-stress limited, whereas vanadium-base alloys will be limited by the pinch between maximum allowable structural temperature and minimum coolant inlet temperature.

(c) Significantly higher neutron wall loadings appear to be achievable with vanadium alloys than with solution-annealed Type 316 stainless steel.

(d) Ignoring the application of advanced power conversion cycles, there is little incentive for structural temperatures in excess of 650°C, since the associated coolant (lithium) exit temperatures ($\geq$550°C) are more than adequate to drive optimized steam turbine cycles.

(e) Overall design and performance objectives for lithium-cooled reactors will be more easily met at lower toroidal fields (8-9 T). Fields as high as 12 T may preclude the use of circulating lithium in all but the most outboard regions of the blanket.

For the case of the helium-cooled stagnant lithium first-wall/blanket concept, the key conclusions are as follows:

(a) A maximum allowable structural temperature $\geq$600°C will be necessary to assure the attainment of attractive operating conditions (i.e., reasonable thermodynamic efficiency) for the helium coolant.

(b) As in the case of the lithium-cooled first-wall/blanket concept, the presence of a divertor increases the allowable wall loading by nearly a factor of two in thermal stress-limited systems.

(c) The transverse cooling arrangement employed in the helium-cooled concept (Fig. 15) requires an enormous number of individual tubes and is probably less attractive (from the standpoint of fabricability and overall thermal hydraulic performance) than the radially cooled helium blanket concept des cribed by Kearney et al. [9].

(d) There appears to be some incentive to provide for augmentation of the heat transfer coefficient in helium-cooled reactors, even though this will undoubtedly be accompanied by increased pressure losses.

Finally, it must be noted that the results given above are for quas-steady-state performance of the first-wall/blanket system. Therefore, the

derived operating conditions (wall loadings, coolant exit temperature, etc.) represent upper limits to the performance of an actual system. The effects of thermal strain and cyclic fatigue act to reduce the allowable wall loading and the peak allowable structural temperature as well. This contention is supported by the work of Majumdar et al. [29] on the fatigue life modeling of the lithium-cooled module in Fig. 15.

9. PLASMA SUBSYSTEM ANALYSIS AND DATA BASE

Among the many parameters which ultimately influence tokamak plasma characteristics, this study has concentrated on twelve of the most important variables: aspect ratio, A; elongation, κ; triangularity, d; peakedness of the pressure profile, α; safety factor, q; toroidal beta, β_t; impurity level, Z_{eff}; average (electron) temperature, $\bar{T}_e$; peakedness of the density profile, α_n; blanket/shield thickness, Δ^i_{BS}; maximum toroidal field, B_m; and major radius, R. The first six of these uniquely specify an ideal magnetohydrodynamic (MHD) equilibrium, and a large number of these equilibria have been surveyed. The parameters Z_{eff}, $\bar{T}_e$, α_n, and α are input to the steady-state, profile-averaged particle and energy transport equations; desirable reactor combinations of these variables are found to be independent of the MHD results. The last three variables, Δ^i_{BS}, B_m, and R, complete the determination of plasma performance, and the relationships among these have been studied. The results of the MHD, transport, and performance calculations are summarized in this section and detailed in Ref. 18. The emphasis has been to examine reactor sensitivity to these variables, to fix the least influential at reference values, and illustrate some of the consequences of various options among the remaining set.

The MHD equilibria, which are solutions to the Grad-Shafranov equation [30, 31] require a specific ratio of plasma current to toroidal field coil

current, I_p/I_{TFC}. Since I_p affects the ohmic heating and equilibrium field power supply requirements, this ratio is significant in determining reactor costs. In the MHD sensitivity studies below we vary one MHD parameter at a time, keeping the others fixed.

The first finding is that triangularity, d, has only mild effects on I_p/I_{TFC}, reverse-D shapes ($d < 0$) requiring slightly smaller I_p/I_{TFC} than normal D's. An overriding consideration then becomes one of stability, and we have chosen to concentrate on values of $d \geq 0$. Hereafter we take d to increase with elongation: $\kappa = 1$, $d = 0$ (circular); $\kappa = 1.3$, $d = 0.25$; $\kappa = 1.65$, $d = 0.5$; $\kappa = 2$, $d = 0.75$ (highly noncircular). The plasma current was next examined as the pressure profile was varied, and I_p/I_{TFC} was found to be independent of α for $1.0 \leq \alpha \leq 2.0$. However, broader pressure profiles ($\alpha \approx 1.0$) tend to have somewhat smoother current density profiles and smaller shifts of the magnetic axis for a given β_t and on an intuitive basis may result in more stable discharges than narrow profiles.

The ratio I_p/I_{TFC} has a strong dependence on the safety factor, essentially being $I_p/I_{TFC} \propto q^{-1}$. In contrast, I_p/I_{TFC} varies very little with β_t, when the other MHD parameters are fixed. The ultimate factor determining reactor values of q and β_t is plasma stability, which we have not quantitatively addressed. For simplicity we set $q = 3$ for the rest of our discussion, but we keep the important quantity β_t as a variable parameter.

We next find that I_p/I_{TFC} increases with κ and decreases with A^2. Since we have required $q(0) = 1$ for all equilibria, which keeps the current density approximately constant, the plasma current is roughly proportional to the plasma's cross-section area.

Turning to the transport calculations [5,18] we focus on two figures of merit for reactor operation, the required containment parameter $\bar{n}_i\tau$ for ignition and the plasma power density P_p. Our first study in this area was to examine

the relative importance of temperature versus density profile effects. For a scalar pressure p = nT, the exponent describing the temperature profile width is $\alpha_T = \alpha - \alpha_n$. We fixed the pressure profile ($\alpha = 1.4$) in flux-coordinate space and varied α_n/α_T for various combinations of $\bar{T}_e$ and Z_{eff}. The power density is insensitive to α_n/α_T at the $\bar{T}_e$ which maximizes P_p. This is to be expected since, approximately [18],

$$P_p \propto (1 + \alpha)^2 \frac{\langle \sigma v[(1 + \alpha_T)\bar{T}] \rangle}{[(1 + \alpha_T)\bar{T}]^2}, \tag{2}$$

and $\langle \sigma v(x) \rangle / x^2$ is slowly varying near its maximum. Likewise $\bar{n}_i\tau$ only varies by a factor of two as α_n/α_T is changed over a realistic range; such a variation is insignificant compared to the present-day uncertainty in predicting the $\bar{n}_i\tau$ attainable in a reactor regime. On this basis we have set the reference value $\alpha_n = 0.3$ (corresponding to relatively broad-density profiles). Proceeding now to vary the total pressure profile parameter, α, we find peaked profiles ($\alpha \sim 2.0$) allow ignition at lower average temperatures than broad profiles ($\alpha \lesssim 1.0$). Also, in accord with Eq. (2), power density maximizes at

$$\bar{T} \approx \frac{13 \text{ keV}}{(1 + \alpha_T)} = \frac{13 \text{ keV}}{(0.7 + \alpha)}.$$

These benefits of peaked profiles confirm the results reported in Ref. 32.

Ignition ($\bar{n}_i\tau < \infty$) was found to be impossible with $Z_{eff} \gtrsim 3$ at low temperatures ($\bar{T}_e \lesssim 10$ keV). However, Z_{eff} has only very small effects on power density, as one can see by writing

$$P_p \propto \overline{n_i^2 \langle \sigma v(T_i) \rangle}.$$

Higher Z_{eff} requires a larger $\langle \sigma v(T_i) \rangle$ in order to balance the enhanced radiation loss with increased fusion power input. This increase in $\langle \sigma v \rangle$ is just offset by

the decrease in n_i^2 with Z_{eff}, since impurities constitute an ever larger portion of the fixed β_t as Z_{eff} increases.

Based on the sensitivity studies, we have chosen a set of transport reference parameters: $\alpha_n = 0.3$, $\alpha = 1.4$, $\bar{T}_e = 8$ keV, and $Z_{eff} = 1.7$. These numbers correspond to nearly maximum power density, reasonable $\bar{n}_i\tau$, and realistic profiles well into the "steady-state" portion of the burn cycle of a typical tokamak reactor, and they are used as input for the remaining calculations.

When analyzing the relationships among Δ_{BS}^i, R, and B_m which determine reactor geometry, the following formulas are useful for reference. The approximate reactor thermal power is

$$P_{th} \approx \beta_t^2 B_0^4 V \, f\left(\alpha, \alpha_n, \bar{T}_e\right) , \tag{3}$$

where the toroidal field at the plasma center is given by Eq. (1) and the plasma volume is

$$V \propto \kappa R^3/A^2 . \tag{4}$$

The vacuum scrape-off width, Δ_v, was set at 0.2 m and the blanket/shield thickness was set at $\Delta_{BS}^i = 1.0$ m.

Figures 18-21 illustrate the options available among the principal reactor design parameters, B_m and I_p versus R for various A, κ, and β_t choices. These variables, which figure prominently in the engineering and economic analysis of Sections 4 and 5, are displayed for 2500 MWt power.

First consider the scaling of β_t with A when κ is fixed. If the maximum beta is independent of A, then we see from Eqs. (1)-(4) that the required R and B_m are smaller as A increases, since $B_0^4 V$ is an increasing function of A. For example, Fig. 18 shows that a reactor with $B_m = 9$ T, $\beta_t = 0.08$, and A = 3.0 requires R = 6.70 m, but at the same B_m and β_t it requires R = 7.00 m if A = 2.5. On the other hand, if $\beta_t\big|_{max}$ increases sufficiently as A is reduced, there may

be motivation to design small aspect ratio devices as shown in Sec. 5. For example [30], suppose $\beta_t|_{max} = 0.08$ at A = 3.0 but $\beta_t|_{max} = 0.12$ at A = 2.5. In this case, Fig. 18 demonstrates the major radius can be reduced from 6.70 m to 5.94 m by going to the lower aspect ratio, with B_m constrained to be 9 T. One price paid for this reduced major radius is a moderate increase in plasma current; as seen in Fig. 19. I_p increases from 11.1 MA at A = 3.0 to 12.7 MA at A = 2.5.

Next we fix A = 3.0 and examine β_t scaling with κ. Again a particular scaling law is required to draw quantitative conclusions. As a purely heuristic case, suppose $\beta_t|_{max} \propto S^2$, where S is the shape factor. The curves labelled $\beta_t = 0.08$ at $\kappa = 1.65$ and $\beta_t = 0.06$ at $\kappa = 1.3$ in Figs. 20 and 21 follow this scaling law, and for a 2500 MW reactor with $B_m = 9$ T, the major radius could be reduced from 7.60 m to 6.37 m by going to the larger elongation. One disadvantage of this larger κ is the increase in I_p from 12.6 MA to 15.3 MA.

In concluding this section we reiterate that the data base presented here is best evaluated in the context of the power plant parametric study of Sections 4 and 5 in which the costs of different choices are quantitatively examined. In these two earlier sections the fixed plasma parameters were $\alpha = 1.4$, $q = 3.0$, $Z_{eff} = 1.7$, $\alpha_n = 0.3$, $\bar{T}_e = 8$ keV, and $\Delta^i_{BS} = 1.0$ m.

10. PLASMA DRIVING SYSTEM REQUIREMENTS

The plasma driving system for a tokamak reactor is composed of an ohmic heating (OH) coil, equilibrium field (EF) coil, and their respective power supplies. Conceptual designs of an Experimental Power Reactor [4-7] (EPR) and scoping studies of a Demonstration Power Reactor [10] have shown that the driving system constitutes a significant part of the overall reactor cost.

The plasma driving system requirements depend upon the reactor design concept, of course. In this section, we summarize our results for a single reactor configuration together with several design concepts for the driving system. Both the reactor configuration and the driving system concepts are natural extensions from the EPR. Thus, the new results presented in this paper can be compared with the previous EPR results [5] to obtain a consistent picture of how the driving system requirements will evolve — for one particular design configuration.

The reactor model used for this study is an 8-m major radius tokamak having a plasma β_t of about 8%, and a thermal power output of 3000 MW. The plasma is D-shaped with κ of 1.3 and has equilibrium parameters $\bar{n}_{DT} = 1.44 \times 10^{20}$ m^{-3}, $I_p = 12.3$ MA, $q(a) = 3$, $\beta_p = 1.85$, $\bar{T}_i = 8$ keV, and $\eta = 3 \times \eta_{spitzer}$. The model and design parameters are based, in part, on data developed by the parametric systems analysis discussed in previous sections. The reactor coil configuration shown in Fig. 22 is conventional, with a central, solenoidal OH coil with a few additional external trimming coils, and a set of EF coils external to the toroidal field coils. Both the OH and EF coils are superconducting and decoupled from one another. The locations of the EF coils and the relative currents in them have been selected so as to obtain the magnetic field in the plasma required to keep the plasma in MHD equilibrium. Four different driving system power supply configurations have been examined as to their suitability for this reactor. All of the configurations studied use a silicon-controlled rectifier (SCR) type power supply for the EF system and for the auxiliary (burn-phase) OH supply but differ in the type of energy transfer device used in the OH system for startup and in the type of central energy storage device. For each power supply configuration, a range of ohmic heating ramp times, Δt_{OH}, and neutral beam turn-on times, t_{B_0}, was simulated.

Configuration No. 1, shown in Fig. 23, uses a homopolar generator for the OH energy transfer device and an energy storage inductor (ESI) as the central storage element, together with the other supplies. An example of the startup, using this configuration is shown in Fig. 24 for the typical case of $\Delta t_{OH} = t_{B_0} = 2$ s. The homopolar generator is connected to the previously charged OH coil at the start of the cycle, t = 0 and disconnected at t = 2 s. During this period the OH current increase serves to induce current in the plasma. Neutral beam heating is initiated at t = 2 s and terminated at about t = 8 s when the plasma reaches an ignited equilibrium. The EF current begins at zero at the start of the cycle, and rises in accordance with the needs of the MHD equilibrium, as determined by the plasma pressure and current. The requirements on the driving system are computed from these waveforms where, for example, the maximum value of V_{OH} determines $\dot{B}_{max}$, and the homopolar generator storage capacity, the amount of ohmic heating flux swing used for startup determines the maximum burn time, etc. Figure 25 shows the sensitivity of some of the requirements for Configuration No. 1 for a range of Δt_{OH}. Similar analysis and sensitivity studies have been made for the other configurations.

In general, feasible startup times for this reactor are about the same as for an EPR; OH reversal times of 1-4 s are followed by a beam heating period of about 5 s. The $\dot{B}$ requirements on the OH coil are considerably less than for an EPR, basically due to the larger radius of the OH coil. The OH power and energy requirements are similar to an EPR but the EF requirements increase considerably. In general, there is a strong degree of coupling between the driving system requirements and the details of the plasma physics, particularly the temperature behavior and the MHD field requirements of the plasma.

Figure 26 summarizes the total driving system power supply cost as a function of the OH ramp time for the different configurations. This data has been

generated by applying cost algorithms developed for the various hardware components to the technological requirements found by the burn cycle analysis. Figure 26 is for the case of the neutral beam turned on just after the OH ramp, generally the best operating mode. The cost of each configuration is extremely sensitive to the ramp time; this illustrates the need for a very precise and coupled analysis of the plasma and the driving system. In general, the cheapest operating point is the most cost effective.

Configuration No. 1 results in the smallest power supply cost: 105 \$M for a Δt_{OH} of 3 s. The energy storage requirement for the homopolar generator, $\dot{B}_{EF}^{max}$ = 2.5 T/s and the ESI storage capacity is 9460 MJ. Based on the OH flux swing used during startup, a burn time of about a half hour would be possible.

In Configuration No. 2 an SCR power supply is used instead of a homopolar generator, as the OH transfer element. At the cheapest operating popint, Δt_{OH} = 2.3 s, the cost is about 25 \$M more than for Configuration No. 1. This is basically because the SCR supply costs more than the homopolar generator. The requirements for this case are P_{OH}^{max} = 2100 MVA, P_{EF}^{max} = 1568 MVA, $\dot{B}_{OH}^{max}$ = 2.0 T/s, and ESI storage = 8350 MJ.

Configuration No. 3 is the most conventional in terms of available technology. Here a motor-generator-flywheel set is used as the central energy storage device along with an SCR-type power supply for the OH transfer element. Although the requirements for this configuration, exclusive of the MGF set, are the same as for Configuration No. 2, the cost is much higher and nearly double that of the homopolar generator-ESI combination at the cheapest operating point. This large additional cost is due almost entirely to the cost of the generator portion of the MGF set. Furthermore, the cost estimates for this configuration assume a voltage compatible power supply-MGF-set combination, i.e. with no transformers used. If transformers were needed the cost of Configuration No. 3 would be even greater.

In Configuration No. 4a a dump resistor is used as the OH energy transfer device, together with an ESI as the central storage device. Use of a dump resistor, which has an essentially trivial cost, eliminates the need for a symmetric OH current swing during startup (needed for the other transfer devices), and so permits the full design value of the OH flux swing to be used. The potential burn time is therefore increased, to about one hour. The use of a dump resistor, however, requires a shorting switch, in the OH circuit. If this switch must be solid state, as has been assumed, it will be expensive. Also, the range of ramp times, for a single dump resistor, is limited to fairly short times, and this increases the EF requirements. For these reasons, Configuration No. 4a is comparatively expensive, about 185 $M for the cheapest case. This may or may not be worth the doubled burn time. Requirements for this case are $\dot{B}_{OH}$ = 3.4 T/s, P_{EF}^{max} = 2576 MVA. If four resistors are used, to obtain a variable resistance during startup, as in Configuration No. 4b, the maximum OH voltage during startup can be lowered and the ramp time increased. This saves on EF supply cost relative to Configuration No. 4a but involves higher switch costs. The cheapest case for Configuration No. 4b costs about the same as Configuration No. 4a. The burn time is about the same, $\dot{B}$ = 2.0 T/s and P_{EF}^{max} = 1568 MVA are lower, while circuit complexity and control would be greater.

11. SUMMARY AND CONCLUSIONS

A parametric systems studies program for simulation of the performance characteristics and economics of tokamak power plants is now in an active stage at ANL. The program has proven to be a powerful tool in addressing critical issues for tokamaks. Parametric systems studies provide a useful framework for identifying the design concepts and the region of parameter space that can make tokamaks economically attractive. The results presented

in this paper represent an example of the usefulness of the parametric systems studies approach. A summary of the conclusions that can be drawn from our work is given below. One should be extremely careful, however, not to extrapolate these results far beyond the scope of work that has been defined in this paper. The reader is encouraged to consult References 16 through 26 for greater detail on each specific topic.

(1) In the entire range of variables examined, the cost of energy for tokamaks varies from ∿25-50 mills/kWh (∿1200-2500 $/kWe). This is comparable to the present range of cost estimates for LMFBR. Cost estimates for other nuclear and coal power plants are in the range of ∿14-20 mills/kWh. Since the fuel cost is negligible in tokamak fusion power plants the present trend of escalation in the fuel cost for other energy sources will make tokamaks competitive in ∿2-4 decades.

(2) Tokamaks exhibit an "economy of scale". Increasing the reactor thermal power from 3000 to 5000 MWt reduces the cost of energy by ∿10-15%. The saving from further increase in reactor power is smaller. The values of parameters that characterize an optimum reactor system are, in many instances, very sensitive to the design value of thermal power output. It is very desirable for the fusion community to select a "target" thermal power for design, analysis, and planning.

(3) The cost of energy is very sensitive to β_t. The choice of the best parameter space for tokamaks is strongly affected by the operating value of β_t. Determining the stability limit of β_t should be a high priority goal for the fusion program.

(4) Much of the economics advantages of tokamaks can be realized at a β_t of ∿6%. <u>Most</u> of the economics potential of tokamaks is achievable with $\beta_t \sim 8\%$. Higher β_t values — if achievable — are always desirable but not crucial to the prospect for economic competitiveness of commercial tokamaks.

(5) The highest desirable toroidal-field strength is ≤ 9 T, which can be achieved by NbTi, if the β_t stability limit is $\gtrsim 6\%$. If $\beta_t < 4\%$ higher fields (>9 T) would be desirable. Such high field (~ 12 T) reactors have to be designed for large power and/or large aspect ratio. The necessity of large aspect ratio for high-field reactors implies poor utilization of the β_t stability limits that will further reduce their benefits if the attainable β_t is inversely proportional to the aspect ratio.

(6) The optimum aspect ratio, A, is sensitive to the variation of β_t with A. If $\beta_t \sim 1/A$, then a favorable aspect ratio is $A \sim 3.5$. If $\beta_t \sim 1/A^2$, then $A \sim 3$ results in an economically favorable design.

(7) The increase in the plasma current and the equilibrium field at larger elongation reduces the benefits of highly shaped plasmas. Assuming the equilibrium-field (EF) coils are located outside the bores of the TF coils, the following conclusions can be derived. If the β_t stability limit is independent of κ there is no motive for employing elongated plasma. If $\beta_t \sim \kappa$ there is a very shallow minimum in the cost of energy in the range $1.3 < \kappa < 1.6$. A significant economic benefit from increasing κ is obtainable if $\beta_t \sim \kappa^2$.

(8) Tokamaks with reactor thermal power in the range of $\sim$3000-6000 MWt have favorable economic conditions with plasma major radii of $\sim$5-8 m.

(9) With proper design concepts, the blanket/shield thickness (distance in midplane from first wall to the point inside the toroidal magnet where the maximum field occurs) can be kept as small as 1 m.

(10) Favorable economic conditions occur when the annealing of the superconducting magnets coincides with the replacement of the first wall.

(11) Experimental data on the radiation damage to organic insulators at low temperatures ($\sim 4°K$) are required. There is an economic incentive to develop insulators suitable for the TF coils that can operate satisfactorily up to 10^{10}-10^{11} rad.

(12) Advanced structural alloys (e.g. vanadium alloys) offer the potential of reducing the cost of energy by ~20-25% compared with stainless steel.

(13) In order to limit the increase in the cost of energy due to the downtime associated with the replacement of the first wall to less than 10%, a long structure lifetime, t_w, and a short downtime, t_d, for replacement are required to meet the following criteria:

$$t_d(\text{days}) < 30 \cdot t_w(\text{years}) .$$

(14) The recommended highest priority goals for structural alloy development are 3 MW/m^2 neutron wall load and 4-yr lifetime. More ambitious goals that can lead to a very significant economic payoff are 5 MW/m^2 and 6 yr.

(15) Detailed engineering and structural analysis of the first wall and blanket is required to quantitatively define the end of life criteria for the structural materials.

(16) Ignoring the application of advanced power conversion cycles, there is little incentive for structural temperatures in excess of 650°C in lithium-coated reactors. Reasonable values for the maximum operating temperature of the structure is 500°C for stainless steel and 650°C for vanadium alloys.

(17) With lithium cooling and a maximum toroidal field of 8 T, the thermomechanical response of the first wall limits the maximum allowable neutron wall load, in the absence of a divertor, to ~8 MW/m^2 for vanadium and 2 MW/m^2 for stainless steel. Higher fields result in a significant reduction in the allowable neutron wall load. Fields as high as 12 T may preclude the lithium cooling option.

(18) The presence of a divertor (or equivalent mechanism to reduce surface heating) can increase the maximum allowable neutron wall load by ~40 to 90% with both helium and lithium coolant.

(19) For the helium coolant option, a maximum structural temperature of $\geq$600°C is necessary to assure the attainment of attractive operating conditions (i.e. reasonable thermodynamic efficiency).

(20) The power supplies for the poloidal coils represent a significant cost item. The use of a conventional motor-generator-flywheel set as a central energy storage device leads to an increase in the plant cost as large as 10%. There is a strong economic incentive for the development of homopolar generators and superconducting energy storage devices.

REFERENCES

[1] MILLS, R. G. et al., A Fusion Power Plant, Princeton Plasma Physics Laboratory, MATT-1050 (1974).

[2] BADGER, B. et al., A Wisconsin Toroidal Fusion Reactor Design, UWMAK-I, University of Wisconsin, UWFDM-68 (1974).

[3] BADGER, B. et al., A Conceptual Tokamak Reactor Design, UWMAK-II, University of Wisconsin, UWFDM-112 (1975).

[4] STACEY, W. M., JR., BAKER, C. C., ROBERTS, M., in Plasma Physics and Controlled Nuclear Fusion Research 1976 (Proc. 6th Int. Conf. Berchtesgaden) IAEA, Vienna, 1977, CN-35/13-2, Vol. III, p. 255.

[5] STACEY, W. M., JR. et al., Tokamak Experimental Power Reactor Conceptual Design, Argonne National Laboratory, ANL/CTR-76-3 (1976); and STACEY, W. M., JR. et al, "Tokamak Experimental Power Reactor Studies, Argonne National Laboratory, ANL/CTR-75-2 (1975).

[6] BAKER, C. et al., Experimental Power Reactor Conceptual Design Study, General Atomic Company, GA-A14000 (1976); and Experimental Power Reactor Conceptual Design Study, General Atomic Company, GA-A13534 (1975).

[7] ROBERTS, M. et al., Oak Ridge Tokamak Experimental Power Reactor Study, Oak Ridge National Laboratory, ORNL/TM-5572 through ORNL/TM-5577 (1976); and Oak Ridge Tokamak Experimental Power Reactor Study Reference Design, ORNL/TM-5402 (1975).

[8] CONN, R. W. et al., UWMAK-III, A Noncircular Tokamak Power Reactor Design, University of Wisconsin, UWFDM-150 (1976).

[9] KEARNEY, D. W. et al., Conceptual Design Study of a Noncircular Tokamak Demonstration Fusion Power Reactor, General Atomic Company, GA-A13992 (1976).

[10] STEINER, D. et al., ORNL Fusion Power Demonstration Study: Interim Report, Oak Ridge National Laboratory, ORNL/TM-5813 (1977).

[11] COHN, D. R. et al., in Technology of Controlled Nuclear Fusion (Proc. 2nd ANL Top. MTG., 1976), USERDA-CONF-760935-P3, p. 931.

[12] STACEY, W. M., JR. et al., EPR-77: A Revised Design for the Tokamak Experimental Power Reactor, Argonne National Laboratory, ANL/FPP/TM-77 (1977).

[13] SAKO, K. et al., in Technology of Controlled Nuclear Fusion (Proc. 2nd ANS Top. Mtg., 1976), USERDA-CONF-760935-P2, p. 607.

[14] MITCHEL, J. T. D., "A Tokamak Reactor with Servicing Capability," in Fusion Technology (Proc. 9th Symp., Commision of the European Communities), Pergamon Press, Oxford and New York (1976).

[15] POWELL, J. R. et al., Preliminary Reference Design of a Fusion Reactor Blanket Exhibiting Very Low Residual Activity, Brookhaven National Laboratory, BNL-19565 (1974).

[16] STACEY, W. M., ABDOU, M. A., "Tokamak Fusion Power Reactors," Nucl. Techn. (in press); also Argonne National Laboratory, ANL/FPP/TM-83 (1977).

[17] ABDOU, M. et al., Wall Load and Structure Life Tradeoffs for Tokamak Power Plants, Argonne National Laboratory, to be published (1977).

[18] EHST, D. et al., A Systematic Survey of Tokamak Reactor Physics Design Parameters, Argonne National Laboratory, ANL/FPP/TM-95 (1977).

[19] BROOKS, J. et al., Plasma Driving Systems Requirements for Commercial Tokamak Fusion Reactors, Argonne National Laboratory, ANL/FPP/TM-87 (1977).

[20] TURNER, L. R., ABDOU, M. A., Computational Model for Superconducting Toroidal-Field Magnets for a Tokamak Reactor, Argonne National Laboratory, ANL/FPP/TM-88 (1977).

[21] MATTAS, R. F., SMITH, D. L., Modeling of Life-Limiting Properties of Fusion Reactor Structural Materials, Argonne National Laboratory, ANL/FPP/TM-84 (1977); also to be published in Nucl. Techn.

[22] MISRA, B., MARONI, V. A., Thermal Hydraulic Analysis of Two Fusion Reactor First-Wall/Blanket Concepts," Argonne National Laboratory, ANL/FPP/TM-94 (1977).

[23] MISRA, B., STEVENS, H. C., MARONI, V. A., "Thermal Hydraulic and Power Cycle Analysis of Liquid Lithium Blanket Designs," in Proc. 1977 National Heat Transfer Conference, August 15-17, 1977, Salt Lake City, Utah.

[24] TURNER, L. R., ABDOU, M. A., Computational Model for Superconducting Toroidal-Field Magnets for a Tokamak Reactor," in Proc. 7th Symp. on Engineering Problems of Fusion Research, Knoxville, Tenn., 1977 (IEEE), to be published.

[25] BROOKS, J., "Plasma Driving System Requirements for Commercial Tokamak Fusion Reactors, in Proc. 7th Symp. on Engineering Problems of Fusion Research, Knoxville, Tenn., 1977 (IEEE), to be published.

[26] ABDOU, M. A., Radiation Considerations for Superconducting Fusion Magnets, Argonne National Laboratory, ANL/FPP/TM-92 (1977); also J. Nucl. Materials to be published.

[27] Guide for Economic Evaluation of Nuclear Reactor Plant Designs, NUS Corp., MUS-531 (1969).

[28] KEARNEY, D. W. et al., General Atomics Company, Private Communication (1977).

[29] MAJUMDAR, S., MISRA, B., HARKNESS, S. D., Argonne National Laboratory, ANL/FPP/TM-99 (1977).

[30] EVANS, K., JR., High β_t Equilibria in Tokamaks, Argonne National Laboratory, ANL/FPP-TM-98; also, Nucl. Fusion (submitted).

[31] CALLEN, J. D., DORY, R. A., Phys. Fluids 15 (1972) 1523.

[32] KESNER, J., CONN, R. W., Nucl. Fusion 16 (1976) 397.

LIST OF TABLES

No.

I Effect of Inner Blanket/Shield Thickness on Maximum Dose to the Insulators in the Toroidal-Field Magnets

II Results of Wall Loading Trade Studies for Lithium-Cooled Stainless Steel and Vanadium-Alloy Blanket Systems

III Trade Study for Helium-Cooled Stagnant Lithium Blanket Using Transverse Cooling Channels Made of Stainless Steel: First-Wall Configuration is a Single Layer of Closed-Packed Tubes

TABLE I. EFFECT OF INNER BLANKET/SHIELD THICKNESS ON MAXIMUM DOSE TO THE INSULATORS IN THE TOROIDAL-FIELD MAGNETS[a]

Δ^{i}_{BS} (m)	Dose to insulator at end of plant Life, 30 yr (rad)	Cost of Energy mills/kWh R = 6
0.7	1.2×10^{12}	55.2
0.8	3×10^{11}	37.6
0.9	7×10^{10}	34.5
1.0	1.8×10^{10}	34.4
1.1	3.3×10^{9}	35.2
1.2	1.2×10^{9}	37.1
1.3	3×10^{8}	40.1
1.4	7×10^{7}	45.4

[a]Based on system with $A = 3$, $\kappa = 1$, $P_w = 3$ MW/m^2.

TABLE II. RESULTS OF WALL LOADING TRADE STUDIES FOR LITHIUM-COOLED STAINLESS STEEL AND VANADIUM-ALLOY BLANKET SYSTEMS[a]

		Lithium-Cooled Vanadium Alloy	Lithium-Cooled Stainless Steel
Criteria			
Maximum allowable temperature (°C)		650	500
Maximum thermal stress (MPa)		351	117
Minimum wall thickness (mm)		2.5	2.5
Maximum wall thickness (mm)		8.0	8.0
Minimum coolant inlet temperature (°C)		235	235
Coolant temperature rise (°C)		325	225
Results			
Maximum neutron wall loading MW/m^2			
F^b = 0.10 (divertor)	8 Tesla	11.2[c]	4.2[d]
	10 Tesla	7.5[e]	3.5[d]
	12 Tesla	5.3[e]	3.0[d]
F^b = 0.25 (no divertor)	8 Tesla	8.0[c]	2.0[d]
	10 Tesla	6.2[c]	2.0[d]
	12 Tesla	4.6[c]	1.8[d]

[a]For a cell diameter of 0.5 m and an inlet tube diameter of 0.1 m.

[b]F = ratio of first-wall surface loading due to particle and radiation effects to neutral wall loading.

[c]Limited by minimum coolant inlet temperature criterion.

[d]Limited by maximum thermal stress criterion.

[e]Limited by MHD pressure stress criterion (i.e. maximum cell wall thickness insufficient to support higher coolant velocity).

TABLE III. TRADE STUDY FOR HELIUM-COOLED STAGNANT LITHIUM BLANKET USING TRANSVERSE COOLING CHANNELS MADE OF STAINLESS STEEL: FIRST-WALL CONFIGURATION IS A SINGLE LAYER OF CLOSED-PACKED TUBES

(* indicates fixed or independent parameter)

Divertor Option	With Divertor				Without Divertor			
General Parameters								
* Maximum Structural Temp., °C [T(MAX)]	500		650		500		650	
* Helium Inlet Pressure, ksi	1.0		1.0		1.0		1.0	
* Pump Power/Thermal Power, %	5		5		5		5	
* Coolant ΔT, °C	200		300		200		300	
* Lithium ΔT, °C [ΔT(Li)]	25		25		25		25	
Neutron Wall Loading, MW/m^2	6.2	12.4	6.0	12.0	2.6	5.3	2.6	5.1
First Wall Parameters								
* Helium Tube Dia., mm	25.4		25.4		25.4		25.4	
* Helium Velocity, ft/s	200		200		200		200	
* Thermal Stress, ksi	17	34	17	34	17	34	17	34
Wall Thickness, mm	1.25		1.25		1.25		1.25	
Channel Length, m	12.2	13.2	17.3	18.5	12.2	13.1	17.3	18.4
HT. TR. Coeff., BTU/hr.ft.^{2}°F	1693	1980	1510	1729	1679	1968	1507	1720
Coolant Inlet Temperature, °C	171	63	217	105	173	67	220	110
Coolant Exit Temperature, °C [T(CE)]	371	263	517	405	373	267	520	410
Wall ΔT, °C	53	106	50	100	53	107	50	100
No. of Tubes, Hundreds[a]	32	29	22	21	32	30	22	21
Total Tube Weight, Tons[a]	35		35		35		35	
Blanket Parameters								
* Void Fraction, % [VF]	5		5		5		5	
Tube Diameter, mm	4.9	3.4	5.2	3.6	7.7	5.4	8.2	5.8
Wall Thickness, mm	0.41	0.37	0.42	0.37	0.48	0.43	0.49	0.43
Channel Length, m	1.1	0.6	1.5	0.8	2.3	1.3	3.3	1.8
HT. TR. Coeff. BTU/hr.ft.^{2}°F	2541	2981	2361	2769	2068	2427	1924	2253
Helium Velocity, ft/s	251	276	263	290	220	244	231	255
Coolant Inlet Temperature, °C	259	249	305	295	268	261	316	308
Coolant Exit Temperature, °C	459	449	605	595	468	461	616	608
Wall ΔT, °C	8.0	11.1	8.0	10.0	6.0	8.0	6.0	8.0
Thermal Stress ksi	2.7	3.4	2.6	3.4	2.0	2.5	1.9	2.5
No. of Tubes, Thousands[a]	939	3435	585	2149	174	644	109	398
Total Tube Weight, Tons[a]	74	96	71	91	54	69	52	66

[a]Based on a reactor with a first wall area of ∿ 1000 m^2

$T(CE) = T(MAX) - 17.9\ P_w - 21.9$

$T(CE) = T(MAX) - 41.3\ P_w - 21.4$

LIST OF FIGURES

No.

1 Variation in the cost of energy with reactor thermal power. ($A = 3$, $\kappa = 1.65$, $q = 3$, $d = 0.5$, $\Delta^i_{BS} = 1$ m, $B_m = 9$ T, $t_d = 80$ d). Results are shown for both stainless steel ($T_{max} = 500°C$, lifetime ~ 3.1 MW-yr/m^2) and a vanadium alloy ($T_{max} = 650°C$, lifetime ~ 34 MW-yr/m^2) as the first wall and blanket structure.

2 Cost of energy as a function of maximum toroidal-field strength and plasma β_t for reactors with thermal power of 3000 MWt ($A = 3$, $\kappa = 1.65$, $q = 3$, $d = 0.5$, $\Delta^i_{BS} = 1$ m, $t_d = 80$ d; lithium-cooled vanadium alloy structure with $T_{max} = 650°C$ and lifetime ~ 34 MW-yr/m^2).

3 Total plant capital cost for the class of reactors shown in Fig. 2.

4 Capital cost of poloidal coils and their power supply for the class of reactors shown in Fig. 2.

5 Cost of energy as a function of maximum toroidal-field strength and plasma β_t for reactors with thermal power of 3000 MWt ($A = 4$, $\kappa = 1.3$, $q = 3$, $d = 0.25$, $\Delta^i_{BS} = 1$ m, $t_d = 80$ d; lithium-cooled vanadium alloy structure with $T_{max} = 650°C$ and lifetime ~ 34 MW-yr/m^2).

6 Cost of energy as a function of maximum toroidal-field strength and plasma β_t for reactors with thermal power of 7000 MWt ($A = 4$, $\kappa = 1.3$, $q = 3$, $d = 0.25$, $\Delta^i_{BS} = 1$ m, $t_d = 80$ d; lithium-cooled vanadium alloy structure with $T_{max} = 650°C$ and lifetime ~ 34 MW-yr/m^2).

7 Cost of energy as a function of the aspect ratio for three scenarios for the β_t dependence on κ.

8 Cost of energy as a function of plasma elongation, κ, for three scenarios for the β_t dependence on κ.

9 Cost of energy as a function of Δ^i_{BS}, the distance in midplane from the first wall to the location of maximum toroidal field ($A = 3$, $P_w = 3$ MW/m^2, $\kappa = 1.0$).

10 Neutron wall load as a function of β_t and toroidal-field strength for reactors with $P_{th} = 3000$ MWt, $\kappa = 1.3$, $A = 4$, $q = 3$, and $\Delta^i_{BS} = 1$ m.

No.

11 Cost of energy versus neutron wall load displayed for lines of constant thermal power (variable β_t) and for lines of constant β_t (variable P_{th}). Results are for A = 3, κ = 1.65, d = 0.5, q = 3, Δ^i_{BS} = 1 m, B_m = 9 T; lithium-cooled structural alloy with vanadium properties and cost, T_{max} = 650°C, lifetime ~34 MW-yr/m^2, t_d = 80 d.

12 Cost of energy versus neutron wall load displayed for lines of constant thermal power (variable β_t) and for lines of constant β_t (variable P_{th}). Results are for A = 3, κ = 1.65, d = 0.5, q = 3, Δ^i_{BS} = 1 m, B_m = 9 T; lithium-cooled structural alloy with stainless steel properties and cost, T_{max} = 500°C, lifetime ~3.1 MW-yr/m^2, t_d = 80 d.

13 Sensitivity of the cost of energy to the lifetime (integrated exposure in MW-yr/m^2) of the first wall at various reactor thermal power and neutron wall load.

14 Simplified model of the lithium blanket cell used in the thermal hydraulic analyses.

15 Simplified model of the helium-cooled stagnant lithium blanket used in the thermal hydraulic analyses.

16 Effect of cell wall thickness and maximum toroidal field on maximum allowable neutron wall loading for the lithium-cooled-stainless steel blanket cell.

17 Effect of cell wall thickness and maximum toroidal field on maximum allowable neutron wall loading for the lithium-cooled-vanadium alloy blanket cell.

18 Toroidal field versus major radius for various aspect ratios and betas; κ = 1.3, d = 0.25, q = 3.0, α = 1.4, Z_{eff} = 1.7, $\bar{T}_e$ = 8 keV, α_n = 0.3, Δ^i_{BS} = 1.0 m, P_{th} = 2500 MW.

19 Plasma current versus major radius; κ = 1.3, d = 0.25, q = 3.0, α = 1.4, Z_{eff} = 1.7, $\bar{T}_e$ = 8 keV, α_n = 0.3, Δ^i_{BS} = 1.0 m, P_{th} = 2500 MW.

No.

20 Toroidal field versus major radius for various elongations and betas; $A = 3.0$, $q = 3.0$, $\alpha = 1.4$, $Z_{eff} = 1.7$, $\bar{T}_e = 8$ keV, $\alpha_n = 0.3$, $\Delta^i_{BS} = 1.0$ m, $P_{th} = 2500$ MW.

21 Plasma current versus major radius; $A = 3.0$, $q = 3.0$, $\alpha = 1.4$, $Z_{eff} = 1.7$, $\bar{T}_e = 8$ keV, $\alpha_n = 0.3$, $\Delta^i_{BS} = 1.0$ m, $P_{th} = 2500$ MW.

22 Schematic view of OH and EF coil locations.

23 Power supply Configuration No. 1.

24 Typical startup, using an SCR-type power supply as the OH transfer element; $V_{OH} = 60$ V/turn, $t_{B_0} = \Delta t_{OH}$.

25 Sensitivity of the driving system requirements to the ohmic heating ramp time, Δt_{OH}. For a homopolar generator used as the OH energy transfer device and for the neutral beam turn-on time, $t_{B_0} = \Delta t_{OH}$.

26 Total driving system power supply cost as a function of the OH ramp time, Δt_{OH}, and power supply configuration. For the neutral beam turn-on time, $t_{B_0} = \Delta t_{OH}$.

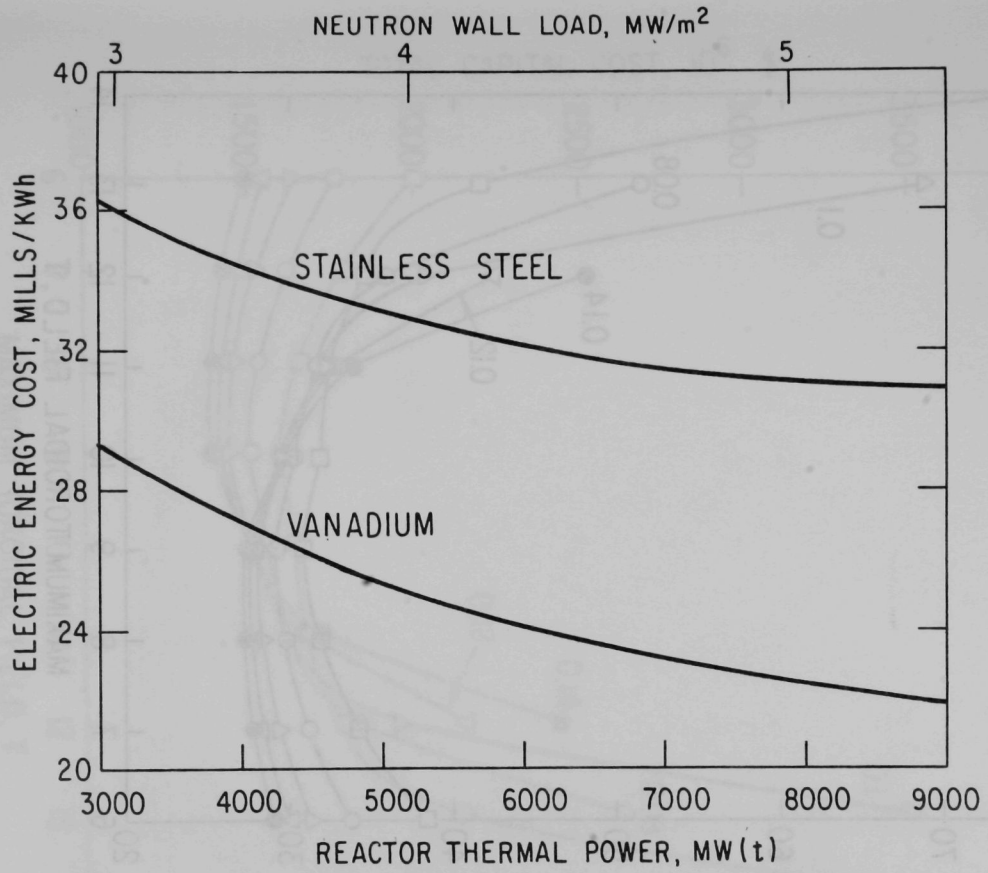

Fig. 1. Variation in the cost of energy with reactor thermal power. ($A = 3$, $\kappa = 1.65$, $q = 3$, $d = 0.5$, $\Delta^{i}_{BS} = 1$ m, $B_m = 9$ T, $t_d = 80$ d). Results are shown for both stainless steel ($T_{max} = 500°C$, lifetime $\sim$3.1 MW-yr/m^2) and a vanadium alloy ($T_{max} = 650°C$, lifetime $\sim$34 MW-yr/m^2) as the first wall and blanket structure.

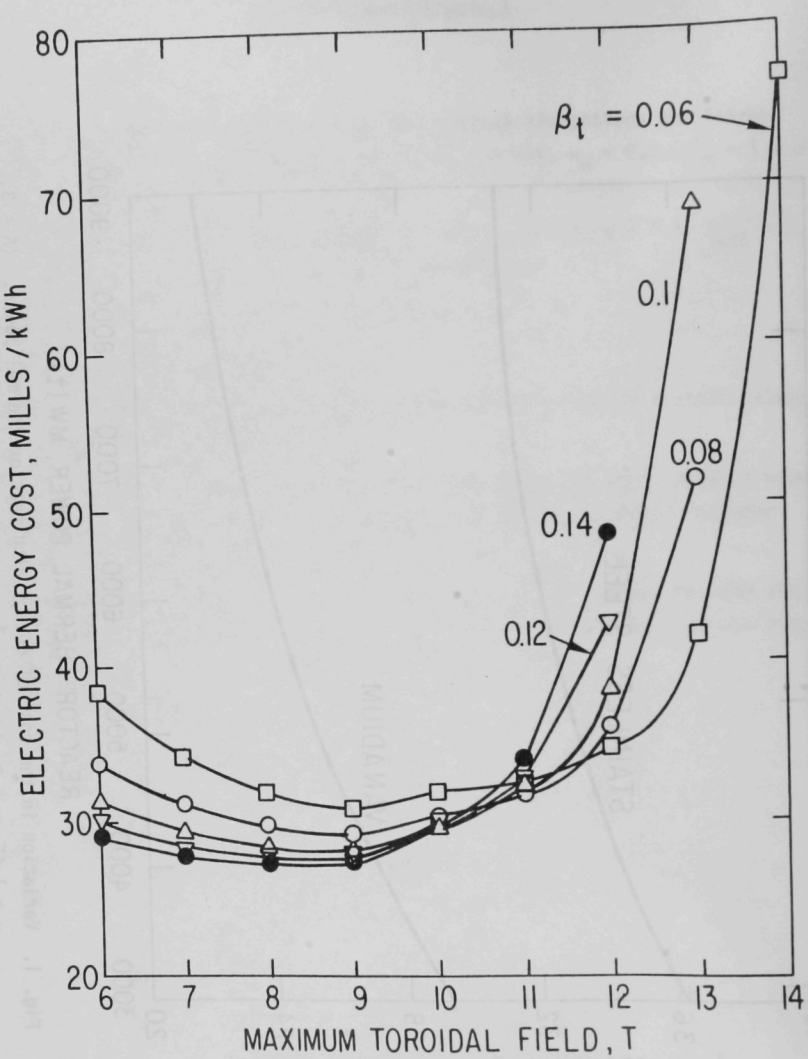

Fig. 2. Cost of energy as a function of maximum toroidal-field strength and plasma β_t for reactors with thermal power of 3000 MWt ($A = 3$, $\kappa = 1.65$, $q = 3$, $d = 0.5$, $\Delta^i_{BS} = 1$ m, $t_d = 80$ d; lithium-cooled vanadium alloy structure with $T_{max} = 650°C$ and lifetime $\sim$34 MW-yr/m^2).

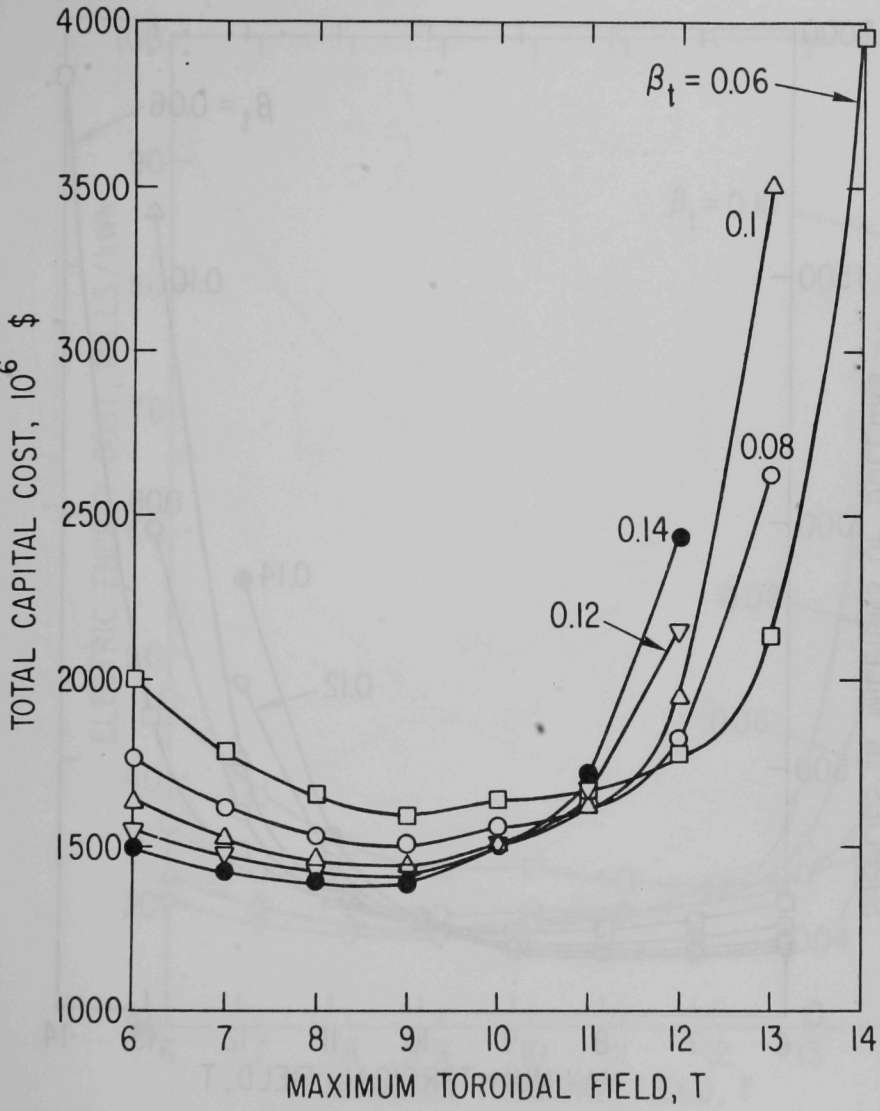

Fig. 3. Total plant capital cost for the class of reactors shown in Fig. 2.

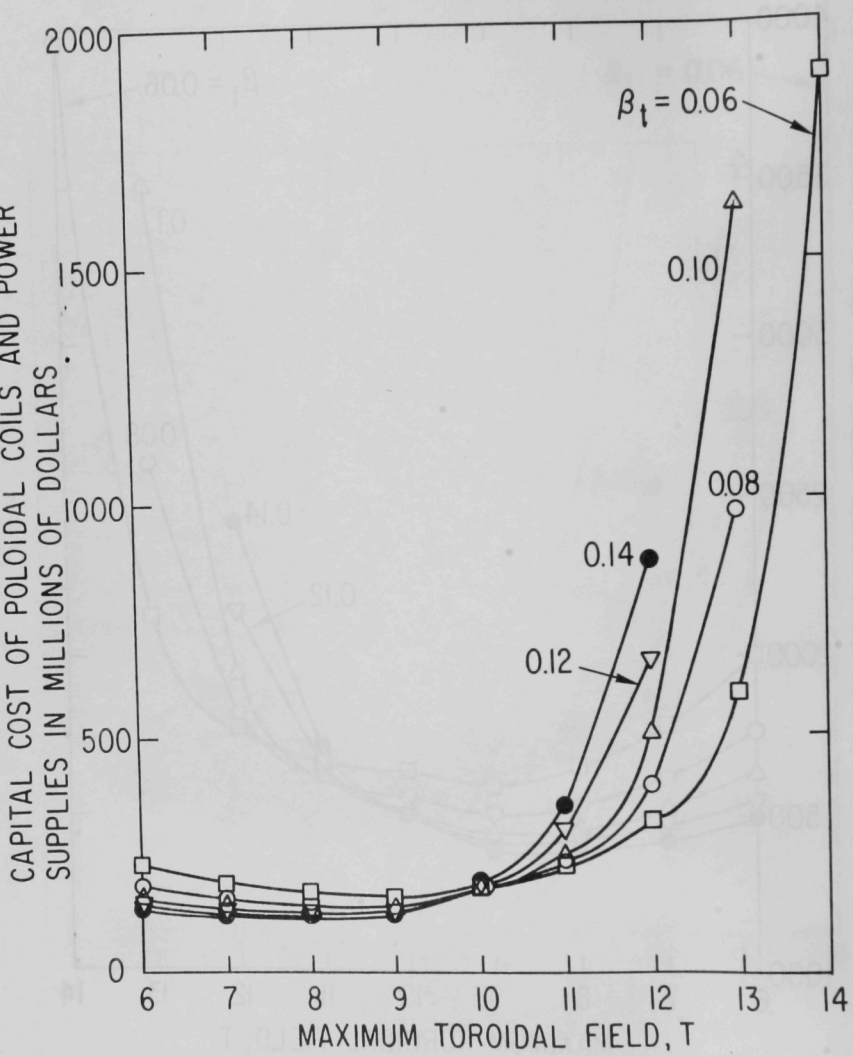

Fig. 4. Capital cost of poloidal coils and their power supply for the class of reactors shown in Fig. 2.

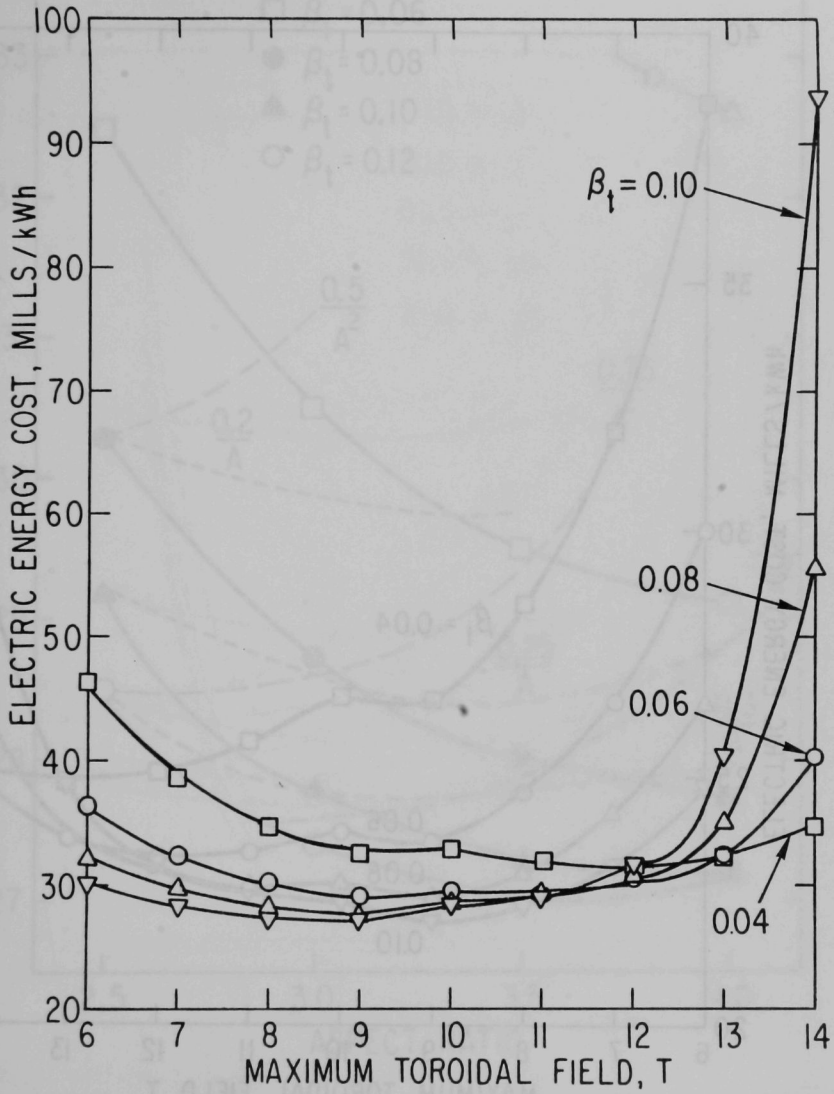

Fig. 5. Cost of energy as a function of maximum toroidal-field strength and plasma β_t for reactors with thermal power of 3000 MWt (A = 4, κ = 1.3, q = 3, d = 0.25, Δ^i_{BS} = 1 m, t_d = 80 d; lithium-cooled vanadium alloy structure with T_{max} = 650°C and lifetime ∿34 MW-yr/m^2).

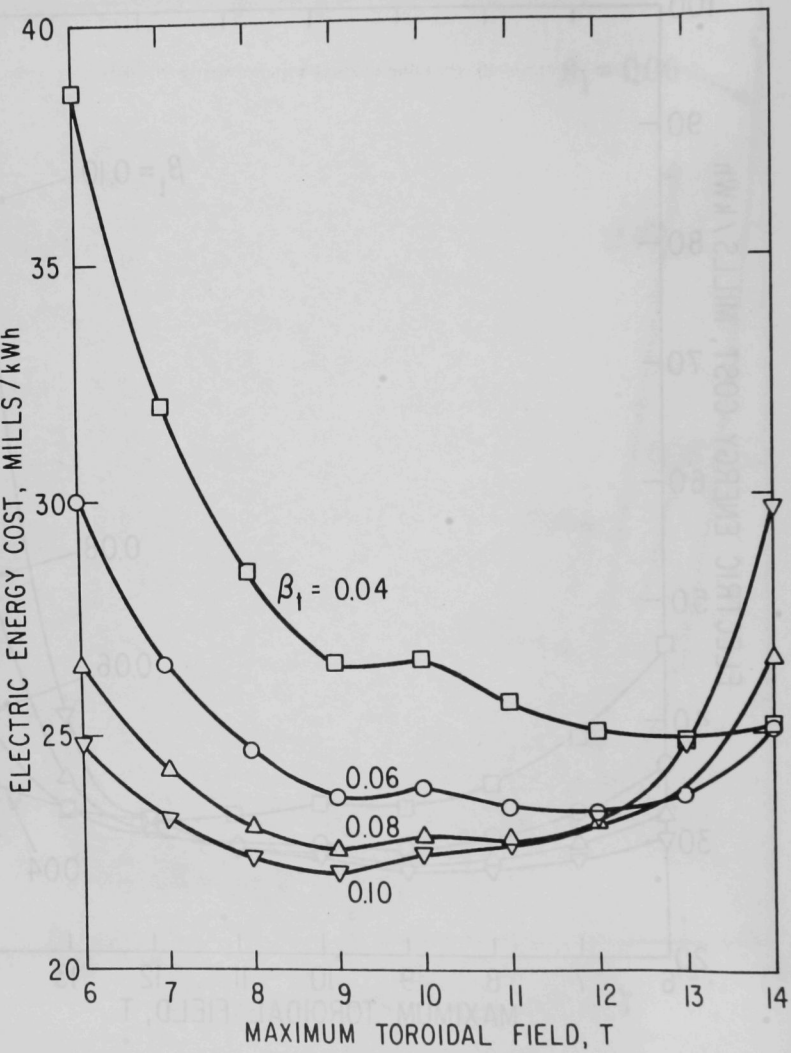

Fig. 6. Cost of energy as a function of maximum toroidal-field strength and plasma β_t for reactors with thermal power of 7000 MWt ($A = 4$, $\kappa = 1.3$, $q = 3$, $d = 0.25$, $\Delta^i_{BS} = 1$ m, $t_d = 80$ d; lithium-cooled vanadium alloy structure with $T_{max} = 650°C$ and lifetime ~34 MW-yr/m^2).

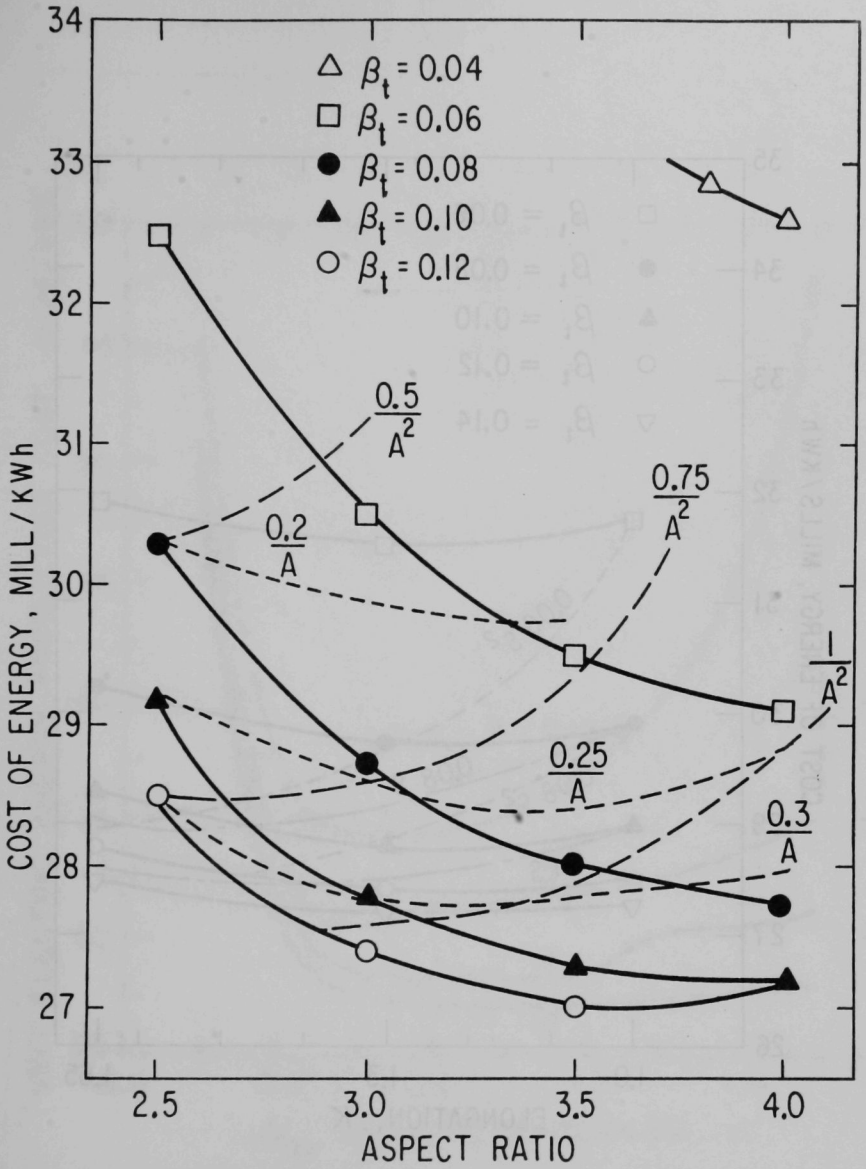

Fig. 7. Cost of energy as a function of the aspect ratio for three scenarios for the β_t dependence on A.

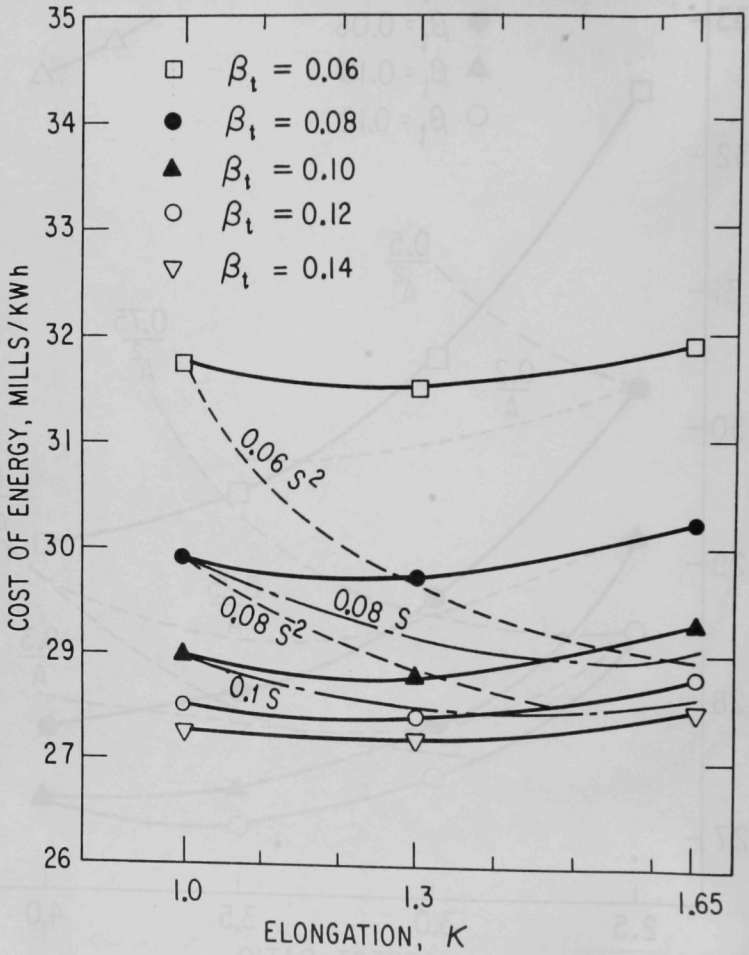

Fig. 8. Cost of energy as a function of plasma elongation, κ, for three scenarios for the β_t dependence on κ.

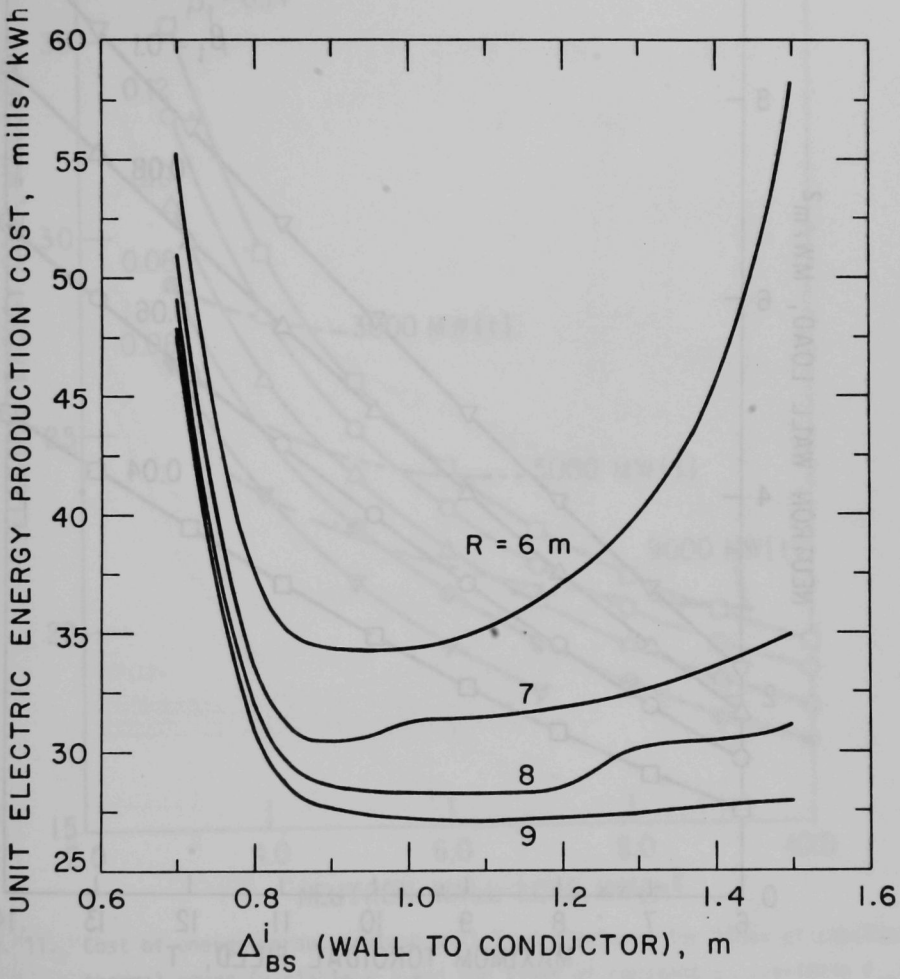

Fig. 9. Cost of energy as a function of Δ^i_{BS}, the distance in midplane from the first wall to the location of maximum toroidal field ($A = 3$, $P_w = 3\ MW/m^2$, $\kappa = 1.0$).

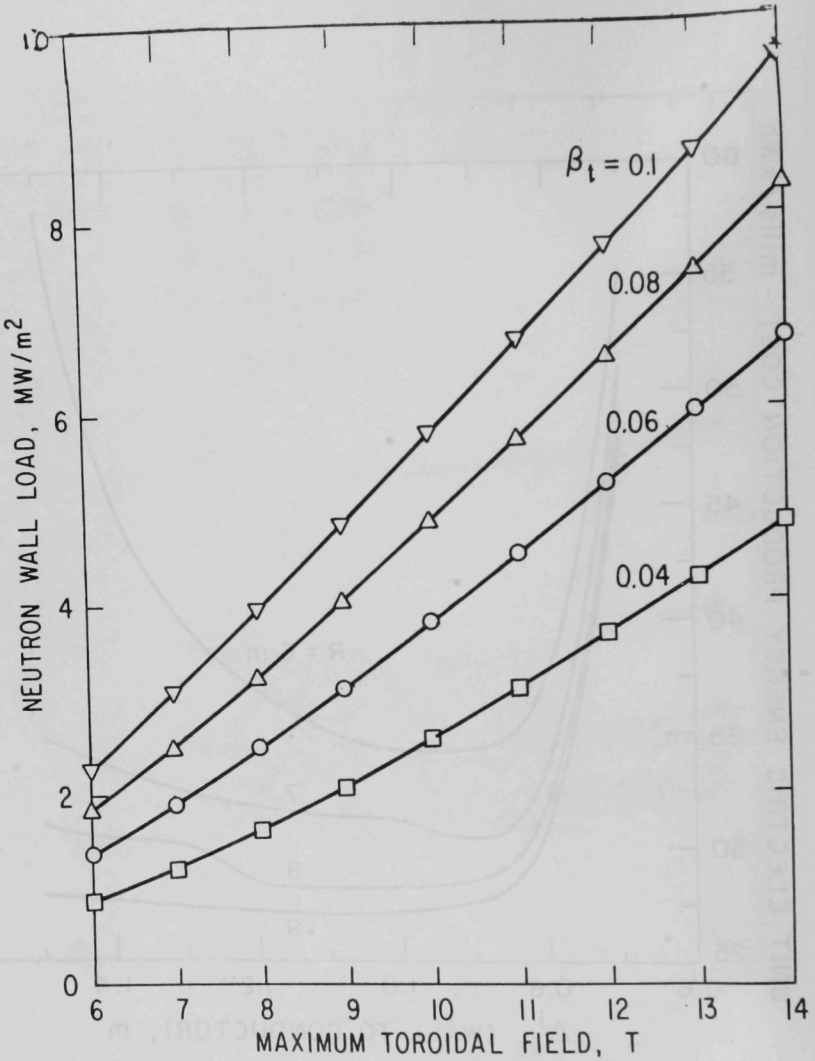

Fig. 10. Neutron wall load as a function of β_t and toroidal-field strength for reactors with P_{th} = 3000 MWt, κ = 1.3, A = 4, q = 3, and Δ^i_{BS} = 1 m.

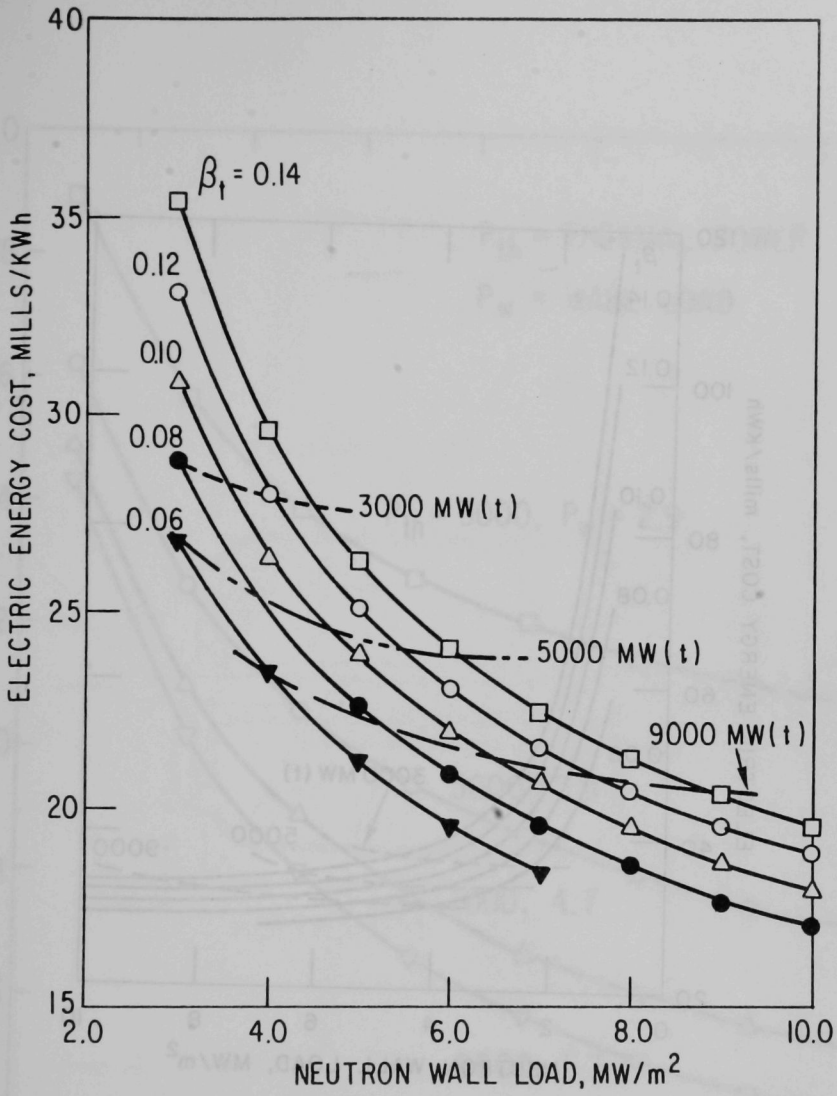

Fig. 11. Cost of energy versus neutron wall load displayed for lines of constant thermal power (variable β_t) and for lines of constant β_t (variable P_{th}). Results are for A = 3, κ = 1.65, d = 0.5, q = 3, Δ^i_{BS} = 1 m, B_m = 9 T; lithium-cooled structural alloy with vanadium properties and cost, T_{max} = 650°C, lifetime ∿34 MW-yr/m², t_d = 80 d.

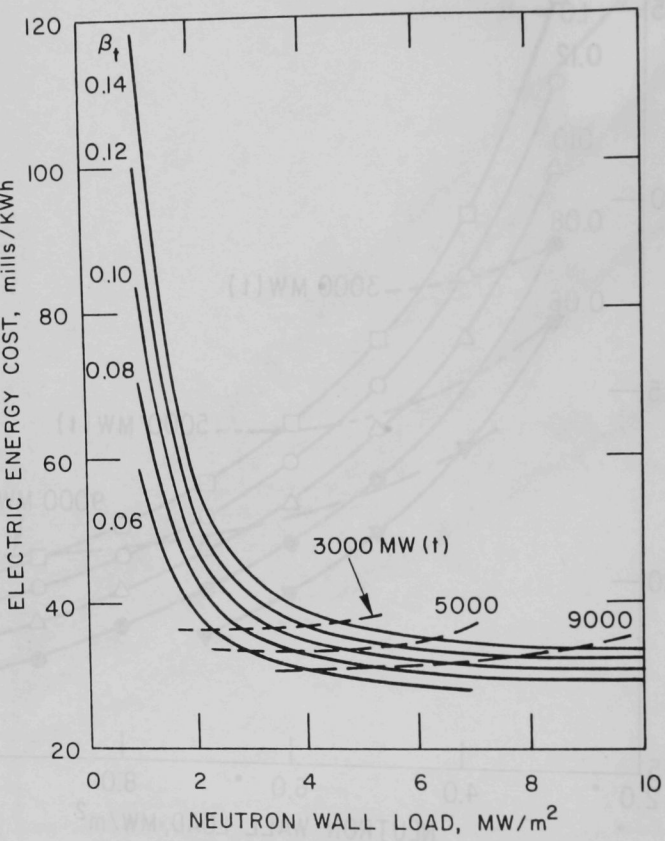

Fig. 12. Cost of energy versus neutron wall load displayed for lines of constant thermal power (variable β_t) and for lines of constant β_t (variable P_{th}). Results are for A = 3, κ = 1.65, d = 0.5, q = 3, Δ^i_{BS} = 1 m, B_m = 9 T; lithium-cooled structural alloy with stainless steel properties and cost, T_{max} = 500°C, lifetime ∿3.1 MW-yr/m^2, t_d = 80 d.

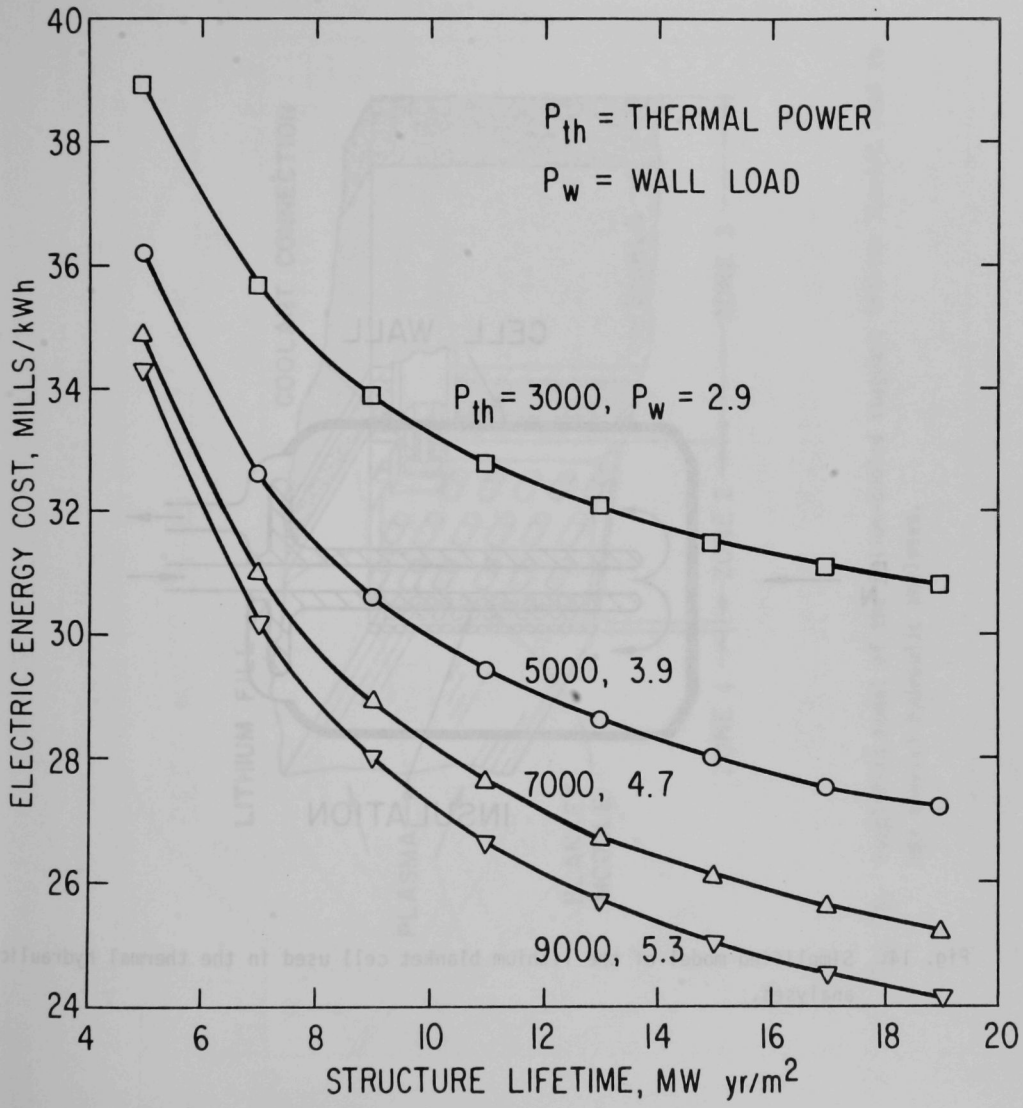

Fig. 13. Sensitivity of the cost of energy to the lifetime (integrated exposure in MW-yr/m^2) of the first wall at various reactor thermal power and neutron wall load.

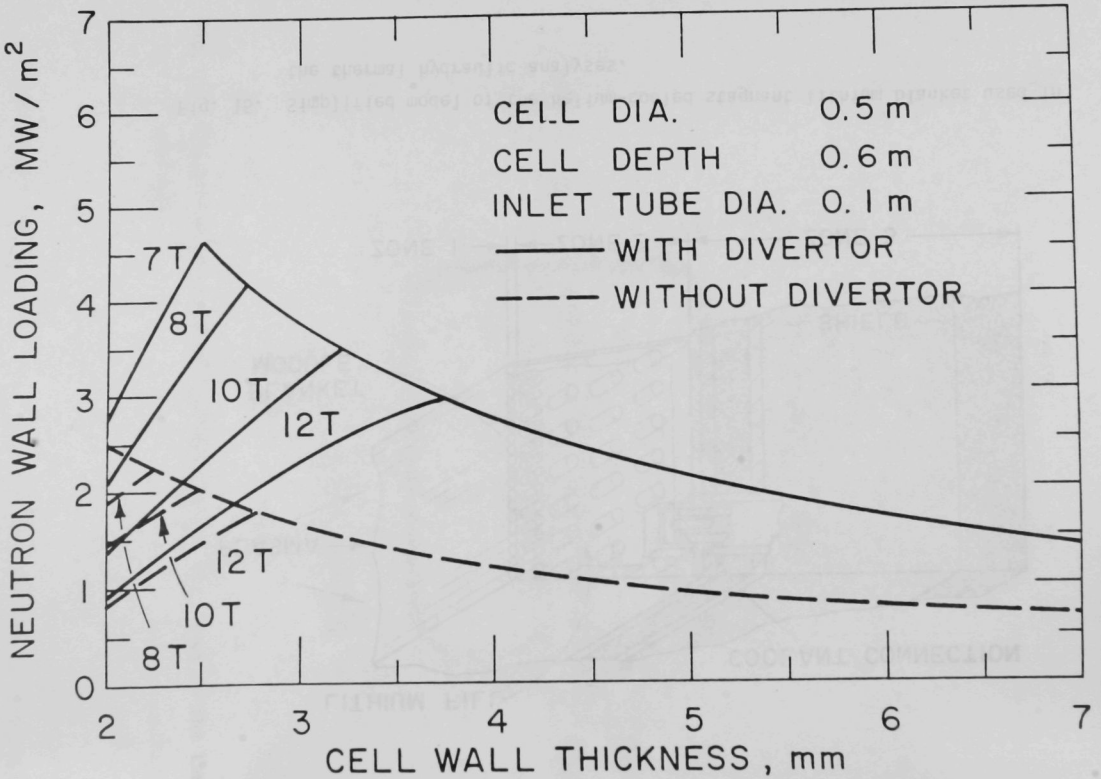

Fig. 16. Effect of cell wall thickness and maximum toroidal field on maximum allowable neutron wall loading for the lithium-cooled-stainless steel blanket cell.

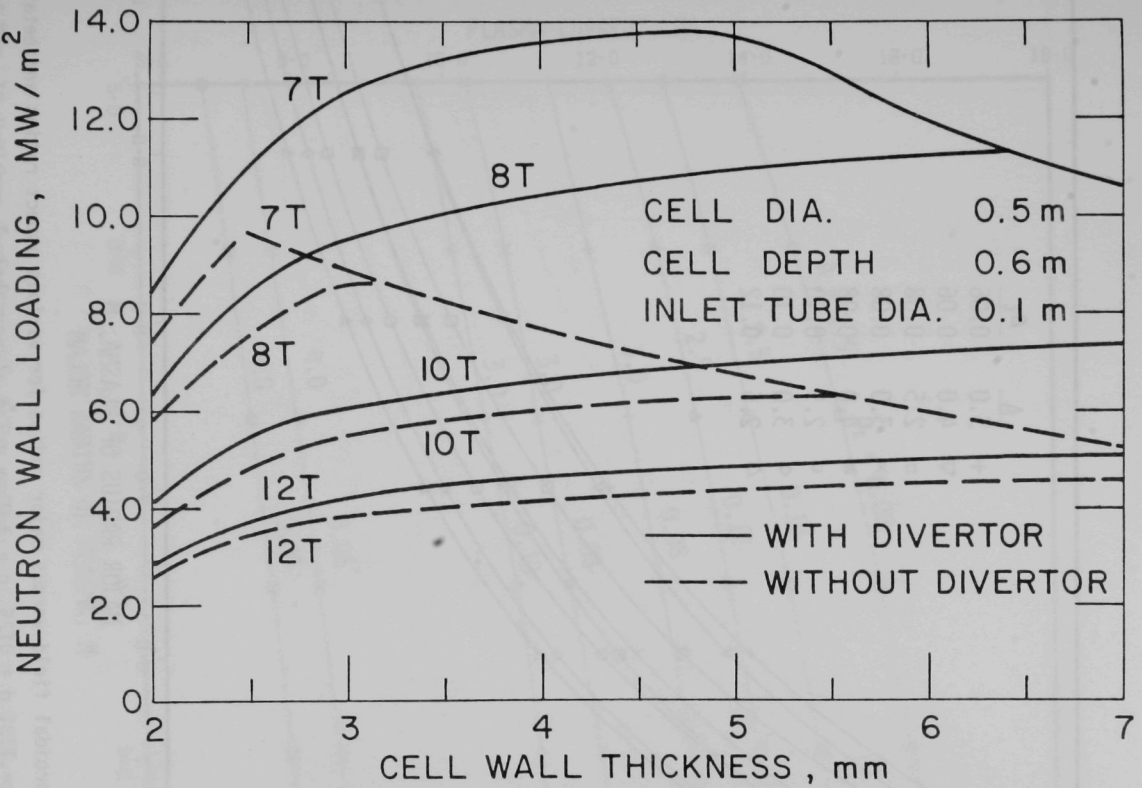

Fig. 17. Effect of cell wall thickness and maximum toroidal field on maximum allowable neutron wall loading for the lithium-cooled-vanadium alloy

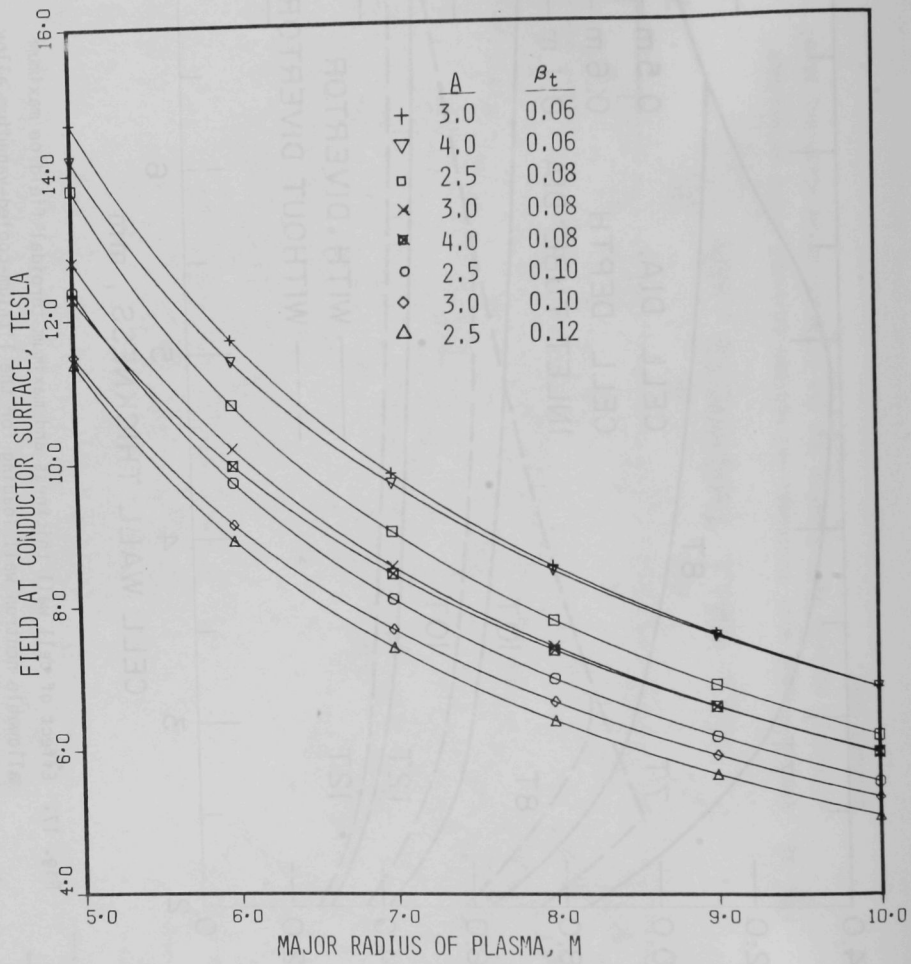

Fig. 18. Toroidal field versus major radius for various aspect ratios and betas; $\kappa = 1.3$, $d = 0.25$, $q = 3.0$, $\alpha = 1.4$, $Z_{eff} = 1.7$, $\bar{T}_e = 8$ keV, $\alpha_n = 0.3$, $\Delta^i_{BS} = 1.0$ m, $P_{th} = 2500$ MW.

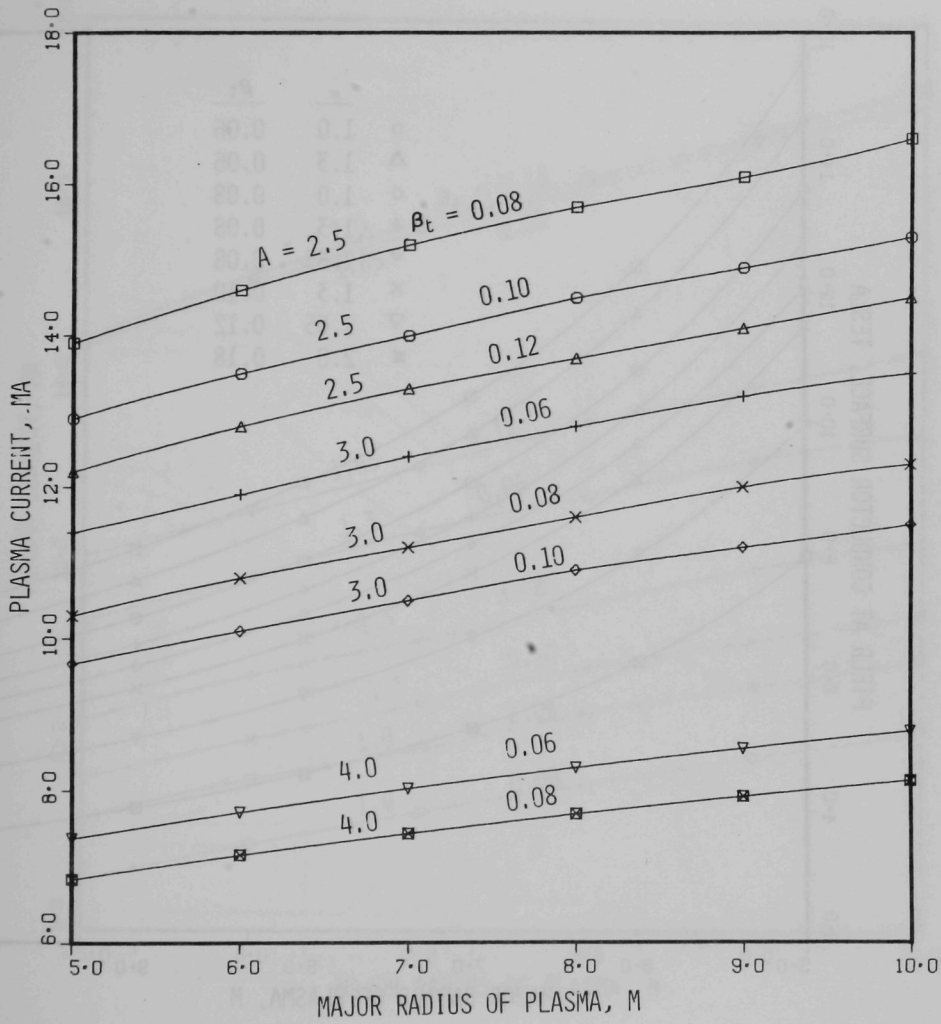

Fig. 19. Plasma current versus major radius; κ = 1.3, d = 0.25, q = 3.0, α = 1.4, Z_{eff} = 1.7, $\bar{T}_e$ = 8 keV, α_n = 0.3, Δ^i_{BS} = 1.0 m, P_{th} = 2500 MW.

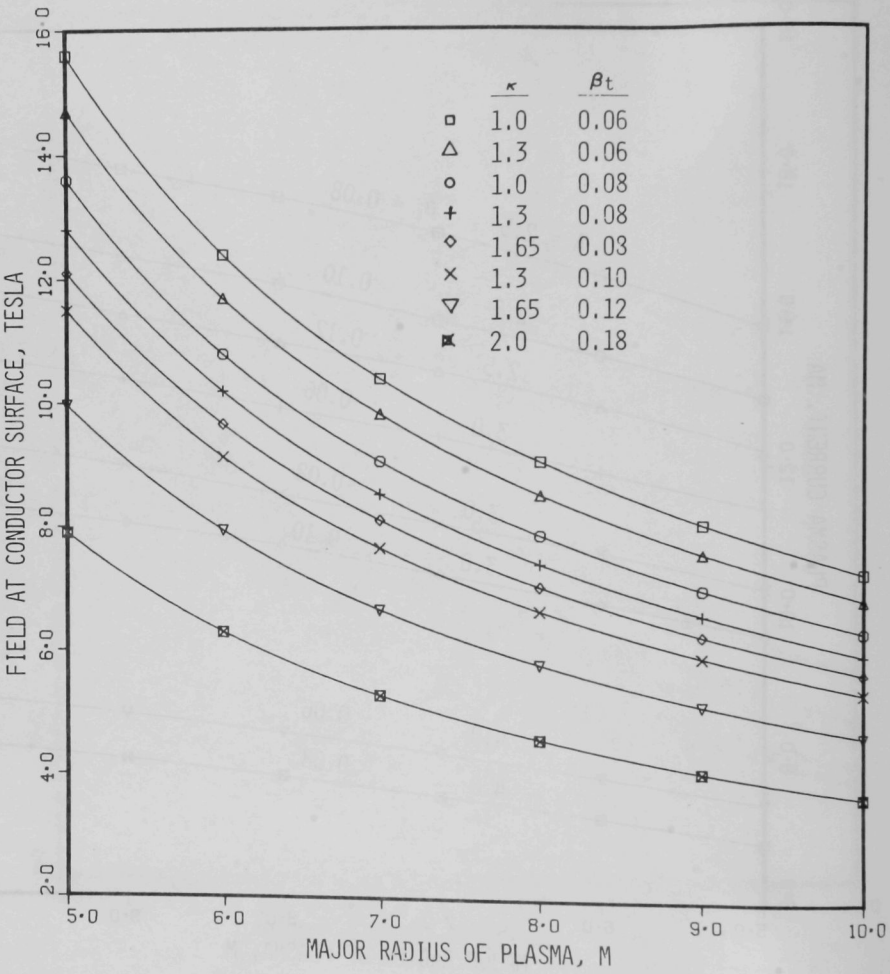

Fig. 20. Toroidal field versus major radius for various elongations and betas; $A = 3.0$, $q = 3.0$, $\alpha = 1.4$, $Z_{eff} = 1.7$, $\bar{T}_e = 8$ keV, $\alpha_n = 0.3$, $\Delta^i_{BS} = 1.0$ m, $P_{th} = 2500$ MW.

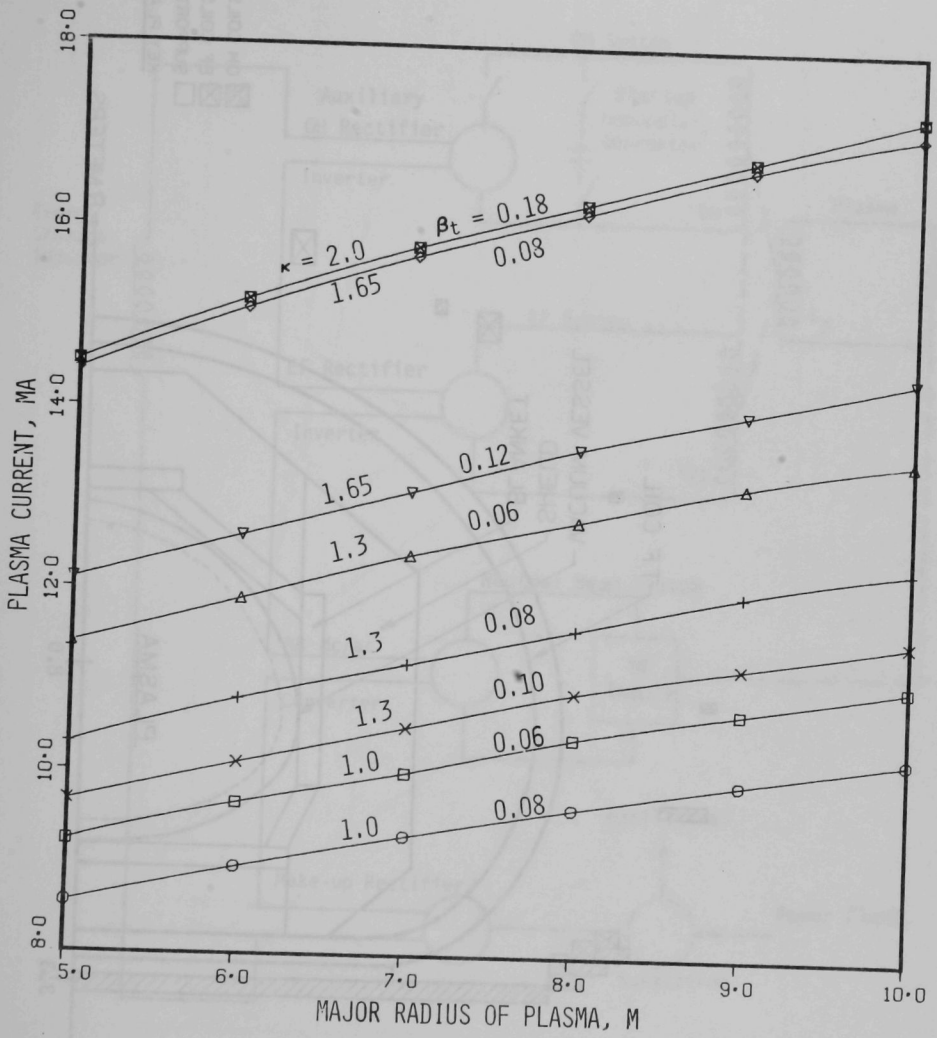

. 21. Plasma current versus major radius; A = 3.0, q = 3.0, α = 1.4, Z_{eff} = 1.7, $\bar{T}_e$ = 8 keV, α_n = 0.3, Δ^i_{BS} = 1.0 m, P_{th} = 2500 MW.

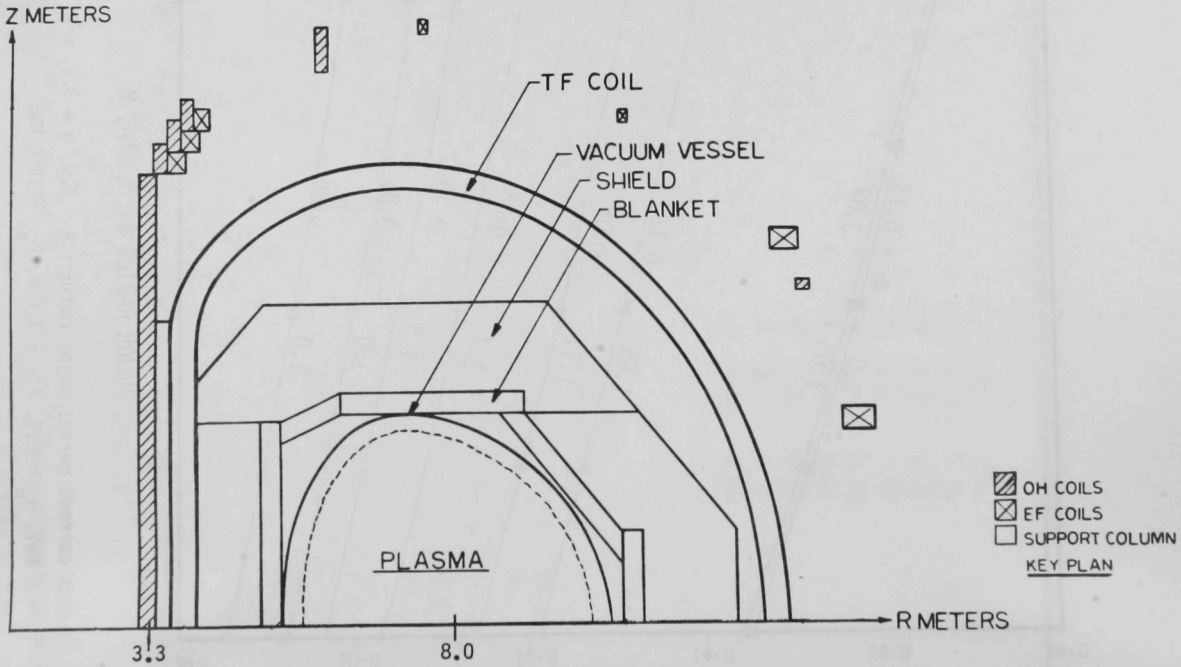

Fig. 22. Schematic view of OH and EF coil locations.

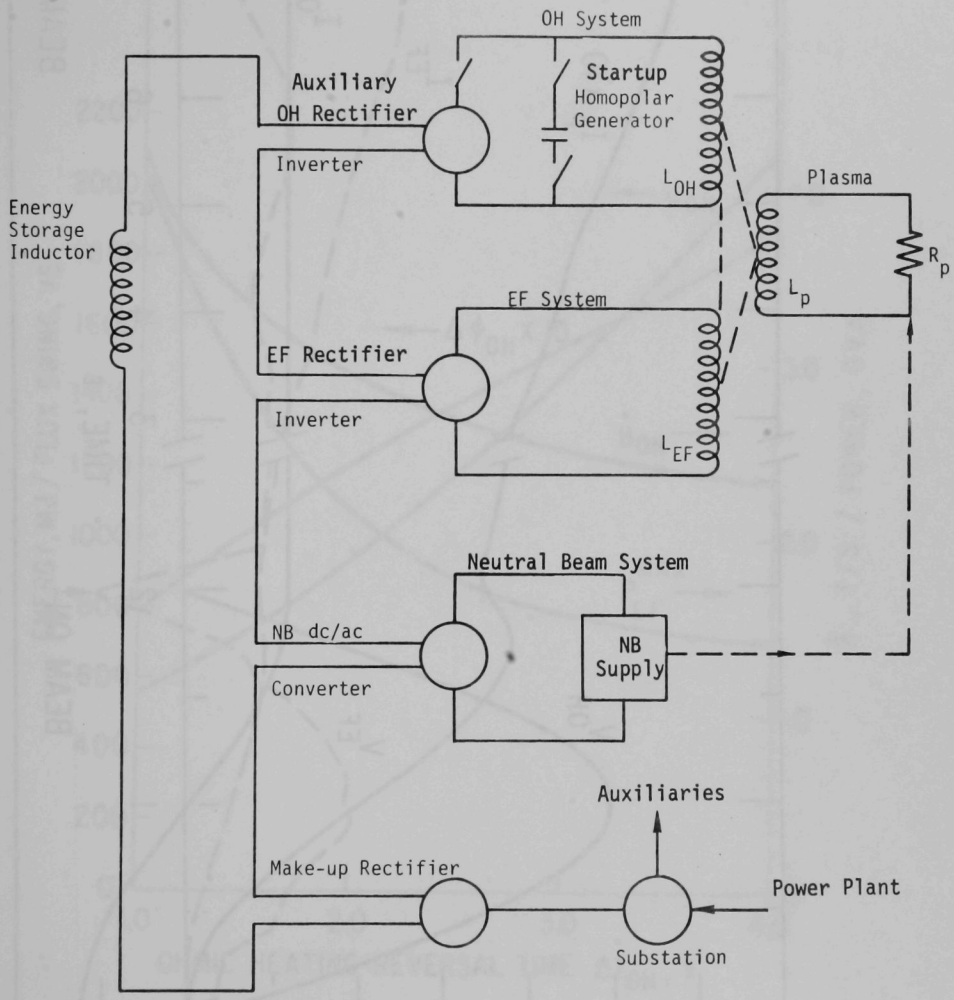

Fig. 23. Power Supply Configuration No. 1.

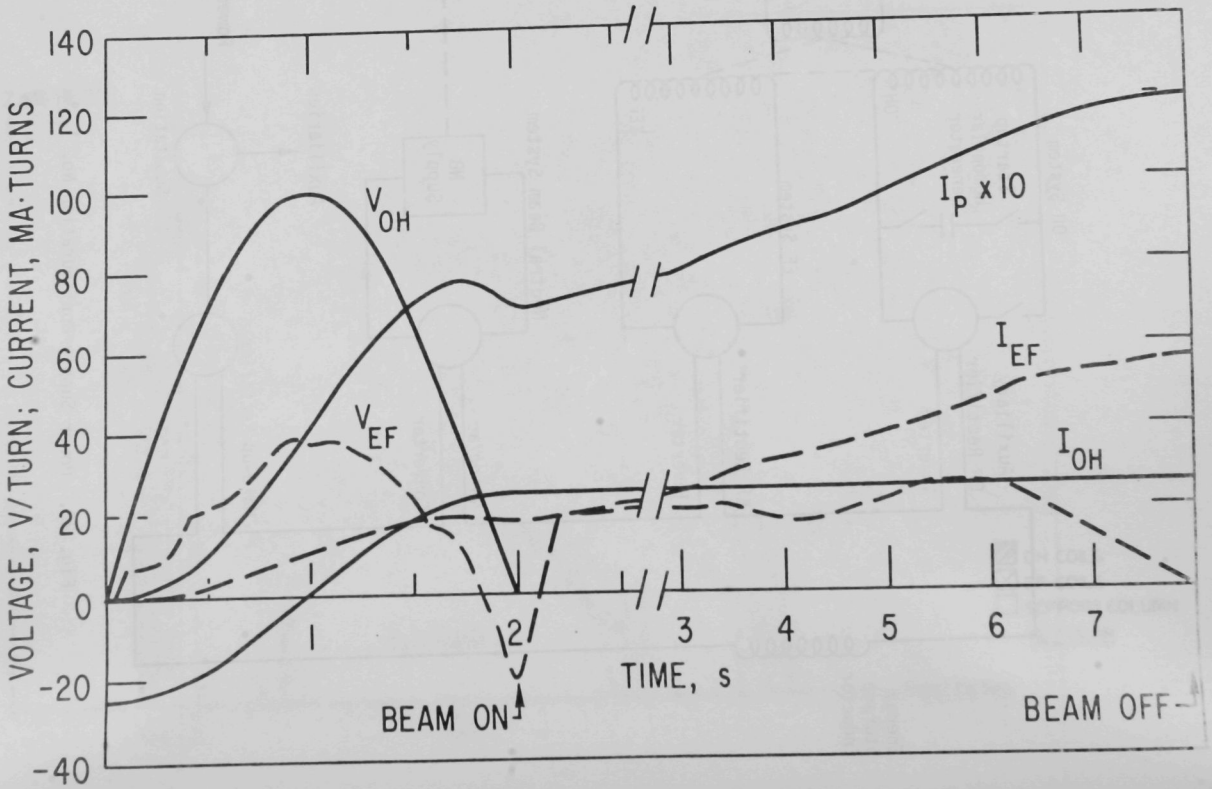

Fig. 24. Typical startup, using an SCR-type power supply as the OH transfer element. V_{OH} = 60 V/turn, $t_{B_0} = \Delta t_{OH}$.

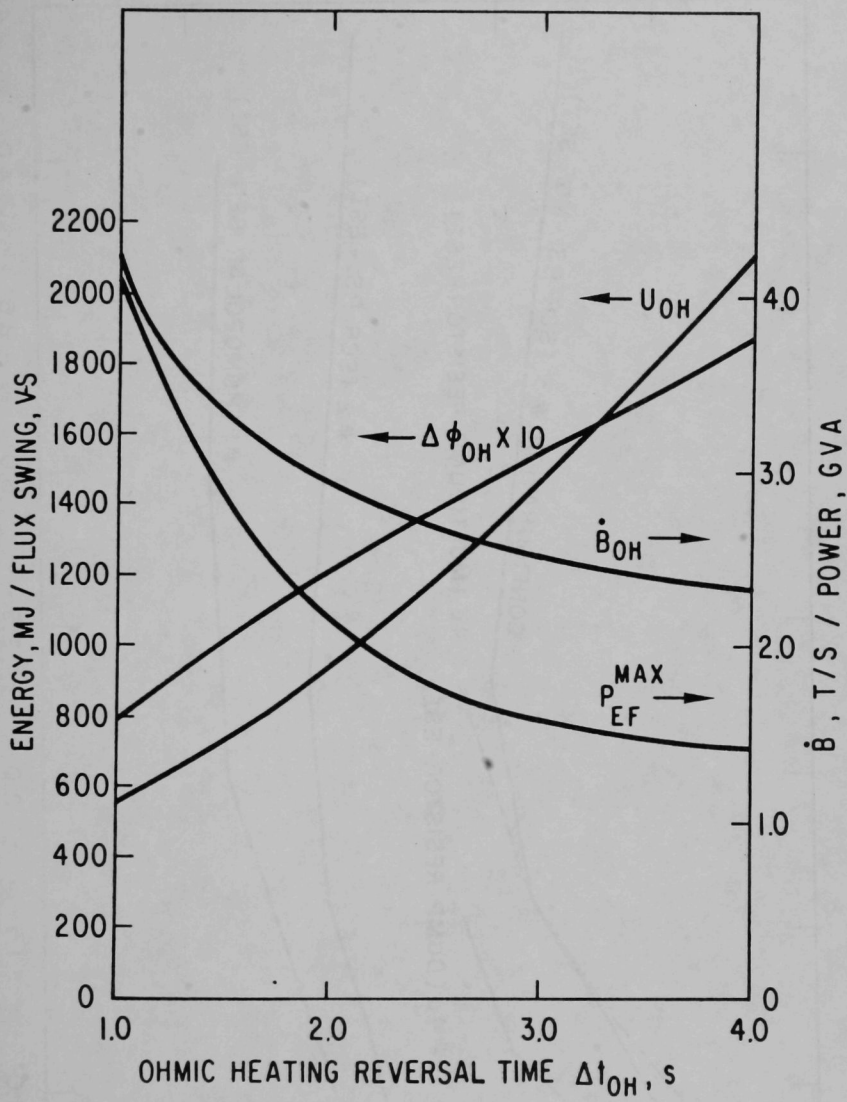

Fig. 25. Sensitivity of the driving system requirements to the ohmic heating ramp time, Δt_{OH}. For a homopolar generator used as the OH energy transfer device and for the neutral beam turn-on time, $t_{B_0} = \Delta t_{OH}$.

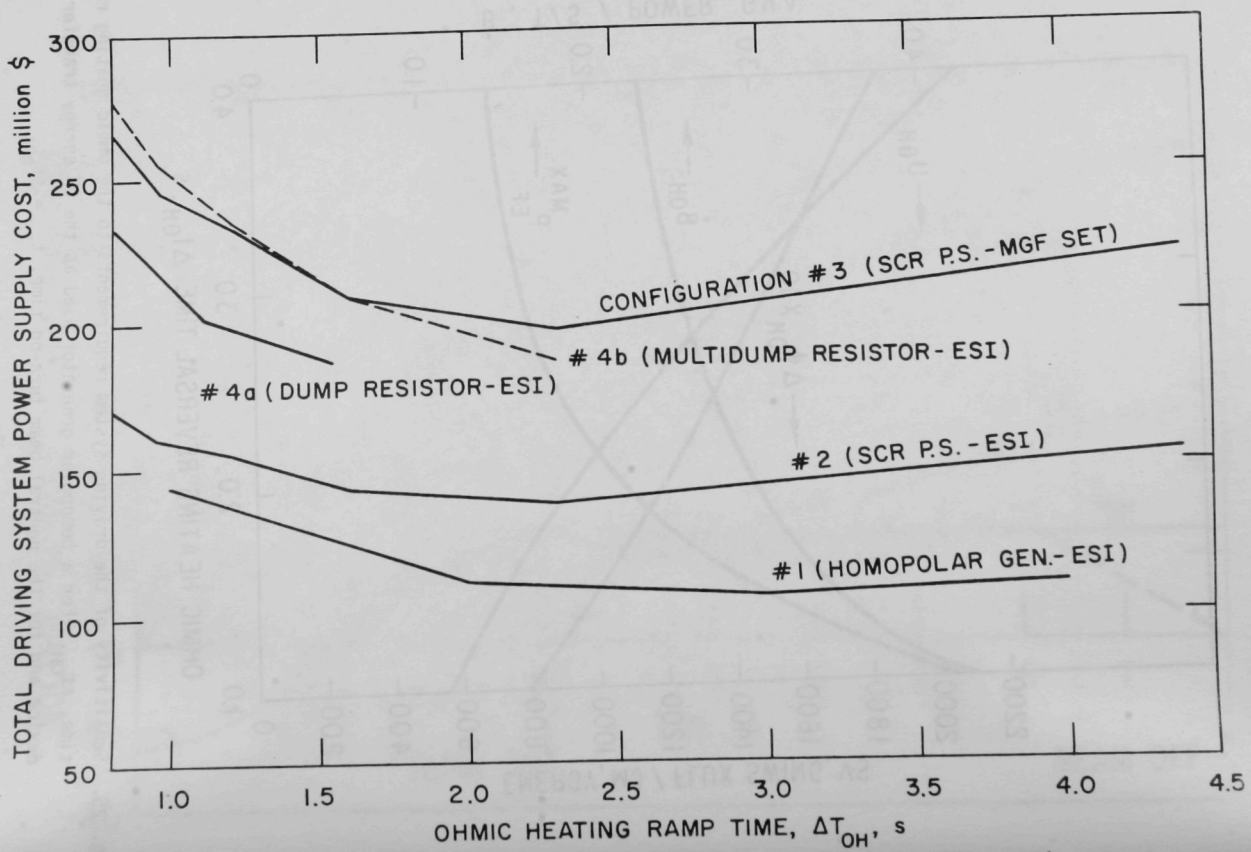

Fig. 26. Total driving system power supply cost as a function of the OH ramp time, Δt_{OH}, and power supply configuration. For the neutral beam turn-on time,

August, 1977 ANL/FPP-TM-94

THERMAL HYDRAULIC ANALYSES OF TWO FUSION REACTOR FIRST WALL/BLANKET CONCEPTS*

Balabhadra Misra and Victor A. Maroni

Fusion Power Program
Argonne National Laboratory
Argonne, Illinois 60439

Results reported in the ANL/FPP/TM series of memoranda frequently are preliminary and subject to revision. Consequently, they should not be quoted nor referenced without the author's permission.

* Work supported by the U.S. Department of Energy.

TABLE OF CONTENTS

	Page
I. Introduction	2
II. Development of the Computational Algorithms	6
A. Flowing Lithium Cooled First Wall/Blanket Concept	6
1. Pressure Loss Calculation	8
2. Heat Transfer Calculations	10
B. Helium Cooled Stagnant Lithium First Wall/Blanket Concept	13
III. Results and Discussion	17
A. Thermal Hydraulic Analyses of the Flowing Lithium Cooled First Wall/Blanket Concept	17
B. Thermal Hydraulic Analyses of the Helium Cooled Stagnant Lithium First Wall/Blanket Concept	25
IV. Conclusions	31
V. Acknowledgements	32
VI. Nomenclature	33
A. Nomenclature for Lithium Cooled First Wall/Blanket Concept	33
B. Nomenclature for Helium-Cooled First Wall/Blanket Concept	35
References	37
APPENDIX A	39

LIST OF FIGURES

Number		Page
1	Lithium-Cooled First-Wall/Blanket System	4
2	Helium Cooled Stagnant-Lithium First Wall/Blanket Concept	5
3	Simplified Model of the Lithium Blanket Cell Used in the Thermal Hydraulic Analyses (cell is assumed to be cylindrical)	7
4	Pressure Drop Diagram for the Lithium Cooled Blanket Cells	9
5	Lithium-cooled Stainless Steel Blanket Cells (cell diameter = 0.5 m, inlet tube diameter = 0.1 m)	20
6	Lithium-cooled Vanadium Alloy Blanket Cells (cell diameter = 0.5 m, inlet tube diameter = 0.1 m)	21
7	Effect of Cell Wall Thickness and Maximum Toroidal Field on Maximum Allowable Neutron Wall Loading for the Lithium Cooled Stainless Steel Blanket Cell . . .	22
8	Effect of Cell Wall Thickness and Maximum Toroidal Field on Maximum Allowable Neutron Wall Loading for the Lithium Cooled Vanadium Alloy Blanket Cell . .	23
9	Coolant Exit Temperature versus Wall Loading for the Helium Cooled Stagnant Lithium Blanket (maximum structural temperature = 500°C)	28
10	Coolant Exit Temperature versus Wall Loading for the Helium Cooled Stagnant Lithium Blanket (maximum structural temperature = 650°C)	29

LIST OF TABLES

Number		Page
1	Reference Design Parameters for Comparisons of Stainless Steel and Vanadium Alloy Systems	3
2	Array of Variables for First Wall/Blanket Thermal Hydraulic Analyses	3
3	Results of Wall Loading Trade Studies for Lithium-Cooled Stainless Steel and Vanadium-Alloy Blanket Systems	18
4	Summary of Trade Studies on Materials Limitations for Lithium-Cooled Stainless Steel Blanket Cells	19
5	Summary of Trade Studies on Materials Limitations for Lithium-Cooled Vanadium Alloy Blanket Cells	19
6	Trade Study for Helium Cooled Stagnant Lithium Blanket Using Transverse Cooling Channels made of Stainless Steel: First Wall Configuration is a Single Layer of Closed-packed Tubes	26
A-1	FORTRAN Listing for Computer Program BLANKET Including Subroutines LITHIUM and HELIUM	45
A-2	Input Data for Subroutine LITHIUM	39
A-3	Input Data for Subroutine HELIUM	42
A-4	Typical Output Format for Subroutine LITHIUM	59
A-5	Typical Output Format for Subroutine HELIUM	61

ABSTRACT

A comparative study has been made of the thermal hydraulic performance of two liquid lithium blanket concepts for tokamak-type reactors. In one concept lithium is circulated through 60-cm deep cylindrical modules oriented so that the module axis is parallel to the reactor minor radius. In the other concept helium carrying channels oriented parallel to the first wall are used to cool a 60-cm thick stagnant lithium blanket. Paralleling studies were carried out wherein the thermal and structural properties of the construction materials were based on those projected for either solution-annealed 316-stainless steel or vanadium-base alloys. The effects of limitations on allowable peak structural temperature, material strength, thermal stress, coolant inlet temperature, and pumping power/thermal power ratio were evaluated. Consequences to thermal hydraulic performance resulting from the presence of or absence of a divertor were also investigated. For the case of lithium cooled modules operated in a reactor without a divertor, the following results were obtained: (a) with stainless steel as construction material and a peak structural temperature of 500°C, the neutron wall loading and coolant exit temperature are limited to ≤ 2 MW/m^2 and ≤ 480°C, respectively, by thermal stress criteria, and (b) with vanadium as construction material and a peak structural temperature of 650°C, the neutron wall loading and coolant exit temperature are limited to ≤ 8 MW/m^2 and ≤ 620°C, respectively, by a combination of constraints involving the peak structural temperature and the minimum coolant exit temperature. For the same cases in a reactor with a divertor, the maximum allowable neutron wall loading increases by from 40% (for vanadium) to 90% (for stainless steel). For the case of a helium cooled stagnant blanket interfaced with a helium cooled stainless steel first-wall assembly, the maximum wall loading is limited by thermal stress criteria to ≤ 2.5 MW/m^2 without a divertor and to ≤ 6.0 MW/m^2 with a divertor.

I. Introduction

In order to shed some light on the question of optimum power cycle concepts for commercial fusion plants, a series of studies has been initiated at ANL to evaluate and compare alternative breeding/heat-transfer/power-conversion systems.[1,2] The objectives of these studies are to (a) examine the range of operating conditions achievable with existing materials, (b) determine the materials properties required to accommodate specified regimes of wall loading and operating temperature, (c) develop a basis for predicting material response and lifetime limits in commercial reactor environments, (d) develop the formalisms required to evaluate thermal-hydraulic and thermomechanical performance of first-wall/blanket systems, (e) develop reliable algorithms for predicting the cost of fabricating and maintaining heat transfer and energy conversion systems, and (f) integrate the above methodology into ongoing systems analyses in order to make comprehensive and meaningful assessments of commercial tokamak reactor energy conversion systems.

To establish the basis for parametric investigations of energy conversion systems for commercial reactors, analyses of first-wall/blanket thermal-hydraulic response were carried out with the life-limiting properties of the structural materials as the primary constraints. The thermal hydraulic calculations are based on a set of reference design parameters as given in Table 1. Table 2 summarizes the important independent and dependent variables that were considered in this study.

As indicated in Table 2, two generically similar blanket concepts were evaluated in the studies reported herein. One involves the use of flowing lithium as a heat transfer and breeding medium in a modular blanket of the type shown in Figure 1. The other uses pressurized helium as the heat transfer fluid flowing (in channels) through a "sea" of stagnant liquid lithium as illustrated in Figure 2. Instead of basing the analyses on arbitrarily selected materials about which little is known regarding behavior in the anticipated harsh radiation environment and compatibility with the proposed coolants, solution-annealed type 316 stainless steel and vanadium-base alloys were selected for initial study as there appeared to be relatively more data available to define life-limiting properties[3] under currently conceived fusion reactor operating conditions.

Table 1. Reference Design Parameters for Comparisons of Stainless Steel and Vanadium Alloy Systems

Reactor Major Radius	8.0 m
Central Core Radius	3.0 m
First-wall Radius	3.4 m
Radiation and Particle Load Factor	
with divertor	0.10
without divertor	0.25
Blanket Thickness	0.6 m
Shield Thickness	0.9 m
Magnet Thickness	0.52 m
Basic Design	Modular

Table 2. Array of Variables for First Wall/Blanket Thermal Hydraulic Analyses

Independent Variables	Dependent Variables
Flowing Lithium Concept	
Reactor Dimensions (Table 1)	Coolant Inlet Temperature
Maximum Toroidal Field	Coolant Exit Temperature
Module Dimensions	Coolant Velocity
Coolant Temperature Rise	Neutron Wall Loading
Material of Construction	Wall Temperature Gradient
Maximum Structural Temperature	Pumping Power/Thermal Power
First Wall Thickness	Total Pressure Drop
Surface Loading Factor	Thermal Stress
Nuclear Heating Rate	Pressure Stress
Helium Cooled Stagnant Lithium Concept	
Reactor Dimensions (Table 1)	Channel Wall Thickness
First Wall Dimensions	Channel Length
Coolant Pressure	Heat Transfer Coefficient
Coolant Temperature Rise	Coolant Inlet Temperature
Material of Construction	Coolant Exit Temperature
Maximum Structural Temperature	Wall Temperature Gradient
Coolant Void Fraction (Blanket)	Coolant Velocity (Blanket)
Coolant Velocity (First Wall)	Thermal Stress (Blanket)
Pumping Power/Thermal Power	Number of Channels
Blanket Temperature Gradient	Gross Channel Weight
Thermal Stress (First Wall)	Neutron Wall Loading
Surface Loading Factor	
Nuclear Heating Rate	

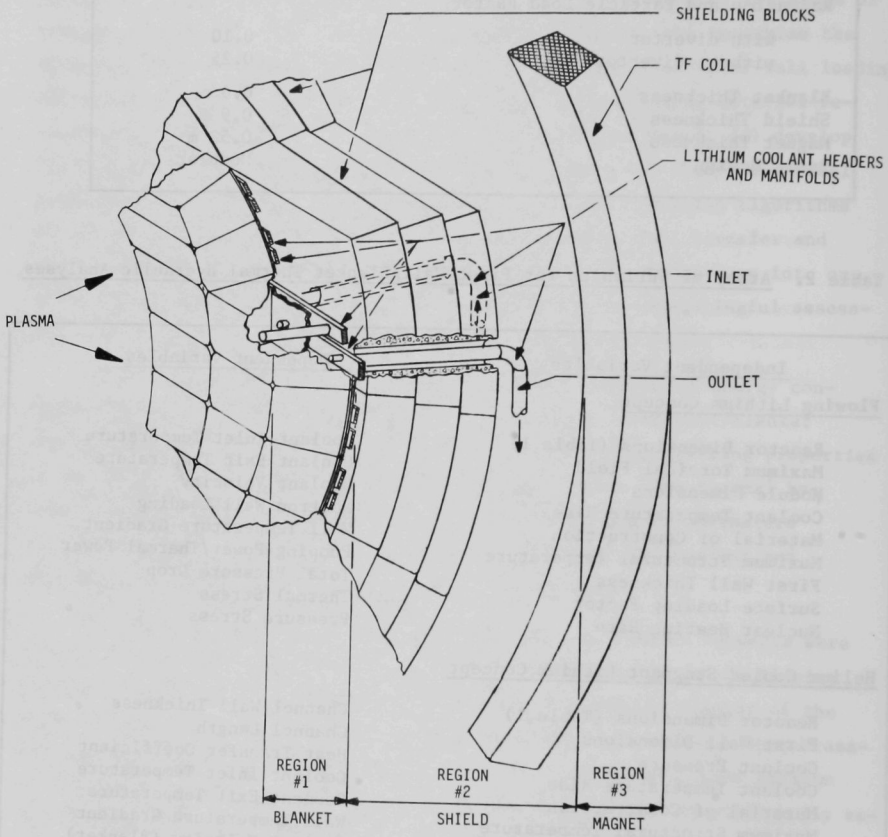

Figure 1. Lithium-Cooled First-Wall/Blanket System.

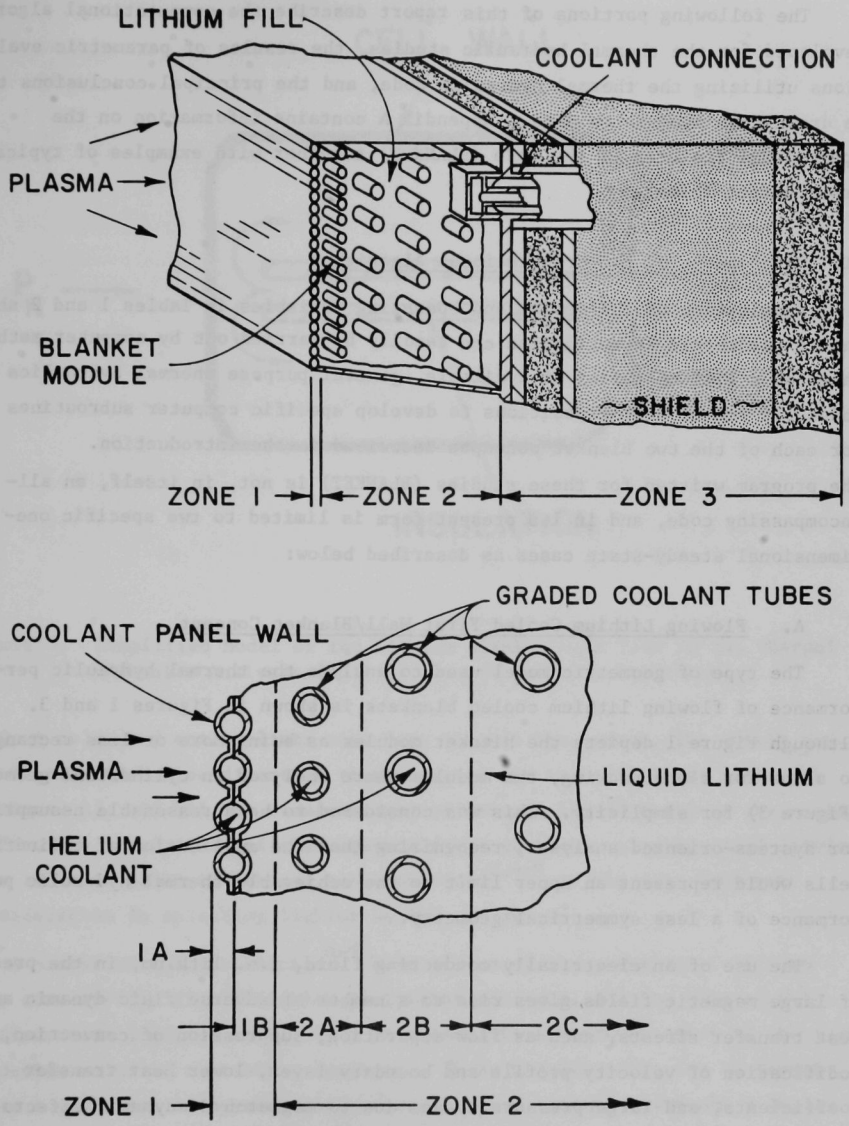

Figure 2. Helium Cooled Stagnant-Lithium First Wall/Blanket Concept.

The following portions of this report describe the computational algorithms developed for the thermal hydraulic studies, the results of parametric evaluations utilizing the thermal hydraulic code, and the principal conclusions to be drawn from studies to date. Appendix A contains information on the operational features of the code (BLANKET) together with examples of typical input/output format.

II. Development of the Computational Algorithms

Examination of the design and operating variables in Tables 1 and 2 shows that a parametric investigation can readily be carried out by computer methods. Based on a limited survey of available, general purpose thermal hydraulics codes, it seemed most expeditious to develop specific computer subroutines for each of the two blanket concepts described in the introduction.
The program written for these studies (BLANKET) is not, in itself, an all-encompassing code, and in its present form is limited to two specific one-dimensional steady-state cases as described below:

A. Flowing Lithium Cooled First Wall/Blanket Concept

The type of geometric model used to analyze the thermal hydraulic performance of flowing lithium cooled blankets is shown in Figures 1 and 3. Although Figure 1 depicts the blanket modules as being more or less rectangular to allow for close packing, the modules where analyzed in cylindrical geometry (Figure 3) for simplicity. This was considered to be a reasonable assumption for systems-oriented analyses, recognizing that the application of cylindrical cells would represent an upper limit to the achievable thermal hydraulic performance of a less symmetrical geometry.

The use of an electrically conducting fluid, i.e. lithium, in the presence of large magnetic fields gives rise to a number of adverse fluid dynamic and heat transfer effects, such as flow separation, suppression of convection, modification of velocity profile and boundary layer, lower heat transfer coefficients, and large pressure losses due to magnetohydrodynamic effects. Because of the nature of the design of tokamak-type fusion reactors, the

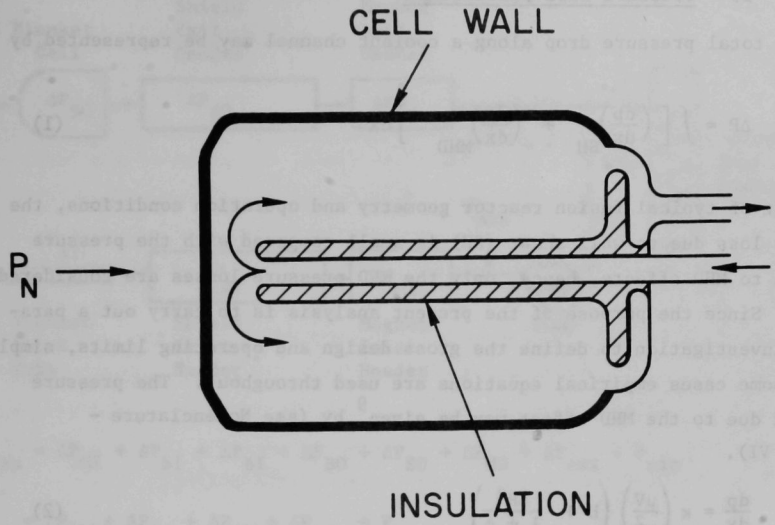

Figure 3. Simplified Model of the Lithium Blanket Cell Used in the Thermal Hydraulic Analyses (cell is assumed to be cylindrical).

coolant inlet and outlet lines must pass through the magnet, the shield and the blanket with flow direction transverse to the magnetic field lines (as in Figure 1). Of all the disadvantages of using a liquid metal as the cooling medium, the interaction of the magnetic field with the velocity field (giving rise to large pressure losses) has been cited[2,4-9] as the most important consideration in selecting lithium as the coolant.

A number of reactor studies[4-9] have addressed the question of optimum flow geometry for liquid lithium in tokamak reactors, and the blanket cell configuration depicted in Figure 3 is a simplified representation of the type of design solution most often employed. These blanket cells may be thought of as a variation of bayonet coolers with coolant entering through a duplex inlet pipe (with an electrically insulated interface) and then returning through the annulus. Several such cells are assumed to be connected in parallel through common inlet and outlet headers.

1. Pressure Loss Calculation

The total pressure drop along a coolant channel may be represented by

$$\Delta P = \int \left[\left(\frac{dp}{dx}\right)_{SH} + \left(\frac{dp}{dx}\right)_{MHD} \right] dx \tag{1}$$

For a set of typical fusion reactor geometry and operation conditions, the pressure loss due to wall shear (SH) is small compared with the pressure loss due to MHD effects, hence, only the MHD pressure losses are considered herein. Since the purpose of the present analysis is to carry out a parametric investigation to define the gross design and operating limits, simple and in some cases empirical equations are used throughout. The pressure gradient due to the MHD effect may be given[9] by (see Nomenclature - Section VI).

$$\frac{dp}{dx} = \kappa \left(\frac{\mu V}{a^2}\right) \left(H + \frac{\phi H^2}{1 + \phi}\right) \tag{2}$$

where

$$H = aB\sqrt{\sigma_L/\mu} \tag{3}$$

$$\phi = \sigma_w t_w / a\sigma_L \tag{4}$$

For large values of Hartman number, H, small values of conductance ratio, ϕ, and $\kappa \simeq 1$, the above equation may be represented[9] by

$$\Delta P = (V\sigma_w t_w/a) \int B^2 dx \tag{5}$$

In calculating the total pressure drop, the coolant path was divided into four regions (see Figure 1): (a) inlet to blanket, (b) return through the blanket cell annulus, (c) inlet and exit through shield, and (d) inlet and exit through magnets. In addition, allowance was made for a minimum inlet pressure to the pump (to suppress cavitation and account for the heat exchanger pressure drop). A schematic representation of the pressure drop terms is shown in Figure 4. As the magnetic field is not constant across the blanket,

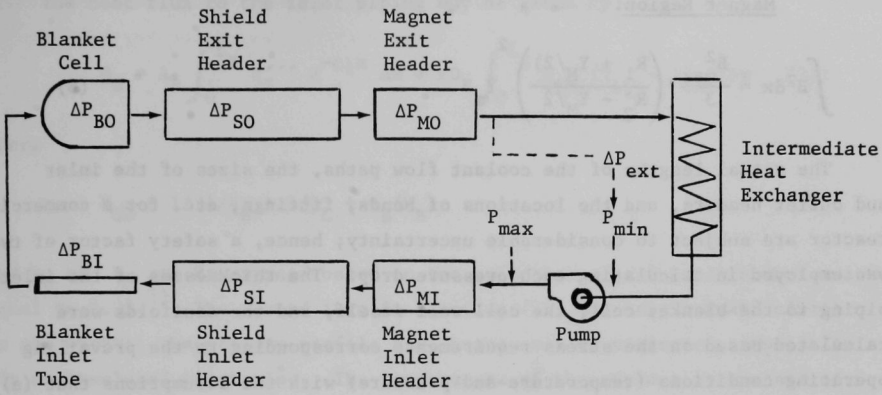

$$P_{max} = \Delta P_{MI} + \Delta P_{SI} + \Delta P_{BI} + \Delta P_{BO} + \Delta P_{SO} + \Delta P_{MO} + \Delta P_{ext} + P_{min}$$

$$P_C = \Delta P_{BO} + \Delta P_{SO} + \Delta P_{MO} + \Delta P_{ext} + P_{min}$$

Figure 4. Pressure Drop Diagram for the Lithium Cooled Blanket Cells.

the shield and the magnet, the integral of B^2dx was calculated using Equations (6), (7), and (8) to obtain a properly averaged value of the gross MHD effect.[10]

Blanket Region:

$$\int B^2dx = \frac{B^2_{max}}{R} \frac{(R_1 + Y_M/2)^2}{(r_1 + Y_C/2)} \left\{ \sqrt{R^2 - r_1^2} - \sqrt{R^2 - (r_1 + Y_C)^2} \right\} \quad (6)$$

Shield Region:

$$\int B^2dx = B^2_{max} (R_1 + Y_M/2)^2 \left\{ \left(\frac{1}{R_1 + r_1 + Y_C} \right) - \left(\frac{1}{R_2 - Y_M} \right) \right\} \quad (7)$$

Magnet Region:

$$\int B^2 dx = \frac{B^2_{max}}{3} \left(\frac{R_1 + Y_M/2)}{R_2 - Y_M/2} \right)^2 Y_m \tag{8}$$

The actual lengths of the coolant flow paths, the sizes of the inlet and outlet headers, and the locations of bends, fittings, etc. for a commercial reactor are subject to considerable uncertainty; hence, a safety factor of two was employed in calculating each pressure drop. The thicknesses of the inlet piping to the blanket cell, the cell wall itself, and the manifolds were calculated based on the stress requirements corresponding to the prevailing operating conditions (temperature and pressure) with the assumptions that (a) the pressure stress cannot exceed one-third the yield strength[3] and (b) the wall thicknesses cannot be less than 2.5 mm in the blanket region and 5 mm in the shield and magnet regions due to fabrication constraints.

2. Heat Transfer Calculations

The heat transfer analysis was performed using standard empirical equations. A one-dimensional steady-state analysis was carried out by dividing the blanket cell into (a) inlet piping, (b) first wall, (c) cell annulus and (d) cell side walls (see Figure 3). These calculations were used to set the optimum coolant velocity for a given wall loading and to establish the general thermal characteristics of the system.

The overall heat balance was determined based on a given wall loading due to (a) particles and radiation that create a first-wall surface flux and (b) neutrons that create internally generated heat. As the particle and surface radiation power fraction depends on whether the reactor has a divertor or not, two cases were considered -- the particle and surface radiation loading factor was set equal to 25% of the neutron wall loading without divertor and 10% of the wall loading with divertor. An overall heat balance gives (see Nomenclature - Section VI)

$$A_C Q_N P_f + Q_v = WC_p \ (T_{EX} - T_{IN}) \tag{9}$$

$$Q_v = A_C \left[\int_0^{t_C} q_1''' \ e^{-c_1 x} \ dx + \int_{t_C}^{L_C - t_C} q_2''' \ e^{-c_2 x} \ dx \right] \tag{10}$$

The heat flux to the inlet piping may be given by

$$Q_B = A_B \int_0^{L_B} q_2''' e^{-c_2 x} dx + \pi D_B \int_0^{L_B} U_{CB} (T_{LC} - T_{LB}) dx \quad (11)$$

where

$$U_{CB} = 1/(1/h_B + 1/h_C + t_B/K_B) \quad (12)$$

and h_B and h_C are determined based on the selection of a Nusselt number value equal to 5.25.[11] The second term in Equation (11) has only a small effect on the overall temperature profile and, hence, may be neglected, especially for an insulated inlet pipe. The temperature of the coolant at the end of the inlet pipe is given by

$$T_{LI} = T_{IN} + Q_B/(WC_p) \quad (13)$$

The temperature of the first wall at the plasma face may be calculated by

$$T_{WO} = T_{LI} + \Delta T_F + \Delta T_v + \Delta T_s \quad (14)$$

where

$$\Delta T_F = \frac{(Q_N P_f + q_{v1} t_C)}{K_L} t_F + \frac{t_F}{2K_L} \int_{t_C}^{t_C + t_F} q_2''' e^{-c_2 x} dx \quad (15)$$

$$\Delta T_v = \frac{q_{v1} t_C^2}{2K_C} \quad (16)$$

$$q_{v1} = q_1'''/t_C \left(\int_0^{t_C} e^{-c_1 x} dx \right) \quad (17)$$

$$\Delta T_s = \frac{(Q_N P_f)\ t_C}{K_C} \quad (18)$$

$$T_{LO} = T_{LI} + \frac{q_{v1} V_{FW} + Q_N A_{FW} P_f}{WC_p} \quad (19)$$

Since the bulk of the heat is generated in the cell annulus and since the internal heat generation rate varies exponentially along the cell length,

the cell annulus was divided into six sections in order to complete the thermal analyses. The temperature of the coolant at any point may be given by

$$(T_L)_n = T_{LO} + \left(A_{Ci}\, q_2''' \int_{L_n}^{L_n + \Delta L_i} e^{-c_2 x}\, dx - Q_{CB_i} \right) / (WC_p) \quad (20)$$

$$Q_{CB_i} = \pi D_B U_{CB_i} \, (T_{LC} - T_{LB})_i \quad (21)$$

The cell wall temperature at any point is given by

$$T_{wi} = T_{Li} + \Delta T_{vi} + \Delta T_{Fi} \quad (22)$$

where ΔT_{vi} and ΔT_{Fi} are, respectively, the temperature drop across the wall due to internal heat generation within the cell wall and the temperature drop across the fluid film. The outer surface of the cell is assumed to be adiabatic.

The thermal power is equal to

$$P_{th} = WC_p \, (T_{EX} - T_{IN}) \quad (23)$$

The pumping power may be expressed as

$$P_{pu} = W \, \Delta P / \rho \quad (24)$$

$$\frac{P_{pu}}{P_{th}} = \frac{\Delta P}{\rho \, C_p \, (T_{EX} - T_{IN})} \quad (25)$$

The thermal stress may be calculated by

$$S = \frac{\alpha E}{2\,(1 - \nu)} \, (\Delta T_s + \Delta T_v) \quad (26)$$

The upper limit for the thermal stresses was assumed[3] to be equal to the yield strength of the construction material at the maximum operating temperature. Further, it is assumed that there is one inlet and one outlet header for each set of ten modular blanket units, and the size of this manifolding is based on the velocity of the coolant in the inlet and the outlet headers

being the same as the velocity of the coolant required at the blanket cell inlet tube.

A listing of the subroutine (LITHIUM) written to carry out the above described analyses is given in Appendix A together with input/output instructions and data sets for test cases.

B. Helium Cooled Stagnant Lithium First Wall/Blanket Concept

The thermal hydraulic analyses of a helium cooled tubular first wall coupled to a stagnant lithium blanket were based on the configuration shown in Figure 2. The first wall is assumed to be made of a single row of tightly packed tubes and the blanket is in essence a "sea" of lithium extending radially outward from the back of the first wall and having an appropriately dispersed array of helium carrying tubes. A realistic boundary condition is set up so that there is no discontinuity in the thermal hydraulic analyses at the first wall/blanket interface. The radiation power deposited on the first wall and the nuclear heat generated within zone 1 (see Figure 2) are removed by the helium flowing through the first wall tube bundle. Zone 2 (blanket) is divided into several regions and the number and size of the coolant tubes throughout these regions are calculated based on the internal heat generation rate so that the coolant exit temperatures for all regions are the same. For purposes of the thermal analysis, zone 1 was subdivided into two regions -- region 1a is constituted by the forward facing half of the coolant tubes and region 1b consists of the rest of zone 1. Two distinct internal heat generation rates were used -- one for region 1a and the other for both region 1b and the blanket region (zone 2). Since the wall loadings (both radiation and neutron) were assumed to be constant along the coolant flow direction, the temperature difference between the wall and the coolant remains essentially constant, and the maximum wall temperature can be based on the coolant exit temperature. (Internal heat generation in the helium was assumed to be zero.) The thermal hydraulic calculations are carried out for each zone separately, with the assumption of an isothermal boundary at the zone 1/zone 2 interface.

The terminology used hereafter to describe locations across zones 1 and 2 is as follows:

$y_1 \longrightarrow$ plasma boundary

$y_2 \longrightarrow$ coolant tube inner surface facing plasma

$y_3 \longrightarrow$ coolant tube inner surface facing blanket

$y_4 \longrightarrow$ coolant tube outer surface facing blanket

$y_5 \longrightarrow$ isothermal boundary between zone 1 and zone 2

$y_2 - y_1 = y_4 - y_3 \rightarrow$ coolant tube wall thickness

For the geometric model as discribed above, the following energy balance equations for steady-state may be written (see Nomenclature - Section VI):

Zone 1

$$\dot{\omega}_f \, Cp \, (T_{EX} - T_{IN}) = q_1 + q_2 + q_3 \tag{27}$$

$$Q = q_1 + q_2 + q_3 = H_f \pi D_f L_f \, (T_{WI} - T_{EX})_f \tag{28}$$

$$\dot{\omega}_f = A_f V_f \rho \tag{29}$$

$$\Delta T_c = T_{EX} - T_{IN} \tag{30}$$

$$q_1 = (D_f + 2t_f) L_f \int_{y_1}^{y_2} q_{v1} \, \overline{e}^{c_1 y} \, dy \tag{31}$$

$$q_2 = (D_f + 2t_f) L_f \int_{y_3}^{y_4} q_{v2} \, \overline{e}^{c_2 y} \, dy \tag{32}$$

$$q_3 = (D_f + 2t_f) L_f \int_{y_4}^{y_5} q_{v2} \, \overline{e}^{c_2 y} \, dy \tag{33}$$

$$R_e = D_f \, u_f \rho / \mu \tag{34}$$

$$f = 0.046 \, x_f / R_e^{0.2} \tag{35}$$

$$P_r = Cp \, \mu / K \tag{36}$$

$$H_f = 0.023 \frac{K}{D_f} R_e^{0.8} P_r^{0.4} x_h \tag{37}$$

$$T_{WI} = T_m - \Delta T_v - \Delta T_s \tag{38}$$

$$Q_s = Q_N P_f \tag{39}$$

$$T_{EX} = T_{WI} - \Delta T_F \tag{40}$$

$$\Delta T_F = Q/[H_f \pi D_f L_f] \tag{41}$$

$$\Delta P_f = R_f \, Cp \, \Delta T_c \, \rho \tag{42}$$

$$L_f = \Delta P_f \, g_c \, D_f \, \rho/[2f \, (\dot{\omega}/A)_f^2] \tag{43}$$

$$t_f = 3 \, P_{in} \, D_f/(4\sigma_y) \tag{44}$$

$$\Delta T = \Delta T_s + \Delta T_v \tag{45}$$

$$P_{th} = \dot{\omega} Cp \, (T_{EX} - T_{IN}) \tag{46}$$

$$P_{pu} = \dot{\omega} \Delta P/\rho \tag{47}$$

$$P_{pu}/P_{th} = \Delta P/[\rho Cp \Delta T_c] \tag{48}$$

$$\sigma_t = \frac{\alpha E}{2(1-\nu)} \Delta T \tag{49}$$

In the calculations described by Equations 27 through 49, the physical and thermodynamic properties are calculated at the average temperature of the coolant and the yield stress is calculated at the maximum allowable temperature for the structural material. Examination of the above set of equations reveals that some of the variables are interrelated, and that Q_N and y_5 are in fact dependent variables.

In order to make the blanket thermal hydraulic calculations for the helium cooled stagnant lithium concept, an equivalent lithium cell was assumed as in Reference 12. A set of assumptions regarding void fraction, temperature difference between the structural material (e.g. coolant tube) and lithium at the isothermal boundary, and the internal heat generation rate within the lithium cell leads to calculations of the diameter of an equivalent lithium cell and the corresponding coolant tube diameter. The following equations are used in the calculations:

$$D_B = 4.0 \sqrt{V_f/(1-V_f)(K_{Li}\ \Delta T_{Li}/Q_v)/[-(1 + \frac{\ell n\ V_f}{1 - V_f})]} \tag{50}$$

$$D_{Li} = D_B/\sqrt{V_f} \tag{51}$$

$$\Delta P = R_B\ Cp\ \Delta T_c\ \rho \tag{52}$$

$$\dot{\omega} = \sqrt[3]{(\pi/4)\ D_{Li}^2\ Q_v\ (1 - V_f)/(Cp\ \Delta T_c)[\Delta P g_c D_B \rho A_B^2/(2f)]} \tag{53}$$

$$Q_v = \frac{1}{(y_6-y_5)} \int_{y_5}^{y_6} q_{v2}\ \overline{e}^{c_2 y}\ dy \tag{54}$$

$$y_6 = y_5 + D_{Li} \tag{55}$$

$$u_B = \dot{\omega}/(A_B\rho) \tag{56}$$

The calculation of overall heat balance, heat transfer coefficients, friction factor, channel length, etc., is similar to that for the first wall region.

An examination of the mathematical relations for the first wall region shows that an iterative scheme can be used to establish the conditions of the coolant and the materials in the various regions. Subroutine HELIUM was written to carry out this portion of the parametric analysis. This subroutine is described in Appendix A.

III. Results and Discussion

A. Thermal Hydraulic Analyses of the Flowing Lithium Cooled First Wall/Blanket Concept

Typical results of thermal hydraulic analyses for four reference cases (stainless steel with and without a divertor and vanadium alloy with and without a divertor) are presented in Tables 3, 4 and 5 and Figures 5 and 6. In Figures 5 and 6 the maximum allowable neutron wall loading, coolant inlet and exit temperatures, thermal stress, coolant inlet velocity and pumping power to thermal power ratio, are plotted as a function of blanket cell wall thickness based on (a) the thermal-hydraulic model described above, (b) a maximum toroidal field of 8 T, and (c) the materials criteria listed in the upper half of Table 3. For stainless steel (with or without a divertor) the maximum neutron wall loading generally occurs at relatively low wall thicknesses and is limited by the thermal stress criterion (maximum thermal stress = material yield strength). For vanadium alloys this maximum occurs at somewhat larger wall thickness values and is limited by the minimum coolant inlet temperature criterion. The values of the maximum allowable neutron wall loading for 8, 10, and 12 T maximum toroidal fields are listed in the lower half of Table 3. The total pressure drops were nominally in the range from 3 to 6 MPa (including the safety factor of 2.0 on all calculated pressure losses).

The effect of maximum toroidal field and cell wall thickness on the maximum allowable neutron wall loading is illustrated more clearly in Figures 7 and 8 for the four cases described above. As can be seen in Figures 7 and 8 and in Table 3, there is some advantage (in terms of overall thermal hydraulic performance) to having the lower toroidal fields. For most cases, the actual advantage is in fact even greater than is indicated in Table 3, because the increased cell wall thicknesses required to support the maximum neutron wall loading at the higher toroidal fields have the concommitant effect of reducing the coolant exit temperature.

Early trade-off studies on the coolant temperature rise showed that the values in Table 3 (i.e. 225°C for stainless steel and 325°C for vanadium alloy) are near to optimum for each material based on the thermal-hydraulic model and maximum structural temperature limits used herein. Also, the pumping power to thermal power ratio (based on geometrically averaged values of the

Table 3. Results of Wall Loading Trade Studies for Lithium-Cooled Stainless Steel and Vanadium-Alloy Blanket Systems[a]

Criteria		Li-Cooled V Alloy	Li-Cooled SS
Maximum Allowable Temp., °C		650	500
Maximum Thermal Stress, MPa		351	117
Minimum Wall Thickness, mm		2.5	2.5
Maximum Wall Thickness, mm		8.0	8.0
Minimum Coolant Inlet Temp., °C		235	235
Coolant Temperature Rise, °C		325	225
Maximum Neutron Wall Loading, MW/m^2			
$F^b = 0.10$	8 Tesla	11.2[c]	4.2[d]
	10 Tesla	7.5[e]	3.5[d]
	12 Tesla	5.3[e]	3.0[d]
$F^b = 0.25$	8 Tesla	8.0[c]	2.0[d]
	10 Tesla	6.2[c]	2.0[d]
	12 Tesla	4.6[c]	1.8[d]

a. For a cell diameter of 0.5 m and an inlet tube diameter of 0.1 m.

b. F = Fractional power loading on first wall surface due to particle and radiation effects.

c. Limited by minimum coolant inlet temperature criterion.

d. Limited by maximum thermal stress criterion.

e. Limited by MHD pressure stress criterion (i.e. maximum cell wall thickness insufficient to support higher coolant velocity).

Table 4. Summary of Trade Studies[a] on Materials Limitations for Lithium-Cooled Stainless Steel Blanket Cells

Parameter	With Divertor			Without Divertor		
Maximum Structural Temperature, °C	500	500	600	500	500	600
Thermal Stress Limit, MPa	117	234	234	117	234	234
Maximum Neutron Wall Loading, MW/m^2	3.8	7.5	7.5	2.0	4.0	4.1
Cell Wall Thickness, mm	3.0	2.5	2.5	2.5	2.5	2.5
Coolant Exit Temperature, °C	485	476	577	493	487	572
Pumping Power/Thermal Power, %	0.3	0.3	0.3	0.1	0.2	0.3
Coolant Velocity, m/s	0.3	0.5	0.5	0.2	0.3	0.3

[a] Criteria: Coolant Inlet Temperature $\geq$ 235°C
Coolant Temperature Rise = 225°C
Safety Factor = 2.0

Table 5. Summary of Trade Studies[a] on Materials Limitations for Lithium-Cooled Vanadium Alloy Blanket Cells

Parameter	With Divertor		Without Divertor	
Maximum Structural Temperature, °C	650	750	650	750
Maximum Neutron Wall Loading, MW/m^2	11.2	13.6	8.0	10.3
Corresponding Cell Wall Thickness, mm	5.5	6.0	3.0	3.0
Thermal Stress, MPa	186	248	152	193
Coolant Exit Temperature, °C	567	571	556	564
Pumping Power/Thermal Power, %	0.9	0.8	0.5	0.4
Coolant Velocity, m/s	0.6	0.7	0.4	0.6

[a] Criteria: Coolant Inlet Temperature $\geq$ 235°C
Coolant Temperature Rise = 325°C
Cell Wall Thermal Stress $\leq$ 351 MPa
Safety Factor = 2.0

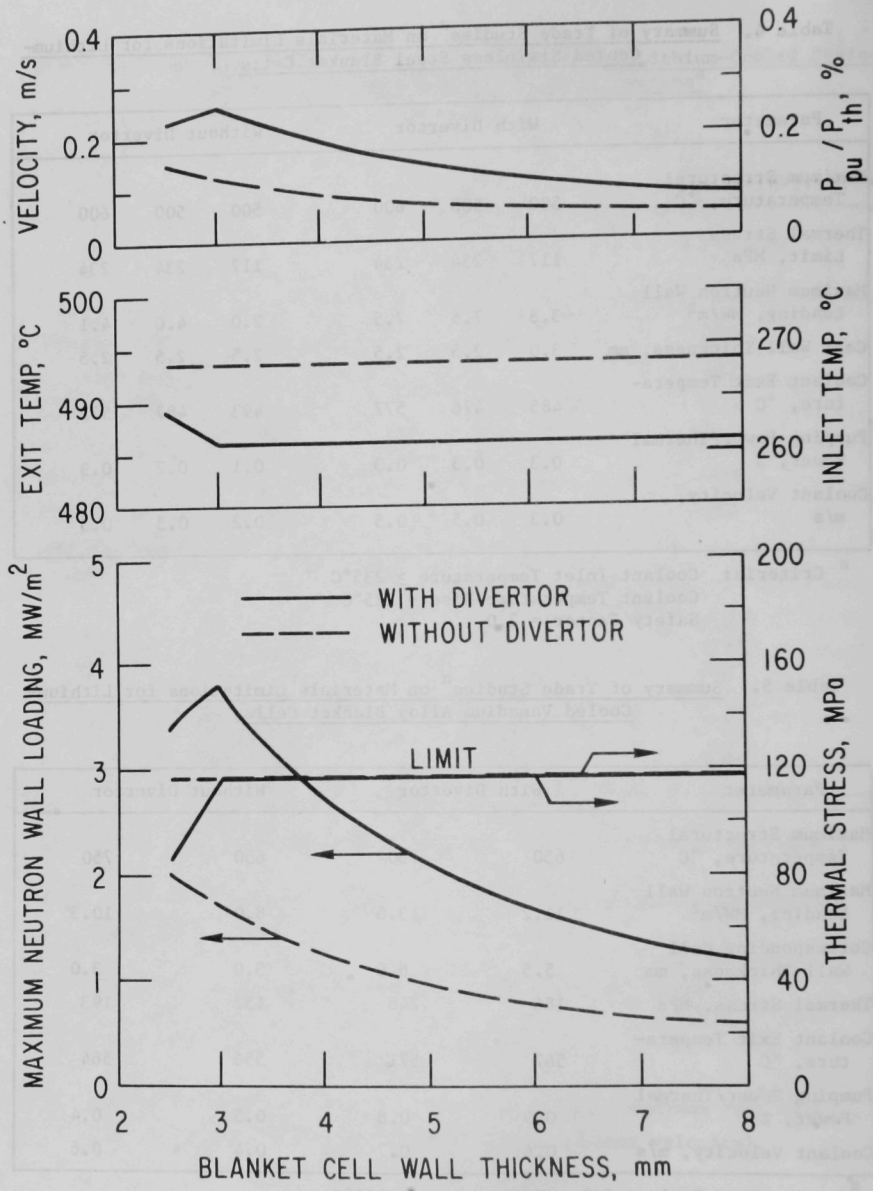

Figure 5. Lithium-cooled Stainless Steel Blanket Cells (cell diameter = 0.5 m, inlet tube diameter = 0.1 m).

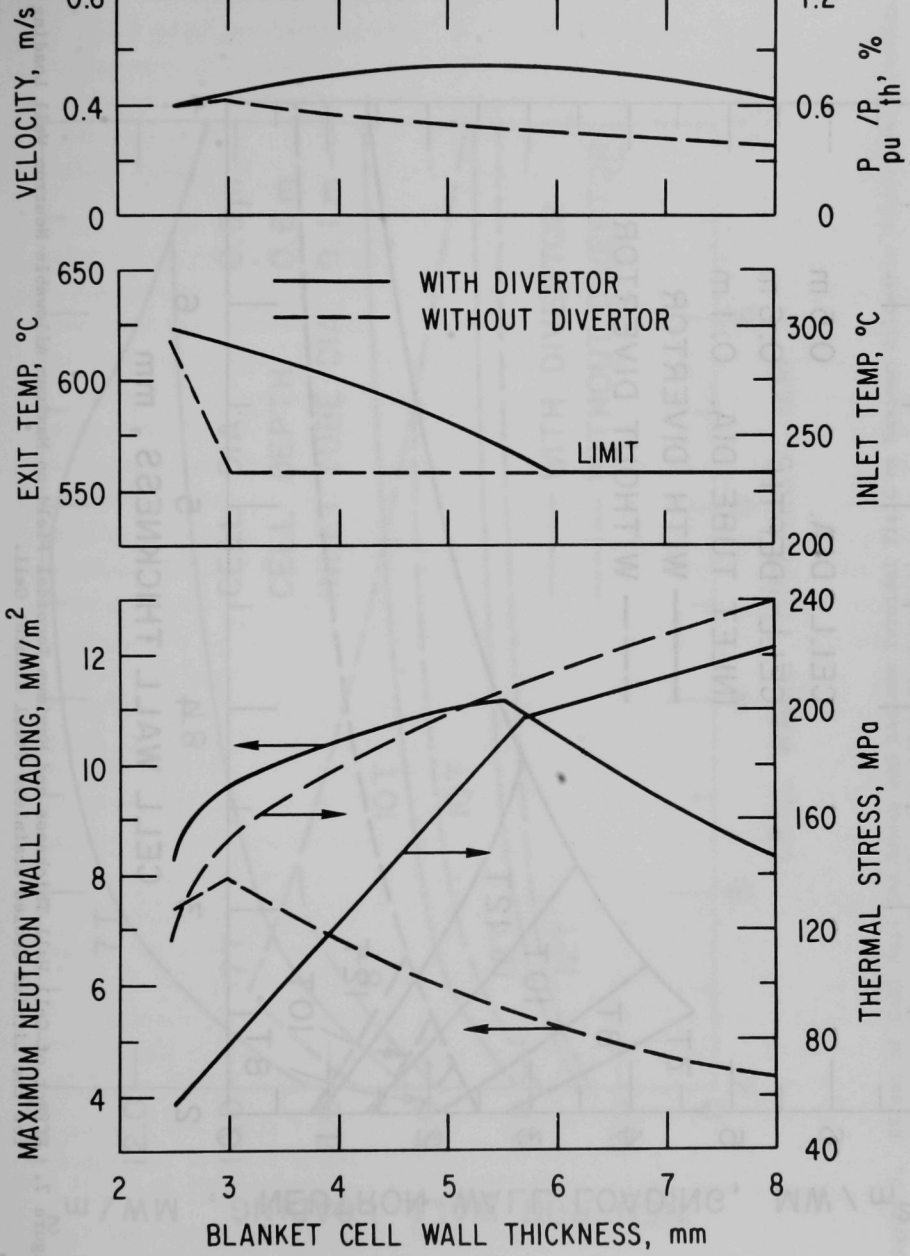

Figure 6. Lithium-cooled Vanadium Alloy Blanket Cells (cell diameter = 0.5 m, inlet tube diameter = 0.1 m).

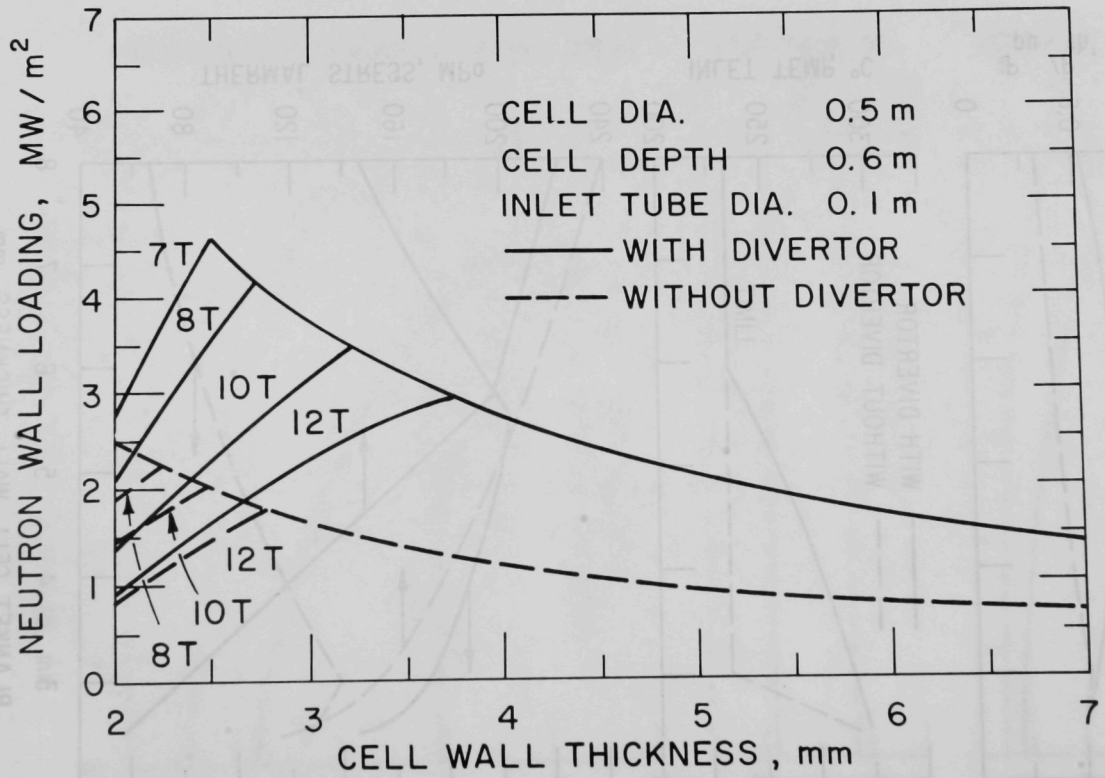

Figure 7. Effect of Cell Wall Thickness and Maximum Toroidal Field on Maximum Allowable Neutron Wall Loading for the Lithium Cooled Stainless Steel Blanket Cell.

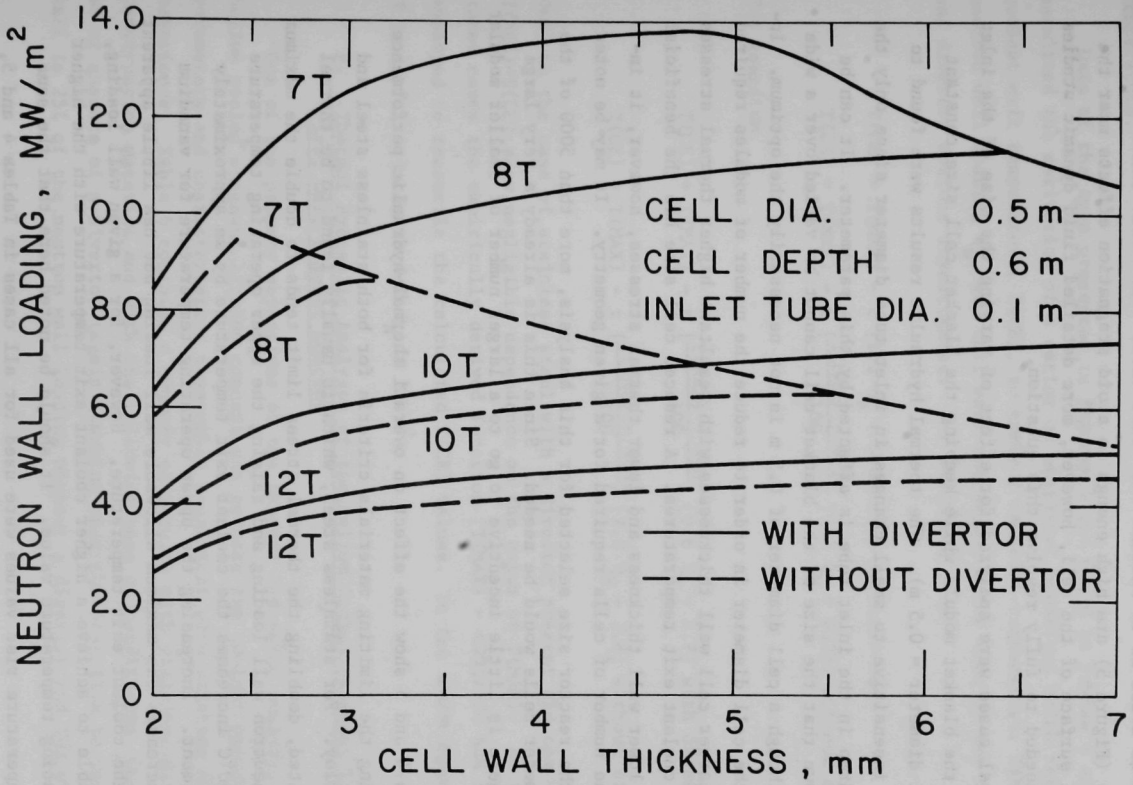

Figure 8. Effect of Cell Wall Thickness and Maximum Toroidal Field on Maximum Allowable Neutron Wall Loading for the Lithium Cooled Vanadium Alloy Blanket Cell.

actual magnetic field strength inside the reactor) was found to be < 1.0, < 1.5 and < 2.0% for maximum toroidal fields of 8, 10 and 12 T, respectively. There is some doubt as to whether the fluid inlet velocities for the stainless steel case (Figure 5) are high enough to avoid stagnation effects near the first-wall surface of the cell, however, more detailed fluid dynamic studies would be needed to fully resolve this question.

Several cases were analyzed for effect of varying the size of the inlet piping to the blanket module while keeping the blanket cell size constant (e.g. cell diameter = 0.5 m). The thermal hydraulic results were found to be rather insensitive to small changes in inlet tube diameter since only the pressure drop in the inlet tube is affected by this parameter. It can be easily shown that the size of the blanket cell cannot be varied over a wide range, although a cell diameter of 0.5 m is not necessarily the optimum. Increasing the cell diameter in order to reduce the number of modules required leads to larger cell wall thicknesses with resultant higher thermal stresses and lower coolant exit temperatures. A reduced cell size has the beneficial effect of lower wall thickness and lower thermal stresses, however, it increases the number of cells required for a given geometry. It may be noted that for the reactor size selected for this analysis, more than 5000 of the 0.5-m diameter cells would be needed. Since this is already a very large number, there is little incentive to go to a larger number of smaller modular units.

Tables 4 and 5 show the effect on overall thermal-hydraulic performance of increasing the limiting materials criteria for both stainless steel and vanadium alloy. For stainless steel, which is usually found to be thermal stress limited, doubling the thermal stress limit tends to double the maximum allowable neutron wall loading and raising the upper operating temperature limit by 100°C increases the coolant exit temperature by an approximately equal increment. Increasing the upper operating temperature for vanadium by 100°C increases the maximum allowable wall loading but has little apparent effect on the coolant exit temperature. However, for a given wall loading, it is possible to achieve a higher coolant exit temperature with the higher upper operating temperature value. It should be noted here that the same coolant temperature rise values were used for all cases in Tables 4 and 5,

although it is known that the coolant temperature rise corresponding to optimum thermal-hydraulic performance increases with peak allowable structural temperature.

Data of the type presented in Figures 5 and 6 and in Tables 4 and 5 have permitted the derivation of a series of empirical equations which relate the coolant exit temperature, T(CE), to maximum material temperature, T(MAX), neutron wall loading Q_N, and cell wall thickness, t, for each of the material and divertor options investigated. For stainless steel

$$T(CE) = T(MAX) - t\,[1.2\,Q_N + 0.5] \text{ with divertor and}$$

$$T(CE) = T(MAX) - t\,\left[\frac{T(MAX) - 400}{100}\right]\,[1.3\,Q_N + 0.25] \text{ without divertor.}$$

For vanadium

$$T(CE) = T(MAX) - t\,\left[\frac{T(MAX) - 400}{100}\right]\,[0.8\,Q_N - 2.7] \text{ with divertor and}$$

$$T(CE) = T(MAX) - t\,\left[\frac{T(MAX) - 400}{100}\right]\,[2.0\,Q_N - 3.8] \text{ without divertor.}$$

Only in the case of stainless steel with a divertor present did the value of T(MAX)-T(CE) show negligible dependence on the value of T(MAX). In the other three cases the empirically derived function [T(MAX) - 400]/100 had to be employed to reconcile the calculated T(CE) values. In the above equations, T is in °C, t is in mm and Q_N is MW/m^2.

B. Thermal Hydraulic Analyses of the Helium Cooled Stagnant Lithium First Wall/Blanket Concept

One of the primary objectives of the thermal hydraulic analysis for the helium cooled stagnant lithium concept was to make the coolant operating parameters and characteristics reasonably consistent with existing HTGR experience. Table 6 contains a summary of results with stainless steel as construction material and with the following sets of conditions: (a) the presence of or absence of a divertor (again assuming that the heat flux to the first wall is 25% of the neutron wall loading without a divertor and 10% with

Table 6. Trade Study for Helium Cooled Stagnant Lithium Blanket Using Transverse Cooling Channels made of Stainless Steel: First Wall Configuration is a Single Layer of Closed-packed Tubes

(* Indicates fixed or independent parameter)

Divertor Option	With Divertor				Without Divertor			
General Parameters								
* Maximum Structural Temp., °C [T(MAX)]	500		650		500		650	
* Helium Inlet Pressure, ksi	1.0		1.0		1.0		1.0	
* Pump Power/Thermal Power, %	5		5		5		5	
* Coolant ΔT, °C	200		300		200		300	
* Lithium ΔT, °C [ΔT(LI)]	25		25		25		25	
Neutron Wall Loading, MW/m^2	6.2	12.4	6.0	12.0	2.6	5.3	2.6	5.1
First Wall Parameters								
* Helium Tube Dia., mm	25.4		25.4		25.4		25.4	
* Helium Velocity, ft/s	200		200		200		200	
* Thermal Stress, ksi	17	34	17	34	17	34	17	34
Wall Thickness, mm	1.25		1.25		1.25		1.25	
Channel Length, m	12.2	13.2	17.3	18.5	12.2	13.1	17.3	18.4
HT. TR. Coeff., BTU/hr.ft.^{2}°F	1693	1980	1510	1729	1679	1968	1507	1720
Coolant Inlet Temperature, °C	171	63	217	105	173	67	220	110
Coolant Exit Temperature, °C [T(CE)]	371	263	517	405	373	267	520	410
Wall ΔT, °C	53	106	50	100	53	107	50	100
No. of Tubes, Hundreds[a]	32	29	22	21	32	30	22	21
Total Tube Weight, Tons[a]	35		35		35		35	
Blanket Parameters								
* Void Fraction, % [VF]	5		5		5		5	
Tube Diameter, mm	4.9	3.4	5.2	3.6	7.7	5.4	8.2	5.8
Wall Thickness, mm	0.41	0.37	0.42	0.37	0.48	0.43	0.49	0.43
Channel Length, m	1.1	0.6	1.5	0.8	2.3	1.3	3.3	1.8
HT. TR. Coeff. BTU/hr.ft.^{2}°F	2541	2981	2361	2769	2068	2427	1924	2253
Helium Velocity, ft/s	251	276	263	290	220	244	231	255
Coolant Inlet Temperature, °C	259	249	305	295	268	261	316	308
Coolant Exit Temperature, °C	459	449	605	595	468	461	616	608
Wall ΔT, °C	8.0	11.1	8.0	10.0	6.0	8.0	6.0	8.0
Thermal Stress ksi	2.7	3.4	2.6	3.4	2.0	2.5	1.9	2.5
No. of Tubes, Thousands[a]	939	3435	585	2149	174	644	109	398
Total Tube Weight, Tons[a]	74	96	71	91	54	69	52	66

[a]Based on a reactor with a first wall area of ∿ 1000 m^2

$T(CE) = T(MAX) - 17.9\ P_w - 21.9$

$T(CE) = T(MAX) - 41.3\ P_w - 21.4$

a divertor), (b) maximum allowable structural temperatures of 500° or 650°C, (c) thermal stress limits of 17 or 34 ksi, and (d) heat transfer coefficient and friction factor multipliers of 2.2 and 4.0, respectively.[13] The asterisked parameters were fixed in the calculation and the primary iteration was done by increasing the neutron wall loading until the thermal stress limit at the first wall was exceeded.

In the thermal hydraulic analysis of the first wall, the coolant velocity is fixed at 200 ft/s, the tube diameter is fixed at 25.4 mm (1 inch), and the tube wall thickness is not allowed to be less than 1.25 mm (50 mil). In the thermal hydraulic analysis of the blanket, the coolant void fraction, VF, is fixed at 5% and the temperature drop through the lithium $\Delta T(Li)$, is set at 25°C. Trade studies on the latter two parameters have been completed for VF = 5, 7, and 10% and $\Delta T(Li)$ = 25, 50, and 100°C. These studies show that, in terms of maximum coolant exit temperature, VF = 5% and $\Delta T(Li)$ = 25°C are closer to optimum than the other values tested. Other parameters that were fixed in these analyses are given in Table 6. The coolant exit temperature, from the first wall region, T(CE), may be represented empirically in terms of the neutron wall loading, Q_N, and the maximum allowable structural temperature, T(MAX), by:

$$T(CE) = T(MAX) - 17.9 \cdot Q_N - 21.9 \text{ (with divertor).}$$

$$T(CE) = T(MAX) - 41.3 \cdot Q_N - 21.4 \text{ (without divertor).}$$

with T in °C and Q_N in MW/m^2.

The coolant exit temperature from the blanket region is nominally 30 to 50°C below the maximum structural temperature and seems to be relatively independent of wall loading or divertor status.

The values arrived at in Table 6 are based largly on attempts to control thermal stress and peak structural temperature, and as a result do not reflect optimum performance from the standpoint of coolant exit temperature. In particular, the cases where coolant exit temperatures from the first wall or the blanket is < 500°C probably do not represent economically attractive systems. Figures 9 and 10 show how these coolant exit temperatures are affected by backing down from the maximum neutron wall loading values given

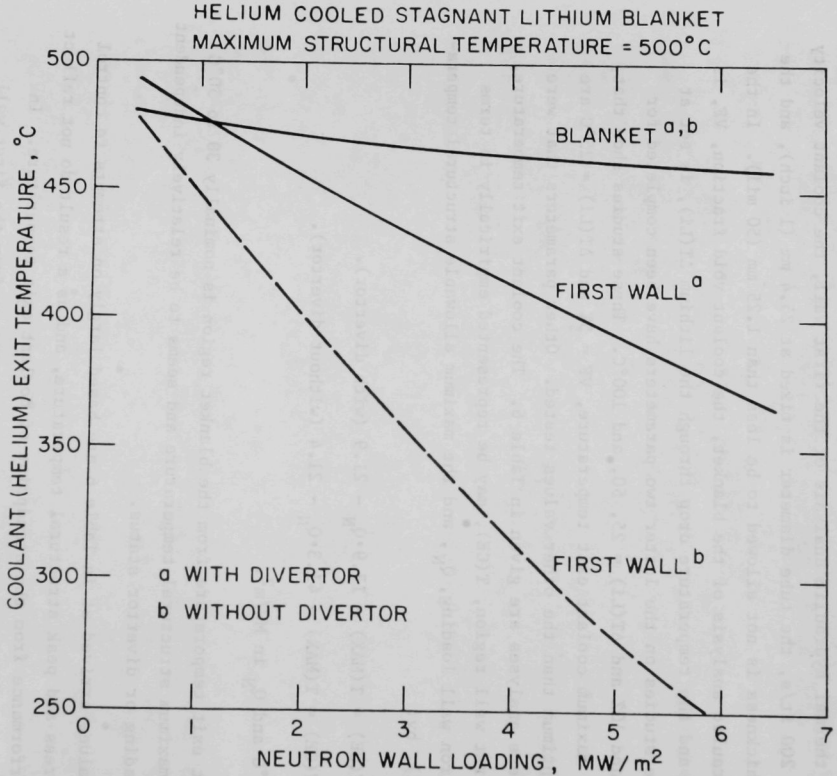

Figure 9. Coolant Exit Temperature versus Wall Loading for the Helium Cooled Stagnant Lithium Blanket (Maximum Structural Temperature = 500°C)

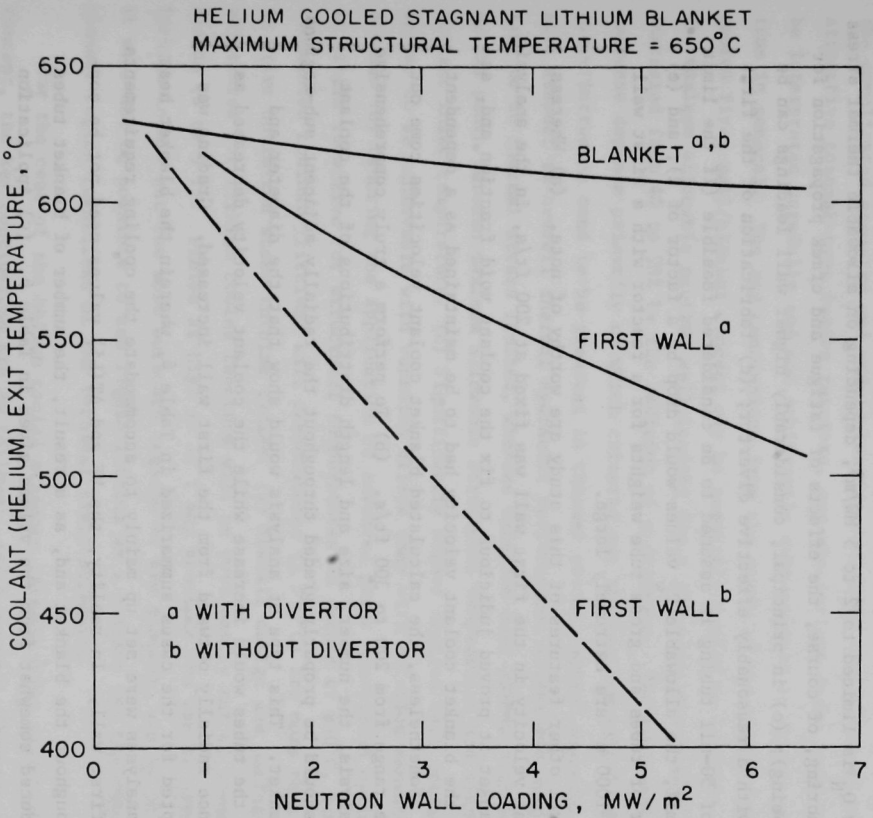

Figure 10. Coolant Exit Temperature versus Wall Loading for the Helium Cooled Stagnant Lithium Blanket (Maximum Structural Temperature = 650°C)

in Table 6 for the 500°C and 650°C stainless steel operating temperatures. Based on these results the helium cooled stagnant lithium blanket would appear to achieve economic attractiveness at wall loading values considerably lower than those in Table 6 and at structural temperatures $\geq$ 650°C.

The principal indications from this study are that (a) T(MAX) $\geq$ 650°C is essential for useful T(CE) with helium, i.e., T(CE) > 500°C; (b) without a divertor Q_N is limited to 2 to 5 MW/m^2, depending on allowable thermal stress level (ignoring, of course, the effects of fatigue and crack propagation for the time being); (c) in principal, considerably higher wall loadings can be achieved with a reasonably effective divertor; (d) fabrication of the first wall out of 50-mil tubing is assumed to be considered feasible (if the limit were 100 mil, the allowable P_w values would drop by a factor of 2); and (e) the number of tubes and gross tube weights for a reactor with a first wall area of $\sim$ 1000 m^2 are extremely large.

Several other features of this study are worthy of note. (a) Whereas the coolant velocity in the first wall was fixed at 200 ft/s, in the analysis of the blanket it proved judicious to fix the coolant void fraction and, as a result, the blanket coolant velocity had to be maintained as a dependent variable. Nonetheless, the calculated blanket coolant velocities come out within the range from 200 to 300 ft/s. (b) To perform a truly comprehensive design analysis, the number, size and length distributions of the coolant channels should be properly graded throughout the radially adjacent sub-regions of the blanket. This type of analysis would show that the diameter and length of the tubes would increase while the coolant velocity decreased as the distance radially outward from the first wall increased. Grading was not attempted for the cases summarized in Table 6, wherein the blanket heat transfer analyses were set up mainly to accommodate the cooling requirements near the first wall, In reality, the VF and $\Delta T(Li)$ values need not be constant throughout the blanket and, as a result, the number of blanket tubes can be reduced somewhat from the values given in Table 6. (c) Application of the multiplier factors for the heat transfer coefficient and frictional pressure drop is based on the assumption that the interior tube walls can be roughened or otherwise modified to augment heat transfer with a resulting modest impact on the pressure drop. Omission of these multiplier factors (i.e., equating them to unity) generally results in substantial increases in

coolant velocity (to > 400 ft/s) and channel length (70 to 80%) with somewhat smaller reductions in heat transfer coefficient (∿ 30%) and coolant exit temperature (4 to 5%).

IV. Conclusions

Because studies of the type described in this report tend to "idealize" the complicated geometry and widely-ranging operating conditions of potentially attractive tokamak-type fusion reactors, any conclusions drawn from them should be interpreted carefully and not arbitrarily extrapolated to fusion power systems in general. The key conclusions from the study of the liquid lithium cooled first wall/blanket concept may be summarily stated as follows: (a) The maximum allowable neutron wall loading for a given reactor design can be increased from 40 to 90% by the addition of a divertor. The magnitude of the increase depends primarily on which criteria set the maximum wall loading, e.g., increases tend to be greatest in thermal stress limited systems. (b) With respect to overall thermal hydraulic performance, austenitic alloys will tend to be thermal stress limited, whereas vanadium-base alloys will be limited by the pinch between maximum allowable structural temperature and minimum coolant inlet temperature. (c) Significantly higher neutron wall loadings appear to be achievable with vanadium alloys than with solution annealed 316-SS. (d) Ignoring the application of advanced power conversion cycles, there is little incentive for structural temperatures in excess of 650°C, since the associated coolant (lithium) exit temperatures (≥ 550°C) are more than adequate to drive optimized steam turbine cycles. (e) Overall design and performance objectives for lithium cooled reactors will be more easily met at lower toroidal fields (8 to 9 T). Fields as high as 12 T may preclude the use of circulating lithium in all but the most outboard regions of the blanket, and by in large it will not be possible to use liquid lithium as a coolant for the innermost blanket region regardless of the toroidal field strength.

For the case of the helium cooled stagnant lithium first wall/blanket concept, the key conclusions are as follows: (a) A maximum allowable structural temperature ≤ 650°C will be necessary to assure the attainment of attractive operating conditions (i.e., reasonable thermodynamic efficiency) for the helium coolant. (b) As in the case of the lithium cooled first

wall/blanket concept, the presence of a divertor increases the allowable wall loading by nearly a factor of two in thermal stress limited system. (c) The transverse cooling arrangement employed in the helium cooled concept (Figure 2) requires an enormous number of individual tubes and is probably less attractive (from the standpoint of fabricability and overall thermal hydraulic performance) than the radially cooled helium blanket concept described by Kearney, et al.[14]. (d) There appears to be some incentive to provide for augmentation of the heat transfer coefficient in helium cooled reactors, even though this will undoubtedly be accompanied by increased pressure losses.

Finally, it must be noted that the studies described herein consider only quasi-steady state performance of the first wall/blanket system, and as a result the derived operating conditions (wall loadings, coolant exit temperatures, etc.) represent upper limits to the performance of an actual system. In the long run, the effects of thermal strain and cyclic fatigue will act to reduce the allowable wall loading and in all likelihood, the peak allowable structural temperature as well. This contention is supported by the more recent work of Majumdar and Misra[15,16] on the fatigue life modeling of the lithium-cooled module in Figure 3.

V. Acknowledgements

The authors are grateful to M. A. Abdou, H. C. Stevens, D. L. Smith, R. F. Mattas, S. D. Harkness, and W. M. Stacey, Jr., for numerous helpful discussions. The equations for computing average values of $\int B^2 dx$ were derived by L. R. Turner. D. W. Kearney (General Atomic Company) provided many useful pieces of information on the helium coolant thermal hydraulics and was kind enough to review portions of the work described in this report. Support for these studies was provided by the Office of Fusion Energy, Department of Energy.

VI. Nomenclature

A. Nomenclature for Lithium Cooled First Wall/Blanket Concept

a	Channel radius or channel half-width.
A	Surface area.
B	Average magnetic field.
B_{max}	Maximum magnetic field.
c_1, c_2	Nuclear attenuation coefficients.
C_p	Heat capacity of coolant.
D	Diameter.
E	Modulus of elasticity.
h	Heat transfer coefficient.
H	Hartman number.
K	Thermal conductivity.
L	Length of coolant passage.
Nu	Nusselt number defined as hD/K.
dp/dx	Pressure gradient.
ΔP	Total pressure drop.
P_f	Power fraction.
P_{pu}	Pumping power.
P_{th}	Thermal power.
Pr	Prandtl number defined as $C_p\mu/K$.
Q	Heat flux.
q_1''', q_2'''	Internal heat generation rate.
q_{v1}	Average volumetric heating rate.
R	Major radius.
R_1	Radius of inner leg of magnet.
R_2	Radius of outer leg of magnet.
r_1	Radius of first wall.
S	Stress.
T	Temperature.
$T(MAX)$	Maximum allowable material temperature.
$T(CE)$	Coolant exit temperature.
ΔT	Temperature difference.
t	Thickness of metal wall.

U	Overall heat transfer coefficient.
V	Velocity of coolant.
W	Coolant mass flow rate.
x	Distance radially outward from first-wall surface.
Y	Thickness.
α	Coefficient of thermal expansion.
κ	Empirical constant.
ν	Poisson's ratio.
μ	Viscosity of coolant.
σ	Electrical conductivity.
ϕ	Conductance ratio.
ρ	Density.

Subscripts

B	Blanket inlet tube.
C	Lithium cell.
CB	Between cell and inlet tube.
EX	Exit.
F	Film.
FW	First wall.
IN	Inlet.
L	Lithium
LB	Blanket inlet tube interior.
LC	Lithium cell interior.
LO	Outlet to cell annulus.
LI	Inlet to cell annulus.
M	Magnet.
MHD	Magnetohydrodynamic.
n,i	Any axial location. (1,2,...6)
N	Nuclear.
S	Shield.
s	Surface.
SH	Wall Shear.
v	Volumetric.
w	Wall.

WI	Inner wall.
WO	Outer wall.

B. Nomenclature for Helium-Cooled First Wall/Blanket Concept

A	Cross-sectional area.
Cp	Heat capacity.
c_1, c_2	Attenuation coefficients.
D	Diameter.
E	Modulus of elasticity.
f	Friction factor.
g_c	Conversion factor.
H	Heat transfer coefficient.
K	Thermal conductivity.
ΔP	Pressure drop.
P_{in}	Inlet pressure.
P_r	Prandtl number, defined as $Cp\mu/k$.
P_f	Fraction of neutron wall loading.
P_{pu}	Pumping power.
P_{th}	Thermal power.
q_{v1}, q_{v2}, q_v	Volumetric heat generation rate.
q_1, q_2, q_3	Heat generation rate.
Q_N	Neutron wall loading.
Q_s	Surface heat flux.
Q	Heat flow rate.
R_e	Reynolds number defined as $Du\rho/\mu$
T_{in}	Coolant inlet temperature.
T_{EX}, T(CE)	Coolant exit temperature.
T_M, T(MAX)	Maximum allowable material temperature.
T_{WI}	Interior wall temperature.
ΔT	Temperature difference.
u	Velocity of coolant.
V_f	Void fraction.
x_f, x_h	Empirical multipliers for frictional pressure drop and heat transfer coefficient respectively.

$y_1, y_2 \ldots y_6$	Radial distances from plasma boundary.
L	Coolant channel length.
t	Thickness of tube wall.
$\dot{\omega}$	Coolant mass flow rate.
α	Coefficient of thermal expansion.
μ	Viscosity of coolant.
ρ	Density of coolant.
ν	Poisson's ratio.
σ	Stress.

Subscripts

B	Blanket.
c	Coolant.
f	First wall.
s	Surface.
v	Volume.
F	Film.
Li	Lithium.
t	Thermal.
y	Yield.

References

1. M. A. Abdou, et al., Fusion Power Program Quarterly Progress Report, October-December, 1976, Argonne National Laboratory, ANL/FPP-76-6 (1977).

2. B. Misra, H. C. Stevens, and V. A. Maroni, "Thermal Hydraulic and Power Cycle Analysis of Liquid Lithium Blanket Designs," Proceedings of the 1977 National Heat Transfer Conference, August 15-17, 1977, Salt Lake City, Utah.

3. R. F. Mattas and D. L. Smith, "Modeling of Life-Limiting Properties of Fusion Reactor Structural Materials," Argonne National Laboratory, ANL/FPP-TM-84 (1977).

4. B. Badger, et al., "A Wisconsin Toroidal Fusion Reactor Design: UWMAK-1," University of Wisconsin, UWFDM-68 (1974); also, B. Badger, et al., "UWMAK-III, A Noncircular Tokamak Power Reactor Design," University of Wisconsin, UWFDM-150 (1976).

5. A. P. Fraas, "Conceptual Design of the Blanket and Shield Region and Related Systems for a Full-Scale Toroidal Fusion Reactor," Oak Ridge National Laboratory, ORNL-TM-3096 (1973).

6. J. R. Stranbridge, et al., "Design of Stainless Steel Blanket Cells for a Fusion Reactor," Culham Laboratory, CLM-R127 (1974).

7. J. T. D. Mitchell and R. Hancox, "A Lithium Cooled Toroidal Fusion Reactor," Culham Laboratory, CLM-P319 (1972).

8. G. A. Carlson, "Magnetohydrodynamic Pressure Drop of Lithium Flowing in Conducting Wall Pipe in a Transverse Magnetic Field - Theory and Experiment," Proceedings of the First Topical Meeting on the Technology of Controlled Nuclear Fusion, CONF-740402-P1, (April, 1974).

9. M. A. Hoffman, et al., "Review of Heat Transfer Problems with Magnetically-Confined Fusion Reactor Concepts," Lawrence Livermore Laboratory, UCRL-78036, (1976).

10. L. R. Turner, Argonne National Laboratory, personal communication (1977).

11. M. M. El-Wakil, Nuclear Heat Transport, International Text Book Company, Scranton, Pennsylvania (1971).

12. G. R. Hopkins, and G. Melese-d'Hospital, "Helium Cooling of Fusion Reactors," Nuclear Engineering and Design, Vol. 26, (1974), pp. 215-230.

13. D. W. Kearney, et al., General Atomic Company (personal communication).

14. D. W. Kearney, et al., "Conceptual Design Study of a Noncircular Tokamak Demonstration Fusion Power Reactor," General Atomic Company, GA-A13992/UC-20 (1976).

15. S. Majumdar and B. Misra, "Thermal Hydraulic and Fatigue-Life Modeling of a Lithium-Cooled First Wall/Blanket System," Transactions of the ANS 1977 Winter Meeting, November 27-December 2, 1977, San Francisco.

16. S. D. Harkness, D. Kummer, et al., "The Establishment of Alloy Development Goals Important to the Commercialization of Tokamak-Based Fusion Reactors," Joint report by Argonne National Laboratory and McDonnell Douglas Corporation - East, ANL/FPP/TM-99 and MDCE-1743 (1977).

APPENDIX A

Description of Computer Code

The computer code BLANKET consists of a driver program and two subroutines -- LITHIUM and HELIUM -- which execute thermal hydraulic calculations based on two distinct blanket cooling concepts as described in the body of the report. The function of the driver program is to read the generalized input data and select the appropriate subroutine(s) for each parametric investigation. FORTRAN listings of the driver program (BLANKET) and the two subroutines (LITHIUM and HELIUM) are given in Table A-1 (included at the end of Appendix A). Tables A-2 and A-3 contain information on the ordering and the units for the input parameters. The following FORMATS are used for all input data cards:

Integer Constants (fixed point): 12I6

Variables (floating point): 6D12.6

Alpha-numeric Information: 9A8

Table A-2. Input Data for Subroutine LITHIUM

Card No.	FORTRAN Name	Description
1	NN	Number of values of magnetic flux.
	NM	Number of values of radiation power fraction.
	NC	Number of incremental values of the neutron wall loading. Note: The neutron wall loading is calculated in a stepwise manner until the desired wall loading is reached as dictated by one of the constraints.
	NT	Number of values of the cell wall thickness.
	KV	Option to select a set of property values: KV = 0, use SS data; KV = 1, use vanadium alloy data.

Table A-2 (Cont'd)

Card No.	FORTRAN Name	Description
	KPR	Option to print out input data: KPR ≥ 1, prints input data.
	KOPT	Option to read, print and execute calculations KOPT = 1, for LITHIUM, KOPT = 2 for HELIUM.
2	TITLE	A set of alpha-numeric characters to identify Input/Output data sets.
3	SF	Safety factor for pressure drop calculations.
	CR	Major radius of reactor, m.
	CR1	Radius of inner leg of magnet, m.
	CR2	Radius of outer leg of magnet, m.
	D_1	Diameter of coolant inlet tube, cm.
	PIN	Minimum pressure of coolant at pump inlet, psia.
4	Q11	Volumetric heating rate, W/cm^3.
	Q12	Volumetric heating rate, W/cm^3.
	SR1	Radius of first wall, m.
	TCB	Wall thickness of inlet tubing, cm.
	TB	Thickness of blanket, m.
	TSH	Thickness of shield, m.
5	TMS	Thickness of magnet, m.
	TIN	Coolant inlet temperature, °C.
	TEX	Coolant exit temperature, °C.
	TM	Maximum material temperature, °C.
	VF	Void fraction in blanket.
	XLB	Length of coolant passage in blanket, cm.
6	XLC	Length of coolant passage in cell, cm.
	XLS	Length of coolant passage in shield, cm.
	XLM	Length of coolant passage in magnet, cm.
	XNU	Nusselt number.
	TCF	Thickness of stagnant lithium layer at the first wall, cm.

Table 2 (Cont'd)

Card No.	FORTRAN Name	Description
7	NN, NT, etc.	Repeat of card 1. Note: It is not necessary to read every value on card 1 twice. The code is set up this way for the sake of convenience.
8	TXX	NT values of wall thickness, cm. Note: Read as many values of wall thickness as desired (6 values per card).
9	BMX	NN values of magnetic flux, tesla. Note: The output format is set up for NN $\leq$ 4.
10	PF	NM values of radiation power fraction.

Note: Cards 7-10 constitute a data set, and may be read as many times as desired to cover the range of variables. A blank card at the end of the data set (cards 7-10) will terminate calculations.

Typical Input Format for Subroutine LITHIUM

```
  4     2   200     6     0     1     1
2.000000D 00   8.000000D 00   3.700000D 00   1.327000D 01   1.000000D 01   3.000000D 01
9.800000D 00   4.000000D 00   3.400000D 00   5.000000D-01   6.000000D-01   9.000000D-01
5.200000D-01   2.500000D 02   4.750000D 02   5.000000D 02   4.000000D-02   6.000000D 01
6.000000D 01   1.350000D 02   1.000000D 02   5.250000D 00   5.000000D-01
```

Table A-3. Input Data for Subroutine HELIUM

Card No.	FORTRAN Name	Description
1	NN	Number of cases to be used in parametric study. Note: The output format is set up for NN equal to multiples of 9. Hence, NN = 9, 18, 27 or 36.
	NM	Not used.
	NC	Number of incremental values of the neutron wall loading.
	NT	Not used.
	KV, KPR, KOPT	Refer to card 1 of Table A-2 for description.
2	TITLE2	A set of alpha-numeric characters to identify input/output data set.
3	DPF	Incremental value of the neutron wall loading factor (PF). Note: A wall loading factor is used to calculate the neutron wall loadings in conjunction with DPF and NC based on Q11 and Q12 (normalized for wall flux - 1 W/cm^3).
	PX	Radiation power fraction.
	PFO	An initial guess value for the wall loading factor (PF).
	Q11, Q12	Refer to card 4 (Table A-2).
	RHOM	Density of coolant channel material, lb_m/ft^3.
4	RFW	Ratio of pumping power to thermal power for first wall region, %.
	RBK	Ratio of pumping power to thermal power for blanket region, %.
	TM	Maximum allowable material temperature, °C.
	VEL1	Coolant velocity in first wall region, ft/s.
	VEL	Not used in the current version of subroutine HELIUM.
	XJH	Empirical multiplier in heat transfer calculations.
7	XJF	Empirical multiplier used in pressure drop calculations.
	XTS	A multiplication factor used to equate yield stress to thermal stress in order to calculate the limiting neutron wall loading.

Note: The thermal stress criterion used to calculate the neutron wall loading is not cmployed when k ≥ (i.e., for vanadium alloy). Hence, when KV = 1, use NC = 1, DPF = 0 and PFO equal to the desired neutron wall loading.

Table 3 (Cont'd)

Card No.	FORTRAN Name	Description
8	TITLE	A set of alpha-numeric characters used to identify individual sets of input data.
9	PIN	Coolant inlet pressure, psia.
	TIN	Coolant inlet temperature, °C.
	TEX	Coolant exit temperature, °C.
	DTLI	Temperature difference between the isothermal boundary and the coolant tube maximum temperature, °C.
	VF	Void fraction for the blanket region.
	X_3	An initial guess of the thickness of the first wall region, cm.

Note: Cards 8 and 9 constitute a set of specific operating variables for the parametric study. Use as many cases as desired using a 2-card input data set. To properly fit into the output format, the number of data sets should be multiples of 9. A blank card at the end of the data set terminates the program calculations.

Computer program BLANKET can be used to carry out simultaneous thermal hydraulic calculations for both cooling concepts or individual calculations for either one of them. For simultaneous calculations, the helium data should follow the lithium data with KOPT = 1 for the first data set, and KOPT = 2 for the second data set. For lithium calculations only, insert a BLANK card at the end of the lithium data set. If calculations for helium only are to be carried out, the first set of data should represent the operating parameters for helium. A blank card at the end of the data set will terminate the calculations.

Typical Numerical Values

A set of typical numerical values of the input parameters are listed below. (The parametric investigations described in the report were limited to the following ranges of the operating variables:)

1. Subroutine LITHIUM

Material:	stainless steel, vanadium alloy
Toroidal field:	7, 8, 10, 12 Tesla
Maximum Material Temperature:	
Stainless Steel	500, 650°C
Vanadium Alloy	600, 700°C

Wall Thickness:	0.20 to 0.8 cm
Radiation power fraction:	0.10, 0.25
Coolant temperature rise:	200 to 350°C
Neutron wall loading	1 to 12 MW/m^2

2. Subroutine HELIUM

Material:	Stainless steel and vanadium alloy
Maximum Material Temperature:	
Stainless Steel	500, 650°C
Vanadium Alloy	600, 700°C
Coolant temperature rise:	200, 300°F
Cooling inlet pressure:	750, 1000, 1500 psia
Void fraction in blanket region:	5, 7, 10%
Radiation power fraction:	0.10, 0.25
Neutron wall loading	1 to 12 MW/m^2
Temperature difference between an isothermal boundary and coolant channel wall:	25, 50, 100°C
Allowable thermal stress:	σ_y, $2\sigma_y$ (σ_y = yield strength)

The results of the analytical calculations for a set of typical input values are given in Tables A-4 and A-5, respectively for the two blanket concepts.

Table A-1

Fortran Listing for Computer Program BLANKET Including Subroutines LITHIUM and HELIUM

```
      IMPLICIT REAL*8 (A-H,O-Z)
      DIMENSION TITLE(9), TITLE1(9), TITLE2(9)
      DIMENSION BMX(5), PF(5), QN(200), TXX(25)
      COMMON/MISRA/NN, NM, NC, NT, KV, KPR, KOPT
      COMMON/MISRA1/SF, CP, D1, DELX, TCB, TB, TSH, TMG, XLB, XLC,
     1XLS, XLM, TCF, TXX
      COMMON/MISRA2/ALF, DPF, PX, PF0, RHOM, RFW, RBK, VEL1, VEL , XJH,
     1XJF, XTS, YME
      COMMON/MISRA3/PIN, Q11, Q12, TIN, TEX, TM, VF, CR, CR1, CR2, SR1
      COMMON/MISRA4/TITLE
   10 READ   1200, NN, NM, NC, NT, KV, KPR, KOPT
      IF ( NN .LE. 0 )  GO  TO  1000
      GO  TO  ( 20, 30 ), KOPT
   20 READ  1150, TITLE1
      READ    1100, SF, CR, CR1, CR2, D1, PIN, Q11, Q12, SR1, TCB,
     1TB, TSH, TMG, TIN, TEX, TM, VF, XLB, XLC, XLS, XLM, XNU, TCF
      GO  TO  40
   30 READ  1150, TITLE2
      READ   1100, DPF, PX, PF0, Q11, Q12, RHOM, RFW, RBK, TM, VEL1,
     1VEL, XJH, XJF, XTS
   40 CONTINUE
      IF ( KPR .LE. 0 )  GO  TO  70
      PRINT  2200
      GO  TO  ( 50, 60 ), KOPT
   50 PRINT  1150, TITLE1
      PRINT  1200, NN, NM, NC, NT, KV, KPR, KOPT
      PRINT  2100,  SF, CR, CR1, CR2, D1, PIN, Q11, Q12, SR1, TCB,
     1TB, TSH, TMG, TIN, TEX, TM, VF, XLB, XLC, XLS, XLM, XNU, TCF
      GO  TO  70
   60 PRINT  1150, TITLE2
      PRINT  1200, NN, NM, NC, NT, KV, KPR, KOPT
      PRINT  2100, DPF, PX, PF0, Q11, Q12, RHOM, RFW, RBK, TM, VEL1,
     1VEL, XJH, XJF, XTS
   70 CONTINUE
C     CALL FOR SUBROUTINES..LITHIUM AND HELIUM
      GO  TO  ( 100, 200 ), KOPT
  100 CALL LITHUM
      GO  TO  10
  200 CALL HELIUM
      GO  TO  10
 1000 STOP
C     FORMAT STATEMENTS
 1100 FORMAT ( 6D12.6 )
 1150 FORMAT ( 9A8 )
 1200 FORMAT ( 12I6 )
 2100 FORMAT ( 1P6D15.6 )
 2200 FORMAT ( '1', ' INPUT CONSTANTS' )
      END
C     PROGRAM TO ESTIMATE PRESSURE DROP IN LITHIUM BLANKET
C     * * * * CALCULATIONS FOR LITHIUM COOLANT * * * *
      SUBROUTINE LITHUM
      IMPLICIT REAL*8 (A-H,O-Z)
      DIMENSION SBMAX(5),SBMB(5), SBMC(5), SBMS(5), SBMM(5), SRPT(5),
     1SDTPW(5), THS(5), QN(200), PF(5), BMX(5), TOI(5), TXX(25)
      DIMENSION DIB(5), DIC(5), DIS(5), DIM(5), TKB(5), TKC(5), TKS(5),
     1TKM(5), VLB(5), VLC(5), VLS(5), VLM(5), DELPB(5), DELPC(5),
     2DELPS(5), DELPM(5),    DPT(5), TPW(5), TCEX(5), TCI(5), MFX(5) ,
     3QNX(5)
      COMMON/MISRA/NN, NM, NC, NT, KV, KPR, KOPT
      COMMON/MISRA1/SF, CP, D1, DELX, TCB, TB, TSH, TMG, XLB, XLC,
     1XLS, XLM, TCF, TXX
```

```
      COMMON/MISRA3/PIN, Q11, Q12, TIN, TEX, TM, VF, CR, CR1, CR2, SR1
      AIF = 1.0D-05
      YME = 25.0D06
      IF ( KV .EQ. 1 )  YME = 17.80D06
      IF ( KV .EQ. 1 )  ALF = 10.50D-06 / 1.80D00
      CP = 4.20D00
      DELX = 10.0D00
      XNS = 0.30D00
      C1 = 0.03D00
      CP = CP * 0.239006
      XNU = 5.25
      QNO = 0.0D00
      DELQ = 0.10D00
      IF ( KV .LE. 0 )  DELQ = 0.05
      DELX = DELX / 30.48
      X3 = 20.0
      X4 = 30.0
      X5 = 40.0
      X6 = 50.0
      X7 = 60.0
      Y1 = 0.0D00
      GC = 32.17 * (3600.0)**2
      PI = 3.141592654D00
      XJ = 778.0D00
      TCC = TCB
      TCS = 0.5
      TCM = 0.5
      RAB = D1 * 0.50
      D2 = 50.0 D00
C     D2 = D1 / DSQRT(VF)
      RAC = D2 * 0.50
      RAS = RAB * DSQRT(10.0D00)
      RAM = RAS
      X = TB
      TM = TM*1.80D00 + 492.0D00
      TIN = TIN * 1.80D00 + 492.0D00
      TINO = TIN
      TEX = TEX * 1.80D00 + 492.0D00
      DTCLNT = TEX - TIN
      DTCB = (TEX-TIN) * 0.50D00
      AX = PI / 4.0 * D1**2
      DF = D1 / 30.48
      AF = PI / 4.0 * DF**2
      CNVF = 1.0D-08 * (3.414/3600.0D00) * XJ * (30.48D00)**3
      TAV = (TEX+TIN)* 0.50 / 1.80
      XKLI = ( 8.24D00 + 7.46D-03 * (TAV-273.3D00) ) * 2.419D00
      XKV = ( 0.0765D00 + 2.80D-05 *(TM/1.80D00-400.0D00) ) * 241.9
      XKSS = 8.093782 + 4.348935D-03 * TM
      IF ( KV .EQ. 1 )  XKSS = XKV
      TW = TM -460.0D00
      SIGH = ( 3.68359D01 - 8.634925D-02*TW + 2.121526D-04*TW**2 -
     13.445285D-07*TW**3+ 3.353186D-10*TW**4 - 1.707864D-13*TW**5 +
     23.429909D-17*TW**6 ) * 1.0D03
      IF ( KV .EQ. 1 )  SIGH = 5.10D04
      CM = 1.4936D00-0.7368D00 * DLOG10(TAV)  + 109.95D00 / TAV
      XMU = 10.0D00 **(CM) * 1.0D-02
      SIGW = 1.0D00/( 70.7D00 + 0.067D00*(TAV-237.3)) * 1.0D06
      SIGL = 1.0D00 / ( 21.55D00 + 0.0262D00 * (TAV-273.1) )* 1.0D06
      RI = 1.0 / SIGL
      SIGV = 1.0D00 / ( 0.075 * (TAV-273.1)) * 1.0D06
      IF ( KV .EQ. 1 )  SIGW = SIGV
      RHO = ( 0.515D00 - 1.01D-04*(TAV-473.1D00)) * 62.4D00
```

```
      HT1 = XNU * XKLI / (D1/30.48)
      HT2 = XNU * XKLI / ((D2-D1)/30.48)
      HB = 1.0 / ( 1.0/HT1 + 1.0/HT2 + (TCB/30.48)/XKSS )
C     * * * * START OF ITERATICN LOOP* * * *
   10 READ   1200, NN, NM, NC, NT, KV, KPR, KOPT
      IF ( NN .LE. 0 )  GO  TO  1000
      XNC = NC
      READ   1100, ( TXX(L), L = 1, NT )
      READ  1100, ( BMX(I), I = 1, NN )
      READ  1100, ( PF(J), J = 1, NM )
      IF ( KPR .LE. 0 )  GO  TO  15
      PRINT  2200
      PRINT  1200, NN, NM, NC, NT, KV, KPR, KOPT
      PRINT  2100, ( TXX(L), L = 1, NT )
      PRINT 2100, ( BMX(I), I = 1, NN )
      PRINT 2100, ( PF(J), J = 1, NM )
   15 CONTINUE
      DO  400  L = 1, NT
      TCC = TXX(L)
      DO  400  J = 1, NM
      DO  260  I = 1, NN
      BMAX = BMX(I)
      BMBS = BMAX**2/(CR*X*(SR1+X/2.0))* (CR1+TMG/2.0)**2 *
     1( DSQRT(CR**2 - SR1**2) -   DSQRT(CR**2 - (SR1+X)**2 ))
      BMB = DSQRT(BMBS)
      BMC = BMB
      XMSS=BMAX**2*(CR1+TMG/2.0)**2 * ( 1.0/(CR+SR1+X) - 1.0/(CR2-
     1TMG/2.0) ) / TSH
      BMS = DSQRT(XMSS)
      BMM = DSQRT(BMAX**2/3.0 * (CR1+TMG/2.0)**2 / (CR2-TMG/2.0)**2 )
      IP = 0
      DO  200 K = 1, NC
      XK = K
      QN(K) = QN0 + DELQ * XK
      QF1 = Q11 * QN(K)
      QF2 = Q12 * QN(K)
      QS0 = QN(K) * PF(J)
      QS1 = QS0 * 3.172D05
      Q0 = QN(K) + QS0
      QS = Q0 * 3.172D05
      WD = Q0 * 9.6674D04 / (CP*DTCLNT)
      ITR = 0
   20 CONTINUE
      ITR = ITR + 1
      IF ( ITR .GT. 15)  GO  TO  90
      VB  = WD/3600.0/RHO / (PI/4.0*(D1/30.48)**2) * 30.48
      VC = VB * D1**2 / (D2**2 - D1**2 )
      VS = VB
      VM = VB
      RE1 = (D1/30.48) * (WD/AF) / (XMU*242.0)
      F1 = 0.046 / (RE1)**0.2
      DPF1 = 2.0*F1 * (XLB/30.48)* (WD/AF)**2 / (GC*D1/30.48*RHO)
      Y2 = TCC
      Y3 = Y2 + TCF
      X1 = Y3
      X2 = 10.0 - Y3
      QX1 = QF1/C1 * ( 1.0D00/DEXP(C1*Y1) - 1.0D00/DEXP(C1*Y2)) /(Y2-Y1)
      QX2 = QF2/C1 * ( 1.0D00/DEXP(C1*Y2) - 1.0D00/DEXP(C1*Y3)) /(Y3-Y2)
      QCW = QX1 * 9.6674D04
      QFW = QX2 * 9.6674D04
      QB1= QS * PI/4.0 * ((D1+2.*TCB)/30.48)**2
      QB2 = PI * D1/30.48 * XLB/30.48 * HB * DTCB* (XK/XNC)
```

```
      QB = QB1 + QB2
      DTS = QS1 * (TCC/30.48) / XKSS
      DTV = QCW * (TCC/30.48)**2 / (2.0*XKSS)
      TSFW = ALF * YME / (2.0D00*(1.0D00-XNS) ) * ( DTS + DTV )
      DTF = (QS1+QCW*TCC/30.48)*TCF/30.48 / XKLI + QFW*(TCF/30.48)**2 /
     1(2.0*XKLI)
      DTT = DTS + DTV + DTF
      QV1 = QF2/C1 * ( 1.0D00/DEXP(C1*X1) - 1.0D00/DEXP(C1*X2)) /(X2-X1)
      QV2 = QF2/C1 * ( 1.0D00/DEXP(C1*X2) - 1.0D00/DEXP(C1*X3)) /(X3-X2)
      QV3 = QF2/C1 * ( 1.0D00/DEXP(C1*X3) - 1.0D00/DEXP(C1*X4)) /(X4-X3)
      QV4 = QF2/C1 * ( 1.0D00/DEXP(C1*X4) - 1.0D00/DEXP(C1*X5)) /(X5-X4)
      QV5 = QF2/C1 * ( 1.0D00/DEXP(C1*X5) - 1.0D00/DEXP(C1*X6)) /(X6-X5)
      QV6 = QF2/C1 * ( 1.0D00/DEXP(C1*X6) - 1.0D00/DEXP(C1*X7)) /(X7-X6)
      DTF1 = QV1 * 9.6674D04 * (TCC/30.48) / HT2
      DTF2 = QV2 * 9.6674D04 * (TCC/30.48) / HT2
      DTF3 = QV3 * 9.6674D04 * (TCC/30.48) / HT2
      DTF4 = QV4 * 9.6674D04 * (TCC/30.48) / HT2
      DTF5 = QV5 * 9.6674D04 * (TCC/30.48) / HT2
      DTF6 = QV6 * 9.6674D04 * (TCC/30.48) / HT2
      DTW1 = QV1 * 9.6674D04 * (TCC/30.48)**2 / (2.0*XKSS)
      DTW2 = QV2 * 9.6674D04 * (TCC/30.48)**2 / (2.0*XKSS)
      DTW3 = QV3 * 9.6674D04 * (TCC/30.48)**2 / (2.0*XKSS)
      DTW4 = QV4 * 9.6674D04 * (TCC/30.48)**2 / (2.0*XKSS)
      DTW5 = QV5 * 9.6674D04 * (TCC/30.48)**2 / (2.0*XKSS)
      DTW6 = QV6 * 9.6674D04 * (TCC/30.48)**2 / (2.0*XKSS)
      DTL1 = QV1 * 9.6674D04 * PI/4.0 * (((D2+2.0*TCC)/30.48)**2 -
     1((D1+2.0*TCB)/30.48)**2) * DELX / ( WD*CP ) - (QB2/6.0)/(WD*CP)
      DTL2 = QV2 * 9.6674D04 * PI/4.0 * (((D2+2.0*TCC)/30.48)**2 -
     1((D1+2.0*TCB)/30.48)**2) * DELX / ( WD*CP ) - (QB2/6.0)/(WD*CP)
      DTL3 = QV3 * 9.6674D04 * PI/4.0 * (((D2+2.0*TCC)/30.48)**2 -
     1((D1+2.0*TCB)/30.48)**2) * DELX / ( WD*CP ) - (QB2/6.0)/(WD*CP)
      DTL4 = QV4 * 9.6674D04 * PI/4.0 * (((D2+2.0*TCC)/30.48)**2 -
     1((D1+2.0*TCB)/30.48)**2) * DELX / ( WD*CP ) - (QB2/6.0)/(WD*CP)
      DTL5 = QV5 * 9.6674D04 * PI/4.0 * (((D2+2.0*TCC)/30.48)**2 -
     1((D1+2.0*TCB)/30.48)**2) * DELX / ( WD*CP ) - (QB2/6.0)/(WD*CP)
      DTL6 = QV6 * 9.6674D04 * PI/4.0 * (((D2+2.0*TCC)/30.48)**2 -
     1((D1+2.0*TCB)/30.48)**2) * DELX / ( WD*CP ) - (QB2/6.0)/(WD*CP)
      Q1   = QS1 * PI/4.0 *( ((D2+2.0*TCC)/30.48)**2- ((D1+2.0*TCB)/
     130.48)**2)
      Q2 = QX1 * 9.6674D04 * PI/4.0 *(((D2+2.0*TCC)/30.48)**2 * Y2/30.48
     1-((D1+2.0*TCB)/30.48)**2*Y2/30.48) +
     2QX2 * 9.6674D04 * PI/4.0 *(((D2+2.0*TCC)/30.48)**2 * Y3/30.48
     3-((D1+2.0*TCB)/30.48)**2*Y3/30.48)
      Q3 = (QV1+QV2+QV3+QV4+QV5+QV6)*9.6674D04*PI/4.0*(((D2+2.0*TCC)/
     130.48)**2 ) * DELX
      QTTL = Q1 + Q2 + Q3
      WD = QTTL / ( CP * DTCLNT )
      DTTL = QTTL / (WD*CP)
      DTLI = QB / (WD*CP)
      DTL0 = (Q1+Q2) / (WD*CP)
      TLI = TIN + DTLI
      TL0 = TLI + DTL0
      TL1 = TL0 + DTL1
      TL2 = TL1 + DTL2
      TL3 = TL2 + DTL3
      TL4 = TL3 + DTL4
      TL5 = TL4 + DTL5
      TL6 = TL5 + DTL6
      DTLX = DTL0 + DTL1 + DTL2 + DTL3 + DTL4 + DTL5 + DTL6 + DTLI
      TW0 = TLI + DTT
      TW1 = TL1 + DTF1 + DTW1
      TW2 = TL2 + DTF2 + DTW2
```

```
      TW3 = TL3 + DTF3 + DTW3
      TW4 = TL4 + DTF4 + DTW4
      TW5 = TL5 + DTF5 + DTW5
      TW6 = TL6 + DTF6 + DTW6
      IF ( ITR .LE. 5 )  GO  TO  60
      IF ( TW6 .GT. TM )  GO  TO  40
      IF ( TW0 .GT. TM )  GO  TO  50
   40 CONTINUE
      IF ( TW0 .GT.TW6 )  GO  TO  50
      TIN = TIN0 - (TW6-TM)
      GO  TO  60
   50 CONTINUE
      TIN = TIN0 - (TW0-TM)
   60 CONTINUE
      TIN0 = TIN
      PHB = SIGW * TCB / ( SIGL*RAB)
      PHC = SIGW * TCC / ( SIGL*RAC)
      PHS = SIGW * TCS / ( SIGL*RAS)
      PHM = SIGW * TCM / ( SIGL*RAM)
      DPB1 = VB * PHB * SIGL * XLB * BMB**2 * CNVF * SF
      DPC1 = VC * PHC * SIGL * XLC * BMC**2 * CNVF * SF
      DPS1 = VS * PHS * SIGL * XLS * BMS**2 * CNVF * SF
      DPM1 = VM * PHM * SIGL * XLM * BMM**2 * CNVF * SF
      HNSQ = RAB**2 * BMB**2 * SIGL/XMU * 981.0 * 1.019716D04 * 1.0D-08
      HMN = DSQRT(HNSQ)
      DPB2 = (XMU*242.0) * (VB*3600.0) * (XLB/30.48) / RAB**2 / GC *
     1( HMN + HMN**2 *PHB/(1.0D00 + PHB )) / 30.48D00 * (30.48)**2
      HMNX = DSQRT( SIGL / XMU * 981.0 * 1.019716D04 ) * 1.0D-04
      HMB = RAB * BMB * HMNX
      HMC = RAC * BMC * HMNX
      HMS = RAS * BMS * HMNX
      HMM = RAM * BMM * HMNX
      DPB2 = (XMU*242.0) * (VB*3600.0) * (XLB/30.48) / RAB**2 / GC *
     1( HMB + HMB**2 *PHB/(1.0D00 + PHB )) / 30.48D00 * (30.48)**2
      DPC2 = (XMU*242.0) * (VC*3600.0) * (XLC/30.48) / RAC**2 / GC *
     1( HMC + HMC**2 *PHC/(1.0D00 + PHC )) / 30.48D00 * (30.48)**2
      DPS2 = (XMU*242.0) * (VS*3600.0) * (XLS/30.48) / RAS**2 / GC *
     1( HMS + HMS**2 *PHS/(1.0D00 + PHS )) / 30.48D00 * (30.48)**2
      DPM2 = (XMU*242.0) * (VM*3600.0) * (XLM/30.48) / RAM**2 / GC *
     1( HMM + HMM**2 *PHM/(1.0D00 + PHM )) / 30.48D00 * (30.48)**2
      DPB1 = DPB1 / 144.0
      DPC1 = DPC1 / 144.0
      DPS1 = DPS1 / 144.0
      DPM1 = DPM1 / 144.0
      DPB2 = DPB2 / 144.0
      DPC2 = DPC2 / 144.0
      DPS2 = DPS2 / 144.0
      DPM2 = DPM2 / 144.0
      DP3 = PIN + DPB1 + DPC1 + 2.0 * ( DPS1+DPM1)
      PMG = DP3
      PSH = PMG - DPM1
      PBK = PSH - DPS1
      PLC = PBK - DPB1
      PLC1 = PIN + DPC1 + DPS1 + DPM1
      TCB = PBK * RAB * 3.0 / SIGH
      TCX = PLC * RAC * 3.0 / SIGH
      TCS = PSH * RAS * 3.0 / SIGH
      TCM = PMG * RAM * 3.0 / SIGH
      IF ( TCB .LT. 0.25 )  TCB = 0.25
      IF ( TCS .LT. 0.50 )  TCS =0.50
      IF ( TCM .LT. 0.50 )  TCM = 0.50
      GO  TO  20
```

```
 90 CONTINUE
    IF (TCX .GT. TCC ) IP=1
    IF ( TSFW .GT. SIGH )  IP = 1
    IF ( (TL6-DTCLNT-492.0D00)/1.8D00 .LT. 235.0D00)  IP = 1
    PPU = WD * (DP3*144.0) / RHO
    PTH = WD * CP * (TEX-TIN) * XJ
    RPT = PPU / PTH * 1.0D02
    DP1 = DPB1 / 144.0
    DP2 = DPB2 / 144.0
    DP3 = DP3 - PIN
    IF ( IP .GT. 0 )  GO  TO  250
200 CONTINUE
250 CONTINUE
    QNX(I) = QN(K)
    SBMAX(I) = BMX(I)
    SRPT(I) = RPT
    SBMB(I) = BMB
    SBMC(I) = BMC
    SBMS(I) = BMS
    SBMM(I) = BMM
    SDTPW(I) = (DTS + DTV ) / 1.80
    DIB(I) = D1
    DIC(I) = D2
    DIS(I) = 2.0 * RAS
    DIM(I) = 2.0 * RAM
    TKB(I) = TCB
    TKC(I) = TCC
    TKS(I) = TCS
    TKM(I) = TCM
    VLB(I) = VB
    VLC(I) = VC
    VLS(I) = VS
    VLM(I) = VM
    DELPB(I) = DPB1
    DELPC(I) = DPC1
    DELPS(I) = DPS1
    DELPM(I) = DPM1
    DPT(I) = DP3
    THS(I) = TSFW
    TCI(I) = ( TL6 - 492.0D00) / 1.80D00
    TPW(I) = ( TW0 - 492.0D00 ) / 1.80D00
    TCEX(I) = ( TW6 - 492.0D00 ) / 1.80D00
    MFX(I) = BMAX
    DTCX = DTCLNT/1.80D00
    TOI(I) = TCI(I) - DTCX
260 CONTINUE
    IF ( KV .EQ. 0 )  PRINT  2300
    IF ( KV .EQ. 1 )  PRINT  2350
    DO  300  M = 1, NN
    PRINT  2400, SBMAX(M), DTCX
    PRINT  2500
    PRINT  2550
    PRINT  2600, DIB(M), DIC(M), DIS(M), DIM(M)
    PRINT  2700, TKB(M), TKC(M), TKS(M), TKM(M)
    PRINT  2800, VLB(M), VLC(M), VLS(M), VLM(M)
    PRINT  2950, SBMB(M), SBMC(M), SBMS(M), SBMM(M)
    PRINT  2960, DELPB(M), DELPC(M), DELPS(M), DELPM(M)
300 CONTINUE
    PRINT  3000, PF(J)
    PRINT  3100, ( SBMAX(M), M = 1, NN )
    PRINT  3150
    PRINT  3175, ( QNX(M)  , M = 1, NN )
```

```
      PRINT  3200, ( DPT(M), M = 1, NN )
      PRINT  3250, ( TKC(M), M = 1, NN )
      PRINT  3300, ( TPW(M), M = 1, NN )
      PRINT  3350, ( SDTPW(M), M = 1, NN )
      PRINT  3375, ( THS(M), M = 1, NN )
      PRINT  3400, ( TCEX(M), M =1, NN )
      PRINT  3500, ( TCI(M), M = 1, NN )
      PRINT  3550, ( TOI(M), M = 1, NN )
      PRINT  3600, ( SRPT(M), M = 1, NN )
  400 CONTINUE
 1000 RETURN
C     * * * * FORMAT STATEMENTS* * * *
 1100 FORMAT ( 6D12.6 )
 1200 FORMAT ( 12I6 )
 2100 FORMAT ( 1P6D15.6 )
 2200 FORMAT ( '1', ' INPUT CONSTANTS' )
 2300 FORMAT ( '1', T14, ' SUMMARY OF CALCULATIONS FOR FLOWING LITHIUM
     1IN STAINLESS STEEL CELLS' )
 2350 FORMAT ( '1', T14, ' SUMMARY OF CALCULATIONS FOR FLOWING LITHIUM
     1IN VANADIUM ALLOY CELLS' )
 2400 FORMAT ( T26, ' MHD PRESSURE LOSSES FOR BMAX =', 1P1D7.1,  'T,',
     1'  DTC=', 3P1D8.0,  'C' )
 2500 FORMAT ( T28, ' BLANKET          LI-CELL          SHIELD          MAGNE
     1T' )
 2550 FORMAT ( T28, ' -------          -------          ------          -----
     1-' )
 2600 FORMAT ( ' PASSAGE DIAMETER, CM  ', 1P4D15.6 )
 2700 FORMAT ( ' CELL WALL TCKNESS, CM ', 1P4D15.6 )
 2800 FORMAT ( ' COOLANT VELOCITY, CM/S', 1P4D15.6 )
 2900 FORMAT ( ' PRESSURE DROP, PSI    ', 1P4D15.6 )
 2950 FORMAT ( ' AVG. BMAX, TESLA      ', 1P4D15.6 )
 3000 FORMAT ( '0',T11, ' SUMMARY OF THERMAL HYDRAULICS CALCULATION, POW
     1ER FACTOR=', ' PF(J)=', 1D8.2 )
 3100 FORMAT ( T26, ' BMAX=', 1P1D7.1,'T', '  BMAX=', 1P1D7.1, 'T','  BM
     1AX=', 1P1D7.1, 'T', '  BMAX=', 1P1D7.1, 'T' )
 3150 FORMAT ( T28, ' --------         -------          -------         -----
     1--' )
 3175 FORMAT ( ' WALL LOADING, MW/M**2 ', 1P4D15.6 )
 3200 FORMAT ( ' TOTAL PRESS. DROP, PSI', 1P4D15.6 )
 3250 FORMAT ( ' WALL THICKNESS, CM    ', 1P4D15.6 )
 3300 FORMAT ( ' PLASMA WALL TEMP., C  ', 1P4D15.6 )
 3350 FORMAT ( ' PLASMA WALL DELT., C  ', 1P4D15.6 )
 3375 FORMAT ( ' FW. THERMAL STRESS,PSI', 1P4D15.6 )
 3400 FORMAT ( ' CELL EXIT WALL TEMP, C', 1P4D15.6 )
 3500 FORMAT ( ' COOLANT EXIT TEMP., C ', 1P4D15.6 )
 3550 FORMAT ( ' COOLANT INLET TEMP., C', 1P4D15.6 )
 3600 FORMAT ( ' RATIO PPU/PTH, %      ', 1P4D15.6 )
      END
C     SUBROUTINE HELIUM MAKES THERMAL HUDRAULIC CALCULATIONS FOR HE
      SUBROUTINE HELIUM
      IMPLICIT REAL*8 (A-H,O-Z)
      DIMENSION SD1(40), SD2(40), STCK(40), SPIN(40), SVEL(40),
     1STIN(40), STEX(40), SQ(40),   SXNT(40), SRBK(40), SVF(40),
     2SHT(40), SWBK(40),  SDTW(40), STM(40), SDTC(40), SDTL(40)
      DIMENSION FD1(40), FD2(40), FDTC(40), FDTW(40), FDTLI(40),
     1FRFW(40), FTCK(40), FHT(40), FVEL(40), FVF(40), FXNT(40), FQ(40),
     2FTEX(40), FTM(40), FWFW(40), STSHT(40), FTSFW(40), PFX(40),
     3FXL(40), SXL(40), FTIN(40)
      DIMENSION TITLE(9)
      COMMON/MISRA/NN, NM, NC, NT, KV, KPR, KOPT
      COMMON/MISRA2/ALF, DPF, PY, PFO, RHOM, RFW, RBK, VEL1, VEL , XJH,
     1XJF, XTS, YME
```

```
      COMMON/MISRA3/PIN, Q11, Q12, TIN, TEX, TM, VF, CR, CR1, CR2, SR1
      COMMON/MISRA4/TITIE
      YME = 25.0D06
      AIF = 1.0D-05
      IF ( KV .LE. 0 )  GO  TO  10
      NC = 1
      ALF = 10.50D00 / 1.80D00
      DPF = 0.0D00
      RHOM = 372.0D00
      YME = 17.8D06
   10 CONTINUE
      IF ( KV .EQ. 0 )  PFO = 1.0D00
      IF ( XTS .GT. 1.0 )  NC = 300
      TMY = TM
      C1 = 0.03D00
      CP = 5.20D00
      CP = CP * 0.239
      PI = 3.141592654D00
      XM = 4.0D00
      GC = 32.17 * (3600.0)**2
      XJ = 778.0D00
      DVF = 0.005
      QN = 1.0D00
      XNU = 0.30D00
      XNS = 0.023D00
C     THE FOLLOWINF ARE A SET OF INITIAL GUESS VALUES
      HT1 = 500.0D00
      DHE = 2.54D00
      AX1 = PI/4.0D00 * ( DHE/30.48)**2
      Y1 = 1.0D-10
      DX = 0.02
      TW = TM * 1.80D00 + 492.0D00
      TM = TM*1.80D00 + 492.0D00
      TMO = TM
      TV1 = TMO / 1.80D00
      XKLI = ( 8.24D00 + 7.46D-03 * (TV1-273.3D00) ) * 2.419D00
      TW1 = TW
      TW = TM -460.0D00
      SIGH = ( 3.68359D01 - 8.634925D-02*TW + 2.121526D-04*TW**2 -
     13.445285D-07*TW**3+ 3.353186D-10*TW**4 - 1.707864D-13*TW**5 +
     23.429909D-17*TW**6 ) * 1.0D03
      SIGX = SIGH * XTS
      IF ( KV .EQ. 1 )  SIGH = 5.1D04
      TW = TW1
C     * * * * START OF ITERATION LOOP* * * *
      DO  150  I = 1, NN
      READ  1200, TITLE
      READ  1000, PIN, TIN, TEX, DTII, VF, X3
      IF ( PIN .LE. 0.0 )  GO  TO  900
      IF ( PX .LT. 0.25 )  GO  TO  20
      IF ( DTLI .EQ. 25.0 )    X3 = 3.50
      IF ( DTLI .EQ. 50.0 )    X3 = 4.0
      IF ( DTLI .EQ. 100.0 )   X3 = 4.5
      GO  TO  30
   20 CONTINUE
      IF ( DTLI .EQ. 25.0 )    X3 = 2.5
      IF ( DTLI .EQ. 50.0 )    X3 = 3.0
      IF ( DTLI .EQ. 100.0 )   X3 = 3.5
   30 CONTINUE
      IF ( TMY .EQ. 500.0 )  TIN = 300.0
      IF ( KPR .LE. 0 )  GO  TO  40
      PRINT  1200, TITLE
```

```
      PRINT  1900
      PRINT  2000, PIN, TIN, TEX, DTLI, VF, X3
   40 CONTINUE
C     * * * * CALCULATIONS FOR THE FIRST WALL * * * *
      TIN = TIN * 1.80D00 + 492.0D00
      TEX = TEX * 1.80D00 + 492.0D00
      TAVG = ( TEX+TIN) * 0.50D00
      RHO = XM/359.0D00 *PIN/14.67D00 * 492.0D00/TAVG
      XKSS = 8.093782 + 4.348935D-03* ( TAVG + TM0 ) * 0.50D00
      XKV = ( 0.0765D00 + 2.80D-05 *(TM/1.80D00-400.0D00) ) * 241.9
      IF ( KV .EQ. 1 )  XKSS = XKV
      DTHE = TEX - TIN
      DTLI = DTLI * 1.80D00
      TCK1 = PIN * DHE* 3.0D00 / (4.0D00*SIGH)
      IF ( TCK1 .LT. 0.125)  TCK1 = 0.125
      Y2 = PI * TCK1*(1.0D00-TCK1/DHE)/2.0D00
      Y3 = DHE + Y2
      Y4 = Y2 + Y3
      Y5 = Y4 + X3
      X1 = ( Y2-Y1) / 30.48D00
      X2 = ( Y4-Y3) / 30.48D00
      ITR = 0
      ITR3 = 0
      IX = 0
   50 CONTINUE
      DO  60  J = 1, NC
      YJ = J
      PF = PF0 + DPF * YJ
      IF ( IX .EQ. 1 )  PF = PF2
      PF1 = PF
      QS0 = QN * PX * PF
      Q0 = Q12 * PF
      QS = QN * PF
      QF1 = Q11 * PF
      QF2 = Q12 * PF
      QF3 = Q12 * PF
      Q23 = QF3 * 9.6674D04
      QS1 = QS0 * 3.172D05
      QV = Q0 * 9.6674D04
      QX1 = QF1/C1 * ( 1.0D00/DEXP(C1*Y1) - 1.0D00/DEXP(C1*Y2)) /(Y2-Y1)
      Q21 = QX1 * 9.6674D04
      FDTS = QS1 * X1 / XKSS
      FDTV = (Q21 * X1**2 / ( 2.0D00*XKSS))
      TSFW = ALF * YME / (2.0D00* (1.0D00-XNU) ) * (FDTS + FDTV)
      IF ( KV .EQ. 1 )  GO  TO  80
      IF ( DABS(SIGX-TSFW) .LE. 100.0D00)  GO  TO  80
      IF ( TSFW .GT. SIGX )  GO  TO  70
   60 CONTINUE
   70 PF2 = PF1 * (1.0-(TSFW-SIGX)/TSFW)
      IX = 1
      ITR3 = ITR3 + 1
      IF ( ITR3 .GT. 10 )  GO  TO  80
      GO  TO  50
   80 CONTINUE
      ITR = ITR + 1
      IF ( ITR .GT. 200 )  GO  TO  90
      Y5 = Y4 + X3
      X1 = Y2-Y1
      X2 = Y4-Y3
      X3 = Y5-Y4
      QX2 = QF2/C1 * ( 1.0D00/DEXP(C1*Y3) - 1.0D00/DEXP(C1*Y4)) /(Y4-Y3)
      QX3 = QF3/C1 * ( 1.0D00/DEXP(C1*Y4) - 1.0D00/DEXP(C1*Y5)) /(Y5-Y4)
```

```
      RT1 = 3.40D00 + 0.50D00 * X1 /1.0D02
      RT2 = 3.40D00 + (Y3+0.50D00*X2)/1.0D02
      RT3 = 3.40D00 + (Y4+0.50D00*X3)/1.0D02
      ST1 = 4.0D00*PI**2*8.0D00*RT1
      ST2 = 4.0D00*PI**2*8.0D00*RT2
      ST3 = 4.0D00*PI**2*8.0D00*RT3
      VT1 = ST1 * X1/1.0D02
      VT2 = ST2 * X2/1.0D02
      VT3 = ST3 * X3/1.0D02
      QVX1 = QX1 * VT1
      QVX2 = QX2 * VT2
      QVX3 = QX3 * VT3
      QVX = QVX1 + QVX2 + QVX3
      QM = 1.20D00 * QS * ST1 - QVX
      Q22 = QX2 * 9.6674D04
      Q23 = QX3 * 9.6674D04
      X1 = ( Y2-Y1) / 30.48D00
      X2 = ( Y4-Y3) / 30.48D00
      X3 = ( Y5-Y4) / 30.48D00
      FDTF = ( QS1 + Q21 * X1 ) / HT1
      TM1 = TM0
      TEX1F= TM0 - FDTV - FDTS - FDTF
      TEX1 = TM0 - (Q21 *X1**2/(2.0D00*XKSS)) - QS1*X1/XKSS - (QS1+Q21 *
     1X1) / HT1
      TIN1 = TEX1 - DTHE
      TM2 = TEX1 + Q22 * X2**2 / (2.0D00*XKSS)+(Q22 * X2 + Q23 * X3 )/
     1HT1
      TM3 = TM2 + (Q23 *X3**2)/(2.0D00*XKLI)
      IF ( DABS(TM1+DTLI-TM3) .LE. 2.0D00 )  GO  TO  90
      X3 = X3 * 30.48D00
      IF ( TM3 .GT. (TM1+DTLI) )  X3 = X3 - DX
      IF ( TM3 .LT. (TM1+DTLI) )  X3 = X3 + DX
      Y5 = Y4 + X3
      X1 = Y2-Y1
      X2 = Y4-Y3
      X3 = Y5-Y4
      WD1 = AX1 * VEL1 * RHO * 3600.0D00
      XMU = 0.05D00 + 5.0D-05 * (TAVG-560.0D00)
      RE1 = DHE  /30.48D00 * WD1 / AX1 / XMU
      FFX1 = 0.046D00 / ( RE1**0.20 )* XJF
      DELP1 = RFW * CP * (TEX-TIN) * RHO * XJ / (100.0D00*144.0D00)
      XL = DELP1 * (GC*DHE/30.48*RHO) / ( 2.0 * FFX1 * (WD1/AX1)**2) *
     1144.0D00 * 30.48D00
      XLF = XL
      QHE = (DHE+2.0D00*TCK1)*XL/(1.D02)**3 * ( X1*QX1 +X2*QX2 +X3*
     1QX3  ) + (DHE+2.0D00*TCK1)*XL*QS0 / (1.0D02)**2
      TAVG = ( TEX1 + TIN1 ) * 0.5D00
      RHO = XM/359.0D00 *PIN/14.67D00 * 492.0D00/TAVG
      XKHE = 0.095D00 + 8.0D-05 * ( TAVG-592.0D00)
      PR = CP * XMU / XKHE
      HT1 = 0.023 * XKHE/(DHE/30.48) * RE1**0.80 * PR**0.40 * XJH
      GO  TO  80
   90 CONTINUE
      XN1 = (QVX + QS0*ST1)/ QHE
      XN2 = 2.0D00 * PI * RT1 * 1.0D02 / ( DHE + 2.0*TCK1 )
      VFW = ( DHE + 2.0D00*TCK1) / Y5
      WFW = PI/4.0D00 * (( DHE+2.0D00*TCK1)**2 - DHE**2 ) * XL/(30.48)
     1**3 * RHOM * XN1
      TM1 = ( TM0 - 492.0D00 ) / 1.80D00
      TM2 = ( TM2 - 492.0D00 ) / 1.80D00
      TM3 = ( TM3 - 492.0D00 ) / 1.80D00
      TEX1 = ( TEX1 - 492.0D00)/ 1.80D00
```

```
      PPF = WD1 * DELP1 * 144.0D00 / RHO / XJ
      PTF = WD1*CP*(TEX-TIN)
      RFWX = PPF/PTF * 1.0D02
      ITR2 = ITR
C     * * * * CALCULATIONS FOR THE BLANKET * * * *
      ITR1 = 0
      XL = XL/(30.48)
      DELT = TEX - TIN
      FFX = FFX1
  100 CONTINUE
      ITR1 = ITR1 + 1
      IF ( ITR1 .GT. 5 )  GO  TO  130
      TAVG = (TIN+TEX) * 0.50D00
      RHO = XM/359.0D00 *PIN/14.67D00 * 492.0D00/TAVG
      XKV = ( 0.0765D00 + 2.80D-05 *(TM/1.80D00-400.0D00) ) * 241.9
      IF ( KV .EQ. 1 )  XKSS = XKV
      XKHE = 0.095D00 + 8.0D-05 * ( TAVG-592.0D00)
      XMU = 0.05D00 + 5.0D-05 * (TAVG-560.0D00)
      PR = CP * XMU / XKHE
      XKSS = 8.093782 + 4.348935D-03* ( TAVG + TMO ) * 0.50D00
      DELP = RBK * CP * ( DELT  ) * RHO * XJ / 100.0D00
      D1 = 4.0D00 * DSQRT( VF/(1.0D00-VF) * (XKLI*DTLI/QV) / (-(1.0D00+
     1DLOG(VF)/(1.0D00-VF))))
      D2 = 4.0D00 * DSQRT(XKLI*DTLI/QV / (-1.0D00 + VF - DLOG(VF)))
      VF1 = (D1/D2)**2
      AX = PI/4.0D00 * D1**2
      Y6 = Y5 + D2 * 30.48D00
      QV4 = QF2/C1 * ( 1.0D00/DEXP(C1*Y5) - 1.0D00/DEXP(C1*Y6)) /(Y6-Y5)
      QV = QV4 * 9.6674D04
      QL = PI/4.0D00 * D2**2 * QV * ( 1.0D00- VF)
      C11 = PI/4.0D00 * D2**2 * QV * (1.0D00-VF) / (CP*DELT)
      C12 = DELP * (GC*D1*RHO) * AX**2 / (2.0D00 * FFX)
      C13 = 1.0D00/3.0D00
      WDOT = (C11*C12)**C13
      VEL = WDOT / RHO / AX / 3600.0D00
      XL = DELP * (GC*D1*RHO) / (2.0 * FFX * (WDOT/AX)**2)
      WD = QL * XL / (CP*DELT)
      WDX  = PI/4.0D00 * D2**2 * XL * QV * ( 1.0D00-VF) / (CP*DELT)
      RE = D1*WDOT/AX/XMU
      RE2 = RE**0.20
      RE8 = RE**0.80
      FFX = 0.046D00 / ( RE**0.20) * XJF
      FF = 1.50D00 * XNS
      HT = 0.023 * XKHF / D1 * PE**0.8 * PR**0.40 * XJH
      TCK = PIN * D1 * 3.0D00 / ( 4.0D00*SIGH)
      IF ( KV .EQ. 1 )  GO  TO  110
      IF(TCK*30.48D00 .LT. 0.052*(D1*30.48D00)**0.326D00 ) TCK = 0.052
     1/30.48D00 * (D1*30.48)**0.326D00
      GO  TO  120
  110 CONTINUE
      IF ( TCK .LT. 0.05D00/30.48D00)   TCK = 0.05D00/30.48D00
  120 CONTINUE
      Q1 = PI/4.0D00 * D2**2 * XL * QV4* 9.66737D04 / 3600.0D00*(1.0-VF)
      DTF = WDOT*CP*(  DELT ) / ( HT*PI*D1*XL)
      DTS = Q1*3600.0D00/(PI*D1*XL) * TCK / XKSS
      DTV = QV * TCK**2 / (2.0D00*XKSS)
      DTW = DTS + DTV
      TEX = TM - DTW - DTF
      TWI = TM - DTW
      TIN = ( WDOT*CP*TEX-HT*PI*D1*XL*(TWI-TEX))/ (WDOT*CP)
      XNS1 = XNS
      XNS = HT/VEL/RHO/CP/3600.0D00
```

```
      Q2 = WDOT * CP * (   DELT ) / 3600.0D00
      Q3 = HT * PI * D1 * XL * (TWI-TEX) / 3600.0D00
      XNT = QM*1.0D06 * 3.414 / ( Q1 * 3600.0D00)
      T1 = TIN/1.8D00 - 273.3D00
      T2 = TEX/1.8D00 - 273.3D00
      T3 = TWI/1.8D00 - 273.3D00
      IF ( DABS(XNS1-XNS) .GT. 1.0D-10)  GO  TO  100
  130 CONTINUE
      PPU = WDOT * DELP / RHO / XJ
      PTH = WDOT * CP * (  DELT )
      RBKX = PPU/PTH  * 1.0D02
      PP = -1.5D00/2.00D00 / (RHO) **2  * (  DELT )/(CP*XNS)**2 *
     1QV*XKLI*DTLI/(TWI-TEX)**3 *(1.0-VF)/VF / ( 1.0 + DLOG(VF)/
     2(1.0-VF))
      PT = CP * ( DELT )
      R2 = PP/PT/(GC*XJ)
      TSHT = ALF * YME / (2.0D00*(1.0D00-XNU) ) * ( DTS + DIV )
      XVF = 4.0D00 * TCK/D1 * (VF/(1.0D00-VF))
      WBK = ((D1+2.0D00*TCK)**2 - D1**2) * XL * XNT * RHOM
      DELPP = DELP/PIN / 144.0D00
      D1 = D1 * 30.48
      D2 = D2 * 30.48
      DELP = DELP/144.0D00
      TCK = TCK * 30.48
      XL = XL * 30.48
      XLB = XL
C     * * * * CALCULATIONS FOR THE BLANKET* * * *
      SD1(I) = D1
      SD2(I) = D2
      SPIN(I) = PIN
      STCK(I) = TCK
      SQ(I) = QS
      SHT(I) = HT
      SVEL(I) = VEL
      SWBK(I) = WBK
      SVF(I) = VF
      SRBK(I) = RBK
      SXL(I) = XLB/1.0D02
      SXNT(I) = XNT
      STIN(I) = T1
      STEX(I) = T2
      SDTW(I) = DTW / 1.80D00
      STM(I) = ( TM - 492.0D00 ) / 1.8D00
      SDTC(I) = ( TEX - TIN ) / 1.8D00
      SDTL(I) = DTLI     / 1.8D00
      STSHT(I) = TSHT
      PFX(I) = PX
C     * * * * CALCULATIONS FOR THE FIRST WALL* * * *
      FD1(I) = DHE
      FD2(I) = Y5
      FTCK(I) = TCK1
      FXL(I) = XLF / 1.0D02
      FHT(I) = HT1
      FVEL(I) = VEL1
      FVF(I) = VFW
      FTM(I) = ( TM0 - 492.0D00) / 1.80D00
      FDTC(I) = (TEX1-TIN1) / 1.80D00
      FDTLI(I) = DTLI / 1.80D00
      FRFW(I) = RFW
      FWFW(I) = WFW
      FXNT(I) = XN1
      FTIN(I) = (TIN1-492.0D00) / 1.80D00
```

```
      FTEX(I) = TEX1
      FDTW(I) = ( FDTV+FDTS) / 1.80D00
      FQ(I) = QS
      FTSFW(I) = TSFW
  150 CONTINUE
C     * * * * CALCULATIONS FOR THE FIRST WALL* * * *
      PRINT  2275
      DO  200  J = 1, 3
      N2 = J * 9
      N1 = N2 - 8
      IF ( KV .EQ. 0 )  PRINT  2300, RFW, VEL1
      IF ( KV .EQ. 1 )  PRINT  2350, RFW, VEL1
      PRINT  2325, STM(N1), SDTC(N1), SDTL(N1), PFX(N1)
      PRINT  2410, (SPIN(I), I = N1, N2 )
      PRINT  2465, ( SQ(I), I = N1, N2 )
      PRINT  2620, ( FVF(I), I = N1, N2 )
      PRINT  2630, ( FD1(I), I = N1, N2 )
      PRINT  2640, ( FD2(I), I = N1, N2 )
      PRINT  2650, (FTCK(I), I = N1, N2 )
      PRINT  2655, ( FXL(I), I = N1, N2 )
      PRINT  2670, ( FHT(I), I = N1, N2 )
      PRINT  2490, ( FTIN(I), I = N1, N2 )
      PRINT  2700, (FTEX(I), I = N1, N2 )
      PRINT  2710, (FDTW(I), I = N1, N2 )
      PRINT  2715, (FTSFW(I), I = N1, N2 )
C     PRINT  2720, ( FRFW(I), I = N1, N2 )
      PRINT  2730, (FXNT(I), I = N1, N2 )
      PRINT  2680, ( FWFW(I), I = N1, N2 )
  200 CONTINUE
C     * * * * CALCULATIONS FOR THE BLANKET* * * *
      PRINT  2250
      DO  300  J = 1, 3
      N2 = J * 9
      N1 = N2 - 8
      IF ( KV .EQ. 0 )  PRINT  2300, RBK, VEL
      IF ( KV .EQ. 1 )  PRINT  2350, RBK, VEL
      PRINT  2325, STM(N1), SDTC(N1), SDTL(N1), PFX(N1)
      PRINT  2410, (SPIN(I), I = N1, N2 )
      PRINT  2465, ( SQ(I), I = N1, N2 )
      PRINT  2420, ( SVF(I), I = N1, N2 )
      PRINT  2430, ( SD1(I), I = N1, N2 )
      PRINT  2440, ( SD2(I), I = N1, N2 )
      PRINT  2450, (STCK(I), I = N1, N2 )
      PRINT  2455, ( SXL(I), I = N1, N2 )
      PRINT  2460, (SVEL(I), I = N1, N2 )
      PRINT  2470, ( SHT(I), I = N1, N2 )
      PRINT  2490, ( STIN(I), I = N1, N2 )
      PRINT  2500, (STEX(I), I = N1, N2 )
      PRINT  2510, (SDTW(I), I = N1, N2 )
      PRINT  2515, ( STSHT(I), I = N1, N2 )
C     PRINT  2520, (SRBK(I), I = N1, N2 )
      PRINT  2530, (SXNT(I), I = N1, N2 )
      PRINT  2480, ( SWBK(I), I = N1, N2 )
  300 CONTINUE
  900 RETURN
C     * * * * FORMAT STATEMENTS * * * *
 1000 FORMAT ( 6D12.6 )
 1100 FORMAT ( 12I6 )
 1200 FORMAT ( 9A8 )
 1900 FORMAT ( '0', '  INPUT DATA' )
 2000 FORMAT ( 1P6D15.6 )
 2250 FORMAT ( '1', T44, ' ANALYTICAL RESULTS FOR THE BLANKET' )
```

```
2275 FORMAT ( '1', T42, ' ANALYTICAL RESULTS FOR THE FIRST WALL' )
2300 FORMAT ( '0', T10, ' SUMMARY OF CALCULATIONS: MATERIAL:STAINLESS
    1STEEL, COOLANT: HELIUM,PPU/PTH=',1P1D8.1,',%', ',V=',1P1D8.1,',FT/
    2SEC' )
2350 FORMAT ( '0', T10, ' SUMMARY OF CALCULATIONS: MATERIAL:VANADIUM
    1ALLOY, COOLANT: HELIUM,PPU/PTH=',1P1D8.1,',%', ',V=',1P1D8.1,',FT/
    2SEC' )
2325 FORMAT ( T26, 'TMAX=',3P1D8.0, ',C',' COOLANT DT=', 3P1D8.0, ',C',
    1' LITHIUM DT=', 2P1D7.0,  ',C', ' PF=', 1P1D8.1 )
2400 FORMAT ( T20,1P9D12.3 )
2410 FORMAT (       ' INLET PR. PSIA     ',        1P9D12.3 )
2420 FORMAT (       ' VOID FRACTION      ',        1P9D12.3 )
2430 FORMAT (       ' HE TUBE DIA. CM    ',        1P9D12.3 )
2440 FORMAT (       ' EQV. LI. CYL., CM  ',        1P9D12.3 )
2450 FORMAT (       ' WALL THICKNESS,CM  ',        1P9D12.3 )
2455 FORMAT (       ' CHANNEL LENGTH,M   ',        1P9D12.3 )
2460 FORMAT (       ' VELOCITY,FT/SEC    ',        1P9D12.3 )
2465 FORMAT (       ' WALL FLUX,MW/M**2  ',        1P9D12.3 )
2470 FORMAT (       ' HT. TR. COEF.      ',        1P9D12.3 )
2480 FORMAT (       ' BLANKET TUBE WT,LB',         1P9D12.3 )
2490 FORMAT (       ' INLET TEMP., C     ',        1P9D12.3 )
2500 FORMAT (       ' EXIT TEMP., C      ',        1P9D12.3 )
2510 FORMAT (       ' WALL TEMP. DROP,C  ',        1P9D12.3 )
2515 FORMAT (       ' HE TUBE TS, PSI    ',        1P9D12.3 )
2520 FORMAT (       ' RATIO OF PP/PT %   ',        1P9D12.3 )
2530 FORMAT (       ' NO. OF HE TUBES    ',        1P9D12.3 )
2620 FORMAT (       ' VOID FRACTION      ',        1P9D12.3 )
2630 FORMAT (       ' HE TUBE DIA. CM    ',        1P9D12.3 )
2640 FORMAT (       ' REGION 1 LENGTH,CM',         1P9D12.3 )
2650 FORMAT (       ' WALL THICKNESS,CM  ',        1P9D12.3 )
2655 FORMAT (       ' CHANNEL LENGTH,M   ',        1P9D12.3 )
2660 FORMAT (       ' VELOCITY,FT/SEC    ',        1P9D12.3 )
2670 FORMAT (       ' HT. TR. COEF.      ',        1P9D12.3 )
2680 FORMAT (       ' FT.WALL TUBE WT,LB',         1P9D12.3 )
2690 FORMAT (       ' INLET TEMP., C     ',        1P9D12.3 )
2700 FORMAT (       ' EXIT TEMP., C      ',        1P9D12.3 )
2710 FORMAT (       ' WALL TEMP. DROP,C  ',        1P9D12.3 )
2715 FORMAT (       ' FW THER. ST, PSI   ',        1P9D12.3 )
2720 FORMAT (       ' RATIO OF PP/PT %   ',        1P9D12.3 )
2730 FORMAT (       ' NO. OF HE TUBES    ',        1P9D12.3 )
     END
```

Table A-4(1)

Typical Output Format for Subroutine LITHIUM

SUMMARY OF CALCULATIONS FOR FLOWING LITHIUM IN STAINLESS STEEL CELLS

MHD PRESSURE LOSSES FOR BMAX =7.0D 00T, DTC=225.D 00C

	BLANKET	LI-CELL	SHIELD	MAGNET
PASSAGE DIAMETER, CM	1.000000D 01	5.000000D 01	3.162278D 01	3.162278D 01
CELL WALL TCKNESS, CM	2.500000D-01	3.000000D-01	5.000000D-01	5.000000D-01
COOLANT VELOCITY, CM/S	2.622727D 01	1.092803D 00	2.622727D 01	2.622727D 01
AVG. BMAX, TESLA	3.681986D 00	3.681986D 00	2.350192D 00	1.230142D 00
PRESSURE DROP, PSI	3.177787D 01	3.177787D-01	1.842382D 01	3.738951D 00

MHD PRESSURE LOSSES FOR BMAX =8.0D 00T, DTC=225.D 00C

	BLANKET	LI-CELL	SHIELD	MAGNET
PASSAGE DIAMETER, CM	1.000000D 01	5.000000D 01	3.162278D 01	3.162278D 01
CELL WALL TCKNESS, CM	2.500000D-01	3.000000D-01	5.000000D-01	5.000000D-01
COOLANT VELOCITY, CM/S	2.622727D 01	1.092803D 00	2.622727D 01	2.622727D 01
AVG. BMAX, TESLA	4.207984D 00	4.207984D 00	2.685934D 00	1.405877D 00
PRESSURE DROP, PSI	4.150579D 01	4.150579D-01	2.406377D 01	4.883528D 00

MHD PRESSURE LOSSES FOR BMAX =1.0D 01T, DTC=225.D 00C

	BLANKET	LI-CELL	SHIELD	MAGNET
PASSAGE DIAMETER, CM	1.000000D 01	5.000000D 01	3.162278D 01	3.162278D 01
CELL WALL TCKNESS, CM	2.500000D-01	3.000000D-01	5.000000D-01	5.000000D-01
COOLANT VELOCITY, CM/S	2.208612D 01	9.202550D-01	2.208612D 01	2.208612D 01
AVG. BMAX, TESLA	5.259980D 00	5.259980D 00	3.357417D 00	1.757346D 00
PRESSURE DROP, PSI	5.461288D 01	5.461288D-01	3.166285D 01	6.425695D 00

MHD PRESSURE LOSSES FOR BMAX =1.2D 01T, DTC=225.D 00C

	BLANKET	LI-CELL	SHIELD	MAGNET
PASSAGE DIAMETER, CM	1.000000D 01	5.000000D 01	3.162278D 01	3.162278D 01
CELL WALL TCKNESS, CM	2.500000D-01	3.000000D-01	5.000000D-01	5.000000D-01
COOLANT VELOCITY, CM/S	1.552930D 01	6.470543D-01	1.552930D 01	1.552930D 01
AVG. BMAX, TESLA	6.311976D 00	6.311976D 00	4.028901D 00	2.108815D 00
PRESSURE DROP, PSI	5.529554D 01	5.529554D-01	3.205864D 01	6.506016D 00

SUMMARY OF THERMAL HYDRAULICS CALCULATION, POWER FACTOR= PF(J)=0.10D 00

	BMAX=7.0D 00T	BMAX=8.0D 00T	BMAX=1.0D 01T	BMAX=1.2D 01T
WALL LOADING, MW/M**2	3.800000D 00	3.800000D 00	3.200000D 00	2.250000D 00
TOTAL PRESS. DROP, PSI	7.642119D 01	9.981544D 01	1.313361D 02	1.329778D 02
WALL THICKNESS, CM	3.000000D-01	3.000000D-01	3.000000D-01	3.000000D-01
PLASMA WALL TEMP., C	3.802905D 02	3.802905D 02	3.651393D 02	3.411499D 02
PLASMA WALL DELT., C	5.340474D 01	5.340474D 01	4.497242D 01	3.162123D 01
FW. THERMAL STRESS,PSI	1.716580D 04	1.716580D 04	1.445541D 04	1.016396D 04
CELL EXIT WALL TEMP, C	5.000000D 02	5.000000D 02	5.000000D 02	5.000000D 02
COOLANT EXIT TEMP., C	4.848367D 02	4.848367D 02	4.872309D 02	4.910217D 02
COOLANT INLET TEMP., C	2.598367D 02	2.598367D 02	2.622309D 02	2.660217D 02
RATIO PPU/PTH,.%	1.629479D-01	1.987682D-01	2.498127D-01	2.569351D-01

Table A-4(2)

Typical Output Format for Subroutine LITHIUM

SUMMARY OF CALCULATIONS FOR FLOWING LITHIUM IN VANADIUM ALLOY CELLS

MHD PRESSURE LOSSES FOR BMAX =7.0D 00T, DTC=325.D 00C

	BLANKET	LI-CELL	SHIELD	MAGNET
PASSAGE DIAMETER, CM	1.000000D 01	5.000000D 01	3.162278D 01	3.162278D 01
CELL WALL TCKNESS, CM	2.500000D-01	3.000000D-01	5.412521D-01	5.699474D-01
COOLANT VELOCITY, CM/S	6.033927D 01	2.514136D 00	6.033927D 01	6.033927D 01
AVG. BMAX, TESLA	3.681986D 00	3.681986D 00	2.350192D 00	1.230142D 00
PRESSURE DROP, PSI	2.300421D 02	2.300421D 00	1.443727D 02	3.085248D 01

MHD PRESSURE LOSSES FOR BMAX =8.0D 00T, DTC=325.D 00C

	BLANKET	LI-CELL	SHIELD	MAGNET
PASSAGE DIAMETER, CM	1.000000D 01	5.000000D 01	3.162278D 01	3.162278D 01
CELL WALL TCKNESS, CM	2.500000D-01	3.000000D-01	5.448073D-01	5.737854D-01
COOLANT VELOCITY, CM/S	4.634056D 01	1.930857D 00	4.634056D 01	4.634056D 01
AVG. BMAX, TESLA	4.207984D 00	4.207984D 00	2.685934D 00	1.405877D 00
PRESSURE DROP, PSI	2.307557D 02	2.307557D 00	1.457715D 02	3.115653D 01

MHD PRESSURE LOSSES FOR BMAX =1.0D 01T, DTC=325.D 00C

	BLANKET	LI-CELL	SHIELD	MAGNET
PASSAGE DIAMETER, CM	1.000000D 01	5.000000D 01	3.162278D 01	3.162278D 01
CELL WALL TCKNESS, CM	2.500000D-01	3.000000D-01	5.366151D-01	5.649424D-01
COOLANT VELOCITY, CM/S	2.944557D 01	1.226899D 00	2.944557D 01	2.944557D 01
AVG. BMAX, TESLA	5.259980D 00	5.259980D 00	3.357417D 00	1.757346D 00
PRESSURE DROP, PSI	2.291032D 02	2.291032D 00	1.425519D 02	3.045679D 01

MHD PRESSURE LOSSES FOR BMAX =1.2D 01T, DTC=325.D 00C

	BLANKET	LI-CELL	SHIELD	MAGNET
PASSAGE DIAMETER, CM	1.000000D 01	5.000000D 01	3.162278D 01	3.162278D 01
CELL WALL TCKNESS, CM	2.500000D-01	3.000000D-01	5.539107D-01	5.836154D-01
COOLANT VELOCITY, CM/S	2.075671D 01	8.648629D-01	2.075671D 01	2.075671D 01
AVG. BMAX, TESLA	6.311976D 00	6.311976D 00	4.028901D 00	2.108815D 00
PRESSURE DROP, PSI	2.325585D 02	2.325585D 00	1.493644D 02	3.193771D 01

SUMMARY OF THERMAL HYDRAULICS CALCULATION, POWER FACTOR= PF(J)=0.10D 00

	BMAX=7.0D 00T	BMAX=8.0D 00T	BMAX=1.0D 01T	BMAX=1.2D 01T
WALL LOADING, MW/M**2	1.250000D 01	9.600000D 00	6.100000D 00	4.300000D 00
TOTAL PRESS. DROP, PSI	5.827929D 02	5.869194D 02	5.774117D 02	5.974883D 02
WALL THICKNESS, CM	3.000000D-01	3.000000D-01	3.000000D-01	3.000000D-01
PLASMA WALL TEMP., C	6.351761D 02	5.778800D 02	5.087294D 02	4.731663D 02
PLASMA WALL DELT., C	1.110090D 02	8.525488D 01	5.417237D 01	3.818708D 01
FW. THERMAL STRESS,PSI	1.481969D 04	1.138152D 04	7.232009D 03	5.097973D 03
CELL EXIT WALL TEMP, C	7.000000D 02	7.000000D 02	7.000000D 02	7.000000D 02
COOLANT EXIT TEMP., C	6.523585D 02	6.634113D 02	6.767509D 02	6.836113D 02
COOLANT INLET TEMP., C	3.273585D 02	3.384113D 02	3.517509D 02	3.586113D 02
RATIO PPU/PTH, %	8.236872D-01	8.680020D-01	9.057300D-01	9.653551D-01

Table A-5(1) Typical Output Format for Subroutine HELIUM

ANALYTICAL RESULTS FOR THE FIRST WALL

SUMMARY OF CALCULATIONS: MATERIAL:STAINLESS STEEL, COOLANT: HELIUM,PPU/PTH= 5.0D 00,%,V= 2.0D 02,FT/SEC
TMAX=500.D 00,C COOLANT DT=200.D 00,C LITHIUM DT=25.D 00,C PF= 1.0D-01

INLET PR. PSIA	7.500D 02	7.500D 02	7.500D 02	1.000D 03	1.000D 03	1.000D 03	1.500D 03	1.500D 03	1.500D 03
WALL FLUX,MW/M**2	6.200D 00	6.200D 00	6.200D 00	6.200D 00	6.200D 00	6.200D 00	4.600D 00	4.600D 00	4.600D 00
VOID FRACTION	5.478D-01	5.478D-01	5.478D-01	5.543D-01	5.543D-01	5.543D-01	5.352D-01	5.352D-01	5.352D-01
HE TUBE DIA. CM	2.540D 00	2.540D 00	2.540D 00	2.540D 00	2.540D 00	2.540D 00	2.540D 00	2.540D 00	2.540D 00
REGION 1 LENGTH,CM	5.093D 00	5.093D 00	5.093D 00	5.033D 00	5.033D 00	5.033D 00	5.370D 00	5.370D 00	5.370D 00
WALL THICKNESS,CM	1.250D-01	1.250D-01	1.250D-01	1.250D-01	1.250D-01	1.250D-01	1.670D-01	1.670D-01	1.670D-01
CHANNEL LENGTH,M	1.166D 01	1.166D 01	1.166D 01	1.221D 01	1.221D 01	1.221D 01	1.299D 01	1.299D 01	1.299D 01
HT. TR. COEF.	1.377D 03	1.377D 03	1.377D 03	1.693D 03	1.693D 03	1.693D 03	2.251D 03	2.251D 03	2.251D 03
INLET TEMP., C	1.531D 02	1.531D 02	1.531D 02	1.706D 02	1.706D 02	1.706D 02	2.023D 02	2.023D 02	2.023D 02
EXIT TEMP., C	3.531D 02	3.531D 02	3.531D 02	3.706D 02	3.706D 02	3.706D 02	4.023D 02	4.023D 02	4.023D 02
WALL TEMP. DROP,C	5.308D 01	5.308D 01	5.308D 01	5.308D 01	5.308D 01	5.308D 01	5.307D 01	5.307D 01	5.307D 01
FW THER. ST, PSI	1.706D 04	1.706D 04	1.706D 04	1.706D 04	1.706D 04	1.706D 04	1.706D 04	1.706D 04	1.706D 04
NO. OF HE TUBES	3.318D 03	3.318D 03	3.318D 03	3.167D 03	3.167D 03	3.167D 03	2.891D 03	2.891D 03	2.891D 03
FT.WALL TUBE WT,LB	6.919D 04	6.919D 04	6.919D 04	6.919D 04	6.919D 04	6.919D 04	9.121D 04	9.121D 04	9.121D 04

SUMMARY OF CALCULATIONS: MATERIAL:STAINLESS STEEL, COOLANT: HELIUM,PPU/PTH= 5.0D 00,%,V= 2.0D 02,FT/SEC
TMAX=500.D 00,C COOLANT DT=200.D 00,C LITHIUM DT=50.D 00,C PF= 1.0D-01

INLET PR. PSIA	7.500D 02	7.500D 02	7.500D 02	1.000D 03	1.000D 03	1.000D 03	1.500D 03	1.500D 03	1.500D 03
WALL FLUX,MW/M**2	6.200D 00	6.200D 00	6.200D 00	6.200D 00	6.200D 00	6.200D 00	4.600D 00	4.600D 00	4.600D 00
VOID FRACTION	5.271D-01	5.271D-01	5.271D-01	5.311D-01	5.311D-01	5.311D-01	5.105D-01	5.105D-01	5.105D-01
HE TUBE DIA. CM	2.540D 00	2.540D 00	2.540D 00	2.540D 00	2.540D 00	2.540D 00	2.540D 00	2.540D 00	2.540D 00
REGION 1 LENGTH,CM	5.293D 00	5.293D 00	5.293D 00	5.253D 00	5.253D 00	5.253D 00	5.630D 00	5.630D 00	5.630D 00
WALL THICKNESS,CM	1.250D-01	1.250D-01	1.250D-01	1.250D-01	1.250D-01	1.250D-01	1.670D-01	1.670D-01	1.670D-01
CHANNEL LENGTH,M	1.166D 01	1.166D 01	1.166D 01	1.221D 01	1.221D 01	1.221D 01	1.299D 01	1.299D 01	1.299D 01
HT. TR. COEF.	1.377D 03	1.377D 03	1.377D 03	1.693D 03	1.693D 03	1.693D 03	2.251D 03	2.251D 03	2.251D 03
INLET TEMP., C	1.531D 02	1.531D 02	1.531D 02	1.706D 02	1.706D 02	1.706D 02	2.023D 02	2.023D 02	2.023D 02
EXIT TEMP., C	3.531D 02	3.531D 02	3.531D 02	3.706D 02	3.706D 02	3.706D 02	4.023D 02	4.023D 02	4.023D 02
WALL TEMP. DROP,C	5.308D 01	5.308D 01	5.308D 01	5.308D 01	5.308D 01	5.308D 01	5.307D 01	5.307D 01	5.307D 01
FW THER. ST, PSI	1.706D 04	1.706D 04	1.706D 04	1.706D 04	1.706D 04	1.706D 04	1.706D 04	1.706D 04	1.706D 04
NO. OF HE TUBES	3.319D 03	3.319D 03	3.319D 03	3.168D 03	3.168D 03	3.168D 03	2.893D 03	2.893D 03	2.893D 03
FT.WALL TUBE WT,LB	6.922D 04	6.922D 04	6.922D 04	6.921D 04	6.921D 04	6.921D 04	9.125D 04	9.125D 04	9.125D 04

SUMMARY OF CALCULATIONS: MATERIAL:STAINLESS STEEL, COOLANT: HELIUM,PPU/PTH= 5.0D 00,%,V= 2.0D 02,FT/SEC
TMAX=500.D 00,C COOLANT DT=200.D 00,C LITHIUM DT=10.D 01,C PF= 1.0D-01

INLET PR. PSIA	7.500D 02	7.500D 02	7.500D 02	1.000D 03	1.000D 03	1.000D 03	1.500D 03	1.500D 03	1.500D 03
WALL FLUX,MW/M**2	6.200D 00	6.200D 00	6.200D 00	6.200D 00	6.200D 00	6.200D 00	4.600D 00	4.600D 00	4.600D 00
VOID FRACTION	4.935D-01	4.935D-01	4.935D-01	4.953D-01	4.953D-01	4.953D-01	4.688D-01	4.688D-01	4.688D-01
HE TUBE DIA. CM	2.540D 00	2.540D 00	2.540D 00	2.540D 00	2.540D 00	2.540D 00	2.540D 00	2.540D 00	2.540D 00
REGION 1 LENGTH,CM	5.653D 00	5.653D 00	5.653D 00	5.633D 00	5.633D 00	5.633D 00	6.130D 00	6.130D 00	6.130D 00
WALL THICKNESS,CM	1.250D-01	1.250D-01	1.250D-01	1.250D-01	1.250D-01	1.250D-01	1.670D-01	1.670D-01	1.670D-01
CHANNEL LENGTH,M	1.166D 01	1.166D 01	1.166D 01	1.221D 01	1.221D 01	1.221D 01	1.299D 01	1.299D 01	1.299D 01
HT. TR. COEF.	1.377D 03	1.377D 03	1.377D 03	1.693D 03	1.693D 03	1.693D 03	2.251D 03	2.251D 03	2.251D 03
INLET TEMP., C	1.531D 02	1.531D 02	1.531D 02	1.706D 02	1.706D 02	1.706D 02	2.023D 02	2.023D 02	2.023D 02
EXIT TEMP., C	3.531D 02	3.531D 02	3.531D 02	3.706D 02	3.706D 02	3.706D 02	4.023D 02	4.023D 02	4.023D 02
WALL TEMP. DROP,C	5.308D 01	5.308D 01	5.308D 01	5.308D 01	5.308D 01	5.308D 01	5.307D 01	5.307D 01	5.307D 01
FW THER. ST, PSI	1.706D 04	1.706D 04	1.706D 04	1.706D 04	1.706D 04	1.706D 04	1.706D 04	1.706D 04	1.706D 04
NO. OF HE TUBES	3.321D 03	3.321D 03	3.321D 03	3.170D 03	3.170D 03	3.170D 03	2.895D 03	2.895D 03	2.895D 03
FT.WALL TUBE WT,LB	6.926D 04	6.926D 04	6.926D 04	6.926D 04	6.926D 04	6.926D 04	9.133D 04	9.133D 04	9.133D 04

Table A-5(2) Typical Output Format for Subroutine HELIUM

ANALYTICAL RESULTS FOR THE BLANKET

SUMMARY OF CALCULATIONS: MATERIAL:STAINLESS STEEL, COOLANT: HELIUM,PPU/PTH= 5.0D 00,%,V= 2.8D 02,FT/SEC
TMAX=500.D 00,C COOLANT DT=200.D 00,C LITHIUM DT=25.D 00,C PF= 1.0D-01

INLET PR. PSIA	7.500D 02	7.500D 02	7.500D 02	1.000D 03	1.000D 03	1.000D 03	1.500D 03	1.500D 03	1.500D 03	1.500D 03
WALL FLUX,MW/M**2	6.200D 00	6.200D 00	6.200D 00	6.200D 00	6.200D 00	6.200D 00	4.600D 00	4.600D 00	4.600D 00	4.600D 00
VOID FRACTION	1.000D-01	7.000D-02	5.000D-02	1.000D-01	7.000D-02	5.000D-02	1.000D-01	7.000D-02	5.000D-02	5.000D-02
HE TUBE DIA. CM	8.355D-01	6.283D-01	4.875D-01	8.347D-01	6.277D-01	4.871D-01	9.772D-01	7.346D-01	5.699D-01	5.699D-01
EQV. LI. CYL., CM	2.642D 00	2.375D 00	2.180D 00	2.640D 00	2.373D 00	2.178D 00	3.090D 00	2.777D 00	2.549D 00	2.549D 00
WALL THICKNESS,CM	4.904D-02	4.469D-02	4.114D-02	4.903D-02	4.468D-02	4.113D-02	6.427D-02	4.831D-02	4.329D-02	4.329D-02
CHANNEL LENGTH,M	1.784D 00	1.228D 00	8.754D-01	2.173D 00	1.496D 00	1.066D 00	3.771D 00	2.588D 00	1.842D 00	1.842D 00
VELOCITY,FT/SEC	2.614D 02	2.661D 02	2.714D 02	2.413D 02	2.457D 02	2.506D 02	2.060D 02	2.099D 02	2.141D 02	2.141D 02
HT. TR. COEF.	1.880D 03	2.022D 03	2.165D 03	2.208D 03	2.374D 03	2.541D 03	2.586D 03	2.778D 03	2.972D 03	2.972D 03
INLET TEMP., C	2.559D 02	2.544D 02	2.528D 02	2.612D 02	2.599D 02	2.585D 02	2.685D 02	2.692D 02	2.683D 02	2.683D 02
EXIT TEMP., C	4.559D 02	4.544D 02	4.528D 02	4.612D 02	4.599D 02	4.585D 02	4.685D 02	4.692D 02	4.683D 02	4.683D 02
WALL TEMP. DROP,C	8.134D 00	8.245D 00	8.436D 00	8.127D 00	8.237D 00	8.428D 00	9.094D 00	7.585D 00	7.553D 00	7.553D 00
HE TUBE TS, PSI	2.614D 03	2.650D 03	2.712D 03	2.612D 03	2.648D 03	2.709D 03	2.923D 03	2.438D 03	2.428D 03	2.428D 03
NO. OF HE TUBES	4.054D 05	7.027D 05	1.142D 06	3.334D 05	5.780D 05	9.393D 05	1.406D 05	2.445D 05	3.977D 05	3.977D 05
BLANKET TUBE WT,LB	2.145D 05	1.774D 05	1.486D 05	2.146D 05	1.776D 05	1.487D 05	2.427D 05	1.636D 05	1.330D 05	1.330D 05

SUMMARY OF CALCULATIONS: MATERIAL:STAINLESS STEEL, COOLANT: HELIUM,PPU/PTH= 5.0D 00,%,V= 2.8D 02,FT/SEC
TMAX=500.D 00,C COOLANT DT=200.D 00,C LITHIUM DT=50.D 00,C PF= 1.0D-01

INLET PR. PSIA	7.500D 02	7.500D 02	7.500D 02	1.000D 03	1.000D 03	1.000D 03	1.500D 03	1.500D 03	1.500D 03	1.500D 03
WALL FLUX,MW/M**2	6.200D 00	6.200D 00	6.200D 00	6.200D 00	6.200D 00	6.200D 00	4.600D 00	4.600D 00	4.600D 00	4.600D 00
VOID FRACTION	1.000D-01	7.000D-02	5.000D-02	1.000D-01	7.000D-02	5.000D-02	1.000D-01	7.000D-02	5.000D-02	5.000D-02
HE TUBE DIA. CM	1.195D 00	8.979D-01	6.963D-01	1.194D 00	8.974D-01	6.959D-01	1.401D 00	1.052D 00	8.157D-01	8.157D-01
EQV. LI. CYL., CM	3.779D 00	3.394D 00	3.114D 00	3.777D 00	3.392D 00	3.112D 00	4.431D 00	3.977D 00	3.648D 00	3.648D 00
WALL THICKNESS,CM	5.511D-02	5.021D-02	4.621D-02	5.510D-02	5.020D-02	4.620D-02	9.215D-02	6.920D-02	5.364D-02	5.364D-02
CHANNEL LENGTH,M	2.153D 00	1.481D 00	1.055D 00	2.618D 00	1.801D 00	1.283D 00	4.568D 00	3.125D 00	2.217D 00	2.217D 00
VELOCITY,FT/SEC	3.005D 02	3.059D 02	3.119D 02	2.775D 02	2.826D 02	2.881D 02	2.367D 02	2.413D 02	2.463D 02	2.463D 02
HT. TR. COEF.	1.992D 03	2.145D 03	2.298D 03	2.336D 03	2.513D 03	2.692D 03	2.737D 03	2.938D 03	3.140D 03	3.140D 03
INLET TEMP., C	2.397D 02	2.377D 02	2.355D 02	2.466D 02	2.450D 02	2.430D 02	2.522D 02	2.541D 02	2.549D 02	2.549D 02
EXIT TEMP., C	4.397D 02	4.377D 02	4.355D 02	4.466D 02	4.450D 02	4.430D 02	4.522D 02	4.541D 02	4.549D 02	4.549D 02
WALL TEMP. DROP,C	1.280D 01	1.300D 01	1.331D 01	1.278D 01	1.297D 01	1.329D 01	1.827D 01	1.524D 01	1.311D 01	1.311D 01
HE TUBE TS, PSI	4.116D 03	4.177D 03	4.278D 03	4.109D 03	4.170D 03	4.271D 03	5.874D 03	4.898D 03	4.215D 03	4.215D 03
NO. OF HE TUBES	1.669D 05	2.895D 05	4.705D 05	1.374D 05	2.384D 05	3.876D 05	5.756D 04	1.004D 05	1.639D 05	1.639D 05
BLANKET TUBE WT,LB	1.693D 05	1.395D 05	1.165D 05	1.693D 05	1.396D 05	1.165D 05	2.474D 05	1.665D 05	1.158D 05	1.158D 05

SUMMARY OF CALCULATIONS: MATERIAL:STAINLESS STEEL, COOLANT: HELIUM,PPU/PTH= 5.0D 00,%,V= 2.8D 02,FT/SEC
TMAX=500.D 00,C COOLANT DT=200.D 00,C LITHIUM DT=10.D 01,C PF= 1.0D-01

INLET PR. PSIA	7.500D 02	7.500D 02	7.500D 02	1.000D 03	1.000D 03	1.000D 03	1.500D 03	1.500D 03	1.500D 03	1.500D 03
WALL FLUX,MW/M**2	6.200D 00	6.200D 00	6.200D 00	6.200D 00	6.200D 00	6.200D 00	4.600D 00	4.600D 00	4.600D 00	4.600D 00
VOID FRACTION	1.000D-01	7.000D-02	5.000D-02	1.000D-01	7.000D-02	5.000D-02	1.000D-01	7.000D-02	5.000D-02	5.000D-02
HE TUBE DIA. CM	1.720D 00	1.291D 00	1.000D 00	1.720D 00	1.290D 00	9.997D-01	2.025D 00	1.519D 00	1.176D 00	1.176D 00
EQV. LI. CYL., CM	5.439D 00	4.879D 00	4.472D 00	5.438D 00	4.877D 00	4.471D 00	6.405D 00	5.741D 00	5.259D 00	5.259D 00
WALL THICKNESS,CM	6.206D-02	5.651D-02	5.200D-02	7.539D-02	5.657D-02	5.199D-02	1.332D-01	9.989D-02	7.734D-02	7.734D-02
CHANNEL LENGTH,M	2.647D 00	1.819D 00	1.295D 00	3.229D 00	2.206D 00	1.570D 00	5.694D 00	3.872D 00	2.736D 00	2.736D 00
VELOCITY,FT/SEC	3.439D 02	3.501D 02	3.569D 02	3.174D 02	3.237D 02	3.301D 02	2.700D 02	2.757D 02	2.817D 02	2.817D 02
HT. TR. COEF.	2.117D 03	2.281D 03	2.447D 03	2.485D 03	2.668D 03	2.860D 03	2.915D 03	3.123D 03	3.335D 03	3.335D 03
INLET TEMP., C	2.177D 02	2.151D 02	2.121D 02	2.226D 02	2.245D 02	2.218D 02	2.248D 02	2.293D 02	2.318D 02	2.318D 02
EXIT TEMP., C	4.177D 02	4.151D 02	4.121D 02	4.226D 02	4.245D 02	4.218D 02	4.248D 02	4.293D 02	4.318D 02	4.318D 02
WALL TEMP. DROP,C	2.012D 01	2.045D 01	2.097D 01	2.446D 01	2.042D 01	2.091D 01	3.684D 01	3.069D 01	2.641D 01	2.641D 01
HE TUBE TS, PSI	6.467D 03	6.573D 03	6.740D 03	7.862D 03	6.565D 03	6.722D 03	1.184D 04	9.866D 03	8.487D 03	8.487D 03
NO. OF HE TUBES	6.711D 04	1.165D 05	1.895D 05	5.505D 04	9.615D 04	1.564D 05	2.272D 04	3.987D 04	6.534D 04	6.534D 04
BLANKET TUBE WT,LB	1.343D 05	1.103D 05	9.179D 04	1.644D 05	1.105D 05	9.181D 04	2.543D 05	1.706D 05	1.185D 05	1.185D 05

October 31, 1977 ANL/FPP/TM-95

A SYSTEMATIC SURVEY OF TOKAMAK REACTOR PHYSICS DESIGN PARAMETERS

David A. Ehst, Kenneth Evans, Jr. and Weston M. Stacey, Jr.

Applied Physics Division
Argonne National Laboratory
Argonne, Illinois 60439

ANL/FPP Technical Memorandum No. 95

Results reported in the FPP series of memoranda frequently are preliminary and subject to revision. They should not be quoted nor referenced without the author's permission.

Work supported by the U. S. Department of Energy.

TABLE OF CONTENTS

	Page
ABSTRACT	1
I. INTRODUCTION	2
II. MHD EQUILIBRIUM	4
III. PARTICLE AND POWER BALANCE	9
IV. REACTOR PERFORMANCE	17
V. SUMMARY	21
APPENDIX: Plasma Physics Subroutine of the ANL Tokamak Systems Code	24
REFERENCES	47
TABLES	49
FIGURES	53
DISTRIBUTION	78

A SYSTEMATIC SURVEY OF TOKAMAK REACTOR PHYSICS DESIGN PARAMETERS

David A. Ehst, Kenneth Evans, Jr. and Weston M. Stacey, Jr.*

Applied Physics Division
Argonne National Laboratory
Argonne, Illinois 60439

ABSTRACT

An in-depth survey of twelve important tokamak reactor parameters is presented. First, a number of MHD equilibria are studied to determine the influences of geometry, pressure profile, safety factor, and plasma beta on the required plasma current. Next, a steady-state transport model is used to study the effects of temperature and density profiles, impurity content, and plasma temperature on the power density and required $\bar{n}_i\tau$. The transport model consists of particle current and power balances averaged in the appropriate flux space over the same profiles used in the MHD calculations. Finally, the influence of the blanket/shield thickness, major radius, and toroidal magnetic field strength on the reactor performance is determined. The relevant design options are presented.

---

*Present address: School of Nuclear Engineering, Georgia Institute of Technology, Atlanta, Georgia 30332.

I. INTRODUCTION

A power producing tokamak reactor will be a highly complex device embodying the results of innumerable design decisions. In order to intelligently assess the impact of some of these design choices on overall power plant performance, a systematic study of tokamak reactors is currently being undertaken [1]. The study has been facilitated by dividing the power plant into several subsystems, and this present report documents the results of the plasma engineering survey. The quantitative impact of plasma engineering choices, (e.g., magnetic field strength) must be determined from the complete reactor systems study (including such considerations as material strengths, economic penalties for downtime, etc.), but valuable information has resulted from the plasma subsystem study itself. In light of the many uncertainties surrounding tokamak plasma physics, a rather broad survey of plasma possibilities has been attempted. For example, the plasma beta has been left an independent variable, and no particular scaling law for beta as a function of geometry has been chosen. Likewise, the impurity content, the safety factor, and other quantities have been left as variable inputs to the calculations. As a consequence we have learned the sensitivity of plasma performance to the various parameters, and this data, used as input to the reactor systems study, will help indicate the attractive directions for future tokamak research.

For convenience of analysis it has been expedient to separate the plasma calculation into three relatively independent parts: the ideal MHD equilibrium; the point model power balance; and the reactor performance characteristics. This report will discuss these three areas in the order listed, and in each case a data base of reactor options will be presented with an analysis of trends among the designs.

We will examine plasma sensitivity to twelve design parameters. The ideal magnetohydrodynamic (MHD) equilibrium is a solution of an inhomogeneous differential equation, so it is a function of the toroidal boundary conditions and the driving terms in the equation. The boundary conditions are represented by the aspect ratio, A, of the torus; the elongation, κ, of the plasma cross section; and the D-shapedness, d, of the cross section. The inhomogeneous terms involve the pressure and diamagnetic effect ($F = \rho B_t$) functions. These are represented by the peak pressure, a parameter, α, related to the pressure profile shape, the vacuum value of F, the depth of the diamagnetic well, and a parameter, γ, related to the F profile shape. The vacuum value of F can be scaled out of the calculation [2], and the peak pressure is determined by requiring the safety factor to be one on axis. The well depth and the F profile shape parameters can be replaced by the equivalent variables β_t, the ratio of the average pressure to the vacuum magnetic field pressure at the major axis, and q, the safety factor at the plasma edge. The MHD equilibrium is then completely determined by the parameters A, κ, d, α, β_t, and q.

The power balance is consistent with the MHD equilibrium. A zero-dimensiona calculation is performed, solving the density and energy transport equations averaged over the flux surfaces of the corresponding MHD solution. We allow the density and temperature profile shapes to be variable parameters, identifying the density profile shape with the independent variable, α_n, and requiring the product of the density and temperature profiles to be the pressure profile of the MHD calculation. The plasma impurity content is another variable, being a function of impurity charges, masses, and concentrations. This set of impurity variables will usually be represented by the single parameter Z_{eff}. While one conventional approach at this point might be to calculate the plasma densities and temperatures for given fueling rates and loss times, we find it convenient

to reverse the role of some of these variables, specifying instead the average electron temperature, $\bar{T}_e$, as an independent variable and calculating the fueling rate and containment time, τ, required for ignition. Thus, our results do not depend *a priori* on any theoretical containment laws, but we are free afterwards to compare the required τ with the values predicted from various theories. We assume a half-deuterium, half-tritium fuel mixture and set particle and energy containment times equal for all species.

The final reactor performance depends on the major radius, R, the magnetic field, B, at the toroidal field (TF) coil, and the blanket/shield thickness, Δ, on the inside of the torus, in addition to the MHD and power balance results. These three parameters are critical in determining reactor performance since power density increases as B_0^4, where B_0 is the magnetic field in the plasma, $B_0 = B\left[1 - A^{-1} - \left(\Delta + \Delta_v\right)/R\right]$, and because R ultimately determines the volume of fusing plasma. Likewise, many other reactor characteristics, such as the theoretical containment time, τ, are significantly dependent on the magnetic field strength and reactor size. We set the vacuum thickness, Δ_v, of the scrape-off layer (limiter width) equal to 0.2 m, which is not varied. Additional energy multiplication in the blanket is not considered. With these three, R, B, and Δ, the set of independent variables is complete, and we will display their influence on the relevant design objectives such as plasma thermal power and wall loading.

The twelve independent variables are listed for reference in Table I.

II. MHD EQUILIBRIUM

A tokamak plasma in ideal MHD equilibrium has a poloidal magnetic flux, $\psi(\rho,z)$, which is a solution to the Grad-Shafranov equation [2,3]

$$\frac{\partial^2\psi}{\partial\rho^2} - \frac{1}{\rho}\frac{\partial\psi}{\partial\rho} + \frac{\partial^2\psi}{\partial z^2} = -4\pi^2\left[\mu\rho^2\frac{dp}{d\psi} + \frac{1}{2}\frac{dF^2}{d\psi}\right],$$

where ρ is the distance from the symmetry axis and z the distance from the equatorial plane. Plasma pressure, $p(\psi)$, and the diamagnetic function, $F(\psi) = \rho B_t$, are functions only of ψ; a scalar pressure is assumed. B_t denotes the actual toroidal magnetic field in the presence of plasma. In reality p and F are determined by the plasma transport properties with associated sources and sinks of particles, energy, and current. Since the transport problem has not been solved, a parametric approach to $p(\psi)$ and $F(\psi)$ is used in this report; we use

$$p = p_0\hat{\psi}^{\alpha} \tag{1}$$

and

$$F^2 = F_0^2\left(1 - \delta\hat{\psi}^{\gamma}\right), \tag{2}$$

where

$$\hat{\psi} = \frac{\psi_{limiter} - \psi}{\psi_{limiter} - \psi_{magnetic\ axis}} \tag{3}$$

and p_0 and F_0 are constants. Knowledge of $\psi(\rho,z)$ permits calculation of the safety factor and the plasma beta. The parameters α, δ, and γ correspond to an equivalent set, α, β_t, and q, the latter variables being the ones used in all our following discussions. We find the functions defined by Eqs. (1)-(3) span a realistic set of centrally peaked pressure distributions, $p(\rho,z)$, which include those obtained experimentally. In the surveys which follow several F functions have been chosen for each pressure profile, corresponding to a range of β_t values.

The boundary condition on the equilibrium solution is taken to be

$$\psi_{limiter} = \text{constant} ,$$

and the limiter shape is defined by

$$\begin{cases} z = \kappa \dfrac{R}{A} \sin t \\ \rho = R + \dfrac{R}{A} \cos(t + d \sin t) , \end{cases} \tag{4}$$

with $0 \leq t \leq 2\pi$. When $d = 0$ an elliptical cross section results, with the ratio of major and minor axes being κ. A value $d > 0$ corresponds roughly to a triangular or "D" shape pointing outwards from the symmetry axis. The aspect ratio A is the ratio of the toroidal major radius to the minor radius in the equatorial plane.

For each equilibrium calculated a large amount of data is produced, such as the differential volume metric $dV/d\psi$, the current density and pressure distributions $j_t(\rho,z)$ and $p(\rho,z)$, the safety factor $q(\psi)$, and the toroidal plasma current. Certain quantities among these may be used to assess stability of the equilibria. Since, however, stability may ultimately depend on details of the $p(\psi)$ and $F(\psi)$ forms, which we have not considered, we consider a wide range of equilibria and do not address the question of which are the highest beta, stable equilibria. The quantity of immediate interest for reactor design is the plasma current I_p required to maintain an equilibrium. In fact, the structure of the equilibrium equation determines I_p to be proportional to the vacuum value of $F = \rho B_t$. Thus, since the toroidal field coil current is $I_{TFC} = 2\pi F/\mu_0$, we display the normalized plasma current, I_p/I_{TFC}, keeping in mind that this ratio is very significant when determining the power supply costs of a tokamak reactor.

The six-dimensional MHD parameter space (A, κ, d, α, β_t, q) naturally requires an extensive survey to cover all the relevant equilibria, but we have

found it instructive to pick a reference point and independently vary one parameter at a time around that point, holding the others fixed. The qualitative dependence of equilibria on these parameters is found to be the same around other reference points. Consequently we will refer to the following point near the center of the interesting parameter space: $A = 3.0$, $\kappa = 1.3$, $d = 0.25$, $q = 3.0$, and $a = 1.4$. For each variation of these parameters we will plot I_p/I_{TFC} versus β_t.

Figure 1 shows the variation of plasma current with the triangularity of the plasma cross section. The reverse D shapes we examined ($d = -0.5, -0.25$) are indistinguishable from circular plasmas ($d = 0.0$) as far as the plasma current requirements are concerned. As d increases above zero, larger plasma currents are required. For a fixed set (A, κ, d, q, a), the mild increase of equilibrium current with β_t is associated with an outward shift of the magnetic axis and a tendency to form skin currents. Since various stability calculations [4] suggest reverse D shapes to be less stable equilibria than D's, we will now concentrate on non-negative values of d. In the remaining parameter surveys we choose correlated values of triangularity and elongation: ($\kappa = 1.0$, $d = 0.0$), ($\kappa = 1.3$, $d = 0.25$), ($\kappa = 1.65$, $d = 0.5$), and ($\kappa = 2.0$, $d = 0.75$)

The equilibrium plasma current was next examined as the pressure profile was varied, and I_p/I_{TFC} was found to be independent of α for $1.0 \leq \alpha \leq 2.0$. However, the broader pressure profiles ($\alpha \approx 1.0$) tend to have somewhat smoother current density profiles and smaller shifts of the magnetic axis for a given β_t and on an intuitive basis may result in more stable discharges than narrow profiles.

The variation of required plasma current with elongation and aspect ratio is displayed in Figs. 2 and 3. The plasma cross-sectional area defined by Eq. (4) is quite accurately given by the formula

$$X = \pi\kappa(R/A)^2[J_0(d) + J_2(d)] , \tag{5}$$

where J_0 and J_2 are Bessel functions and where we assume $0 \leq d \leq 1$. Comparison of Eq. (5) with the figures shows plasma current is roughly proportional to the area of the plasma cross section (except for the dependence on d, discussed above). The reason is that requiring q(0) = 1 keeps the current density approximately the same in all cases. The effects of κ and A on I_p/I_{TFC}, which partly determines the reactor power supply costs, must be compared with the effects of κ and A variations on the total thermal power of the reactor. Reactor power, which will be quantitatively analyzed in Sec. IV, may be estimated as

$$P = \beta_t^2 B_0^4 f\left(\alpha_n, \alpha_T, \bar{T}_e\right) V . \tag{6}$$

Here B_0 is the toroidal magnetic field at the point $\rho = R$, $Z = 0$, which is related to the field at the TF coil by

$$B_0 = B\left[1 - A^{-1} - \frac{\left(\Delta + \Delta_v\right)}{R}\right] , \tag{7}$$

where Δ_v is the thickness of the vacuum scrape-off region. The quantity f is the reaction rate, which is a function of profiles and temperatures. The toroidal plasma volume, V, may be gotten by rotating the cross section given by Eq. (4) around the centerline:

$$V = 2\pi RX \cdot \left(1 - \frac{0.233\ d}{A}\right)$$

$$= 2\pi^2 \frac{R^3}{A^2} \kappa[J_0(d) + J_2(d)]\left(1 - \frac{0.233\ d}{A}\right) . \tag{8}$$

A comparison of Eq. (8) with our numerical results shows the formula to be correct within 1% for the geometry range we are considering.

If we now increase κ and d with all other parameters fixed, we note that the increase in I_p in Fig. 2 is compensated by an increase in the reactor power from Eqs. (6) and (8). On the other hand, the increase of I_p/I_{TFC} with decreasing aspect ratio is not compensated by increases in reactor power if β_t remains constant since the product B_0^4V decreases with decreasing A in the geometry range of interest. (Stability limits may allow higher β_t at low aspect ratios, motivating low A designs.)

The strong dependence of I_p/I_{TFC} on safety factor is given in Fig. 4 and is essentially $I_p/I_{TFC} \propto q^{-1}$.

III. PARTICLE AND POWER BALANCE

By adding the electron and D-T ion power balance equations, we find the overall steady-state relation for ignition is

$$0 = \frac{n_i^2 \langle \sigma v(T_i) \rangle E}{4} - W_R - \frac{3}{2}\frac{n_i}{\tau}\left(T_i + \frac{n_e}{n_i} T_e\right),$$

where E is 3.52 MeV/event, W_R is the radiation loss, and τ is the energy containment time. Ohmic heating is negligible in the reactor regime. Dividing by the square of the D-T ion density, n_i^2, and using explicit expressions for synchrotron, bremsstrahlung, line and recombination radiation [5,6], we have

$$\frac{\langle\sigma v(T_i)\rangle E}{4} = K_s \frac{n_e}{n_i}\frac{B_t^{5/2}}{n_i^{3/2}}\left(T_e^{11/4} + 0.0049\, T_e^{15/4}\right)$$

$$+ \frac{n_e}{n_i}\sum_z \frac{n_z}{n_i}\left(K_B Z^2 T_e^{1/2} + K_1 Z^4 T_e^{-1/2} + K_2 Z^6 T_e^{-3/2}\right)$$

$$+ \frac{3}{2n_i\tau}\left(T_i + \frac{n_e}{n_i}T_e\right) . \tag{9}$$

The ratio n_e/n_i in Eq. (9) is determined from charge neutrality, $n_e = n_i + 2n_\alpha + \sum_z n_z Z$, or,

$$\frac{n_e}{n_i} = 1 + \frac{2n_\alpha}{n_i} + \sum_z \frac{n_z}{n_i} Z . \tag{10}$$

The alpha particle density is derived from the condition

$$0 = \frac{dn_\alpha}{dt} = \frac{n_i^2\langle\sigma v(T_i)\rangle}{4} - \frac{n_\alpha}{\tau} ,$$

or

$$\frac{n_\alpha}{n_i} = \frac{\langle\sigma v(T_i)\rangle}{4} n_i\tau . \tag{11}$$

A final independent relation is the ion power balance (divided by n_i^2),

$$0 = \frac{\langle\sigma v(T_i)\rangle E\, f_{\alpha i}}{4} - K_{ie}\frac{n_e}{n_i}\frac{T_i}{T_e^{3/2}}\left(1 - \frac{T_e}{T_i}\right)A_i \sum_z \frac{n_z}{n_i}\frac{Z^2}{A_z} - \frac{3T_i}{2n_i\tau} , \tag{12}$$

where $f_{\alpha i}$, the fraction of alpha particle energy transferred to D-T ions, is

a function of T_e, n_e/n_i, n_α/n_i, and the impurity content. In the D-T ion-electron energy transfer term A_j denotes the mass of the j-th species. If synchrotron radiation, the first term on the right-hand side of Eq. (9), could be neglected, then the four equations, (9)-(12), could be solved for T_i, $n_i\tau$, n_e/n_i, and n_α/n_i by merely specifying T_e and the impurity parameters n_z/n_i, Z, and A_z. In fact, for an average $\bar{T}_e \lesssim 20$ keV we find synchrotron radiation is negligible, which means the relationships between $n_i\tau$, T_e, T_i, and impurity content are independent of the D-T ion density, n_i, and of B_t. Thus, in this temperature range, which we will find is most attractive for tokamak operation, the power balance calculation is essentially independent of the MHD equilibrium results.

Recall that all the densities and temperatures are associated with profiles in flux coordinate space:

$$\begin{cases} n_j = n_{j0}\hat{\psi}^{\alpha_n} \\ T_j = T_{j0}\hat{\psi}^{\alpha_T} . \end{cases}$$

Comparing these expressions with Eq. (1) and requiring the pressure to be the product of particle density and temperature, we see

$$\alpha = \alpha_n + \alpha_T . \tag{13}$$

In solving Eqs. (9)-(12) all expressions are evaluated at ten points in ψ, and the spatial averages $\bar{n}_i\tau$ and $\bar{T}_i$ are found which balance the total power production and loss. (No significant change is found if more than ten points are used.)

Besides the required $\bar{n}_i\tau$ for ignition, another useful result of the power balance calculation is the alpha power density in the plasma,

$$w = \frac{n_i^2 \langle \sigma v(T_i) \rangle E}{4} . \tag{14}$$

A qualitative appreciation of profile effects on the power density may be gained by expanding Eq. (3) around the magnetic axis, assuming circular, concentric flux surfaces. Then, denoting the minor radius coordinate as $r = \sqrt{(\rho - R)^2 + z^2}$,

$$\begin{cases} n_j \approx n_{j0}\left(1 - r^2/a^2\right)^{\alpha_n} \\ T_j \approx T_{j0}\left(1 - r^2/a^2\right)^{\alpha_T} , \end{cases} \tag{15}$$

where $a = R/A$; the volume averaged values are

$$\bar{n}_j = \frac{n_{j0}}{1 + \alpha_n}$$

$$\bar{T}_j = \frac{T_{j0}}{1 + \alpha_T} . \tag{16}$$

Inserting Eq. (15) into Eq. (14) the total alpha power in a circular cross section reactor would be

$$P \approx (2\pi)^2 R \int_0^a \frac{dr\, r\, n_i(r)^2 \langle \sigma v[T_i(r)] \rangle E}{4} .$$

After $\langle \sigma v(T_i) \rangle$ has been determined from Eqs. (9)-(12) the D-T ion density is found from the results of the MHD calculation, i.e. n_i is constrained by the equilibrium value of plasma beta. Denoting a spatial average by a bar,

$$\beta_t \equiv \frac{\overline{n_i T_i + n_e T_e + \sum_z n_z T_i + \text{alpha pressure}}}{B_0^2/2\mu} . \tag{17}$$

For the purpose of the present illustration we set $T_e = T_i$ and neglect alpha and impurity contributions in Eqs. (10) and (17), so

$$P \approx (2\pi)^2 R \frac{\beta_t^2 B_0^4}{64\mu^2} \left(\frac{1+\alpha}{1+\alpha_T}\right)^2 \int_0^a dr\, r \left(1 - \frac{r^2}{a^2}\right)^{2\alpha_n} \left\langle \sigma v[T(r)] \right\rangle E \ .$$

Using the analytic expression [7]

$$\left\langle \sigma v(T) \right\rangle = bT^{-2/3} \exp\left(-cT^{-1/3}\right) ,$$

the integral is easily performed:

$$P \approx 6\pi^2 R\, a^2 \frac{\beta_t^2 B_0^4}{64\mu^2} E \left(\frac{1+\alpha}{1+\alpha_T}\right)^2 \frac{bT_0^{-2/3}}{\alpha_T} u^{-m} \Gamma(m,u) ,$$

where

$$u = cT_0^{-1/3}$$

and

$$m = 2 - \frac{3 + 6\alpha_n}{\alpha_T} .$$

The incomplete gamma function may be expressed in terms of a continued fraction and the result is a close fit in the profile and temperature range of interest with

$$P \approx 6\pi^2 R\, a^2 \frac{\beta_t^2 B_0^4}{64\mu^2} E \left\{ (1+\alpha)^2 \frac{\left\langle \sigma v \left[\left(1+\alpha_T\right)\bar{T}\right] \right\rangle}{\left[\left(1+\alpha_T\right)\bar{T}\right]^2} H(\alpha,\bar{T}) \right\} , \tag{18}$$

where

$$H(\alpha,\bar{T}) \equiv \left[\frac{0.095}{\alpha^{3/4}} + 0.00139\ \bar{T}\right] .$$

The function of α_n, α_T, and $\bar{T}$ in braces in Eq. (18) is proportional to the reactor average power density. Let us first consider holding the pressure profile (α) and average energy ($\bar{T}$) constant so the power density only varies with the function $\left\langle \sigma v\left[\left(1 + \alpha_T\right)\bar{T}\right]\right\rangle \Big/ \left[\left(1 + \alpha_T\right)\bar{T}\right]^2$. This latter function has a maximum near $\left(1 + \alpha_T\right) = 13$ keV, so we expect power density to increase with increasing α_T (decreasing α_n) for $\left(1 + \alpha_T\right)\bar{T} < 13$ keV and to decrease with α_T for $\left(1 + \alpha_T\right)\bar{T} > 13$ keV. These conclusions are supported by the numerical results, such as those in Fig. 5. Due to the slow variation of $\langle \sigma v(x)\rangle/x^2$ near $x = 13$ keV we see that power density is almost independent of the ratio of α_T to α_n as long as $\left(1 + \alpha_T\right)\bar{T} \approx 13$ keV. Physically, most of the fusion is occurring for particles at the peak of the temperature profile. Another noteworthy point about Fig. 5 is the insensitivity of power density to impurity concentration. While $\langle \sigma v\rangle$ is an increasing function of Z_{eff} $\left(= \sum_j n_j Z_j^2/n_e\right)$ at constant β_t [cf. Eq. (9)], n_i must decrease with Z_{eff} at constant β_t [see Eq. (17)], and consequently the product in Eq. (14) remains fairly constant.

The variation of ignition $\bar{n}_i\tau$ with the ratio of α_T to α_n is displayed in Fig. 6 for fixed α and various temperatures and Z_{eff} values. Again the results vary slowly with α_n, especially for clean plasmas characteristic of the steady-state portion of the burn cycle. Due to this very mild dependence of power density and $\bar{n}_i\tau$ on α_n at a fixed α we feel comfortable in selecting a reference value for α_n for the remaining investigations. We have chosen $\alpha_n = 0.3$ in anticipation that a reactor will have a broader density profile than present experiments [8] because of such factors as increased activity near the walls

and the difficulty of a neutral beam in penetrating the plasma during the initiation phase.

In analyzing the power balance results we should be aware of the limitations of describing plasma impurity content with the quantity Z_{eff}. We have solved the power balance for two different plasma compositions both having $Z_{eff} = 1.7$, and this illustration is given in Fig. 7. For all cases in this report the alpha particle concentration is the result of the steady-state power balance calculation [cf. Eq. (11)], and a background oxygen content with $n_0/n_i \equiv 0.5\%$ is assumed. Then $Z_{eff} = 1.7$ results from an additional contribution of either 0.07% iron or 5.0% beryllium, for the example given here. The figure shows both $\bar{n}_i\tau$ and power density versus $\bar{T}_e$ for typical density and temperature profiles. The main effect of a "good quality" plasma with mainly low atomic number impurities contributing to Z_{eff} (the beryllium curves) is to reduce the the minimum $\bar{T}_e$ for ignition. On the other hand, the plasma dominated by higher-Z atoms tends to result in a slightly larger power density, even though β_t, B, and all other independent variables are fixed. However, for the present survey the important observation is that the average temperatures for maximum power production and minimum $\bar{n}_i\tau$ are essentially unchanged, $\bar{T}_e \approx$ 8 keV and 17 keV, respectively. We will use iron as the reference impurity in the remaining calculations.

In order to appreciate the strong influence of impurity quality on reactor performance we have included a plot of maximum allowable impurity concentration versus atomic number of the dominant impurity, Fig. 8. The differences between our radiation formula, a modified version of that in Eq. (9), which is a simple fit to the theory [5,6], and the detailed line and recombination coronal equilibrium model of Ref. 9 result in the surprisingly small discrepancies between the solid and dashed curves. Despite numerical disagreements, it is

evident that allowable impurity levels decrease almost exponentially with Z. The importance of impurity quality to burn cycle dynamics, first-wall design, and impurity control methods is readily acknowledged but is outside the purview of our present study.

Turning now to Fig. 9 we see the ignition value of $\bar{n}_i\tau$ increases with Z_{eff}, as expected. The three solid $\bar{n}_i\tau$ curves (with $\alpha = 1.5$) show ignition is impossible around $\bar{T}_e = 10$ keV for $Z_{eff} \gtrsim 2$-3. Note that $Z_{eff} = 1.3$ assumes only alpha particles and the 0.5% oxygen background. If we next fix Z_{eff} and increase α (the three curves with $Z_{eff} = 1.7$) we find $\bar{n}_i\tau$ decreases as the pressure profile peaks, for $\bar{T}_e \lesssim 12$ keV. Also, the value of $\bar{T}_e$ required to minimize $\bar{n}_i\tau$ shifts from over 20 keV, characteristic of flat profiles with $\alpha < 1.0$, to almost 10 keV for narrow profiles with $\alpha = 2.0$. These beneficial profile effects have been previously noted by Kesner and Conn [10], whose conclusions agree qualitatively with ours. For $\bar{T}_e \gtrsim 15$-20 keV our values of $\bar{n}_i\tau$ are significantly larger than those of Kesner and Conn since they did not include synchrotron radiation, which becomes dominant at large temperatures. From the figure we conclude that the required $\bar{n}_i\tau$ varies only by a factor of two or three as long as $\bar{T}_e$ is not near the ignition cutoff point, i.e., for 8 keV $\lesssim \bar{T}_e \lesssim$ 17 keV, $Z_{eff} \lesssim 2.0$, and $1.0 \lesssim \alpha \lesssim 2.0$. In view of the orders of magnitude uncertainty in predicting the achievable energy containment time, τ, it seems unwarranted at present to concern ourselves further with the detailed dependence of $\bar{n}_i\tau$ on $\bar{T}_e$, Z_{eff}, and α.

Therefore, we focus on the power density as a more relevant measure of the plasma behavior. The significant effect of increasing α is to reduce the $\bar{T}_e$ at which maximum thermal power is produced [10]. Referring to Eq. (18) and ignoring the slow variation of $H(\bar{T})$ we see power density can maximize well below the usual $\bar{T} \approx 13$ keV of a flat pressure profile. Since $\langle\sigma v(x)\rangle/x^2$ peaks

at $x \approx 13$ keV, the power density peaks at $\bar{T} \approx 13\ \text{keV}\left(1 + \alpha_T\right)^{-1}$, as illustrated in Figs. 7 and 9. This reduction in the optimum $\bar{T}$ can be large ($\bar{T}_e < 5$ keV for maximum power with $Z_{eff} = 1.3$, $\alpha_n = 0.3$, and $\alpha = 2.0$), making peaked profiles quite attractive. As found in Ref. 10 the other effect of increasing α is to generally increase the power density at a fixed value of $\bar{T}_e$. For example, increasing α from 1.4 to 2.0 can increase power density by 8% at $\bar{T}_e = 8$ keV if $\alpha_n = 0.3$, $Z_{eff} = 1.7$, and if β_t is kept constant. Of course, the pressure profile parameter α will affect the achievability and stability of the MHD equilibria, making it unclear what freedom exists in choosing β_t as α varies

There remain subtle consequences of geometry (A, κ, d) and finite β_t which determine the $\psi(\rho,z)$ metric. These details, which are accounted for by the numerical volume integration of Eq. (14), have only small effects on power density curves and the $\bar{n}_i\tau$ parameter. Thus, based on the sensitivity studies so far, we can choose a set of power balance reference parameters: $\alpha_n = 0.3$, $\alpha = 1.4$, $\bar{T}_e = 8$ keV, and $Z_{eff} = 1.7$. These numbers correspond to nearly maximum power density, reasonable $\bar{n}_i\tau$, and realistic profiles well into the "steady-state" portion of the burn cycle of a typical tokamak reactor.

IV. REACTOR PERFORMANCE

The last stage in our tokamak physics survey probes the relationships among the major radius, magnetic field, and blanket/shield thickness. These three figure prominently in the engineering and economic analysis of reactor design for which our results serve as a data base [1]. In this section we set $\alpha_n = 0.3$, $\bar{T}_e = 8$ keV, $Z_{eff} = 1.7$, and let d increase with κ as given in Sec. II. Our approach will be to examine alternatives among the major cost items, B, R, and I_p, for a fixed reactor thermal power (2500 MW, considering 17.58 MeV per fusion event). The section concludes with a brief look at reactor scaling with

power level around an attractive design point, including neutron wall load and containment times computed from theoretical and empirical laws.

From Eqs. (6)-(8) we see $B \propto R^{-3/4}$ at constant power when $\Delta + \Delta_v << R$, which is evident in Fig. 10. If the TF coils are NbTi superconductor with $B \lesssim 9$ T, the minimum major radius is in the 6-7 m range, for $A = 3.0$, $\kappa = 1.3$, and $\beta_t = 0.08$. A small reduction in R requires a substantial increase in B, which may necessitate the use of a more advanced type of conductor. Equation (7) shows a small increase in Δ at constant R requires a concommitant increase in B if B_0 and the thermal power are to remain constant. On the other hand, the figure shows that a 0.25 m reduction in the blanket/shield thickness allows about a 0.50 m reduction in the major radius for a fixed B at this reference design point. Other studies [11] indicate $\Delta = 1.0$ m is probably near the optimum thickness for a tokamak reactor, and we will take this as our reference value for the remaining part of this study.

A series of pressure profiles, from $\alpha = 1.2$ to $\alpha = 2.0$, was examined, and the two limiting cases are plotted in Fig. 11. As noted in Sec. III, narrow profiles are preferable for reducing the required magnetic field or major radius for a given reactor power. The plot shows only a 4% change in B or R for $1.2 \leq \alpha \leq 2.0$, so our reference choice, $\alpha = 1.4$, is reasonably representative of reactor possibilities.

The most timely questions surrounding tokamak reactors concern the magnitude and scaling of plasma beta with geometry; the next series of figures shows the consequences of various trends. First, Figs. 12 and 13 detail the design options for a number of A and β_t combinations when κ is fixed. As implied in Sec. II, if the thermal power is fixed then either B or R or both may be reduced if A is increased at constant β_t. However, plasma stability considerations may dictate that the maximum β_t decrease as the aspect ratio increases,

which could affect our choice of a desirable aspect ratio. If, for example, $\beta_t\big|_{max} = cA^{-1/2}$, a weak dependence on aspect ratio, we would compare curves such as β_t = 10% at A = 2.5 with β_t = 8% at A = 4.0, shown in Fig. 12. For this case a low field (B = 6 T) reactor must have R = 9.3 m if A = 2.5 but requires R = 10.0 m if A = 4.0. Yet, for the same scaling, a compact tokamak (B $\geq$ 12 T, R $\lesssim$ 5.0 m) actually requires a smaller major radius if A = 4.0 and β_t = 8%! (Keep in mind that the coefficient c in the $\beta_t(A)$ scaling is also presently unknown; the A and β_t combinations used here are only hypothetical examples.) If we postulate a stronger scaling such as $\beta_t\big|_{max} = cA^{-3/2}$, then instructive curves for comparison would be β_t = 8% at A = 2.5 and β_t = 6% at A = 3.0. Now we see the lower aspect ratio plasma always results in a smaller major radius, although the difference becomes small at high magnetic field (B $\approx$ 14 T).

The required plasma current for these options is shown in Fig. 13. For a fixed power at constant β_t and constant R the needed I_p decreases dramatically with increasing A, due to the decrease in the ratio I_p/I_{TFC} (see Fig. 3) and due to a decrease in I_{TFC}, which is proportional to B (Fig. 12). For a fixed aspect ratio and major radius we see I_p decreases with increasing β_t since the magnetic field decreases faster than the ratio I_p/I_{TFC} increases. The inference drawn from these two figures, Figs. 12 and 13, is that, if β_t is sufficiently increased by reducing A at constant power with all other parameters fixed, then the major radius and magnetic field may possibly decrease while the required plasma current will certainly increase. Since R, B, and I_p are strong determinants of reactor cost the economic consequences of the $\beta_t(A)$ scaling are important and can be quantitatively assessed only with an overall power plant systems study [1].

Next we fix A = 3.0 and examine β_t scaling with κ. Again the particular scaling law is needed to make quantitative conclusions. As a heuristic case,

suppose $\beta_t|_{max} = c'S^2$, where S is the shape factor, the ratio of plasma perimeter to the circumference of an inscribed circle. In order of increasing ellipticity and triangularity the four cross sections considered here have S = 1.0, 1.2, 1.4, and 1.6. The curves labelled β_t = 8% at κ = 1.65 and β_t = 6% at κ = 1.3 in Figs. 14 and 15 follow the scaling law in question. At a fixed magnetic field strength and constant power the change from the κ = 1.3 to the κ = 1.65 design results in a 15% decrease in major radius but a 22% increase in plasma current. As with the aspect ratio variations the relative merits of various designs ultimately depend on the engineering/economics considerations of the overall power plant systems study [1].

The influence of the safety factor on design criteria is shown in Figs. 16 and 17. We see if β_t is constant then the q value has very little impact on B versus R, only changing the volume metric slightly. One motivation for reducing q is that the maximum stable plasma beta is often thought to scale inversely with q provided the Kruskal-Shafranov limit is not violated ($q \lesssim 1$). For example, the curves β_t = 16% at q = 2.0 and β_t = 8% at q = 4.0 correspond to $\beta_t|_{max} \propto q^{-1}$. In this case the lower q requires about a 25% smaller major radius and 15% larger plasma current for fixed field strength and reactor power.

The final sequence of figures depicts the scaling of a few design features with reactor thermal power production. The tokamak parameters were fixed with A = 3.0, κ = 1.65, β_t = 8%, q = 3.0, and Δ = 1.0 m while the major radius was varied for P = 2500, 1250, and 650 MW. Figure 18 illustrates the power dependence on B and R, indicated by Eqs. (6)-(8). Note especially at high field the modest increase in major radius needed to substantially increase power production. The plasma current, Fig. 19, also is a slowly increasing function of power level, typically requiring only a 20% increase for twice the power output. Neutron wall loading might impose a significant constraint on our design

options. As seen in Fig. 20 this consideration is especially relevant to small volume, high-field tokamaks. The concluding plot, Fig. 21, compares the energy containment time τ required for steady-state ignition to the values τ_{EMP} and τ_{TIM} predicted by empirical scaling and trapped ion mode theory [6], respectively. We have used $\tau_{EMP} = 4 \times 10^{-21}\, n_e q^{\frac{1}{2}} (as)^2$, where the shape factor is an *ad hoc* attempt to model diffusion in a noncircular plasma. The ratios τ/τ_{EMP} and τ/τ_{TIM} are less than one, as required if energy loss is not to exceed fusion energy production. However, when we acknowledge the myriad uncertainties in plasma transport theory we hesitate to draw any final conclusions from this figure.

V. SUMMARY

Assuming β_t is fixed, the plasma power density in tokamak reactors is very insensitive to certain characteristics of the MHD equilibrium, and the following trends were observed.

(1) Power density and ignition $\bar{n}_i\tau$ are only slowly varying functions of α_n/α_T for a fixed pressure profile. We chose $\alpha_n = 0.3$, representative of a relatively broad density distribution, for subsequent analysis.

(2) Power density and $\bar{n}_i\tau$ values become more favorable for peaked pressure profiles compared to flat profiles. We set $\alpha = 1.4$ as a typical value, although future MHD stability analyses should indicate more clearly which pressure profiles are actually attainable.

(3) Power density is insensitive to Z_{eff}, except that ignition becomes impossible ($\bar{n}_i\tau \to \infty$) at low $\bar{T}_e$ as Z_{eff} increases. By taking $Z_{eff} = 1.7$, ignition is assured for $\bar{T}_e$ as low as 8 keV.

(4) Power density tends to peak at $\bar{T}_e \approx 13\ \text{keV}\left(1 + \alpha_T\right)^{-1}$. This, plus the fact that $\bar{n}_i\tau$ is slowly varying for $\bar{T}_e$ in the range 8-15 keV, motivated our standard choice $\bar{T}_e = 8$ keV.

Reactor costs are strong functions of magnetic field, major radius, and blanket/shield thickness. Our choices among these parameters are influenced by the nature of the MHD equilibrium and result in the following observations.

(5) Triangularity of the plasma cross section has only mild effects on I_p for a fixed B and R; it has only small effects on plasma volume and consequently does not change the B versus R curve at constant reactor power. Thus our arbitrary choice of the d and κ relationship was permissible for our purposes. If high beta stability is significantly dependent on triangularity, some other sequence of d values could be more pertinent.

(6) Pressure profile effects are negligible on I_p and B versus R for $1.0 \leq \alpha \leq 2.0$, if β_t is fixed. However, MHD stability may vary with α.

(7) There is substantial motivation to reduce Δ as far as possible; Δ = 1.0 m was considered a practical minimum.

(8) We saw from Figs. 12 and 13 that $\beta_t|_{max}$ must increase substantially as A decreases in order to benefit from low aspect ratio designs when κ is fixed. This is especially true of small-size, large field tokamaks.

(9) When the aspect ratio is fixed, the advantages of large κ designs are straightforward, as shown in Fig. 14, even if β_t does not increase with κ. The high current requirements at large κ are equally apparent, in Fig. 15.

(10) Large increases in I_p are required if q is reduced. Hopefully, these increases may be compensated by increases in $\beta_t|_{max}$.

It should be obvious that one shortcoming of the present systems study is the inability to predict the optimum path of investigation through the multidimensional parameter space. For example, future stability studies may shed light on the proper relationships among A, κ, d, q, and α needed to maximize β_t. It also seems plausible that the path of stability through MHD space may have poorly defined boundaries since mild deviations from the path may simply

result in plasmas with degraded confinement properties. Finally, we stress that the data base presented here is best evaluated in the context of the overall power plant parametric study [1] in which the costs and benefits of different choices are quantitatively examined.

ACKNOWLEDGMENTS

We wish to thank E. Goldstick for compiling much of the MHD data base and C. Dennis for extensive computational assistance.

APPENDIX

Plasma Physics Subroutine of the ANL Tokamak Systems Code

1. General Description

The plasma physics subroutine is a flexible package designed to accommodate many modes of data handling for tokamak reactor analysis and was built upon capabilities developed at ANL for detailed design activities. The package consists of a plasma driver, which specifies the independent variables, controls the calculation procedure, and organizes the output data, and various subroutines which perform the actual calculations. The calculations fall into three categories: MHD equilibrium, particle and power balance, and reactor design interface, which are detailed below.

To facilitate quick surveys of reactor possibilities this code has been tailored for rapid turnaround. The equilibrium computation is by far the most time consuming requiring about 13 s on the IBM-370/195. However, once an equilibrium has been computed, all the relevant parameters are stored in a library (MHDLIB) for use in all future calculations with that equilibrium. The particle and power balance is relatively fast running, typically using 1.5 s of computer time, and the final reactor design interface portion requires the least time, less than a few milliseconds. Table II presents benchmark calculations documenting the running time for four different cases using the plasma physics package.

Output data has been selected on the basis of its usefulness to the tokamak systems study. Important quantities like thermal power, wall loads, and plasma current are numerically determined in detail. Other quantities, such as the plasma self-inductance and equilibrium vertical field, are very time consuming

to be calculated numerically and are therefore approximated from analytical formulas. A steady-state, zero-dimensional transport calculation is performed over the density and temperature profiles determined from the MHD equilibrium. Burn cycle dynamics, which introduce many new variables and uncertainties, are not addressed by this subroutine but are treated separately in the Tokamak Systems Program. Likewise, the stability of high beta equilibria is not calculated quantitatively. The plasma-wall model incorporated in the code permits studies of impurity generation and control.

2. Variables and Assumptions

2.1 Glossary of variables

Variable Name in Code	Symbol in this Document	Description
ACX	A_{cx}	Charge exchange albedo for neutral D-T.
ACXEXT	A_{cx}^{ext}	Charge exchange albedo for neutral D-T for refueling.
ALFEMP		Ratio of τ to containment time from empirical scaling.
ALFPC		Ratio of τ to containment time from pseudoclassical theory.
ALFTEM		Ratio of τ to containment time from trapped electron theory.
ALPHA		Ratio of τ to containment time from trapped ion theory.
ALPHAJ	α_J	Measure of diamagnetism.
ANIMI(J)	A_j	Atomic mass of j-th species.
AREAP		Surface area of plasma.
AREAW	A_w	Surface area of first wall.
ASP	A	Aspect ratio of plasma.
BETAP	β_p	Poloidal beta.
BETAT	β_t	Toroidal beta.
BMAX	B	Maximum toroidal field at TFC.

BMAXQ		Toroidal field specified as input.
BPLAS	B_0	Toroidal field at plasma center.
CAPPA	κ	Height-to-width ratio.
CI	$\bar{I}_c$	Source of D-T ions.
CLNGTH		Length of perimeter of plasma cross section.
CSNLTY	ν_*	Ratio of electron effective collision and bounce frequencies.
DEITY	d	Measure of cross-section triangularity.
DELB	Δ_B	Inner blanket thickness.
DELS	Δ_S	Inner shield thickness.
DELSQ		Shield thickness specified as input.
DELV	Δ_v	Inner scrapeoff (vacuum) width.
DELTA	δ	Magnitude of diamagnetism.
DPHI		Inductive volt-seconds of OHC.
DPHIDT		e.m.f. required to maintain current.
EA		Average alpha particle energy.
ETAAL	η_α	Alpha removal efficiency.
ETADT	η_{DT}	D-T ion removal efficiency.
ETAIM	η_I	Impurity removal efficiency.
FAL	f_α	Effective alpha recycle fraction.
FB	f_{bu}	Fractional burnup.
FDT	f_{DT}	Effective D-T recycle fraction.
FIM	f_I	Effective impurity recycle fraction.
FNEXT	F_{DT}^{ext}	Refueling rate required by D-T source.
FWALAL	F_{wall}^{α}	Alpha wall flux.
FWALDT	F_{wall}^{DT}	D-T wall flux (including neutrals).
FWALIM	F_{wall}^{I}	Impurity wall flux.
FWALL	F_0	Magnetic field - major radius product in vacuum.

FWALL0		Reference value of FWALL used for MHD scaling.
GAMMA	Γ	Ratio of injection energy density to plasma energy density.
HEIGHT		Height of plasma cross section.
OHMIC		Ohmic heating power density.
P	p	Tritium fraction.
PA		Alpha particle energy density.
PCUR	I_p	Plasma toroidal current.
PIMP(J,I)	n_I	Density of I-th impurity at point J.
PIB(J)		Density of beam particles at point J.
PNI(J)	n_i	Density of D-T ions at point J.
POHM	P_Ω	Ohmic heating power.
PROFF	γ	Shape factor for diamagnetism.
PROFN	α_n	Density profile shape factor.
PROFP	α	Pressure profile shape factor.
PROFT	α_T	Temperature profile shape factor.
PT	P	Total thermal power.
PTE(J)	T_e	Electron temperature at point J.
PTI(J)	T_i	Ion temperature at point J.
PTQ		Thermal power specified as input.
PW	W	Neutron wall load.
PWQ		Neutron wall load specified as input.
PZI(J,I)		Charge state of I-th impurity at point J.
QGAIN	Q_p	Ratio of fusion power to power input from external sources.
QSAFE	q	Safety factor at the limiter.
RADB	$\bar{P}_{rad}$	Average power density of line, recombination, and bremsstrahlung.

RADC	$\bar{P}_c$	Average cyclotron power density.
RDT	R_{DT}	D-T wall reflection coefficient.
REFB		Wall reflection coefficient for line, recombination and bremsstrahlung.
REFC		Wall reflection coefficient for cyclotron radiation.
RM		Distance from center line of maximum toroidal field.
RMAJ	R	Major radius.
RMAJO		Reference value of RMAJ used for MHD scaling.
RNIMI(J)	n_j/n_i	Relative density of species j to D-T ion density.
RPLAS	a	Plasma minor radius.
RWALL		First-wall minor radius.
SN	S_n	Neutron sputtering coefficient.
SAL	S_α	Alpha sputtering coefficient.
SDT	S_{DT}	D-T sputtering coefficient.
SIM	S_I	Impurity sputtering coefficient.
SQUIG	ξ	Ratio of enhanced beam power to alpha heating power.
SV	$\overline{\langle \sigma v \rangle_f}$	Average fusion reaction rate.
TALPHA	τ_α^{SD}	Alpha slowing-down time.
TE	$\bar{T}_e$	Average electron temperature.
TI	$\bar{T}_i$	Average ion temperature.
TRANS	P_L	Transport power loss.
VAE		Alpha energy transferred to electrons.
VAI		Alpha energy transferred to ions.
VOLUM	V	Plasma volume.
VPRIM	V'	Volume metric.
WBEAM	U_B	Beam energy.
XJDT		D-T flux to wall.
XJFA		Fast alpha flux to wall.

XJN	J_w	Neutron wall flux.
XJSA		Slow (thermal) alpha wall flux.
XL		Plasma dimension for cyclotron radiation.
XNALFA	$\bar{n}_\alpha$	Average alpha particle density.
XNE	$\bar{n}_e$	Average electron density.
XNI	$\bar{n}_i$	Average D-T ion density.
XNITAU	$\bar{n}_i\tau$	Density-containment time product.
XSB		Line, recombination, and bremsstrahlung wall load.
XSC		Cyclotron radiation wall load.
ZEFF	Z_{eff}	Effective plasma charge state.
ZI(J)	Z	Charge of J-th species.
ZI2(J)		Square of charge of J-th species.
ZL		Shape factor (ratio of CLNGTH to circumference of inscribed circle).

2.2 *Tokamak model assumptions*

The code has been designed to analyze circular or mildly noncircular axisymmetric tokamaks. In cylindrical coordinates the plasma surface has the equation

$$z = \kappa \frac{R}{A} \sin t$$

$$\rho = R + \frac{R}{A} \cos(t + d \sin t) ,$$

where $0 \leq t \leq 2\pi$, $\kappa \lesssim 2$, and $|d| \lesssim 1$.

A scalar pressure is assumed, and stationary flux surfaces are determined by solving the Grad-Shafranov equation; the pressure and diamagnetic functions of ψ are characterized by the parameters α, γ, and δ. A fixed boundary calculation of the equilibrium is done, and the safety factor on the magnetic axis is constrained to be unity. By specifying α, γ, and α_J (which is equivalent to

specifying α, γ, and δ) the values β_t and q will be found. An extensive survey of tokamak equilibria has been performed, and those with favorable stability characteristics ($q \geq 2$, smooth current density profiles, no reversed current regions, only mild shift of the magnetic axis) have been stored in the MHD library where they may be recalled by merely specifying the parameters A, κ, d, α, β_t, and q.

The vacuum region, Δ_v, is assumed uniform all over the plasma surface.

Plasma self-inductance, which determines the inductive transformer volt-seconds, is approximately found from the analytic expression for a large aspect ratio, uniform current density discharge. The transformer flux change required to maintain the plasma current is found assuming uniform current density and resistivity in the plasma. Spitzer resistivity is assumed, with no neoclassical or anomalous enhancement.

A steady-state transport model is assumed with losses described by a containment time τ (point model); energy and particle containment times for all species are assumed equal. The equations are averaged over $\psi(\rho,z)$ with specified density and temperature profiles, such that $\sum_j n_j(\psi)T_j(\psi) = p(\psi)$, the pressure for the MHD equilibrium.

The fuel is a deuterium-tritium mixture, treated as a single ion species. Spatial absorption profiles for beam fueling and heating are ignored, as well as spatial variation of alpha particle energy deposition. Impurity and thermal alpha particle temperatures are equated to the fuel ion temperature. Suprathermal (non-Maxwellian) fusion probability for beam injection is determined. Alpha particle thermalization time and energy transfer to ions and electrons is calculated from standard slowing-down theory. A fixed fraction (7%) of the alphas are assumed to be born on unconfined orbits.

An unlimited number of impurity species may be handled. Electron density

is determined by assuming quasineutrality. Cyclotron radiation is calculated as suggested by Rose [12], and bremsstrahlung, line, and recombination radiation are computed with a modification of Hopkins' model [5].

3. Input/Output Options

3.1 MODSYS options

3.1.1 Independent versus dependent variables

A conventional mode of data processing results in a reactor design determined by the following thirteen independent variables: A, κ, d, α, q, β_t, Z_{eff}, $\bar{T}_e$, α_n, Δ_v, R, B, and $\Delta(=\Delta_B + \Delta_S)$. Numerous other inputs must be specified, but in practice they are fixed at constant values and rarely considered variables for reactor surveys. The first six variables in this list uniquely describe an ideal MHD equilibrium and determine the important pressure distribution inside the torus. In the event the diamagnetic function $F(\psi) = \rho B_t$ is not known *a priori*, the plasma code must be given a function F, described by profile parameters γ and α_J, and q, β_t will be calculated. The input Z_{eff} is in fact a function of a multitude of independent variables (the densities and charge states of all plasma species), but it is convenient to consider this as one independent variable. The quantities Z_{eff}, $\bar{T}_e$, α_n, and the pressure distribution (from the MHD calculation) are sufficient (except for an insignificant dependence on magnetic field) to determine $\bar{T}_i$, $\overline{\langle\sigma v\rangle}$, etc. from a power balance calculation. At this point specification of the last four independent variables allows a detailed calculation of the reactor's plasma characteristics. Two of the most important dependent variables are

$$\begin{cases} P = \text{reactor thermonuclear power} \\ W = \text{reactor neutron wall loading.} \end{cases}$$

In addition, plasma current, alpha flux, $\bar{n}_i\tau$ required for ignition, fractional burn, and many other dependent variables are calculated. This conventional procedure of data handling is identified by assigning the value one to the index named MODSYS.

The plasma calculation also allows more flexible data handling, viz.: either (or both) P or W may be specified as an independent variable with options for calculating any one (or two) of R, B, or Δ as a dependent variable. The specific options are identified by MODSYS numbers and are cataloged below for reference. To illustrate the calculational logic consider the MODSYS = 2 option. In this mode the reactor major radius R, blanket/shield thickness Δ, and thermal power P are specified and the magnetic field B is to be determined. In practice, the code takes R, Δ, and a reference magnetic field $\tilde{B}$ and first calculates an associated reference thermal power $\tilde{P}$. Since $\tilde{P} \propto \tilde{B}^4$ and $P \propto B^4$, the program makes the simple determination

$$B = \tilde{B}[P/\tilde{P}]^{\frac{1}{4}} .$$

All the options are based on this type of scaling from reference calculations.

3.1.2 *Sequence of data processing*

A brief description of the data handling follows; we refer to the flow chart in Fig. 22. The first step feeds the independent variables into the plasma driver where, depending on the mode of calculation, a reference value is assigned to the dependent variable (see example below). The MHD library is searched (or a new solution to the Grad-Shafranov equation is calculated if necessary) for the appropriate equilibrium. The MHD calculation is relatively time-consuming so library storage represents a considerable savings. The library equilibria are stored for R = 6.3 m and F_0 = 25 T-m, and the reference values of the MHD quantitites (i.e., the metric $\tilde{V}'$, plasma current $\tilde{I}_p$, etc.)

are set in the SCALE MHD subroutine from the reference values $\tilde{R}$ and $\tilde{F}_0$ via simple algebraic scaling. Next the radial temperature and density distribution are set up in PROFIL and the ion temperature and density, $\bar{n}_i\tau$, etc., are solved in EQULIB from the power balance. The results of the power balance are independent of R, B, and Δ except for the cyclotron radiation term, but in regimes of interest for reactors other radiation losses dominate this term by orders of magnitude. Consequently EQULIB is only called once from the plasma driver even though R, B, or Δ may be changed from reference values to the final target values in the course of the data handling. Now the DESIGN subroutine calculates the reference power and wall loading, $\tilde{P}$ and $\tilde{W}$, from the reference variables, and these are returned to the plasma driver where the proper (target) value of R, B, or Δ, depending on the mode of operation, is calculated from the target P or W. Finally, SCALE MHD and DESIGN are called a second time with all the desired reactor parameters (R, B, and Δ), and all the other dependent quantities (e.g., fast alpha flux, thermal alpha flux, bremsstrahlung power density, plasma current, etc.) are self-consistently calculated.

3.1.3 Data processing example: MODSYS = 2

For this example, A, κ, d, α, β_t, q, α_n, $\bar{T}_e$, Z_{eff}, and Δ_v are given values which will remain unchanged. In addition, R = 8 m, Δ = 0.75 m, and P = 10,500 MW. The object is to determine the required B. Initially, the plasma driver selects a reference $\tilde{B}$ = 8 T. Then the MHD library is searched for the equilibrium corresponding to the given A, κ, d, α, q, and β_t, and the metric $\tilde{V}'$ as well as other quantities, all previously calculated for $\tilde{\tilde{R}}$ = 6.3 m and $\tilde{\tilde{F}}_0$ = 25 T-m, are read from the library. SCALE MHD adjusts the metric to $\tilde{V}'$ corresponding to R = 8 and $\tilde{B}$ = 8. Next the power balance is established for α_n, $\bar{T}_e$, Z_{eff}, $\tilde{V}'$, R, and $\tilde{B}$, yielding $\bar{T}_i$, $\bar{n}_i\tau$, etc. The DESIGN routine then finds the reference power $\tilde{P}$ = 4300 corresponding to $\tilde{B}$ = 8. Using the relation

$B = \tilde{B}(P/\tilde{P})^{1/4}$, the driver computes the target value B = 10 T corresponding to the stipulated P = 10,500 MW. Finally, V′ and the other MHD parameters are found by SCALE MHD for R = 8, B = 10, and DESIGN computes W and the other reactor parameters in a consistent manner.

3.1.4 MODSYS option catalog

The nine MODSYS options are presented in Table 3. For all options, ten independent variables must first be specified: A, κ, d, α; (q, β_t) or (γ, α_J); Z_{eff}, $\bar{T}_e$, α_n; Δ_v. In developing these options the following equations were utilized:

$$P = B^4\left[1 - A^{-1} - \left(\Delta + \Delta_v\right)/R\right]^4 R^3A^{-2}f ,$$

$$W = \frac{P}{R\left(R + A\Delta_v\right)} g ,$$

where neither f nor g is a function of R, B, or Δ. Modes 2, 4, 5, and 7 require only a simple expression to be evaluated in the scaling to the target B or Δ; modes 3 and 6 require the solution to a quartic equation in R for the scaling, and modes 8 and 9 naturally require the solution of two simultaneous equations.

3.2 MODE options

If the index MODE is set equal to one the amount of beam injection must be specified as an input, and $\bar{n}_i\tau$ required for a steady-state solution is determined. For example, if MODE = 1 and one sets ξ = 0 (no beam heating) the output is the $\bar{n}_i\tau$ required for ignition. When MODE equals two, the input variable is $\bar{n}_i\tau$ and the beam heating required to maintain fusion is computed.

4. Plasma Subroutine Equations

For clarity, in this section alone, we denote the D-T fuel species with the

the subscript DT rather than i.

4.1 Global model

4.1.1 Balance equations

Particle and power balance equations which have been averaged over given spatial profiles are used to represent the plasma during the burn phase.

D-T Ions

$$0 = \frac{d\bar{n}_{DT}}{dt} = \overline{I_B(1 - 2f)} - \overline{2p(1 - p)n_{DT}^2\langle\sigma v\rangle_f} + \bar{I}_c - \frac{\bar{n}_{DT}\left(1 - f_{DT}\right)}{\tau} \qquad \text{(A-1)}$$

$$0 = \frac{3}{2}\frac{d}{dt}\overline{n_{DT}T_{DT}} = \overline{p(1 - p)\langle\sigma v\rangle_f n_{DT}^2\left[U_\alpha f_{\alpha DT} - 3T_{DT}\right]} - \bar{K}_{ie}$$

$$+ \overline{I_B\left[G_B U_B \hat{f}_{BDT} + \frac{3}{2}T_{DT}(1 - 2f)\right]} - \frac{3}{2}\frac{\overline{n_{DT}T_{DT}}}{\tau}, \qquad \text{(A-2)}$$

where

$$K_{ie} = 1.2 \times 10^{-18}\frac{n_e n_{DT} T_{DT}}{T_e^{3/2}}\left(1 - \frac{T_e}{T_{DT}}\right) A_{DT}\sum_j \frac{Z_j^2 r_j}{A_j}. \qquad \text{(A-3)}$$

In these equations I_B is the injected source of energetic deuterons, p is the tritium fraction, f is the suprathermal fusion probability, U_B is the beam energy, G_B is the suprathermal fusion enhancement of the injected beam energy, $\hat{f}_{BDT}$ is the fraction of the beam energy acquired by the D-T ions, $\langle\sigma v\rangle_f$ is the Maxwellian-averaged fusion cross section, I_c is the source of D-T ions, τ is the particle and energy confinement time, n_j and T_j are the particle density and temperature of plasma species j, U_α = 3.52 MeV is the fusion alpha energy, $f_{\alpha DT}$ is the fraction of the fusion alpha energy acquired by the D-T ions, A_j is the atomic mass, Z_j is the atomic number, and r_j is the fractional concentration of

plasma species j. A bar over a quantity denotes a spatial average. The sum is over all ions. All quantities are in mks units except that temperatures and energies are in keV.

The quantity f_{DT} is the effective recycle fraction, including the effect of charge-exchange,

$$f_{DT} \equiv \left(1 - \eta_{DT}\right) R_{DT} \frac{\left(1 - A_{cx}\right)}{\left(1 - R_{DT} A_{cx}\right)} , \tag{A-4}$$

where η_{DT} is the D-T ion removal efficiency, R_{DT} is the wall reflection coefficient (including backscattering and re-emission), and A_{cx} is the charge-exchange albedo for neutral D-T atoms incident upon the plasma. (See Appendix B of Ref. 6 for a discussion of the plasma-wall interaction model.)

If the charge-exchange albedo for neutral D-T atoms used to refuel the plasma (by whatever mechanism) is A_{cx}^{ext}, the actual refueling rate per unit volume which is required to supply the refueling source $\bar{I}_c$ is

$$F_{DT}^{ext} = \bar{I}_c \Bigg/ \left[\left(1 - A_{cx}^{ext}\right) + R_{DT} A_{cx}^{ext} \frac{\left(1 - A_{cx}\right)}{\left(1 - R_{DT} A_{cx}\right)} \right] . \tag{A-5}$$

The wall flux of D-T particles (ions + neutrals) is

$$F_{wall}^{DT} = \frac{F_{DT}^{ext} A_{cx}^{ext}}{1 - R_{DT} A_{cx}} + \frac{\eta_{DT}}{\tau} \left(1 - \eta_{DT}\right) \left(\frac{1}{1 - R_{DT} A_{cx}} \right) . \tag{A-6}$$

<u>Alpha Particles</u>

$$0 = \frac{d\bar{n}_\alpha}{dt} = \overline{p(1 - p)\langle \sigma v \rangle_f n_{DT}^2} + \overline{f I_B} - \frac{\bar{n}_\alpha \left(1 - f_\alpha\right)}{\tau} , \tag{A-7}$$

where

$$f_\alpha \equiv \left(1 - \eta_\alpha\right) R_\alpha \ . \tag{A-8}$$

The wall flux of alpha particles is

$$F^\alpha_{wall} = \frac{\bar{n}_\alpha}{\tau}\left(1 - \eta_\alpha\right) \ . \tag{A-9}$$

Impurities

$$0 = \frac{d\bar{n}_I}{dt} = \left[\overline{p(1 - p)\langle\sigma v\rangle_f n^2_{DT}} + \overline{fI_B}\right] S_n + F^{DT}_{wall} S_{DT} + F^\alpha_{wall} S_\alpha$$

$$+ F^I_{wall} S_I - \frac{\bar{n}_I\left(1 - f_I\right)}{\tau} \ , \tag{A-10}$$

where the S's are the sputtering coefficients, f_I is defined as in Eq. (A-8) with $\alpha \to I$, and F^I_{wall} is defined as in Eq. (A-9) with $\alpha \to I$.

Electrons

$$\bar{n}_e = \bar{n}_{DT} + 2\bar{n}_\alpha + \sum_I \overline{Z_I n_I} \ , \tag{A-11}$$

$$0 = \frac{3}{2}\frac{d}{dt}\overline{n_e T_e} = \overline{p(1 - p)\langle\sigma v\rangle_f n^2_{DT} U_\alpha f_{\alpha e}} + \overline{G_B I_B U_B \hat{f}_{Be}} + \eta \bar{J}^2$$

$$+ \bar{K}_{ie} - \bar{W}_R - \frac{3}{2}\frac{\overline{n_e T_e}}{\tau} \ , \tag{A-12}$$

where

$$\eta = \frac{2.8 \times 10^{-8}\ \bar{Z}_{eff}}{\bar{T}_e^{3/2}} \tag{A-13}$$

is the resistivity, $\bar{J}$ is the average plasma current density, and W_R is the radiative power (see Appendix B of Ref. 6). The sum in Eq. (A-11) is over

impurities, I. $W_R = P_{rad} + P_c$, where P_{rad} accounts for bremsstrahlung, line, and recombination radiation, as defined in Appendix B of Ref. 6, and P_c accounts for cyclotron radiation

$$P_c = \frac{3.7 \times 10^3 \; n_e B_0^{5/2} \left(T_e^{11/4} + 0.0049 \; T_e^{15/4} \right)}{\sqrt{n_{DT}}} .$$

The density profiles for all plasma species are taken to be the same and all temperature profiles are taken to be the same; the beam deposition profile is taken to be flat ($\alpha = 0$). In the balance equations and in expressions for the various powers, wall loadings, etc., the various reaction rates are calculated as a function of ψ, then averaged. An exception is that the transport loss terms are calculated in terms of averaged values, $\bar{n}_{DT}$, $\bar{T}_{DT}$, etc.

Thermalization of injected deuterons and of the fusion alpha particles is computed as a function of ψ from a model of a test particle slowing down in a multicomponent plasma. From this calculation the distribution of fast ion energy among the plasma components and the suprathermal fusion rate are determined. The thermalization model is described in Appendix A of Ref. 13.

4.1.2 Transport model

The expressions used for τ are consistent with Ref. 14, and are written here for the confinement parameter $\bar{n}_{DT}\tau$.

Pseudoclassical

$$\bar{n}_{DT}\tau^{PC} = \frac{1.8 \times 10^8 \; I_p^2 \bar{T}_e^{1/2}}{\bar{Z}_{eff}} . \qquad \text{(A-14)}$$

Trapped Electron Mode

$$n_{DT}\tau^{TEM} = \frac{6.35 \times 10^6 \; \tilde{A}^{3/2}}{\bar{Z}_{eff}} \bar{T}_e^{1/2} I_p^2 \left[1 + \left(\nu_{ei}/\omega_0 \right)^2 \right] . \qquad \text{(A-15)}$$

This is a combination, of the form given by Ref. 15, which approaches the asymptotic limits given in Ref. 14 for TEM-1 and TEM-2.

Trapped Ion Mode

$$\bar{n}_{DT}\tau^{TIM} = \frac{2.05 \times 10^{-5}\beta_{pe}^{2} I_p^4 \bar{Z}_{eff} B_0^2 \tilde{A}^{5/2}}{\bar{T}_e^{11/2}} \left[1 + \left(\frac{\bar{T}_e}{\bar{T}_{DT}}\right)\right]^2 . \tag{A-16}$$

Empirical Scaling

$$\bar{n}_{DT}\tau^{EMP} = 4 \times 10^{-21}\bar{n}_{DT}\bar{n}_e q^{1/2}\tilde{a}^2 . \tag{A-17}$$

I_p is the plasma current, $\bar{T}_{DT}$ and $\bar{T}_e$ are the average ion and electron temperatures, $\tilde{A} = R/\tilde{a}$ is the average aspect ratio, R is the major radius, $\tilde{a}$ is the average radius of the cross section,

$$Z_{eff} = \sum_{ions} n_j Z_j^2 \Big/ \sum_{ions} n_j Z_j$$

is the effective charge,

$$\nu_{ei} = \frac{1.6 \times 10^{-15}\bar{Z}_{eff}\bar{n}_{DT}}{\bar{T}_e^{3/2}}$$

is the electron-ion collision frequency,

$$\nu_{eff} = \frac{3}{2}\tilde{A}\,\nu_{ei}$$

is the effective collision frequency,

$$\omega_0 = \frac{0.19\,\bar{T}_e^{1/2} I_p}{\tilde{A}^{1/2} B_0 \tilde{a}^2}$$

is the frequency where TEM peaks, and B_0 is the toroidal magnetic field at the center of the chamber.

4.2 MHD equilibrium model

The axisymmetric, ideal MHD equilibrium model used in this report is essentially that of Callen and Dory [3]. The equations used are the ideal MHD equilibrium equation

$$\nabla p = \vec{J} \times \vec{B}$$

and the Maxwell equations

$$\nabla \cdot \vec{B} = 0$$

$$\nabla \times \vec{B} = \mu \vec{J} .$$

For azimuthal symmetry [$(\partial/\partial\phi) = 1$], the magnetic field can be written

$$\vec{B} = \vec{B}_t + \vec{B}_p = B_t \hat{\phi} + \frac{\hat{\phi}}{2\pi\rho} \times \nabla\psi ,$$

where $\psi = 2\pi\rho A_\phi$ is the flux function, and $\vec{A}$ is the vector potential. It can be shown that the poloidal field lines are tangent to the surfaces ψ = constant. The pressure, p, and the quantity $F \equiv \rho B_t$ must be constant on the flux surfaces,

$$p = p(\psi)$$

$$F = F(\psi) ,$$

and the current flows in the flux surfaces. The components of the current density are:

$$J_p = -\frac{2\pi B_p}{\mu} \frac{dF}{d\psi}$$

$$J_t = -\frac{2\pi F}{\mu\rho} \frac{dF}{d\psi} - 2\pi\rho \frac{dp}{d\psi} .$$

The equilibrium equation for the flux function is:

$$\frac{\partial^2\psi}{\partial\rho^2} - \frac{1}{\rho}\frac{\partial\psi}{\partial\rho} + \frac{\partial^2\psi}{\partial z^2} = -4\pi^2\left[\mu\rho^2\frac{dp}{d\psi} + F\frac{dF}{d\psi}\right] . \tag{A-18}$$

This equation is solved by specifying $p(\psi)$ and $F(\psi)$, then solving for $\psi(\rho,z)$. The parameterization of p and F used in this report is:

$$p = p_0\hat{\psi}^{\alpha}$$

$$F^2 = F_0^2\left(1 - \delta\hat{\psi}^{\gamma}\right) ,$$

where

$$\hat{\psi} = \frac{\psi_\ell - \psi}{\psi_\ell - \psi_m} ,$$

where ψ_ℓ and ψ_m are the values of ψ at the limiter and magnetic axis, respectively

The definitions of the plasma current, I_p, the safety factor q [16], and the pressure ratios, β_p and β_t are given in terms of integrals around a poloidal flux line defined by a value, ψ, of the flux function:

$$\mu I_{enc}(\psi) = \oint_\psi B_p \, d\ell$$

$$\mu I_p = \oint_{\psi_\ell} B_p \, d\ell$$

$$q(\psi) = \frac{F(\psi)}{2\pi}\oint_\psi \frac{d\ell}{\rho^2 B_p}$$

$$\beta_p = \frac{2\mu\bar{p}}{\left\langle B_p^2\right\rangle_{\psi_\ell}}$$

$$\beta_t = \frac{2\mu\bar{p}}{B_0^2} , \tag{A-19}$$

where $\bar{p}$ is the average pressure over the plasma cross section, the flux line average is defined as:

$$\langle x \rangle = \oint_\psi x \, d\ell \Big/ \oint_\psi d\ell ,$$

and B_0 is the vacuum toroidal field at the center of the chamber. It should be noted that other definitions of β_p are in use.

It can be seen that if ψ is a solution of Eq. (A-18), then $\psi \to \psi' = \lambda\psi$ is a solution provided:

$$\vec{B}_p \to \vec{B}_p = \lambda \vec{B}_p$$

$$I \to I' = \lambda I$$

$$p \to p' = \lambda^2 p$$

$$F_0 \to F_0' , \quad \text{arbitrary}$$

$$F^2 \to F'^2 = F_0'^2 + \lambda^2 \int_{\psi_\ell}^{\psi} F'^2 \, d\psi$$

$$\beta_p \to \beta_p' = \beta_p$$

$$\frac{\beta_t}{F_0} \to \frac{\beta_t'}{F_0'} = \frac{\lambda^2 \beta_t}{F_0'}$$

$$\frac{q}{F_0} \to \frac{q'}{F_0'} = \frac{q}{\lambda F_0'} .$$

Since p and F are known only as a function of ψ, but $\psi(\rho,z)$ is not known, one cannot specify a quantity such as I_p or q *a priori*. Once a solution is known, however, it can be scaled to give the required value (provided F^2 stays non-negative). All of the solutions that vary only by scaling have the same magnetic axis, and if one does not have reversed toroidal currents, then none do.

Equation (A-18) is solved with the fixed boundary method in which the flux line at the outer perimeter of the plasma is specified in space. The solution is scaled to give, for example, the desired current or $q(\psi_m) = 1$, and the other quantities are determined for given α, γ, and δ. The vector potential (and hence the flux function) due to the plasma loop alone is then calculated explicitly. The part of the flux function not supplied by the plasma loop must be supplied by the external coils. The fixed boundary method gives the required external field for any equilibrium and has exactly the plasma cross section desired.

4.3 Global model parameters

4.3.1 Plasma pressure

In computing the plasma pressure, or equivalently β_t, not only the pressure of the thermalized particles but the fast alpha particles and deuterons from the beam which are in the process of thermalizing are included.

$$\beta_t = \frac{\overline{n_{DT}T_{DT}} + \overline{n_e T_e} + \overline{n_\alpha T_{DT}} + \sum \overline{n_I T_{DT}} + \frac{2}{3}\overline{n_\alpha^f E_\alpha} + \frac{2}{3}\overline{n_B^f E_B}}{B_0^2/2\mu}, \qquad \text{(A-20)}$$

where the sum in the numerator is over impurities, E_α and E_B are the mean energies of the thermalizing alpha particles and deuterons, respectively, and n_α^f and n_B^f are the corresponding densities of such particles at any given instant. These latter quantities are computed from the general consideration that the number of particles in the process of thermalizing at any time is equal to the source rate times the thermalization time. The formulas are

$$n_\alpha^f = \overline{\left[p(1-p)\langle\sigma v\rangle_f n_{DT}^2 + fI_B\right]\tau_\alpha^{SD}},$$

and

$$n_B^f = \overline{I_B \tau_B^{SD}} ,$$

where τ^{SD} is the thermalization time defined in Appendix A of Ref. 13.

For the static global calculations, the value of β_t is determined from Eq. (A-19) for a given MHD equilibrium state, then Eq. (A-20) determines the upper limit on $\bar{n}_{DT}$, hence the maximum power.

4.3.2 Reactor performance parameters

The neutron power flux through the first wall is

$$W(MW/m^2) = 2.26 \times 10^{-18} J_w(n/m^2/s) ,$$

where

$$J_w = \left| \overline{p(1-p)\langle\sigma v\rangle_f n_{DT}^2} + \overline{fI_B} \right| \frac{V}{A_w} ,$$

is the 14-MeV neutron current density at the first wall, A_w is the surface area of the first wall, and V is the plasma volume. The total power output is

$$P(MW) = 1.602 \times 10^{-22} E_{fus} \left[\overline{p(1-p)\langle\sigma v\rangle_f n_{DT}^2} + \overline{fI_B} \right] + \overline{I_B U_B} V + \bar{P}_\Omega ,$$

where

$$E_{fus}(keV) = \left[14.1 \, \varepsilon_{bkt} + 3.52 \right] \times 10^3 ,$$

with ε_{bkt} accounting for the energy enhancement in the blanket, and $\bar{P}_\Omega$ is the ohmic heating power,

$$\bar{P}_\Omega(MW) = 10^{-6} \eta \bar{J}^2 V .$$

The neutron power is

$$P_N = \varepsilon_{bkt} W A_w .$$

The radiation power is

$$P_R(MW) = 1.602 \times 10^{-22} \left(\bar{P}_{rad} + \bar{P}_c \right) V .$$

The power loss by transport processes is

$$P_L(MW) = 1.602 \times 10^{-22} \left[\frac{3}{2} \overline{\frac{n_{DT} T_{DT}}{\tau}} + \frac{3}{2} \overline{\frac{n_\alpha T_{DT}}{\tau}} + \frac{3}{2} \overline{\frac{n_e T_e}{\tau}} \right] V .$$

4.3.3 Additional parameters

There are four additional parameters which are useful in characterizing the performance of the plasma in a tokamak (for that matter, in any reactor). The plasma Q_p is defined as the thermonuclear power generated by the plasma (including the blanket enhancement) divided by the total power put into the plasma from external sources. In a steady-state situation

$$Q_p \equiv \frac{P - \left(P_B + P_\Omega \right)}{P_B + P_\Omega} ,$$

where $P_B = P_{inj} V$ is the beam power injected into the plasma, and $P_{inj} = \bar{I}_B U_B$. The quantity, Q_p, becomes very large for devices approaching ignition and provides a measure of the gain when neutral beam injection is used to maintain the plasma in a subignition condition.

The ratio of the energy density of the injected deuterons to the plasma energy density is

$$\Gamma = \frac{\overline{I_B U_B \tau_B^{SD}}}{\left[\frac{3}{2}\left(\overline{n_{DT}T_{DT}} + \overline{n_e T_e} + \overline{n_\alpha T_{DT}} + \sum \overline{n_I T_{DT}}\right) + \overline{n_\alpha^f E_\alpha} + \overline{n_B^f E_B}\right]},$$

where the sum is over impurities.

The fractional burnup is

$$f_{bu} = \frac{\left[\overline{2\,p(1-p)\langle\sigma v\rangle_f n_{DT}^2} + \overline{fI_B}\right]}{2\left[\overline{p(1-p)\langle\sigma v\rangle_f n_{DT}} + \overline{fI_B}\right] + \left(\bar{n}_{DT}\tau\right)}.$$

The parameter ξ is defined as the ratio of the enhanced beam power to the alpha heating power

$$\xi = \frac{\overline{I_B G_B U_B}}{p(1-p)\langle\sigma v\rangle_f n_{DT}^2 U_\alpha}.$$

The plasma self-inductance is approximated by $L = \mu_0 R[\ln(8A) - 1.75]$.

REFERENCES

[1] ABDOU, M. A., et al., Parametric Systems Analysis for Tokamak Power Plants, Argonne National Laboratory, ANL/FPP/TM-97 (1977).

[2] EVANS, K., JR., High β_t Equilibria in Tokamaks, Argonne National Laboratory Report, to be published.

[3] CALLEN, J. D., DORY, R. A., Phys. Fluids 15 (1972) 1523.

[4] GALVÃO, R. M. O., Nucl. Fusion 15 (1975) 785; DOBROTT, D., HELTON, F. J., Nucl. Fusion 16 (1976) 491; PENG, Y-K. M., DORY, R. A., NELSON, D. B., SAYER, R. O., Magnetohydrodynamic Equilibria and Local Stability of Axisymmetric Tokamak Plasmas, to be published in Phys. Fluids.

[5] HOPKINS, G. R., in Proc. Symp. on Technology of Controlled Thermonuclear Fusion Experiments and the Engineering Aspects of Fusion Reactors, Nov. 20-22, 1972, Austin, Texas, USAEC Rep. CONF-721111 (1974), p. 795.

[6] STACEY, W. M., JR. et al., Tokamak Experimental Power Reactor Conceptual Design, Argonne National Laboratory Report ANL/CTR-76-3 (1976), Vol. II.

[7] BOOK, D. L., Revised and Enlarged Collection of Plasma Physics Formulas and Data, Naval Research Laboratory Memorandum Report 3332.

[8] BERLIZOV, A. B. et al., in Plasma Physics and Controlled Nuclear Fusion Research 1976 (Proc. 6th Int. Conf. Berchtesgaden, 1976) 1, IAEA, Vienna (1977) 3; GROVE, D. et al., in Plasma Physics and Controlled Nuclear Fusion Research (1976) op cit., p. 21.

[9] JENSEN, R. V., POST, D. E., JASSBY, D. L., Critical Impurity Concentrations for Power Multiplication in Beam-Heated Toroidal Fusion Reactors, Princeton Plasma Physics Laboratory Rep. PPPL-1350 (1977).

[10] KESNER, J., CONN, R. W., Nucl. Fusion 16 (1976) 397.

[11] ABDOU, M. A., Radiation Considerations for Superconducting Fusion Magnets, Argonne National Laboratory Report ANL/FPP/TM-92 (1977); to be published in J. Nucl. Materials.

[12] ROSE, D. J., Nucl. Fusion 9 (1969) 183.

[13] STACEY, W. M., JR. et al., Tokamak Experimental Power Reactor Studies, Argonne National Laboratory Report ANL/CTR-75-2 (1975).

[14] DEAN, S. O. et al., Status and Objectives of Tokamak Systems for Fusion Research, USAEC Report WASH-1295 (1974).

[15] KADOMTSEV, B. B., POGUTSE, O. P., Nucl. Fusion 11 (1971) 67.

[16] MOROZOV, A. S., SOLOV'EV, L. S., in Reviews of Plasma Physics, Consultants Bureau, New York (1966) Vol. 2, p. 18.

LIST OF TABLES

No.

I Independent Variables and Their Influence on the Plasma Subsystem

II Benchmark Runs

III MODSYS OPTIONS

TABLE I. INDEPENDENT VARIABLES AND THEIR INFLUENCE ON THE PLASMA SUBSYSTEM

Symbol	Quantity	Data Base		
A	Plasma aspect ratio	MHD		Reactor performance
κ	Plasma elongation	MHD		Reactor performance
d	Plasma triangularity	MHD		Reactor performance
q	Limiter safety factor	MHD		Reactor performance
β_t	Average plasma beta	MHD		Reactor performance
α	Pressure profile	MHD	Power balance	Reactor performance
α_n	Density profile		Power balance	Reactor performance
Z_{eff}	Impurity content		Power balance	Reactor performance
$\bar{T}_e$	Average electron temperature		Power balance	Reactor performance
R	Major radius		Power balance	Reactor performance
B	Maximum toroidal field			Reactor performance
Δ	Inner shield/blanket thickness			Reactor performance

TABLE II. Benchmark Runs

Run	No. 1: Compute MHD	No. 2: MHDLIB (Table Search)	No. 3: Survey $\bar{T}_e$ Effects	No. 4: Survey R vs B
Mode for obtaining MHD data; A = 3.0, κ = 1.3, d = 0.25, α = 1.4, q = 3.0, β_t = 0.08.	Solve Grad-Shafranov equation directly.	Retrieve from MHD library.	Retrieve from MHD library.	Retrieve from MHD library.
Time required (s):	13.0	0.012	0.013	0.35
Particle and power balance; Z_{eff} = 1.7, α_n = 0.3.	$\bar{T}_e$ = 8 keV	$\bar{T}_e$ = 8 keV	$\bar{T}_e$ = 5-15 keV by 0.5 keV.	$\bar{T}_e$ = 8 keV
Total time (s) all designs:	1.6	1.4	34.0	35.0
Design; Δ = 1.0 m	R = 6.65 B = 9	R = 6.65 B = 9	R = 6.65 B = 9	Compute R required for P = 2460 MW with B = 6-16 T by 0.5 T.
Total time (s) all designs:	0.0018	0.0018	0.042	0.042
Description of run	MHD data calculated directly for one reactor design.	MHD library; one reactor design.	MHD library; sweep $\bar{T}_e$ to generate 21 reactor designs.	MHD library; sweep B to generate 21 reactor designs with fixed thermal power (MODSYS = 3)
Total running time (s):	18 CPU 20 WAIT	4 CPU 16 WAIT	37 CPU 18 WAIT	38 CPU 26 WAIT

TABLE III. MODSYS OPTIONS

MODSYS No.	Independent Variables	Dependent Variables
1	R,B,Δ	P,W
2	R,Δ,P	B,W
3	B,Δ,P	R,W
4	R,B,P	Δ,W
5	R,Δ,W	B,P
6	B,Δ,W	R,P
7	R,B,W	Δ,P
8	Δ,P,W	R,B
9	B,P,W	R,Δ

NOTE: R,P,W do not form a set of independent variables and thus do not result in a unique B,Δ solution.

LIST OF FIGURES

No.

1 Plasma current versus β_t and triangularity.

2 Plasma current versus β_t and elongation.

3 Plasma current versus β_t and aspect ratio.

4 Plasma current versus β_t and safety factor.

5 Power density versus density profile width, α_n, for fixed pressure profile width (α = 1.4); curves are independent of impurity concentration (Z_{eff} = 1.3-2.9).

6 Required $\bar{n}_i\tau$ for ignition versus density profile width, α_n, for fixed pressure profile width (α = 1.4) and various temperatures and (iron) impurity concentrations.

7 Power density and ignition $\bar{n}_i\tau$ versus average electron temperature for low and intermediate atomic number impurities resulting in Z_{eff} = 1.7; α = 1.4, α_n = 0.3.

8 Maximum impurity concentration for ignition versus atomic number of dominant impurity; Jensen's model is described in Ref. 8.

9 Power density and ignition $\bar{n}_i\tau$ versus average electron temperature; results are for three values of Z_{eff} at α = 1.4 and three values of α at Z_{eff} = 1.7; α_n = 0.3.

10 Required magnetic field versus major radius for various blanket/shield thicknesses; P = 2500 MW, A = 3.0, κ = 1.3, q = 3.0, β_t = 0.08, α = 1.4.

11 Required magnetic field versus major radius for different pressure profiles; P = 2500 MW, A = 3.0, κ = 1.3, q = 3.0, β_t = 0.08, Δ = 1.0 m.

12 Required magnetic field versus major radius for various aspect ratios and β_t's; P = 2500 MW, κ = 1.3, q = 3.0, α = 1.4, Δ = 1.0 m.

13 Plasma current versus major radius; same parameters as in Fig. 12.

No.

14 Required magnetic field versus major radius for various elongations and β_t's; P = 2500 MW, A = 3.0, q = 3.0, α = 1.4, Δ = 1.0 m.

15 Plasma current versus major radius; same parameters as in Fig. 14.

16 Required magnetic field versus major radius for various safety factors and β_t's; P = 2500 MW, A = 3.0, κ = 1.3, α = 1.4, Δ = 1.0 m.

17 Plasma current versus major radius; same parameters as in Fig. 16.

18 Required magnetic field versus major radius for various thermal power levels; A = 3.0, κ = 1.65, q = 3.0, β_t = 0.08, Δ = 1.0 m.

19 Plasma current versus major radius; same parameters as in Fig. 18.

20 Neutron wall load versus major radius; same parameters as in Fig. 18.

21 Ratio of τ required for ignition to τ predicted by theory versus major radius for empirical (EMP) and trapped ion mode (TIM) scaling; same parameters as in Fig. 18.

22 Flow chart diagramming MODSYS options.

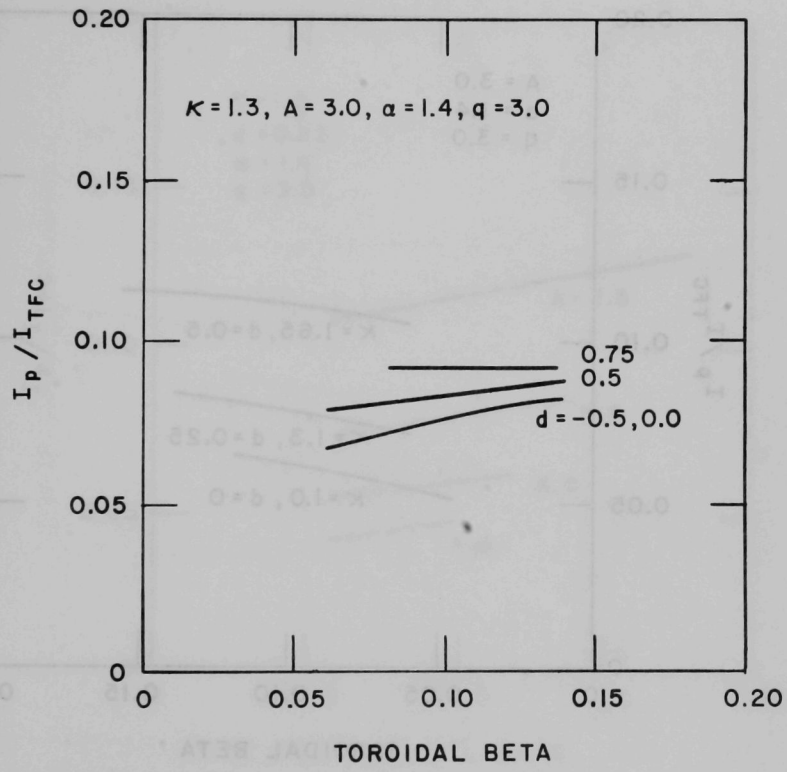

Fig. 1. Plasma current versus β_t and triangularity.

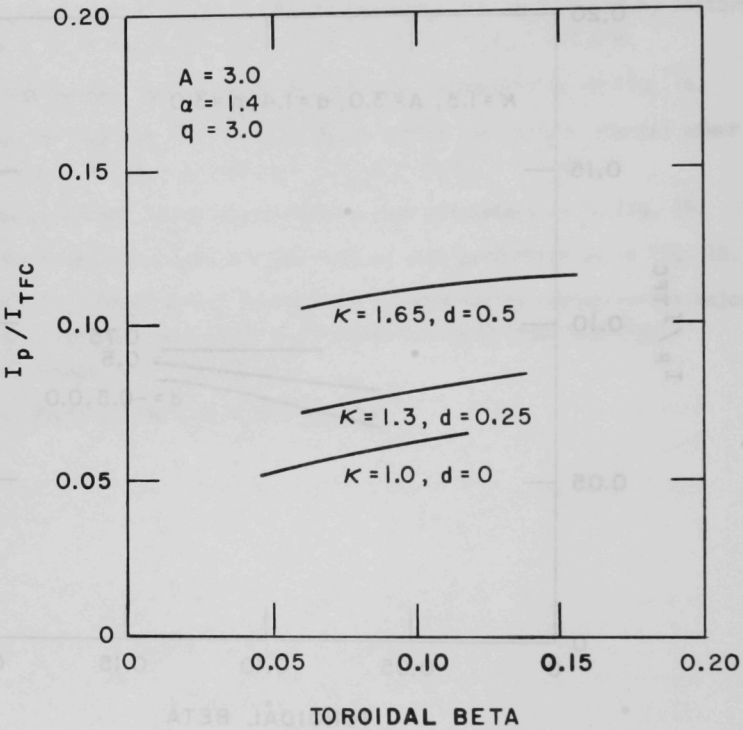

Fig. 2. Plasma current versus β_t and elongation.

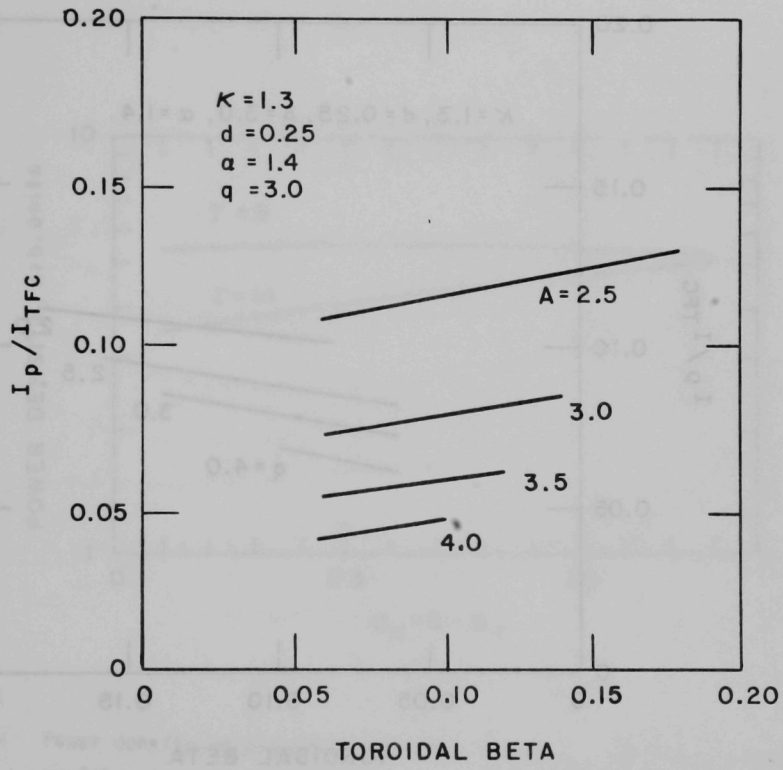

Fig. 3. Plasma current versus β_t and aspect ratio.

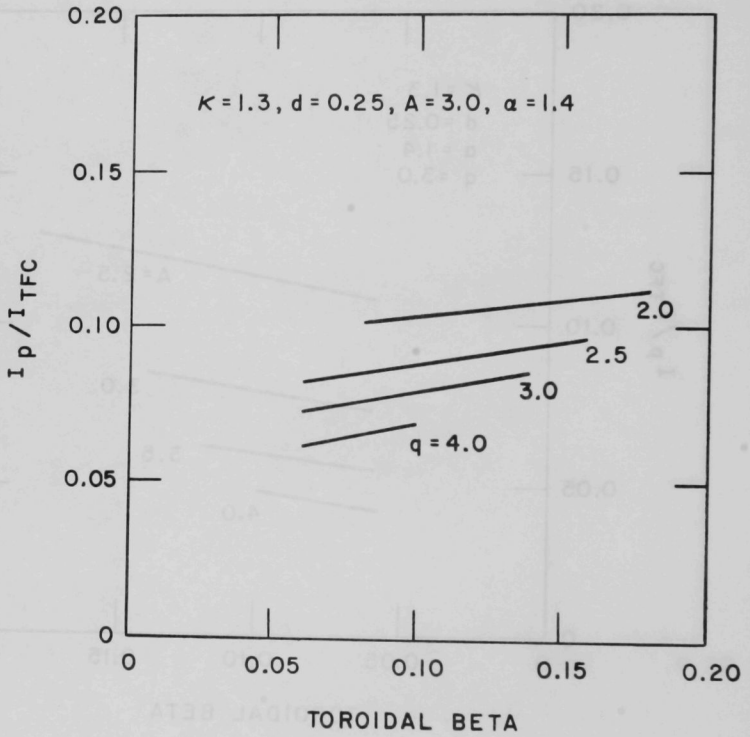

Fig. 4. Plasma current versus β_t and safety factor.

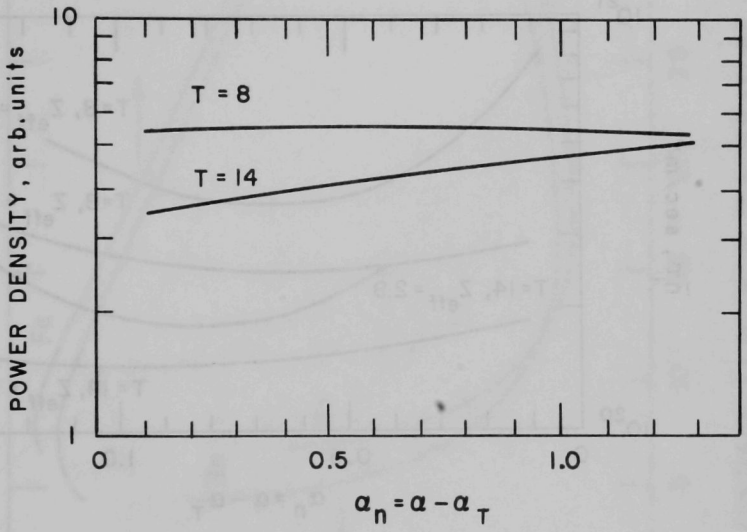

Fig. 5. Power density versus density profile width, α_n, for fixed pressure profile width (α = 1.4); curves are independent of impurity concentration (Z_{eff} = 1.3-2.9).

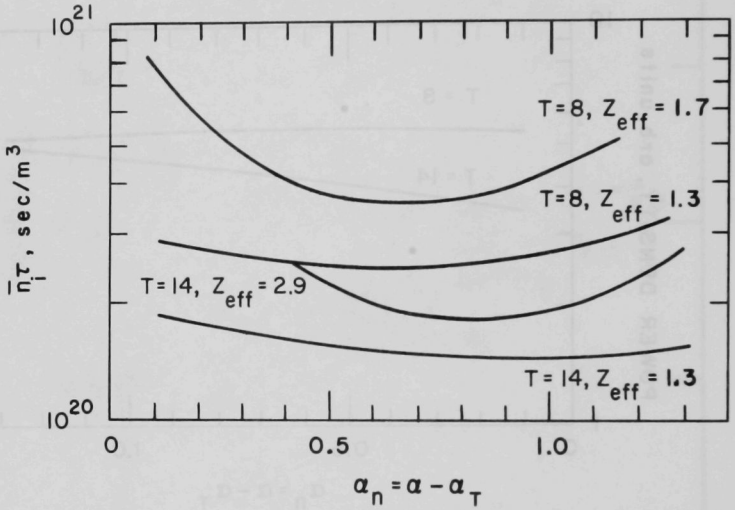

Fig. 6. Required $\bar{n}_i\tau$ for ignition versus density profile width, α_n, for fixed pressure profile width (α = 1.4) and various temperatures and (iron) impurity concentrations.

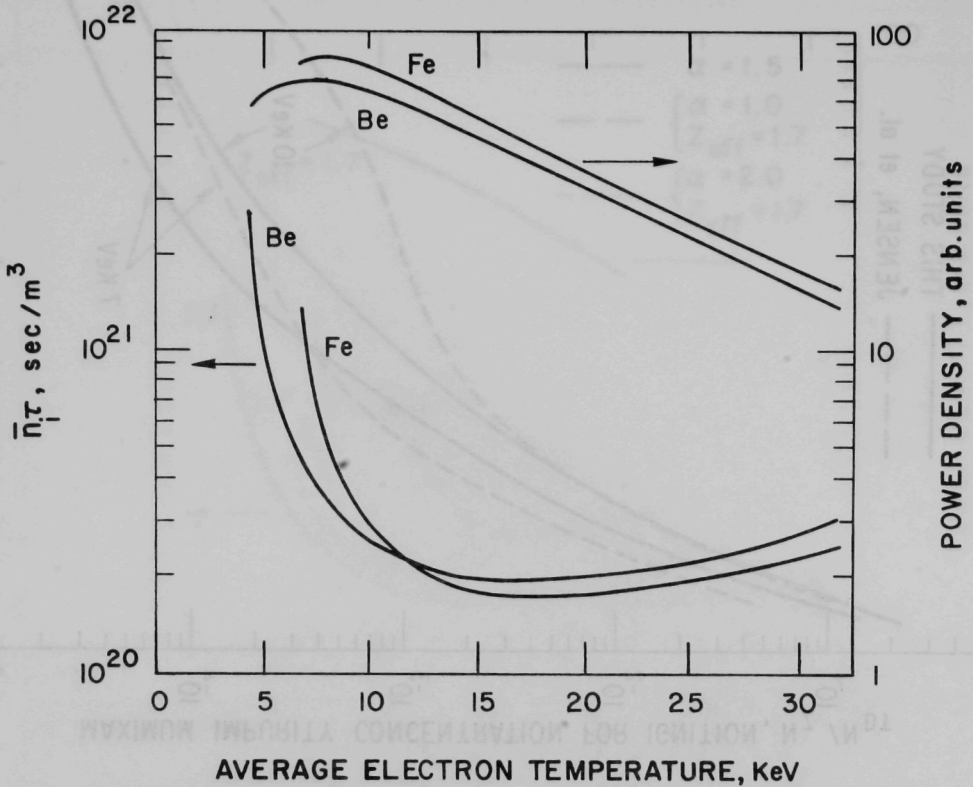

Fig. 7. Power density and ignition $\bar{n}_i\tau$ versus average electron temperature for low and intermediate atomic number impurities resulting in $Z_{eff} = 1.7$; $\alpha = 1.4$, $\alpha_n = 0.3$.

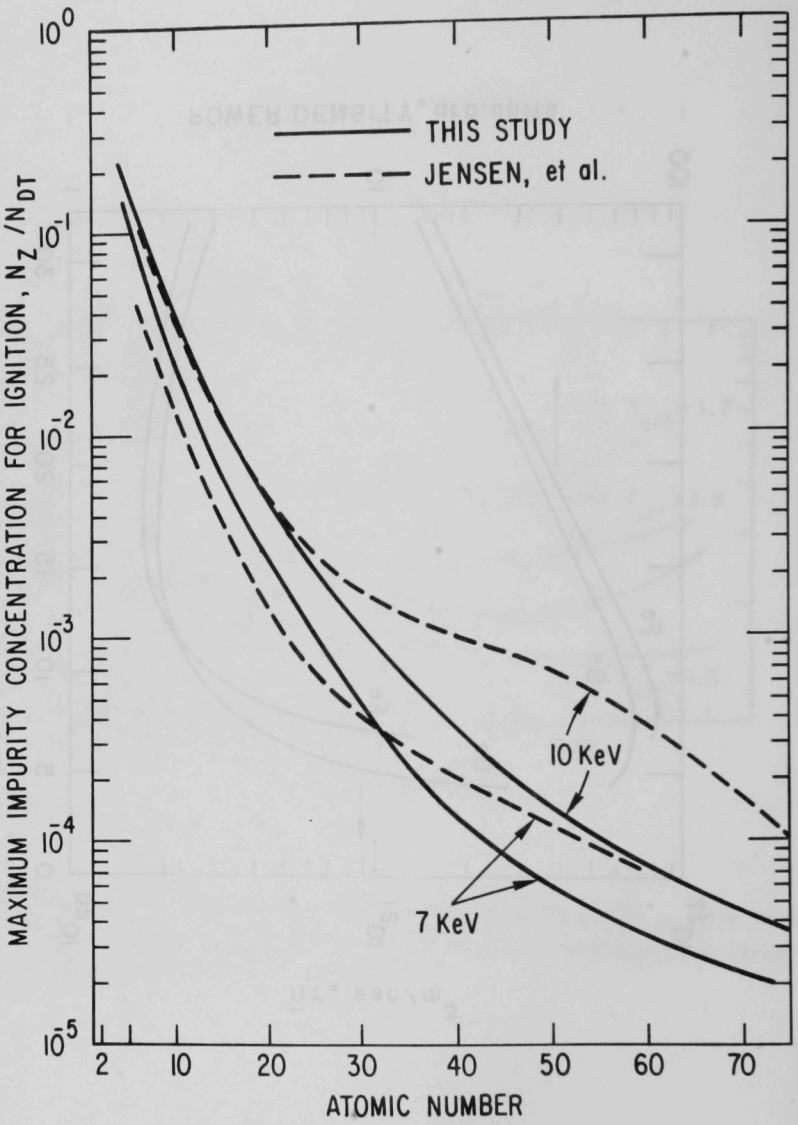

Fig. 8. Maximum impurity concentration for ignition versus atomic number of dominant impurity; Jensen's model is described in Ref. 8.

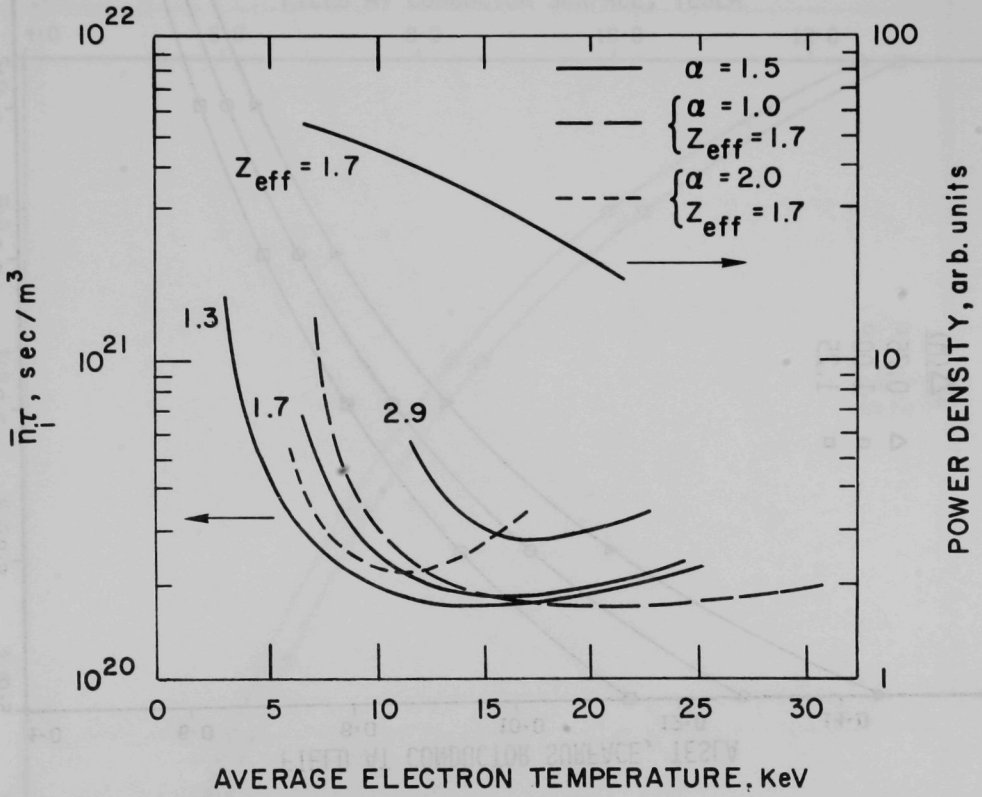

Fig. 9. Power density and ignition $\bar{n}_i\tau$ versus average electron temperature; results are for three values of Z_{eff} at α = 1.4 and three values of α at Z_{eff} = 1.7; α_n = 0.3.

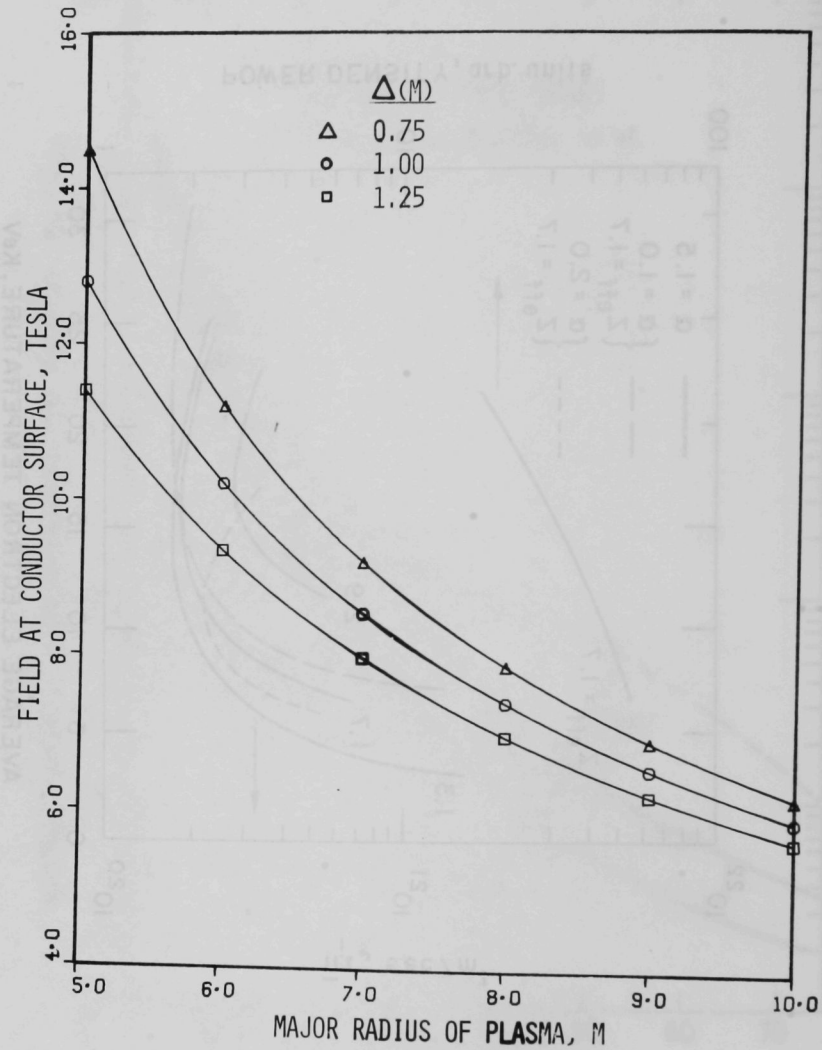

Fig. 10 Required magnetic field versus major radius for various blanket/shield thicknesses; P = 2500 MW, A = 3.0, κ = 1.3, q = 3.0, β_t = 0.08, α = 1.4.

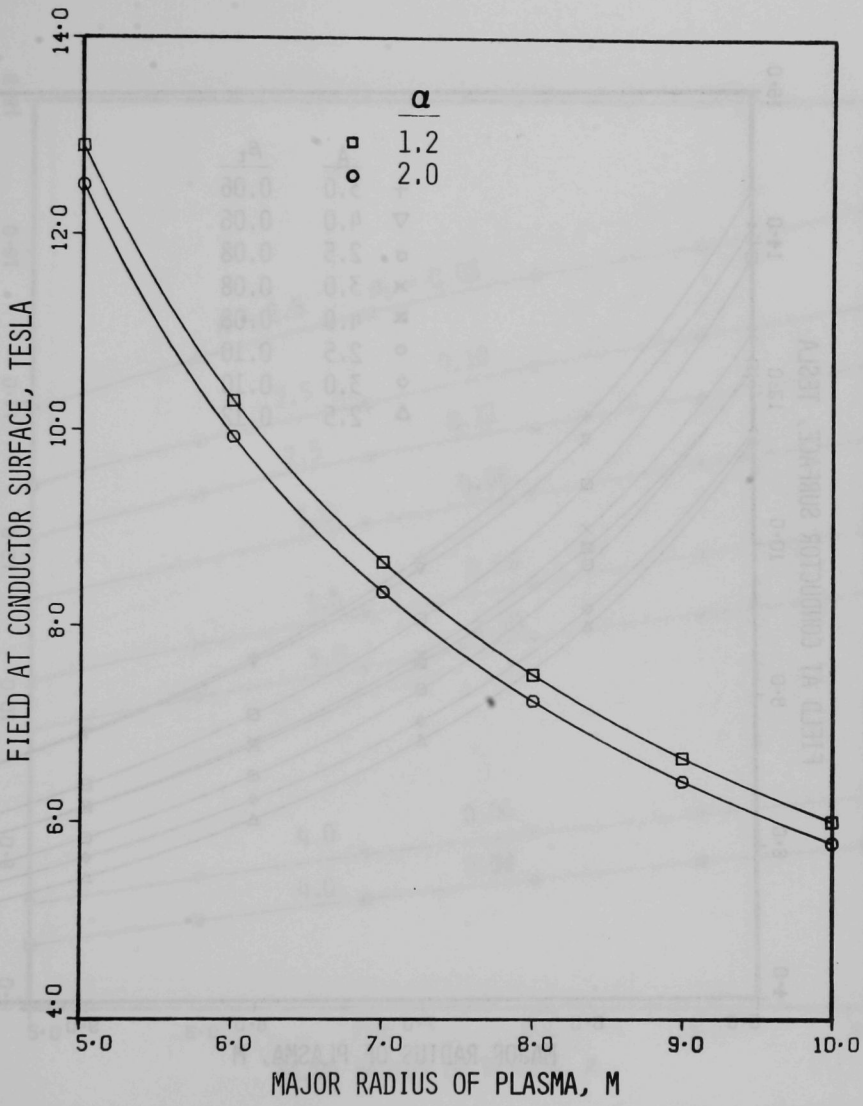

Fig. 11. Required magnetic field versus major radius for different pressure profiles; P = 2500 MW, A = 3.0, κ = 1.3, q = 3.0, β_t = 0.08, Δ = 1.0 m.

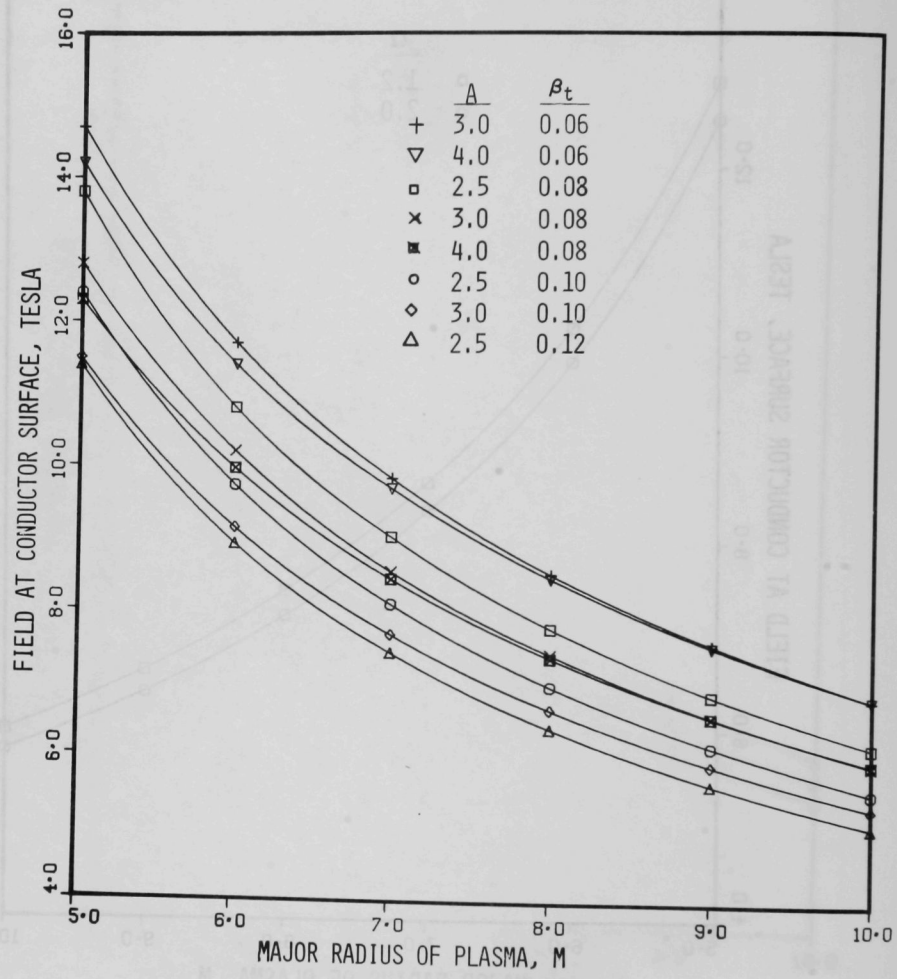

Fig. 12. Required magnetic field versus major radius for various aspect ratios and β_t's; P = 2500 MW, κ = 1.3, q = 3.0, α = 1.4, Δ = 1.0 m.

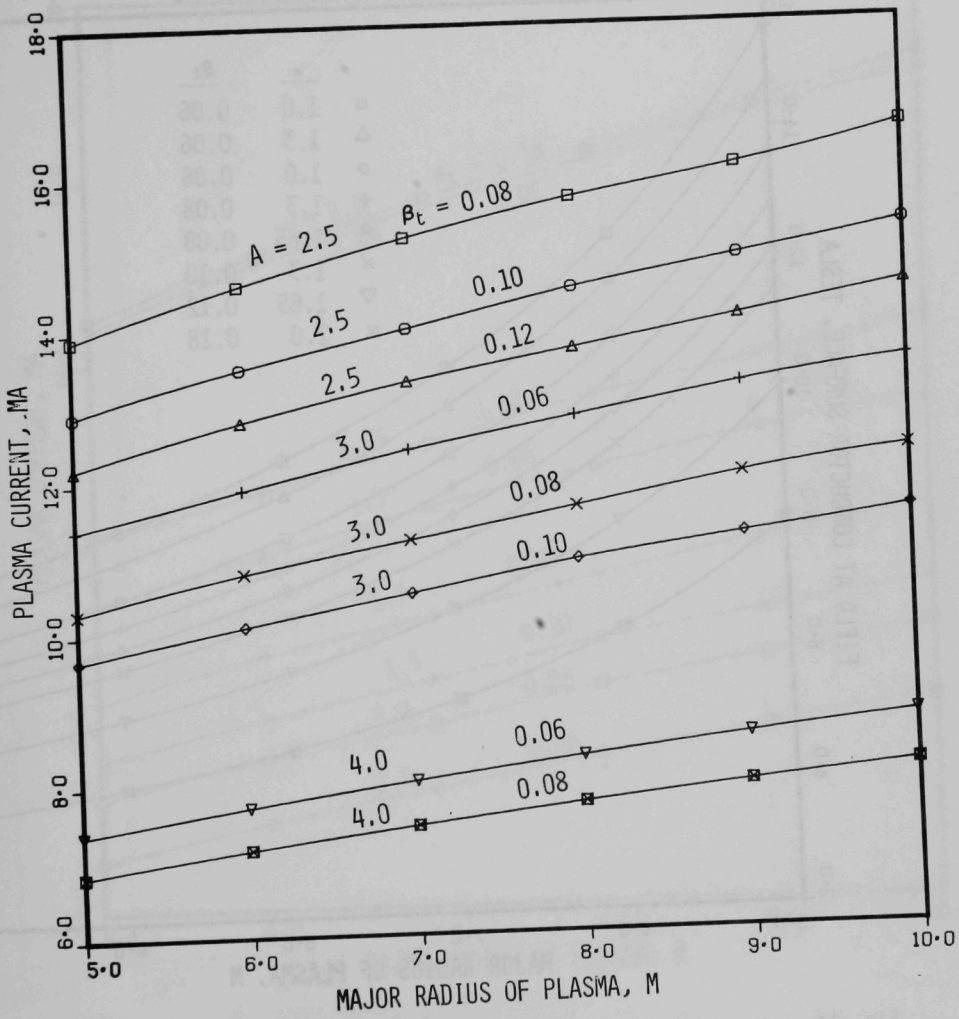

Fig. 13. Plasma current versus major radius; P = 2500 MW, κ = 1.3, q = 3.0, α = 1.4, Δ = 1.0 m.

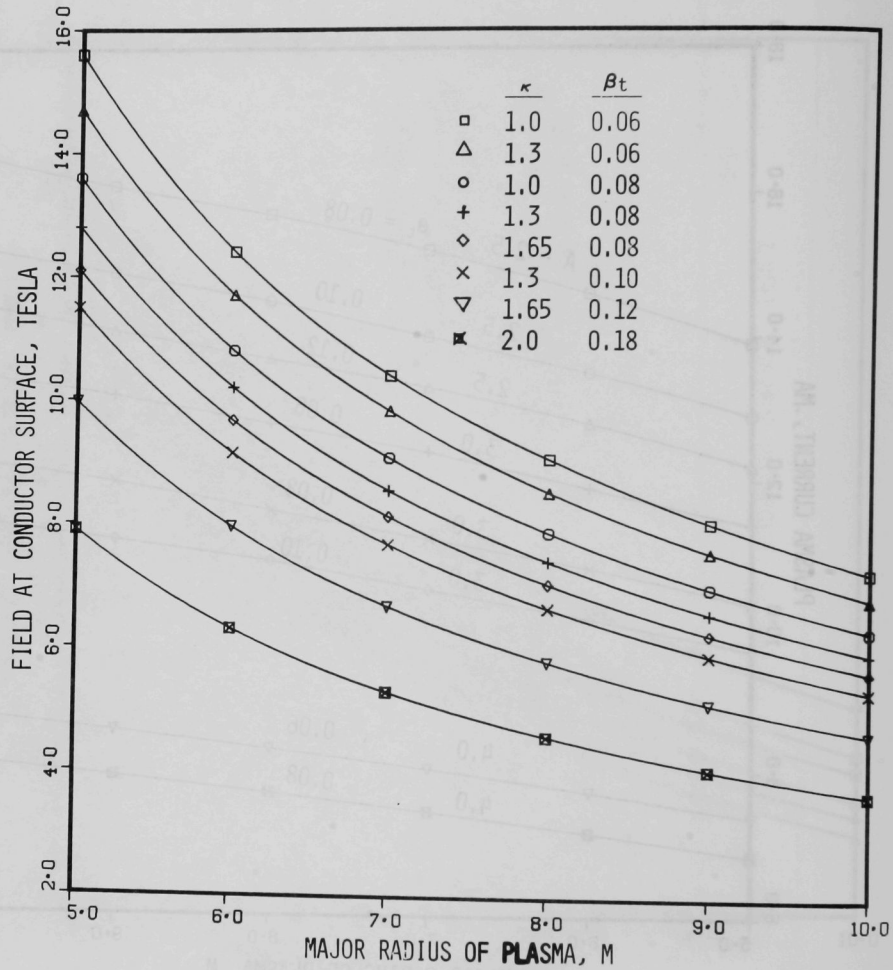

Fig. 14. Required magnetic field versus major radius for various elongations and β_t's; P = 2500 MW, A = 3.0, q = 3.0, α = 1.4, Δ = 1.0 m.

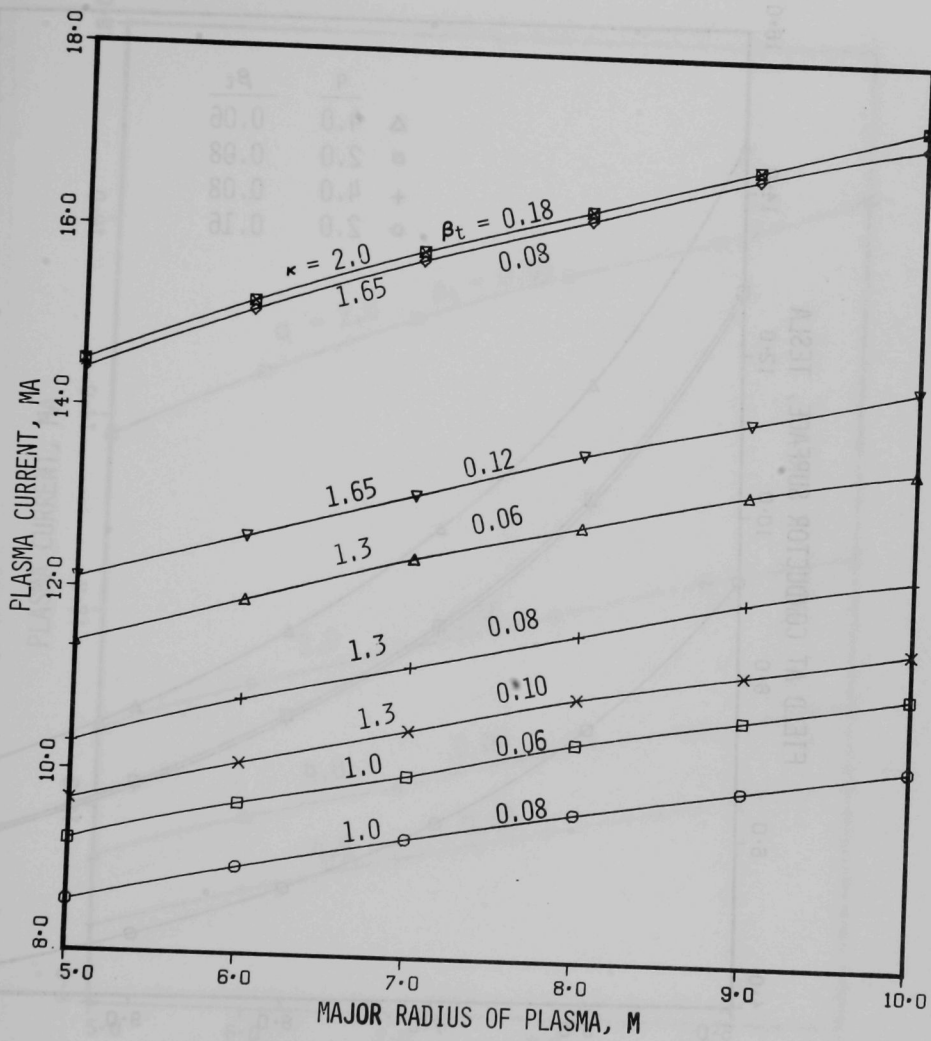

Fig. 15. Plasma current versus major radius; P = 2500 MW, A = 3.0, q = 3.0, α = 1.4, Δ = 1.0 m.

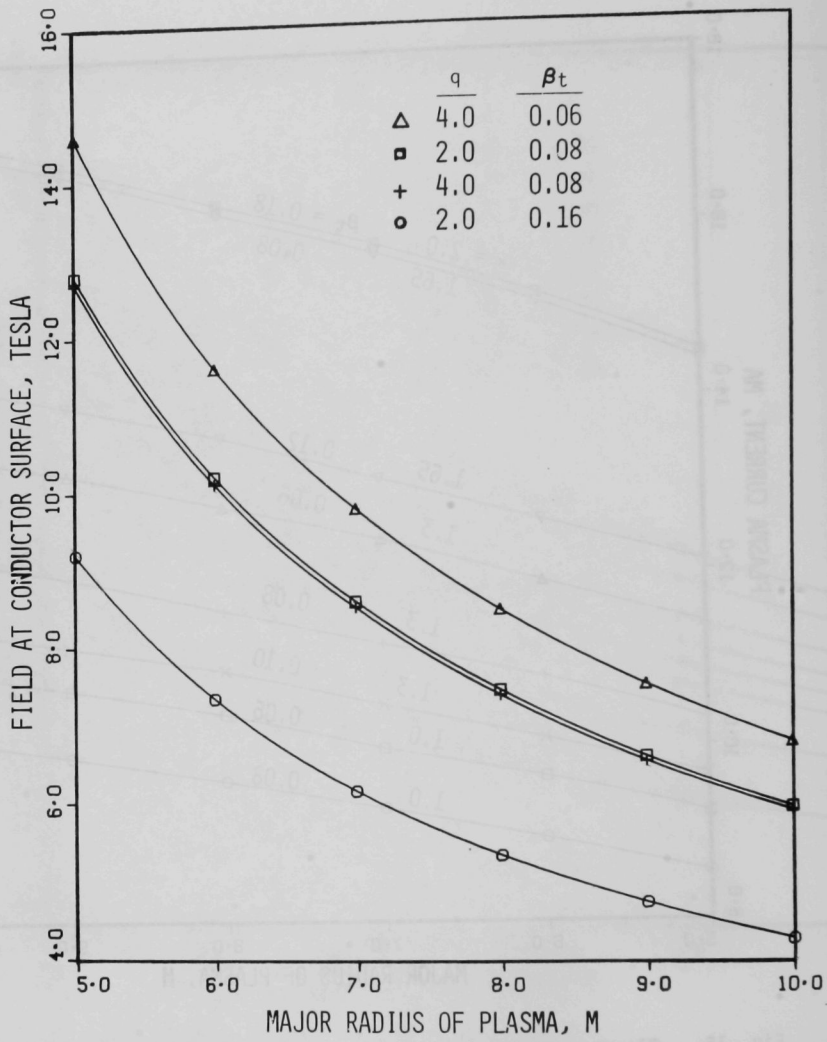

Fig. 16. Required magnetic field versus major radius for various safety facto and β_t's; P = 2500 MW, A = 3.0, κ = 1.3, α = 1.4, Δ = 1.0 m.

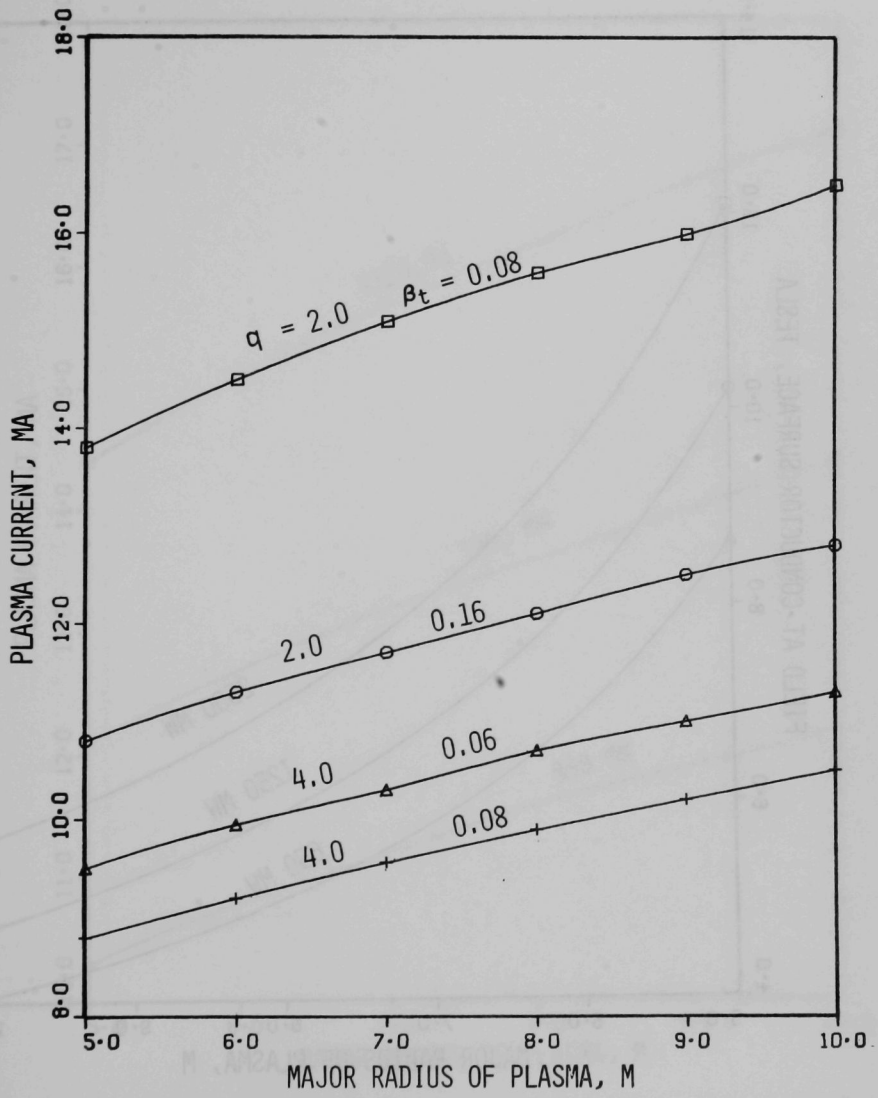

Fig. 17. Plasma current versus major radius; P = 2500 MW, A = 3.0, κ = 1.3, α = 1.4, Δ = 1.0 m.

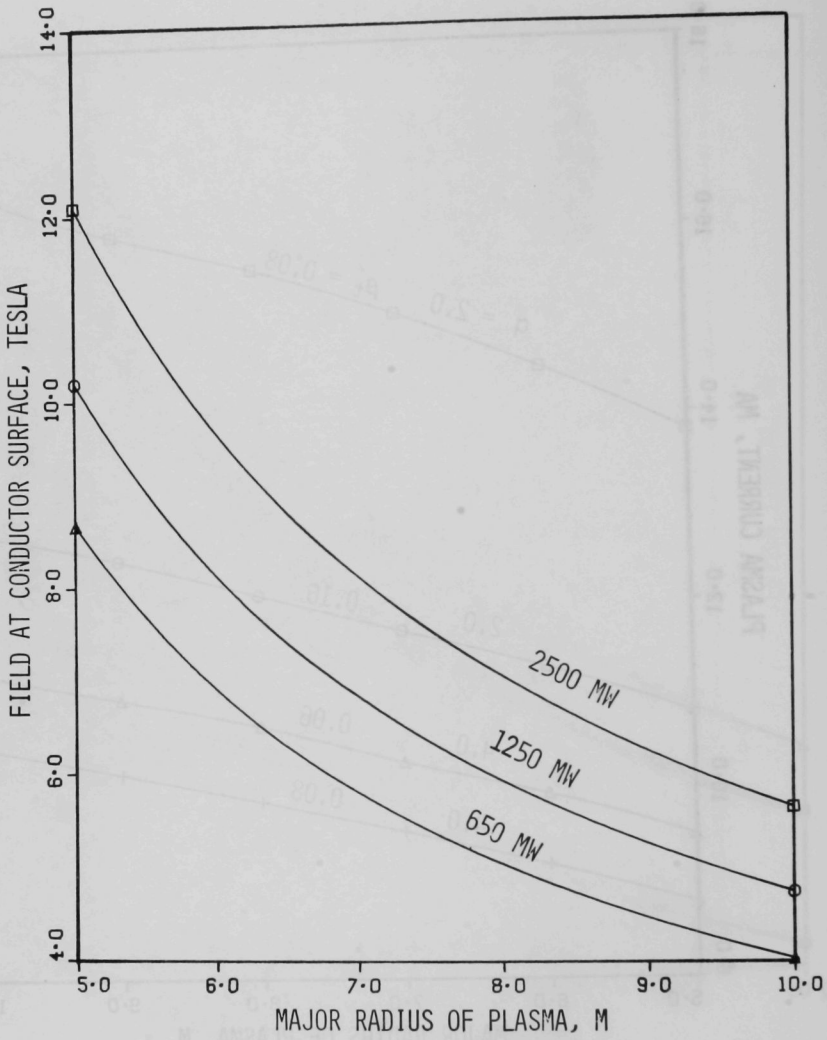

Fig. 18. Required magnetic field versus major radius for various thermal power levels; A = 3.0, κ = 1.65, q = 3.0, β_t = 0.08, Δ = 1.0 m.

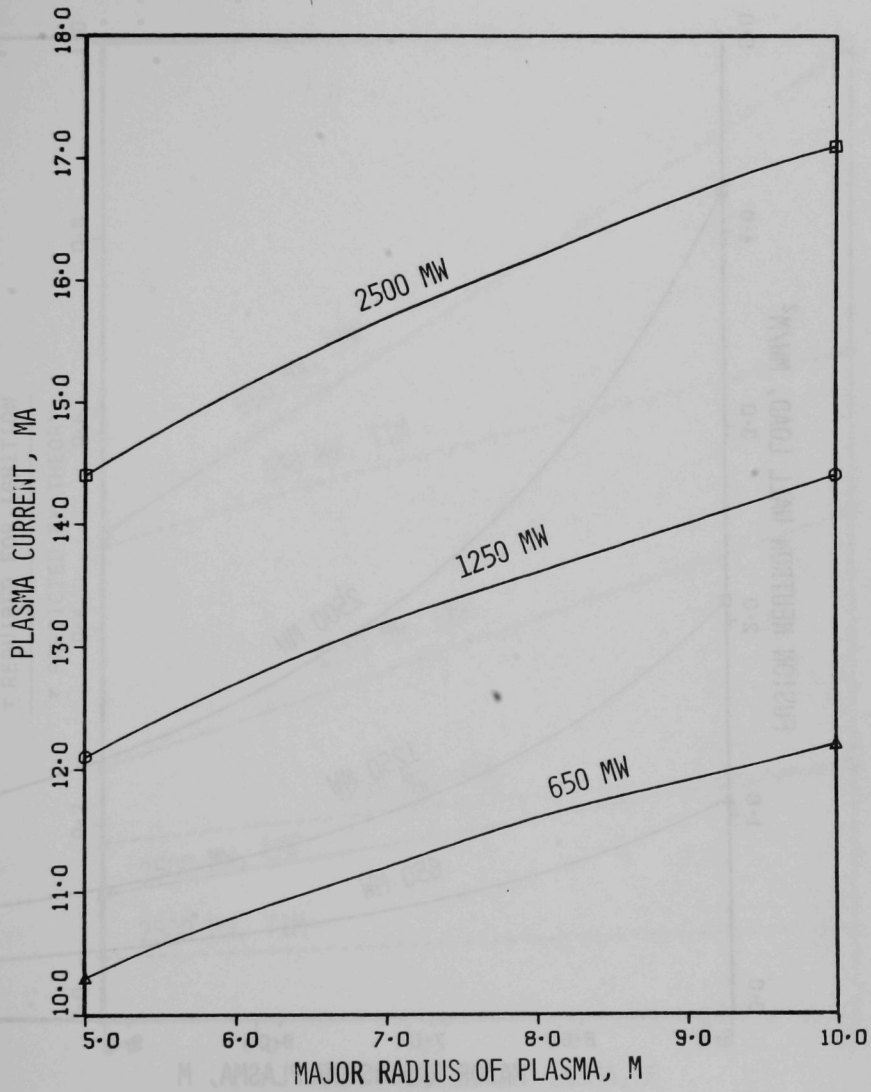

Fig. 19. Plasma current versus major radius; A = 3.0, κ = 1.65, q = 3.0, β_t = 0.08, Δ = 1.0 m.

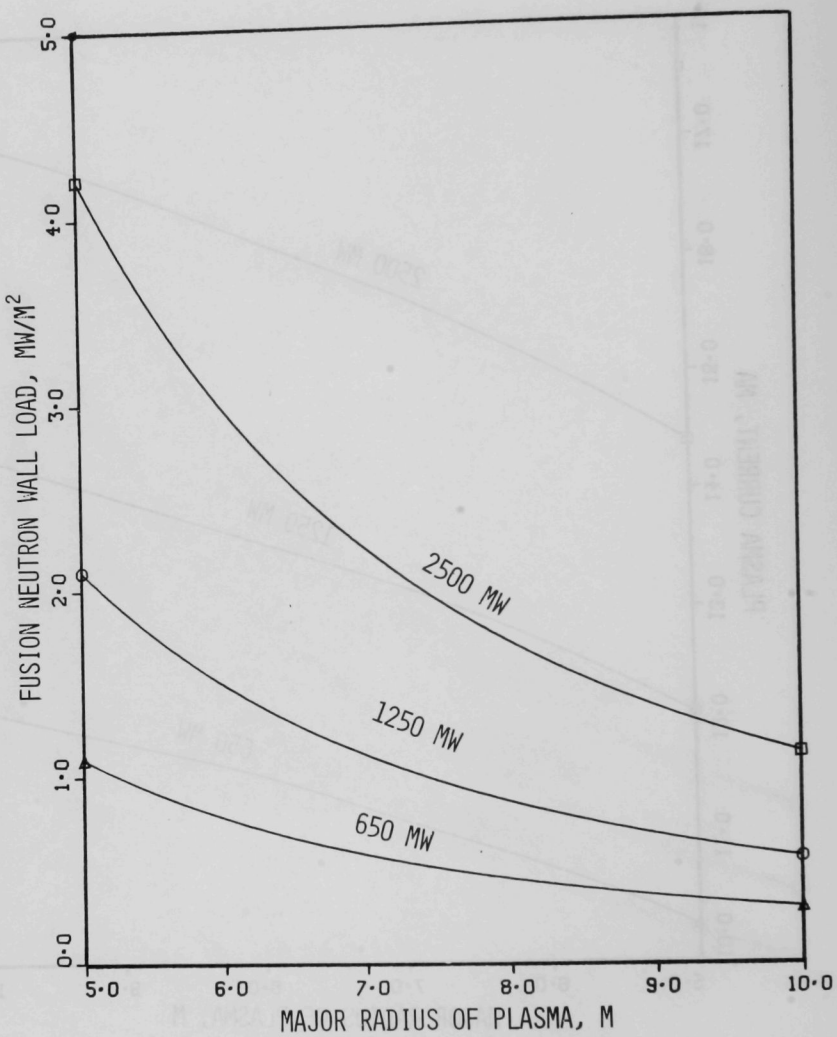

Fig. 20. Neutron wall load versus major radius; A = 3.0, κ = 1.65, q = 3.0, β_t = 0.08, Δ = 1.0 m.

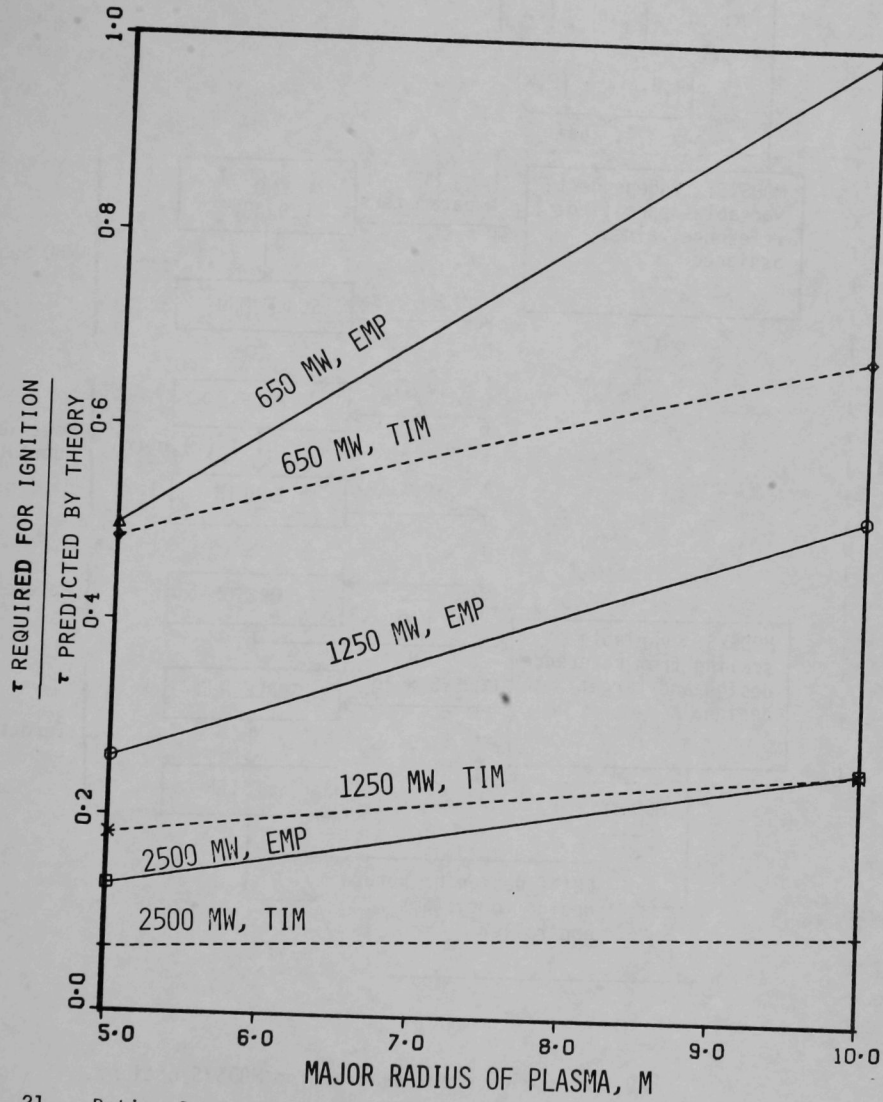

Fig. 21. Ratio of τ required for ignition to τ predicted by theory versus major radius for empirical (EMP) and trapped ion mode (TIM) scaling; $A = 3.0$, $\kappa = 1.65$. $q = 3.0$, $\beta_t = 0.08$, $\Delta = 1.0$ m.

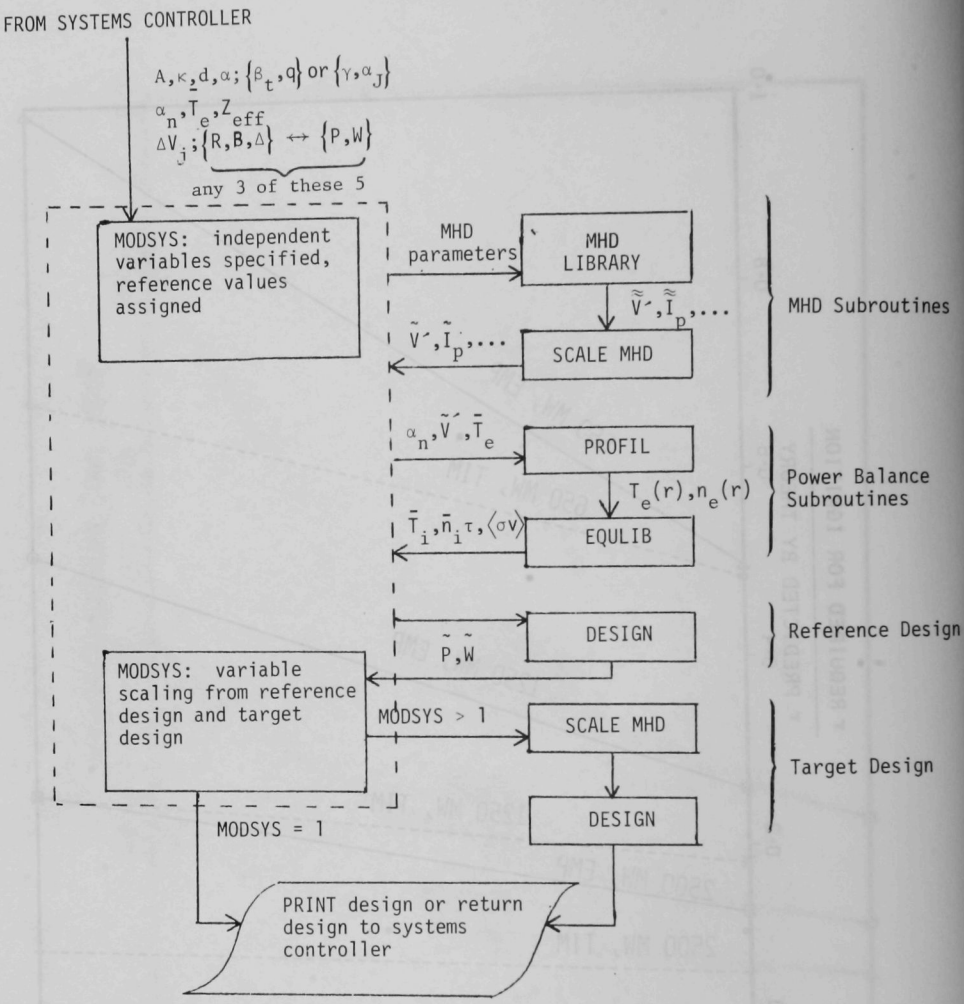

Fig. 22. Flow chart diagramming MODSYS options.

September 20, 1977 ANL/FPP/TM-87

PLASMA DRIVING SYSTEMS REQUIREMENTS FOR COMMERCIAL TOKAMAK FUSION REACTORS

Jeffrey N. Brooks, Robert L. Kustom, and Weston M. Stacey, Jr.*

Fusion Power Program
Argonne National Laboratory
Argonne, Illinois 60439

ANL/FPP Technical Memorandum No. 87

---

*Present address: School of Nuclear Engineering, Georgia Institute of Technology, Atlanta, Georgia 30332.

TABLE OF CONTENTS

	Page
ABSTRACT	1
I. INTRODUCTION	2
II. REACTOR MODEL	3
III. POWER SUPPLY CONFIGURATIONS	6
IV. COMPUTATIONAL MODEL AND BURN CYCLE SCENARIO	16
V. RESULTS OF BURN CYCLE SIMULATIONS	22
A. Homopolar Generator - Configuration No. 1	22
1. Typical Case	22
2. Sensitivity Study	25
B. Configuration No. 2 - SCR Power Supply	30
1. Typical Case	30
2. Sensitivity Study	33
3. Alternate Operation	37
C. Configuration No. 3 - MGF Set	38
D. Configuration No. 4a - Single Dump Resistor	38
1. Typical Case	40
2. Sensitivity Study	43
E. Configuration No. 4b - Multi-dump Resistor	43
VI. SUMMARY AND CONCLUSIONS	46
APPENDIX. Cost Algorithms	52
REFERENCES	54

LIST OF TABLES

No.	Title	Page
I	Steady-State Plasma and Reactor Parameters	5
II	Hardware Configurations	7
III	Summary of Driving System Requirements for Configuration No. 1 (Homopolar Generator-Energy Storage Inductor)	27
IV	Summary of Driving System Requirements for Configuration No. 2 (SCR Power Supply - Energy Storage Inductor)	36
V	Summary of Driving System Requirements for Configuration No. 3 (SCR Power Supply - MGF Set)	39
VI	Summary of Driving System Requirements for Configuration No. 4a (Single Dump Resistor - Energy Storage Inductor)	42
VII	Summary of Driving System Requirements for Configuration No. 4b (Multi-resistor, Energy Storage Inductor - Constant OH Voltage During Reversal)	47

LIST OF FIGURES

No.	Title	Page
1	Schematic view of OH and EF coil locations	4
2	Power supply configuration No. 1	8
3	Power supply configuration No. 2	9
4	Power supply configuration No. 3	10
5	Power supply configuration No. 4	11
6	Simplified equivalent circuit of driving system	17
7	Typical startup using a homopolar generator as the OH transfer element. Δt_{OH} = 2 s, t_{B_0} = 2 s	23
8	Sensitivity of the driving system requirements to the ohmic heating ramp time, Δt_{OH}. For a homopolar generator used as the OH energy transfer device and for the neutral beam turn on time, $t_{B_0} = \Delta t_{OH}$	26
9	Sensitivity of the driving system requirements to the ohmic heating ramp time, Δt_{OH}. For a homopolar generator used as the OH energy transfer device and for the neutral beam turn-on time, $t_{B_0} = \Delta t_{OH}/2$	29
10	Poloidal beta, β_p, versus time, during startup, for a homopolar generator; Δt_{OH} = 2 s and for t_{B_0} = 1 and 2 s	31
11	Typical startup, using an SCR-type power supply as the OH transfer element; V_{OH} = 60 V/turn, $t_{B_0} = \Delta t_{OH}/2$	32
12	Sensitivity of the driving system requirements to the flat-top OH voltage. For a constant voltage SCR-type power supply used as the OH energy transfer device and for $t_{B_0} = \Delta t_{OH}$	34
13	Sensitivity of the driving system requirements to the flat-top OH voltage. For a constant voltage SCR-type power supply used as the OH energy transfer device and for $t_{B_0} = \Delta t_{OH}/2$	35

LIST OF FIGURES (Contd.)

No.	Title	Page
14	Typical startup using a dump resistor as the OH transfer element; V_{OH}^{max} = 115 V/turn, $t_{B_0} = \Delta t_{OH}$	41
15	Sensitivity of the driving system requirements to the maximum OH voltage. For a single dump resistor used as the OH transfer element and for $t_{B_0} = \Delta t_{OH}$	44
16	Sensitivity of the driving system requirements to the maximum OH voltage. For a single dump resistor used as the OH transfer element and for $t_{B_0} = \Delta t_{OH}/2$	45
17	Total driving system power supply cost as a function of the OH ramp time, Δt_{OH} and power supply configuration. For the neutral beam turn-on time, $t_{B_0} = \Delta t_{OH}$	49

PLASMA DRIVING SYSTEMS REQUIREMENTS FOR COMMERCIAL TOKAMAK FUSION REACTORS

Jeffrey N. Brooks, Robert L. Kustom, and Weston M. Stacey, Jr.

Fusion Power Program
Argonne National Laboratory
Argonne, Illinois 60439

ABSTRACT

The requirements on the plasma driving system (OH and EF coils and their power supplies) for a typical commercial tokamak fusion reactor (R = 8 m, P = 1000 MWe) have been analyzed. The analysis made use of a plasma burn cycle simulation code fully coupled to a model of the driving system. Technological requirements and cost estimates have been made for five possible driving system components: homopolar generators, SCR-type power supplies, dump resistors, superconducting energy storage inductors, and motor-generator-flywheel sets.

I. INTRODUCTION

The plasma driving system for a tokamak reactor is composed of an ohmic heating (OH) coil equilibrium field (EF) coil, and their respective power supplies. Conceptual designs of an Experimental Power Reactor[1,3] (EPR) and scoping studies of a Demonstration Power Reactor[4] have shown that the driving system constitutes a significant part of the overall reactor cost. The capabilities of the driving system also set or help set important parameters of the burn cycle, such as the startup time, shutdown time, and the net power output. Previous detailed studies[1-3,5-6] on driving system dynamics have helped to define the required characteristics for fast-pulsed superconducting magnets, homopolar generators, and very high power (GVA) power supplies for an EPR.

The driving system requirements for commercial reactors have not been examined in detail to date. Plasma driving systems requirements are needed to guide studies of commercial reactor systems, to define research and development needs and to provide some perspective as to how well design options for near-term tokamaks extrapolate to commercial reactors. The plasma driving system requirements depend upon the reactor design concept, of course. In this paper, a single reactor configuration together with several design concepts for the driving system are considered. Both the reactor configuration and the driving system concepts are natural extensions from the EPR. Thus, the new results presented in this paper can be compared with the previous EPR results[1-3] to obtain a consistent picture of how the driving system requirements will evolve — for one particular design configuration. Subsequent studies will examine different design configurations for the poloidal (OH and EF) coil system.

The main focus of this work is on the cost and technological requirements of the OH and EF energy storage and transfer systems. Other related points addressed are: (1) the likely duration of the plasma startup period — this affects several other subsystems as well as the overall power performance; (2) the maximum burn time obtainable, assuming volt-seconds are limiting; and (3) the $\dot{B}$ requirements of the OH coil. The specific designs and the costs of the OH and EF coils themselves are not included.

II. REACTOR MODEL

The reactor model used for this study is an 8-m major radius tokamak having a plasma β of about 8% and a power output of 1000 MWe. The plasma is D-shaped with a height-to-width ratio of 1.3. It is believed that this model represents a typical choice of a commercial reactor design, from today's standpoint. The model and design parameters are based, in part, on data developed by the parametric systems analysis project at ANL.[7] The reactor coil configuration, shown in Fig. 1, is conventional, with a central, solenoidal OH coil with a few additional external trimming coils, and a set of EF coils external to the toroidal field coils. Both the OH and EF coils are superconducting and decoupled from one another. The locations of the EF coils and the relative currents in them have been selected so as to obtain the magnetic field in the plasma required to keep the plasma in MHD equilibrium. Table I lists the main design parameters and the steady-state plasma parameters for this reactor. The peak field of the OH coils is 8 T. This and the OH coil radius of 3.3 m determine the available flux swing of the OH coil.

The plasma data, at equilibrium, was obtained by means of a static energy and particle balance code and an MHD equilibrium code, both of which are described in Appendix C of Ref. 2. Both the static and time-dependent calcula-

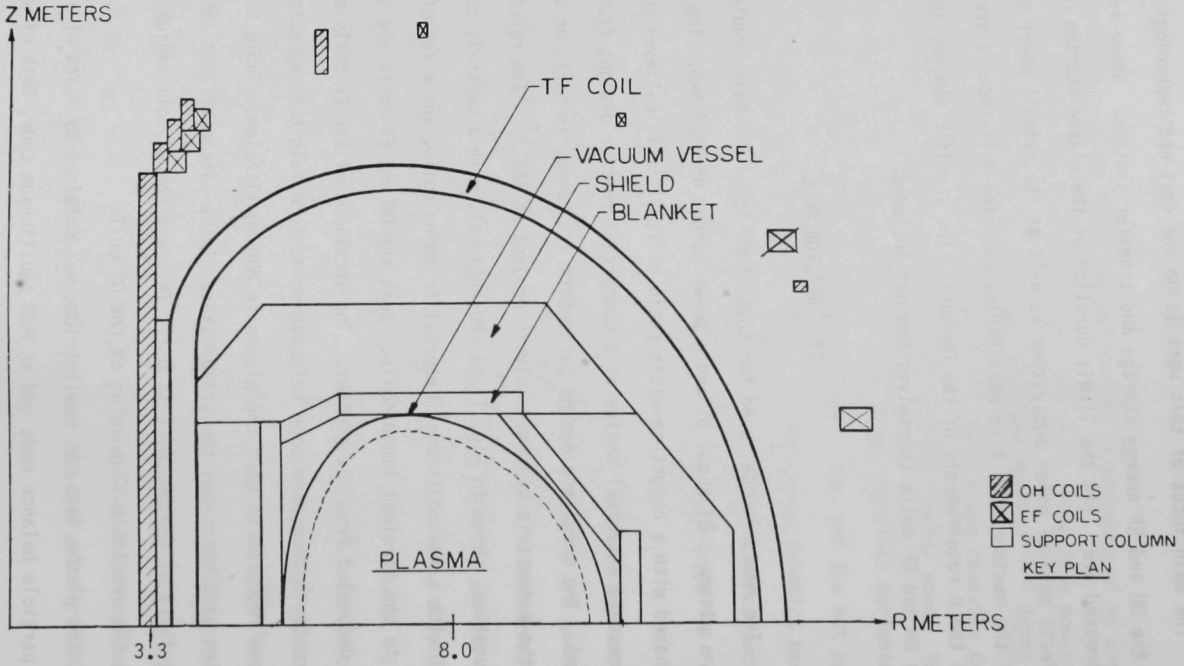

Fig. 1. Schematic view of OH and EF coil locations.

TABLE I

Steady-State Plasma and Reactor Parameters

Major radius, R	8.0 m
Aspect ratio, A	3.0
Height-to-width ratio, κ	1.3
Toroidal beta, β_T	7.9%
Poloidal beta, β_P	1.85
Safety factor	
magnetic axis, q(0)	1.0
plasma surface, q(a)	3.0
Average ion temperature, $\bar{T}_i$	8 keV
Peak field, B_{max}	
at TF coils	8.0 T
at OH coils	8.0 T
Effective radius of OH coil, R_v	3.3 M
Field at plasma centerline, B_{t_0}	4.03 T
Plasma current, I_p	12.3 MA
Resistivity, η	$3 \times \eta_{spitzer}$
Average D-T ion density, $\bar{N}_{DT}$	1.44×10^{20} m^{-3}
Background impurity	0.5% oxygen
Wall-sputtered impurity	beryllium
Neutral beam heating power, P_B	200 MW
Power output	
thermal, P_t	3330 MWt
electrical, P_E	≈1000 MWe

tions used in this analysis are 0-D, with spatial effects incorporated by averaging all quantities over specified density, temperature, and flux function profiles.

The value of the neutral beam heating power, 200 MW, was selected on the basis of an initial sensitivity study which identified this value as an adequate one for effective operation. This choice is set by, among other things, the need to break through the radiation barrier imposed by the oxygen background impurity.

III. POWER SUPPLY CONFIGURATIONS

Four power supply configurations have been analyzed. Each configuration contains an energy transfer device for use with the OH coil during startup and a central energy storage device used to provide large power demands when necessary. Three types of possible OH transfer devices have been considered: (1) a homopolar generator; (2) an SCR-type rectifier-inverter power supply (SCR P.S.); and (3) a dump resistor. Two types of central energy storage devices have also been considered: (1) a superconducting energy storage inductor (ESI); and (2) a motor-generator-flywheel (MGF) set. These transfer and central storage devices have been combined into four configurations, the most important elements of which are listed in Table II.

The equivalent circuit of these configurations is shown in Figs. 2-5. All configurations use several common elements. The EF power supply is an SCR P.S. in all cases because the EF current cannot be free-running; it must be precisely controlled to keep the plasma in MHD equilibrium. (The MHD requirements depend on the plasma current and plasma pressure.) The requirements on the EF supply and the cost of it do, however, depend greatly on the type of OH transfer device used and upon details of the startup. The exact design of the

TABLE II

Hardware Configurations

Hardware Configuration No.	OH Transfer Device	EF Transfer Device	Central Energy Storage Device
I	Homopolar generator	SCR-type power supply	Energy storage inductor
II	SCR-type power supply	SCR-type power supply	Energy storage inductor
III	SCR-type power supply	SCR-type power supply	Motor-generator-flywheel
IV	Dump resistor	SCR-type power supply	Energy storage inductor

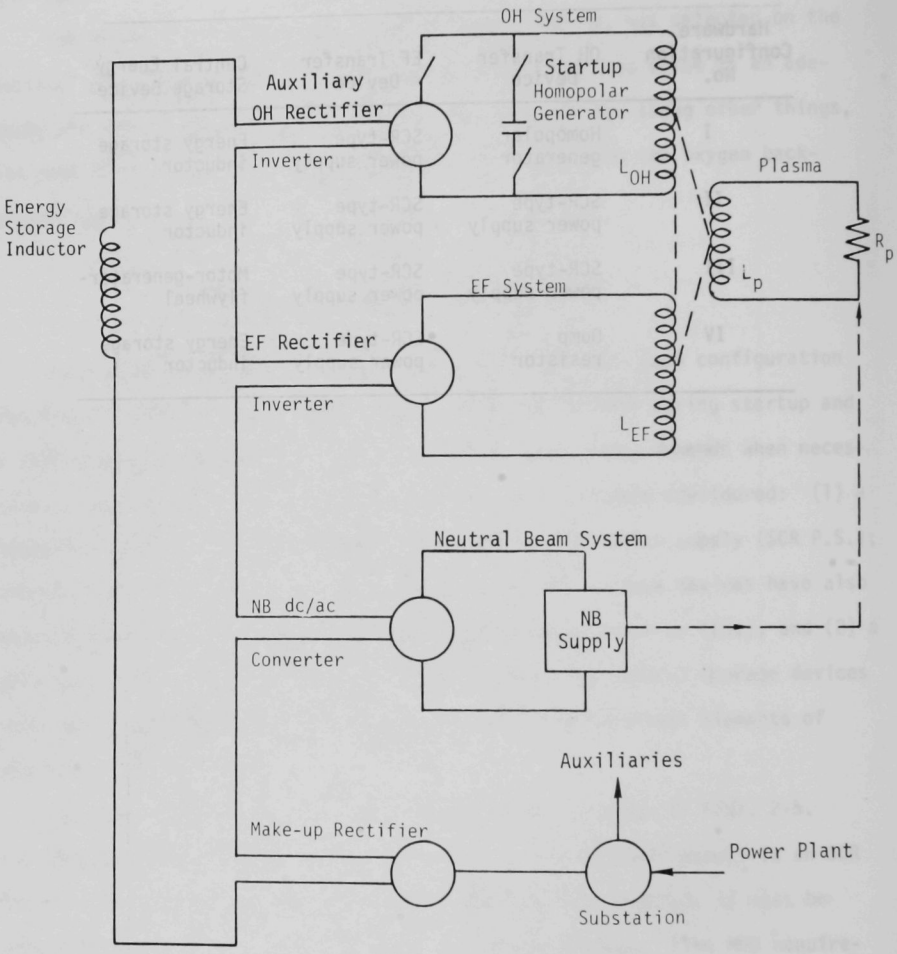

Fig. 2. Power supply configuration No. 1.

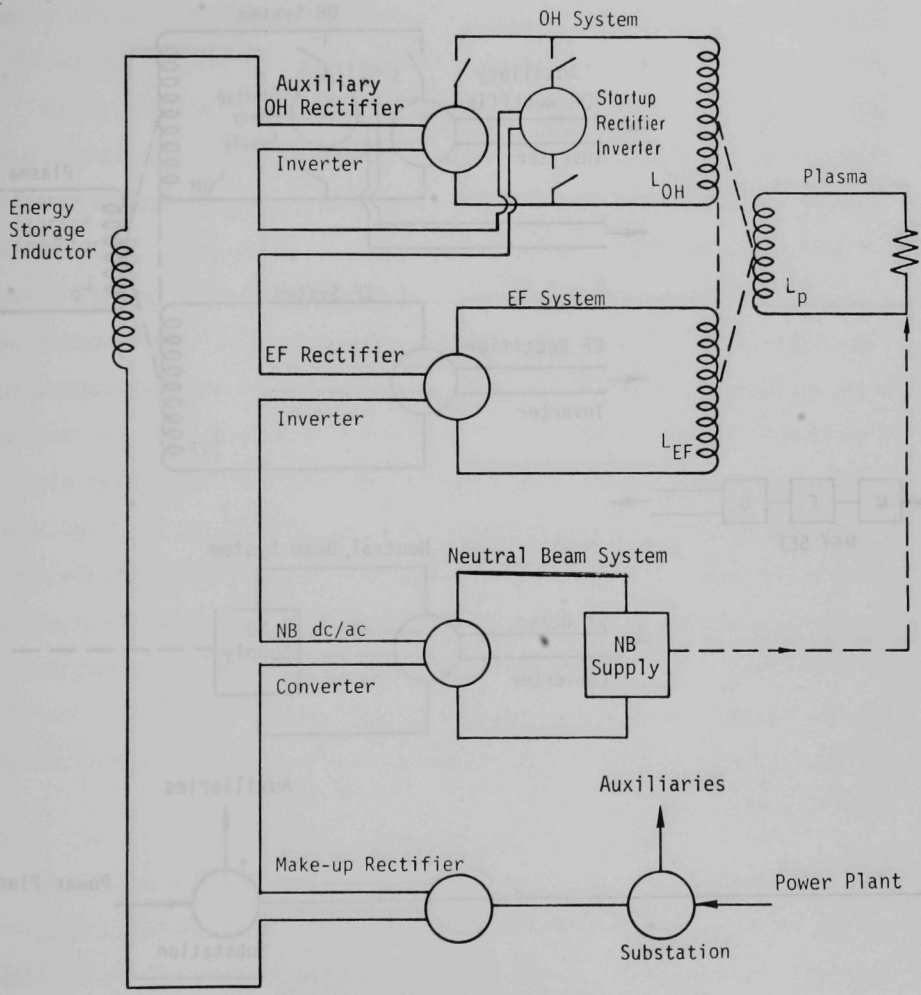

Fig. 3. Power supply configuration No. 2.

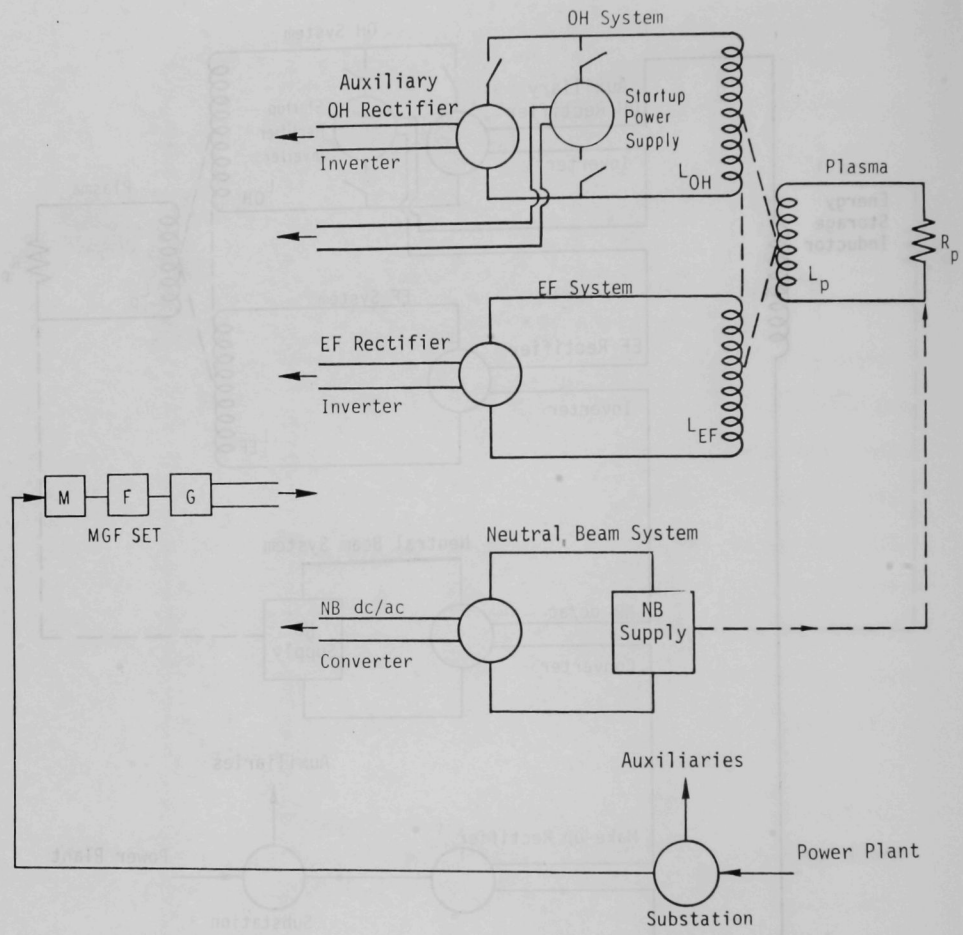

Fig. 4. Power supply configuration No. 3.

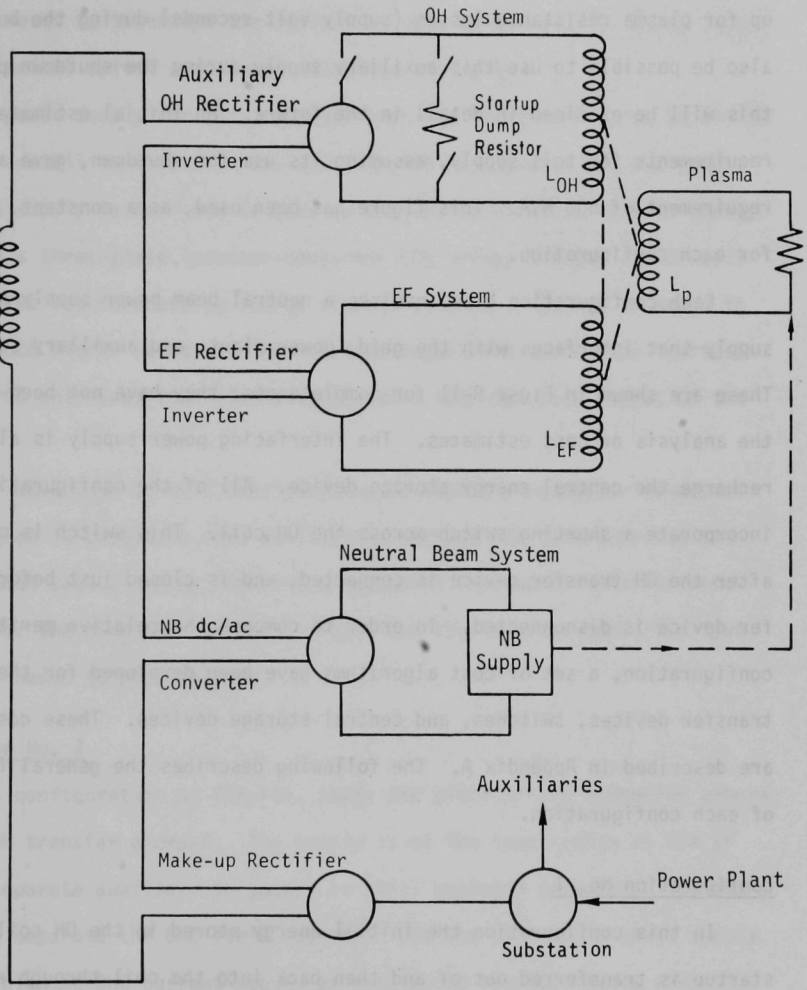

Fig. 5. Power supply configuration No. 4.

EF supply also depends on whether it will operate out of an ESI or an MGF. All four configurations also use an auxiliary SCR P.S. in the OH circuit. This auxiliary supply is used to charge the OH coil prior to startup, and to make up for plasma resistance losses (supply volt-seconds) during the burn. It may also be possible to use this auxiliary supply during the shutdown period; this will be examined in detail in the future. An initial estimate of the requirements for this supply, assuming its use for shutdown, gave a peak power requirement of 500 MVA. This figure has been used, as a constant, in costing for each configuration.

Each configuration also involves a neutral beam power supply and a power supply that interfaces with the grid, power plant, and auxillary subsystems. These are shown in Figs. 8-11 for completeness; they have not been included in the analysis or cost estimates. The interfacing power supply is also used to recharge the central energy storage device. All of the configurations also incorporate a shorting switch across the OH coil. This switch is opened just after the OH transfer device is connected, and is closed just before the transfer device is disconnected. In order to compare the relative merits of each configuration, a set of cost algorithms have been developed for the various transfer devices, switches, and central storage devices. These cost algorithms are described in Appendix A. The following describes the general functioning of each configuration.

Configuration No. 1

In this configuration the initial energy stored in the OH coil prior to startup is transferred out of and then back into the coil through an inertial energy storage device in the form of radially stacked, drum-type homopolar generators to obtain a half-sinusoid voltage waveform. The wavelength of the half sinusoid is controlled by adjusting the effective capacitance of the

homopolar generators to match the inductance of the OH coil. A description of the homopolar generator design is given in Refs. 1-3. The start-and-stop action is controlled by the shorting switch (not shown) across the OH coil. This switch only needs to interrupt the current at zero voltage, so a fairly inexpensive mechanical switch arrangement might be possible.

The EF power supply for this configuration and the others using an ESI is described in detail in Ref. 2 . The auxiliary OH supply also has the same design. The supply is designed to have an actively controlled rate of energy change using a three-phase inductor-convertor SCR bridge between the EF coil and the central superconducting energy storage inductor. Energy is added to the ESI at much higher rates than the average input rate during the startup. The power grid only sees the relatively constant 1000-MWe peak output of the reactor.

A clear advantage of this configuration is that the homopolar generator can be designed to provide a free oscillation between the generator and the OH coil without costly energy conversion equipment inbetween. However, the technology for the homopolar generator, ESI, and the inductor-converter-type power supply needs to be developed.

Configuration No. 2

In this configuration an SCR P.S. takes the place of the homopolar generator as the OH transfer element. The supply is of the same design as the EF supply. A separate auxiliary OH supply is still employed because it is cost effective to separate the OHC field reversal from the burn cycle power supply because the highest OHC current occurs at the end of the burn cycle when the coil voltage is relatively low. A mechanical shorting switch is also used across the OH coil in connection with power supply changeover. However, the mechanical shorting switch would probably have to be a combination of a high

duty cycle slow-acting mechanical switch in parallel with a fast-acting, low-duty cycle switch.

Configuration No. 3

In this configuration an MGF set is used, instead of an ESI, as the central energy storage device. The MGF set consists of an ac motor needed to make up energy losses in the system, a flywheel to store energy, and an ac generator to convert the mechanical energy into electrical energy. The generator also functions reversibly as a high power motor. An SCR-type power supply is used, in this configuration, for the OH transfer device. The rectifier supply for the MGF system is a conventional ac-dc multiphase converter, rather than a dc-ac-dc inductor-converter of the type needed for use with the ESI. If the MGF system can be optimized (i.e., so that the generator terminal voltage is slightly higher than the peak coil voltage), no intermediate transformers are needed between the generator terminals and the rectifier stacks. However, if the optimal system cannot be designed, intermediate transformers are needed. The impact of adding the transformers represents about 30% in cost. For coating purposes this report assumes an optimized system. The advantage of this configuration is that it uses technology that is commercially available today. The tokamak fusion test reactor (TFTR), for example, will use an MGF set to operate the driving system power supplies.

Configuration No. 4

This configuration is similar to No. 1 or No. 3 except that a dump resistor is used as the OH transfer element. The dump resistor can be either a single unit, or a combination of resistors switched in at appropriate times to change the effective resistance.

In this configuration some (actually most) of the initial energy stored in the OH coil prior to startup is dissipated ("dumped") in the passive resistor element.

The time constant of the OH current decay can be controlled by adjusting the resistance of the single dump resistor and/or by switching in different resistors during the startup with a multi-resistor combination. An initial design study for a suitable dump resistor has been performed by R. Fuja of ANL's Accelerator Research Facility Division. The initial design is quite simple, basically consisting of a stainless steel drum filled with oil and with electrodes at both ends of the drum. Current flows through the oil and is dissipated as heat. A heat exchanger, heat distribution system, and several miscellaneous components are also needed. The resistor appears to be straightforward to build. The switch system for a dump resistor is, however, much more involved than for the other configurations because the shorting switch across the OH coil must now close across high voltage. The resistor, like the other transfer devices, must be switched out of the circuit when enough voltseconds have been supplied by the OH coil to the plasma. Unlike the other transfer elements the voltage across the dump resistor is never zero; therefore, necessitating the non-zero voltage closing capability of the shorting switch. For a multi-resistor combination, more switches with similar capability are needed. Although mechanical switches could potentially be developed to serve this function, response time consideration and reliability questions may force the need for a solid-state switch. It is assumed, therefore, for costing purposes that an SCR-type isolation switch will be used in this configuration. The use of thyristors in a switch configuration is much less expensive than their use in a polyphase rectifier since phase control circuits and transformers are not needed. However, the cost of heat sinks, current balancing inductors, scrubbers, etc.,

still represent a significant cost, about one-fourth of the price per kVa of a rectifier power supply unit.

COMPUTATIONAL MODEL AND BURN CYCLE SCENARIO

The burn cycle and driving system requirements for this reactor have been analyzed by means of a spatial-profile-averaged, time-dependent, plasma code coupled to a driving system code. The plasma code solves particle balance equations for each constituent plasma ion species (D-T, alpha, wall-sputtered impurity) and solves energy balance equations for the ions and the electrons. Plasma heating by alpha and neutral beam slowing down is treated. Radiative (bremsstrahlung, line, recombination) and transport losses are treated, the latter with a multi-regime (neoclassical ions/empirical-classical electrons at large collision frequencies and trapped-particle mode at small collision frequencies) confinement model. The overall model is described in Appendix C of Ref. 2. For the purposes of analyzing the driving system requirements, the coupled dynamics of the plasma and poloidal coil systems has been simulated with the simplified three-mesh equivalent circuit shown in Fig. 6. In Fig. 6 it is understood that the individual elements operate out of the central energy storage device as appropriate. The inductance matrix for the system was computed on the basis of the coil locations shown in Fig. 1. Values are normalized to the number of turns in the respective coils.

The coupled system of Fig. 6 is described by the following set of equations:

$$L_{OH} \frac{dI_{OH}}{dt} - M_{OH,p} \frac{dI_p}{dt} = V_{OH} \tag{1}$$

$$L_p \frac{dI_p}{dt} + R_p I_p = M_{OH,p} \frac{dI_{OH}}{dt} + M_{EF,p} \frac{dI_{EF}}{dt} \tag{2}$$

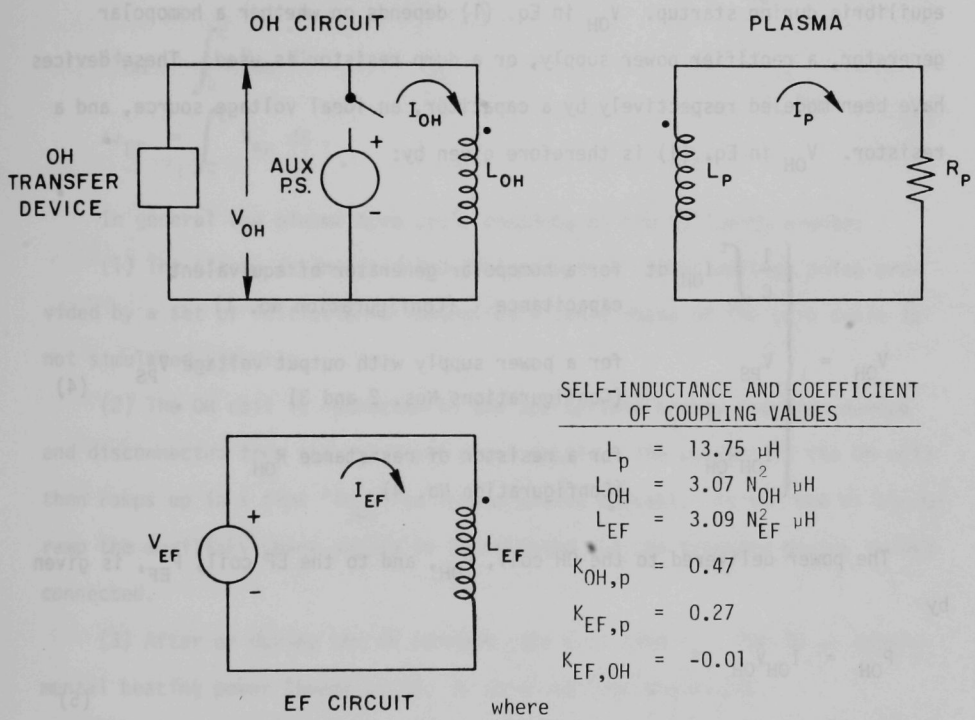

SELF-INDUCTANCE AND COEFFICIENT OF COUPLING VALUES

$L_p = 13.75\ \mu H$

$L_{OH} = 3.07\ N_{OH}^2\ \mu H$

$L_{EF} = 3.09\ N_{EF}^2\ \mu H$

$K_{OH,p} = 0.47$

$K_{EF,p} = 0.27$

$K_{EF,OH} = -0.01$

where

N_{OH} = No. of turns of OH coil

N_{EF} = No. of turns of EF coil

Fig. 6. Simplified equivalent circuit of driving system.

$$I_{EF} = f\left(I_p, \beta_p\right) , \tag{3}$$

where β_p is the ratio of the kinetic-to-poloidal magnetic pressures. The required current, I_{EF}, in the EF coils is determined through the use of a separate MHD equilibrium code as the plasma evolves through a sequence of equilibria during startup. V_{OH} in Eq. (1) depends on whether a homopolar generator, a rectifier power supply, or a dump resistor is used. These devices have been modeled respectively by a capacitor, an ideal voltage source, and a resistor. V_{OH} in Eq. (1) is therefore given by:

$$V_{OH} = \begin{cases} \frac{1}{C}\int_0^t I_{OH}\, dt & \text{for a homopolar generator of equivalent capacitance C (Configuration No. 1)} \\ V_{PS} & \text{for a power supply with output voltage } V_{PS} \text{ (Configurations Nos. 2 and 3)} \\ I_{OH}R_{OH} & \text{for a resistor of resistance } R_{OH} \text{ (Configuration No. 4)} \end{cases} \tag{4}$$

The power delivered to the OH coil, P_{OH}, and to the EF coil, P_{EF}, is given by

$$\begin{aligned} P_{OH} &= I_{OH}V_{OH} \\ P_{EF} &= I_{EF}V_{EF} \end{aligned} \tag{5}$$

where

$$V_{EF} = L_{EF}\frac{dI_{EF}}{dt} - M_{EF,P}\frac{dI_p}{dt} \tag{6}$$

is the voltage across the EF coil.

The energy delivered to the respective coils are

$$U_{OH} = \int_0^t P_{OH}\, dt$$

$$U_{EF} = \int_0^t P_{EF}\, dt \tag{7}$$

and the flux swings across the coils are

$$\Delta\phi_{OH} = \int_0^t V_{OH}\, dt$$

$$\Delta\phi_{EF} = \int_0^t V_{EF}\, dt\ . \tag{8}$$

In general the plasma burn cycle consists of the following events:

(1) The plasma is injected and ionized with a 10-ms voltage pulse provided by a set of initiation-trimming coils (this phase of the burn cycle is not simulated directly.

(2) The OH coil is connected to the appropriate energy transfer device and disconnected from the auxiliary power supply. The current in the OH coil then ramps up in a time "Δt_{OH}" to induce plasma current. At the end of the OH ramp the auxiliary power supply is reconnected and the transfer device is disconnected.

(3) After or during the OH current ramp at a time t_{B_0}, 200 MW of supplemental heating power (beams or RF) is injected into the plasma.

(4) When the plasma reaches its equilibrium point, $\bar{T}_i$ = 8 keV, supplemental heating is terminated. The startup period is over and the main burn phase begins. The EF current increases during the startup and in so doing also induces plasma current. At the end of the startup, both the EF and plasma currents are at their maximum values. The OH current continues to rise slowly during the burn phase to make up for resistive losses in the plasma.

(5) The plasma burns until the maximum flux swing of the OH coil is reached, or for any shorter time desired.

(6) The shutdown period is started by causing a temperature reduction (e.g. by impurity injection). The plasma and EF currents are reduced.

(7) When the thermal energy content of the plasma has been reduced sufficiently, the OH current is ramped down by means of the energy transfer device and the burn pulse is terminated.

(8) The vacuum chamber is evacuated, the OH current is brought to the required starting value by the auxiliary power supply, and preparations are made for the next burn pulse.

Most of the driving system requirements are set during the startup period, i.e. events (1)-(4) in the listing above, and so the focus of this work is on this period. These requirements (set during startup) are the maximum $\dot{B}$ ($\dot{B}$ = dB/dt) and voltage on the OH coil, the energy and power needs of the EF power supply and the OH transfer device, and the energy storage requirement of the central storage device. The requirements on the auxiliary power supply are set after startup and depend on the voltage needed to sustain the plasma current during the burn and/or the voltage needed for shutdown if the same supply is used for this purpose as well. As mentioned previously, a value of P_{max} = 500 MVA has been estimated for this supply.

The maximum burn time is another important parameter for a commercial reactor. The burn time depends on either the degree of impurity buildup in the plasma or else on the volt-second limitations of the OH coil. An estimate of the maximum burn time has been made for the various cases studied, assuming that some impurity control is, in fact, used (e.g. edge temperature control, low sputter surface, divertor action, etc.) and hence volt-seconds are limiting. (Impurity buildup with a beryllium coating has virtually no effect on the startup requirements because there is not enough time for appreciable buildup even without special impurity control measures.)

The maximum burn time is reached when the OH field reaches its maximum value; B_{OH}^{max} = 8 T is assumed for this reactor. The difference between this 8 T value and the field reached just after startup therefore determines the burn time, and computations have been made on this basis. It is not clear, at this time, just how long the burn cycle needs to be or should be for effective operation of commercial reactors; however, knowledge of the maximum burn time possible is important in at least determining the range of options.

In order to assess the driving system requirements, burn cycle simulations were performed for each configuration, using a range of Δt_{OH}. This parameter can be controlled by varying the appropriate parameter of the OH transfer device. Another possibly important control variable is t_{B_0}, the neutral beam turn-on time. Potential plasma physics questions, however, can limit the choice of t_{B_0}; in particular a strong skin effect due to excess heating may prevent adequate current penetration and hence may preclude turning on the beam very early in the cycle. It may be that the skin effect in large tokamaks could be reduced spontaneously by MHD turbulent activity; in any event this subject is not predictable or modelable at this time, but should be borne in mind with regard to early heating. In order to keep the number of cases analyzed tractable, and at the same time to cover the general possibilities, two generic beam options were used: (1) $t_{B_0} = \Delta t_{OH}$; and (2) $t_{B_0} = \Delta t_{OH}/2$. Case 1 is conservative in the sense that all the plasma current that will be induced by the OH coil is already in the plasma before the beam is turned on and strong heating occurs. This avoids skin effect problems to the extent possible. Case 2 is riskier because (as will be shown), much less of the current is present when strong heating begins; skin effect problems, if they are going to occur, would be more likely. As it turns out, the choice of t_{B_0} is quite important in the driving system analysis for other reasons also.

V. RESULTS OF BURN CYCLE SIMULATIONS

A. Homopolar Generator - Configuration No. 1

1. Typical Case

A homopolar generator when connected to the OH coil forms an equivalent L-C circuit. Δt_{OH} for this circuit is actually a "reversal" time in the sense that the original OH current in the coil will reverse symmetrically. As mentioned previously, Δt_{OH} can be varied by changing the effective capacitance of the homopolar generator. The startup phase of the reactor, using configuration No. 1 has been simulated for reversal times of from 1 to 5 s. Figure 7 shows the current and voltage waveforms for the typical case of $\Delta t_{OH} = t_{B_0} = 2$ s, and this case is summarized as case 2 of Table III. The starting value of I_{OH} was adjusted to give the required amount of flux swing needed by the plasma. At t = 2 s the homopolar generator is disconnected and the auxiliary supply switched in. The OH current rises very slowly thereafter to compensate for the resistive losses in the plasma. The rise is slow because the plasma resistance is very small once the beam is turned on and the plasma heats up. During the OH field reversal, 0-2 s, both I_{OH} and V_{OH} are nearly sinuisoidal; nonlinearities arising through the coupled plasma resistance, and the EF-dependent voltage source have a major effect on the plasma current and on the OH requirements, but not much effect on OH waveforms. The OH voltage peaks at t = 1.0 s with V_{OH}^{max} = 100 V/turn. This sets the $\dot{B}_{OH}$ requirement and the homopolar generator energy storage requirement as

$$\dot{B}_{OH}^{max} = \frac{V_{OH}^{max}}{R_v^2} = 2.9 \text{ T/S}$$

$$U_{OH}^{max} = \frac{1}{2} C_{OH} \left(V_{OH}^{max}\right)^2 = 937 \text{ MJ}$$

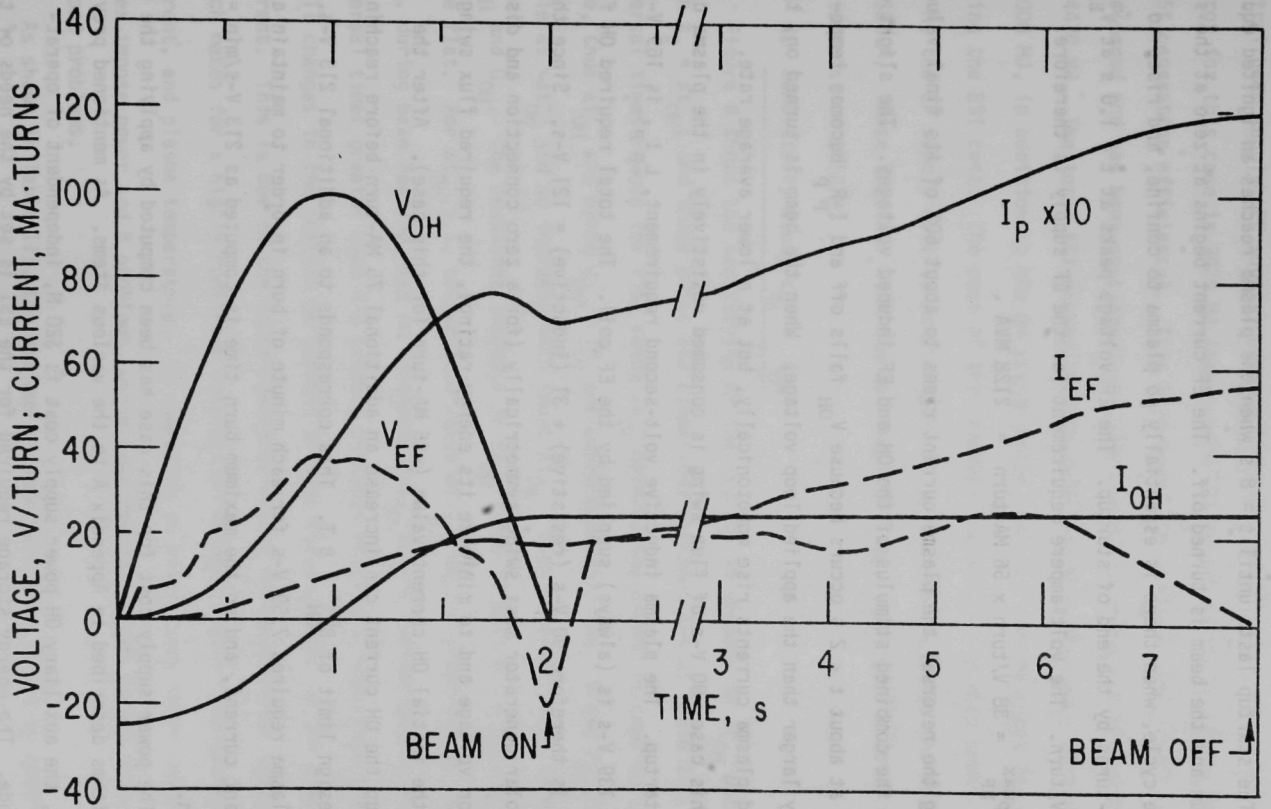

Fig. 7. Typical startup using a homopolar generator as the OH transfer element. Δt_{OH} = 2 s, t_{B_0} = 2 s.

The startup lasts until $t \approx 8$ s when the plasma reaches an ignited equilibrium and the beam is turned off. The EF current begins at zero at the start of the cycle, when there is essentially no plasma to confine, and rises to 56 MA-turns by the end of startup. The EF voltage peaks at $t = 1.0$ s at V_{EF}^{max} = 38 V/turn. The volt-ampere requirement for the EF supply is therefore:

$$P_{EF}^{max} = 38 \text{ V/turn} \times 56 \text{ MA turn} = 2128 \text{ MVA} .$$

During the reversal the plasma current rises to about 60% of its final value under the combined stimulus of the OH and EF induced voltages. The slight dip in I_p at about $t \lesssim 2$ s occurs because V_{OH} falls off and $I_p R_p$ becomes temporarily larger than the applied loop voltage. When the beam is turned on, the EF and plasma currents rise monotonically, but at a lower average rate. For this case, 90 V-s of flux swing is consumed resistively in the plasma during the startup. The plasma inductive volt-second requirement, $L_p I_p$, is 169 V-s of which 139 V-s is (always) supplied by the EF coil. The total required OH flux swing is therefore 90 V-s (resistive) + 31 (inductive) = 121 V-s. Since the homopolar generator must swing symmetrically (for a zero connection and disconnection voltage and to minimize its energy rating), the required flux swing sets the initial OH current value (-25 MA-turn for this case). After the startup the OH current can increase an additional 75 MA-turn before reaching the design limit of $B_{OH}^{max} = 8$ T. This corresponds to an additional 213 V-s. The plasma requires 7.59 V-s for each minute of burn in order to maintain a constant current, and so the maximum burn time is computed as 213 V-s/min = 28 min.

The power supply cost for this case has been computed by applying the cost algorithms described in Appendix A to the various items. As mentioned previously, the auxiliary OH power supply cost is \$20 M, independent of operating mode. The energy storage required for the ESI is set by the needs of the

neutral beam supply, EF supply, and the homopolar generator. The neutral beam energy for this case is 3429 MJ (based on ≈1200 MJ delivered to the plasma and a 35% generation efficiency). This is practically constant for all of the cases considered and has been considered so. The maximum EF energy is always constant at 4470 MJ. The total ESI energy storage requirement is therefore 3429 + 4470 ≈ 8000 MJ, in addition to the OH system needs, and this is the basis for computing the ESI cost. The cost of the homopolar generator, in this case, is \$14 M, the EF supply cost is considerably larger, at \$53 M, while the ESI cost is \$23 M. These together with the auxiliary OH supply cost give a total driving system cost of \$110 M.

2. Sensitivity Study $t_{B_0} = t_{OH}$

Figure 8 shows the sensitivity of the results to changes in Δt_{OH} but still with $t_B = \Delta t_{OH}$; and these cases are summarized as cases 1-4 of Table III. Short reversal times reduce the flux swing $\Delta\phi_{OH}$ because the plasma is cool for a shorter time, thus ΔI_{OH} and hence $U_{OH} \sim I_{OH}^2$ are correspondingly low. $\dot{B}$ and P_{EF}, however, scale as $\sim\Delta t_{OH}^{-1}$ and so increase with short Δt_{OH}. Long reversal times increase $\Delta\phi_{OH}$ and U_{OH}. The resulting increase in ΔI_{OH} tends to make $\dot{B} \sim \Delta I_{OH}/\Delta t_{OH}$ become flat. For $\Delta t_{OH} \geq 3$, the maximum value of V_{EF} occurs after the OH reversal, i.e. during beam heating, and so increasing Δt_{OH} has no further effect on P_{EF}. Reversal times greater than 4 s produce unstable results in the sense that small changes in the initial OH current produce large changes in the plasma current. This is due to the large resistive losses encountered for long Δt_{OH}, which makes for a highly nonlinear interaction between plasma resistance, plasma current, and plasma temperature. To summarize in brief, very short reversal times impose power and $\dot{B}$ problems, while long reversal times impose volt-second problems.

As shown in Table III, the maximum allowed burn time varies by only ≈25% over the range of Δt_{OH}, and the power supply costs vary from \$143 M to \$109 M.

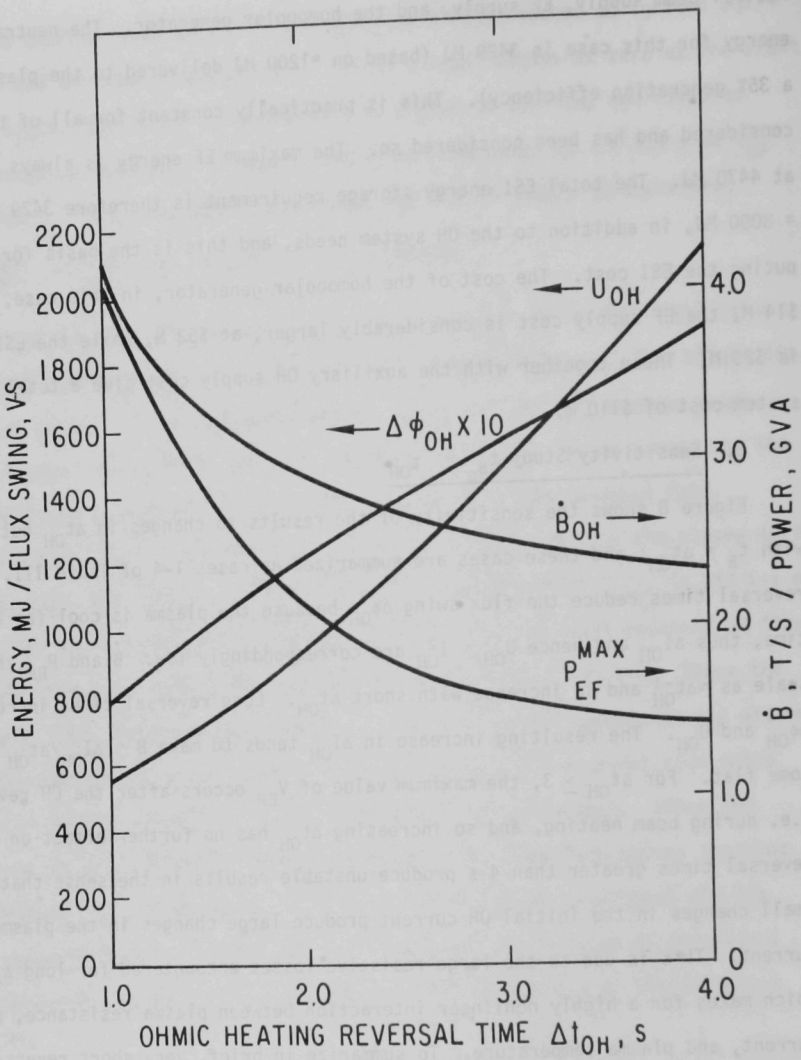

Fig. 8. Sensitivity of the driving system requirements to the ohmic heating ramp time, Δt_{OH}. For a homopolar generator used as the OH energy transfer device and for the neutral beam turn-on time, $t_{B_0} = \Delta t_{OH}$.

TABLE III

Summary of Driving System Requirements for Configuration No. 1
(Homopolar Generator-Energy Storage Inductor)

			Startup Requirements				Power Supply Costs				
Case No.	Δt_{OH} (s)	t_{B_0} (s)	$\Delta\phi_{OH}$ (V-s)	U_{OH}^{max} (MJ)	$\dot{B}_{OH}^{max}$ (T/s)	P_{EF}^{max} (MVA)	OH[a] Homopolar Generator ($M)	EF[b] SCR P.S. ($M)	ESI[c] ($M)	Total[d] ($M)	Max. Burn Time (min)
1	1.0	Δt_{OH}	80	543	4.2	4032	10	91	22	143	31
2	2.0		121	937	2.9	2128	14	53	23	110	28
3	3.0		156	1460	2.5	1568	20	41	24	105	26
4	4.0		187	2100	2.3	1400	26	38	25	109	24
5	1.0	$\Delta t_{OH}/2$	66	410	3.6	4424	9	98	22	149	32
6	2.0		85	606	2.3	3024	11	70	22	123	31
7	3.0		104	813	1.9	2800	13	66	23	122	29
8	4.0		123	1040	1.6	2520	15	60	23	118	28

[a] Cost = \$5 M + \$0.01 × U_{OH}^{max}.

[b] Cost = \$10 M + \$0.02 × P_{EF}^{max}.

[c] Cost = \$5 M + \$0.002 × $\left[U_{OH}^{max} + 8000 \times 10^6\right]$.

[d] Total = (homopolar generator) + (EF P.S.) + (ESI) + Aux. P.S.).

In all cases the EF supply is the largest single cost. The cheapest and probably the most cost-effective choice of operating mode is case 3, which has Δt_{OH} = 3 s, would allow a burn time of 26 min, a fairly low $\dot{B}$, and would involve power supply costs of $105 M.

Sensitivity Study $t_{B_0} = \Delta t_{OH}/2$

Figure 9 shows the results for configuration No. 1 with the beam turned on in the middle of the reversal, $t_B = \Delta t_{OH}/2$, and these cases are summarized as cases 5-8 in Table III. This mode of operation is considered an important option for an EPR because it reduces the resistive flux losses during startup — a critical point for reactors with a small OH coil radius. Similarly, $\Delta\phi_{OH}$ and $\dot{B}_{OH}$ for this reactor are all reduced relative to the cases with the same Δt_{OH} but with $t_B = \Delta t_{OH}$. The drawback of this method is that P_{EF}^{max} becomes considerably higher when $t_B = \Delta t_{OH}/2$. The reason is that the plasma is heated rapidly at the same time that the current is being increased rapidly and so $\dot{\beta}_p$ is large at the same time as V_{OH} is large. The dependence of V_{EF} on $\dot{\beta}_p$ can be shown by analytically representing the MHD requirements for the reactor in a form valid for low β as:

$$I_{EF} \simeq I_p\left(2.5 + \beta_p\right) , \qquad \beta_p << \beta_p^{max} \tag{9}$$

together with Eqs. (1), (2), and (8) gives the dependence of V_{EF} on V_{OH} and $\dot{\beta}_p$:

$$V_{EF} = C\left[V_{OH} - R_p I_p\right] + \frac{d\beta_p}{dt}\left[CM_{EF,p} + L_3\right] I_p , \tag{10}$$

where

$$C = \frac{L_{EF}\left(2.5 + \beta_p\right) - M_{EF,p}}{L_p - M_{OH,p} - M_{EF,p}\left(2.5 + \beta_p\right)} \approx 1 .$$

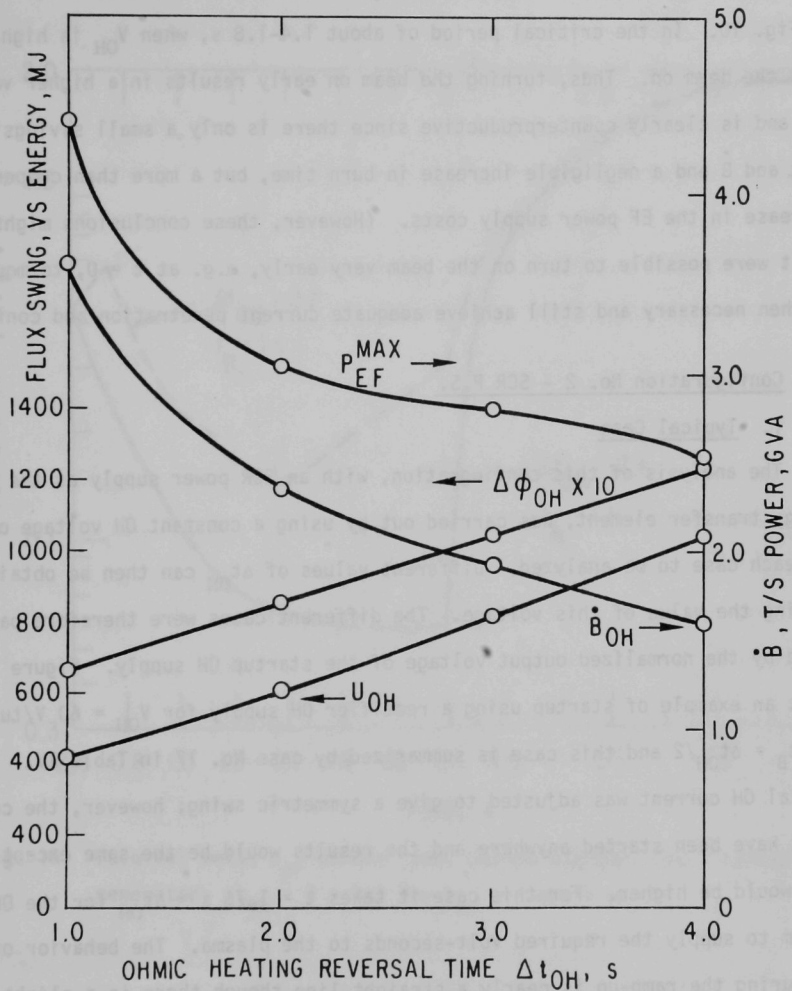

Fig. 9. Sensitivity of the driving system requirements to the ohmic heating ramp time, Δt_{OH}. For a homopolar generator used as the OH energy transfer device and for the neutral beam turn-on time, $t_{B_0} = \Delta t_{OH}/2$.

The second term in Eq. (7) represents the contribution to the required EF voltage arising from a change in β_p. A comparison of the effect on β_p versus t of the two modes of beam operation, for a reversal time of 2 s, is shown in Fig. 10. In the critical period of about 1.4-1.8 s, when V_{OH} is high, $\dot{\beta}_p > 0$ with the beam on. Thus, turning the beam on early results in a higher value of V_{EF} and is clearly counterproductive since there is only a small savings in OH cost and $\dot{B}$ and a negligible increase in burn time, but a more than compensating increase in the EF power supply costs. (However, these conclusions might change if it were possible to turn on the beam very early, e.g. at t = 0, to modulate it when necessary and still achieve adequate current penetration and confinement.)

B. Configuration No. 2 - SCR P.S.

1. Typical Case

The analysis of this confiugration, with an SCR power supply as the OH energy transfer element, was carried out by using a constant OH voltage output for each case to be analyzed. Different values of Δt_{OH} can then be obtained by varying the value of this voltage. The different cases were therefore parametrimized by the normalized output voltage of the startup OH supply. Figure 11 shows an example of startup using a rectifier OH supply for V_{OH} = 60 V/turn and for $t_B = \Delta t_{OH}/2$ and this case is summarized by case No. 17 in Table IV. The initial OH current was adjusted to give a symmetric swing; however, the current could have been started anywhere and the results would be the same except that P_{OH}^{max} would be higher. For this case it takes t = 1.75 s = Δt_{OH} for the OH system to supply the required volt-seconds to the plasma. The behavior of I_{OH} during the ramp-up is nearly a straight line though there is a slight deviation due to the back EMF from the plasma current. The neutral beam is turned on at $t_{B_0} = \Delta t_{OH}/2$ = 0.85 s and off at about 7.2 s. An abrupt change in the slope of I_p is noticeable at t = t_{B_0} when the plasma starts to heat rapidly and

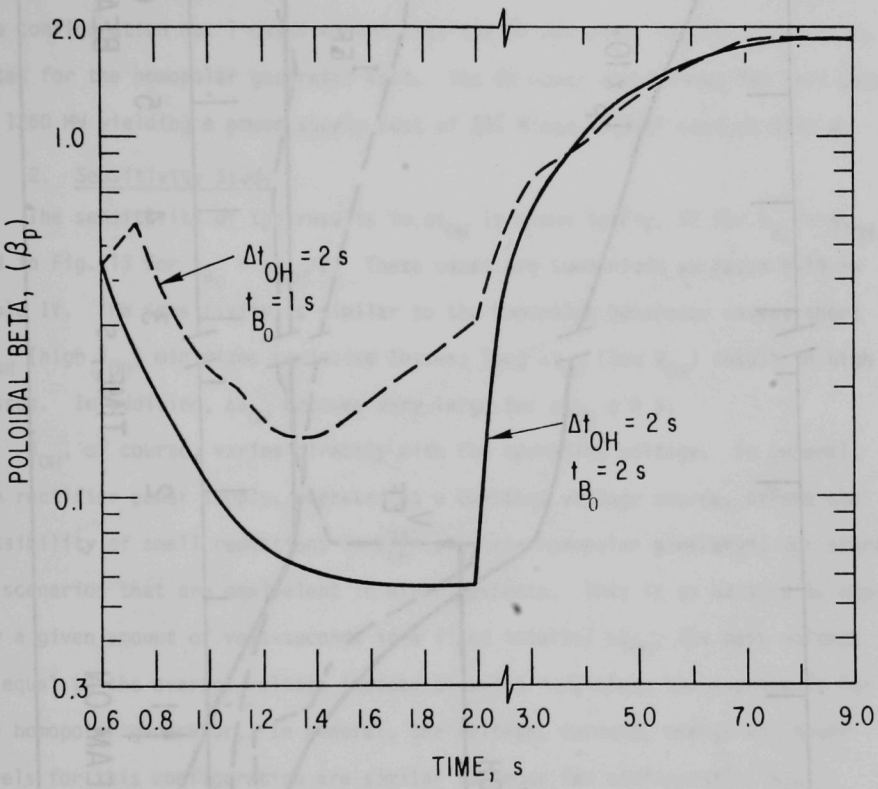

Fig. 10. Poloidal beta, β_p, versus time, during startup, for a homopolar generator; Δt_{OH} = 2 s and for t_{B_0} = 1 and 2 s.

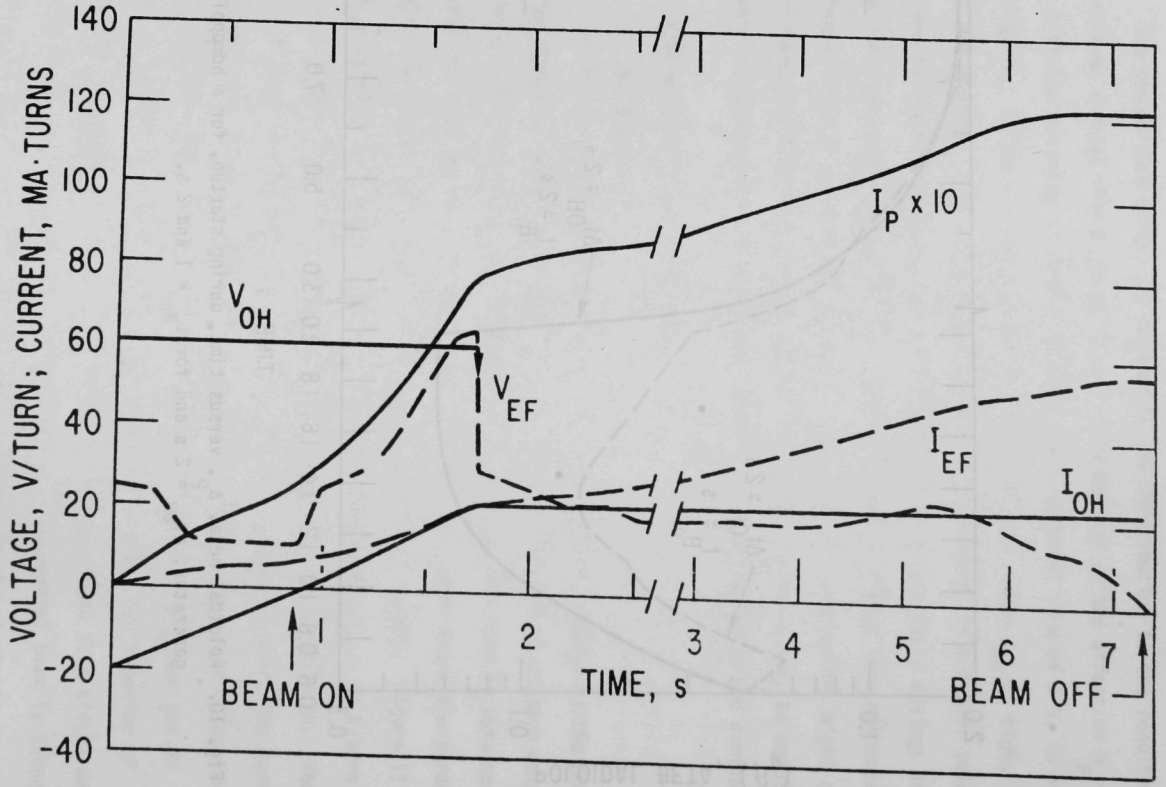

Fig. 11. Typical startup, using an SCR-type power supply as the OH transfer element; V_{OH} = 60 V/turn, $t_{B_0} = \Delta t_{OH}$.

and resistive losses decrease, and at $t = \Delta t_{OH}$ when the OH voltage is removed. V_{EF} peaks at $t = \Delta t_{OH}$ when I_p is at a maximum. The behavior after $t = \Delta t_{OH}$ is basically similar to the homopolar generator cases.

The driving system cost for this case is computed in a similar manner to the configuration No. 1 cases except that the OH SCR power supply cost substitutes for the homopolar generator cost. The OH power requirement for this case is 1260 MW yielding a power supply cost of $35 M and a total cost of $159 M.

2. Sensitivity Study

The sensitivity of the results to Δt_{OH} is shown in Fig. 12 for $t_{B_0} = \Delta t_{OH}$ and in Fig. 13 for $t_{B_0} = \Delta t_{OH}/2$. These cases are summarized as cases 9-19 in Table IV. The sensitivity is similar to the homopolar generator cases; short Δt_{OH} (high V_{OH}) minimizes resistive losses; long Δt_{OH} (low V_{OH}) result in high losses. In addition, $\Delta\phi_{OH}$ becomes very large for $\Delta t_{OH} \gtrsim 4$ s.

$\dot{B}_{OH}$, of course, varies directly with the operating voltage. In general, the rectifier power supply, operated as a constant voltage source, offers the possibility of small reductions in $\dot{B}_{OH}^{max}$ over the homopolar generator, for start-up scenarios that are equivalent in other respects. This is so because to supply a given amount of volt-seconds in a fixed interval Δt_{OH}, the peak voltage is equal to the average voltage instead of being $\approx\pi/2$ times the average as for the homopolar generator. In general, the voltage, current, energy and power levels for this configuration are similar to those for configuration No. 1. The costs for the EF supply and the ESI are likewise similar but the range of cost of the OH supply is substantially higher than the range for the homopolar generator. The lowest OH supply costs are obtained by turning on the beam early but then the increasing EF costs compensate. There appears to be a very slight saving over the cheapest case with $t_{B_0} = \Delta t_{OH}/2$, i.e. case No. 18 in comparison with the cheapest case with $t_{B_0} = \Delta t_{OH}$, i.e. case No. 13. However, this

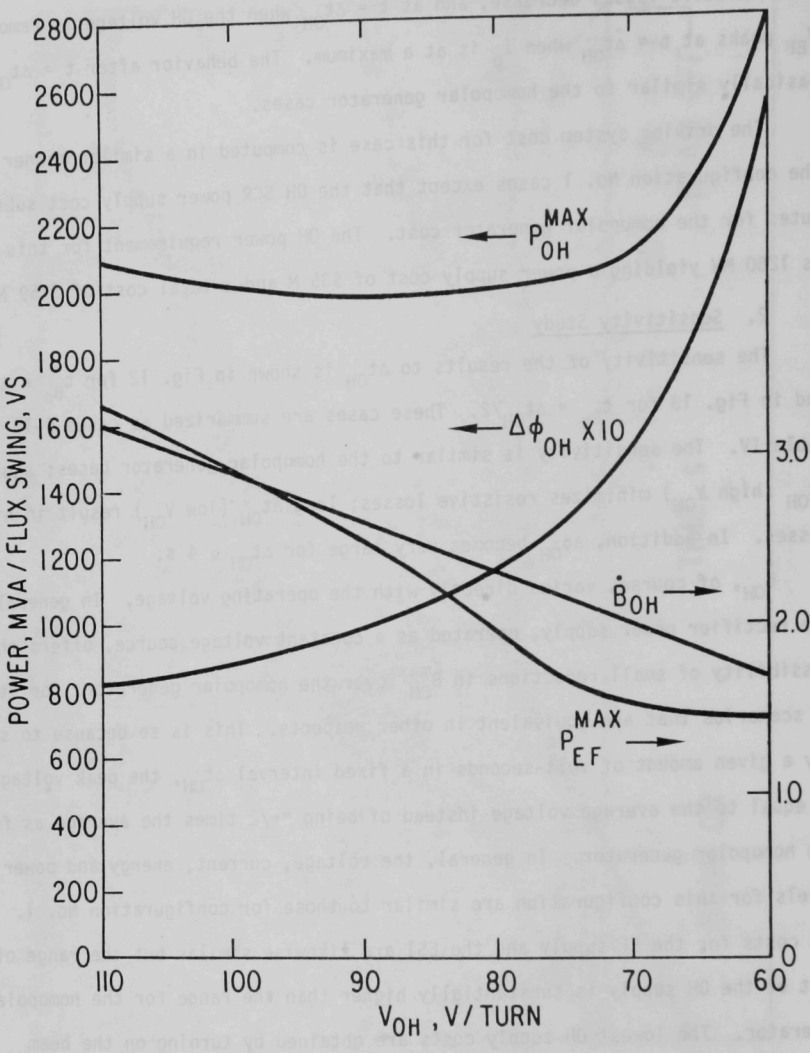

Fig. 12. Sensitivity of the driving system requirements to the flat-top OH voltage. For a constant voltage SCR-type power supply used as the OH energy transfer device and for $t_{B_0} = \Delta t_{OH}$.

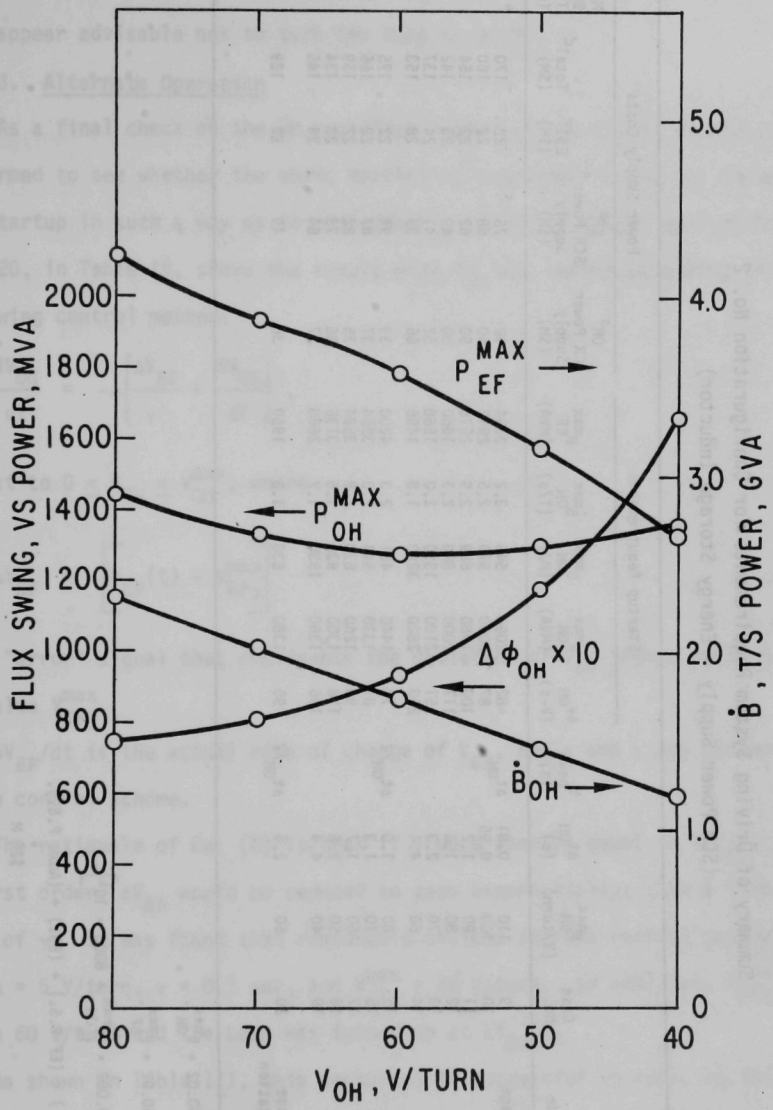

Fig. 13. Sensitivity of the driving system requirements to the flat-top OH voltage. For a constant voltage SCR-type power supply used a the OH energy transfer device and for $t_{B_0} = \Delta t_{OH}/2$.

TABLE IV

Summary of Driving System Requirements for Configuration No. 2
(SCR Power Supply - Energy Storage Inductor)

Operating Mode	Case No.	V_{OH}^{max} (V/turn)	Δt_{OH} (s)	t_{beam} (s)	Startup Requirements: $\Delta\phi_{OH}$ (V-s)	P_{OH}^{max} (MVA)	U_{OH}^{max} (MJ)	$\dot{B}_{OH}^{max}$ (T/s)	P_{EF}^{max} (MVA)	Power Supply Costs: OH[a] SCR Power Supply ($M)	EF[b] SCR Power Supply ($M)	ESI[c] ($M)	Total[d] ($M)	Max. Burn Time (min)
Constant OH voltage during reversal	9	110	0.81	Δt_{OH}	82	2090	546	3.2	3304	52	76	22	170	31
	10	100	0.96		87	2000	579	2.5	2912	50	68	22	160	30
	11	90	1.2		100	1980	689	2.9	2576	50	62	22	154	30
	12	80	1.6		117	2000	888	2.3	1960	50	49	23	142	28
	13	70	2.3		151	2100	1350	2.0	1568	52	41	24	137	26
	14	60	4.4		253	2820	3280	1.8	1456	66	39	28	153	19
	15	80	1.0	$\Delta t_{OH}/2$	74	1440	401	2.3	4200	39	94	22	175	31
	16	70	1.3		81	1330	544	2.0	3864	37	87	22	166	31
	17	60	1.7		93	1260	670	1.8	3584	35	82	22	159	30
	18	50	2.6		118	1300	936	1.5	3136	36	73	23	134	28
	19	40	4.4		166	1360	1530	1.2	2688	37	64	24	145	25
Variable OH voltage using V_{EF} minimization algorithm	20	60	2.6	$\Delta t_{OH}/2$	99	1380	633	1.8	1960	38	49	22	129	30

[a] Cost = \$10 M + \$0.02 × P_{OH}^{max}.

[b] Cost = \$10 M + \$0.02 × P_{EF}^{max}.

[c] Cost = \$5 M + \$0.002 × $\left[U_{OH}^{max} + 8000 \times 10^6\right]$.

[d] Total = (OH P.S.) + (EF P.S.) + (ESI) + (Aux. P.S.).
↓
\$20 M

the resulting increase in uncertainty in the plasma physics. It would therefore appear advisable not to turn the beam on early.

3. Alternate Operation

As a final check on the OH rectifier method of operation, an analysis was performed to see whether the ohmic heating voltage could be varied throughout the startup in such a way as to minimize P_{EF} and still obtain good performance. Case 20, in Table IV, shows the result when V_{OH} was varied according to the following control method:

$$\frac{dV_{OH}}{dt} = -\alpha\left(\frac{\Delta V_{EF}}{\gamma} + \frac{dV_{EF}}{dT}\right), \tag{11}$$

subject to $0 \leq V_{OH} \leq V_{OH}^{max}$, where

$$\Delta V_{EF} = \left[V_{EF}(t) - V_{EF_0}^{max}\right] \tag{12}$$

is an "error" signal that represents the deviation of V_{EF} from a desired maximum value $V_{EF_0}^{max}$.

dV_{EF}/dt is the actual rate of change of V_{EF}, and α and γ are parameters of the control scheme.

The rationale of Eq. (8) is that if γ were exactly equal to $\partial V_{EF}/\partial t$, then to first order, ΔV_{EF} would be reduced to zero exponentially, with a time constant of γ. It was found that reasonable choices for the control parameters were α = 5 V/turn, γ = 0.1 sec, and $V_{EF_0}^{max}$ = 30 V/turn. In addition, $V_{EF_0}^{max}$ was set to 60 V/turn and the beam was turned on at $\Delta t_{OH}/2$.

As shown in Table III, this technique is successful in reducing the combined power supply costs to the lowest of any associated with configuration No. 2 (cases 9-19) while still giving an acceptable burn time and $\dot{B}$. However, even the resulting cost of $129 M is higher than is obtainable with a homopolar

generator. It is also not clear how well such a control scheme, Eqs. (11) and (12), could be implemented.

C. Configuration No. 3

The simulation of this configuration is identical to that of configuration No. 2. The only thing that changes is that the MGF set replaces the ESI in the cost computation. The resulting cases 9b-20b are the analog of cases 9-20 and are shown in Table IV. As shown, the MGF set in configuration No. 3 cost turns out to be much more expensive than the ESI cost in configuration No. 2 and so the total driving system cost is considerably greater.

D. Configuration No. 4a - Single Dump Resistor

The motivation of using a resistor as the OH transfer device is to enable use of the full potential OH flux swing by starting the OH current at its maximum (negative) value, i.e. corresponding to a field of $B_{OH} = -8$ T. This could potentially be done with a homopolar generator or a rectifier power supply, by use of the same sort of switch arrangement as configuration No. 4 but then the cost of the transfer devices would be prohibitive, compared to the resistor. When the resistor is connected to the OH coil it forms an equivalent R-L circuit; the resistor dissipates magnetic energy as heat, and the current decays. Since only one polarity of the OH current can be used, the use of a dump resistor is restricted to situations where enough flux is available in one direction to support startup. (This consideration would exclude the use of a resistor for an EPR device, also the energy dissipated in the resistor would make the production of net power almost impossible for the short burn cycle of an EPR.) By changing the value or R, Δt_{OH} can be varied. For convenience the cases involving a dump resistor have been parameterized by the maximum voltage $|V_{OH}| = |I_{OH}(0)|R_{OH}$ that would appear across the OH coil and a range of values of V_{OH} has been analyzed.

TABLE V

Summary of Driving System Requirements for Configuration No. 3
(SCR Power Supply - MGF Set)

Operating Mode	Case No.	V_{OH}^{max} (V/turn)	Δt_{OH} (s)	t_{B_0} (s)	Startup Requirements: $\Delta\phi_{OH}$ (V-s)	P_{OH}^{max} (MVA)	$\dot{B}_{OH}^{max}$ (T/s)	P_{EF}^{max} (MVA)	Power Supply Costs: OH[a] SCR Power Supply ($M)	EF[b] SCR Power Supply ($M)	MGF[c] ($M)	Total[d] ($M)
Constant OH voltage during reversal	9b	110	0.81	Δt_{OH}	82	2090	3.2	3304	52	76	118	266
	10b	100	0.96		87	2000	2.5	2912	50	68	108	246
	11b	90	1.2		100	1980	2.9	2576	50	62	101	233
	12b	80	1.6		117	2000	2.3	1960	50	49	89	208
	13b	70	2.3		151	2100	2.0	1568	52	41	83	196
	14b	60	4.4		253	2820	1.8	1456	66	39	96	221
	15b	80	1.0	$\Delta t_{OH}/2$	74	1440	2.3	4200	39	94	123	276
	16b	70	1.3		81	1330	2.0	3864	37	87	114	258
	17b	60	1.7		93	1260	1.8	3584	35	82	107	244
	18b	50	2.6		118	1300	1.5	3136	36	73	99	228
	19b	40	4.4		166	1360	1.2	2688	37	64	91	212
Variable OH voltage using V_{EF} minimization algorithm	20b	60	2.6	$\Delta t_{OH}/2$	99	1380	1.8	1960	38	49	77	184

[a] Cost = \$10 M + \$0.02 × P_{OH}^{max}.

[b] Cost = \$10 M + \$0.02 × P_{EF}^{max}

[c] Cost = \$10 M + \$0.02 × $\left[P_{OH}^{max} + P_{EF}^{max}\right]$.

[d] Total = (OH P.S.) + (EF P.S.) + (MGF set) + (Aux. P.S.).
↓
\$20 M

1. Typical Case

Figure 14 shows the waveforms for the case of $|V_{OH}|^{max}$ = 115 V/turn and $t_B = \Delta t_{OH}$ and this case is summarized as case 25 in Table VI. I_{OH} is started at -90 MA-turns, corresponding to B_{OH} = -8 T. Both V_{OH} and I_{OH} show, to first order, the exponential decay characteristic of a conventional L-R circuit. By t = 1.5 s = Δt_{OH}, the proper amount of volt-seconds has been delivered. At this time, therefore, the resistor is removed from the circuit. To reiterate this process, the shorting switch is closed, thereby reducing V_{OH} to 0 and terminating the OH current decay. The resistor is then switched out and the auxiliary power supply switched in. The shorting switch is then opened completing the process. The shorting switch must handle a maximum current of 90 MA-turns and must isolate against a maximum voltage of 115 V/turn for a maximum reactive power capability of 10,350 GVA. Using the cost algorithm of 0.8¢/VA, the switch cost is computed to be $82 M. The cost of the resistor, at $0.6 M is negligible in comparison. The other features of the startup are similar to those for the other configurations except that V_{EF} peaks at t = 0, when V_{OH} is maximum. The value of V_{EF}^{max} is also more than for the other configurations. Another difference is that energy is dissipated in the resistor, a total of 8071 MJ for this case, instead of being returned to the OH coil. This is probably not significant, at least for long burn pulses, since it represents only 8-s worth of output from the reactor.

The advantage of the dump resistor is evident from Fig. 10; at the end of the startup I_{OH} is much lower than for the other transfer devices. The OH coil can therefore swing through much more flux, nearly double that for the other devices. This gives a maximum burn time capability of 57 min, for this case. Thus, the major advantage of using a dump resistor is to achieve a much longer burn time for a given B_{OH}^{max}.

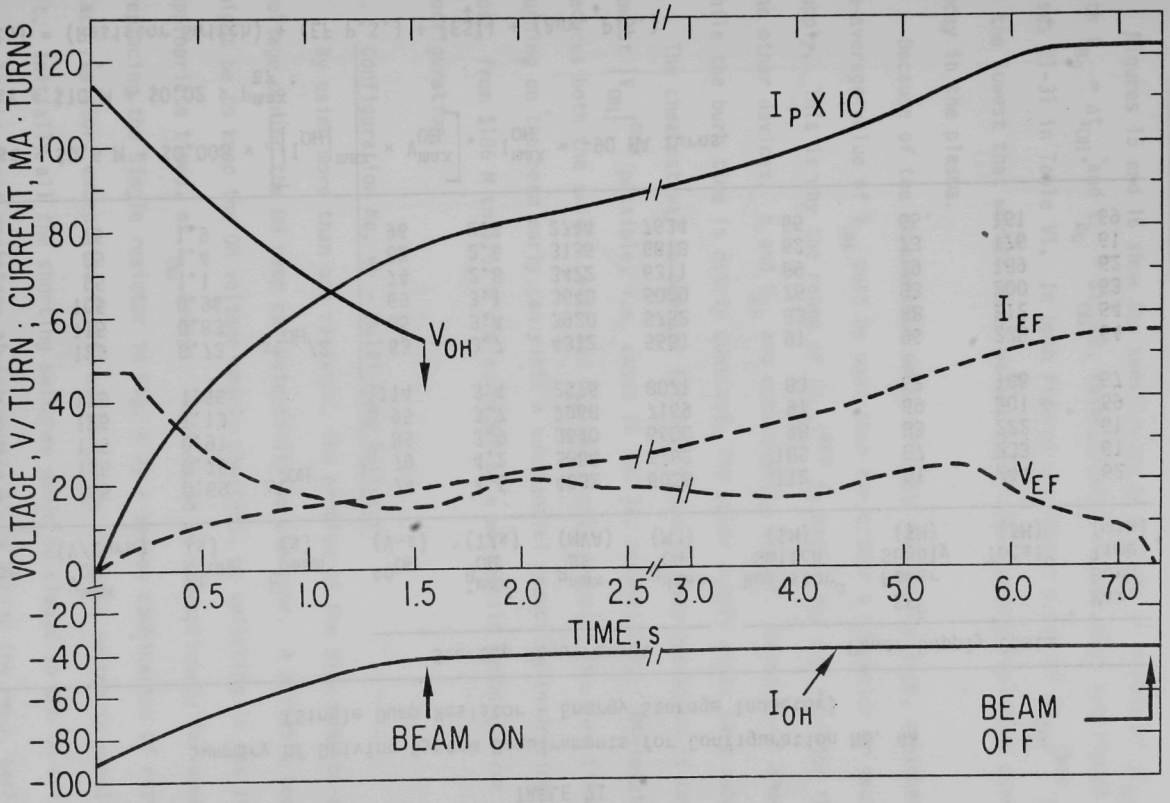

Fig. 14. Typical startup using a dump resistor as the OH transfer element; V_{OH}^{max} = 115 V/turn, $t_{B_0} = \Delta t_{OH}$.

TABLE VI

Summary of Driving System Requirements for Configuration No. 4a
(Single Dump Resistor - Energy Storage Inductor)

				Startup Requirement				Power Supply Costs			
Case No.	V_{OH}^{max} (V/turn)	Δt_{OH} (s)	t_{beam} (s)	$\Delta\phi_{OH}$ (V-s)	$\dot{B}_{OH}^{max}$ (T/s)	P_{EF}^{max} (MVA)	U_{OH}^{diss} (MJ)	Resistor[a] Switch ($M)	EF[b] Power Supply ($M)	Total[c] ($M)	Max. Burn Time (min)
21	155	0.69	Δt_{OH}	74	4.5	4032	6028	112	91	244	62
22	145	0.78		79	4.2	3864	6282	105	87	233	61
23	135	0.91		85	3.9	3640	6600	98	83	222	61
24	125	1.13		95	3.7	2968	7169	91	69	201	59
25	115	1.55		114	3.4	2576	8071	83	62	186	57
26	125	0.73	$\Delta t_{OH}/2$	63	3.7	4312	5581	91	96	228	64
27	115	0.83		65	3.4	3920	5752	83	88	212	64
28	105	0.96		69	3.1	3640	6000	76	83	200	63
29	95	1.1		74	2.8	3472	6311	69	79	189	62
30	85	1.4		82	2.5	3136	6818	62	73	176	61
31	75	1.9		96	2.2	2744	7634	55	65	161	59

[a] Cost = \$0.6 M + \$0.008 × $\left[\left|I_{OH}\right|^{max} \times V_{OH}^{max}\right]$, I_{OH}^{max} = -90 MA turns.

[b] Cost = \$10 M + \$0.02 × P_{EF}^{max}.

[c] Total = (Resistor Switch) + (EF P.S.) + (ESI) + (Aux. P.S.).
(ESI) → \$21 M; (Aux. P.S.) → \$20 M

2. Sensitivity Study

Figures 15 and 16 show the sensitivity to a range of values of $|V_{OH}|^{max}$ with $t_{B_0} = \Delta t_{OH}$ and $t_{B_0} = \Delta t_{OH}/2$, respectively. These cases are listed in cases 21-31 in Table VI. In both figures the lowest value of $|V_{OH}|^{max}$ shown is the lowest that works; lower values result in complete resistive current decay in the plasma.

Because of the exponential decay of ohmic heating voltage, a higher peak-to-average value of V_{OH} must be used than for either a homopolar or rectifier supply. This is why the range of $|V_{OH}|^{max}$ is higher for the resistor than for the other devices. $\dot{B}$ and P_{EF} are consequently higher. Cases 21-31 show that while the burn time is nearly constant, the power supply costs vary substantially.

The cheapest way to operate for both modes of beam operation is to use the lowest $|V_{OH}|^{max}$ possible, i.e. cases 25 and 31, respectively. Minimizing V_{OH} reduces both the switch costs and P_{EF} while only reducing the burn time slightly. Turning on the beam early can yield a substantial reduction in driving system cost, from $186 M to $161 M and so might be a worthwhile technique for this configuration.

E. Configuration No. 4b - Multi-Dump Resistor

By using more than one resistor, the problem of the high peak-to-average voltage during the OH ramp can potentially be overcome. A suitable technique might be to keep the OH voltage nearly constant, by switching in resistors at appropriate times, as I_{OH} decays. This could be accomplished, for example, by replacing the single resistor in Fig. 4 by a series combination of resistors. Each resistor, except the first, would have a shorting switch in parallel with it. Initially all the shorting switches would be closed so the OH coil would see only the first resistor, at successive times during the ramp, each shorting switch would be opened, thereby placing the corresponding resistor in the

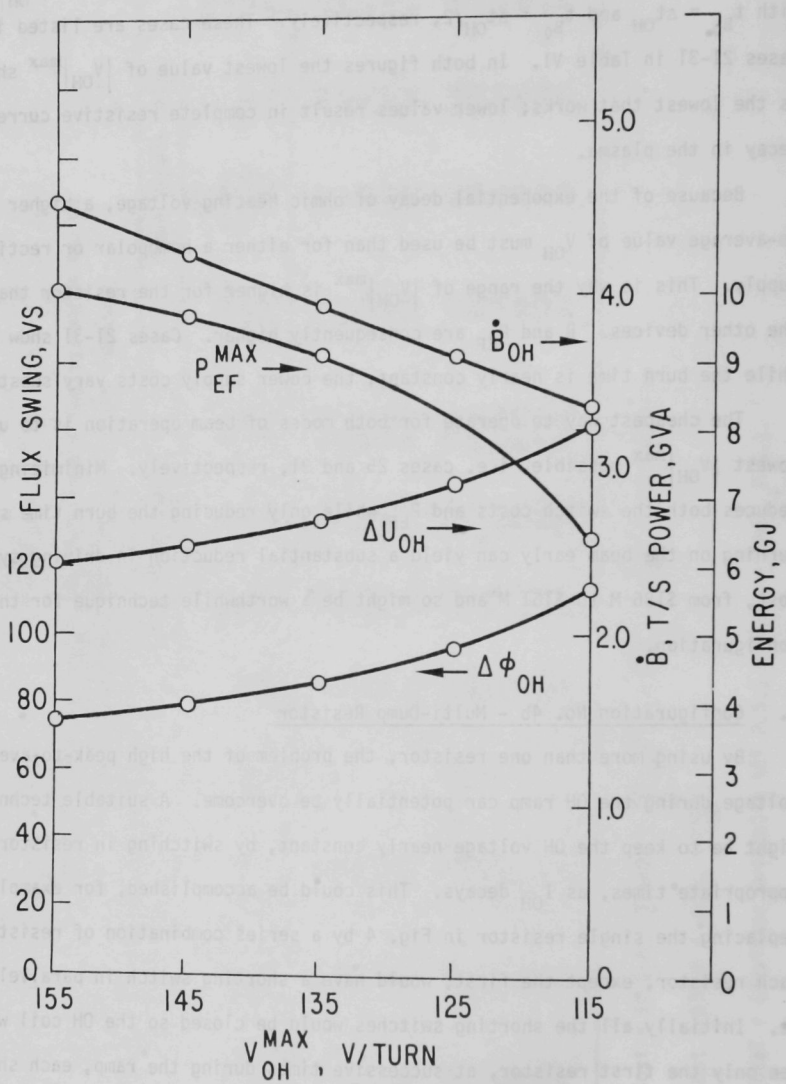

Fig. 15. Sensitivity of the driving system requirements to the maximum OH voltage. For a single dump resistor used as the OH transfer element and for $t_{B_0} = \Delta t_{OH}$.

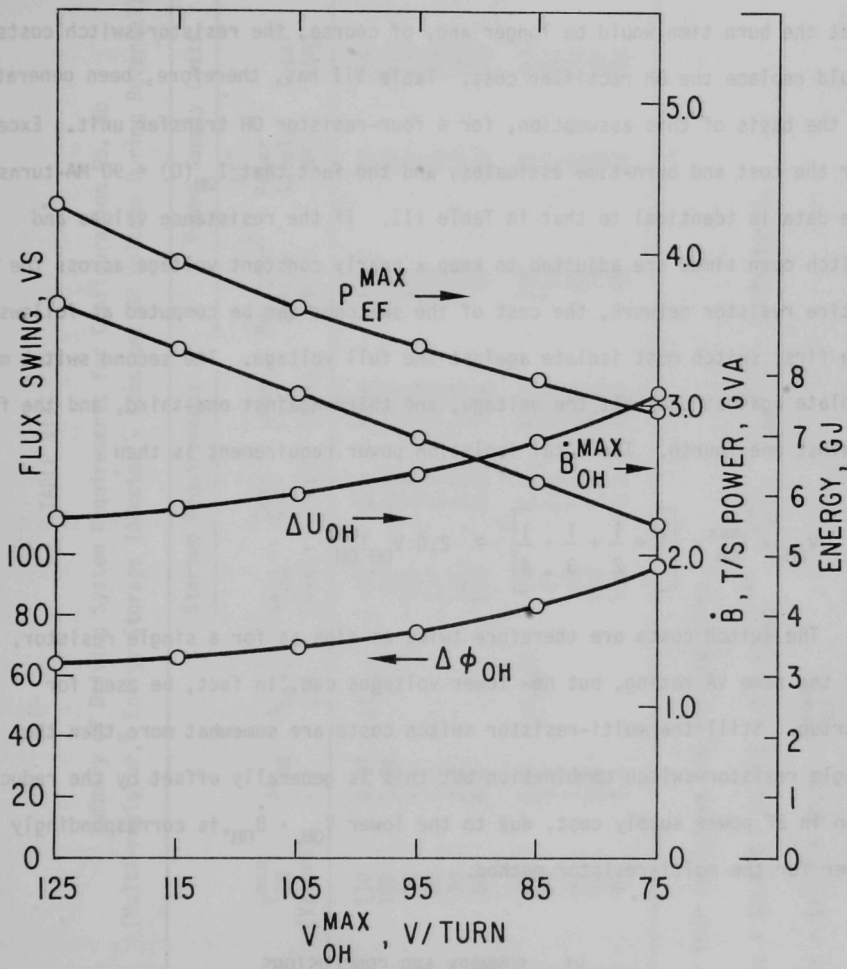

Fig. 16. Sensitivity of the driving system requirements to the maximum OH voltage. For a single dump resistor used as the OH transfer element and for $t_{B_0} = \Delta t_{OH}/2$.

circuit and increasing the total series resistance. The OH voltage could then be made nearly flat with small ripples. To the extent that V_{OH} could be made flat, the startup scenario for configuration No. 4b would be essentially similar to those for the constant voltage rectifier, cases 9-19 of Table II except that the burn time would be longer and, of course, the resistor-switch costs would replace the OH rectifier cost. Table VII has, therefore, been generated, on the basis of this assumption, for a four-resistor OH transfer unit. Except for the cost and burn-time estimates, and the fact that $I_{OH}(0)$ = 90 MA-turns, the data is identical to that in Table III. If the resistance values and switch open times are adjusted to keep a nearly constant voltage across the entire resistor network, the cost of the switches can be computed as follows: The first switch must isolate against the full voltage. The second switch must isolate against one-half the voltage, the third against one-third, and the fourth against one-fourth. The total isolation power requirement is then

$$V_{OH} \times I_{OH}^{max} \times \left[1 + \frac{1}{2} + \frac{1}{3} + \frac{1}{4}\right] \approx 2.0\ V_{OH} I_{OH}^{max} .$$

The switch costs are therefore twice as high as for a single resistor, for the same VA rating, but now lower voltages can, in fact, be used for startup. Still the multi-resistor switch costs are somewhat more than the single resistor-switch combination but this is generally offset by the reduction in EF power supply cost, due to the lower $V_{OH} \cdot \dot{B}_{OH}$ is correspondingly lower for the multi-resistor method.

VI. SUMMARY AND CONCLUSIONS

An analysis of the driving system requirements for a typical commercial fusion reactor has been performed. The reactor is an 8-M major radius tokamak

TABLE VII

Summary of Driving System Requirements for Configuration No. 4b
(Multi-resistor,[a] Energy Storage Inductor - Constant OH Voltage During Reversal)

				Startup Requirements			Power Supply Costs			
Case No.	V_{OH}^{max} (V/turn)	Δt_{OH} (s)	t_{beam} (s)	$\Delta\phi_{OH}$ (V-s)	$\dot{B}_{OH}^{max}$ (T/s)	P_{EF}^{max} (MVA)	Resistor[b] Switch ($M)	EF[c] Power Supply ($M)	Total[d] ($M)	Max. Burn Time (min)
9c	110	0.81	Δt_{OH}	82	3.2	3304	161	76	278	61
10c	100	0.96		87	2.5	2912	147	68	256	61
11c	90	1.2		100	2.9	2576	132	62	235	59
12c	80	1.6		117	2.3	1960	118	49	208	57
13c	70	2.3		151	2.0	1568	103	41	185	57
14c	60	4.4		253	1.8	1456	89	39	169	39
15c	80	1.0	$\Delta t_{OH}/2$	74	2.3	4200	118	94	253	62
16c	70	1.3		81	2.0	3864	103	87	231	61
17c	60	1.7		93	1.8	3584	89	82	212	60
18c	50	2.6		118	1.5	3136	74	73	188	57
19c	40	4.4		166	1.2	2688	60	64	165	50

[a]For four resistors and four switches.

[b]Cost = \$2.4 M + \$0.008 × 2 × $|I_{OH}|^{max} \times V_{OH}^{max}$, $|I_{OH}|^{max}$ = 90 MA-turns.

[c]Cost = \$10 M + \$0.02 × P_{EF}^{max}.

[d]Total = (Resistors-Switches) + (EF P.S.) + (ESI) + (Aux. P.S.).
(ESI) → \$21 M; (Aux. P.S.) → \$20 M

with a power output of 1000 MWe. The reactor has the conventional coil configuration of a central, solenoidal OH coil, and an EF coil externally located to the TF coil. Four different driving system power supply configurations have been examined as to their suitability for this reactor. The analysis used a plasma burn cycle dynamics code fully coupled to a driving system code. For each power supply configuration, a range of ohmic heating ramp times, Δt_{OH}, and neutral beam turn-on times, t_{B_0}, was simulated.

In general, feasible startup times for this reactor are about the same as for an EPR; OH reversal times of 1-4 s followed by a beam heating period of about 5 s. The $\dot{B}$ requirements on the OH coil are considerably less than for an EPR, basically due to the larger radius of the OH coil. The OH power and energy requirements are similar to an EPR but the EF requirements increase considerably. In general, there is a strong degree of coupling between the driving system requirements and the details of the plasma physics, particularly the temperature behavior and the MHD field requirements of the plasma.

Figure 17 summarizes the total driving system power supply cost as a function of the OH ramp time for the different configurations. This data has been generated by applying cost algorithms developed for the various hardware components to the technological requirements found by the burn cycle analysis. Figure 17 is for the case of the neutral beam turn turned on just after the OH ramp, generally the best operating mode. The cost of each configuration is extremely sensitive to the ramp time; this illustrates the need for a very precise and coupled analysis of the plasma and the driving system. In general, the cheapest operating point is the most cost effective.

All of the configurations studied use an SCR-type power supply for the EF system and for the auxiliary (burn-phase) OH supply but differ in the type of energy transfer device used in the OH system for startup and in the type of central energy storage device.

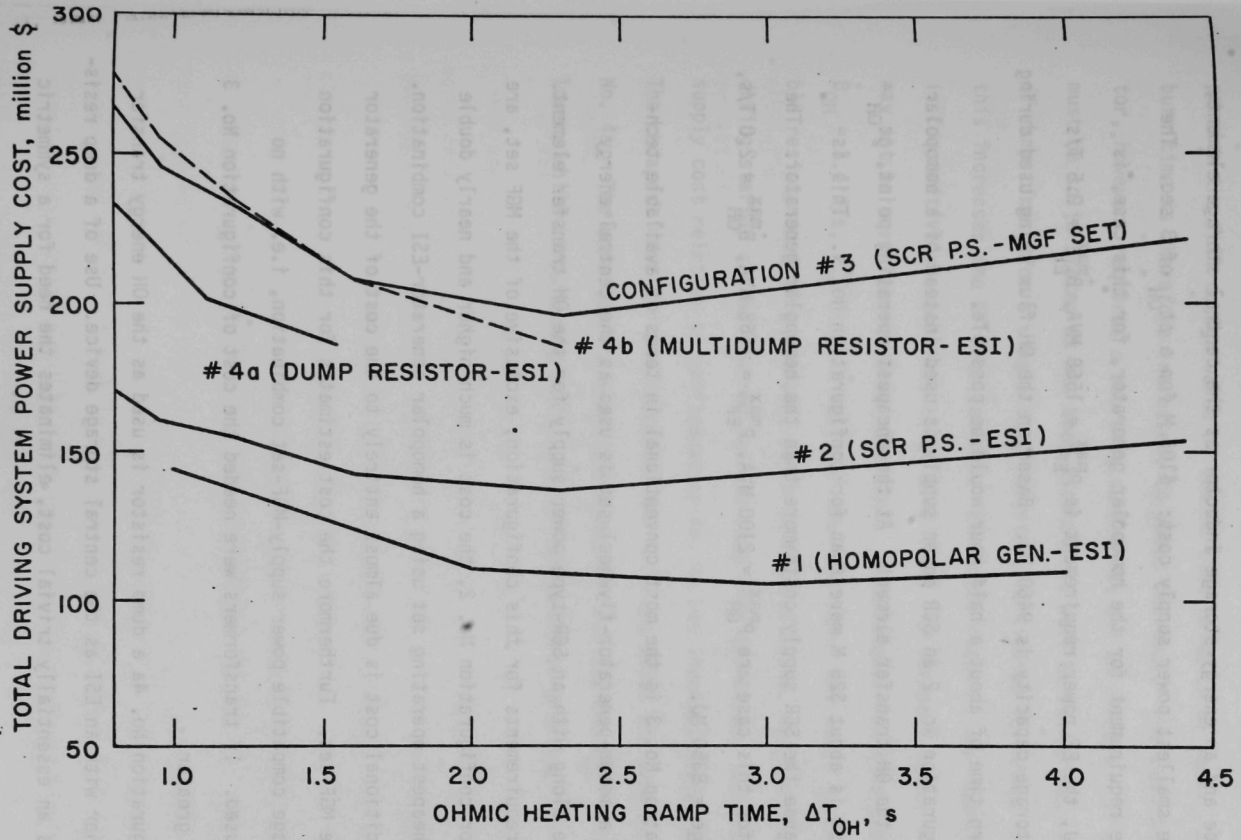

Fig. 17. Total driving system power supply cost as a function of the OH ramp time, Δt_{OH} and power supply configuration. For the neutral beam turn-on time, $t_{B_0} = \Delta t_{OH}$.

Configuration No. 1, which uses a homopolar generator for the OH energy transfer device and an energy storage inductor as the central storage element, results in the smallest power supply cost: \$105 M for a Δt_{OH} of 3 sec. The energy storage requirement for the homopolar generator, for this case, is U_{OH}^{max} = 1460 MJ, the EF power requirement is P_{EF}^{max} = 1568 MVA, $\dot{B}_{EF}^{max}$ = 2.5 T/s and the ESI storage capacity is 9460 MJ. Based on the OH flux swing used during startup, a burn time of about a half hour would be possible.

In configuration No. 2 an SCR power supply is used instead of a homopolar generator, as the OH transfer element. At the cheapest operating point, Δt_{OH} = 2.3 s, the cost is about \$25 M more than for configuration No. 1. This is basically because the SCR supply costs more than the homopolar generator. The requirements for this case are P_{OH}^{max} = 2100 MVA, P_{EF}^{max} = 1568 MVA, $\dot{B}_{OH}^{max}$ = 2.0 T/s, and ESI storage = 8350 MJ.

Configuration No. 3 is the most conventional in terms of available technology. Here a motor-generator-flywheel set is used as the central energy storage device along with an SCR-type power supply for the OH transfer element. Although the requirements for this configuration, exclusive of the MGF set, are the same as for configuration No. 2, the cost is much higher and nearly double that of the cheapest operating set using a homopolar generator-ESI combination. This large additional cost is due almost entirely to the cost of the generator portion of the MGF set. Furthermore the cost estimates for this configuration assume a voltage compatible power supply-MGF-set combination, i.e. with no transformers used. If transformers were needed the cost of configuration No. 3 would be even greater.

In configuration No. 4a a dump resistor is used as the OH energy transfer device, together with an ESI as the central storage device. Use of a dump resistor, which has an essentially trivial cost, eliminates the need for a symmetric

permits the full design value of the OH flux swing to be used. The potential burn time is therefore increased, to about one hour. The use of a dump resistor, however, requires a shorting switch in the OH circuit. If this switch must be solid state, as has been assumed, it will be expensive. Also, the range of ramp times, for a single dump resistor, is limited to fairly short times and this increases the EF requirements. For these reasons, configuration No. 4a is comparatively expensive, about $185 M for the cheapest case. This may or may not be worth the doubled burn time. Requirements for this case are $\dot{B}_{OH}$ = 3.4 T/s, P_{EF}^{max} = 2576 MVA. If four resistors are used, to obtain a variable resistance during startup, as in configuration No. 4b, the maximum OH voltage during startup can be lowered and the ramp time increased. This saves on EF supply cost relative to configuration No. 4a but involves higher switch costs. The cheapest case for configuration No. 4b costs about the same as configuration No. 4a. The burn time is about the same, $\dot{B}$ = 2.0 T/s and P_{EF}^{max} = 1568 MVA are lower, while circuit complexity and control would be greater.

APPENDIX

Cost Algorithms

The cost algorithms described here are based on current prices where the systems involved, such as MGF sets and ac-dc converters, are commercially available; otherwise they are based on best-guess estimates extrapolated from similar installations when possible.

Homopolar Generator

The cost is determined by the maximum required energy storage of the unit rather than peak power:

$$\text{Cost} = \$5\ \text{M} + \$0.01/\text{J}\ .$$

Homopolar generators of the type described in this report are not commercially available, and as a result any cost projections are based on predicted technical complexity and the construction of other equipment with similar complexity. The cost "figures" used in this report are about 60% higher than those used by Westinghouse[8] for the Reference Theta Pinch Reactor primarily because a higher voltage-type homopolar is assumed.

SCR-Type Power Supply

The cost is determined by the maximum power requirement:

$$\text{Cost} = \$10\ \text{M} + \$0.02/\text{V-A}\ .$$

The power supply operating out of an ESI is different than one operating off an MGF. The costs are predicted on the basis of the current costs of large ac/dc/ac conversion systems with about a 30% reduction because large power trans-

formers should not be needed. Of course, the same might be true for MGF sets which are voltage optimized to the coil system.

Dump Resistor

Cost = $0.6 M for each resistor used.

Superconducting Energy Storage Inductor

The cost is based on the maximum stored energy:

Cost = $5 M + $0.002/J .

ESI costs are based on extrapolation from existing large magnet systems, most of which were not designed as energy storage coils so the costs might be overstated. The estimates include all the cryogenic equipment and instrumentation.

MGF Set

The variable cost is primarily based on the maximum power requirement of the generator while the fixed cost includes the cost of the motor and flywheel:

Cost = $10 M + $0.02/V-A .

Switch Costs

For a mechanical switch the costs are basically trivial and have been included in the fixed cost portion of the other algorithms.

For the solid state switch used in connection with the dump resistor, the estimated cost is based on the maximum isolation voltage and maximum series current handled by the switch:

Cost = $0.008/V-A .

SCR switch costs used here are about one-fourth the cost per KVA of an ac/dc/ac convertor.

REFERENCES

1. W. M. STACEY, JR., ET AL., "EPR-77: A Revised Design for the Tokamak Experimental Power Reactor," Argonne National Laboratory, ANL/FPP/TM-77 (1977).

2. W. M. STACEY, JR., ET AL., "Experimental Power Reactor Conceptual Design Argonne National Laboratory, ANL/CTR-76-3 (1976).

3. W. M. STACEY, JR., ET AL., "Tokamak Experimental Power Reactor Studies," Argonne National Laboratory, ANL/CTR-75-2 (1975).

4. D. STEINER, ET AL., "ORNL Fusion Power Demonstration Study: Interim Report," ORNL/TM-5813 (1977).

5. F. E. MILLS, Ed., "Plasma Driving Systems for a Tokamak Experimental Power Reactor," in *Proc. Second ANS Top. Mtg. on Technology of Controlled Nuclear Fusion*, USERDA CONF-760935, Vol. IV, p. 1233.

6. J. N. BROOKS and W. M. STACEY, JR., "Driving Requirements for the Ohmic Heating and Equilibrium Coils of a Tokamak Experimental Power Reactor," in *Proc. Sixth IEEE Symp. on Engineering Problems of Fusion Research*, Nov. 18-21, 1975, San Diego, Calif., IEEE Pub. No. 75CH1097-5-NPS, p. 43.

7. M. ABDOU, ET AL., "Parameteric Systems Analysis for Tokamak Power Plants," Argonne National Laboratory, to be published.

8. "Design Studies of Reversible Energy Storage and Transfer Systems for the Reference Theta Pinch Reactor," Westinghouse Electric Co., Chesnick, Pa., Report No. E.M. 4620 (1974).

August 15, 1977 ANL/FPP/TM-92

RADIATION CONSIDERATIONS FOR SUPERCONDUCTING FUSION MAGNETS

Mohamed A. Abdou

Applied Physics Division
Argonne National Laboratory
Argonne, Illinois 60439

Invited Paper Presented at

"International Meeting on Radiation Effects on Superconductivity"
Argonne, Illinois, June 13-16, 1977

RADIATION CONSIDERATIONS FOR SUPERCONDUCTING FUSION MAGNETS*

Mohamed A. Abdou

Applied Physics Division
Argonne National Laboratory
Argonne, Illinois 60439

Abstract

Superconducting magnets are believed to be necessary for fusion power reactors. High flux levels of neutrons and seccondary gamma rays in these reactors require extensive radiation shielding to protect the components of the superconducting magnets from intolerable radiation damage and energy deposition. In this paper, radiation environment for the magnets is characterized for various conditions expected for tokamak power reactor operation. The radiation levels are translated into radiation effects using available experimental data. The impact of the tradeoffs in radiation shielding and the change in the properties of the superconducting magnets on reactor performance and economics is examined. It is shown that (1) superconducting magnets in fusion reactors will operate at much higher radiation level than was previously anticipated; (2) additional data on radiation damage is required to better accuracy than is presently available in order to accurately quantify the change in properties in the superconducting magnet components; and (3) there is a substantial penalty for increasing (or overestimating) the shielding requirements. Therefore there is a strong incentive to explore all important options that lead to lower radiation damage at a given radiation level.

Work supported by the U. S. Energy Research and Development Administration.

1. Introduction

Fusion reactors based on magnetic confinement employ a variety of magnets for initiating, driving, confining, and shaping the plasma. Many of these magnets are large in size and are required to provide a high field. Although fusion reactors appear to be viable with normal magnets, the development of superconducting magnets is believed to be necessary for these reactors on the grounds of better economics and reliability. Much of the energy liberated in a fusion reactor operated on the D-T or D-D cycle is carried away with neutrons. Therefore, knowledge of radiation effects in the components of superconducting magnets is of great importance to fusion reactor research and development.

The largest effort in the world fusion power reactor research and development program is devoted to tokamaks operated on the D-T cycle. The scope of this paper is limited to this class of reactors but many of the ideas can be extrapolated to other types of magnetic confinement reactors.

The need for radiation protection of superconducting magnets has been realized [1-5] by tokamak shield designers since the early stages of tokamak development. Attempts were made to derive tolerable radiation levels in superconducting magnets as a necessary step in arriving at a sound radiation shield design. Until recently there was a lack of information to permit quantifying the radiation effects in the components of the superconducting magnets. Refrigeration requirements were generally used as the limiting factor for shield design. The general guiding philosophy for shield designers was to reduce the radiation field at the magnet to the lowest possible level. Consequently, earlier iterations on tokamak reactor designs resulted in very thick radiation shields. Later, attempts were made to review the characteristics of the radiation environment in the superconducting magnets. Unfortunately, these reviews used the results of the earlier designs as a fixed target for tokamak reactors

and arrived at a misleading conclusion that radiation effects in the magnet were negligible.

At present, a second generation of tokamak reactor designs is evolving [6]. This second generation of designs is based on a better understanding of the trade-offs and interrelations within and among reactor components. In addition, codes are becoming available that allow parametric analyses and economic comparisons of a wide range of design parameters and options [7]. These studies show that the overall reactor performance and economics favor shields that are considerably thinner than those employed in earlier designs. Consequently, the radiation level in the superconducting magnets is one to two orders of magnitude higher than was generally assumed in previous studies. These results have identified a greater need for more accurate information on radiation effects in the components of superconducting magnets than is presently known.

The next section provides a brief review of tokamak reactor systems with emphasis on the interrelation between radiation shield and various types of magnets. Section 3 examines the results of trade-off studies pertinent to the shield design and radiation effects in superconducting magnets. In Section 4, radiation environment for the magnets is characterized for various conditions expected for tokamak power reactor operation.

2. Review of Tokamak Magnets and Shields

The purpose of this section is to briefly review the major features of tokamaks; particularly, the geometrical relationship between the radiation shield and the various types of magnets. Figures 1 and 2 show a perspective view and a vertical cross section of a typical tokamak reactor. The plasma is confined in a toroidal geometry with the cross section of the torus being circular, D-shaped, or doublet. In a D-T cycle, the fusion energy is liberated

as kinetic energy of 3.5 MeV α-alpha particles and 14.1 MeV neutrons. The plasma region is surrounded by a vacuum vessel (first-wall) that serves as the vacuum boundary for the plasma chamber. The first wall is surrounded by a blanket that converts the kinetic energy of the neutrons into heat. The blanket has lithium in one form or another for tritium regeneration. The magnet shield surrounds the blanket. The basic function of the magnet shield is to provide the radiation attenuation necessary for protection of the components of the toroidal-field magnets.

2.1 Types of magnets

The toroidal-field (TF) coils constitute the largest magnet system in a tokamak. These coils generate a strong steady-state toroidal magnetic field in the plasma region. The TF coils are closely packed on the inner side of the torus and the spacing between each pair of coils increases in the outward direction and reaches its maximum on the outside at the midplane. Each coil has a cross section that can be circular, oval or D-shaped. Constant tension D-shape is currently believed to be the most appropriate geometry for the TF coils. Tokamak operation requires a toroidal magnetic field at the plasma centerline of ∿4-8 T which corresponds to a maximum magnetic field at the coil windings of ∿7-14 T depending on the reactor design characteristics.

In addition to the toroidal-field coil system, tokamaks require a poloidal coil system. The poloidal coils vary in position and requirements but they have the common geometrical feature of being a concentric set of circles with the toroidal axis as the common axis. The ohmic heating (OH) coil system, a part of the poloidal coils, consists generally of a solenoid located inside the central core formed by the inner leg of the toroidal field coils and a number of smaller coils as indicated in figs. 1 and 2. The OH coils act as the primary of a transformer with the plasma as the secondary. Energizing the

primary side induces and drives a toroidal current in the plasma. The plasma current, in addition to providing for initial plasma heating, produces a pulsed poloidal magnetic field which together with the steady-state toroidal field confine the plasma. The pulsed OH coils can be normal or superconducting. It has been shown that a pulsed superconducting magnet is generally superior to a pulsed normal magnet unless the maximum field for a normal coil could be designed so as to be twice as high as the maximum field for a superconducting coil [8]. The OH coil system as described above and as shown in Figs. 1 and 2 is located outside the TF coil system. In this location, the winding configurations can be arranged so that the pulsing fields and the torques imposed on the TF coils are minimized. In addition, they receive less radiation than the TF coils do. However, another concept for tokamak reactor design has been proposed [9], in which the OH coils are located inside the bore of the TF coils. This concept is meritorius for several reasons but it causes the OH coils to be closer to the high radiation field.

A tokamak plasma requires a pulsed vertical field to provide control on the position of the plasma column. This field is provided by the equilibrium-field (EF) coils. Lower ampere-turn and better coupling to the plasma can be obtained by placing the EF coils in the blanket as close as possible to the first wall. However, the high radiation field and the high temperature make it difficult to design even normal copper coils for placement in the blanket. Much easier assembly, maintenance, and replacement of the EF coils can be accomplished by placing them outside the TF coils. Whether these coils can be normal or superconducting and whether they are in a severe or moderate radiation environment will depend on their location either inside or outside the TF coils. Detailed studies remain to be carried out to determine the best compromise for the location and type of the EF coils. Knowledge of radiation effects in

superconducting magnets provides an important contribution to these studies.

Tokamaks with Doublet plasma require field-shaping coils (F-coils) to actively shape the plasma [10] (see fig. 3). Because of the extensive shaping capability requirements on these coils they must be sufficiently close to the plasma. Moving the F-coils away from the plasma increases significantly the total current requirements. On the other hand, coils located in proximity to the first wall will be subjected to a very intensive radiation field which will certainly shorten considerably the useful lifetime of any type of magnet. All poloidal coils such as the F-coils that are located inside the toroidal-field coils are extremely difficult to repair and replace. This is particularly complicated by the fact that remote handling is a necessity. Normal, cryoresistive, and superconducting magnet options have been considered [10] for the F-coils. Operation of normal coils will involve large Joule heating losses but superconducting magnets will also require a high refrigeration power requirement for removal of nuclear energy deposition. Radiation effects in superconducting coils are very large but they are also of considerable concern for normal coils as well. Therefore, the best option for the type of F-coils is not clear yet. However, designing workable and maintainable F-coils with tolerable power losses in an intense radiation environment appears at present to be the most challenging engineering problem for Doublet tokamaks.

2.2 Material options for the magnets

The number of materials that have been proposed for superconducting fusion magnets is rather limited. These materials are discussed below to provide a guideline for priorities in experimental programs concerned with radiation effects in superconducting fusion magnets.

Both NbTi and Nb_3Sn have been proposed for the superconductor. NbTi is generally preferred because of its ductility but it has the disadvantage that

operated at much higher field but its brittleness cast some doubt on its viability as a superconductor in large magnets. The brittleness of Nb_3Sn dictates that the magnets be designed to a relatively low strain level of ~0.05 to 0.1%. At a low strain level, toroidal-field magnets with a peak field of 10-14 T are very thick and it becomes extremely difficult to design a workable OH coil system with a solenoid located in the central core [11]. It has been shown [6] that under these conditions tokamaks are best operated with NbTi superconductors in the range of 8-9 T. However, high-field superconductors such as Nb_3Sn remain as strong contenders for fusion magnets.

The toroidal-field magnet system in tokamaks has a tremendous amount of stored energy of $\sim 10^{10}$-10^{12} Joules. Therefore, it is necessary that these magnets be well protected and designed so that they do not quench. Cryostatically stable magnets are presently the preferred design option but intrinsically stable magnets have also been considered. Both copper and aluminum have been considered for the conductor stabilizer. Aluminum has a potential for lower intrinsic resistivity and magneto-resistance than for copper. In addition, the long-term radiation-induced activity in aluminum is much lower than that induced in copper. However, aluminum has a low yield stress and under some circumstances the resistivity increases excessively with strain. In addition, the radiation-induced resistivity in aluminum is approximately 2.5 times that in copper. At present, copper is assumed to be the preferred choice for near-term fusion magnets with aluminum as a very attractive long-term possibility.

Steel is generally considered to be the primary choice for structural material in the magnet. However, aluminum alloys have been considered as the structural materials in magnets that employ aluminum stabilizers.

A variety of insulators are required in the magnets. Up to the present, only organic insulators have been considered for the TF magnets because they exhibit the ductility required for large coil windings. As will be shown later in this paper, the low threshold for radiation damage in organic insulators result in significant economic penalty for tokamaks. The higher threshold for radiation damage in inorganic insulators makes them attractive for fusion magnets but their brittleness presents a very serious limitation on their practical use, particularly in large coils such as the TF magnets. All coils that have to be located inside the blanket/shield must be designed, however, to employ inorganic insulators as it appears very doubtful that organic insulators can withstand the harsh radiation environment in the blanket/shield for a reasonably long operation time.

2.3 Radiation shields

Figure 4 is a vertical cross section of a tokamak which is similar in many respects to fig. 2 but many of the engineering details are omitted to facilitate the following discussion. The sector of the blanket and shield on the inner side of the torus is normally called the inner blanket/shield. The rest of the blanket and shield on the top, bottom, and outer regions of the torus is referred to as the outer blanket/shield.

The inner blanket/shield occupies the high magnetic field region where space is at a premium. Therefore, the main objective of the design for the inner blanket/shield is to provide protection for the TF coils with the smallest possible thickness, Δ^{i}_{BS}, from the first wall to the magnet. One means of accomplishing this goal is to use very efficient shielding materials. A combination of stainless steel (SS) and/or tungsten and boron carbide (B_4C) has been found to be a reasonably good choice for this purpose [12,13]. In addition, it is essential that shielding requirements for the TF coils are not overestimated.

The next section presents results of the trade-offs concerned with Δ^{i}_{BS}.

The space restrictions are much less severe on the outer blanket/shield. The outer blanket incorporates the tritium breeding medium which generally results in lower attenuation efficiency than that in the inner blanket. Several materials have been proposed for use in the outer shield; e.g. lead, lead mortar, borated graphite, water, boron carbide, and nonmagnetic concrete. Combinations of two (high mass number and lighter material) or more of these materials provide good shielding compositions but they generally result in less attenuation efficiency than a mixture of stainless steel-boron carbide or tungsten-boron carbide generally employed in the inner shield. Therefore, the outer blanket/shield thickness, Δ^{0}_{BS}, is generally considerably greater than Δ^{i}_{BS} to provide the same level of radiation attenuation. In some design concepts, additional attenuation is provided for on the outside by further increase in Δ^{0}_{BS} in order to reduce the overall refrigeration power requirement in the TF magnets. Because of these considerations, toroidal-geometry, and the particular geometrical shapes of the TF magnets, the neutron and gamma-ray fluxes vary from one position to the other along the circumference (in the poloidal direction) of the TF magnets. The maximum fluxes in almost all designs occur in the midplane at the inner side of the torus at the inner layer of the magnet that is closest to the shield, i.e. the location marked A in fig. 4. Neutrons and secondary gamma rays are also attenuated within the magnet (e.g. along lines C-D and A-B in fig. 4) as the composition of the magnet (copper or aluminum and stainless steel) is a good radiation attenuator.

Tokamak reactors require that the blanket and magnet shield accommodate a variety of penetrations, including those for vacuum pumping, auxiliary heating, divertor, and maintenance access. Many of these penetrations are large open regions which extend from the first wall radially outward through the blanket/shield and between the TF coils. Figure 2 shows an example of penetrations for

neutral beams. These penetrations seriously affect the attenuation efficiency of the magnet shield and cause considerable radiation streaming into the toroidal and poloidal coils. Special penetration shields have to be designed to protect the magnets and other reactor equipment [14,15]. However, even fully shielded penetrations cause a considerable change in the characteristics of the radiation field within the magnets.

3. Radiation Shield/Superconducting Magnet Tradeoff

A very notable characteristic of a tokamak reactor is a strong and complex interface among reactor components. The interface between the toroidal field magnet and the radiation shield is particularly strong and involved. Understanding and accounting for this interface is extremely important for shield and magnet designers and those involved in information development for these reactor subsystems. This section delineates this interface and its important impact on the overall reactor performance.

A primary function of the blanket/shield system is to protect the superconducting toroidal-field coils from excessive radiation. The radiation level at the magnet depends on the composition and thickness of the blanket/shield. The problem of finding an effective shield composition has been examined in detail earlier [3,4,12] but the designer's choice is limited to available materials as well as engineering considerations. For the same shield composition, varying the shield thickness has many counteracting effects on the reactor performance and economics. The contradicting requirements on the shield thickness are discussed next as they demonstrate the large impact that radiation effects in superconducting magnets have on tokamaks. The discussion in this section should also clarify why the present generation of tokamak designs involve higher radiation levels at the magnets than those in earlier design generations.

3.1 *Motives for smaller shield thickness*

The power density in a tokamak can be written as

$$P \propto \beta_t^2 B_t^4 , \tag{1}$$

where β_t is the plasma kinetic-to-magnetic pressure ratio and B_t is the toroidal field strength at the center of the plasma. Thus, increasing B_t and/or β_t can result in significant increase in reactor power. Practical reactors operate with a power density of ~1 to 10 MW/m^3. The magnetic field strength required to obtain a power density in this range depends strongly on β_t. The plasma stability limit on β_t has not been established yet. Current investigation in the field of plasma physics indicates that β_t is likely to be in the range of 0.04 to 0.1. Therefore, the most desirable value for B_t is not certain at present. Tokamak reactor designs have considered B_t in the range 3-8 T.

A limit on B_t comes from technological constraints on the maximum practical magnetic field, B_m, at the TF magnet windings. The value of B_t depends upon B_m and upon the geometry according to

$$B_t = B_m \left(1 - \frac{1}{A} - \frac{\Delta_v}{R} - \frac{\Delta_{BS}^i}{R} \right) , \tag{2}$$

where A is the aspect ratio (typically 2.5-5), R is the major radius of the plasma torus (4-14 m), and Δ_v is the thickness of the scrape-off region between the plasma and first wall (0.1-0.5 m). The parameter Δ_{BS}^i is the distance in midplane on the inner side of the torus from the first wall to the TF coil windings. The largest portion of Δ_{BS}^i is occupied by the inner blanket/shield but it also includes maintenance clearance space, and the cryostat dewar, thermal and magnetic shield, and bobbin of the TF coils. The maximum toroidal field strength B_m is limited by the type of superconductors. Fields $B_m \lesssim 9$ T are

achievable with NbTi superconductors but at higher fields Nb_3Sn would be required.

Equations (1) and (2) show the importance of the inner blanket/shield thickness, Δ^i_{BS}. For a given B_m, increasing the blanket/shield thickness reduces the field in the plasma region and results in a significant decrease in the reactor power. Curve a in Fig. 5 shows the reactor power as a function of Δ^i_{BS} for a reactor with A = 2.5 and R = 8 m and blanket shield composition of SS/SS-B_4C. As can be observed from the graph, increasing Δ^i_{BS} from 0.8 m to 1.4 m reduces the power by roughly a factor of 2.

Another way to illustrate the importance of reducing the blanket/shield thickness on the inner side of the torus is to examine a reactor with a fixed aspect ratio, major radius, and magnetic field at plasma centerline. Under these conditions the reactor power output is fixed for the same plasma parameters. Two effects can now be noted if the blanket/shield thickness, Δ^i_{BS}, is increased:

(1) It is clear from eq. (2) that the maximum field, B_m at the TF windings increases. The cost of the TF magnet increases as $\sim B_m^2$.

(2) The thickness, Δ_m, of the TF magnet increases roughly as $\sim B_m$. If B_m exceeds $\sim$9 T then NbTi cannot be used and Nb_3Sn superconductor (or alternative) has to be employed. Because of Nb_3Sn brittleness the maximum permissible strain is a factor of $\sim$2 to 3 lower than that with NbTi. This dictates a large increase in the magnet thickness since Δ_m is inversely proportional to the design strain. As shown in figs. 1 and 2, a central support cylinder is required to take up the compressive force pushing the TF coils toward the tokamak axis. The thickness of the support cylinder, Δ_{sp}, increases as B_m increases. The flux core radius, r_v, for the OH coils is given by

$$r_v = R - r_w - \Delta^i_{BS} - \Delta_m - \Delta_{sp} , \quad (3)$$

where r_w is the minor radius of the first wall. Therefore, increasing Δ^i_{BS} increases also Δ_m and Δ_{sp} and results in significant reduction in r_v. The maximum ohmic heating field, B_{OH}, increases as r_v is decreased, $B_{OH} \sim 1/r_v^2$. Increasing B_{OH} increases the cost of the pulsed OH coils and more importantly the cost of the OH power supplies.

These effects are demonstrated numerically in figs. 6, 7, and 8. Shown in these figures are B_m, r_v, and B_{OH} as functions of Δ^i_{BS} for R = 6, 7, 8, and 9 m. In calculating these results NbTi magnets with a design strain of 0.2% were employed for $B_m \leq 9$ T and Nb_3Sn magnets with a design strain of 0.1% were used at higher fields. In all cases shown in these figures, the plasma is circular with an aspect ratio of 3 and a fixed neutron wall loading of 3 MW/m^2.

3.2 Motives for Larger Shield Thickness

All the effects discussed so far indicate very strong reasons for reducing the blanket/shield thickness. Magnet protection, on the other hand, requires increasing this thickness. The neutron flux, ϕ_m, at the inner TF coil winding is correlated to the neutron flux, ϕ_w, at the first wall by the approximate relationship

$$\phi_m = \phi_w e^{-\mu_{bs}\Delta^i_{BS}} , \quad (4)$$

where μ_{bs} is an effective attenuation coefficient which depends strongly on the material composition of the blanket/shield and for typical shielding materials it varies from $\sim$0.08 cm^{-1} to $\sim$0.14 cm^{-1}. From magnet protection viewpoint, it is desirable to use a large Δ^i_{BS}. This conflicts with the deletorius effects that an excessively large Δ^i_{BS} has on reactor performance and economics. Therefore, a prudent compromise on Δ^i_{BS}, and hence the operating radiation level at the magnet, has to be found. A crucial step for doing this is to accurately

quantify the performance and economics effects of radiation on the superconducting magnets. An attempt to perform this is made next.

Radiation damage to the magnets is particularly important in three areas: (a) effects on the individual magnet components under steady-state irradiation; (b) possible synergistic effects in large superconducting coils; and (c) any effects that may result from periodic magnet annealing. In general, no data exists at the present time to evaluate effects in (b) and (c). On the other hand, very useful, but limited experimental inforamtion are available with which to evaluate radiation effects in the magnet components. The components of concern are (1) the superconductor; (2) the normal (stabilizing) conductor; (3) insulators; and (4) structural materials.

We will now utilize the available experimental information on radiation effects in individual magnet components to examine their impact on the magnet and reactor performance and economics. Our concern here is not to survey and investigate radiation damage in magnets but rather is to study the implications of changes in crucial performance properties. The former is covered elsewhere in the *Proceedings* of this meeting.

3.2.1 Superconductor

It has been shown that high neutron fluences result in a change in the transition temperature T_c and the critical current density, J_c of superconductors. Furthermore, radiation effects in NbTi alloys are significantly different from those in the Nb_3Sn compounds. To focus this discussion, we will consider only the case of NbTi. For NbTi, the change in T_c is very small, and the irradiation-induced changes in J_c are quite sensitive to the metallurgical structure in the unirradiated material [16]. Results on the change in J_c have been reported in the literature as a function of neutron fluences. Figure 9 shows the neutron fluence, ϕt, in a NbTi superconductor as a function of the

inner blanket/shield thickness, Δ^i_{BS} for I_w = 1 and 30 MW-yr/m^2, where I_w, integral neutron wall loading, is the product of P_w, the neutron wall loading, and an operational time period, t_0. The composition of the blanket/shield is similar to that of fig. 5, i.e. stainless and boron carbide. The value of Δ^i_{BS} in this figure, and everywhere else in this paper, includes provision for 10% of the blanket/shield volume as void to account for a variety of cooling, clearance, and other engineering requirements in addition to a fixed 0.05-m vacuum gap generally required in the TF coils for thermal insulation.

Experimental results for the change in the critical current density of NbTi with neutron fluence up to 5×10^{22} m^{-2} can be approximated [17] as

$$J_c = J_{c0} e^{-\alpha\phi t} , \tag{5}$$

where J_{c0} is the unirradiated value for the critical current density and $\alpha = 3.5 \times 10^{-24}$ m^2.

Figure 9 shows three horizontal lines that are representative of the experimental results on the relative change in the NbTi critical current density, $\Delta J/J_c$ as a function of neutron fluences. As can be inferred from these results, no or little change in J_c occurs at fluences $\lesssim 10^{21}$ n/m^2. The decrease in J_c is moderate for fluences up to $\sim 3 \times 10^{22}$ n/m^2 where $\Delta J/J_c \sim -10\%$. At higher fluences, the decrease in J_c is relatively large for small increments in the neutron fluences.

The decrease in the critical current density can be accommodated by adding more superconductors to produce the same ampere-turn. This involves increasing the cost of the magnet but this increase can be offset by the benefits achievable when Δ^i_{BS} is reduced. Thus, the permissible decrease in the critical current density is not a fixed value but it is an economics problem that is amenable to optimization.

3.2.2 *Normal conductor*

Low-temperature irradiation of normal conductors serving as the stabilizers in superconducting magnets results in an increase in the electric resistivity. The experimental data of Brown, et al [18] were used to derive the following formula for radiation-induced resistivity in copper:

$$\rho_r = 3 \times 10^{-7}[1 - \exp(-563\ d)]\ \Omega\text{-cm}\ , \tag{6}$$

where the saturation resistivity for copper, ρ_s, is equal to 3×10^{-7} Ω-cm and d is the total number of atomic displacements. A displacement energy, E_d, of 40 eV was used for copper. The value of E_d has very little effect except through normalization of the numerical factor (563) in the exponent of the exponential term in the above equation. A similar expression can be derived for aluminum:

$$\rho_r = 8 \times 10^{-7}[1 - \exp(-366\ d)]\ \Omega\text{-cm}\ , \tag{7}$$

where the value of E_d for aluminum was taken as 26 eV. Figure 10 shows the maximum radiation-induced resistivity in copper as a function of the blanket/shield thickness, Δ^i_{BS}, for integral wall loadings, I_w, of 1 and 30 MW-yr/m^2. At small values of Δ^i_{BS}, the radiation-induced resistivity is equal to the saturation value and does not change when Δ^i_{BS} is increased up to ∿0.6 m for I_w = 30 MW-yr/m^2. Further increase in Δ^i_{BS} reduces ρ_r rather rapidly.

Cryogenic stabilization criterion requires that the heat transfer from the stabilized superconducting matrix must be sufficient to transfer the I^2R heat generated in the stabilizing material when a flux jump occurs, i.e.,

$$I^2\rho \leq aqP\ , \tag{8}$$

where I is the oeprating current in the stabilizer of a composite conductor which has gone normal, ρ is the total resistivity of the stabilizer, a is

the normal conductor cross-sectional area, q is the heat flux, and P is the cooled perimeter of the composite. The total resistivity ρ is given by

$$\rho = \rho_0 + \rho_m + \rho_r , \tag{9}$$

where ρ_0 is the intrinsic resistivity, ρ_m is the magnetoresistivity, and ρ_r is the radiation-induced resistivity.

The increase in the resistivity of the stabilizer can be accommodated without violating the cryostability condition by adding more stabilizer and modifying the conductor design [19]. This results in an increase in the magnet cost. This increase in cost can be compensated for by the economics gain achievable with smaller Δ^i_{BS}. Thus, the problem of radiation damage to the stabilizer is primarily an economics consideration.

3.2.3 Magnet anneal

The experimental observation that most of the radiation damage to the superconductor and stabilizer can be recovered by magnet annealing brings another important factor into the performance and economic tradeoffs. The neutron fluence at the magnet varies, of course, linearly with the irradiation period, t_0, or equivalently, the integral neutron wall loading, I_w, is proportional to t_0, for the same neutron wall loading, P_w. From the results shown in figs. 9 and 10, it can be seen that for the same radiation-induced change in the properties of the superconductor and stabilizer, reducing I_w (i.e. reducing t_0 for the same P_w) permits the selection of a significantly smaller Δ^i_{BS}. Thus, it is logical that tokamak reactor designs plan on periodic magnet annealing. However, there are other additional problems involved here. Magnet warmup and cooldown require that the power plant be shut down. The downtime involved results in a reduced capacity factor for the plant and an increased cost of energy, depending on the necessary downtime for magnet anneal. The

minimum time period required for magnet warmup and cooldown without inducing intolerable strains in large magnets has not been established yet. Preliminary estimates of approximately two to three months have been made but a detailed study is required to provide more definitive information. This study must also account for the accumulated effects, if any, resulting from repeating the magnet anneal several to tens of times during the plant lifetime (∿30 yr).

3.2.4 *Insulators*

Superconducting magnets employ a variety of electrical and thermal insulation. Organic insulators are believed to be necessary for large magnets since inorganic insulators are very brittle. There is a serious lack of irradiation data on insulators at low temperature [20]. It is known, however, that organic insulators are much less resistant to radiation damage than inorganic insulators. Furthermore, radiation damage in these insulators is irreversible. Therefore, the insulators in the TF coils must be designed to function properly for the lifetime of the plant, typically ∿30 yr. Figure 11 shows the maximum dose in the TF coil insulators as a function of Δ^{i}_{BS} at 30 and 300 MW-yr/m^2. Extrapolation of neutron irradiation data suggests dose limits of ∿10^8 rad and ∿10^9 to 5×10^9 rad for mylar and epoxy, respectively. (Regions indicated by the letters M and E in fig. 11.) Thus, the minimum Δ^{i}_{BS} is ∿1.0-1.3 m for epoxy, and ∿1.28-1.48 for mylar. Region I in fig. 11 shows that with radiation damage limits on inorganic insulators of ∿10^{12} to 5×10^{12} rad, the minimum Δ^{i}_{BS} is ∿0.5 to 0.8 m.

3.2.5 *Refrigeration requirements*

Another effect in the superconducting magnets that calls for a thicker shield is the refrigeration power required to remove the nuclear energy deposition since ∿300 W of electric power are required per watt of thermal input to

4°K refrigerators. Curve b in fig. 5 shows the net reactor power, i.e. the gross reactor power minus the power required to run the magnet refrigerators, as a function of Δ^i_{BS}. At $\Delta^i_{BS} \sim 0.45$ m, the reactor power is barely sufficient to run the refrigerators. At $\Delta^i_B \sim 0.8$ m half the reactor power is wasted on refrigeration requirements. At larger Δ^i_{BS}, the refrigeration power requirements decrease rapidly. The maximum net power occurs at $\Delta^i_{BS} \sim 0.91$ m. The value of Δ^i_{BS} at which the net power is maximum is not overly sensitive to reactor parameters but it depends greatly on the material composition of the shield. Examining curves a and b in fig 5, one finds that the maximum net power occurs when the fraction of the reactor electrical output spent on the refrigerators is ~1.5%. This is about a factor of 15 higher than the limit on refrigeration power suggested earlier in the literature [1-5].

3.3 Results of tradeoffs

An important conclusion to be made from the results shown above is that the design of the magnet shield in terms of material composition and thickness must evolve from a trade-off study for the particular system. A system program [7] for fusion power plants recently developed at Argonne National Laboratory (ANL) has built-in capabilities for performing this type of trade-off studies. This system program can parametrize performance and economic variables of all components in a tokamak power plant. All interrelations within and among reactor components are mathematically modeled into the program. For example, radiation levels at the magnet, as predicted by a neutronics model, are transformed into property changes of the magnet components, which are fully accounted for in the magnet design and hence the cost [11].

An extensive study of the tradeoffs in the magnet/shield design has been carried out using the ANL System Program. An example of the results is shown in fig. 12. This figure shows the cost of energy as a function of the inner

blanket/shield thickness for tokamaks with aspect ratio of 3, and neutron wall loading of 3 MW/m^2. The blanket/shield material composition is the same as that described earlier in this section (stainless steel-boron carbide) with the same provision for vacuum, engineering, and maintenance space. Results are shown for tokamaks with major radius R = 6, 7, 8, and 9 m. Annealing of the superconducting toroidal-field magnets was assumed to coincide with the first-wall replacement which occurs every 11.4 yr and requires downtime of 80 days. Niobium-titanium was employed for fields ≤ 9 T and Nb_3Sn was used for higher fields. The plant capacity factor, F, is 0.9. The reference parameters fixed for all cases in fig. 12 are shown in table 1.

The results in fig. 12 show that the minimum energy cost is obtainable with $\Delta^i_{BS} \sim 1$ m. The maximum values at the TF magnets for the radiation-related parameters at the optimum blanket/shield thickness are shown in table 2. The results of these parametric studies show that with the present information, superconducting magnets can tolerate neutron and gamma-ray fluxes of $\sim 10^{14}$ m^{-2}-sec^{-1}. Neutron and gamma-ray fluences of 5×10^{22} m^{-2} and 3×10^{22} m^{-2}, respectively can be expected. This level of radiation is much higher than has been predicted from earlier generations of tokamak designs that employed much thicker shields. At $\Delta^i_{BS} \sim 1$ m, the radiation-induced resistivity is $\sim 10^{-7}$ Ω-cm and the change in the NbTi critical current density is $\Delta J/J_c \sim -14\%$. Figures 9-11 show that radiation effects in the magnet are very sensitive to Δ^i_{BS} in the neighborhood of $\Delta^i_{BS} \sim 1$ m and $I_w = 30$ MW-yr/m^2. Therefore, there is a great demand for high accuracy on neutron and gamma-ray transport calculations, nuclear data, and radiation damage information in the superconducting magnet.

Additional interesting remarks can be made about the results in fig. 12. Increasing Δ^i_{BS} beyond the optimum value increases the cost of energy due to the larger capital cost when B_m and B_{OH} increase. The relative increase in the cost

of energy is more significant at smaller major radius, R. This can be readily explained by examining eq. (2) which shows that the ratio B_m/B_t increases as the ratio Δ^i_{BS}/R increases. In other words, the gradient of the TF field is steeper and the space on the inner side of the torus is more valuable for smaller-size machines. On the other hand, decreasing Δ^i_{BS} below the optimum value results in a dramatic increase in the cost of energy that is not overly sensitive to R. This increase in the cost of energy results from an increase in the refrigeration power requirements and an increase in the capital cost of the magnet to accommodate the increased radiation level at the magnet. The radiation level at the magnet is not sensitive to R when the neutron wall load is fixed.

Figure 13 shows the TF coil thickness as a function of Δ^i_{BS} for the same cases of fig. 12. For $\Delta^i_{BS} > 1$ m increasing Δ^i_{BS} increases the magnet thickness because of the increase in B_m (see fig. 6). The abrupt increase in the magnet thickness for R = 7 m and R = 8 m at $\Delta^i_{BS} \sim 0.9$ m and $\Delta^i_{BS} \sim 1.2$ m, respectively is due to the "switch" from NbTi to Nb_3Sn when B_m exceeds 9 T. The important observation to be made from fig. 13 is that for small values of Δ^i_{BS} the magnet thickness <u>increases</u> as Δ^i_{BS} is <u>decreased</u> despite the fact that B_m is smaller. The reason is primarily due to the additional amount of copper required at higher radiation level to compensate for the increase in ρ_r. A much smaller contribution to the increase in the magnet thickness comes from increasing the amount of superconductor to compensate for the decrease in J_c.

In carrying out the parametric study discussed above, we purposely assumed that all insulators will perform satisfactorily for the lifetime of the plant in all cases. However, table 3 shows the actual dose in the TF magnet insulators as a function of Δ^i_{BS} at the end of plant life of 30 yr. Shown also in the table is the cost of energy for R = 6 m. For the optimum shield, $\Delta^i_{BS} \sim 1$ m, the maximum dose in the insulator is 1.8×10^{10} rad. Therefore, TF insulators that can function properly up to that dose level are required in order to operate

tokamaks in economically optimum conditions. As mentioned earlier, radiation damage data on organic insulators at ~4°K are lacking. Extrapolation of irradiation data at higher temperatures show that mylar can be operated up to a dose of $\sim 10^8$ rad (region M in fig. 11) and that epoxy-base insulators can withstand higher doses of $\sim 10^9$-5×10^9 rad (region E in fig. 11). Table 3 shows that such limits would dictate the use of a thicker shield and result in higher costs of energy than what is achievable otherwise. Therefore, accurate low-temperature irradiation data for organic insulators is necessary. These results may prove the need for development of new ductile and more radiation-resistant insulators or new concepts for magnet design that can permit the utilization of inorganic insulators.

It should be recalled that the values of Δ^i_{BS} used in this section represent the actual physical distance from the first wall to the inner edge of the TF coil winding (location of maximum magnetic field) in the midplane. Thus, the dimension of Δ^i_{BS} includes not only the blanket/shield thickness but also the non-attenuating space for maintenance, clearance, and thermal-insulation vacuum gap. For $\Delta^i_{BS} \sim 1$ m, the net thickness of the blanket/shield based on theoretical density of the shield materials is only 0.87 m.

4. *Radiation Characteristics in Superconducting Magnets*

In the previous sections, typical characteristics of the radiation environments expected in tokamak superconducting TF magnets were given. The purpose of this section is to discuss in more detail the radiation levels and spectra at and within the tokamak magnets. It should be clearly noted that tokamak reactors are in a stage of active research and development. Present design concepts are continually revised and new ones are developed. Therefore, it is not possible to predict today all the specific features of the ultimate commercial tokamak power reactors that will prove the most attractive. To reach the goal of defining the most promising design point for a tokamak, a great deal of new knowledge has to

be acquired and extensive experimental and analytical information needs to be developed. This information should cover a wide range of variables and a broad spectrum for each variable. An example of such information is the quantitative radiation effects in superconducting magnets. In the previous section we derived, based on present knowledge, an optimum design point and defined the corresponding maximum radiation levels in the TF magnets. These levels should not be considered as the maximum required for new experimental and analytical information. Accurate inforamtion that extends to higher radiation levels is needed in order to quantify to a better accuracy all the tradeoffs in tokamak designs. Results presented below should be useful in defining the range of interest for radiation environment in superconducting magnets.

Figures 14-18 show the neutron flux and various radiation damage indicators in the elemental components of a TF magnet as a function of the spatial depth within the magnet. Prior to any specific discussion of these figures, one should note a few general rules about the absolute values and the spatial dependence of radiation-related parameters in the TF magnets. The maximum value of neutron and gamma flux, atomic displacement, gas production, or any other neutronics response rate in the magnet depends on (1) the material composition in the blanket shield; (2) Δ^{i}_{BS} and/or Δ^{0}_{BS}; and (3) the neutron wall loading. The results that we selected for presentation in these figures are based on the blanket/shield system that evolved from the tradeoff studies discussed in the previous section. The inner blanket/shield in this system consists of stainless steel and boron carbide with Δ^{i}_{BS} = 1 m. Variation of the neutronics response values in the magnet with Δ^{i}_{BS} can be easily inferred from results in the previous section. There is approximately an order of magnitude reduction in the maximum values at the TF magnet for every ~0.17 m increase in Δ^{i}_{BS}. Dependence of these values on the blanket/shield composition and specific design considerations is available in the literature (see

for example, ref. 12). All neutron and gamma-ray fluxes, reaction, atomic displacement, and nuclear heating rates, vary linearly with the neutron wall loading, P_w. Tokamaks will operate in the range of $P_w \sim 1\text{-}5$ MW/m^2. Time-integrated quantities such as atomic displacements and gas production are also linearly proportional to the operation time t_0, and hence they vary linearly with the integral neutron wall loading $I_w = P_w t_0 F$. The range of t_0 was discussed in the previous section. For radiation effects that can be recovered, a reasonable range for I_w = 5-50 MW-yr/m^2 and for irreversible radiation effects, the range of interest is I_w = 30-150 MW-yr/m^2. For convenience, fig. 14 is normalized to P_w = 1 MW/m^2 and figs. 15-18 are normalized to 1 MW-yr/m^2.

Figure 14 shows the total neutron flux and gamma-ray flux within the TF magnet. There is a factor of 10 reduction in every ~0.3 m. This attenuation factor depends on the amount of helium and vacuum space which was assumed here to be 15% of the magnet volume. Shown also in the figure is the neutron flux for neutrons with energies >8 MeV. About 2% of the neutrons at the edge of the magnet have such high energies. This fraction also varies with Δ^i_{BS} and the composition of the shield.

Figure 15 shows the spatial distribution of atomic displacements in aluminum, copper, and niobium in units of dpa/(MW-yr/m^2). Displacement energies employed in these calculations are 26, 40, and 60 eV for aluminum, copper, and niobium, respectively. The radiation-induced resistivity in copper and aluminum varies exponentially with the dpa level as discussed earlier in this paper. It should be noted here that the radiation-induced resistivity is higher in aluminum than in copper because of the higher dpa and larger saturation resistivity in aluminum.

Hydrogen and helium production rates within the TF magnet are shown in figs. 16 and 17 for stainless steel, copper, aluminum, and niobium. Helium and hydrogen productions in stabilizing materials (aluminum and copper) are higher than in the

superconductor (Nb_3Sn or NbTi). Both are in the range of 10^{-4} to 10^{-3} appm/(MW-yr/m^2). Thus, total gas production in the range of 0.001 to 0.1 appm is expected in the TF magnet conductors at the end of plant life. The concentration of impurities due to all transmutations by nuclear reactions is heavily dependent on the neutron spectrum at the magnet but it is generally one to two orders of magnitude higher than the gas production. About 70% of all neutron transmuting reaction rates come from the (n,γ) reaction. The important impurities produced by nuclear transmutations are nickel, zinc, and cobalt in copper; and silicon and magnesium in aluminum. The total impurity concentration in copper and aluminum is 0.01 and 0.002 appm/(MW-yr/m^2), respectively. Thus, at the end of the plant lifetime, the maximum impurity concentration in the magnet is roughly 1 appm. Figure 18 shows that the total absorbed dose in two typical insulators, mylar and epoxy.

Figure 19 shows three neutron spectra, A, B, and C. Curves A and B represent the neutron spectra obtainable in tokamaks with an inner blanket/shield of stainless steel-boron carbide in two locations. Location B is the innermost layer of the TF coil located 1 m away from the first wall. Location A is 0.6 m away from the first wall which is a typical location for the equilibrium-field (EF) coils if they are located inside the shield. Curve C represents the neutron spectrum obtainable in the ANL low-temperature fast flux facility [18]. Figure 20 shows the fraction, $f(E_0)$, of the total neutron flux with neutron energies above E_0, as a function of E_0 for the same three fluxes, A, B, and C. The two figures show that a typical fission spectrum such as that of C can simulate very well the neutron spectra in tokamak superconducting magnets for energies below ~5 MeV. The fraction of neutrons above 0.1 MeV in C (90%) is considerably greater than in A and B (~60%). However, the fission spectrum (C) has a very small component (1.5%) above 5 MeV and essentially no neutrons above 8 MeV. The typical spectra in tokamak magnets (A and B) have ~5% of the

neutrons of energies >5 MeV. Many neutron-induced reactions [e.g. n,α), (n,p), (n,n'p), etc.] occur in typical magnet materials only at high energies. In addition, the recoil energy for a given reaction increases with neutron energy. Therefore, high-energy neutrons are more capable of producing radiation damage than low-energy neutrons. Thus, while fission spectra seem to be adequate for radiation damage experiments on superconducting magnets, the spectral differences in the fusion environments must be taken into account. It should be noted in this regard that the total neutron flux is a poor radiation damage indicator in the wide fusion spectra that extends from ~0-15 MeV. Other radiation damage indicators, e.g. atomic displacements, that account, to some extent, for the energy dependence of the radiation effects should be used in correlating radiation damage and radiation levels. It would be useful to establish reference sets of damage functions for materials in superconducting magnets that can be used by radiation damage experimentalists and fusion reactor designers.

The neutron spectra at the TF magnet will change for other shielding material compositions. In general, the fraction of neutrons at high energy will decrease as the shield thickness is increased.

References

[1] Proceedings of BNES Nuclear Fusion Conference, Culham (1969).

[2] A. J. Impink, Jr., "Neutron Economy in Fusion Reactor Blanket Assemblies," Technical Report No. 434, MIT Research Laboratory of Electronics, Cambridge Mass. (1965).

[3] J. T. Driese and D. Steiner, "Magnet Shield Design for Fusion Reactors," ORNL-TM-4853, Oak Ridge National Laboratory (1973).

[4] M. A. Abdou and C. W. Maynard, "Nuclear Design of the Magnet Shield for Fusion Reactors," *Proceedings of the First Topical Meeting on the Technology of Controlled Nuclear Fusion*, USAEC-CONF-740402-P1, Vol. 1 (1974), p. 685.

[5] G. M. McCracken and S. Blow, "The Shielding of Superconducting Magnets in a Fusion Reactor," CLM-R120, Culham Laboratory (1972).

[6] W. M. Stacey, Jr. and M. A. Abdou, "Tokamak Fusion Power Reactors," ANL/FPP/TM-83, Argonne National Laboratory (1977).

[7] M. A. Abdou, C. Dennis, D. Ehst, W. M. Stacey, Jr. and L. Turner, "Parametric Systems Analysis for Tokamak Power Plants," Argonne National Laboratory, to be published.

[8] W. M. Stacey, Jr., M. A. Abdou, P. J. Bertoncini, C. C. Bolta, J. N. Brooks, K. Evans, J. A. Fasolo, J. C. Jung, R. L. Kustom, V. A. Maroni, R. F. Mattas, F. E. Mills, B. Misra, J. S. Moenich, A. Moretti, J. H. Norem, J. S. Patten, W. F. Praeg, P. Smelser, D. L. Smith, H. C. Stevens, L. Turner, S-T Wang, C. K. Youngdahl, "Tokamak Experimental Power Reactor Conceptual Design," ANL/CTR-76-3, Argonne National Laboratory (1976).

[9] D. R. Cohn, D. Jassby, R. Parker and J. Williams, "A High Density, High Field Tokamak Demonstration Power Reactor," *Proceedings of the Second Topical Meeting on the Technology of Controlled Nuclear Fusion*, USERDA-CONF-760935-P3 (1976), p. 931.

[10] D. W. Kearney, R. Bourque, W. Chen, J. Dalessandro, E. Hager, R. Harder, B. McHarg, M. Mintz, S. Rosenwasser, K. Schultz, R. Thomas, "Conceptual Design Study of Noncircular Tokamak Demonstration Fusion Power Reactor," GA-A13992, General Atomics (1976).

[11] L. R. Turner and M. A. Abdou, "Computational Model for Superconducting Toroidal-Field Magnets for a Tokamak Reactor," ANL/FPP/TM-88, Argonne National Laboratory (1977).

[12] M. A. Abdou, "Nuclear Design of Blanket/Shield System for a Tokamak Experimental Power Reactor," *Nucl. Techn.* 29 (1976) 7.

[13] M. A. Abdou, "Important Aspects of Radiation Shielding for Fusion Reactor Tokamaks," ANL/FPP/TM-81, Argonne National Laboratory (1977).

[14] M. A. Abdou, L. Milton, J. Jung and E. Gelbard, "Multidimensional Neutronics Analysis of Major Penetrations in Tokamaks," *Proceedings of the Second ANS Topical Meeting on the Technology of Controlled Nuclear Fusion,* USERDA-CONF-760935-P3 (1976), p. 848.

[15] R. T. Santora, T. S. Tang, R. G. Alsmiller, Jr. and J. M. Barnes, "Monte Carlo Analysis of the Effects of a Blanket-Shield Penetration on the Performance of a Tokamak Fusion Reactor," ORNL/TM-5874, Oak Ridge National Laboratory (1977).

[16] B. S. Brown, "Radiation Effects on Superconductivity," in *Radiation Damage in Metals,* N. L. Peterson and S. D. Harkness, Eds. (American Society of Metals, 1975), p. 330.

[17] M. Soll, "The Influence of Radiation Damage on the Properties of a Superconductor," IPP-4/104, Max-Planck Institute fur Plasmaphysik.

[18] B. S. Brown, T. H. Blewitt, T. L. Scott and A. C. Klank, "Low-Temperature Fast Neutron Radiation Damage Studies in Superconducting Materials," *J. Nucl. Mater.* 52, (1974) 215.

[19] G. L. Kulcinski, R. G. Brown, R. G. Lott and P. A. Sanger, "Radiation Damage Limitations on the Design of the Wisconsin Tokamak Fusion Reactor," *Nucl. Techn.* 22 (1974) 20.

[20] C. A. M. Van der Klein, "The Organic Insulators in Fusion Reactor Magnet Systems," RCN-240, Reactor Centrum Mederland (1975).

Table 1

Reference parameters for cases in fig. 11

Neutron wall loading, MW/m^2	3
Reactor thermal power, MW	
R = 6 m	1950
R = 7 m	2620
R = 8 m	3390
R = 9 m	4260
Aspect ratio	3
Period between magnet anneals, yr	11.4
Downtime for magnet anneal, days	80

Radiation parameters (maximum values) in the TF superconducting magnet at Δ^{i}_{BS} = 1 m

Neutron flux, m^{-2}-sec^{-2}	1.4×10^{14}
Gamma-ray flux, m^{-2}-sec^{-1}	9×10^{13}
Maximum neutron fluence prior to magnet anneal, m^{-2}	4.5×10^{22}
Maximum gamma-ray fluence prior to magnet anneal, m^{-2}	2.9×10^{22}
Radiation-induced resistivity in copper, Ω-cm	1.05×10^{-7}
Decrease in NbTi critical current density, $\Delta J/J_c$	∿14%
Nuclear energy deposition, kW	
R = 6 m	5.9
R = 7 m	7.9
R = 8 m	10.3
R = 9 m	12.9

Table 3

Effect of inner blanket/shield thickness on maximum dose to the insulators in the toroidal-field magnets*

Δ^{i}_{BS} (m)	Dose to insulator at end of plant Life, 30 yr (rad)	Cost of Energy mills/kWh R = 6
0.7	1.2×10^{12}	55.2
0.8	3×10^{11}	37.6
0.9	7×10^{10}	34.5
1.0	1.8×10^{10}	34.4
1.1	3.3×10^{9}	35.2
1.2	1.2×10^{9}	37.1
1.3	3×10^{8}	40.1
1.4	7×10^{7}	45.4

*Based on system with A = 3, κ = 1, P_w = 3 MW/m^2.

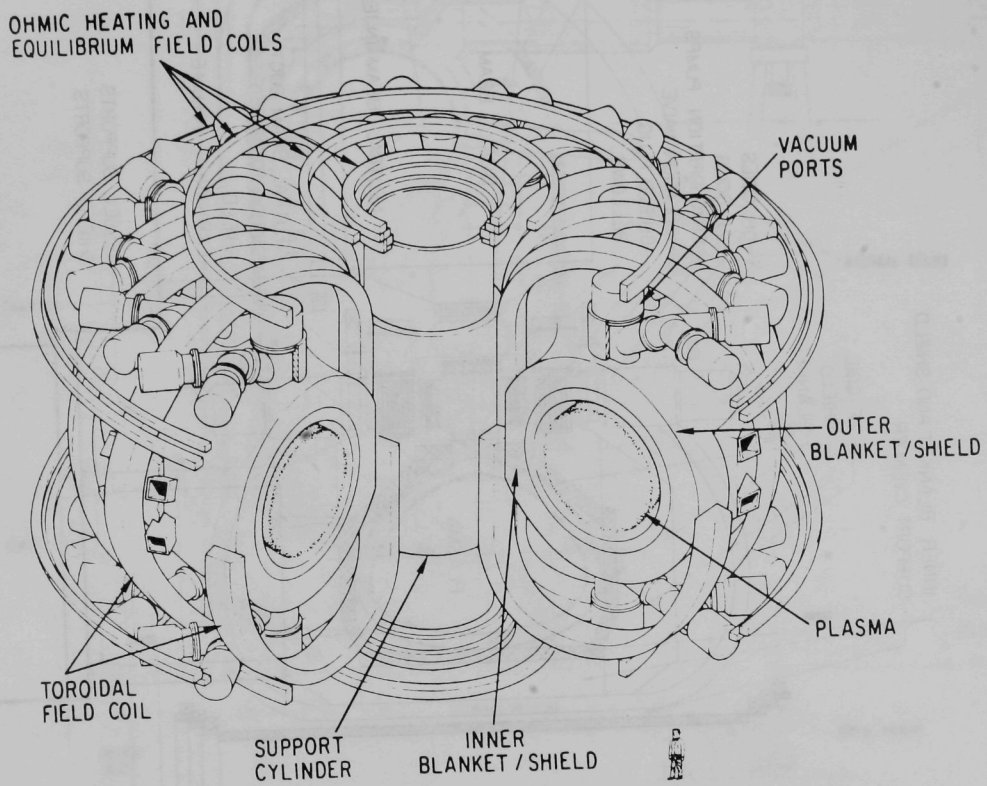

Fig. 1. Perspective view of a tokamak.

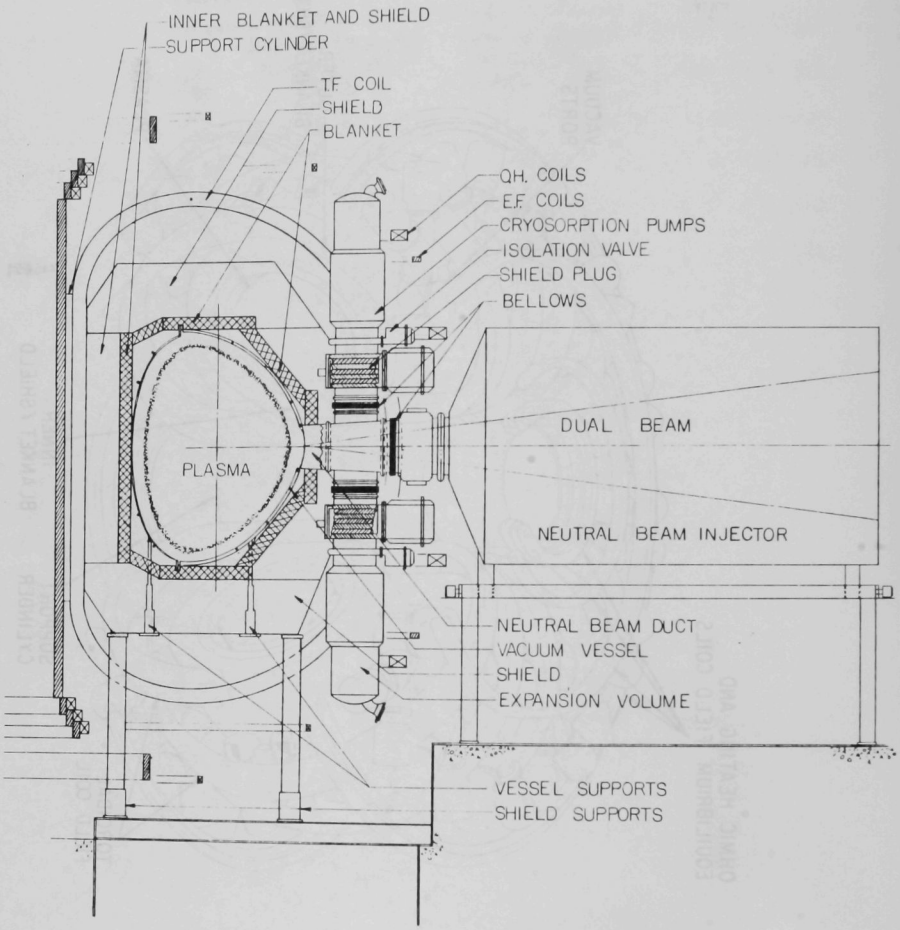

Fig. 2. Vertical cross section of a tokamak with a representative neutral beam penetration.

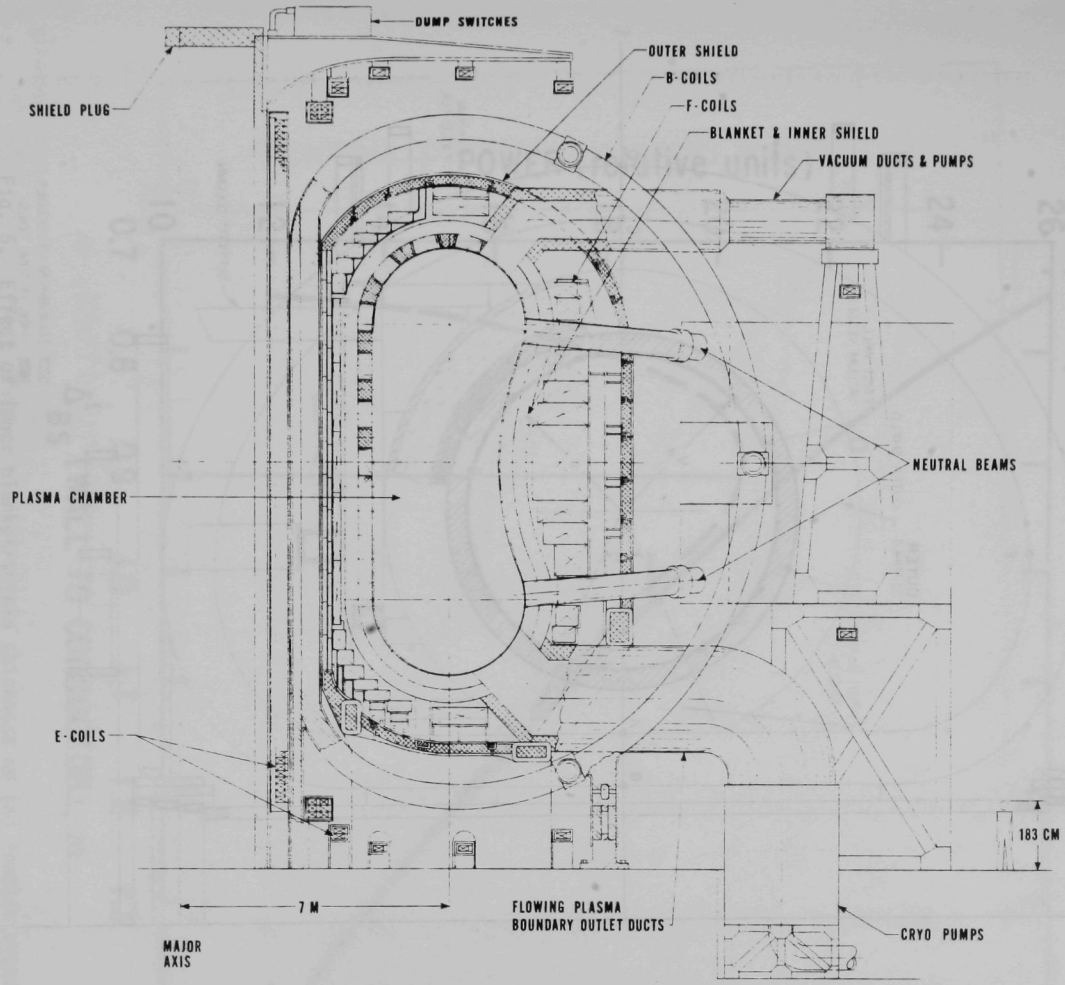

Fig. 3. Vertical cross section of a Doublet tokamak. (Reproduced from ref. 10.)

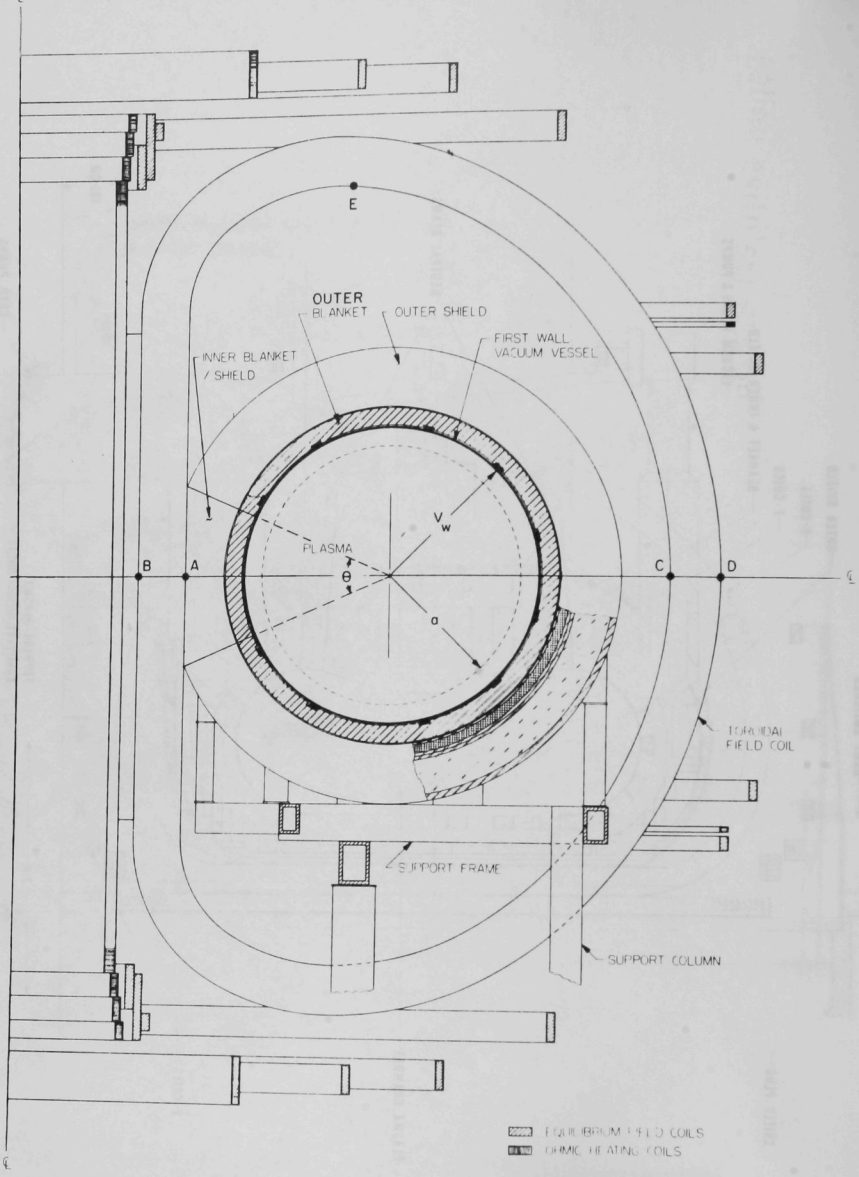

Fig. 4. A simplified vertical cross section of a representative tokamak with circular plasma.

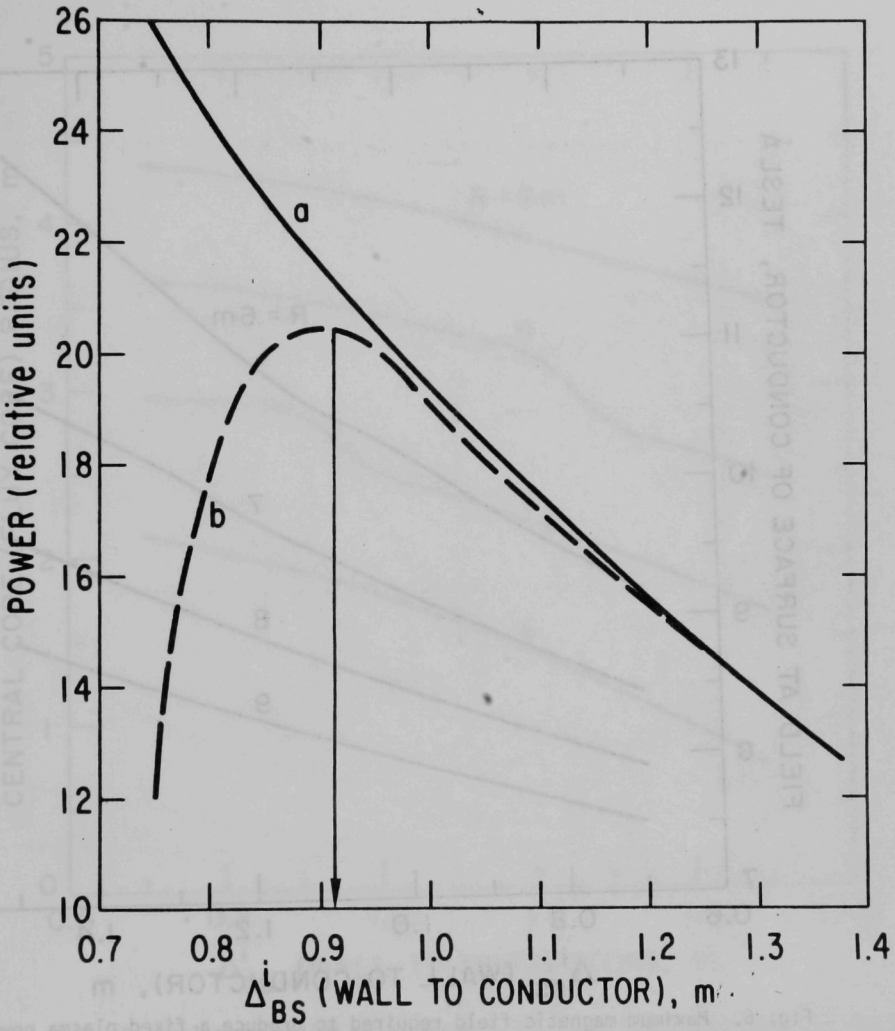

Fig. 5. Effect of inner blanket/shield thickness on (a) reactor gross electric power; and (b) reactor net electric power (= gross power-TF magnet refrigeration power).

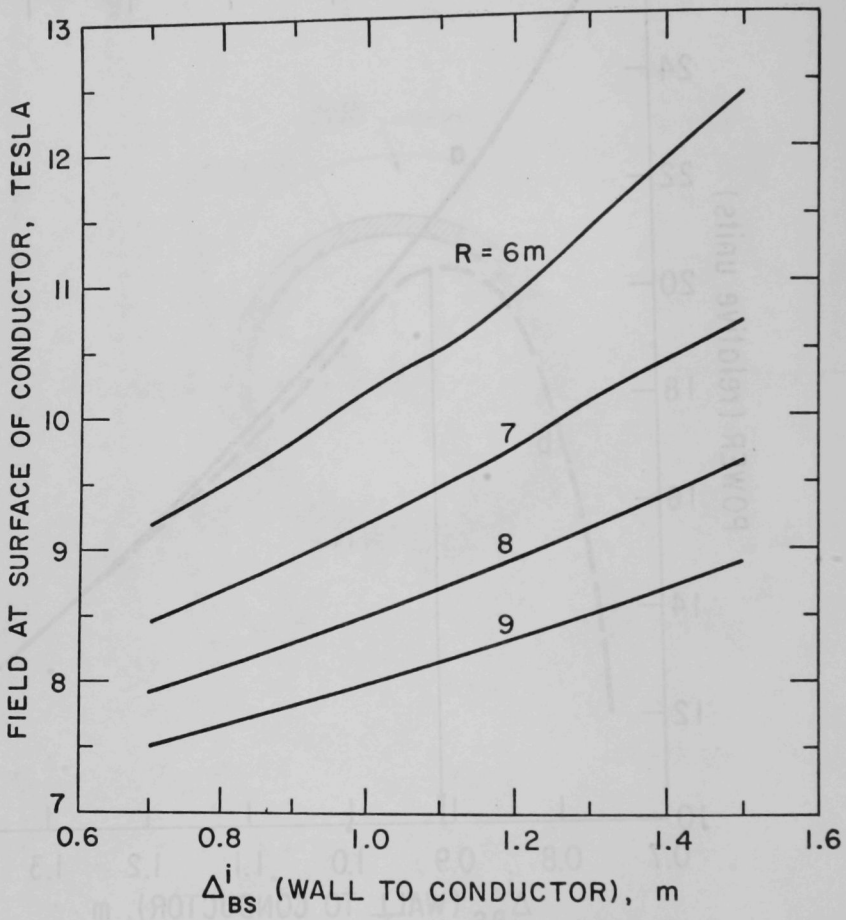

Fig. 6. Maximum magnetic field required to produce a fixed plasma power density as a function of the inner blanket/shield thickness. Results are shown for several values of the major radius, R, aspect ratio of 3, and neutron wall load of 3 MW/m^2 for circular plasma.

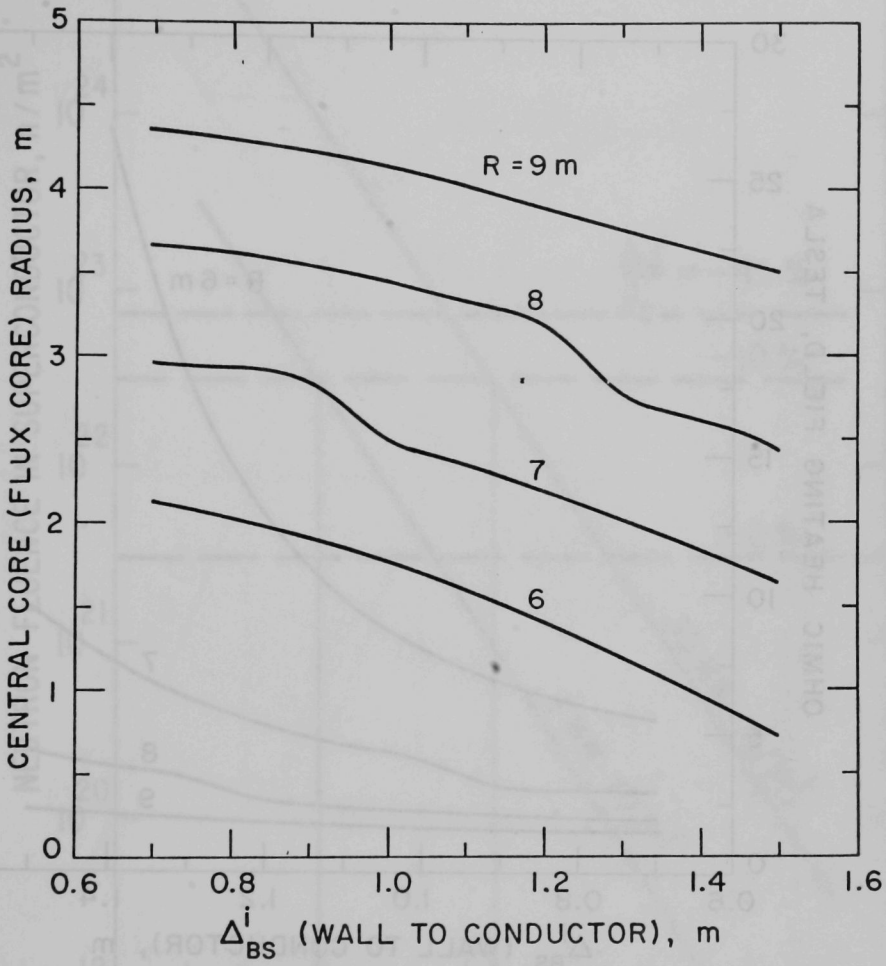

Fig. 7. Central core radius as a function of inner blanket/shield thickness for several size tokamaks (A = 3, P_W = 3 M/m^2, circular plasma).

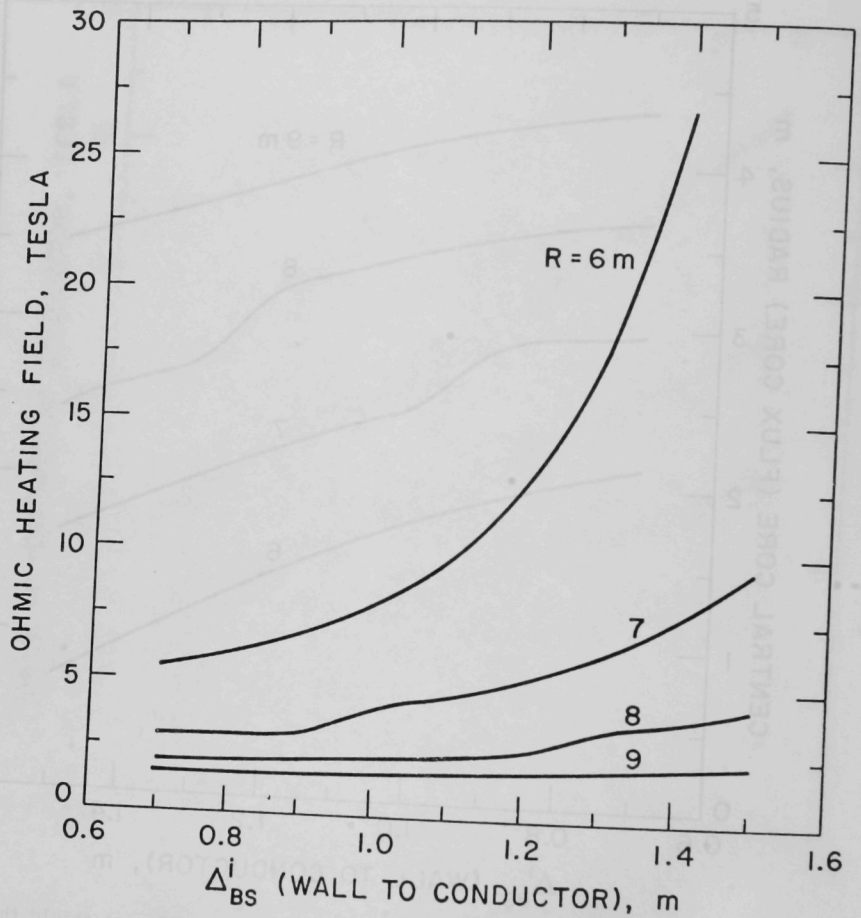

Fig. 8. Maximum ohmic heating field required in several size tokamaks as a function of inner blanket/shield thickness ($A = 3$, $P_w = 3$ MW/m^2, circular plasma).

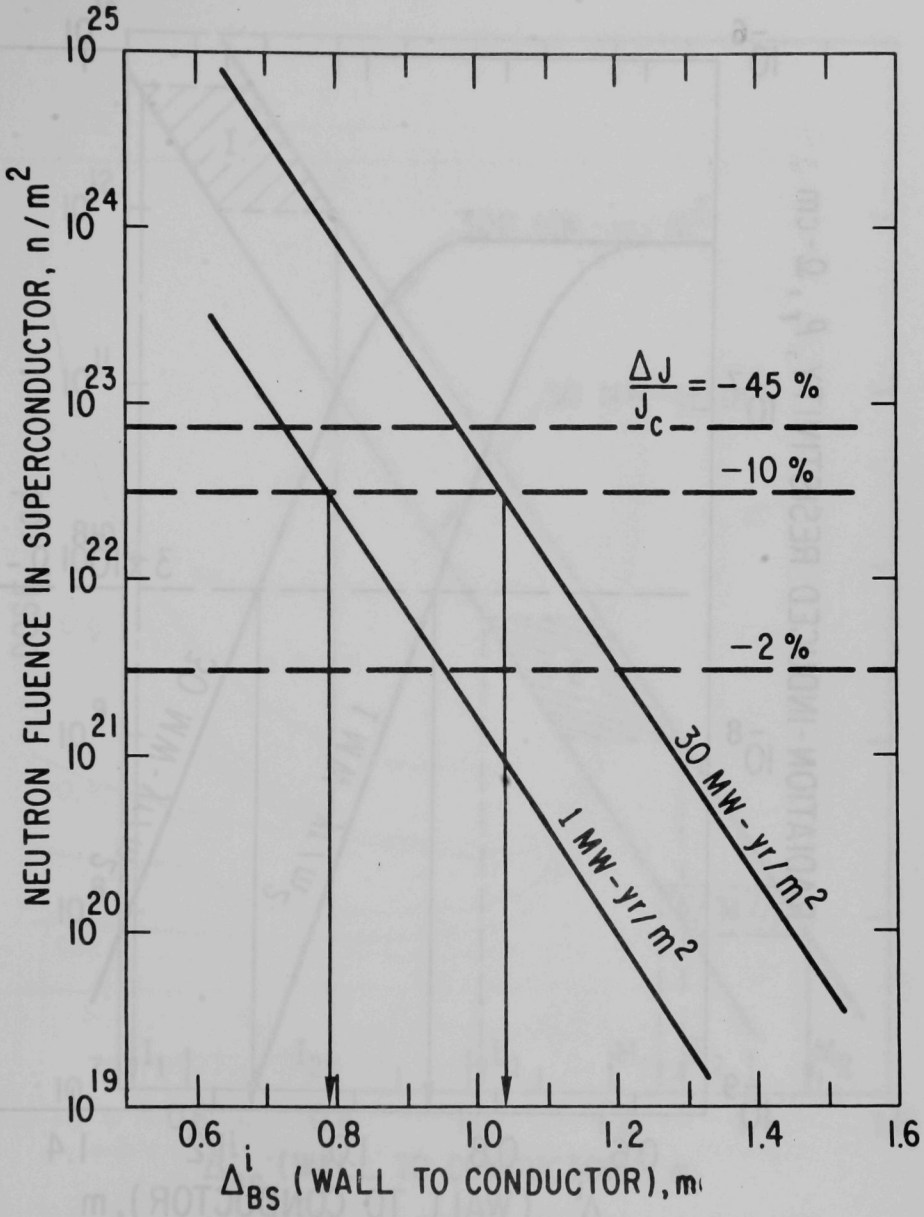

Fig. 9. Maximum neutron fluence in TF magnet as a function of inner blanket/shield thickness.

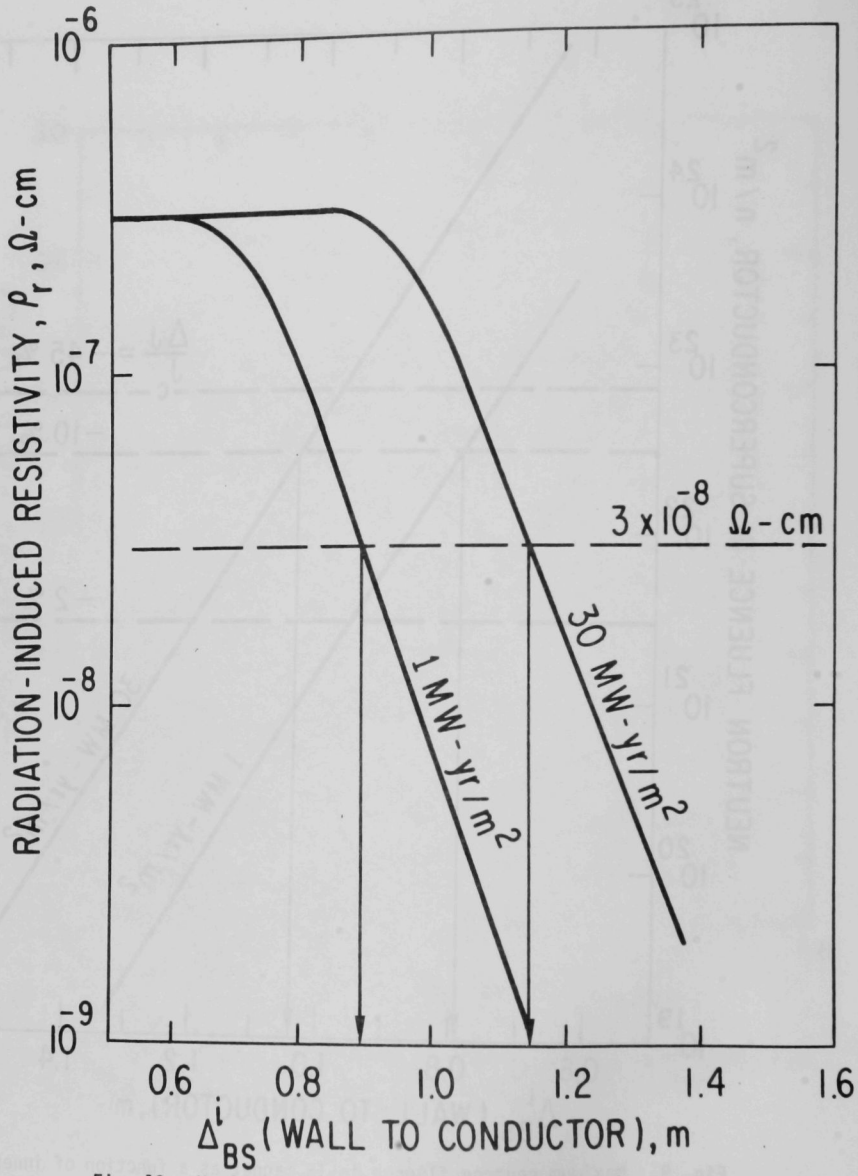

Fig. 10. Maximum radiation-induced resistivity in copper stabilizer as a function of inner blanket/shield thickness.

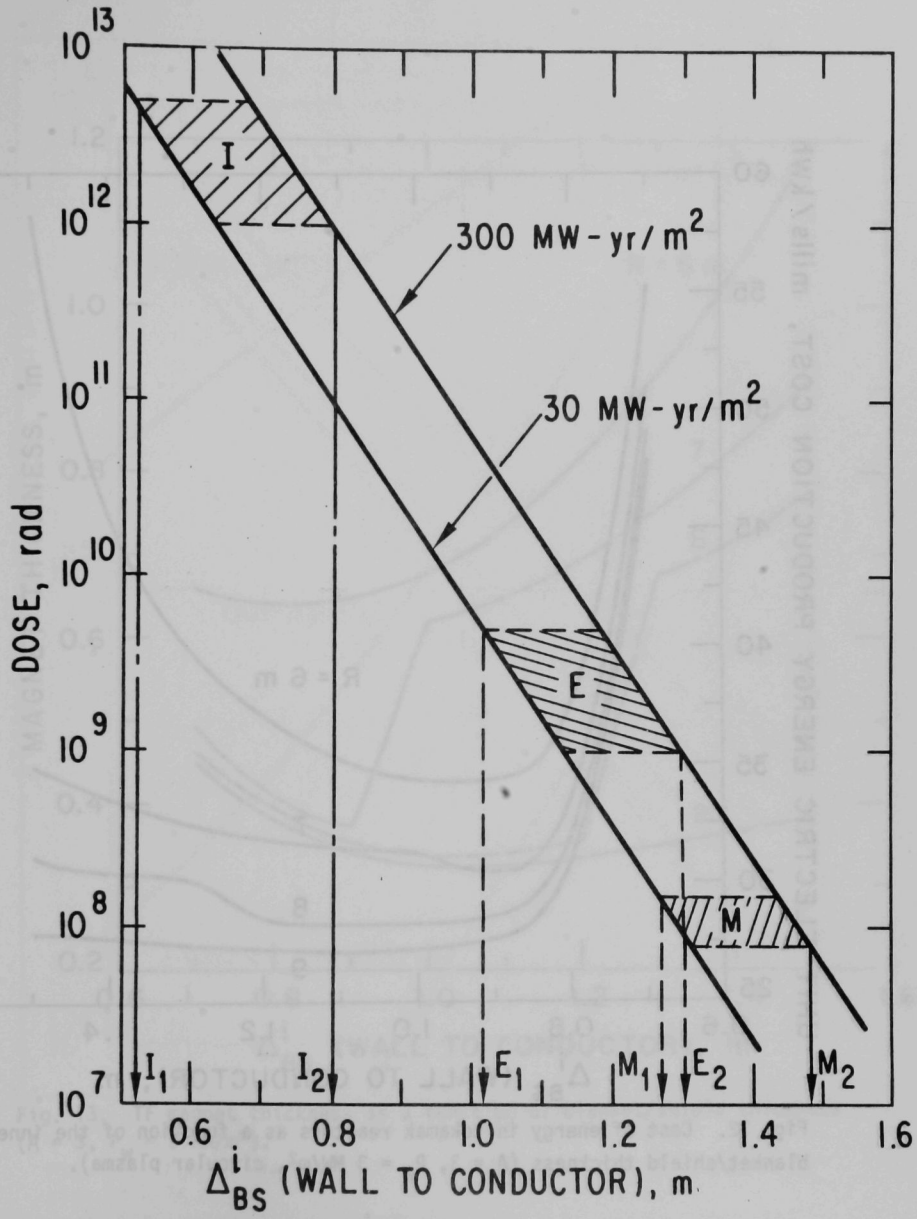

Fig. 11. Variation of radiation dose in TF magnet insulators with inner blanket/shield thickness.

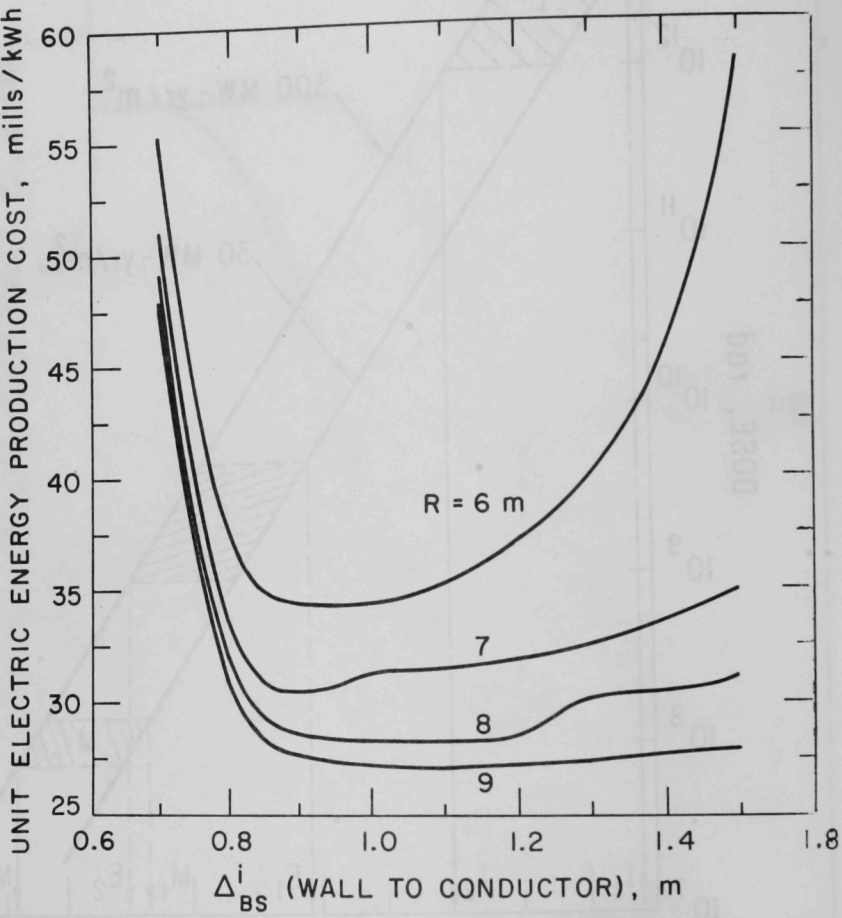

Fig. 12. Cost of energy in tokamak reactors as a function of the inner blanket/shield thickness (A = 3, P_W = 3 MW/m^2, circular plasma).

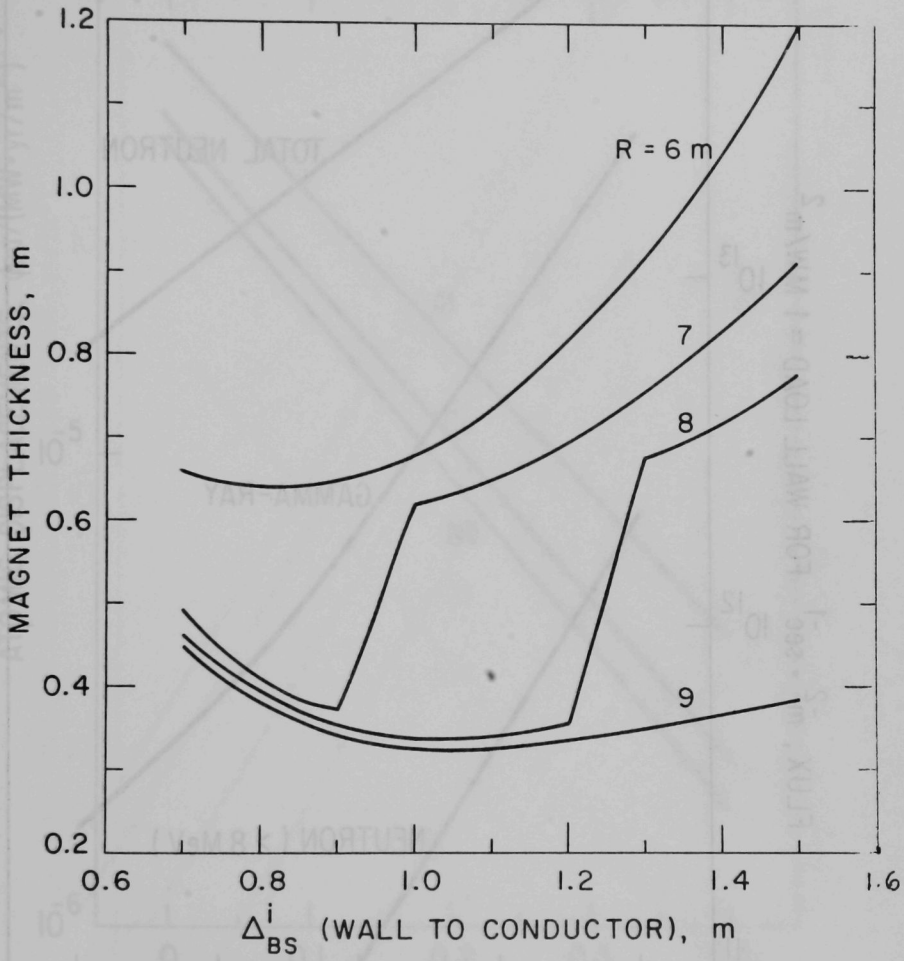

Fig. 13. TF magnet thickness as a function of blanket/shield thickness ($A = 3$, $P_w = 3$ MW/m^2).

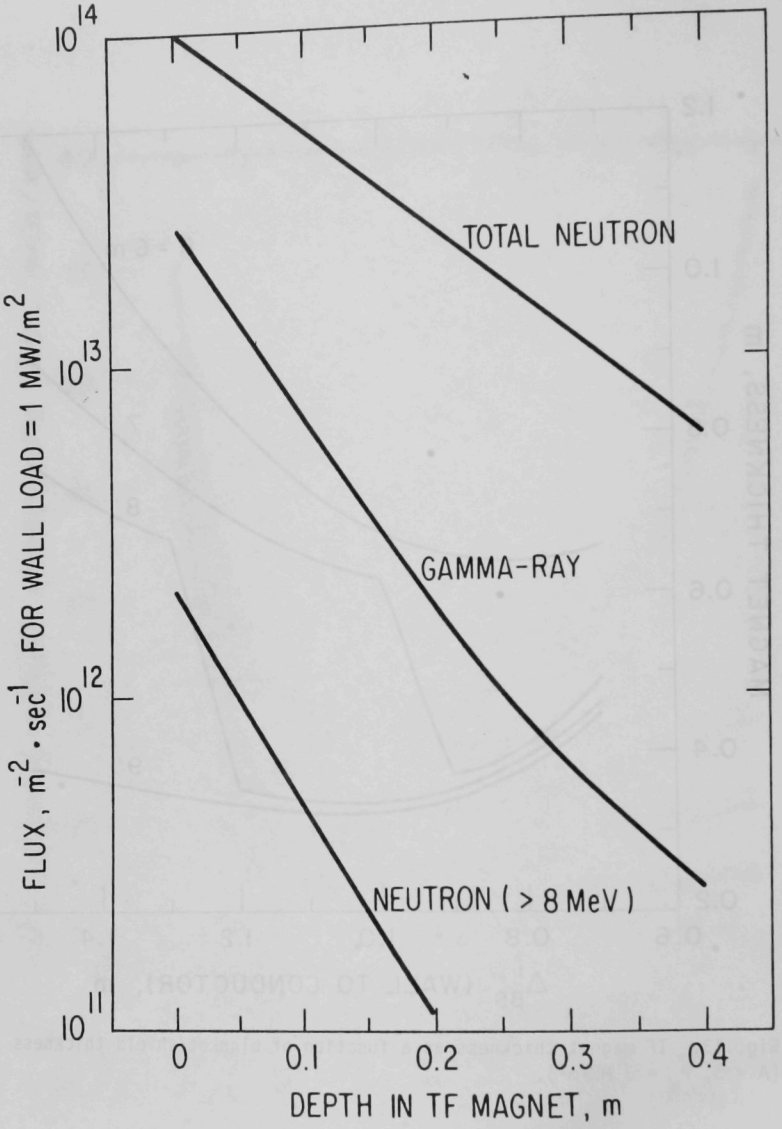

Fig. 14. Neutron and gamma-ray fluxes as a function of depth on the innerside of a TF magnet.

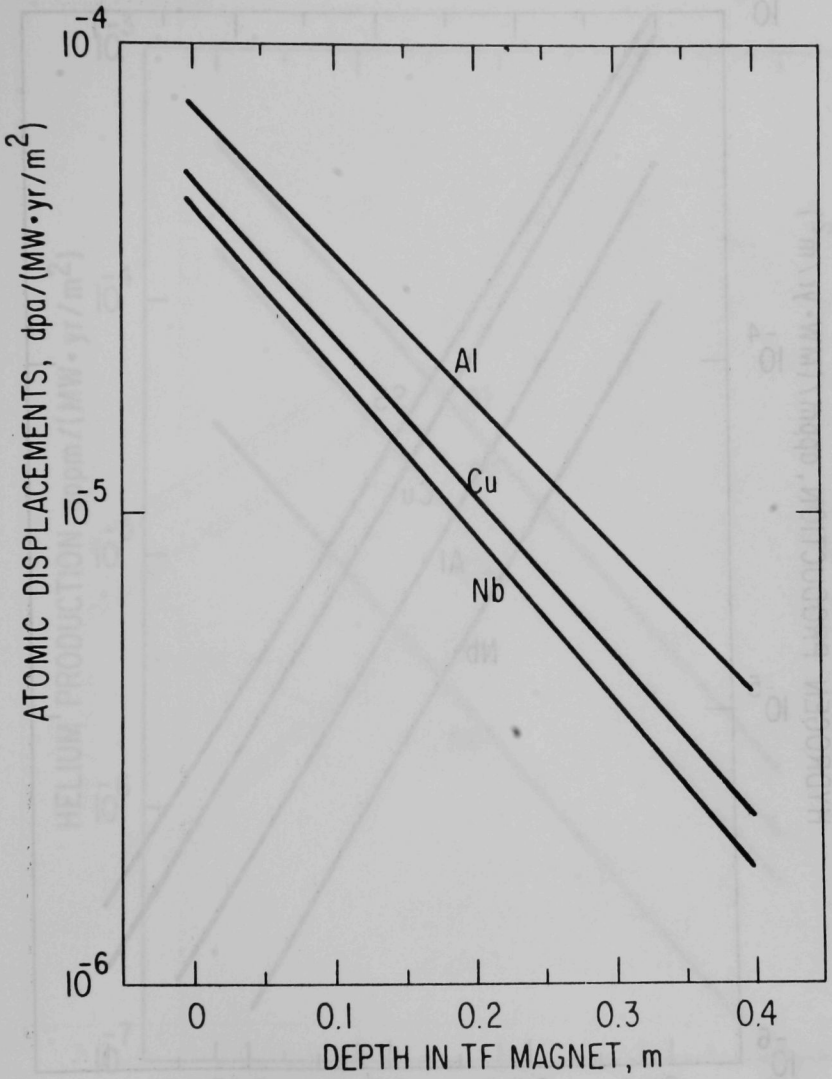

Fig. 15. Atomic displacements as a function of depth on the inner side of a TF magnet.

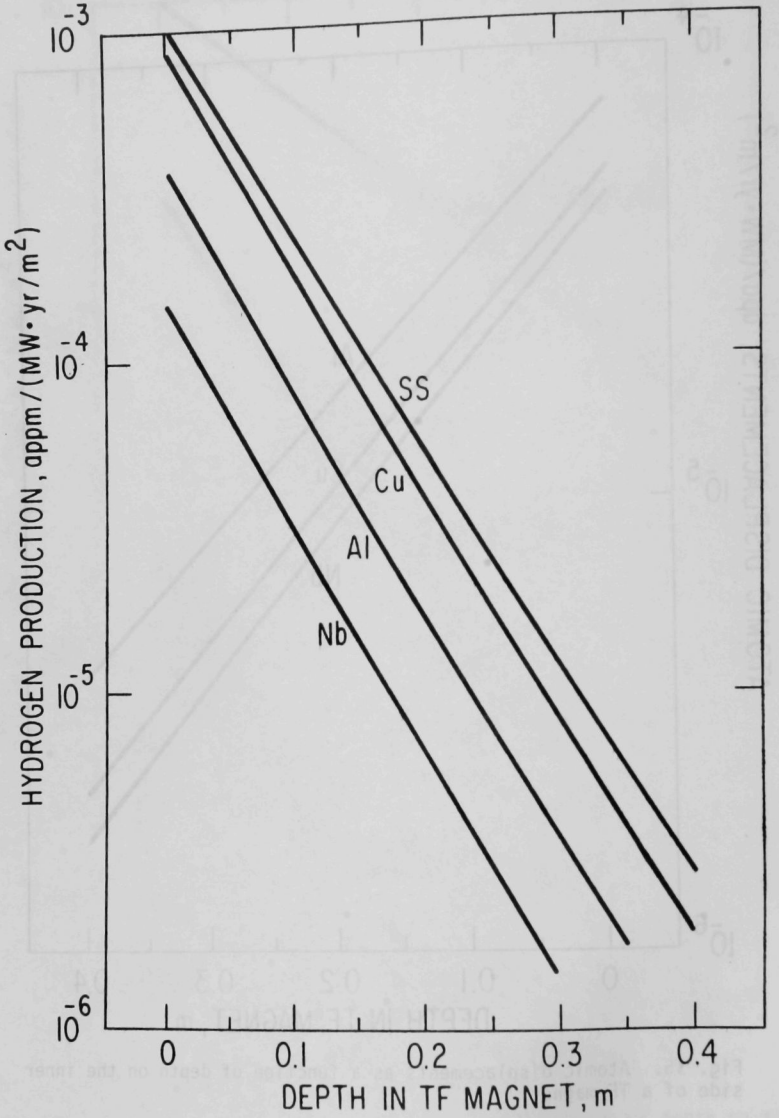

Fig. 16. Hydrogen production as a function of depth on the inner side of a TF magnet.

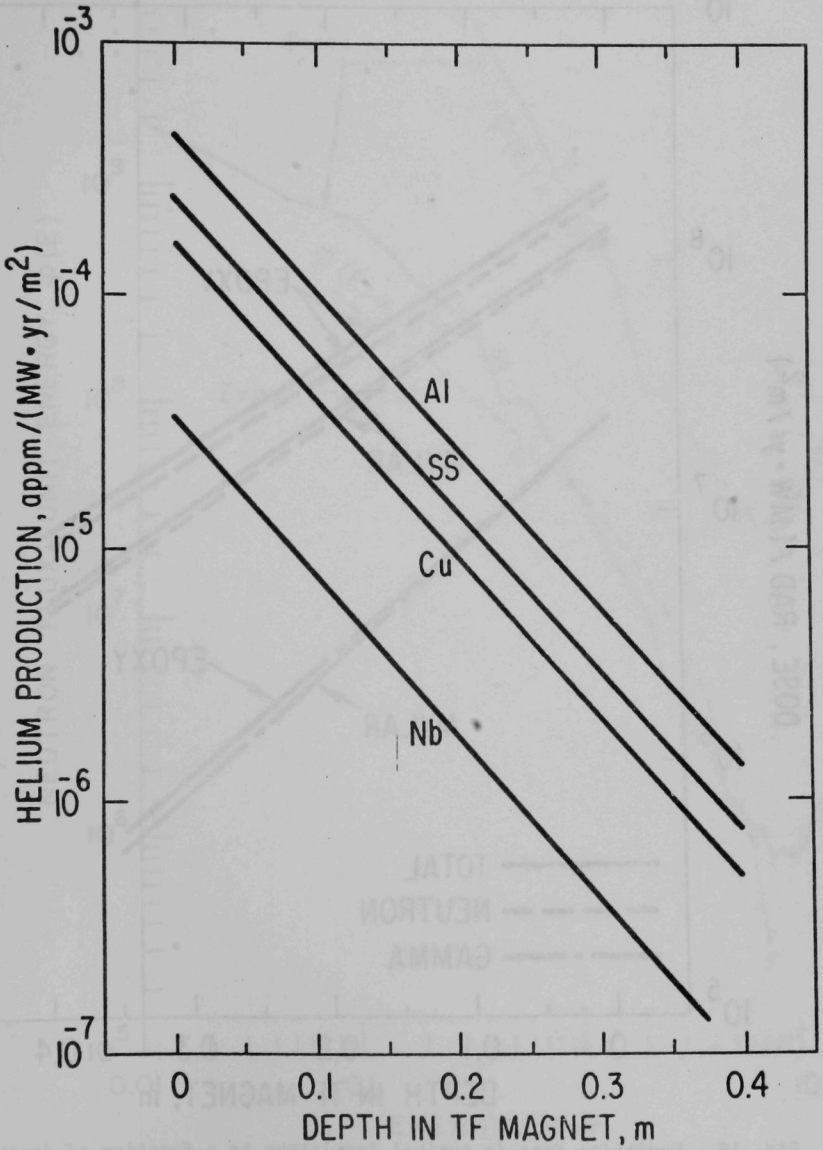

Fig. 17. Helium production as a function of depth on the inner side of a TF magnet.

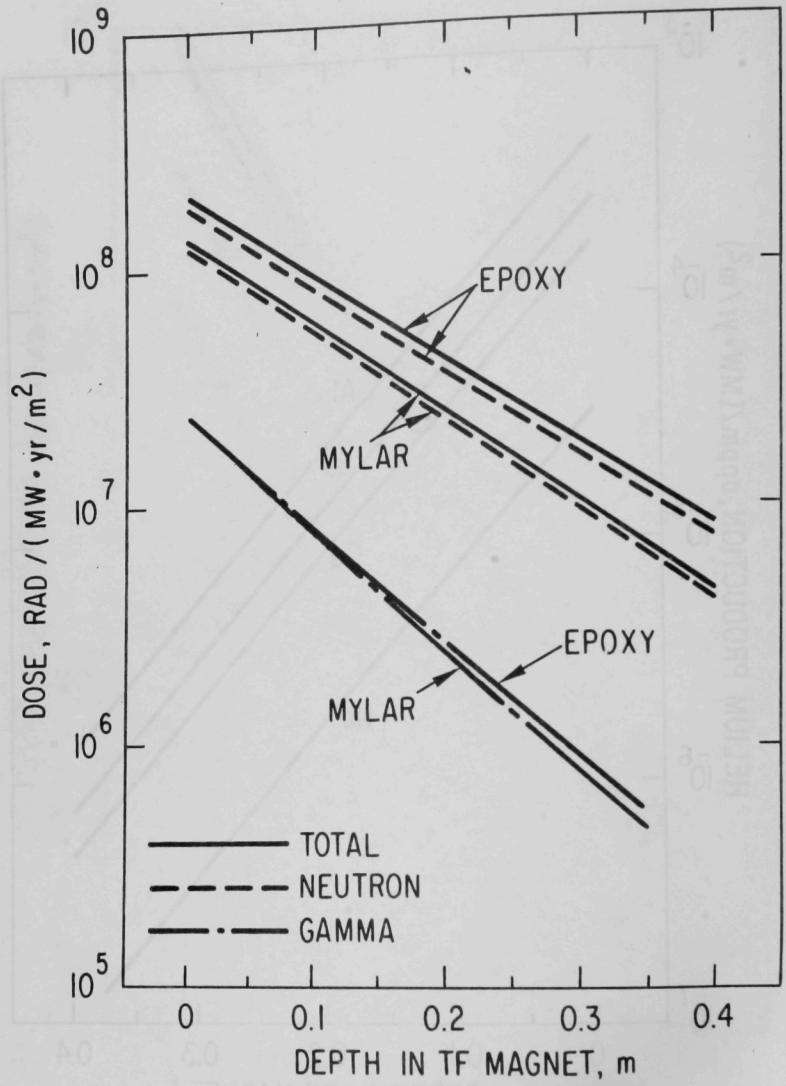

Fig. 18. Radiation dose in typical insulators as a function of depth on the inner side of a TF magnet.

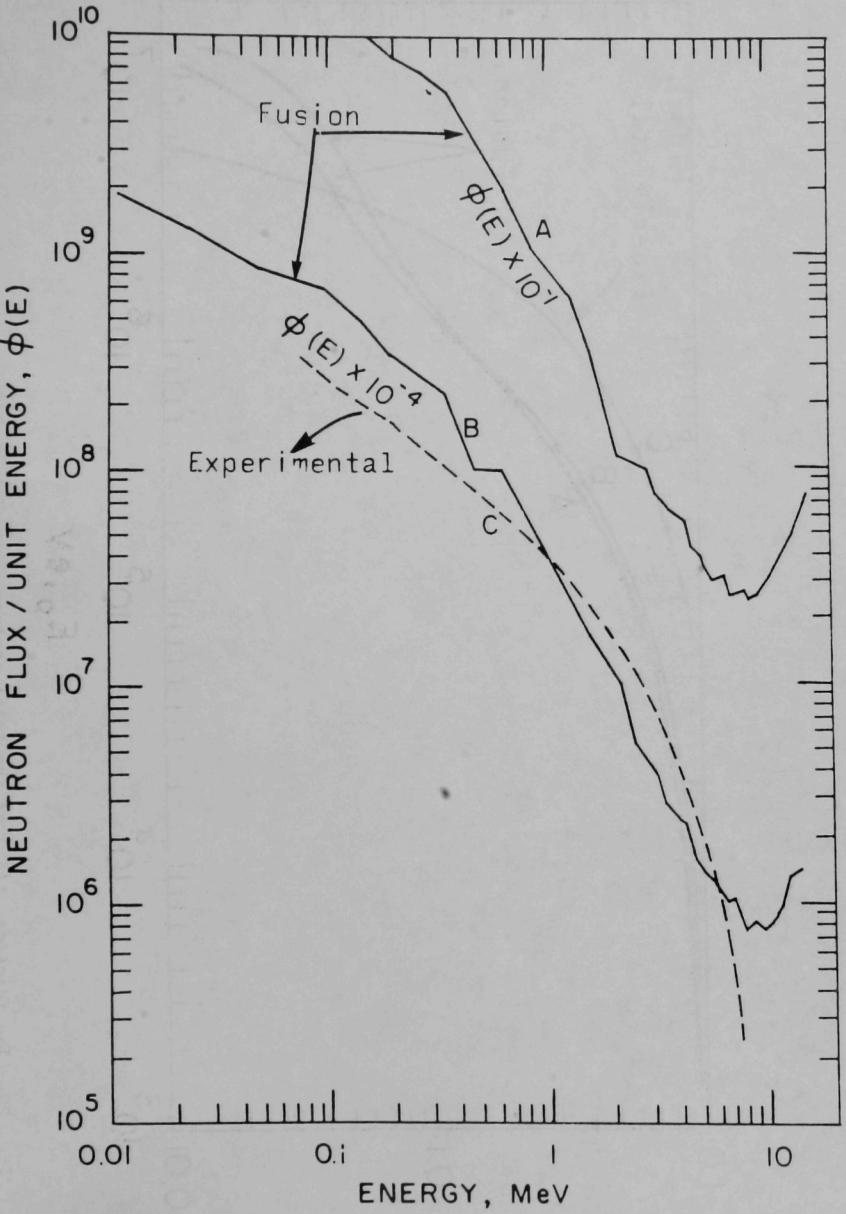

Fig. 19. Comparison of typical neutron spectra in tokamak magnets with typical experimental (fission) spectrum: (a) neutron spectrum in a magnet located 0.6 m away from first wall; (b) neutron spectrum in TF magnet with inner blanket/shield of SS and B_4C (Δ^i_{BS} = 1 m); and (c) neutron spectrum for the ANL low-temperature facility.

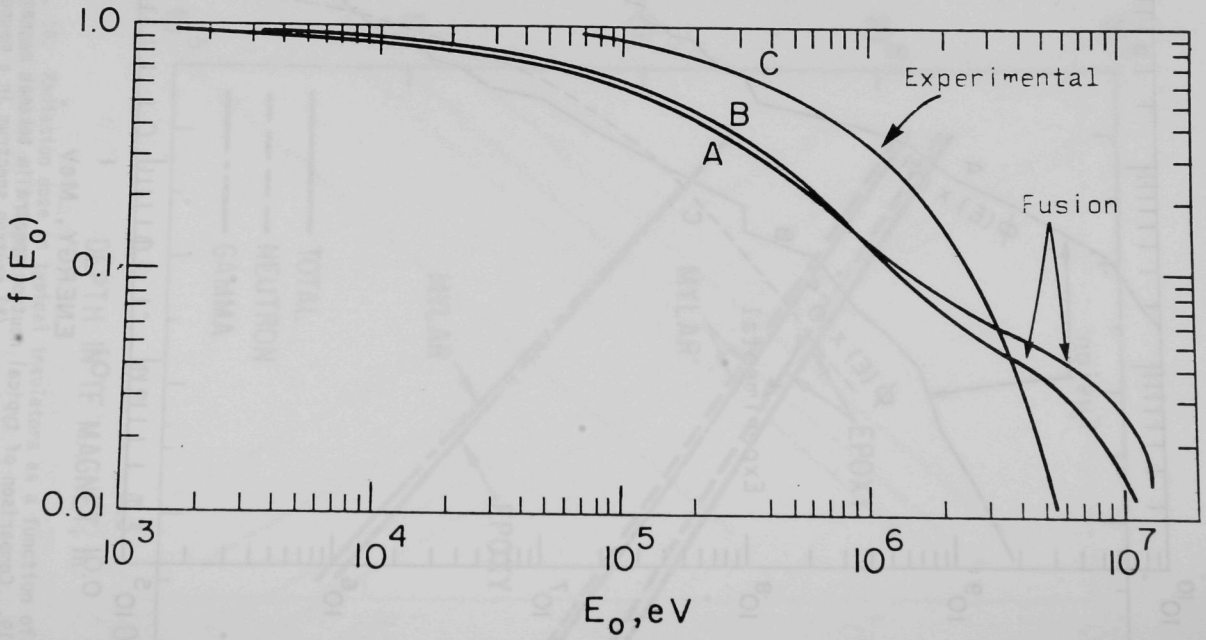

Fig. 20. The fraction, $f(E_0)$ of the total neutron flux with neutron energies above E_0 as a function of E_0 for the three cases A, B, and C shown in Fig. 19.

May 1977

ANL/FPP/TM-84

MODELING OF LIFE-LIMITING PROPERTIES OF FUSION REACTOR STRUCTURAL MATERIALS

R. F. Mattas and D. L. Smith

Materials Science Division
Fusion Power Program
Argonne National Laboratory
Argonne, Illinois 60439

ANL/FPP Technical Memorandum Number 84

Results reported in the FPP series of memoranda frequently are preliminary and subject to revision. Consequently, they should not be quoted nor referenced without the authors' permission.

Work supported by the U.S. Energy Research and Development Administration.

ABSTRACT

A computer model based on available materials-property data has been developed to predict the lifetimes of first-wall structural materials under a variety of reactor conditions. The model combines the materials-property data with the appropriate ranges of limiting criteria to establish design lifetimes as functions of relevant parameters such as temperature and integrated neutron wall loading. Empirical equations developed from existing literature data were used to interpolate and extrapolate the required materials properties over the desired ranges. The present effort has concentrated on the evaluation of two candidate structural materials, viz., Type 316 stainless steel and a vanadium-base alloy (V-15Cr-5Ti). Curves have been derived that show the estimated lifetime and life-limiting property as a function of temperature for a specified set of design criteria, e.g., maximum swelling of 4%, minimum uniform elongation of 1%, and total creep strain of < 1% for an applied stress of 103 MPa (15 ksi). The results obtained indicate a much longer design lifetime for the vanadium-base alloy than for stainless steel under the conditions of interest. The computational model has been incorporated into the tokamak power plant systems program at Argonne National Laboratory.

		Page
I.	INTRODUCTION	1
II.	MATERIALS MODEL	1
III.	MATERIALS-PROPERTY DATA	3
	A. Swelling	4
	B. Tensile Ductility	7
	C. Thermal and Radiation Creep	10
	D. Fatigue	17
IV.	RESULTS AND DISCUSSION	19
	A. Swelling	19
	B. Ductility	19
	C. Creep	24
	D. Fatigue	24
	E. Combined Property Analysis	28
V.	SUMMARY AND CONCLUSIONS	32
REFERENCES		34

LIST OF FIGURES

Number		Page
1.	Temperature Dependence of Radiation Swelling for Annealed Type 316 Stainless Steel	5
2.	Swelling Curve as a Function of Radiation Fluence for Annealed Type 316 Stainless Steel	6
3.	Estimated Radiation Swelling Response as a Function of Temperature for a Low-swelling Vanadium Alloy	8
4.	Estimated Swelling Curve as a Function of Radiation Fluence for a Low-swelling Vanadium Alloy	9
5.	Uniform Elongation as a Function of Radiation Damage for Type 316 Stainless Steel	11
6.	Temperature Dependence of Uniform Elongation for Highly-Irradiated Type 316 Stainless Steel	12
7.	Uniform Elongation as a Function of Radiation Damage for Reference Vanadium Alloy	13
8.	Derived Curve for Temperature Dependence of Uniform Elongation for Highly-Irradiated Vanadium Alloy	14
9.	Creep Strain Curves for V-15 Cr-5 Ti Alloy Under 21 ksi Stress at 650°C	16
10.	Design Strain Range - Lifetime Curves for 18-8 Stainless Steels (ASME Code Case 1331-8) for Temperatures to 700°C	18
11.	Predicted Operating Lifetime as a Function of Temperature for Type 316 Stainless Steel When Limited by Radiation Swelling	20
12.	Predicted Operating Lifetime as a Function of Temperature for V-15 Cr-5 Ti Alloy When Limited by Radiation Swelling	21
13.	Predicted Operating Lifetime as a Function of Temperature for Stainless Steel When Limited by Loss of Ductility	22
14.	Predicted Operating Lifetime as a Function of Temperature for V-15 Cr-5 Ti Alloy When Limited by Loss of Ductility	23
15.	Predicted Operating Lifetime as a Function of Temperature for Stainless Steel Under Specified Stresses When Limited by 2% Creep Strain	25

Number		Page
16.	Predicted Operating Lifetime as a Function of Temperature for V-15 Cr-5 Ti Alloy Under Specified Stresses When Limited by 2% Creep Strain	26
17.	Predicted Fatigue Lifetimes as a Function of Temperature for Stainless Steel Cycled at Specified Strain Ranges	27
18.	Predicted Lifetime for Crack Propagation as a Function of Temperature for Stainless Steel with Specified Initial Flaw Sizes	29
19.	Predicted Lifetime for Crack Propagation as a Function of Temperature for Stainless Steel Under Specified Cyclic Stresses (initial crack size = 0.01 in.)	30
20.	Composite Lifetime Curves as a Function of Temperature for Stainless Steel and V-15 Cr-5 Ti Alloy When Limited Either by Swelling, Loss of Ductility, or Creep Strain for Specified Criteria	31

I. INTRODUCTION

The severe operating conditions imposed by a fusion-reactor environment can seriously affect the integrity of proposed structural materials and limit the lifetime of critical reactor components. The resultant costs of commercial fusion power will depend heavily upon the useful lifetime of the various components. A computer model based on available materials-property data has been developed to predict the lifetime of first-wall structural materials under a variety of reactor operating conditions. Results from this model will aid in the assessment of the viability of various structural materials and the optimal operating conditions for different components and will contribute to maintenance scheduling and overall cost estimates for commercial fusion power.

Critical materials properties that could limit the operating lifetime of a reactor provide input for the model. The pertinent property data for candidate structural materials have been obtained from the literature. A range of limiting criteria representative of conditions anticipated for a variety of reactor components has been used to establish the design lifetime. Initial phases of the present work have concentrated on the analysis of an austenitic stainless steel (annealed Type 316) and an appropriate vanadium-base alloy. Stainless steel has been proposed as a structural material in near-term experimental power reactor designs, and vanadium-base alloys are representative of advanced higher-temperature structural materials. Property data for other materials can be incorporated into the model to assess the viability and determine the limitations of other candidate structural alloys. The present materials model has been integrated into a more extensive Fusion Power Plant System program,[1] which can parametrically describe economic, design, operating, and maintenance trade-offs in conceptual fusion power reactors.

II. MATERIALS MODEL

The materials model to be described provides a capability for predicting the design lifetime of structural components operating under a variety of conditions in a fusion-reactor environment. Pertinent bulk-materials property

data are combined with appropriate ranges of limiting design criteria to evaluate the useful lifetimes of candidate alloys. The critical properties evaluated include radiation swelling and creep that can lead to excessive dimensional instabilities, and tensile and fatigue damage which can result in failure by fracture. The specific properties investigated as well as the relevant parameters that affect the properties are summarized in Table I. The tensile and swelling properties are assumed to be dependent only on the radiation fluence and temperature. The creep properties include the stress level as an added variable, whereas the fatigue properties depend upon such additional variables as stress or strain range associated with the burn cycle, burn-cycle frequency, initial crack size, and component geometry. In the present analysis, effects on the individual properties are assumed to be independent of effects that occur simultaneously on other properties. In general, sufficient data are not available at the present time for an evaluation of possible synergistic effects. It is anticipated that the lifetime will be limited primarily by a single property under most conditions of interest. Other properties such as (a) sputtering and blistering behavior, (b) coolant corrosion, and (c) magnetic interactions are expected to be more critical to overall reactor performance than to degradation of the mechanical integrity of the structural material. Therefore, these types of properties are not included in the present materials model.

Table I. Properties and Variables Considered for Lifetime Program

Property	Independent Variables
Radiation Swelling	Fluence, temperature
Tensile Ductility and Strength	Fluence, temperature
Radiation and Thermal Creep	Fluence, temperature, stress
Fatigue	Fluence, temperature, strain range, stress range, burn-cycle frequency, initial crack length, component geometry

In general, the materials properties used in the model are based primarily on available experimental data. Empirical equations were developed to represent the property responses as a function of the independent variables for the ranges of interest. The independent variables considered for each of the properties are listed in Table I. A detailed analysis of the data and the formalism used is given in Section III for the two alloy systems considered in the present investigation, viz., Type 316 stainless steel and a representative vanadium-base alloy. If subsequent changes in these data are warranted, they can be accommodated in the model. These changes could include incorporation of additional independent variables and consideration of synergistic effects as well as upgrading of the existing data base.

An important aspect of the lifetime assessment relates to the establishment of the life-limiting criteria for the individual properties. These are the values at which the material is considered to fail because of separation, i.e., fracture or excessive dimensional instability. The life-limiting parameters for the different properties are expected to vary with component geometry, function, and location in the reactor. For example, the limiting criteria for a relatively thin first-wall section may be substantially different than for a thick structural member. A range of limiting criteria are incorporated in the model so that lifetimes of different types of components can be evaluated. This also permits one to obtain both optimistic and conservative lifetime estimates.

The normal output of the program is the component lifetime for a given set of input parameters. For the case of fatigue, however, the number of cycles to failure are determined by the program.

III. MATERIALS-PROPERTY DATA

The materials-property data and the empirical equations developed to represent the behavior of the two structural alloys investigated in the initial phases of the present study are described. Annealed Type 316 stainless steel is representative of a well-characterized structural material that has been proposed for near-term experimental power reactors, and the vanadium-chromium-titanium alloy is an advanced material which possesses many favorable

properties for fusion-reactor applications. The V-15% Cr-5% Ti alloy is selected as the reference alloy; however, because of limited data, values obtained for other vanadium-base alloys are sometimes used to represent the properties of the reference alloy.

A. Swelling

The swelling characteristics of annealed Type 316 stainless steel have been studied extensively. Neutron-radiation data have been compiled in the Nuclear Systems Materials Handbook[2] and described by an empirical equation of the form

$$\Delta V/V = R \left\{ \phi t + \frac{1}{\alpha} \ln \left[\frac{1 + \exp[\alpha(\tau - t)]}{1 + \exp(\alpha t)} \right] \right\} , \qquad (1)$$

where $\Delta V/V$ is the total swelling; R, α, and τ are materials constants that vary with temperature; ϕ is the radiation damage rate; and t is time. A simpler empirical expression, which incorporates the temperature dependence directly into the equation, has been developed in the present investigation. The swelling responses of both stainless steel and the vanadium alloy have been fit to a gaussian equation of the form

$$\Delta V/V = 0, \text{ for } \phi t \leq \phi t_o \qquad (2)$$

and

$$\Delta V/V = A\phi \, (t - t_o)^{n_s} \exp \left[\frac{-(T - T_p)^2}{w^2} \right], \text{ for } \phi t > \phi t_o , \qquad (3)$$

where $\Delta V/V$, ϕ, and t are the same as in Equation (1); A is a materials constant; t_o is the incubation period; n_s is the swelling exponent; w is the half width of the swelling peak; T_p is the peak swelling temperature; and T is the operating temperature. Figures 1 and 2 show the swelling response of annealed Type 316 stainless steel as a function of temperature and fluence, respectively, for the derived expression. Also shown in the two figures are the swelling responses obtained with Equation (1), which give quite similar results.

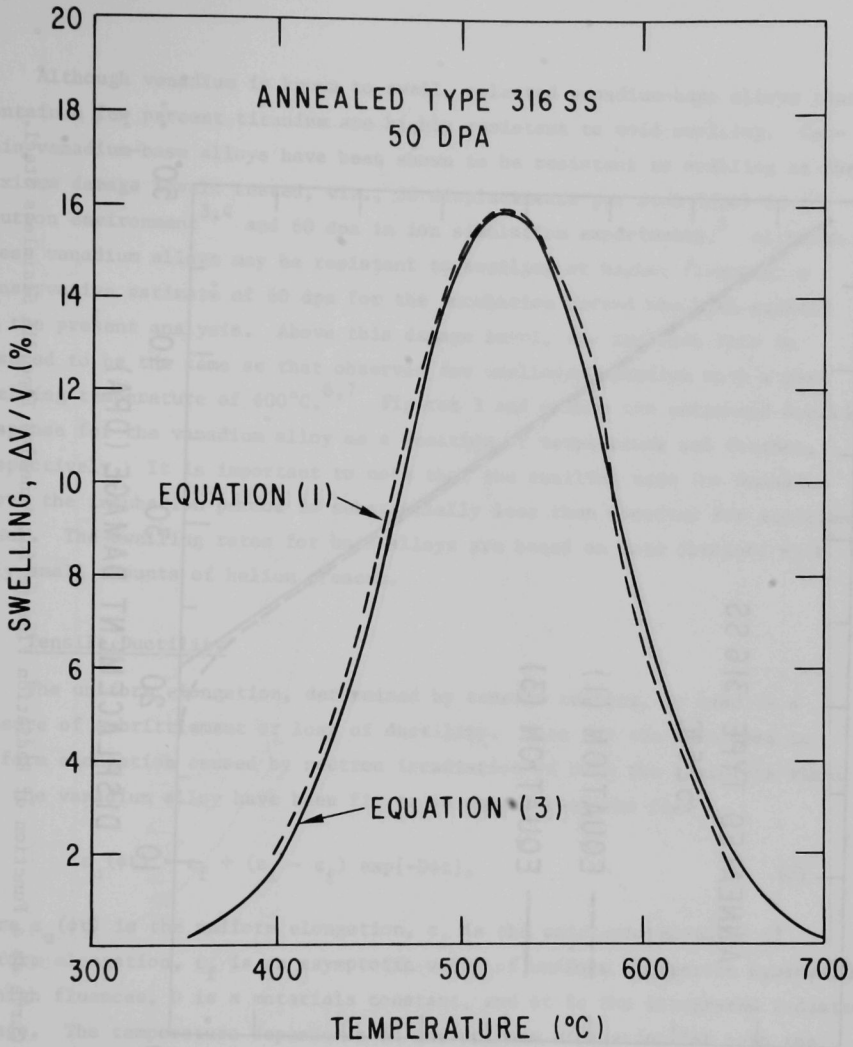

Figure 1. Temperature Dependence of Radiation Swelling for Annealed Type 316 Stainless Steel.

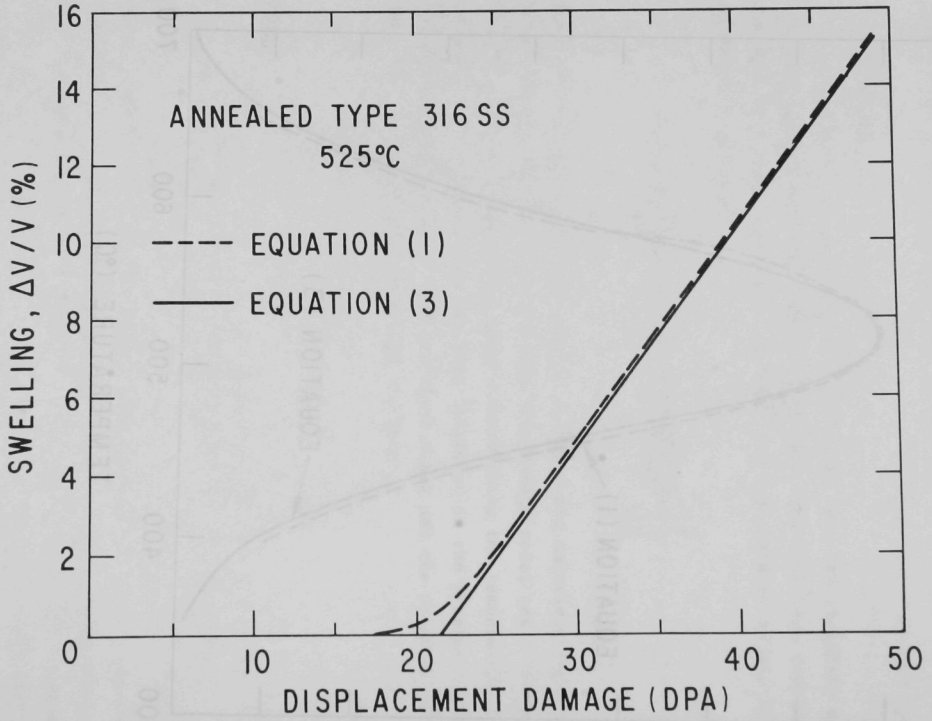

Figure 2. Swelling Curve as a Function of Radiation Fluence for Annealed Type 316 Stainless Steel.

Although vanadium is known to swell, selected vanadium-base alloys that contain a few percent titanium are highly resistant to void swelling. Certain vanadium-base alloys have been shown to be resistant to swelling at the maximum damage levels tested, viz., 30 displacements per atom (dpa) in a neutron environment[3,4] and 60 dpa in ion simulation experiments.[5] Although these vanadium alloys may be resistant to swelling at higher fluences, a conservative estimate of 60 dpa for the incubation period has been assumed in the present analysis. Above this damage level, the swelling rate is assumed to be the same as that observed for unalloyed vanadium with a peak swelling temperature of 600°C.[6,7] Figures 3 and 4 show the estimated swelling response for the vanadium alloy as a function of temperature and fluence, respectively. It is important to note that the swelling rate for vanadium above the incubation period is substantially less than observed for stainless steel. The swelling rates for both alloys are based on data obtained with only small amounts of helium present.

B. Tensile Ductility

The uniform elongation, determined by tensile testing, is used as a measure of embrittlement or loss of ductility. Data for the reduction in uniform elongation caused by neutron irradiation of both the stainless steel and the vanadium alloy have been fit to an equation of the form

$$\varepsilon_u(\phi t) = \varepsilon_f + (\varepsilon_i - \varepsilon_f)\exp[-D\phi t], \tag{4}$$

where $\varepsilon_u(\phi t)$ is the uniform elongation, ε_i is the unirradiated value of uniform elongation, ε_f is an asymptotic value of uniform elongation approached at high fluences, D is a materials constant, and ϕt is the integrated radiation damage. The temperature dependence of the uniform elongation for both the stainless steel and the vanadium alloy is expressed by an equation of the form

$$\varepsilon_u(\phi t,T) = \varepsilon_u(\phi t)\left\{B\,e^{-CT} + \frac{1}{\exp[(T - T_{emb})/2\Delta T] + 1}\right\}, \tag{5}$$

where B and C are materials constants, T_{emb} is the temperature at which helium embrittlement dominates fracture, ΔT is the temperature range over which helium embrittlement becomes important, and T is the operating temperature.

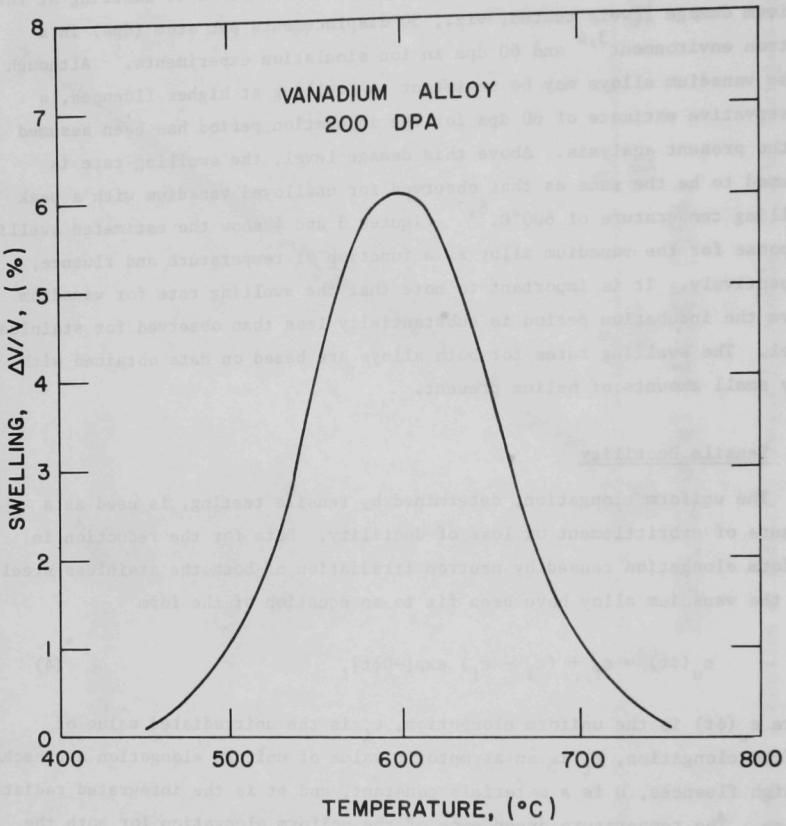

Figure 3. Estimated Radiation Swelling Response as a Function of Temperature for a Low-swelling Vanadium Alloy.

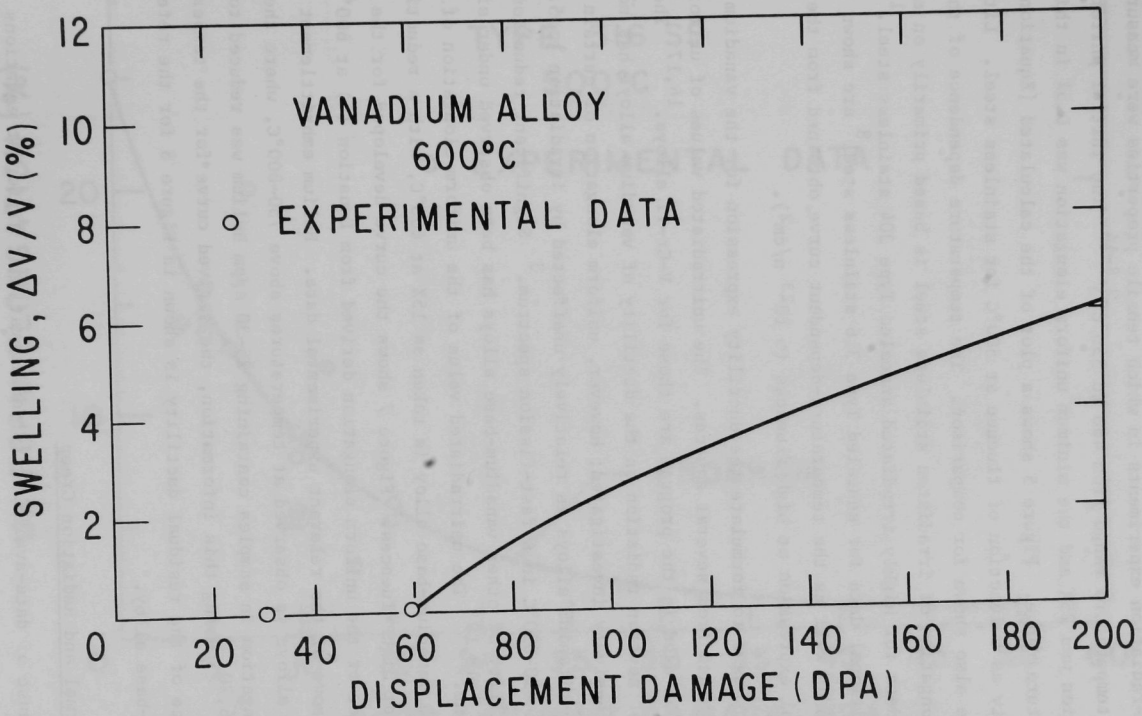

Figure 4. Estimated Swelling Curve as a Function of Radiation Fluence for a Low-swelling Vanadium Alloy.

The loss of ductility in neutron-irradiated stainless steel has been measured extensively. The data used to fit Equation (4) were taken from neutron-radiation experiments in which tensile properties were measured in the temperature range from 480 to 530°C.[2,8-14] The initial uniform elongation was 25% and the minimum uniform elongation was 0.5% in this temperature range. Figure 5 shows a plot of the calculated [Equation (4)] ductility as a function of fluence at 500°C for stainless steel. Literature data are also shown for comparison. The temperature dependence of the uniform elongation of irradiated stainless steel is based primarily on experimental data for highly irradiated annealed Type 304 stainless steel.[15] These and additional data for annealed Type 316 stainless steel[8] are shown in Figure 6 as well as the temperature-dependent curve obtained from the empirical expression at high fluences ($\sim 10^{23}$ n/cm^2).

Data used to formulate the ductility expression for the vanadium alloy were obtained from several sources. The unirradiated values of uniform elongation used in the program are those for V-Cr-Ti alloys.[16,17] The effect of neutron radiation on the ductility of vanadium alloys has not been extensively investigated; however, uniform elongation of certain vanadium-titanium alloys is relatively unaffected by irradiation to 5.4×10^{22} n/cm^2 at 450-650°C in a fast-fission spectrum.[3] Significant reduction in the ductility of other vanadium-base alloys has been observed under similar conditions.[18,19] The unirradiated value of the uniform elongation of the reference vanadium-base alloy is taken as 15% at 600°C, with a reduction to 1.5% at high fluences. Figure 7 shows the curve developed for the fluence dependence of the uniform elongation derived from Equation (4) at 600°C as well as some of the relevant experimental data. Helium embrittlement of vanadium alloys is observed at temperatures above 750-800°C, where the uniform elongation in samples containing 25-30 appm helium was reduced to $\sim$ 3%.[6,16,20] Using this information, the derived curve for the temperature dependence of the residual ductility is shown in Figure 8 for the reference vanadium-base alloy.

C. Thermal and Radiation Creep

Because of data-availability considerations, different equations have been used to represent creep in the stainless steel and the vanadium-base

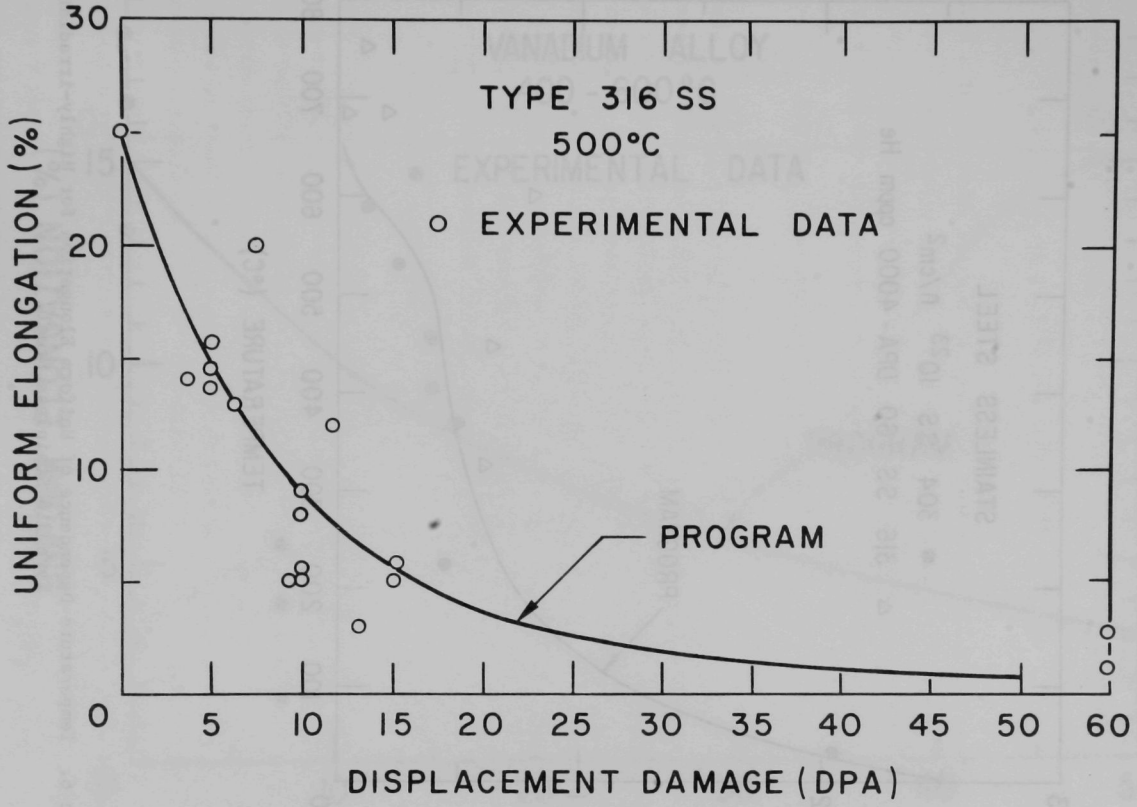

Figure 5. Uniform Elongation as a Function of Radiation Damage for Type 316 Stainless Steel.

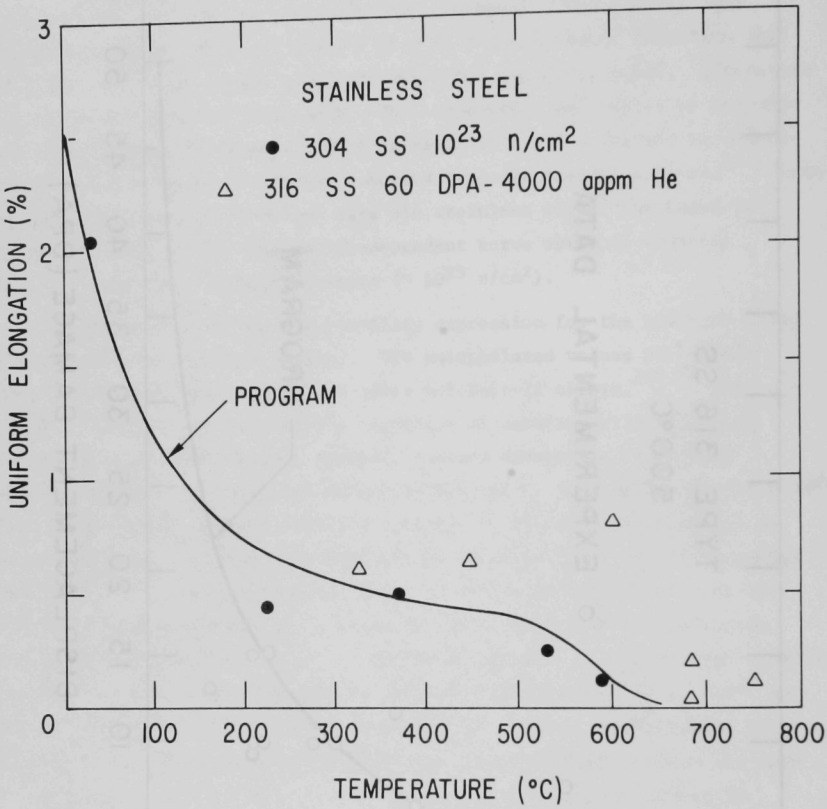

Figure 6. Temperature Dependence of Uniform Elongation for Highly-irradiated Type 316 Stainless Steel.

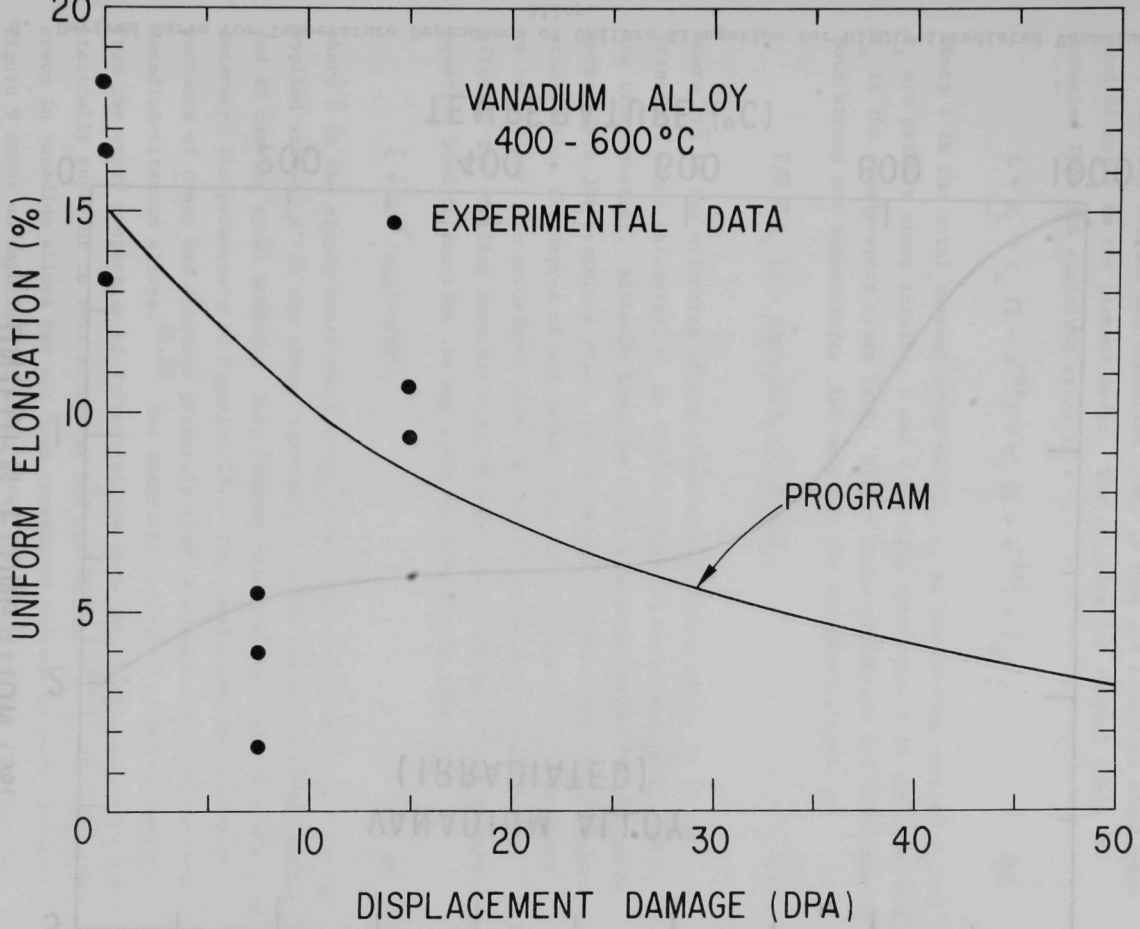

Figure 7. Uniform Elongation as a Function of Radiation Damage for Reference Vanadium Alloy.

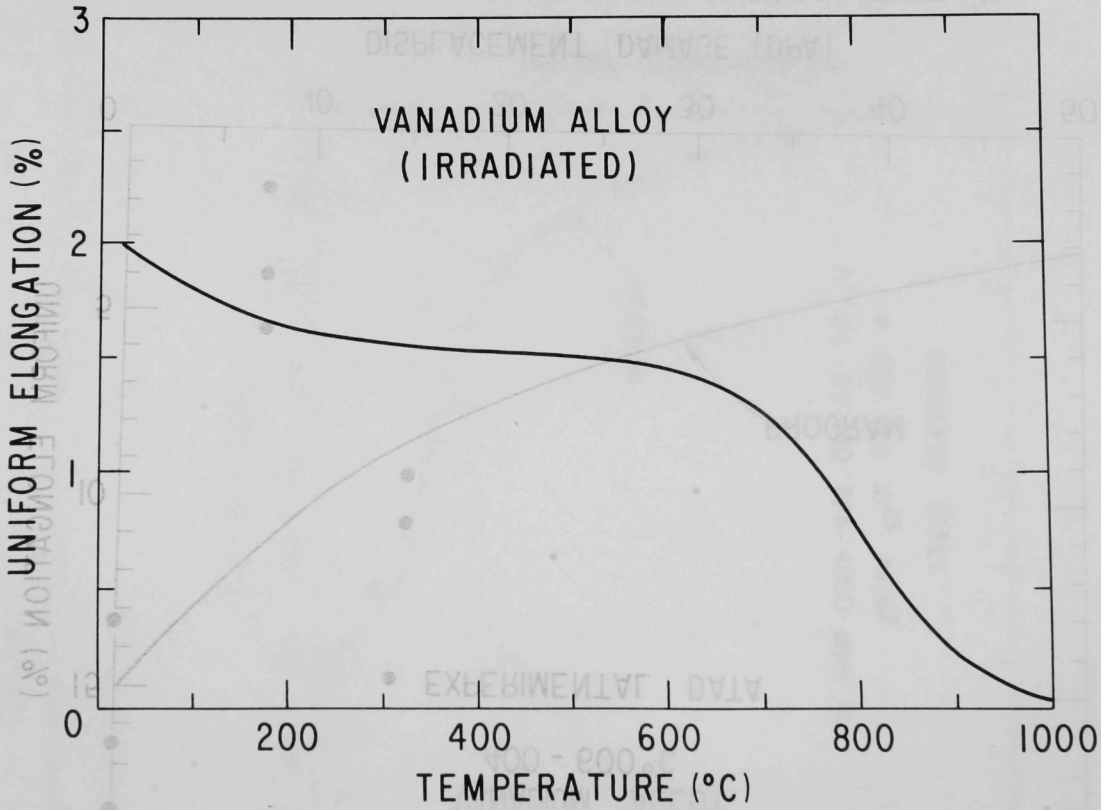

Figure 8. Derived Curve for Temperature Dependence of Uniform Elongation for Highly-irradiated Vanadium Alloy.

alloy. The empirical equations from the Nuclear Systems Materials Handbook[2] that describe thermal and radiation creep in Type 316 stainless steel were used directly in the present model. The equation for thermal creep in annealed Type 316 stainless steel is

$$\varepsilon = \varepsilon_L + \varepsilon_x (1 - e^{-St}) + \varepsilon_t (1 - e^{-rt}) + \dot{\varepsilon}_m t , \qquad (6)$$

where ε is the total thermal creep strain, ε_L is the loading strain, ε_x and ε_t are primary creep strains, S and r are time constants, t is the time, and $\dot{\varepsilon}_m$ is the steady-state creep rate. All of these parameters are functions of both stress and temperature. The equation for irradiation creep is

$$\overline{\varepsilon}/\overline{\sigma} = A_1 [1 - \exp(-\phi t/B_1)] + C_1 \phi t , \qquad (7)$$

where $\overline{\varepsilon}/\overline{\sigma}$ is the effective strain-to-effective stress ratio, A_1 is the transient creep parameter, C_1 is the steady-state creep parameter, and B_1 is the time constant. Although Equation (7) has been developed for 20% cold-worked Type 316 stainless steel, it has been applied to annealed stainless steel, since the degree of radiation creep in both materials is expected to be similar. In accordance with the initial exclusion of synergistic effects, the swelling term has been omitted from Equation (7). A general equation used to describe thermal creep in vanadium is given by

$$\dot{\varepsilon} = K\sigma^{n'} \exp[-Q/RT], \qquad (8)$$

where $\dot{\varepsilon}$ is the steady-state creep rate, K is a materials constant, σ is the applied stress, n' is the stress exponent, Q is the creep activation energy, and RT has its usual meaning. Only limited data are available with which to determine the parameters in Equation (8). The temperature and stress dependence of creep was obtained primarily from experiments in vanadium and vanadium-titanium alloys.[21,22] The materials constant, K, was determined from the creep properties of V-Cr-Ti alloys that have creep properties substantially superior to V-Ti alloys at 650 and 700°C.[17,23,23] The radiation creep in vanadium alloys has not been considered because of lack of data. Figure 9 shows an experimental creep curve for the V-15 Cr-5 Ti alloy at 650°C under a stress of 21 ksi[23] and the comparable curve derived from Equation (8).

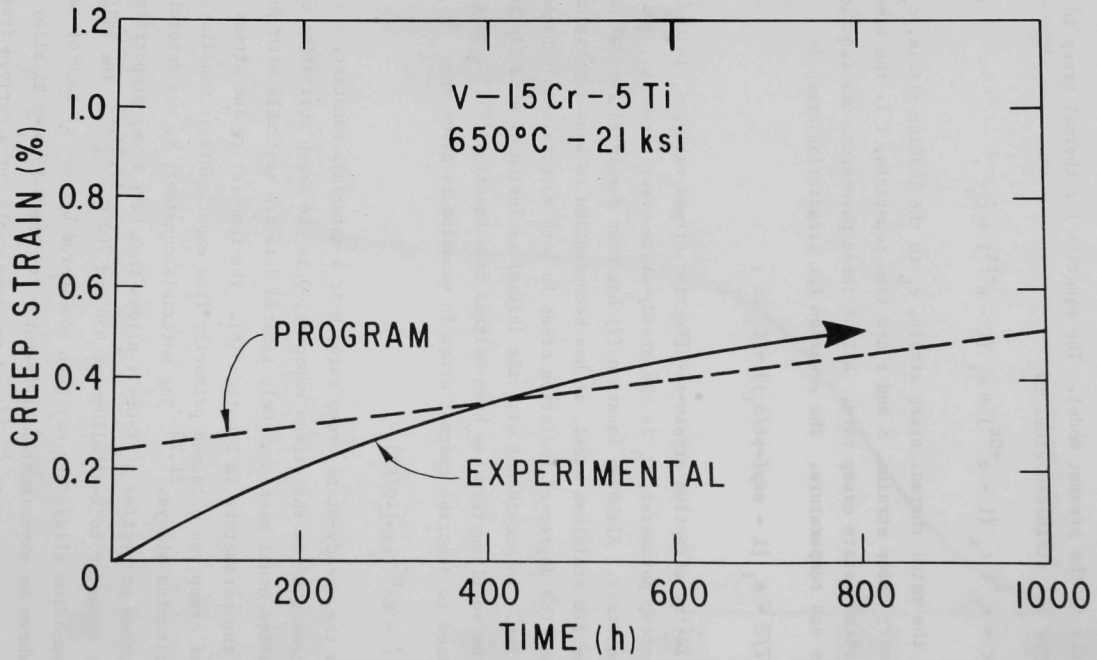

Figure 9. Creep Strain Curves for V-15 Cr-5 Ti Alloy Under 21 ksi Stress at 650°C.

D. Fatigue

Only the stainless steel fatigue properties have been modeled in the present investigation because of insufficient data for vanadium-base alloys. Although a substantial effort has been expended on studies of the fatigue properties of unirradiated stainless steels,[25,26] studies of the fatigue properties of irradiated stainless steel are much more limited.[27,28] As a result, the effects of radiation on fatigue life have not been incorporated into the present model. Both the strain-range-life and the linear-elastic fracture mechanics approaches have been used to evaluate the fatigue behavior of stainless steel.

The strain-range-life fatigue curves for 18-8 stainless steels from ASME code case 1592-8 were used as a basis for prediction of fatigue lifetimes.[29] These curves were fit to a modified universal slopes equation of the form[30]

$$\Delta\varepsilon_t = G\, N_f^{-0.6} + H\, N_f^{-0.12} \quad , \tag{9}$$

where $\Delta\varepsilon_t$ is the total strain range during a fatigue cycle, N_f is the number of cycles to failure, and G and H are constants determined from the code-case curves. The curves of strain range versus N_f from the code case are plotted in Figure 10 for temperatures to 700°C.

A linear-elastic fracture mechanics analysis was also used to evaluate the fatigue behavior of stainless steel. The data used were taken from a recent review of crack propagation in stainless steel.[26] Since the amount of data on irradiated material is limited, these effects were not incorporated into the model. The equation used to relate crack propagation rate per cycle is[26]

$$da/dN = M \left[K_{max}\,(1 - R)^m\right]^n \quad , \tag{10}$$

where da/dN is the crack-growth rate, M is a materials parameter that depends on temperature, K_{max} is the maximum stress-intensity factor during the cycle, R is the stress ratio which is defined as the minimum stress during a fatigue cycle divided by the maximum stress during the cycle, and m and n are experimentally determined exponents. The values for K_{max} depend

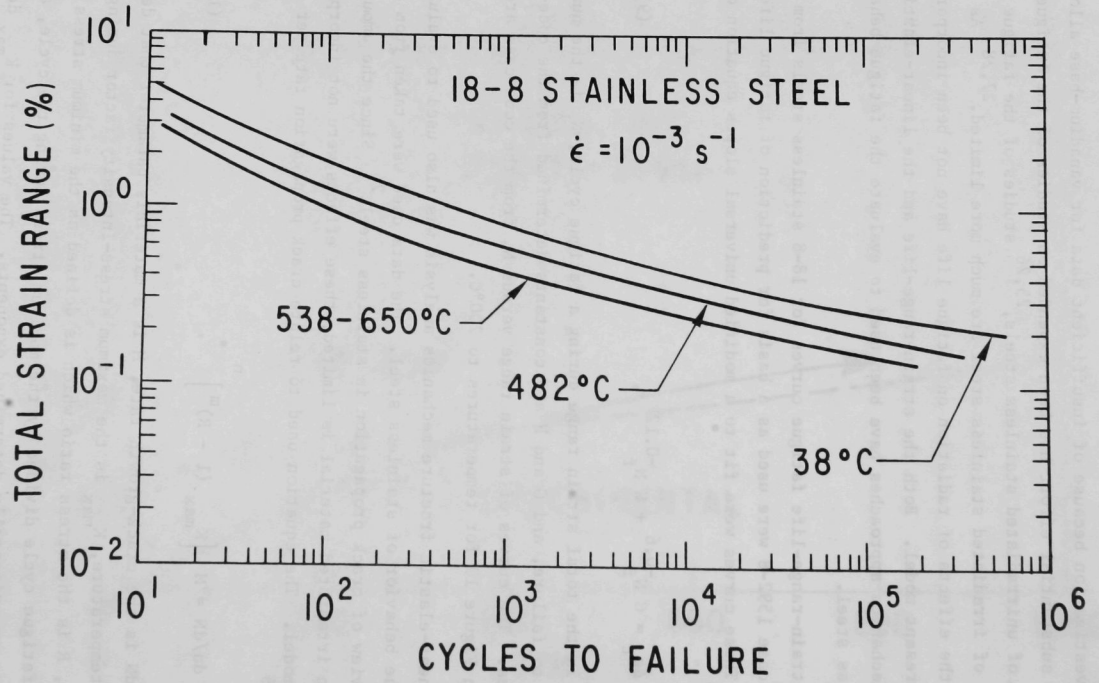

Figure 10. Design Strain Range - Lifetime Curves for 18-8 Stainless Steels (ASME Code Case 1331-8) for Temperatures to 700°C.

upon the component and crack geometry as well as the applied stress. The geometry included in the life program is that of a plate under a tensile stress with a crack present on one edge.

IV. RESULTS AND DISCUSSION

The properties described in Section III were individually programmed to determine the lifetime sensitivity to various parameters. The calculations are based on a constant neutron wall loading of 2 MW/m^2, and the component lifetime curves for a particular property are plotted as a function of operation temperature. The uncertainties in calculated lifetimes are greater in the case of the vanadium alloy, since less data are available on the bulk properties of this material.

A. Swelling

Figures 11 and 12 show the predicted operating lifetimes for the annealed Type 316 stainless steel and the vanadium alloy for a range of swelling criteria. In general, the shape of the lifetime curves are the inverse of the shape of the swelling versus temperature curves, with the minimum lifetime occurring at the peak swelling temperature. The calculated lifetimes limited by swelling are substantially shorter for the stainless steel than for the vanadium alloy. In addition, raising the swelling limit of stainless steel from 2 to 10% increased the lifetime from only 1 year to 1-3/4 years at the peak swelling temperature of 525°C, whereas a similar increase in the swelling limit of the vanadium alloy increased the lifetime from 4 years to over 15 years at the peak swelling temperature of 600°C. The predicted lifetime is more strongly dependent on the limiting swelling criteria at temperatures just below the peak swelling temperature.

B. Ductility

Figures 13 and 14 are plots of the predicted operating lifetimes of the stainless steel and the vanadium alloy when a minimum ductility, measured by the uniform elongation, is used as the limiting criterion. The curves tend toward a decrease in lifetime with an increase in temperature. More rapid decreases in lifetime generally occur at temperatures where helium

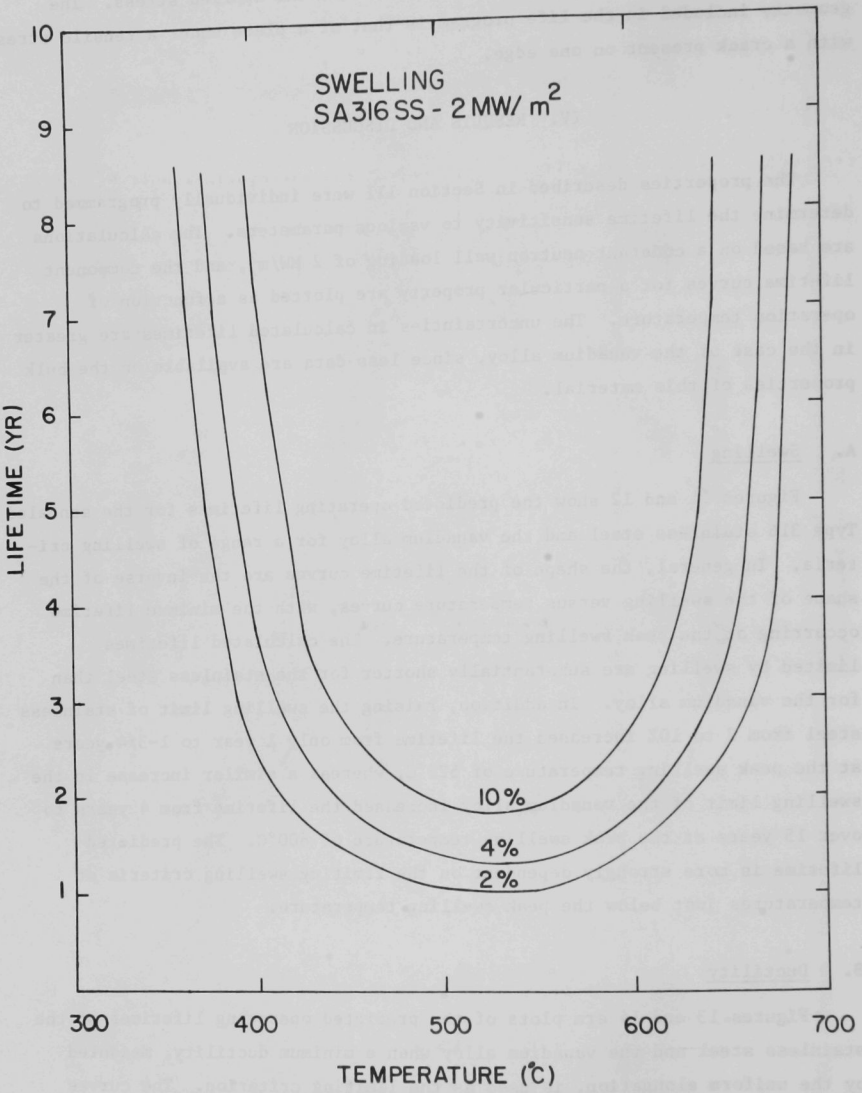

Figure 11. Predicted Operating Lifetime as a Function of Temperature for Type 316 Stainless Steel When Limited by Radiation Swelling.

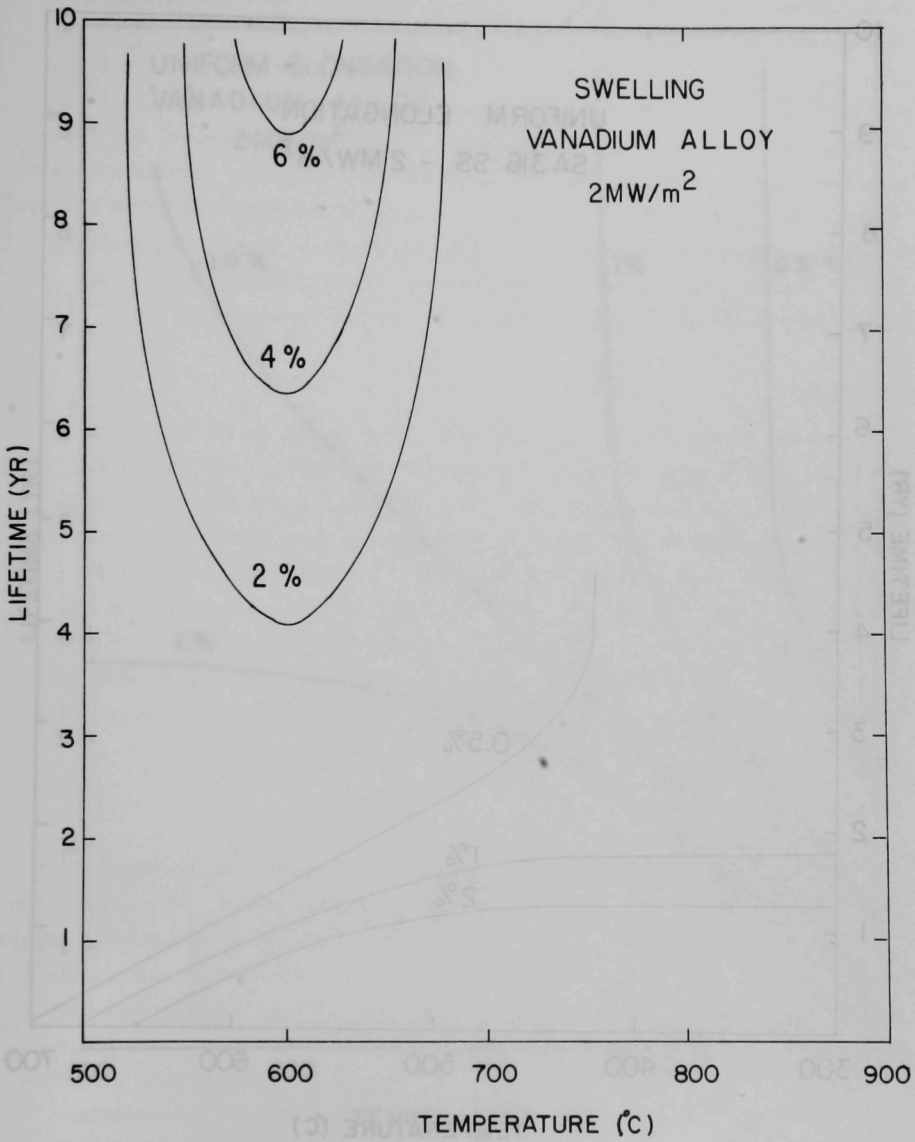

Figure 12. Predicted Operating Lifetime as a Function of Temperature for V-15 Cr-5 Ti Alloy When Limited by Radiation Swelling.

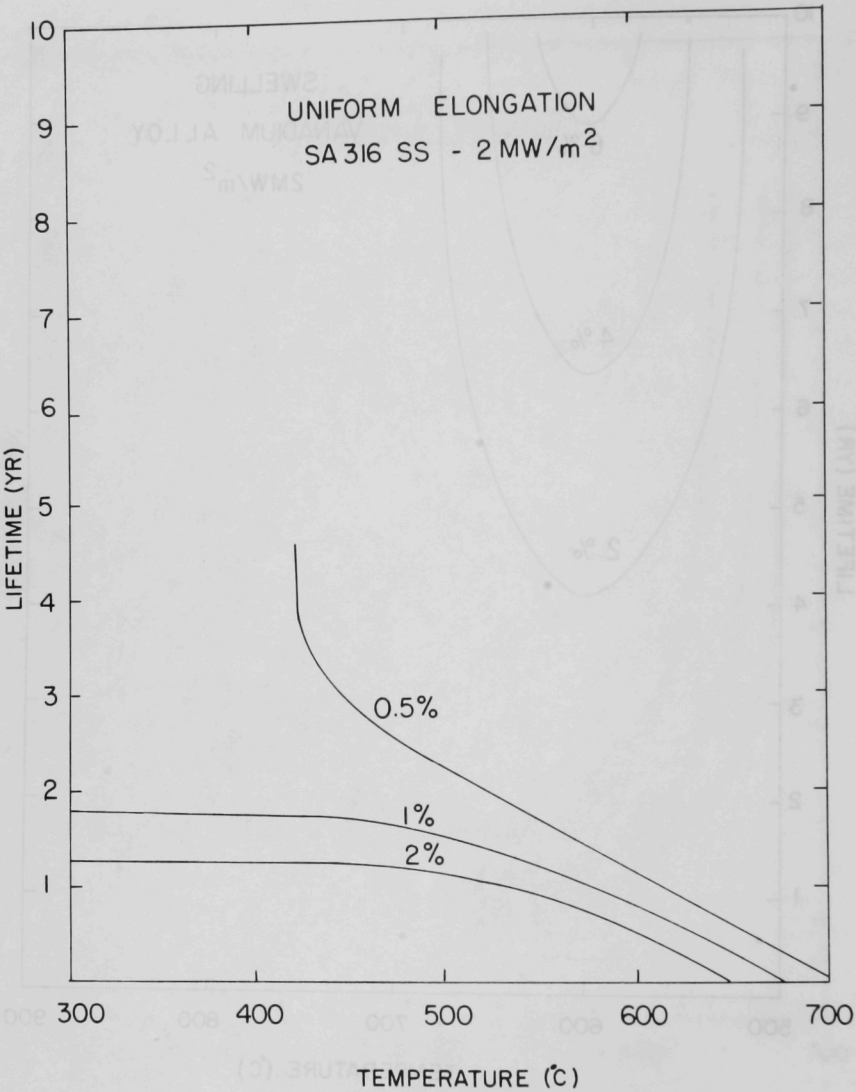

Figure 13. Predicted Operating Lifetime as a Function of Temperature for Stainless Steel when Limited by Loss of Ductility.

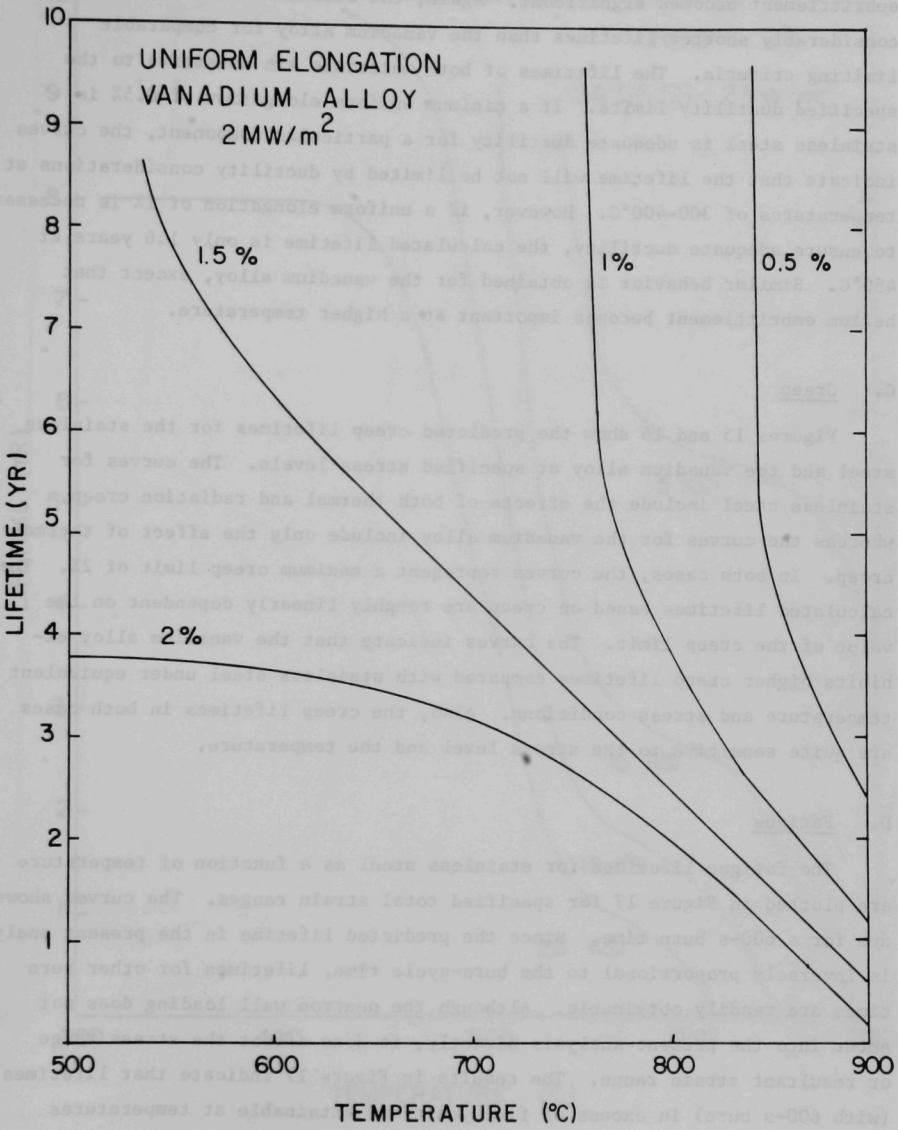

Figure 14. Predicted Operating Lifetime as a Function of Temperature for V-15 Cr-5 Ti Alloy when Limited by Loss of Ductility.

embrittlement becomes significant. Again, the stainless steel exhibits considerably shorter lifetimes than the vanadium alloy for comparable limiting criteria. The lifetimes of both materials are sensitive to the specified ductility limits. If a minimum uniform elongation of 0.5% in stainless steel is adequate ductility for a particular component, the curves indicate that the lifetime will not be limited by ductility considerations at temperatures of 300-400°C. However, if a uniform elongation of 1% is necessary to ensure adequate ductility, the calculated lifetime is only 1.6 years at 450°C. Similar behavior is obtained for the vanadium alloy, excect that helium embrittlement becomes important at a higher temperature.

C. Creep

Figures 15 and 16 show the predicted creep lifetimes for the stainless steel and the vanadium alloy at specified stress levels. The curves for stainless steel include the effects of both thermal and radiation creep, whereas the curves for the vanadium alloy include only the effect of thermal creep. In both cases, the curves represent a maximum creep limit of 2%. The calculated lifetimes based on creep are roughly linearly dependent on the value of the creep limit. The curves indicate that the vanadium alloy exhibits higher creep lifetimes compared with stainless steel under equivalent temperature and stress conditions. Also, the creep lifetimes in both cases are quite sensitive to the stress level and the temperature.

D. Fatigue

The fatigue lifetimes for stainless steel as a function of temperature are plotted in Figure 17 for specified total strain ranges. The curves shown are for a 600-s burn time. Since the predicted lifetime in the present analysis is inversely proportional to the burn-cycle time, lifetimes for other burn times are readily obtainable. Although the neutron wall loading does not enter into the present analysis directly, it does affect the stress range or resultant strain range. The results in Figure 17 indicate that lifetimes (with 600-s burn) in excess of five years are attainable at temperatures below 500°C if the total cyclic strain range can be maintained below 0.15%.

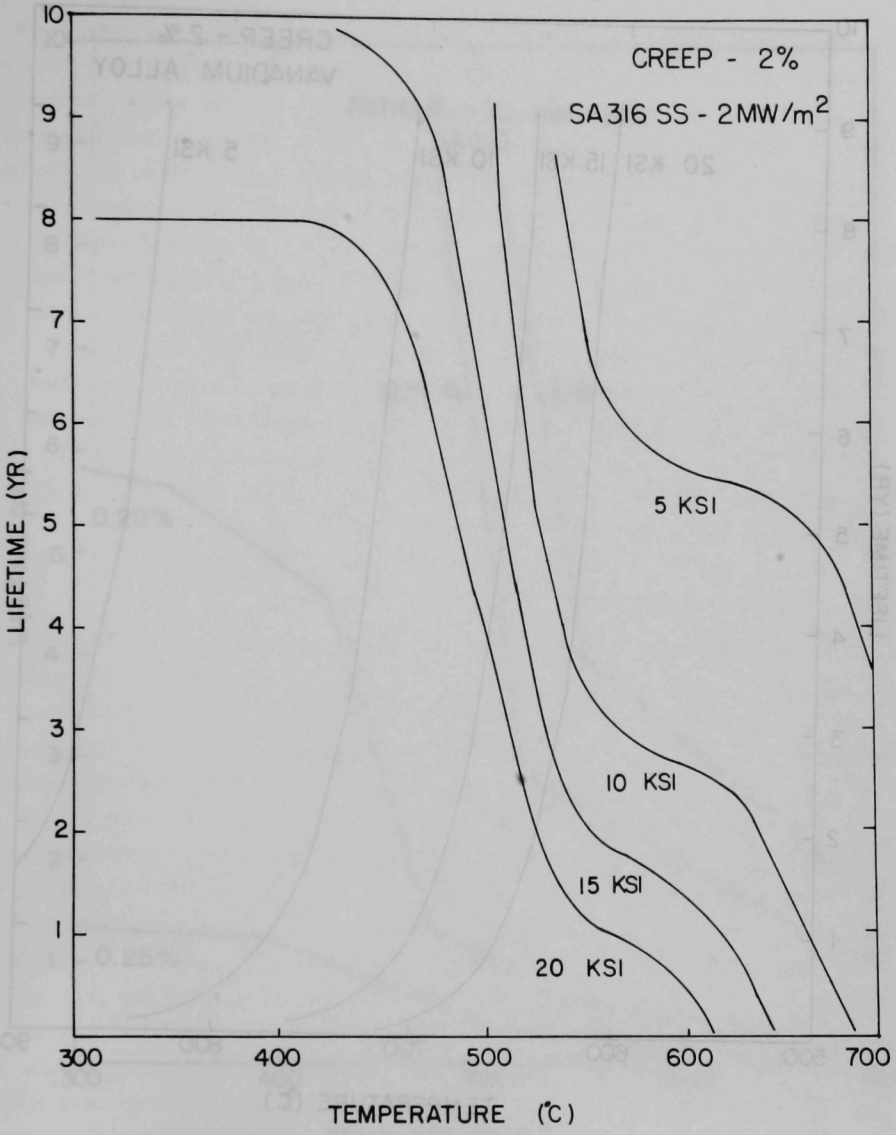

Figure 15. Predicted Operating Lifetime as a Function of Temperature for Stainless Steel Under Specified Stresses when Limited by 2% Creep Strain.

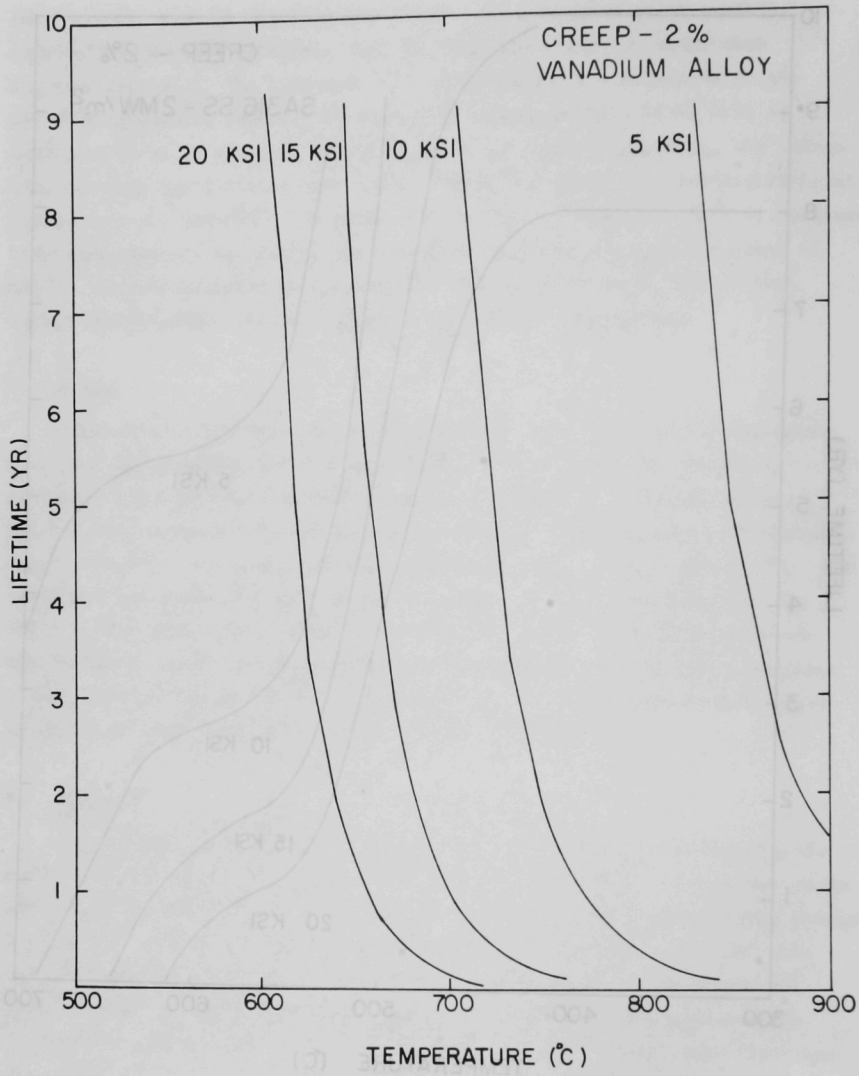

Figure 16. Predicted Operating Lifetime as a Function of Temperature for V-15 Cr-5 Ti Alloy under Specified Stresses when Limited by 2% Creep Strain.

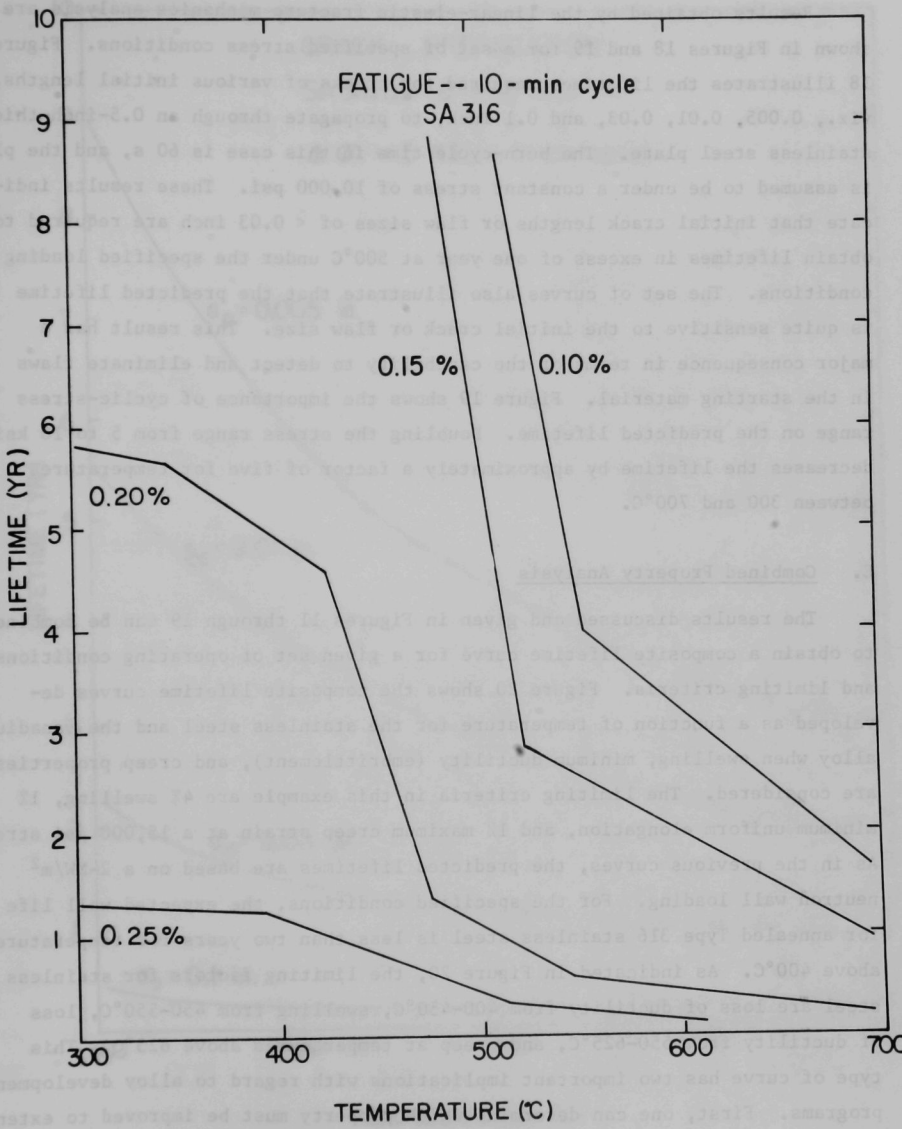

Figure 17. Predicted Fatigue Lifetimes as a Function of Temperature for Stainless Steel Cycled at Specified Strain Ranges.

Results obtained by the linear-elastic fracture mechanics analysis are shown in Figures 18 and 19 for a set of specified stress conditions. Figure 18 illustrates the lifetimes required for cracks of various initial lengths, viz., 0.005, 0.01, 0.03, and 0.1 inch, to propagate through an 0.5-inch-thick stainless steel plate. The burn-cycle time in this case is 60 s, and the plate is assumed to be under a constant stress of 10,000 psi. These results indicate that initial crack lengths or flaw sizes of < 0.03 inch are required to obtain lifetimes in excess of one year at 500°C under the specified loading conditions. The set of curves also illustrate that the predicted lifetime is quite sensitive to the initial crack or flaw size. This result has a major consequence in terms of the capability to detect and eliminate flaws in the starting material. Figure 19 shows the importance of cyclic-stress range on the predicted lifetime. Doubling the stress range from 5 to 10 ksi decreases the lifetime by approximately a factor of five for temperatures between 300 and 700°C.

E. Combined Property Analysis

The results discussed and given in Figures 11 through 19 can be combined to obtain a composite lifetime curve for a given set of operating conditions and limiting criteria. Figure 20 shows the composite lifetime curves developed as a function of temperature for the stainless steel and the vanadium alloy when swelling, minimum ductility (embrittlement), and creep properties are considered. The limiting criteria in this example are 4% swelling, 1% minimum uniform elongation, and 1% maximum creep strain at a 15,000 psi stress. As in the previous curves, the predicted lifetimes are based on a 2-MW/m^2 neutron wall loading. For the specified conditions, the expected wall life for annealed Type 316 stainless steel is less than two years for temperatures above 400°C. As indicated in Figure 20, the limiting factors for stainless steel are loss of ductility from 400-450°C, swelling from 450-550°C, loss of ductility from 550-625°C, and creep at temperatures above 625°C. This type of curve has two important implications with regard to alloy development programs. First, one can determine which property must be improved to extend the life of the wall for a given set of conditions. The quality of the data used to obtain the particular life-limiting curve of interest can also be reviewed to better assess the uncertainty. Second, the overall gain achieved

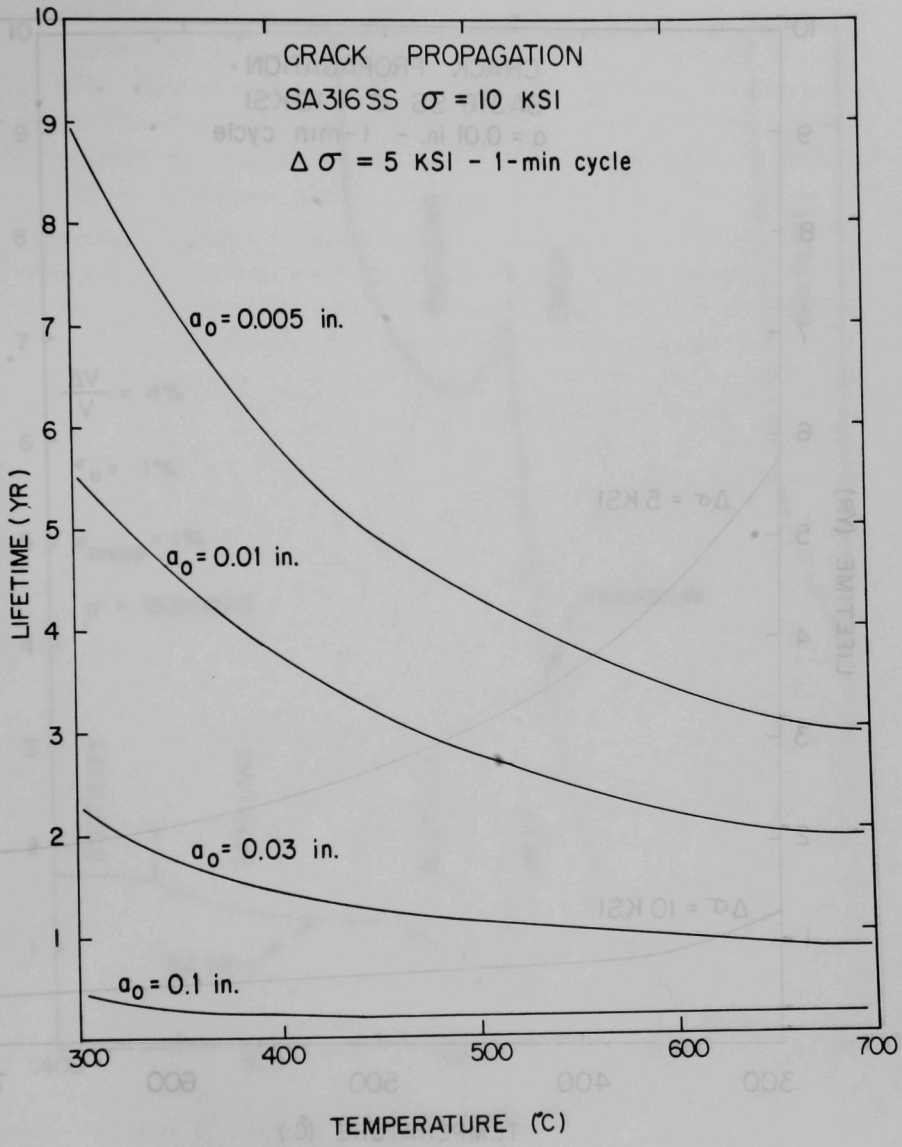

Figure 18. Predicted Lifetime for Crack Propagation as a Function of Temperature for Stainless Steel with Specified Initial Flaw Sizes.

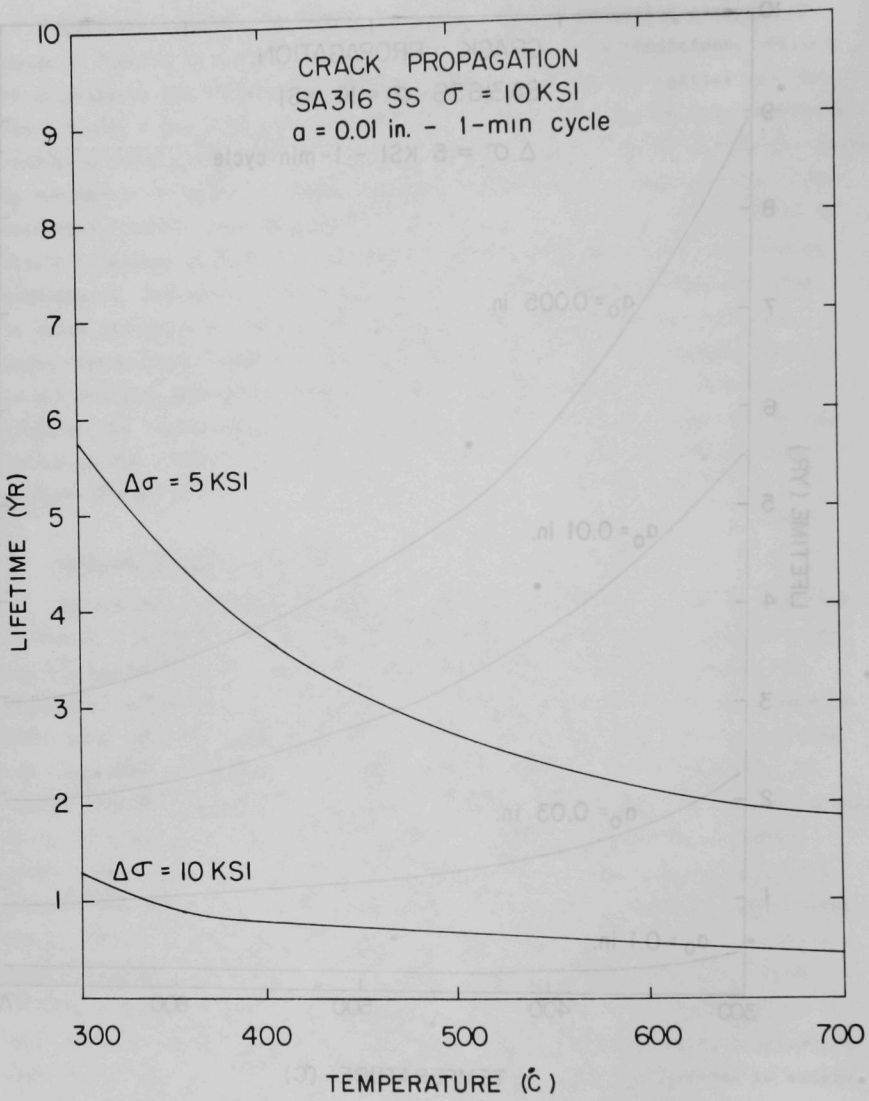

Figure 19. Predicted Lifetime for Crack Propagation as a Function of Temperature for Stainless Steel Under Specified Cyclic Stresses (initial crack size = 0.01 in.).

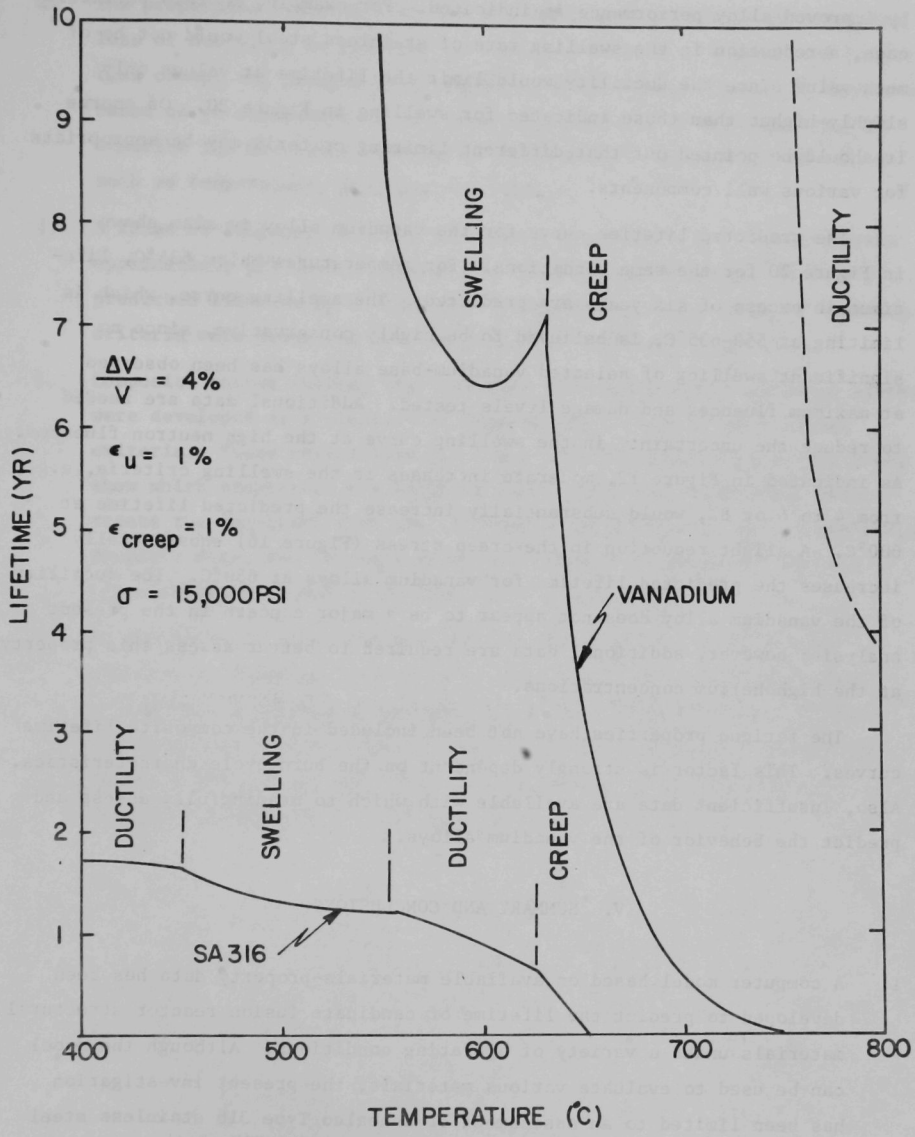

Figure 20. Composite Lifetime Curves as a Function of Temperature for Stainless Steel and V-15 Cr-5 Ti Alloy when Limited Either by Swelling, Loss of Ductility, or Creep Strain for Specified Criteria.

by improved alloy performance is indicated. For example, in this particular case, a reduction in the swelling rate of stainless steel would not be of much value since the ductility would limit the lifetime at values only slighly higher than those indicated for swelling in Figure 20. Of course it should be pointed out that different limiting criteria may be appropriate for various wall components.

The predicted lifetime curve for the vanadium alloy is also shown in Figure 20 for the same conditions. For temperatures below 635°C, lifetimes in excess of six years are predicted. The swelling curve, which is limiting at 550-635°C, is believed to be highly conservative, since no significant swelling of selected vanadium-base alloys has been observed at maximum fluences and damage levels tested. Additional data are needed to reduce the uncertainty in the swelling curve at the high neutron fluences. As indicated in Figure 12, moderate increases in the swelling criteria, e.g., from 4 to 6 or 8%, would substantially increase the predicted lifetime at 600°C. A slight reduction in the creep stress (Figure 16) substantially increases the predicted lifetime for vanadium alloys at 650°C. The ductility of the vanadium alloy does not appear to be a major concern in the present analysis; however, additional data are required to better assess this property at the high helium concentrations.

The fatigue properties have not been included in the composite lifetime curves. This factor is strongly dependent on the burn-cycle characteristics. Also, insufficient data are available with which to meaningfully assess and predict the behavior of the vanadium alloys.

V. SUMMARY AND CONCLUSIONS

1. A computer model based on available materials-property data has been developed to predict the lifetime of candidate fusion reactor structural materials under a variety of operating conditions. Although the model can be used to evaluate various materials, the present investigation has been limited to an assessment of annealed Type 316 stainless steel and the V-15% Cr-5% Ti alloy. Stainless steel has been proposed as a structural material in near-term power reactors, and the vanadium alloy is representative of advanced higher-temperature structural materials.

2. The properties evaluated for the two structural materials are swelling, loss of ductility as measured by uniform elongation, thermal and radiation creep, and fatigue (for stainless steel only). Empirical equations based on an assessment of available literature data were developed to describe the materials behavior as functions of independent variables such as temperature, fluence, and stress.

3. A range of limiting criteria considered appropriate for fusion-reactor applications was used to define the materials limitations. Curves of predicted lifetime as a function of temperature for a range of limiting criteria were developed for the different materials properties.

4. Composite curves showing the predicted life and the life-limiting property were developed as a function of temperature for specified limiting criteria. These curves form the basis for first-wall life predictions, show which properties are limiting under different conditions, demonstrate the sensitivity of the lifetime to uncertainties in the available property data, and indicate potential benefits to be gained through improvements achieved by further alloy development.

5. On the basis of available data for the properties considered and appropriate limiting criteria, the reference vanadium alloy appears to have the capability of operating for considerably longer lifetimes and at somewhat higher temperatures than stainless steel. Additional property data, particularly for the vanadium alloy, are required to confirm and improve the basis for these predictions.

REFERENCES

1. M. A. Abdou, et al., "Parametric Systems Analysis for Tokamak Power Plants," Argonne National Laboratory, to be published.

2. Nuclear Systems Materials Handbook, Vol. 1, Design Data.

3. R. Carlander, S. D. Harkness, and A. T. Santhanum, "Effect of Fast Neutron Irradiation on Tensile Properties and Swelling Behavior of Vanadium Alloys," Effects of Radiation on Substructure and Mechanical Properties of Metals and Alloys, ASTM STP 529, 399 (1973).

4. J. Bentley and F. W. Wiffen, "Swelling and Microstructural Changes in Irradiated Vanadium Alloys," Nucl. Tech. 30, 376 (1976).

5. A. T. Santhanum, A. Taylor, B. J. Kestel, and C. Steves, "Swelling Studies of Vanadium and Vanadium-Titanium Alloys Using Ion-Simulation Techniques," J. Vac. Sci. Tech. 12, 528 (1975).

6. A. T. Santhanum, A. Taylor, and S. D. Harkness, "Charged Particle Simulation Studies of Vanadium and Vanadium Alloys," Defects and Defect Clusters in BCC Metals and Their Alloys, R. J. Arsenault, ed., Nucl. Metall. 18, 302 (1973).

7. S. C. Agarwal and A. Taylor, "Dose Dependence of Void Swelling in Vanadium Irradiated with Self Ions," Proc. Conf. on Radiation Effects and Tritium Technology for Fusion Reactors, CONF-750989, Vol. 1, I-150 (1975).

8. E. E. Bloom and F. W. Wiffen, "The Effects of Large Concentrations of Helium on the Mechanical Properties of Neutron-Irradiated Stainless Steel, J. Nucl. Mater. 58, 171 (1975).

9. G. L. Kulcinski, R. G. Brown, R. G. Lott, and P. A. Sang, "Radiation Damage Limitations in the Design of the Wisconsin Tokamak Fusion Reactor," Nucl. Tech. 22, 20 (1974).

10. E. E. Bloom, "Correlation of Structure and Ductility of Irradiated Stainless Steels," Irradiation Embrittlement and Creep in Fuel Cladding and Core Components, Brit. Nucl. Energy Soc. (1972), p. 93.

11. K. R. Garr, C. G. Rhodes, and D. Kramer, "Effects of Microstructure on Swelling and Tensile Properties of Neutron Irradiated Type 316 and 405 Stainless Steels," Effects of Radiation on Substructure and Mechanical Properties of Metals and Alloys, ASTM STP 529, 109 (1973).

12. D. Fahr, E. E. Bloom, and J. O. Steigler, "Post Irradiation Tensile Properties of Annealed and Cold-Worked Type 316 Stainless Steel," in Irradiation Embrittlement and Creep in Fuel Cladding and Core Components, Brit. Nucl. Energy Soc. (1972), p. 167.

13. R. L. Fish, A. J. Lovell, H. R. Brager, and J. J. Holmes, "Tensile and Creep Behavior of Cold-Worked 316 Stainless Steel after EBR-II Irradiation," Irradiation Embrittlement and Creep in Fuel Cladding and Core Components, Brit. Nucl. Energy Soc. (1972), p. 187.

14. P. Soo and J. McAndrew, Type 304 and Type 316 Stainless Steel Data for High Temperature Design, Westinghouse Electric Company, WARD-3045T2C-3 (1972).

15. R. L. Fish and C. W. Hunter, "Tensile Properties of Fast Reactor Irradiated Type 304 Stainless Steel," Presented at ASTM Symposium on the Effects of Radiation on Structural Materials, May 4-6, 1976.

16. R. F. Mattas, H. Wiedersich, D. G. Atteridge, A. B. Johnson, and J. F. Remark, "Elevated-Temperature Tensile Properties of V-15Cr-5Ti Containing Helium Introduced by Ion Bombardment and Tritium Decay," Proc. of the Second ANS Topical Meeting on the Technology of Controlled Thermonuclear Fusion, Hanford, Washington, CONF-760935, September 1976.

17. W. C. Kramer, W. R. Burt, Jr., F. J. Karasek, J. C. Flinn, and R. M. Mayfield, "Vanadium Alloy Screening Studies and Fabrication of V-15 wt % Ti-7.5 wt % Cr Tubing for Nuclear Fuel Cladding, Argonne National Laboratory, ANL-7206 (1966).

18. F. W. Wiffen, "The Tensile Properties of Fast Reactor Neutron Irradiated BCC Metals and Alloys," Defects and Defect Clusters in BCC Metals and Their Alloys, R. J. Arsenault, ed., Nucl. Metall. 18, 176 (1973).

19. H. Böhm, W. Dienst, H. Hauck, and H. J. Laue, "Irradiated Effects on the Mechanical Properties of Vanadium-Base Alloys," Effects of Radiation on Structural Materials, ASTM STP 426, 95 (1967).

20. D. Kramer, "Helium Embrittlement," Fusion Reactor First Wall Materials, WASH-1206, (1971), p. 50.

21. H. Böhm and M. Schirra, "Einfluss der Kaltverformung und Wärmebehandlung anf das Zeitstand und Kriechverbalten von Vanadium-Legierunger," Z. Metallkde 59, 715 (1968).

22. K. R. Wheeler, E. R. Gilbert, F. L. Yaggee, and S. A. Duran, "Minimum-Creep-Rate Behavior of Polycrystalline Vanadium from 0.35 to 0.87 T_m," Acta. Met. 19, 21 (1971).

23. F. L. Yaggee, unpublished data.

24. C. G. Collins, J. Moteff, and B. A. Chandler, "Evaluation of the Potential of Selected Alloys for Use as a Fuel Cladding Material in an LMFBR," General Electric Company, GEMP-573 (1969).

25. R. W. Weeks, D. R. Diercks, and C. F. Cheng, "ANL Low-cycle Fatigue Studies Program, Results, and Analysis," Argonne National Laboratory, ANL-8009 (1973).

26. L. A. James, "Fatigue-Crack Propagation in Austenitic Stainless Steels," Atomic Energy Review 14, 1 (1976).

27. C. R. Brinkman, G. E. Korth, J. M. Beeston, "Influence of Irradiation on the Creep/Fatigue Behavior of Several Austenitic Stainless Steels and Incoloy 800 at 700°C," Effects of Radiation on Substructure and Mechanical Properties of Metals and Alloys, ASTM STP 529, 473 (1973).

28. C. R. Brinkman, G. E. Korth, and R. R. Hobbins, "Estimates of Creep-Fatigue Interaction in Irradiated and Unirradiated Austenitic Stainless Steel," Nucl. Tech. 16, 297 (1972).

29. Interpretations of ASME Boiler and Pressure Vessel Code, Code Case 1592-8 (1976).

30. A. D. Tetelman and A. J. McEvily, Jr., Fracture of Structural Materials, John Wiley and Sons, Inc., New York, (1967), p. 377.

August, 1977

ANL/FPP/TM-88

COMPUTATIONAL MODEL FOR SUPERCONDUCTING TOROIDAL-FIELD MAGNETS FOR A TOKAMAK REACTOR*

by

L. R. Turner and M. A. Abdou

Fusion Power Program
Argonne National Laboratory
Argonne, Illinois 60439

ANL/FPP Technical Memorandum Number 88

Results reported in the FPP series of memoranda frequently are preliminary and subject to revision. They should not not be quoted nor referenced without the author's permission.

* *Work supported by the U.S. Energy Research and Development Administration.*

ABSTRACT

A computational model for predicting the performance characteristics and cost of superconducting toroidal-field (TF) magnets in tokamak reactors is presented. The model, essentially a parameterization of various design algorithms, can be used to compare the technical and economic merits of different approaches to the design of TF magnets for a reactor system. The model has been integrated into the ANL Systems Analysis Program. Samples of results obtainable with the model are presented.

I. Introduction

Parametric systems anlaysis provides the means for identifying technically feasible and economically attractive fusion reactor systems. An integrated systems computer program for simulation of tokamak power plants has been developed at ANL.[1] The program consists of modular units with each unit corresponding to a reactor subsystem. The function of a subsystem model is to predict the performance characteristics for the subsystem, account for the interrelation with other subsystems and provide information required for estimating the cost of the subsystem. The purpose of this report is to describe a model that has been developed for the toroidal-field (TF) coils.

The algorithms included in the model should be simple enough to keep computational time and cost down and to permit an intuitive understanding of their workings, but at the same time complete enough to incorporate variation with all important parameters. Compromises, some of them painful, have had to be made between these conflicting aims.

The model has proved useful not only in overall systems studies, but also in finding quickly and easily the implications of proposed design options.

Section II gives a qualitative overview of the model, which is developed in detail in Section III. Representative results obtained with the model are presented in Section IV. Symbols used are defined in Appendix A.

II. The Model in Outline

The TF coils are taken to be of the constant tension shape;[2] the shape is calculated by the approximate method of Moses and Young.[3]

Several material choices are permitted in specifying the magnet. The magnet may be superconducting or conventional; if it is superconducting, the superconductor may be NbTi or a hybrid with NbTi in the low-field turns and Nb_3Sn in the high-field turns. The superconductor may be graded or ungraded. The magnet may be cryostable or intrinsically stable; the stabilizer may be copper or aluminum and graded or ungraded. The support material may be

stainless steel or aluminum alloy. The options of conventional magnets and of aluminum stabilizer and support material have not been implemented yet. The options of intrinsically stable coils and of ungraded superconductor and stabilizer have been included but have not been fully tested.

The amount of the different materials is determined by the coil circumference and by the following factors. The superconductor is determined by the total number of amp-turns and by the critical current density, which in turn is determined by the maximum magnetic field and the design temperature. The amount of stabilizer is generally determined by cryostability considerations. The amount of support material is determined by the tension in the coils and the allowable stress or strain; it is diminished by the tension that the stabilizer can support. The thickness of the support cylinder is determined by the allowed stress and by stability against buckling.

The simplified flow diagram in Figure 1 shows how the model operates. The maximum magnetic field and the space requirements inside the TF coil are first specified; from these the coil thickness is estimated and the inner and outer mid-radii R_1 and R_2 of the coil calculated. These in turn determine the total amp turns required nNI.

At this point the choice between cryostable or intrinsically stable coils occurs. If the coils are to be cryostable, the operating temperature, T_o, and temperature safety margin, ΔT, are specified; their sum is the design temperature, T. If, instead, the coils are to be intrinsically stable, the percentage of short-sample current density at which the magnet is to operate is also specified.

In either case, the choice between NbTi or hybrid coils is made at this point on the basis of the maximum field. The critical current density, J_c, the cross sectional area, A_{sc}, and the reduced area if the superconductor is to be graded complete the specification of the superconductor.

For an intrinsically stable conductor, the ratio of copper to superconductor is specified; for a cryostable conductor the amount of copper is determined from cryostability considerations involving heat transfer to the helium and electrical resistivity. The resistivity is the sum of the intrinsic resistivity, magnetoresistivity and radiation-induced resistivity. Since the

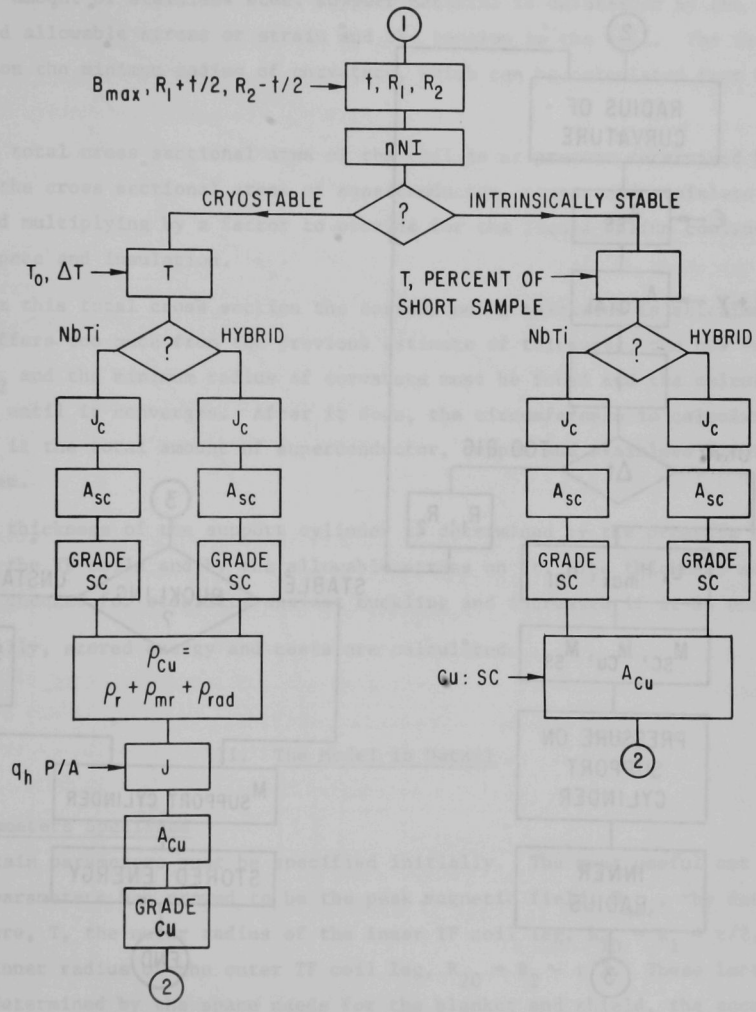

Figure 1a. Simplified Flow Diagram for the TF Magnet Model

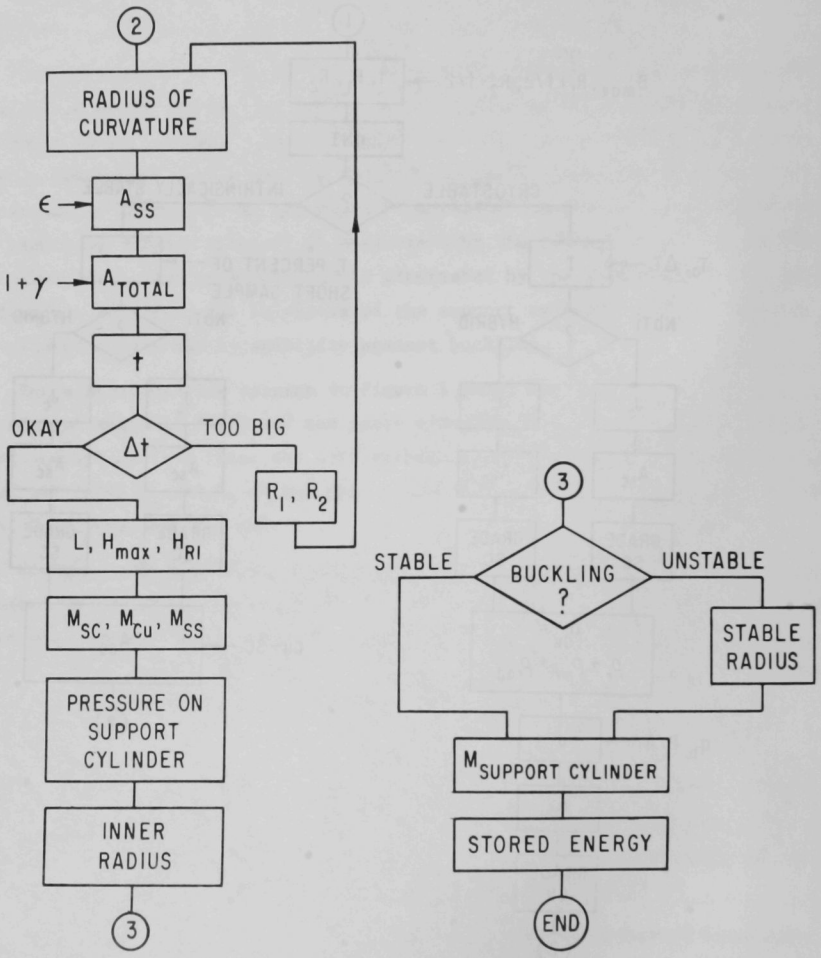

Figure 1b. Simplified Flow Diagram for the TF Magnet Model

magnetoresistivity and radiation-induced resistivity vary across the thickness of a coil, the copper can be graded.

The amount of stainless steel support material is determined by the specified allowable stress or strain and the tension in the coil. The tension depends on the minimum radius of curvature, which can be calculated from R_1 and R_2.

The total cross sectional area of the coil is at present determined by summing the cross sectional areas of superconductor, copper and stainless steel and multiplying by a factor to provide for the liquid helium coolant, vacuum space and insulation.

From this total cross section the corresponding thickness is calculated. If it differs too much from the previous estimate of thickness, the new values of R_1, R_2 and the minimum radius of curvature must be found and the calculation iterated until it converges. After it does, the circumference is calculated; and from it the total amount of superconductor, copper and stainless steel in the system.

The thickness of the support cylinder is determined by the pressure exerted on it by the TF coils and by the allowable stress on it. The thickness so found is checked for stability against buckling and increased if it is unstable.

Finally, stored energy and costs are calculated.

III. The Model in Detail

A. Parameters Specified

Certain parameters must be specified initially. The most useful set of initial parameters has proved to be the peak magnetic field, B_{max}, the design temperature, T, the outer radius of the inner TF coil leg, $R_{10} = R_1 + t/2$, and the inner radius of the outer TF coil leg, $R_{20} = R_2 - t/2$. These latter two are determined by the space needs for the blanket and shield, the access space between coils and the permissible field ripple. If the shape generated from R_{10} and R_{20} fails to provide sufficient height, H_{max}, for a very elongated plasma, a diverter or other feature of a particular design, then R_1 and H_{max},

rather than R_1 and R_2, are taken as the design parameters for the shape. The design temperature T is the sum of the operating temperature, generally 4.2 K, and the temperature safety margin, generally 0.5 K.

Another parameter to be specified is the permissible stress or strain in the conductor. For a Nb_3Sn-Cu composite conductor, the strain is limited by the brittleness of the Nb_3Sn; but for a NbTi-Cu composite conductor, it is limited only by the strain-induced resistivity of the copper.

B. The Superconductor

Two kinds of coils are envisioned; for fields B_{max} up to 8 or 10 T, NbTi is used. For higher values of B_{max}, hybrid coils are considered, with NbTi in the outer turns and Nb_3Sn in the inner turns where the field is higher. The choice is an input option.

In either case, the total current NnI is given by Ampere's Law

$$NnI = 2\pi\ (R_1 + t/2)\ B_{max}/\mu o$$

Superconducting TF coils for a tokamak reactor would almost certainly be cryostable as opposed to intrinsically stable. An intrinsically stable magnet may spontaneously quench; a cryostable one will not unless its coolant is disrupted. The magnet system for a tokamak reactor is so large that it may be impossible to build it to survive a quench. Moreover, a power plant should not be subject to a probable spontaneous shutdown. However, it may prove interesting to compare cryostable and intrinsically stable coils, so provision was made in the magnet model for intrinsically stable coils as well.

1. Critical Current Density

For NbTi, the critical current density[4] as a function of temperature T in Kelvin and field B in Tesla is shown in Figure 2. The data in Figure 2 are fit by the expression

$$J_c = (T_c - T)\ (3.352 - 0.3607\ B + 11.929/T) \times 10^4\ A/cm^2 \qquad (2)$$

where the critical temperature T_c can be found by

$$T_c = 8.56\ (1 - B/14.7)^{1/2} \qquad (3)$$

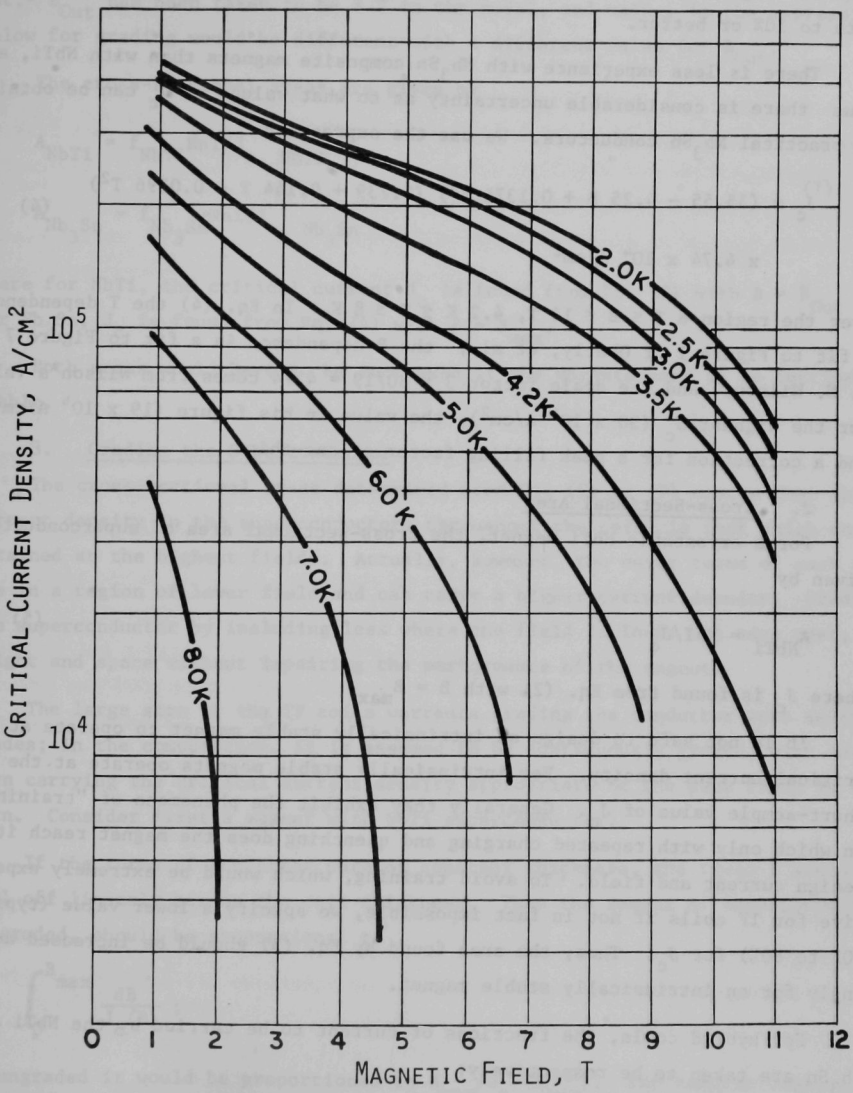

Figure 2. J-H Curve for NbTi Versus Temperature

Over the region $1\ T \le B \le 11\ T$, $3\ K \le T \le 6\ K$, $T_c - T > 1\ K$, Eq. (2) fits the data to 10% or better.

There is less experience with Nb_3Sn composite magnets than with NbTi, and thus there is considerable uncertainty as to what values of J_c can be obtained in practical Nb_3Sn conductors. We use the expression

$$J_c = (35.55 - 4.25\ B + 0.1375\ B^2)\ (0.739 + 0.144\ T - 0.0196\ T^2) \times 4.74 \times 10^4\ A/cm^2 \tag{4}$$

over the region $6\ T \le B \le 14\ T$, $4.2\ K \le T \le 8\ K$. In Eq. (4) the T dependence is a fit to Figure 1 of Oberly, et al.;[5] the B dependence is a fit to Figure 7 of M. N. Wilson;[6] and the scale factor 3 x 30/19 = 4.74 comes from Wilson's value for the highest J_c ($30 \times 10^4\ A/cm^2$), the value in his figure ($19 \times 10^4\ A/cm^2$), and a correction for a peak filling factor of one-third.

2. Cross-Sectional Area

For a cryostable NbTi magnet, the cross-sectional area of superconductor is given by

$$A_{NbTi} = NnI/J_c \tag{5}$$

where J_c is found from Eq. (2) with $B = B_{max}$.

It is not safe to design an intrinsically stable magnet to operate at the critical current density. Few intrinsically stable magnets operate at the short-sample value of J_c. Generally they exhibit the phenomena of "training," in which only with repeated charging and quenching does the magnet reach its design current and field. To avoid training, which would be extremely expensive for TF coils if not in fact impossible, we specify a lower value (typically 70% to 80%) for J_c. Thus, the area found by Eq. (5) should be increased accordingly for an intrinsically stable magnet.

For hybrid coils, the fractions of current to be carried by the NbTi and Nb_3Sn are taken to be respectively:

$$\left.\begin{aligned} f_{NbTi} &= B_{Cut}/B_{max} \\ \text{and} \quad f_{NbTi} &= 1 - f_{NbTi} \end{aligned}\right\} \tag{6}$$

where B_{Cut} is the highest field at which NbTi is to be used in the hybrid magnet. B_{Cut} has been taken to be 8 T in the model, and values in the expressions below for grading would be different with a different value for B_{Cut}.

The cross-sectional areas are given by

$$A_{NbTi} = f_{NbTi} NnI/J_{c,\ NbTi}$$

$$A_{Nb_3Sn} = f_{Nb_3Sn} NnI/J_{c,\ Nb_3Sn} \qquad (7)$$

where for NbTi, the critical current J_c is found from Eq. (2) with $B = B_{Cut}$ and for Nb_3Sn, J_c is found from Eq. (4) with $B = B_{max}$.

Both areas would have to be increased if the magnets were to be intrinsically stable.

3. Grading the Superconductor

The cross-sectional areas determined from Eq. (5) or (7) assume that the current density in the superconductors throughout the coils is that which can be attained at the highest fields. Actually, however, the outer turns of each coil are in a region of lower field and can carry a higher current density. Grading the superconductor by including less where the field is lower can save cost, weight and space without impairing the performance of the magnet.

The large size of the TF coils warrants grading the conductor into several grades; in the computation, it is assumed to be continuously graded, with each turn carrying the critical current density appropriate to the peak field in that turn. Consider first a magnet with NbTi superconductor.

If the turns of conductor were of constant thickness, the field B would fall off linearly across the coil thickness. Then the amount of superconductor, if graded, should be proportional to

$$\int_0^{B_{max}} \frac{dB}{J_c(B)} ;$$

If ungraded it would be proportional to $B_{max}/J_c\ (B_{max})$. For computational reasons, it was preferable to take the lower limit of the integral as $B_{min} = 1.31$ T rather than zero. The grading factor, GF, is the ratio of the two expressions:

$$GF_{NbTi} = \frac{J_c(B_{max})}{B_{max}} \left[\frac{B_{min}}{J_c(B_{min})} + \int_{B_{min}}^{B_{max}} \frac{dB}{J_c(B)} \right] \tag{8}$$

A curve of $1/J_c$ vs B at T = 4.2 K was fit to the quadratic expression $1/J_c = (0.00493 - 0.00917\ B + 0.0035\ B^2) \times 10^{-4}\ cm^2/A$. With that expression incorporated, Eq. (8) was integrated analytically. Values of GF_{NbTi} for various values of B_{max} were fit numerically to give:

$$GF_{NbTi} = 1.309 - 0.1909\ B_{max} + 0.0102\ B_{max}^2 \tag{9}$$

over the range $4\ T \le B_{max} \le 8\ T$. The correct value for A_{NbTi} then is that given by Eq. (5) multiplied by GF_{NbTi} from Eq. (9).

For hybrid coils, A_{NbTi} should be multiplied by GF_{NbTi} with $B_{max} = B_{Cut}$ or $GF_{NbTi} = 0.4266$. The grading factor for Nb_3Sn is found in much the same way as the one for NbTi. The lower limit of the integral is B_{Cut}

$$GF_{Nb_3Sn} = \frac{J_c(B_{max})}{B_{max} - B_{Cut}} \int_{B_{Cut}}^{B_{max}} \frac{dB}{J_c(B)} \tag{10}$$

Again $1/J_c$ as a function of B was fit by a quadratic and integrated. The results of several values for B_{max} were fit to give

$$GF_{NB_3Sn} = 2.096 - 0.1747\ B_{max} = 0.00472\ B_{max}^2 \tag{11}$$

for $8\ T \le B_{max} \le 14\ T$ and $B_{Cut} = 8\ T$.

Equations (8) through (11) were derived assuming a constant thickness per turn. If the copper stabilizer is graded as well as the superconductor, this assumption does not hold. Even so, the equations are expected to give some indication of the effect of grading.

4. Radiation Damage

Low temperature irradiation results in change of properties of superconductors and normal metals.[7] In particular, there is a change in the transition temperature T_c and the critical current density J_c at high fluences.

Radiation effects in NbTi alloys are significantly different from those in the Nb_3Sn compounds.

The important features of irradiation experiments on NbTi alloy superconductor are that the change in T_c is very small and that the change in J_c is very sensitive to the metallurgical structure in the unirradiated material. In general, J_c increases with irradiation for materials with low unirradiated J_{co} and decreases for materials with high J_{co}, with the magnitude of the decrease larger for larger J_{co}. The variation of J_c in NbTi with the neutron fluence is obtained from a fit of experimental data as

$$J_c = J_{co}\, e^{-\alpha\phi t}$$

where α is a constant. A representative value of α is taken in the model to be 3.5×10^{-24} m^2 but it can be varied by input. The neutron flux, ϕ, varies with position within the magnet as determined from the neutronics model. The irradiation time, t, is the product of the time period between magnet anneals and the plant capacity factor.

Irradiation of Nb_3Sn compounds up to a neutron fluence of $\sim 4 \times 10^{18}$ n/cm^2 showed ~ 1 K reduction in T_c. The value of J_c increases with neutron irradiation at low neutron fluences. The increase in J_c saturates with increasing fluence and then decreases. The saturation dose is higher at higher magnetic fields. The change in J_c as a function of magnetic field and neutron fluence was formulated in the model according to Figure 10 of Reference 7.

C. <u>The Copper Stabilizer</u>

For an intrinsically stable magnet the copper to superconductor ratio R_{CuSC} is generally specified between 1.5 and 3.0. The cross-sectional area is given by

$$A_{Cu} = R_{CuSC}\, A_{NbTi}$$

or (12)

$$A_{Cu} = R_{CuNbTi}\, A_{NbTi} + R_{CuNb_3Sn}\, A_{Nb_3Sn}$$

for NbTi and hybrid coils respectively. The question of whether the copper for an intrinsically stable magnet should be graded differently than the superconductor has not been investigated.

A cryostable magnet must obey the cryostability condition

$$J^2 \rho A_{Cu} \leq q_h p \tag{13}$$

where J is the current density in the copper of a composite conductor which has gone normal, ρ is the total resistivity of the copper, A_{Cu} is the cross-sectional area of the copper, p is its wetted perimeter and q_h is the effective heat flux into the helium. To determine J and thus

$$A_{Cu} = NnI/J \tag{14}$$

we consider each of these factors in turn. Cryostability is discussed in more detail in the 1976 ANL/EPR design report.[8]

1. Resistivity

The total resistivity includes the intrinsic resistivity, ρ_o, the magnetoresistivity, ρ_{mr}, and the radiation induced resistivity, ρ_{rad}.

$$\rho = \rho_o + \rho_{mr} + \rho_{rad} \tag{15}$$

There is uncertainty in the value $\rho_o = 6 \times 10^{-9}\ \Omega$ cm, but it is dominated by ρ_{mr} and ρ_{rad} anyway. The magnetoresistivity[9] is given by

$$\rho_{mr} = 4.55 \times 10^{-9}\ \Omega \text{ cm} \cdot B \tag{16}$$

and the radiation-induced resistivity[10] by

$$\rho_{rad} = 3 \times 10^{-7}\ (1 - \exp(-563d))\ \Omega \text{ cm} \tag{17}$$

where d is the total atomic displacements.

2. Copper Area and Wetted Perimeter

The ratio A_{Cu}/p is design-dependent; in particular, it depends on the operational current I. However, for a sheet conductor of the kind described in the 1976 ANL/EPR design,[11] the ratio depends primarily on the thickness of the sheet and, for a 50% wetted surface, equals the thickness. We take $A_{Cu}/p = 0.45$ cm, the value in the 1976 ANL/EPR design.

3. Heat Transfer to Helium

As it appears in Eq. (13), q_h includes the effect of heat transfer along the conductor or between turns as well as into the helium. So interpreted[8] q_h may be less than 0.06 W/cm^2 or greater than 2.2 W/cm^2, but it is customary to take q_h = 0.35 W/cm^2.

With these factors specified, J can be found from Eq. (13) and A_{Cu} from Eq. (14).

4. Grading the Copper

The resistivity of the copper, expressed in Eq. (15), is dominated by the magnetoresistivity and the radiation-induced resistivity, both of which are smaller for the outer turns than for the inner ones. Thus, there can be savings in grading the copper as there are in grading the superconductor.

To find the grading factor, we approximate ρ by a quadratic polynomial in x, the distance from the high field side of the TF coil; ρ_o contributes only to the constant term, ρ_{mr} to the constant and linear terms, but ρ_{rad} to all three. The two terms for ρ_{mr} are found by evaluating Fq. (16) at x = o and x = t using B = 0.2 T rather than B = o at x = t for conservatism. The three terms for ρ_{rad} are found by evaluating Eq. (17) at x = o, x = t/2 and x = t using

$$d = d_o \exp(-\mu x) \tag{18}$$

where μ is an effective attenuation coefficient (typically ~ 0.1 cm^{-1}) and d_o is the maximum atomic displacements in the copper. The value of d_o is specified by other parts of the systems analysis program according to values calculated for the atomic displacement rate, period between magnet anneals and plant capacity factor. The grading factor, GF_{Cu}, is given by

$$GF_{Cu} = \frac{J(x = o)}{t} \int_o^t \frac{dx}{J(x)}$$

which with the dependence of J on ρ of Eq. (13) becomes

$$GF_{Cu} = \int_o^t \sqrt{\rho(x)}\; dx / \sqrt{\rho(x = o)}\; t. \tag{19}$$

Using $\rho = a_0 + a_1 x + a_2 x^2$, Eq. (19) becomes

$$GF_{Cu} = \frac{1}{\sqrt{a_o}\, t} \left[\frac{(2\, a_2\, t + a_1)\sqrt{\rho(t)}}{4\, a_2} - \frac{a_1 \sqrt{a_o}}{4\, a_2} + \frac{4\, a_0\, a_2 - a_1^{\,2}}{8\, a_2^{\,3/2}} \right.$$

$$\left. \ln \left\{ \frac{\sqrt{\rho(t)} + (t + a_1/2)/\sqrt{a_2}}{\sqrt{a_o} + a_1/2\sqrt{a_2}} \right\} \right] \tag{20}$$

D. Stainless Steel Reinforcement for Coils

Enough stainless steel reinforcement must be included with the coils to withstand the tension, τ, in the coils and limit the stress or strain in the coils to the allowable value.

For constant tension coils, at every cross-section the tension is the product of the current, the radius of the curvature and the mean field over that cross section. In particular, where the field is a maximum

$$\tau = nNI\rho_1\, B_{max}/2 \tag{21}$$

since the field decreases linearly across the coil, ρ_1 is the minimum radius of curvature.

The tension is related to the stresses through the relation

$$\tau = A_{Cu}\, \sigma_{Cu} + A_{SS}\, \sigma_{SS} \tag{22}$$

where σ_{Cu} and σ_{SS} are the allowable stresses in the copper and stainless steel respectively. If A_{SS} as calculated by Eq. (22) is negative, it means that no stainless steel reinforcement is required.

In general, a specified σ_{Cu} and σ_{SS} occur simultaneously only if the coil is wound with the copper in precompression and the stainless steel in pretension. The model calculates the required prestresses before and after cool-down and confirms that they do not exceed σ_{Cu} or σ_{SS}.

Alternatively, the allowable strain, ε, can be specified rather than the stresses σ_{Cu} and σ_{SS}; in this case no pretension is assumed.

E. Geometry of Coils

The exact shape of the TF coils can be generated by the magnet code MARIA.[12] However, Moses and Young[3] have shown how the geometrical parameters of a constant-tension coil shown in Figure 3 can be generated numerically. We have integrated their expression for a family of parametric values, and fit the results as functions of R_1 and R_2 as follows:

$$\rho_1 = 0.095\ R_2 + 0.575\ R_1 - 0.750\ R_1^2/R_2 \tag{23}$$

$$\rho_2 = 1.116\ R_2 - 2.375\ R_1 + 1.475\ R_1^2/R_2 \tag{24}$$

$$H_{R1} = 0.793\ R_2 - 2.280\ R_1 + 1.700\ R_1^2/R_2 \tag{25}$$

$$H_{max} = 0.944\ R_2 - 1.790\ R_1 + 0.950\ R_1^2/R_2 \tag{26}$$

$$R_{Hmax} = 0.245\ R_2 + 1.238\ R_1 - 0.562\ R_1^2/R_2 \tag{27}$$

$$L = \text{Circumference} = 4.846\ R_2 - 7.960\ R_1 + 3.400\ R_1^2/R_2 \tag{28}$$

Equations (23) through (28) are derived for a torus of N = 16 coils, but should give satisfactory accuracy for N between 12 and 24.

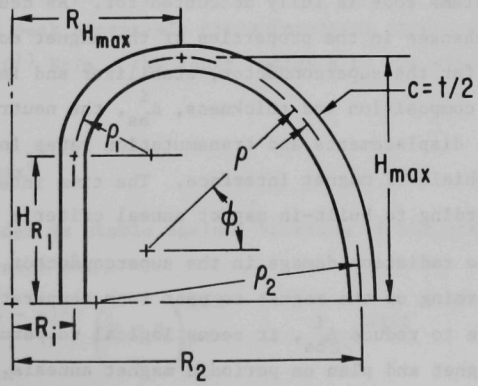

Figure 3. Geometric Parameters for a Constant-Tension Coil.

F. Iteration for Thickness, t

The total area of the coils exceeds that occupied by the superconductor, copper and stainless steel by a factor of $1 + \gamma$, corresponding to helium space, cryostat walls, insulation, etc. Assuming no gaps between coils on the inner leg, we find the thickness, t, by

$$t = (1 + \gamma)\ (A_{SC} + A_{Cu} + A_{SS})/2\pi\ R_1 \tag{29}$$

The model as described up to this point requires iteration over the coil thickness t. To find A_{SS} by Eq. (22) we need ρ_1. To find ρ_1 by Eq. (23) we need R_1 and R_2. To find R_1 and R_2 from the initial values of $R_1 + t/2$ and $R_2 - t/2$, we need t. (We need t also in order to grade the superconductor and copper.) And to find t by Eq. (29), we need A_{SS} and R_1. It is, therefore, necessary to take some initial value for t and iterate through the calculation until the value for t converges. A suitable starting value is

$$t_o = 6 \times 10^{-4}\ B^2_{max}\ (R_2 - t/2) \tag{30}$$

After the calculation for t converges, R_1 and R_2, or for height limited coils R_1 and H_{max}, can be found and from them the other shape parameters of Figure 3.

G. Magnet Anneal

The interface among the magnet subsystem model, the shield model and the rest of the systems code is fully accounted for. As described earlier, irradiation-induced changes in the properties of the magnet components are built into the model for the superconductor, stabilizer and insulators. For a given blanket/shield composition and thickness, Δ^i_{bs}, the neutron and gamma-ray fluxes, heating, atomic displacements and transmutation rates in the magnet are provided via the shield-TF magnet interface. The time integrated responses are calculated according to built-in magnet anneal criteria discussed below.

Most of the radiation damage in the superconductor and normal metal can be recovered by warming up the magnet to near room temperature. Since there is a strong incentive to reduce Δ^i_{bs}, it seems logical to permit a higher radiation level at the magnet and plan on periodic magnet anneals. However, magnet warm up and cooldown require two to three months of plant downtime. Therefore, it

is apparent that for any given system, there is an optimum time span between magnet anneals. At present the program permits specifying t_a in one of two modes: either t_a is an input variable, or t_a is defined to be equal to the lifetime of the first wall. The second mode has proven to be economically favorable since it permits the magnet anneal to coincide with the first wall replacement, which results in less downtime for the plant.

H. The Support Cylinder

There is a compressive force pushing all TF coils toward the axis of the tokamak; this force must be taken up by the support cylinder, assumed to be a hollow cylinder of stainless steel of inner radius a and outer radius b. Generally we assume $A = R_1 - t/2$. The pressure acting on the cylinder is given by:

$$p = \frac{(H_{max} + H_{R1} - 2_{\rho 1})\ nNI\ B_{max}}{8\pi\ (R_1 - t/2)\ H_{R1}} \tag{31}$$

if we assume that the full force per unit length $nNI\ B_{max}/2$ acts between $\pm H_{R1}$, half that force per unit length acts between H_{R1} and H_{max}, and that the force is diminished by twice the tnesion, τ. If the wedge-shaped coils can partially react on each other, ρ as found in Eq. (31) can be decreased by the factor $(1 + t/2b)$. The force is taken to act uniformly over the length $\pm H_{R1}$.

The stresses in the support cylinder are discussed in the 1975 ANL/EPR design study.[13] For a peak acceptable circumferential stress σ_{max}, (typically 50,000 psi or 3.45×10^{11} Nt/m^2) the inner radius a of the support cylinder is given by

$$a = b\ (1 - 2\ p/\sigma_{max})^{1/2} \tag{32}$$

The support cylinder is stable against buckling if the pressure p is less than the critical pressure p^1.

$$p^1 = \frac{0.807\ Y_{SS}\ (b - a)^2}{2\ a\ H_{max}} \left(\frac{b - a}{a}\right)^{1/2} (1 - \nu_{SS})^{-3/4} \tag{33}$$

where ν_{SS} is Poisson's ratio for stainless steel. If it is unstable, the inner radius a must be decreased until it is stable.

I. Stored Energy

The stored energy of the TF coil system is an important parameter in its own right; in addition, attempts have sometimes been made[14] to scale the costs of magnet systems according to stored energy.

The energy is found from the volume integral

$$E = \frac{1}{2\mu_o} \int B^2 \, dV.$$

We assume that B is zero outside the coils and has a 1/r dependence inside; i.e.,

$$B = B_{max} \, (R_1 + t/2)/r$$

Thus

$$E = \frac{B^2_{max} \, (R_1 + t/2)^2}{2\mu_o} \int_{R_1}^{R_2} \frac{1}{r^2} \, 2h \, (r) \, 2\pi \, rdr$$

If we approximate h (r), the half height as a function of radius, by a parabola passing through the points (R_1, H_{R1}) and $(R_2, 0)$ and of height H_{max}, then we can write $h(r) = a + br + cr^2$, with

$$a = R_2 \, (H_{R1} \, R_2 - 2 \, R_1 \, \Omega)/(R_2 - R_1)^2$$

$$b = 2 \, [(R_1 + R_2) \, \Omega - H_{R1} \, R_2]/(R_2 - R_1)^2$$

$$c = (H_{R1} - 2 \, \Omega)/(R_2 - R_1)^2$$

with $\Omega = H_{max} \, (1 + \sqrt{1 - H_{R1}/H_{max}})$.

Integration yields

$$E = \frac{2 \, B^2_{max} \, (R_1 + t/2)^2}{\mu_o \, (R_2 - R_1)^2} \, [R_2 \, (H_{R1} \, R_2 - 2R_1 \, \Omega) \ln (R_2/R_1) + (R_2^2 - R_1^2) \, \Omega - (R_2 - R_1) \, H_{R1}/2] \tag{34}$$

J. TF Magnet Costs

The volume of superconductor, copper stabilizer or stainless steel reinforcement is found by multiplying the circumference, found with Eq. (28) by the cross-sectional area, incorporating grading if appropriate. Multiplication by the density then yields the mass. The cost of materials is calculated assuming a unit material cost of \$2/kg, \$6/kg, \$60/kg and \$130/kg for copper, stainless steel, NbTi and Nb_3Sn, respectively. The electrical insulation is assumed to be 10% of the magnet volume with a unit cost of $\$4000/m^3$. The superinsulation cost is taken as $\$100/m^2$ with an area equal to twice the surface area of the magnet. The unit cost for the dewar is assumed to be $\$3000/m^2$.

The magnet cost is equal to the material plus fabrication and winding cost. At present, the fabrication plus winding cost is taken as three times the material cost. Investigation is underway to derive an algorithm for the fabrication and winding cost that takes into account the complexity and details of the magnet design.

The refrigeration load is calculated as the sum of the nuclear energy deposition and thermal leakage. Other heating loads will be included in the future. The nuclear heating is calculated by the neutronics/shield model and the thermal leakage is assumed to be 1 W/m^2 of the magnet surface area. The refrigeration cost at a unit price of \$583/W plus the cost of helium supply at \$3/liter. The refrigeration load is converted to electric power requirements using a multiplicative factor of 300 for 4.2 K cooling and 500 for 3 K cooling. The electric power requirements are passed into another part of the system code that calculates the plant net electric power output.

IV. Results

The model was used to study how magnet parameters vary with major radius, peak magnetic field and material properties. One or two parameters were changed for each study. During variation with major radius, the aspect ratio R/a was held at a constant value of three.

A. Coil Thickness

The coil thickness is shown in Figure 4 as a function of major radius for several peak fields. The tension increases with both radius and field, and consequently the coils must be thicker to withstand the tension. Moreover, the lower permissible strain with hybrid coils accentuates the increase in thickness with field.

B. Thickness Variation with Strain

Variation of coil thickness with allowable strain is shown in Figure 5 for an 8 T field and in Figure 6 for a 12 T field. In each case, major radii of 5 m to 13 m are treated. The rapid increase in thickness as athe strain is decreased below 0.1% is striking. For a 12 T field, 0.05% strain, and an aspect ratio of 3, there is not enough room for TF coils with major radius of 5 m or less. Under the same conditions there is not enough room for the support cylinder in reactors with 7 m or less major radius.

C. Stored Energy

The energy stored in the TF coil system is shown in Figure 7 as a function of major radius for fields between 8 T and 14 T. The rapid increase with both field and major radius is evident.

D. Cost

The cost of a TF coil system is shown in Figure 8 as a function of major radius for fields between 8 T and 14 T. Here too the rapid increase with both field and major radius is evident.

The cost as a function of allowable strain for major radii between 5 m and 13 m is shown in Figure 9 for a field of 8 T and in Figure 10 for a field of 12 T. The increased thickness required for low strain, shown in Figure 5 and Figure 6, represent increased material requirements and thus increased cost.

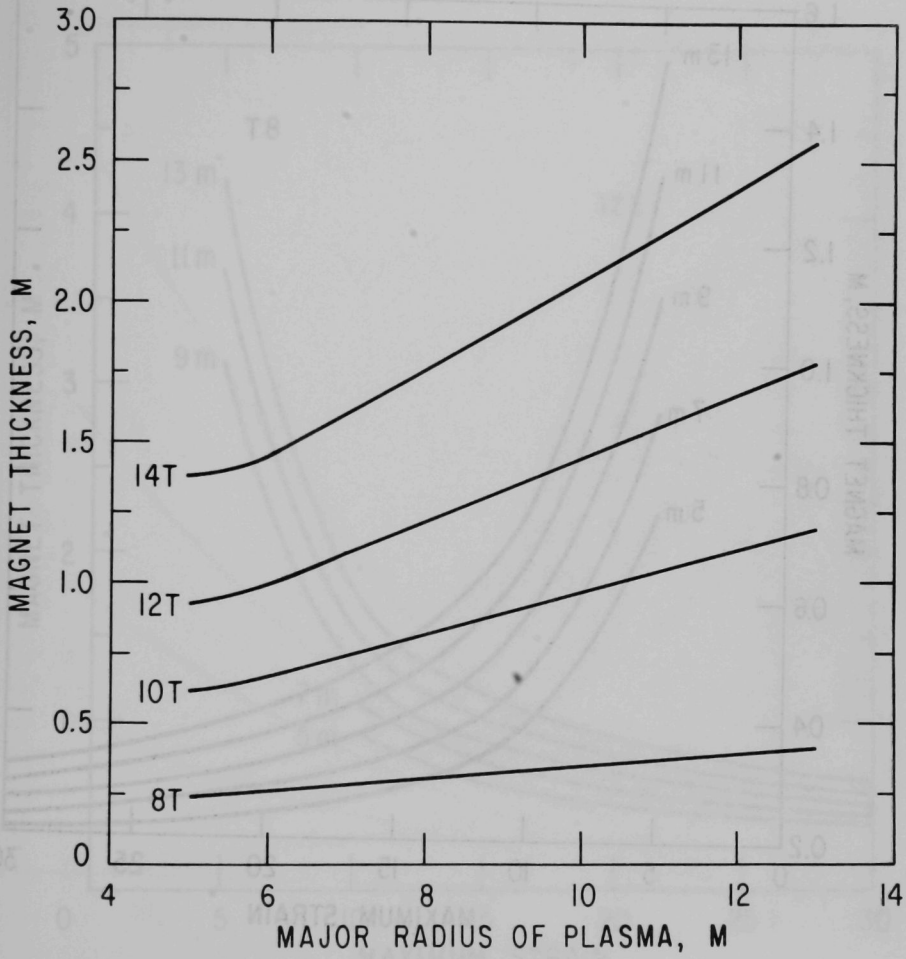

Figure 4. Magnet Thickness as a Function of Major Radius at Several Values for the Maximum Magnetic Field.

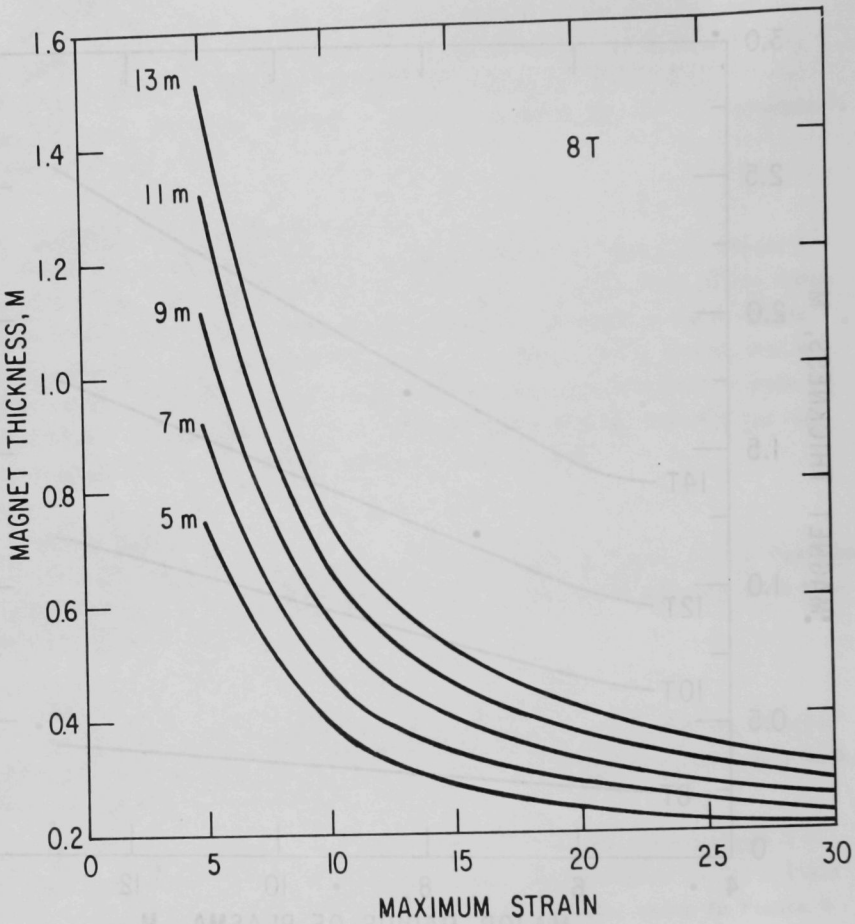

Figure 5. Sensitivity of the Magnet Thickness to the Permissible Strain. Results are shown for a maximum magnetic field of 8 T and several values for the major radius.

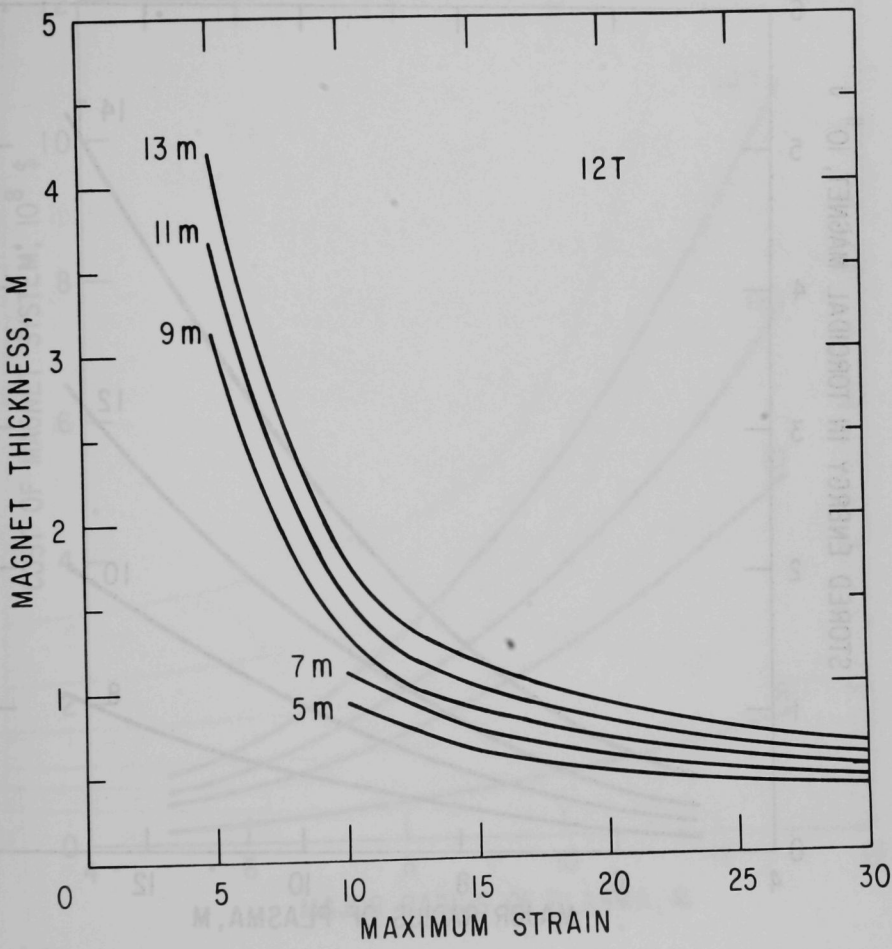

Figure 6. Sensitivity of the Magnet Thickness to the Permissible Strain. Results are shown for a maximum magnetic field of 12 T and several values for the major radius.

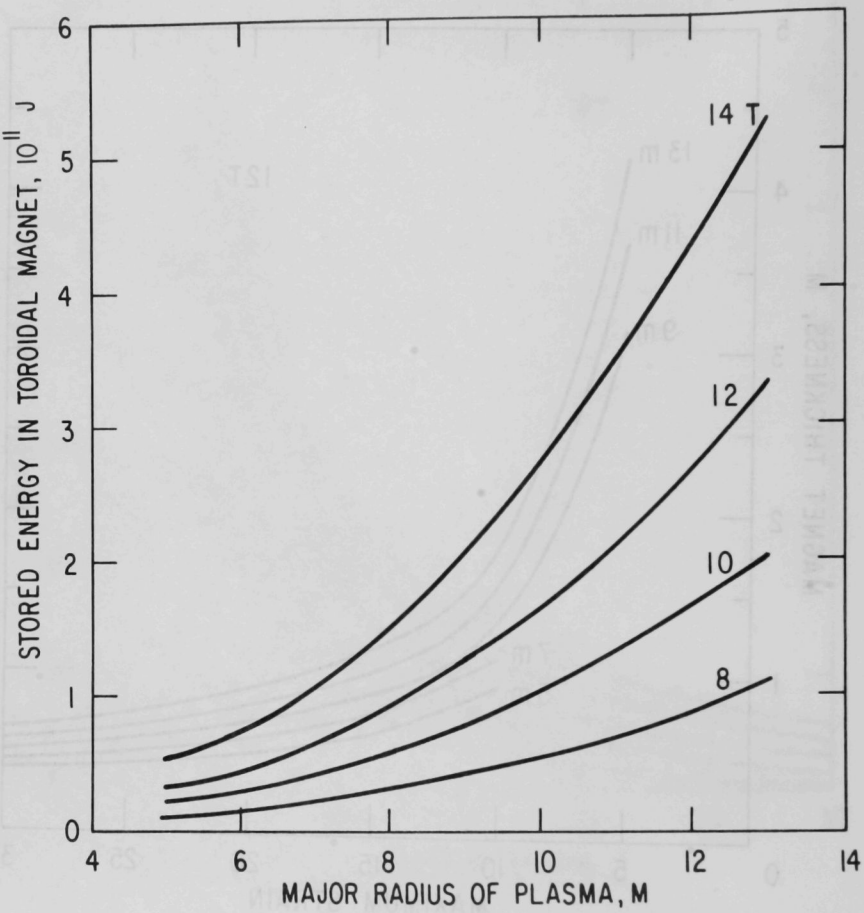

Figure 7. Stored Energy as a Function of the Major Radius at Several Values of the Maximum Magnetic Field.

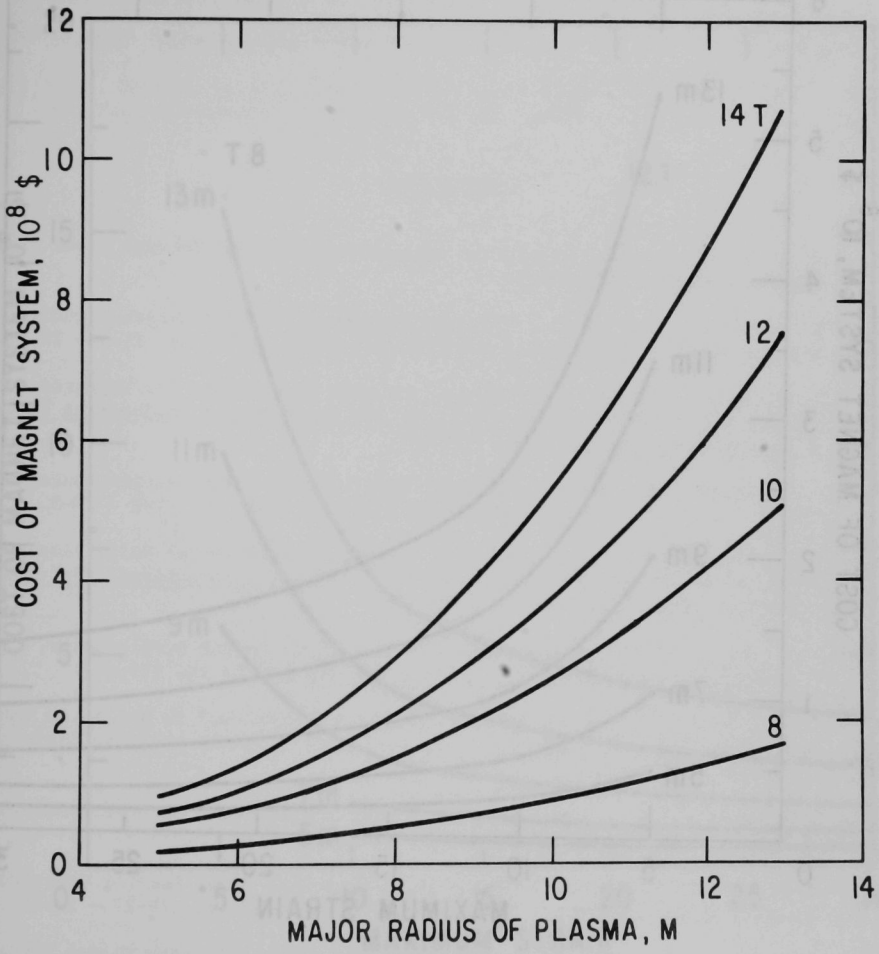

Figure 8. Cost of the TF Magnet as a Function of Reactor Size and Maximum Field.

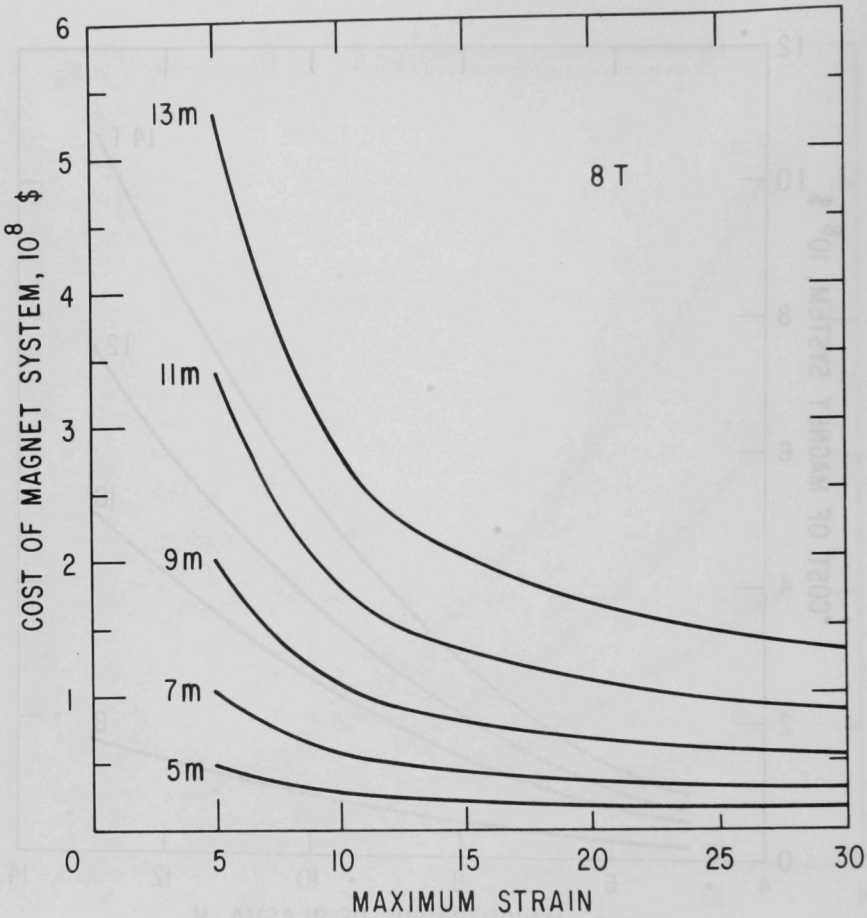

Figure 9. Sensitivity of the Magnet Cost to the Permissible Strain for a Maximum TF Field of 8 T.

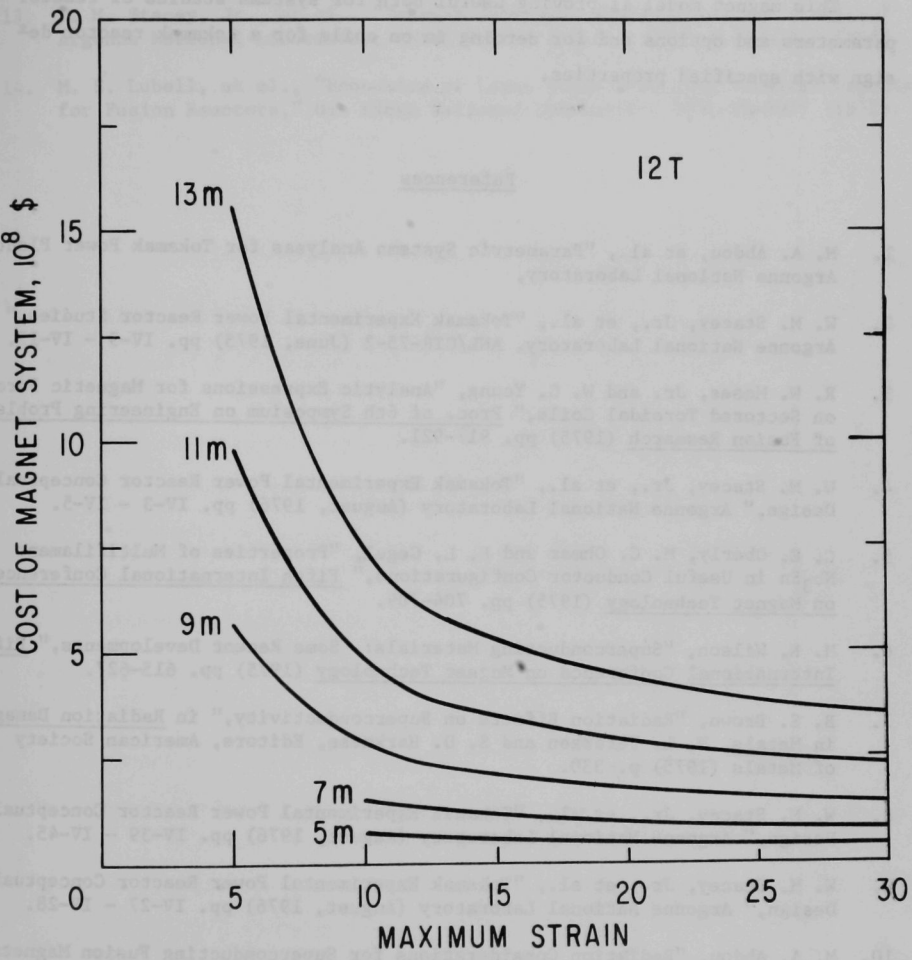

Figure 10. Sensitivity of the Magnet Cost to the Permissible Strain for a Maximum TF Field of 12 T.

V. Conclusions

This magnet model is proving useful both for systems studies of reactor parameters and options and for zeroing in on coils for a tokamak reactor design with specified properties.

References

1. M. A. Abdou, et al., "Parametric Systems Analyses for Tokamak Power Plants," Argonne National Laboratory,

2. W. M. Stacey, Jr., et al., "Tokamak Experimental Power Reactor Studies," Argonne National Laboratory, ANL/CTR-75-2 (June, 1975) pp. IV-9 - IV-17.

3. R. W. Moses, Jr. and W. C. Young, "Analytic Expressions for Magnetic Forces on Sectored Toroidal Coils," Proc. of 6th Symposium on Engineering Problems of Fusion Research (1975) pp. 917-921.

4. W. M. Stacey, Jr., et al., "Tokamak Experimental Power Reactor Conceptual Design," Argonne National Laboratory (August, 1976) pp. IV-3 - IV-5.

5. C. E. Oberly, M. C. Ohmer and H. L. Gegel, "Properties of Multifilament Nb_3Sn in Useful Conductor Configurations," Fifth International Conference on Magnet Technology (1975) pp. 704-709.

6. M. N. Wilson, "Superconducting Materials: Some Recent Developments," Fifth International Conference on Magnet Technology (1975) pp. 615-627.

7. B. S. Brown, "Radiation Effects on Superconductivity," in Radiation Damage in Metals, N. L. Peterson and S. D. Harkness, Editors, American Society of Metals (1975) p. 330.

8. W. M. Stacey, Jr., et al., "Tokamak Experimental Power Reactor Conceptual Design," Argonne National Laboratory (August, 1976) pp. IV-39 - IV-45.

9. W. M. Stacey, Jr., et al., "Tokamak Experimental Power Reactor Conceptual Design," Argonne National Laboratory (August, 1976) pp. IV-27 - IV-28.

10. M. A. Abdou, "Radiation Considerations for Superconducting Fusion Magnets," International Meeting on Radiation Effects on Superconductivity, Argonne, Illinois (1977); to be published in *J. Nucl. Materials*.

11. W. M. Stacey, Jr., et al., "Tokamak Experimental Power Reactor Conceptual Design," Argonne National Laboratory (August, 1976) pp. IV-47 - IV-50.

12. S. T. Wang, J. R. Purcell, D. W. DeMichele and L. R. Turner, "Pure Tension Superconducting Toroidal-Field Coil System Design Studies," Proc. of 6th Symposium on Engineering Problems of Fusion Research (1975) pp. 1084-1088.

13. W. M. Stacey, Jr., et al., "Tokamak Experimental Power Reactor Studies," Argonne National Laboratory, ANL/CTR-75-2 (June, 1975) pp. IV-25 - IV-26.

14. M. S. Lubell, et al., "Economics of Large Superconducting Toroidal Magnets for Fusion Reactors," Oak Ridge National Laboratory, ORNL-TM-3927 (1972).

Appendix A

Symbols used in the Magnet Model

Symbol	Parameter
a	Inner radius of support cylinder.
A	Cross-sectional area of conductor.
A_x	Cross-sectional area of material x, x = Cu, SS, NbTi, Nb_3Sn.
b	Outer radius of support cylinder.
B	Toroidal magnetic field.
B_{cut}	Highest field at which NbTi is used in a hybrid coil.
B_{max}	Peak value of magnetic field, occurs at $R_1 + t/2$.
d	Atomic displacements.
d_o	Maximum atomic displacements.
E	Energy stored in the TF coil system.
f_x	Fraction of the current carried by material x, x = NbTi, Nb_3Sn.
F_{SS}	Fraction of short-sample current which an intrinsically-stable magnet is expected to reach.
GF_x	Grading factor for material x, x = NbTi, Nb_3Sn.
H_{max}	Maximum height of TF coil above mid-plane (see Figure 3).
H_{R_1}	Height of straight section of TF coil above mid-plane (see Figure 3).
I	Current in one turn of a TF coil.
J	Overall current density in superconductor plus copper.
J_c	Critical current density in superconductor.
L	Circumference of a TF coil.
m_x	Mass of material x, x = Cu, SS, NbTi, Nb_3Sn, cylinder.
n	Turns in one TF coil.

Symbol	Parameter
N	Number of TF coils.
p	Wetted perimeter of conductor.
p	Pressure on support cylinder.
p^1	Critical load on support cylinder.
q_h	Heat transfer coefficient to pool-boiling helium.
$R_{Cu:x}$	Ratio of copper to superconductor x, x = NbTi, Nb_3Sn, Sc (superconductor).
R_1	Radial distance to center of inner leg of TF coil (see Figure 3).
R_2	Radial distance to center of outer leg of TF coil (see Figure 3).
R_{Hmax}	Radial distance to highest point of TF coil (see Figure 3).
t	Thickness of TF coil.
t_o	Initial estimate of thickness of TF coil.
T	Design temperature for TF coil.
T_c	Critical temperature for the superconductor.
T_o	Initial estimate of thickness of TF coil.
Y_x	Young's modulus of material x, x = Cu, SS
γ	Additional fractions of cross section of coil for helium, vacuum, insulator, etc. Area of coil = $(1 + \gamma)(A_{Cu} + A_{SS})$
ΔT	Safety margin in temperature.
ε	Allowable strain in conductor.
μ	Effective attenuation coefficient for neutrons.
μ_o	$4 \pi \times 10^{-7}$ Tesla m/amp.
ν_{SS}	Poisson's ratio for stainless steel.
ρ	Total electrical resistivity of copper.
ρ_o	Intrinsic resistivity of copper.
ρ_{mr}	Magneto-resistive resistivity of copper.

Symbol	Parameter
ρ_{rad}	Radiation-induced resistivity of copper.
ρ_1	Minimum radius of curvature of the TF coil (see Figure 3).
ρ_x	Mass density of material x, x = Cu, SS, NbTi, Nb_3Sn.
σ_{max}	Maximum permitted circumferential stress in support cylinder.
σ_x	Allowed stresses in coils, x = Cu, SS
τ	Tension in TF coils.
Ω	Parameter used in calculating stored energy $\Omega = H_{max}\,(1 + \sqrt{1 - H_{R_1}/H_{max}})$.

May, 1977

ANL/FPP/TM-83

"TOKAMAK FUSION POWER REACTORS"

by

Weston M. Stacey, Jr.
Mohamed A. Abdou

Fusion Power Program
Argonne National Laboratory
Argonne, Illinois 60439

ANL/FPP Technical Memorandum Number 83

Results reported in the FPP series of memoranda frequently are preliminary and subject to revision. They should not be quoted nor referenced without the author's permission.

Work supported by the U. S. Energy Research and Development Administration.

ABSTRACT

The major parameters and corresponding economic characteristics of a representative class of commercial tokamak fusion power reactors are examined as a function of four major design parameters -- plasma β_t, toroidal magnetic field strength, first-wall lifetime and power output. Representative design parameters, costs, schedule and technology advances are presented for a sequence of three reactors that could lead to the demonstration of commercial feasibility of this class of tokamak fusion power reactors near the turn of the century.

INTRODUCTION

The first generation of designs for commercial[1-3] and experimental[4-7] (EPR) tokamak fusion power reactors served to elucidate many of the technological problems of fusion reactors and to identify possible solutions. Because these studies were based, by and large, upon conservative assumptions regarding the plasma physics and the extrapolation of technology, the reactor designs were large and expensive. Moreover, the conservative, first-cut solutions to engineering design problems sometimes led to somewhat complex designs. While these first-generation designs were a valuable and necessary first step in defining the characteristics of tokamak fusion power reactors, they created an overly pessimistic impression of tokamak reactors as large, complex and expensive devices. They also stimulated a search for better design solutions and a re-examination of the plasma physics bases of the design.

Presently, second-generation designs for commercial,[8] pre-commercial demonstration[9-11] (DEMO) and experimental[12] reactors are evolving. In addition, codes are becoming available that allow a parametric analysis[13] of a wide range of design parameters. This second generation of designs is generally smaller because of a higher power density, simpler because of better design solutions and potentially less expensive than the first generation of designs. The higher power densities are postulated on the basis of shaping the plasma cross section to allow confinement of the plasma at higher pressure (i.e. higher β_t), a favorable re-evaluation of previously supposed MHD limits on the maximum β_t which could be confined and/or the use of higher magnetic fields to confine higher density plasmas.

In addition to the power reactor design activities, there are two substantial design efforts, one at General Atomic Company and Argonne National Laboratory and the other at Oak Ridge National Laboratory and Westinghouse Electric Company, for plasma ignition experiments, which are currently envisioned as the next step (TNS) in the tokamak program after the Tokamak Fusion Test Reactor (TFTR). Design solutions that are being developed in the TNS designs are, in some instances, extrapolatable to power reactors.

Thus, the perception of a tokamak power reactor that is emerging from ongoing work is more encouraging than the earlier perception based upon the first-generation design studies.

The purposes of this report are: 1) to identify the size and economic characteristics of one particular class of commercial tokamak fusion reactors and to assess the sensitivity of these characteristics to four important parameters -- plasma β_t, toroidal magnetic field strength, first-wall lifetime and power output; and 2) to describe a plausible path along which tokamak power reactors could evolve towards a commercial reactor. A single geometric configuration has been chosen in order to limit the scope of the study -- an extensive parametric study is in progress and will be reported elsewhere.[13]

I. COMMERCIAL TOKAMAK POWER REACTORS

One of the principle lessons learned from the first-generation design studies was that it was necessary to increase the fusion power density in the plasma in order to reduce the size, hence cost, of the reactor. The power density in a β_t-limited tokamak may be written

$$P \propto \beta_t^2 B_t^4 (1 + \kappa^2)^2, \tag{1}$$

where β_t is the plasma kinetic-to-magnetic pressure ratio, B_t is the toroidal field strength at the center of the plasma and κ is the plasma height-to-width ratio or elongation. Plasmas with D-shaped cross sections and elongations in the range $1 \leq \kappa \leq 2$ and plasmas with connected double-teardrop, or Doublet, shaped cross sections and elongations in the vicinity of $\kappa = 3$ have been the most extensively studied. In this report, a single D-shaped plasma with $\kappa = 1.65$ will be considered.

The magnetic field, B_t, depends upon the maximum magnetic field, B_{TFC}, at the coil and upon the geometry according to

$$B_t = B_{TFC} \left(1 - \frac{1}{A} - \frac{\Delta_{BS} + \Delta_V}{R}\right), \tag{2}$$

where $A \equiv R/a$ is the aspect ratio, R is the major radius of the plasma torus, a is the plasma minor radius, Δ_{BS} is the thickness of the blanket and shield on the inside of the torus and Δ_V is the thickness of the scrape-off region between the plasma and chamber wall. In this report, a single set of geometric parameters ($A = 3$, $\Delta_{BS} = 1$ m, $\Delta_V = 0.2$ m) will be considered. The 1-m blanket/shield thickness has been found to be economically optimum.[13] Toroidal field strengths $B_{TFC} \lesssim 9$ T are believed to be achievable with NbTi superconductor, which allows magnets to be designed to a strain level of 0.2%. At fields $B_{TFC} \gtrsim 9$ T, Nb_3Sn superconductors would be required and the magnets probably must be designed to a much lower strain level -- 0.1% is used in this report, although a smaller strain level may well be necessary.

The limits on β_t will be determined by MHD stability constraints. These limits have not been established yet, so a plausible range of β_t-values will be considered.

This part of the study will examine the range of possibilities for a tokamak reactor that would produce 3000 MW(t) -- this roughly corresponds to a 1000 MW(e) reactor. The size of such a reactor is indicated in Figure 1, as a function of B_{TFC} and β_t. Based upon this range of parameter space, parametric studies were performed to evaluate the economic characteristics of reactors. Lithium-cooled reactors with an intermediate sodium coolant and thermal energy storage loop and a conventional steam cycle were considered. Superconducting magnets and advanced electromagnetic energy storage and transfer systems were assumed. Costs were estimated for the entire reactor facility, including the nuclear island, balance of plant and facilities. The plasma physics, reactor systems and cost algorithms employed in developing the data displayed in Figure 1 and in assessing its reactor implications are discussed in reference 13.

The capital cost per unit electric power of 3000 MW(t) tokamak reactors is displayed in Figures 2 and 3, as a function of B_{TFC} and β_t -- the corresponding size can be determined from Figure 1. The capital cost includes direct cost plus indirect (engineering, contingency, interest during construction) costs, the latter amounting to approximately 50% of the former.

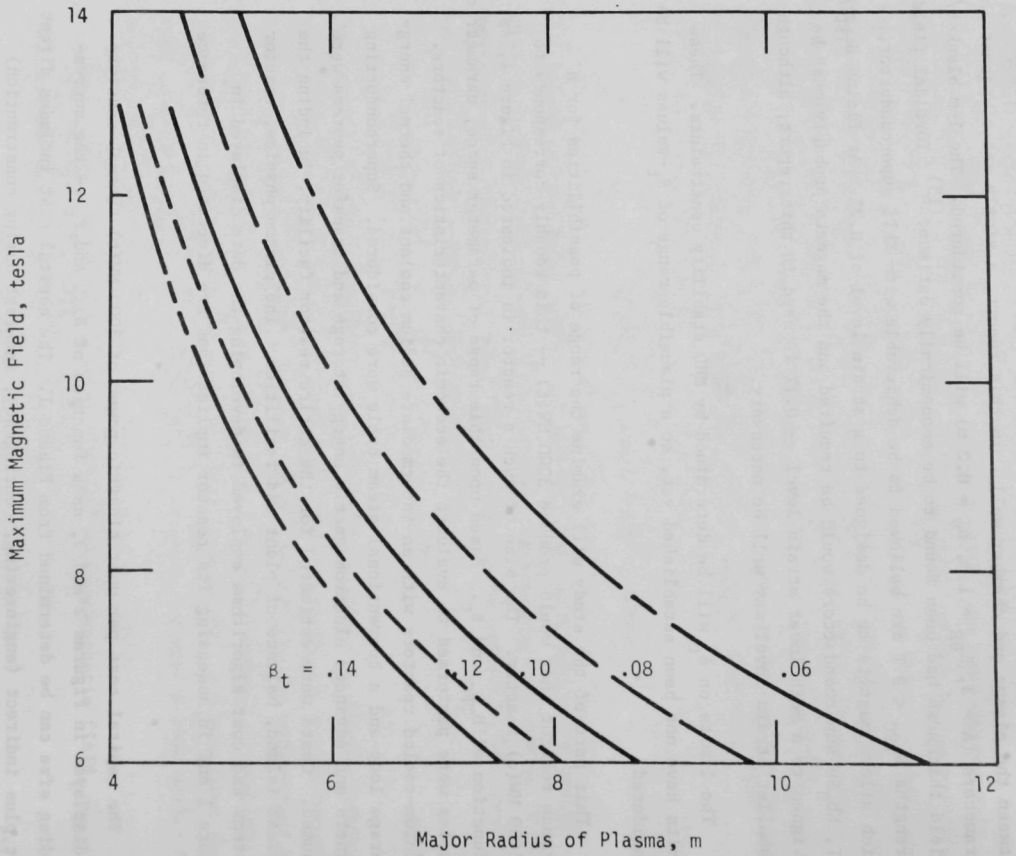

Figure 1. Effect of Toroidal Magnetic Field Strength and Plasma β_t on the Size of a Tokamak Reactor for a Fixed Thermal Power Output of 3000 MW(t). (Aspect ratio = 3, plasma D elongation = 1.65, plasma safety factor = 3, inner blanket/shield thickness = 1 m)

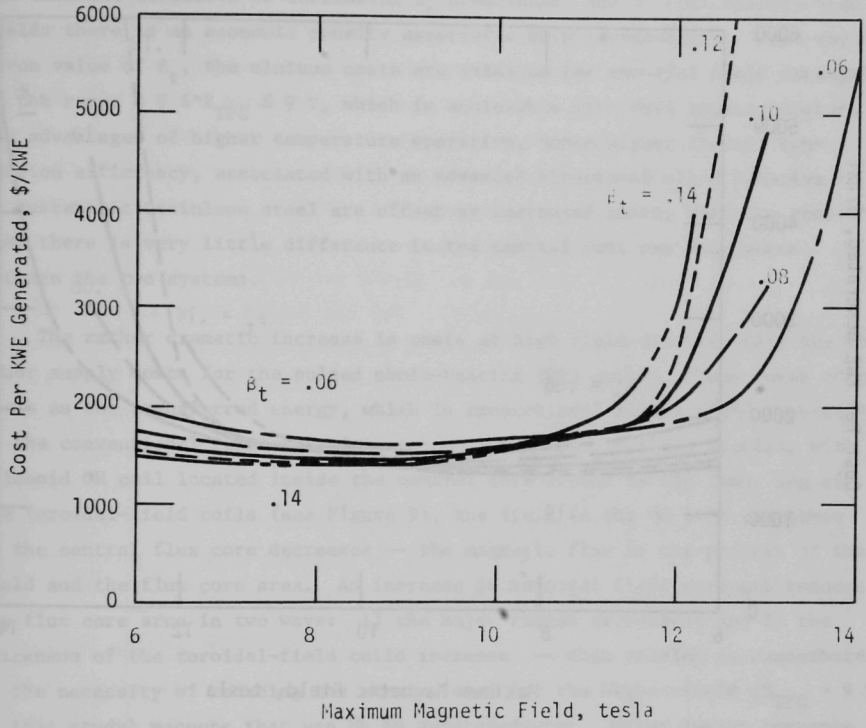

Figure 2. Effect of Toroidal Magnetic Field Strength and Plasma β_t on the Capital Cost per Unit Power for a Fixed Thermal Power Output of 3000 MW(t) in a Lithium-cooled Tokamak Reactor with Stainless Steel Structural Material. (Aspect ratio = 3, plasma D elongation = 1.65, plasma safety factor = 3, inner blanket/shield thickness = 1 m, maximum structure temperature = 500°C, electrical power output ≈ 940 MW(e))

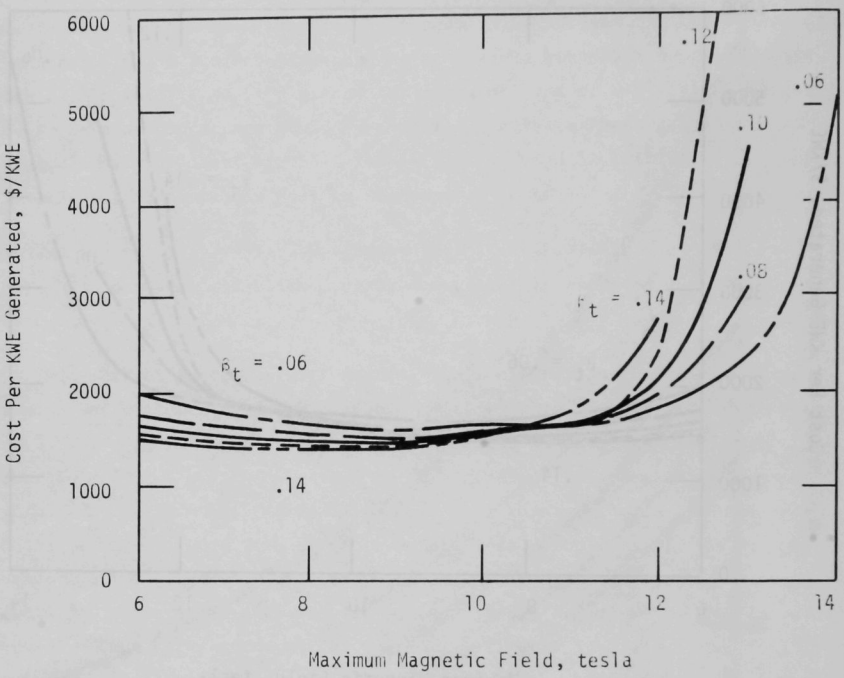

Figure 3. Effect of Toroidal Magnetic Field Strength and Plasma β_t on the Capital Cost per Unit Power for a Fixed Thermal Power Output of 3000 MW(t) in a Lithium-cooled Tokamak Reactor with Vanadium-alloy Structural Material. (Aspect ratio = 3, plasma D elongation = 1.65, plasma safety factor = 3, inner blanket/shield thickness = 1 m, maximum structural temperature = 650°C, electrical power output ≈ 1060 MW(e))

Several interesting trends are evident in Figures 2 and 3. At low magnetic fields the cost is quite sensitive to β_t -- increasing β_t from 6% to 14% for B_{TFC} = 6 T reduces the major radius of the reactor from 11.4 m to 7.5 m, and the cost is reduced by ∿ 30%. However, at higher magnetic fields the economic incentive of increasing β_t diminishes, and at sufficiently high fields there is an economic penalty associated with increasing β_t. For any given value of β_t, the minimum costs are obtained for toroidal field strengths in the range 8 T ≤ B_{TFC} ≤ 9 T, which is achievable with NbTi superconductor. The advantages of higher temperature operation, hence higher thermal conversion efficiency, associated with an advanced structural alloy relative to an austenitic stainless steel are offset by increased costs, with the result that there is very little difference in the capital cost per unit power between the two systems.

The rather dramatic increase in costs at high field are primarily due to power supply costs for the pulsed ohmic-heating (OH) coils. These costs roughly scale as the transferred energy, which is proportional to the field squared.* In the conventional reactor design concept considered in these studies, with a solenoid OH coil located inside the central core formed by the inner leg of the toroidal-field coils (see Figure 9), the field in the OH coil increases as the central flux core decreases -- the magnetic flux is the product of the field and the flux core area. An increase in toroidal field strength reduces the flux core area in two ways: 1) the major radius decreases; and 2) the thickness of the toroidal-field coils increase -- this problem is exacerbated by the necessity of reducing the strain level for the higher-field (B_{TFC} > 9 T in this study) magnets that use Nb_3Sn superconductor. Other design concepts for the OH system, which would ameliorate this particular problem with high-field tokamak reactors, have been suggested. However, the present studies indicate that costs tend to increase at high field even when power supply costs are factored out, albeit not so dramatically as shown in these figures.

---

* No technological limit has been imposed upon the field in the OH coil. Imposing such a limit would eliminate some of the high-field high-β_t cases and/or would limit the burn time, hence duty cycle, increasingly as β_t and B_{TFC} increase. The net effect is the same as shown here -- the cost increases dramatically at high field, particularly with high β_t.

The incentive for an advanced structural alloy is better illustrated by considering cost of energy production -- the ratio of the annual cost to the annual energy production. The annual cost is computed as 15% of the capital cost as an annual return on capital plus the operation and maintenance cost plus the prorated first-wall/blanket replacement cost plus a trivial fuel cost. The annual energy production computation allows for 28 days miscellaneous outage time and a prorated share of an 80-day first-wall and blanket rebuilding time. The cost of energy production with an austenitic stainless steel (type 316) and an advanced vanadium alloy structure are shown in Figures 4 and 5. The structural material lifetimes are computed from the best current estimates of materials data.[14] The end of life criteria used for the structural materials are ≤ 8% void swelling, ≥ 1% uniform elongation ductility and ≤ 2% creep elongation. Stress levels of 7,000 psi and 12,000 psi were used for stainless steel and vanadium alloys, respectively. For the design temperatures considered in this report, violation of the void swelling criterion was the lifetime limiting factor. The materials data base for stainless steel[14] is considerably more complete than for a vanadium alloy, of course, and Figure 5 should be viewed as illustrating the economic incentive of using an advanced structural material rather than as the prediction for a specific material. This incentive is emphasized in Figure 6, where cost of energy production is displayed as a function of wall lifetime. Clearly, there is a strong economic incentive to develop structural alloys with lifetimes in the range of 10-20 $MW \cdot yr/m^2$.

Up to this point, the study has compared reactors with a fixed thermal power output. The "economy of scale" in going to reactors with larger power outputs is illustrated in Figure 7. Greater benefits of increasing the reactor power output are realized in reactors with an advanced structural alloy than in reactors with type-316 stainless steel, because of the more frequent wall replacement associated with the latter.

II. PATH TO COMMERCIAL TOKAMAK FUSION POWER REACTORS

Many, if not all, of the presently outstanding plasma physics questions about transport and energy confinement, limits on β_t, plasma shape optimization, impurity control, heating and fueling should be resolved by existing and planned

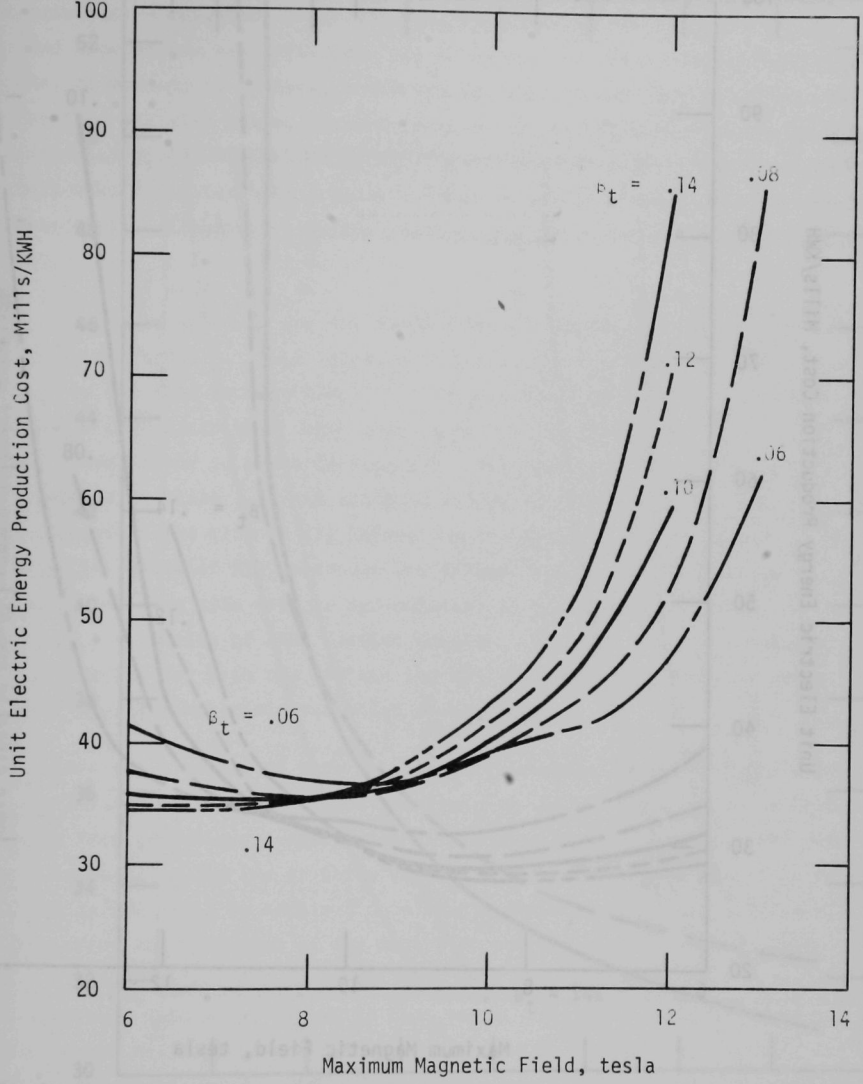

Figure 4. Effect of Toroidal Magnetic Field Strength and Plasma β_t on the Cost of Energy Production for a Fixed Thermal Power Output of 3000 MW(t) in a Lithium-cooled Tokamak Reactor with Stainless Steel Structural Material. (Aspect ratio = 3, plasma D elongation = 1.65, plasma safety factor = 3, inner blanket/shield thickness = 1 m, maximum structural temperature = 500°C, first-wall lifetime = 3.1 MW•yr/m^2, electrical power output ≈ 940 MW(e))

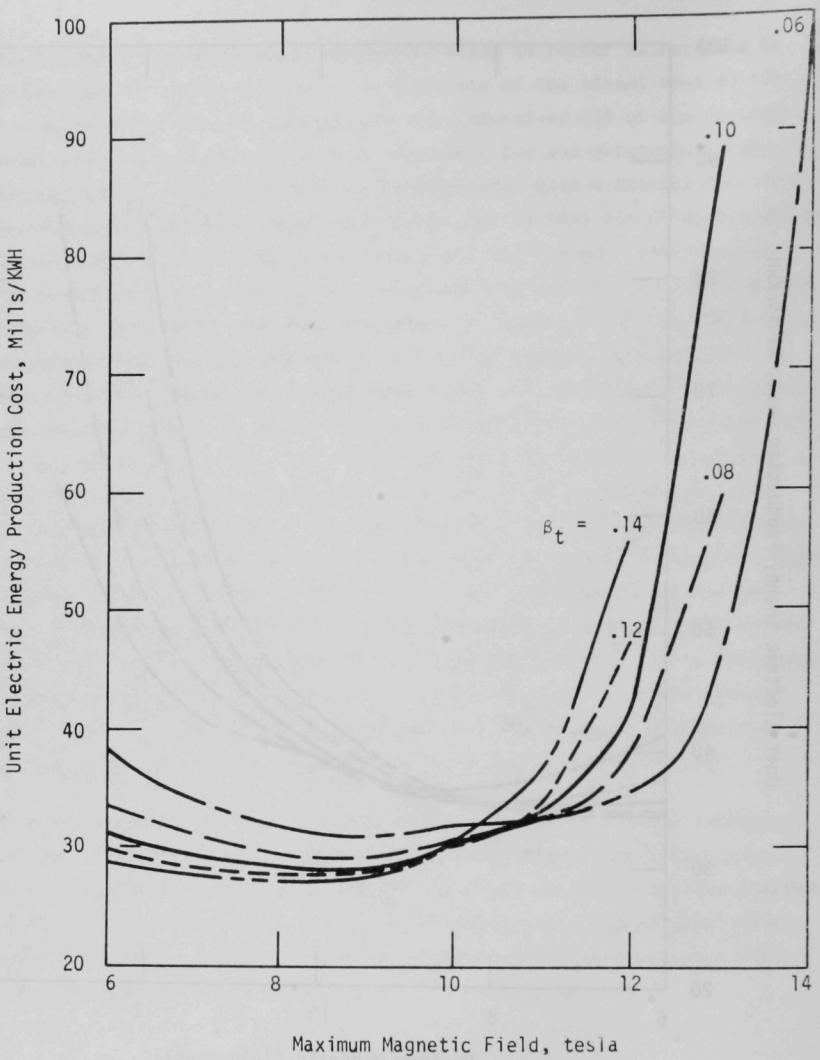

Figure 5. Effect of Toroidal Magnetic Field Strength and Plasma β_t on the Cost of Energy Production for a Fixed Thermal Power Output of 3000 MW(t) in a Lithium-cooled Tokamak Reactor with Vanadium-alloy Structural Material. (Aspect ratio = 3, plasma D elongation = 1.65, plasma safety factor = 3, inner blanket/shield thickness = 1 m, maximum structural temperature = 650°C, first-wall lifetime = 34 MW•yr/m^2. electrical power output ≈ 1060 MW(e))

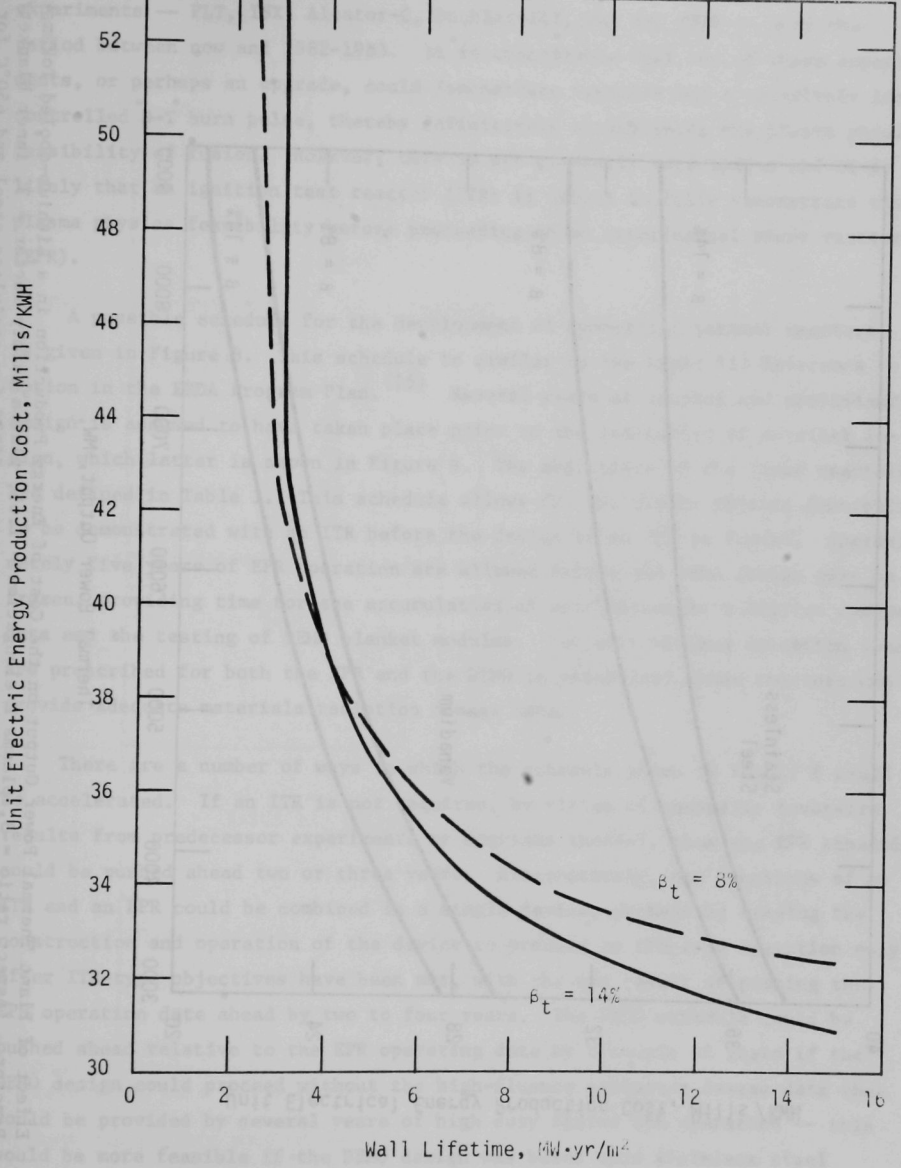

Figure 6. Effect of First-wall Lifetime on the Cost of Energy Production for a Fixed Thermal Power Output of 3000 MW(t) in a Lithium-cooled Tokamak Reactor. (Aspect ratio = 3, plasma D elongation = 1.65, plasma safety factor = 3, inner blanket/shield thickness = 1 m, maximum toroidal field strength = 9 T)

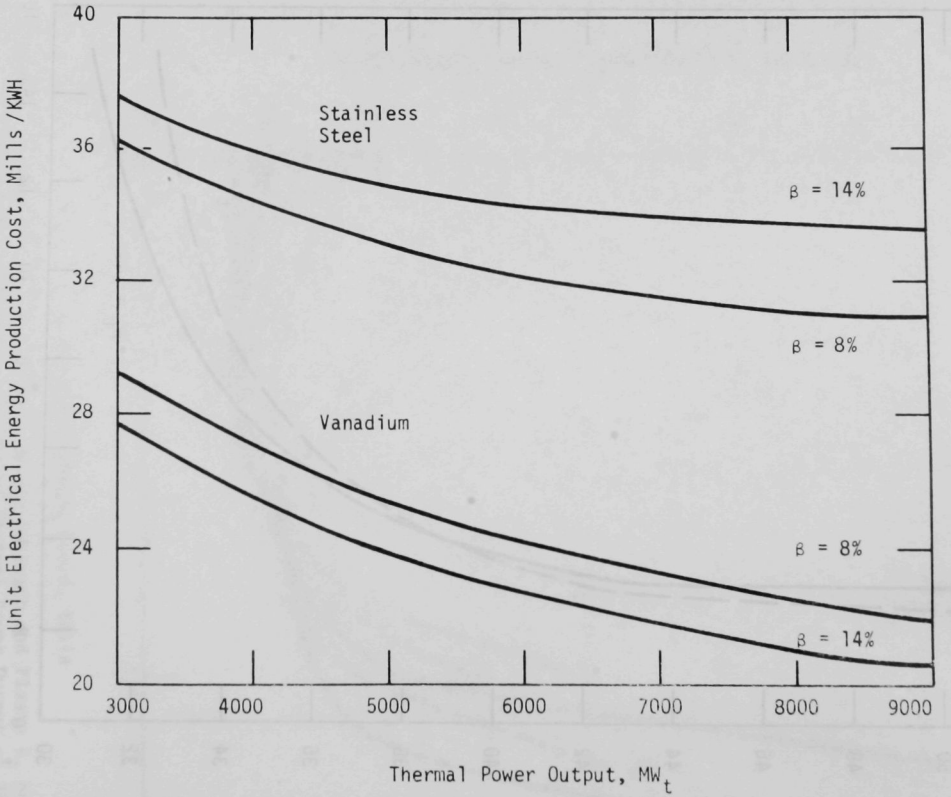

Figure 7. Effect of Plant Thermal Power Output on the Cost of Energy Production in a Lithium-cooled Tokamak Reactor. (Aspect ratio = 3, plasma D elongation = 1.65, plasma safety factor = 3, inner blanket/shield thickness = 1 m, maximum structural temperature = 500°C for stainless steel and 650°C for vanadium alloy, first-wall lifetime = 3.1 MW•yr/m^2 for stainless steel and 34 MW•yr/m^2 for vanadium alloy, maximum toroidal field strength = 9 T)

experiments -- PLT, ISX, Alcator-C, Doublet-III, PDX and TFTR -- over the period between now and 1982-1983. It is conceivable that one of these experiments, or perhaps an upgrade, could demonstrate ignition and a relatively long, controlled D-T burn pulse, thereby definitively establishing the plasma physics feasibility of fusion. However, this is not generally anticipated and it is likely that an ignition test reactor (ITR) is needed to fully demonstrate the plasma physics feasibility before proceeding to an experimental power reactor (EPR).

A possible schedule for the development of commercial tokamak reactors is given in Figure 8. This schedule is similar to the Logic III Reference Option in the ERDA Program Plan.[15] Several years of scoping and preliminary design is assumed to have taken place prior to the initiation of detailed design, which latter is shown in Figure 8. The objectives of the three reactors are defined in Table 1. This schedule allows for the plasma physics feasibility to be demonstrated with an ITR before the design of an EPR is frozen. Approximately five years of EPR operation are allowed before the DEMO design must be frozen, providing time for the accumulation of some materials radiation damage data and the testing of DEMO blanket modules. Ten year minimum operation times are prescribed for both the EPR and the DEMO in order that these reactors can provide adequate materials radiation damage data.

There are a number of ways in which the schedule shown in Figure 8 could be accelerated. If an ITR is not required, by virtue of unusually favorable results from predecessor experiments or upgrades thereof, then the EPR schedule could be pushed ahead two or three years. Alternatively, the functions of an ITR and an EPR could be combined in a single device, perhaps by staging the construction and operation of the device to proceed to EPR-type operation only after ITR-type objectives have been met, with the net result of pushing the EPR operation date ahead by two to four years. The DEMO schedule could be pushed ahead relative to the EPR operating date by a couple of years if the DEMO design could proceed without the high-fluence radiation damage data that would be provided by several years of high duty factor EPR operation -- this would be more feasible if the DEMO design was based upon stainless steel rather than an advanced structural alloy.

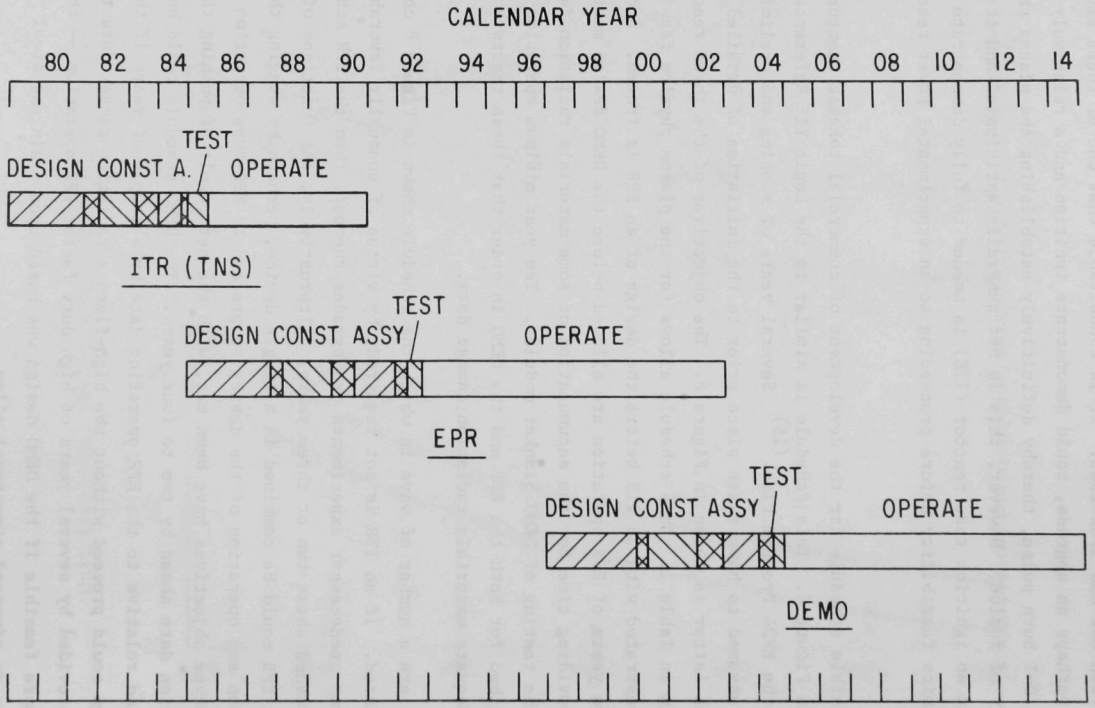

Figure 8. Possible Schedule for the Achievement of Commercial Tokamak Fusion Power Reactors.

TABLE 1. Tokamak Reactors on Path to Commercial Fusion Power Reactor Development

Ignition Test Reactor (ITR)	Primary:	Demonstrate plasma physics feasibility of fusion power.
	Secondary:	Demonstrate those fusion technologies required to achieve primary objective.
Experimental Power Reactor (EPR)	Primary:	Produce electrical power from fusion and demonstrate the technological feasibility of fusion power reactors. Physics and technology systems integration.
	Secondary:	Demonstrate fusion technologies and serve as an engineering/materials test reactor.
Demonstration Power Reactor (DEMO)	Primary:	Demonstrate the commercial feasibility of electrical power production from fusion.
	Secondary:	Serve as a test reactor for advanced fusion technologies.

TABLE 2. Tokamak Reactor Cost Estimates

	ITR	EPR	DEMO
Total Capital Costs* ($M)	400	600	1050
Annual Operating Costs† ($M)	4.1	5.4	5.8

* Does not include supporting research and development or unusual expenses associated with the development of first-of-type manufacturing capability.

† Does not include cost of materials and engineering testing.

Estimated costs of the three reactors are given in Table 2. These cost estimates are based upon a low-duty cycle ITR about 4 m in major radius and an EPR and a DEMO as will be subsequently discussed.

The two ongoing TNS designs are considering a range of options varying from an ITR up to a reactor with characteristics approaching those of the EPR. Hence, the designs and research and development requirements of an ITR should be reasonably well defined in the near future.

The first-generation EPR designs[4-7] have been reviewed in detail and a revised design has recently been defined.[12] Major parameters which characterize one of the revised EPR design options are given in Table 3 and a cross section view is shown in Figure 9. The EPR requires a number of advanced technologies, as indicated in Table 5, but does not require advanced structural alloys or coolant technology. This particular EPR design could be upgraded somewhat to obtain a more adequate materials radiation facility -- this question is being examined in the continuing EPR design activity.

The integration in a power reactor of all of the advanced technologies that are required for commercial tokamak fusion reactors must be accomplished in the DEMO. A range of possible DEMO parameters is shown in Figure 10 for a geometric configuration and plasma conditions which are consistent with those of the EPR and the commercial reactors discussed in this report. The discontinuity at 9 T is a result of switching from NbTi to Nb_3Sn as a superconductor. Representative parameters for both type-316 stainless steel and advanced vanadium alloy designs are given in Table 4. A stress level (15,000 psi) higher than the actual design stress (12,000 psi) and a stringent requirement on creep not to exceed 1% were assumed in predicting a conservative limit on the lifetime of the vanadium-base alloys shown in Table 4. This avoids having to base the DEMO design on an uncomfortable extrapolation beyond the radiation damage data and blanket engineering information that could be provided by EPR. However, extrapolation of present data for the actual design and operating conditions of the DEMO shows that the lifetime for the vanadium alloys will be considerably longer than that shown in Table 4.

TABLE 3. Representative Tokamak Experimental Power Reactor Parameters

Major radius, meters	4.7
Aspect ratio (A)	3.5
Plasma D elongation (κ)	1.65
Maximum toroidal field, tesla	9.0
Superconductor	NbTi
Average plasma β_t, %	8
Plasma safety factor (q)	3
Thermal power, MW(t)	270
Electric power, MW(e)	67
Net electric power, MW(e)	39
Plasma current, MA	7.6
Maximum OH field, tesla	4.0
Coolant	H_2O
Structural material	Stainless Steel
Maximum structural temperature, °C	500
Wall lifetime, yr	8
Direct capital cost, $M	420
Total capital cost,* $M	600

* Including contingency and engineering.

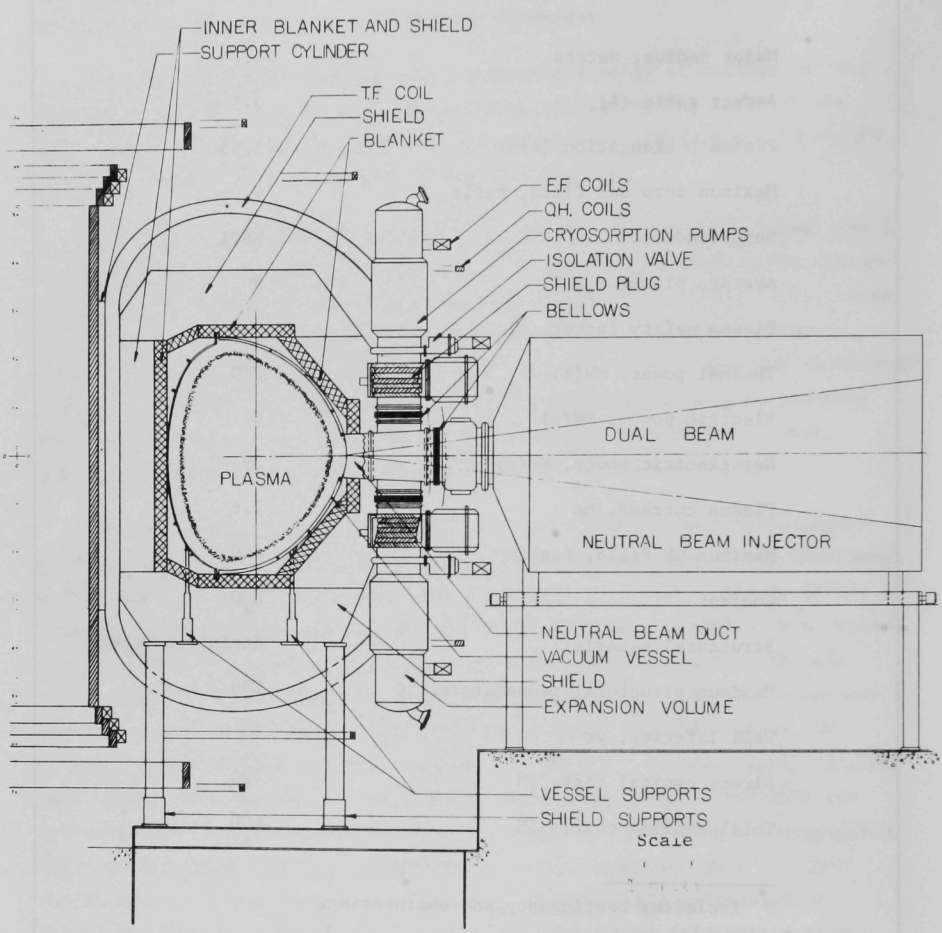

Figure 9. Cross Section of a Tokamak Experimental Power Reactor.

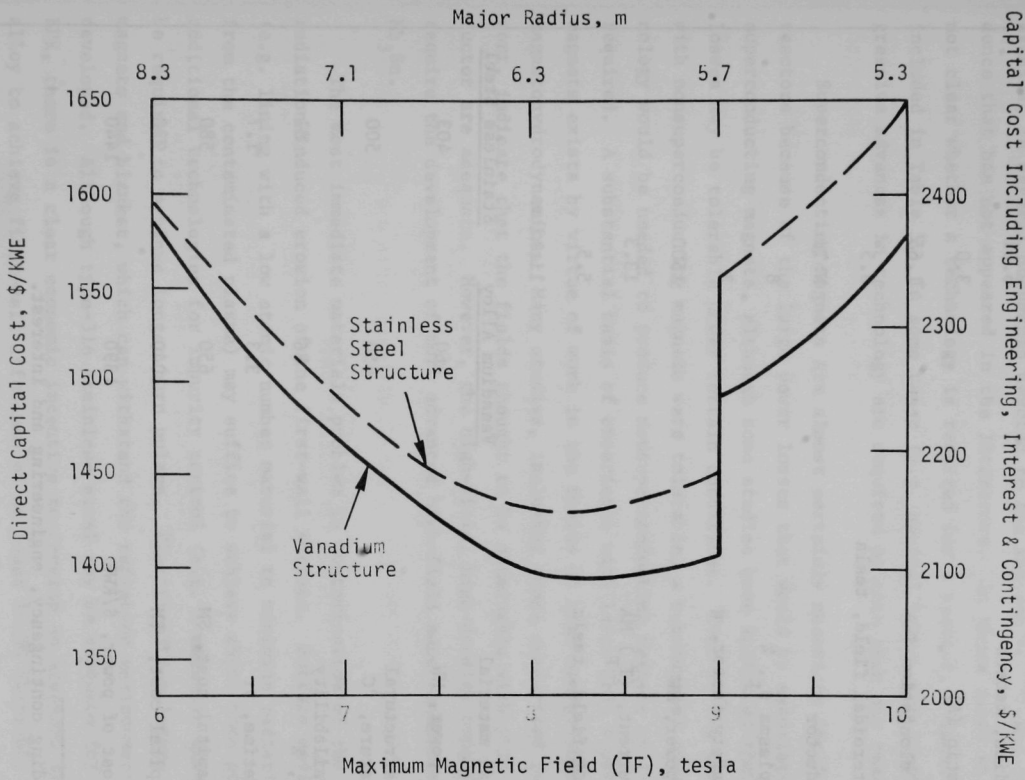

Figure 10. Effect of Toroidal Magnetic Field Strength and Structural Material on the Capital Cost per Unit Power for a Fixed Thermal Power Output of 1500 MW(t) of a Lithium-cooled Tokamak Demonstration Reactor. (Aspect ratio = 3, plasma D elongation = 1.65, plasma safety factor = 3, plasma β_t = 8%, inner blanket/shield thickness = 1 m, maximum structural temperature = 500°C for stainless steel and 650°C for vanadium alloy, electrical power output = 403 MW(e) with stainless steel and 460 MW(e) with vanadium alloy)

TABLE 4. Representative Tokamak Demonstration Plant Parameters

Major radius, meters	6.01	
Aspect ratio (A)	3.0	
Plasma D elongation (κ)	1.65	
Maximum toroidal field, tesla	8.5	
Superconductor	NbTi	
Average plasma β_t, %	8	
Plasma safety factor, q	3	
Thermal power, MW	1500	
Plasma current, (I_p) MA	13.3	
Maximum OH field, tesla	5.5	
Coolant	lithium	
Structural material	Vanadium Alloy	Stainless Steel
Electric power, MW	460	403
Maximum structural temperature, °C	650	500
Plant availability factor, %	86	81
Wall lifetime, yr	3.3	1.7
Direct capital cost, $M	650	580
Total capital cost,* $M	1040	930
Direct cost of power, $/KWE	1390	1440

* Including contingency, engineering and interest.

The principal technology advances required for the development of commercial fusion power are indicated in Table 5. The general features of these technology requirements have been identified in the previously cited design studies, in several documents devoted to the subject[16-18] and in correspondence that has not appeared in the literature. In those cases in which it is not clear whether a technology is required for a reactor, a question mark is included in Table 5. In some cases (e.g. neutral beams) substantial and progressive advances in technology are required at more than one reactor stage.

Superconducting magnets are almost certainly necessary for fusion power reactors because of the large power losses that would be associated with nonsuperconducting magnets, although some studies have indicated that these power losses may be tolerable under certain conditions. Even if the power losses with nonsuperconducting magnets were tolerable, a substantial advance in technology would be needed to produce nonsuperconducting magnets on the scale required. A substantial basis of experience with large NbTi superconducting magnets exists by virtue of work in the fields of high energy physics and magnetohydrodynamics. Many studies, including those summarized in this report, indicate that the fields thought to be obtainable with NbTi superconductor are adequate. However, the high-field, high-density concept[11] would require the development of more advanced high-field superconductors such as Nb_3Sn.

The most immediate materials problem is contamination of the plasma by radiation-induced erosion of the first-wall surface. Surface modifications (e.g. lining with a low atomic number material to minimize radiation losses from the contaminated plasma) may suffice to achieve short burn pulses, but additional technologies for impurity control (e.g. a magnetic divertor) may be required to achieve longer burn pulses. Electrical insulators for the magnets and blanket, which can withstand the radiation environment, must be developed. Although type-316 stainless steel may be adequate for TNS and EPR, there is a clear economic incentive to develop an advanced structural alloy to achieve first-wall lifetimes of at least 10-20 $MW \cdot yr/m^2$.

Neutral beams have been demonstrated to be effective in heating plasmas, but the increasing plasma size and/or density in the progression of reactors shown in Figure 8 requires increasing technology for the ion source and the

TABLE 5. Advanced Technology Requirements for the Development of Commercial Fusion Power

Advanced Technology	Reactor for which Technology must be available
Superconducting Magnets	
Steady-state toroidal field coils	ITR
Pulsed poloidal field coils	ITR?, EPR
Impurity Control	
Short burn pulse (~ 1 min)	TFTR?, ITR
Long burn pulse (>> 1 min)	DEMO
Materials	
Insulators	ITR?, EPR
Advanced structural alloy	DEMO*
Heating and Fueling	
Neutral beams	TFTR, ITR
Radio frequency	(backup)
Fueling	ITR
Energy Storage and Transfer	
Pulsed coil energy transfer	EPR
Central energy storage	EPR
Storage, switching, recovery for neutral beams	ITR?, EPR
Blanket/Shield	
Radiation shielding	TFTR, ITR
High-temperature operation	EPR*
Lithium (or alternative) coolant	DEMO*
Tritium	
Fuel cycle and containment	ITR
Breeding and blanket extraction	DEMO*
Vacuum	TFTR, ITR
Engineering	
Assembly and disassembly	TFTR, ITR
Remote maintenance	TFTR, ITR

* Could be tested in earlier reactors.

energy transfer and recovery systems at each stage. Radio frequency wave heating of the plasma may be less demanding technologically and lead to more attractive designs, but the plasma physics feasibility has yet to be definitely established.

If gas injected into the vacuum chamber is drawn into the plasma core, as appears to be the case in some experiments, then refueling is trivial. Otherwise, technology for injecting fresh fuel into the plasma core (e.g. as high-speed pellets) must be developed.

The large, pulsed energy transfer in and out of the poloidal coil system and into the plasma heating system during startup and shutdown requires the development of advanced technologies for storing, transferring, switching and recovering energy. Although some of these functions could be met with existing technologies, there appears to be a substantial economic incentive to develop new energy storage and transfer technologies.

The problems of radiation shielding, primary energy conversion into heat and heat removal are similar to those encountered in fission reactors, so a substantial technology base exists upon which to build. However, there are some unique new problems arising from the geometry and the interaction of the magnetic field with the structural material and a flowing liquid metal coolant. Although there are other possible coolants (e.g. helium, molten salt), liquid lithium appears to offer significant advantages.

Experience in the weapons program provides a basis upon which the technology for the tritium fuel cycle can be developed. Chemical processing technology of a different type will be required to extract the tritium bred in fusion reactor blankets from the lithium-containing breeding medium.

Advances in high-vacuum technology will be required because of the large volumes involved, although a substantial basis exists upon which to build, particularly in the aerospace industry.

The low aspect ratio, toroidal geometry of a tokamak calls for the development of innovative engineering designs, procedures for assembling and disassembling the reactor and remote maintenance technology.

III. SUMMARY

The major parameters and corresponding economic characteristics of a representative class of commercial tokamak fusion power reactors have been examined as a function of four major design parameters -- the plasma β_t, the toroidal magnetic field strength, the first-wall lifetime and the power output. An economically optimum value of the toroidal field strength was found. This optimum value was in the range of $6\ T \leq B_{TFC} \leq 9\ T$, depending upon the value of β_t and the first-wall lifetime. The costs of electrical energy production were found to decrease rapidly with first-wall lifetime up to about 10-20 $MW \cdot yr/m^2$ and more gradually beyond this range. An economy of scale was found. Reactors with a large thermal power output (6000 - 9000 MW(t)) and based upon an advanced structural alloy design were predicted to have electrical energy production costs in the range of 20-24 mills/kilowatt•hr.

A possible sequence of three reactors -- an ignition test reactor to establish plasma physics feasibility, an experimental power reactor to establish technological feasibility and a demonstration power reactor to establish commercial feasibility -- was outlined which could lead to a demonstration of fusion power in the last decade of this century and to a demonstration of commercial feasibility near the turn of the century. Representative design parameters and costs were presented for such a sequence of reactors that would lead to the class of commercial reactors discussed in this report. The principal technological advances that would be required to support this sequence of reactors were discussed.

ACKNOWLEDGEMENTS

This report was based, both directly and indirectly, upon the body of experience and analysis capability in the fusion reactor design group at Argonne. In addition, we wish to acknowledge the valuable contribution of H. C. Stevens in the development of reactor construction and assembly schedules and in assisting with the development of cost estimates for the ITR, EPR and DEMO.

REFERENCES

1. R. G. Mills, et al., "A Fusion Power Plant," Princeton Plasma Physics Laboratory, MATT-1050 (1974).

2. G. L. Kulcinski, et al., "A Wisconsin Toroidal Fusion Reactor Design, UWMAK-I," University of Wisconsin, UWFDM-68 (1974).

3. R. W. Conn, et al., "A Conceptual Tokamak Reactor Design, UWMAK-II," University of Wisconsin, UWFDM-112 (1975).

4. W. M. Stacey, Jr., C. C. Baker and M. Roberts, "Tokamak Experimental Power Reactor Studies," Presented at the Sixth International Conference on Plasma Physics and Controlled Nuclear Fusion Research, October 6-13, 1976, Berchtesgaden, Federal Republic of Germany; also, ERDA-76/139.

5. W. M. Stacey, Jr., et al., "Tokamak Experimental Power Reactor Conceptual Design," Argonne National Laboratory, ANL/CTR-76-3 (August, 1976); and W. M. Stacey, Jr., et al., "Tokamak Experimental Power Reactor Studies," Argonne National Laboratory, ANL/CTR-75-2 (June, 1975).

6. "Experimental Power Reactor Conceptual Design Study," General Atomic Company, GA-A14000 (July, 1976); and "Experimental Power Reactor Conceptual Design Study," General Atomic Company, GA-A13534 (July, 1975).

7. "Oak Ridge Tokamak Experimental Power Reactor Study," Oak Ridge National Laboratory, ORNL/TM-5572 through ORNL/TM-5577 (1976); and M. Roberts and E. S. Bettis, "Oak Ridge Tokamak Experimental Power Reactor Study Reference Design," Oak Ridge National Laboratory, ORNL/TM-5042 (1975).

8. R. W. Conn, et al., "UWMAK-III, A Noncircular Tokamak Power Reactor Design," University of Wisconsin, UWFDM-150 (July, 1976).

9. D. W. Kearney, et al., "Conceptual Design Study of a Noncircular Tokamak Demonstration Fusion Power Reactor," General Atomic Company, GA-A13992 (1976).

10. D. Steiner, et al., "ORNL Fusion Power Demonstration Study: Interim Report," Oak Ridge National Laboratory, ORNL/TM-5813 (1977).

11. D. R. Cohn, et al., "A High Density, High Field Tokamak Demonstration Power Reactor," Conference on Technology of Controlled Nuclear Fusion, CONF-760935-P3 (1977) p. 931.

12. W. M. Stacey, Jr., et al., "EPR-77: A Revised Design for the Tokamak Experimental Power Reactor," Argonne National Laboratory, ANL/FPP/TM-77 (March, 1977).

13. M. Abdou, et al., "Parametric Systems Analyses for Tokamak Power Plants," Argonne National Laboratory, to be published.

14. R. F. Mattas and D. L. Smith, "Modeling of Life-limiting Properties of Fusion Reactor Structural Materials," Argonne National Laboratory, ANL/FPP/TM-84 (May, 1977).

15. "Fusion Power by Magnetic Confinement-Program Plan," Energy Research and Development Administration/Division of Magnetic Fusion Energy, ERDA-76/110 (1976).

16. F. E. Mills, Ed., "Research and Development Required for the Tokamak Experimental Power Reactor," Argonne National Laboratory, ANL/CTR/TM-65 (1976).

17. M. Roberts, et al., "Research, Development and Demonstration Needs," Oak Ridge National Laboratory, ORNL/TM-5577 (1977).

18. J. R. Powell, Ed., "Proceedings of the Magnetic Fusion Energy Blanket and Shield Workshop," CONF-760343 and ERDA-76/117 (1975).

INTERNAL DISTRIBUTION

M. Abdou
F. Adams
S. Agarwal
B. Ancker-Johnson
C. Baker
M. Benson
P. Bertoncini
T. H. Blewitt
C. Boley
C. C. Bolta
J. N. Brooks
K. Burba
R. J. Burke
F. A. Cafasso
I. Charak
R. Clemmer
J. B. Darby
S. G. Das
J. Dawson
C. Dennis
J. E. Draley
P. Dusza
D. Ehst
K. Evans, Jr.
J. A. Fasolo
G. Fenske
R. Fuja
M. Y. Gohar
E. Goldstick
L. Greenwood
H. L. Griffin
D. M. Gruen
R. R. Heinrich
S. Harkness
C. E. Johnson
J. Jung
M. S. Kaminsky
S. H. Kim
Y. K. Kim
A. Krauss
T. Kurkowski
R. Kustom
S. K. Lam
B. A. Loomis
V. A. Maroni
R. Mattas
B. Misra
J. Moenich
A. Moretti
F. Nolfi
J. Norem
D. Patterson
P. J. Persiani
R. B. Poeppel
D. Potter
W. Praeg
J. L. Robinson
D. Rose
B. Siskind
A. B. Smith
D. L. Smith
D. Y. Smith
R. Smith
H. Stevens
F. Thalgott
K. Thompson
L. Turner
S. T. Wang
H. Wiedersich
C. Youngdahl
W. Praeg
R. Avery
L. Burris, Jr.
E. J. Croke
S. A. Davis
P. R. Fields
T. H. Fields
B. R. T. Frost
P. F. Gustafson
R. V. Laney
R. L. Martin
M. V. Nevitt
E. N. Pettitt
E. G. Pewitt
D. C. L. Price
R. J. Royston
R. G. Sachs
W. K. Sinclair
R. G. Staker
C. E. Till
R. S. Zeno
G. T. Garvey
FP Program

EXTERNAL DISTRIBUTION

R. G. Alsmiller, Jr., Oak Ridge National Laboratory
N. Amherd, Electric Power Research Institute
R. Axtmann, Princeton University
J. Baublitz, OFE/DOE
J. W. Beal, OFE/DOE
J. W. Bennett, OFE/DOE
R. Blanken, OFE/DOE
S. Locke Bogart, OFE/DOE
R. Boom, University of Wisconsin
G. Bosler, Los Alamos Scientific Laboratory
J. A. Borders, Sandia Laboratories
R. Botwin, Grumman Aerospace Corporation
W. Briggs, McDonnellDouglas Corporation
J. D. Callen, Oak Ridge National Laboratory
G. A. Carlson, Lawrence Livermore Laboratory
R. A. Carruthers, Culham Laboratory
J. F. Clarke, OFE/DOE
M. Clarke, Combustion Engineering
F. Coffman, OFE/DOE
M. Cohen, OFE/DOE
R. Conn, University of Wisconsin
B. Coppi, Massachusetts Institute of Technology
E. Dalder, OFE/DOE
R. C. Davidson, OFE/DOE
N. Anne Davies, OFE/DOE
J. Davis, McDonnell Douglas Corporation
S. O. Dean, OFE/DOE
J. F. Decker, OFE/DOE
D. Dingee, Battelle - Pacific Northwest Laboratory
W. L. Ellis, OFE/DOE
C. Finfgeld, OFE/DOE
H. K. Forsen, Exxon Nuclear Company, Inc.
T. K. Fowler, Lawrence Livermore Laboratory
H. P. Furth, Princeton University
M. B. Gottlieb, Princeton University
W. C. Gough, Electric Power Research Institute
J. N. Grace, OFE/DOE
D. Grafstein, Exxon Research Engineering Co.
S. A. Gralnick, Princeton University
R. A. Gross, Columbia University
C. Henning, OFE/DOE
G. Hess, OFE/DOE
A. Hill, Massachusetts Institute of Technology
G. Hopkins, General Atomic Company
R. J. Impara, OFE/DOE
G. R. Ingram, OFE/DOE
D. L. Jassby, Princeton University
T. Kammash, University of Michigan
D. Kiefer, EG & G - Broadway Factory

E. E. Kintner, OFE/DOE
D. Klein, Westinghouse Electric Corporation
A. Knoblock, Max-Planck Institute fur Plasmaphysik
R. Kostoff, OFE/DOE
H. Kouts, Brookhaven National Laboratory
G. L. Kulcinski, University of Wisconsin
D. Kummer, McDonnell Douglas Corporation
S. C. Kuo, United Technologies Research Center
B. Langley, Sandia Laboratories
Librarian, Culham Laboratory
Library, C.E.A., FRANCE
L. Lidsky, Massachusetts Institute of Technology
P. S. Lykoudis, Purdue University
B. Ma, Iowa State University
C. W. Maynard, University of Wisconsin
D. McAlees, Exxon Nuclear Co., Inc.
J. McGoff, OFE/DOE
G. H. Miley, University of Illinois
R. G. Mills, Princeton University
K. Moses, OFE/DOE
M. Murphy, OFE/DOE
J. Neff, OFE/DOE
T. Ohkawa, General Atomic Company
J. J. Osher, Lawrence Livermore Laboratory
G. D. Pine, Massachusetts Institute of Technology
J. Powell, Brookhaven National Laboratory
L. K. Price, OFE/DOE
R. E. Price, OFE/DOE
J. Purcell, General Atomic Company
P. Reardon, Princeton University
T. C. Reuther, OFE/DOE
F. Ribe, University of Washington
M. Roberts, Oak Ridge National Laboratory
D. J. Rose, Massachusetts Institute of Technology
J. L. Scott, Oak Ridge National Laboratory
W. M. Stacey, Jr., Georgia Institute of Technology
D. M. C. Stauber, Grumman Aerospace Corporation
D. Steiner, Oak Ridge National Laboratory
F. H. Tenney, Princeton University
V. L. Teofilo, Battelle - Pacific Northwest Laboratory
K. Thomassen, Los Alamos Scientific Laboratory
R. Turnbull, University of Illinois
B. Twining, OFE/DOE
C. Taylor, Lawrence Livermore Laboratory
P. E. Thress, Catholic University
R. W. Werner, Lawrence Livermore Laboratory
J. Williams, OFE/DOE
W. R. Wilkes, Monsanto Research Corporation
H. Willenberg, Battelle - Pacific Northwest Laboratory
L. Wood, Lawrence Livermore Laboratory
G. L. Woodruff, University of Washington
E. J. Ziurys, OFE/DOE
K. Zwilsky, OFE/DOE
CEA Fusion, FRANCE
Bibliothek, Max-Planck-Institut fur Plasmaphysik

☆ U.S. GOVERNMENT PRINTING OFFICE: 1977 750-133